Applications of Synthesis in Copolymer Upcycling, Reduction of CO_2, Ligand Non-Innocence, and New Weakly-Coordinating Anions

Thesis by

Meaghan Ann Bruening

In Partial Fulfillment of the Requirements for the Degree of

Doctor of Philosophy

CALIFORNIA INSTITUTE OF TECHNOLOGY

Pasadena, California

2024

(Defended on May 23rd, 2024)

Meaghan Ann Bruening
ORCID: 0000-0001-8132-9497

Dear reader

If it feels like a trap…

You're already in one.

Dear reader

Get out your map…

Pick somewhere and just run.

Dear reader

Burn all the files…

Desert all your past lives.

And if you don't recognize yourself…

That means you did it right.

—Taylor Swift

Midnights

"Dear Reader"

ACKNOWLEDGEMENTS

The process of writing my thesis has been both stressful (as expected) and reflective. This has not been the PhD journey I expected, but I would like to use this space in my thesis to acknowledge the individuals who have helped me reach this point.

First and foremost, I must thank my advisor, Prof. Theodor Agapie. I want to thank him for allowing me to be part of this group. I was drawn to the group by his excitement and enthusiasm about the many diverse projects. I thank him for his endless suggestions, advice, and guidance. I have learned a great deal from him.

I would also like to thank the rest of my committee, Prof. Jonas Peters, Prof. Greg Fu, and Prof. Harry Gray for the insightful discussions, comments, and ideas about my proposals and research.

I owe immense gratitude to Prof. John Bercaw. I had the privilege of learning how to use a high vacuum line and swivel frit from the legend himself. John is one of the kindest *and* most brilliant chemists that I've ever met. Conversations on the second floor of Noyes were always an eclectic mix of hare-core chemistry and funny tales from John. I have nothing but respect and admiration for him, and I thank him for the profound impact he had on my graduate experience.

I overlapped with many remarkable graduate students and postdocs. I want to first thank Marcus, my mentor. He taught me the techniques required for rigorous air-free chemistry. I will always remember how my first introduction to Schlenk technique was a light-sensitive filtration (on a Schlenk frit!!). Marcus was full of boundless wisdom and kindness (and he was an amazing chef and baker)! I also want to thank many individuals from the beginning of my graduate career, especially Josh and Naoki—wonderful examples of rigorous chemists with high standards and remarkable work ethics—they truly instilled high standards and shaped my early time in the group. Angela was a wonderful friend (and even more remarkable chemist!), and she endured many of

these years with me, including a few terms of teaching Chem5B! To those I have overlapped with—especially those who are still here—Mike, Matt, Fernando, Adjeoda, and Max—thank you for your kindness.

I have had the opportunity to work collaboratively with many individuals, each side bringing a diverse perspective to the work. In particular, I thank Jessica, Sam, Gavin, Mike, and the See group (and many other individuals who I do not have space to mention). My overlap with Jessica at Caltech was brief, but I was able to follow up on polymer characterization from her Zr-catalysts. Sam and I worked together on the α,ω diene project. Gavin and I collaborated on our CO_2 reduction project using ionomer coatings.

Mike deserves his own paragraph in these acknowledgments as we worked together very closely for the last few years. I remember when he first started working on silicates, and I am so grateful that he welcomed me to the project where we further diversified the silicates and explored the chemistry of these new anions. He is a remarkable chemist and a wonderful friend.

Caltech has fantastic individuals running excellent facilities. I want to thank Dave Vander Velde for NMR, and Larry Henling and Mike Takase for the X-ray crystallography facility. So much of the chemistry discussed in this thesis would be impossible without their well-run facilities.

There are also individuals outside of Caltech that I would like to acknowledge. My initial pursuit of chemistry was because of my undergraduate advisor, Prof. Daron Janzen. I am so very grateful that he encouraged me to get involved in undergraduate research both at St. Kate's and outside universities (University of Minnesota and Northwestern). It was transformative to have an advisor who truly believed in me and my ability to be a real scientist, and I am so grateful for everything he has done. While I have been at Caltech, I have always appreciated his outside perspective.

I thank my family, especially my parents, Jenny and Bill, and my older brother, Robert—for everything. I would be nowhere without their love and support. While Caltech is 2000 miles from home, they were always just a phone call away. I thank them for pushing me to follow my "dreams" (even when they had the wisdom to know better). They encouraged me to make my own decisions, and they were always there to support me.

At the expense of sounding childish and naïve, I would also like to thank my feline companion, Zuri. She has been my faithful sidekick in Noyes for the last 5 years (and I am so grateful that I have been able to bring her to the office with me). She has seen me through some of the toughest times, especially when I was not very welcome within the group. I hope she's brought joy to others in Noyes with her furry friendliness. She was very appreciative of all the petting, treats, and kindness bestowed upon her while she traversed the 3rd floor of Noyes.

Finally, in a manner to save the best, most important person for last: Kevin. My partner, Kevin, has been my absolute, unwavering support for the last 3.5 years. He has given me a life and a future to fight for. He has helped me see reason and logic, and he has helped me create a life outside the walls of Noyes. Sometimes I feel this accomplishment also belongs to him since he endured so much of it with me. He is the reason that I stayed, and he is the reason I am still here.

There is so much more that I wish I was allowed to say, but I realize it would all be removed in the revision process, so here's the short version:

To those who listened—to those who really mattered—to those who did the right thing—to those who believed me …*Thank you.*

PUBLISHED CONTENT AND CONTRIBUTIONS

Parts of this thesis have been adapted from both published articles.

CHAPTER 2

In Chapter 2, the synthesis of pyridines with oximes was originally developed by a visiting scholar (Miku Oi). Preparation of the Zr-CO_2-Alkyne complex was first reported by Choon Heng Low (Marcus).

CHAPTER 3

Bruening, M.A.; Xiong, S.; Agapie, T. α, ω-Diene Generation from Ethylene and Butadiene by Copolymer Upcycling. *ACS Sustainable Chem. Eng.*; **2023**, *11*, (27), 9918-9923. 10.1021/acssuschemeng.3c02569.

M.A.B. prepared all polymers, conducted all metathesis reactions, and collected all ^{1}H and ^{13}C NMR and GC-MS spectra. All authors analyzed data and prepared the manuscript.

CHAPTER 4

Heim, G.P.[†]; **Bruening, M.A.**[†]; Musgrave III, C.B.; Goddard III, W.A. Peters, J.C.; Agapie, T. Potassium ion modulation of the Cu electrode-electrode interface with ionomers enhances CO_2 reduction to C_{2+} products. *Joule.* **2024.** *8*, 1-10 10.1016/j.joule.2024.03.019.

[†] denotes equal contribution

M.A.B. synthesized and characterized all the polymers. G.P.H carried out electrochemistry experiments. C.B.M performed computations. All authors analyzed data and prepared the manuscript.

CHAPTER 5

He, T. †; **Bruening, M.A.**†; Stradley, S.H; See, K.A; Agapie, T. Novel Silicate Platform as Weakly-Coordinating Anions for Diverse Organometallic and Electrochemical Applications. *Manuscript Prepared*

† denotes equal contribution

M.A.B. developed the route from $RSiCl_3$ reagents and associated compounds. T.H. developed $RSi(OEt)_3$ route and associated compounds. M.A.B. and T.H. jointly conducted electrochemical experiments. M.A.B, T.H., and T.A. analyzed data and prepared the manuscript.

CHAPTER 6

He, T. †; **Bruening, M.A.**†; Stradley, S.H; See, K.A; Agapie, T. Novel Silicate Platform as Weakly-Coordinating Anions for Diverse Organometallic and Electrochemical Applications. *Manuscript Prepared*

† denotes equal contribution

M.A.B. and T.H. each prepared large batch of electrolyte. All electrochemical experiments were collected jointly by M.A.B. and T.H. M.A.B., T.H., and T.A. analyzed data and prepared the manuscript.

Appendix A

Sampson, J.; **Bruening, M.A.**; Akhtar, M.N.; Jaseer, E.A.; Theravalappil, R.; Garcia, N; Agapie, T. Copolymerization of Ethylene and Long-Chain Functional α-Olefins by Dinuclear Zirconium Catalysts. *Organometallics,* **2021**, *40*, (12), 1854-1858. 10.1021/acs.organomet.1c00126.

M.A.B. acquired all ^{1}H and ^{13}C polymer data. All authors analyzed data and prepared the manuscript.

ABSTRACT

This dissertation focuses on a very diverse series of studies with synthetic applications to organometallic systems supported by a redox non-innocent ligand architecture, α,ω diene generation, ionomers for tuning performance of electrochemical CO_2 reduction, and design of new weakly coordinating anions.

Chapter 2 discusses the reactivity of a 9,10-anthracenediyl *bis*(phenoxide) titanium complex, where the polyaromatic anthracene motif functions as a non-innocent ligand. This enables access to a reduced Ti complex which is competent for oxidative coupling of alkyne and nitrile substrates, and pyrimidines and substituted benzenes can be accessed catalytically. Additional reactivity with oximes and oxidative coupling of alkynes and CO_2 is explored.

Chapter 3 reports a two-step method for generation of a distribution of α,ω-dienes from ethylene and butadiene. Copolymers are prepared with variable butadiene content, where 1,4-butadiene incorporation ensures the double bonds are in the polymer backbone. Subsequent ethenolysis of the copolymers produces α,ω-dienes in the C_{10}-C_{20} range. The conditions can be modified to control product selectivity.

Chapter 4 presents a series of polystyrene-based ionomers to probe the impact of local $[K^+]$ in the Cu electrode microenvironment on CO_2R performance (Part A). Partial current density towards C_{2+} products ($|j_{C2+}|$) increases with $[K^+]$ in ionomer, up to 225 mA cm^{-2}. When K^+ is replaced with $[Me_4N]^+$, performance lowers to the level of bare Cu, highlighting the crucial role of K^+ in improving C_{2+} product selectivity. Molecular dynamics simulations and partial pressure CO_2 experiments support enhanced CO_2 mass transport with the ionomers. An expanded series of ionomers is presented (Part B), where the incorporation of different neutral comonomers (vinyl biphenyl) and cross-linking monomers (biphenyl and terphenyl) dramatically boosts performance.

Direct tends between K^+ content and CO_2R performance are not observed with the expanded series, highlighting the non-innocent role of the neutral monomer and polymer structure.

Chapter 5 presents a new, Si-based weakly-coordinating anion. A library of anions bearing a variety of R groups is prepared, enabling facile tuning of sterics and solubility. A range of cations employed in chemical reactivity is supported by these anions, including ether-free alkali cations, Ph_3C^+, and an ethylene/CO copolymerization catalyst $[Pd(dppe)(NCMe)Me]^+$ (generated by salt metathesis or protonation of a metal-alkyl bond). Electrochemical studies on the $[Bu_4N]^+$ variant show an exceptionally wide stability window for the $[^{Me}SiF]^-$ anion of 7.5 V in MeCN. The $[^{C6F5}SiF]^-$ variant can be readily modified to access additional diverse and/or dianionic variants.

Chapter 6 discusses the electrochemical performance of a new class of magnesium electrolytes for next-generation batteries. $[Mg(DME)_3][^{Me}SiF]_2$ demonstrates remarkable performance with good stability, moderate conditioning, high coulombic efficiency (> 96%), and high current density (~100 mA cm^{-2}). However, the sensitivity of the experiments requires careful study of many parameters including impact of MgR_2 additives (identity and concentration), cycling protocol, synthetic route, and Pt working electrode to understand how the electrochemical performance is impacted. While addition of $MgMe_2$ improves electrochemical performance, it is not inherently required for reversible Mg deposition and stripping. Following an extensive investigation of the cyclic voltammetry (CV) performance of $[Mg(DME)_3][^{Me}SiF]_2$, preliminary screening of additional $[Mg(DME)_3][^{R}SiF]_2$ variants is discussed.

Appendix I discusses the characterization of ethylene/α-olefin copolymers generated from monometallic and bimetallic Zr catalysts. The decreased polar monomer incorporation for the bimetallic vs. monometallic catalysts is attributed to the steric clash of larger comonomers with the distal metal site in bimetallic catalysts.

Appendix II discusses the preparation of bulky anthracene phenoxide ligands for Ti and Ta.

Appendix III discusses the preparation of mixed aryl/hydride borates as electrolytes for next-generation Mg batteries.

TABLE OF CONTENTS

LIST OF FIGURES

Note: Figures listed below correspond to those included in the main text of each chapter. Remaining figures can be found in the respective Experimental Sections.

LIST OF SCHEMES

Note: Schemes listed below correspond to those included in the main text of each chapter. Remaining schemes can be found in the respective Experimental Sections.

LIST OF TABLES

Note: Tables listed below correspond to those included in the main text of each chapter. Remaining tables can be found in the respective Experimental Sections.

CHAPTER 1. General Introduction

This dissertation focuses on a very diverse series of studies, with projects and applications ranging from organometallic systems supported by a redox non-innocent ligand architecture to α,ω diene generation to the use of ionomers to improve electrochemical CO_2 reduction to the design of new weakly coordinating anions. While these projects are exceptionally wide-ranging, they are unified by the key concept of chemical synthesis for specific, targeted applications. A detailed background with the appropriate references is incorporated in the introduction of each chapter, and this chapter aims to provide a very general overview of the main concepts that are tackled with this research.

Within Chapter 2, the chemistry and reactivity of a Ti system supported by a bisphenoxide ligand tethered to a redox non-innocent anthracene core is discussed. The ligand design and the reactivity of the Zr system was reported by a previous graduate student, Marcus Low, where the simultaneous change in the redox state of the ligand *and* coordination framework enabled access to a "Zr^{II}" species. This work explores the analogous Ti system, as well as an expanded range of reactivity for both systems.

In Chapter 3, a different approach to synthesis is considered, focusing specifically on accessing α,ω dienes by pairing reported polymerization and ethenolysis catalysts. While α-olefins are industrially prepared by the Shell-Higher Olefin Process, α,ω-dienes do not have a well-established synthetic method for generation. Within this work, a two-step method is developed, with initial ethylene/butadiene copolymerization and subsequent ethenolysis to access the desired species. Modification of the system and reaction conditions is used to control product selectivity and distribution of the produced α,ω dienes.

Chapter 4 considers yet another challenge, specifically the distribution of products generated during CO_2 reduction (CO_2R) with Cu. While Cu is desirable because it is the only type of metallic

electrodes that can facilitate the formation of multi-carbon products (C_{2+} products), it is hindered by poor selectivity and insufficient activity. Alkali cations can facilitate CO_2R. Within Part A, a series of potassium-containing copolymers is prepared, where the potassium content is controlled by modulating monomer ratios during the polymerization reactions. When tested as Cu coatings for CO_2R, a trend is observed where performance increases with increasing potassium content in the ionomer coating. This specifically highlights how synthesis can facilitate generation of a series of materials that allows for careful and targeted study of specific hypotheses. In Part B, a more diverse collection of polymeric coatings is examined, leveraging less soluble monomers (vinyl biphenyl) and cross-linking monomers to decrease polymer solubility, facilitating testing of materials with higher potassium content.

Chapter 5 uses synthesis to target new silicon-based weakly coordinating anions. Reminiscent to the design strategy for $[BAr^F{}_{24}]^-$ where a weakly coordinating anion is prepared by addition of an anionic aryl group to a highly Lewis acidic fragment, five-coordinate silicon-based WCAs can be designed from a silicon Lewis super acid. These new anions are readily diversified, where the "R" group provides a facile handle for tuning sterics and solubility. This new class of weakly-coordinating anions supports routine organometallic chemistry, and the anion has a remarkably wide window of electrochemical stability (7.5 V!). Leveraging the electrochemical window, this new class of $Mg[^RSiF]_2$ anions demonstrates remarkable electrochemical performance as an electrolyte for next-generation Mg batteries. While the overall performance is impacted by many variables (discussed in Chapter 6), stable and consistent performance can be obtained.

These projects are diverse and wide-ranging, but they convey how well-thought, careful synthesis can be the key strategy for many challenging problems.

CHAPTER 2. A Redox-Active 9,10-Anthracenyl-linked Bisphenoxide-supported Titanium Complex: Comparison to the Zr System, Preparation of Pyridines with Oximes, Reactivity with CO_2

For author contributions, see Page vii.

ABSTRACT

Redox-active ligands have widely expanded the scope and reactivity of early transition metals, facilitating oxidative and reductive coupling rather than redox-neutral processes which are more common for Ti and Zr. Herein, we report the synthesis, characterization, and reactivity of a Ti^{IV} species supported by a 9,10-anthracenediyl-linked bisphenoxide ligand. Upon metalation, the complex readily undergoes a photolytic reduction to afford $TiO_2AnthTHF_2$ where the Ti^{IV} is bound to the central arene in an η^4-fashion as the anthracene motif is reduced. Similar to the Zr-congener; $TiO_2AnthTHF_2$ is competent for the [2+2+2] trimerization of alkynes and nitriles to afford pyrimidines, albeit with attenuated selectivity compared to the Zr system. Stoichiometric reactivity reveals $TiO_2AnthTHF_2$ has two active competing pathways, explaining the decrease in selectivity. The reducing equivalents of $TiO_2AnthTHF_2$ and $ZrO_2AnthTHF_3$ can be harnessed for a variety of additional transformations including stoichiometric pyridine formation using oximes and stoichiometric reactivity with alkynes and CO_2.

GENERAL INTRODUCTION

Redox-active ligands can be employed to mediate multi-electron chemical transformations.[1-4] For early metals, including Ti and Zr, redox-neutral processes (olefin polymerization, etc.) are common, but redox-active ligands facilitate access to different reactivity.[5-10] In typical transformations, a redox change occurs at the ligand, with minimal changes in the coordination environment around the metal center. However, redox-active ligands which can change the coordination environment around the metal depending on the oxidation state are expected to result in improved reactivity when matched to the appropriate electronic and steric demands of the metal center.

Our group (and others) have explored the utility of redox non-innocent pendant arene ligands, where expanded reactivity is accessible, including metal phosphide coupling, CO bond cleavage and coupling, CO_2 bond cleavage, ammonia borane dehydrogenation, etc.[11-20] While many of these pendant arene systems are based on substituted benzene rings, where very negative potentials are necessary for formal reduction, an arene system based on a substituted anthracene core displays a milder reduction potential,[21] allowing for more accessible redox chemistry.

In our group, we have demonstrated a Zr system with a pendant anthracene.[22] When the ligand is in the reduced (dianionic) state, the Zr coordinates in the bridgehead position; and this system can be leveraged for [2+2+2] cycloaddition of alkynes and nitriles to afford pyrimidine products with high selectivity. Herein we report the preparation of the corresponding $Ti^{IV}Anth(THF)_2$ and

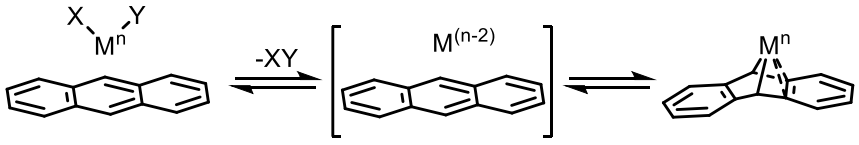

Figure 2.1: Reductive elimination with noninnocent anthracene moiety.

an expanded range of reactivity observed for both the Ti and Zr complexes including pyridine formation and reactivity with CO_2.

RESULTS AND DISCUSSION

Beginning from previously reported syn-9,10-anthracenediyl-linked *bis*(phenol) (LH_2) (Scheme 2.1),[22] protonolysis with tetrabenzyl titanium at elevated temperatures affords the bisbenzyl complex **1-[Ti]**. Preliminary single-crystal X-ray diffraction (XRD) studies confirm the identity of **1-[Ti]** and displays no significant Ti-arene interactions with distances of ~3.6A (Figure 2.2).

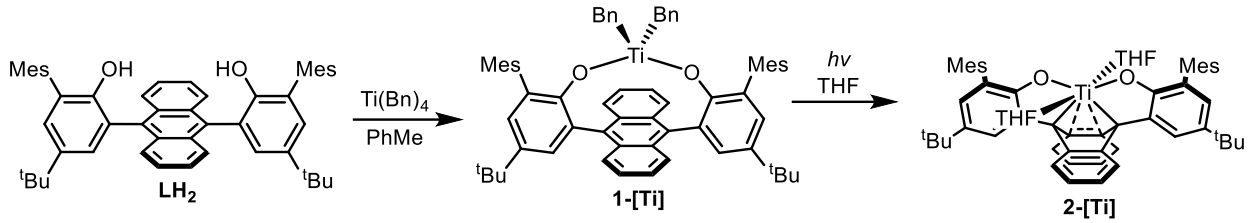

Scheme 2.1: Synthesis of Titanium Complex with Pendant Anthracene.

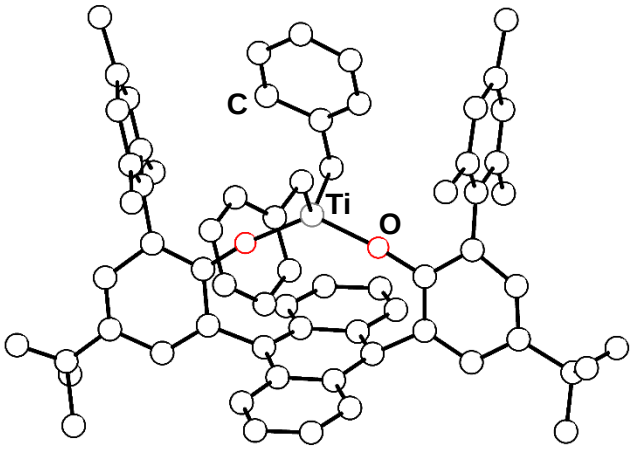

Figure 2.2: Preliminary structure of **1-[Ti]**. Due to data quality, only connectivity was determined. Hydrogen atoms omitted for clarity.

Analogous to the preparation of $Zr^{IV}Anth(THF)_3$, the reduced Ti compound can be prepared by photolysis of **1-[Ti]** in tetrahydrofuran. The new species, $Ti^{IV}Anth(THF)_2$ (**2-[Ti]**), can be cleanly prepared after 16 h of irradiation in THF, detected by ^1H NMR by loss of the benzylic signals of **1-[Ti]**, generation of bibenzyl (the reaction byproduct), and formation of a new species. Solid-

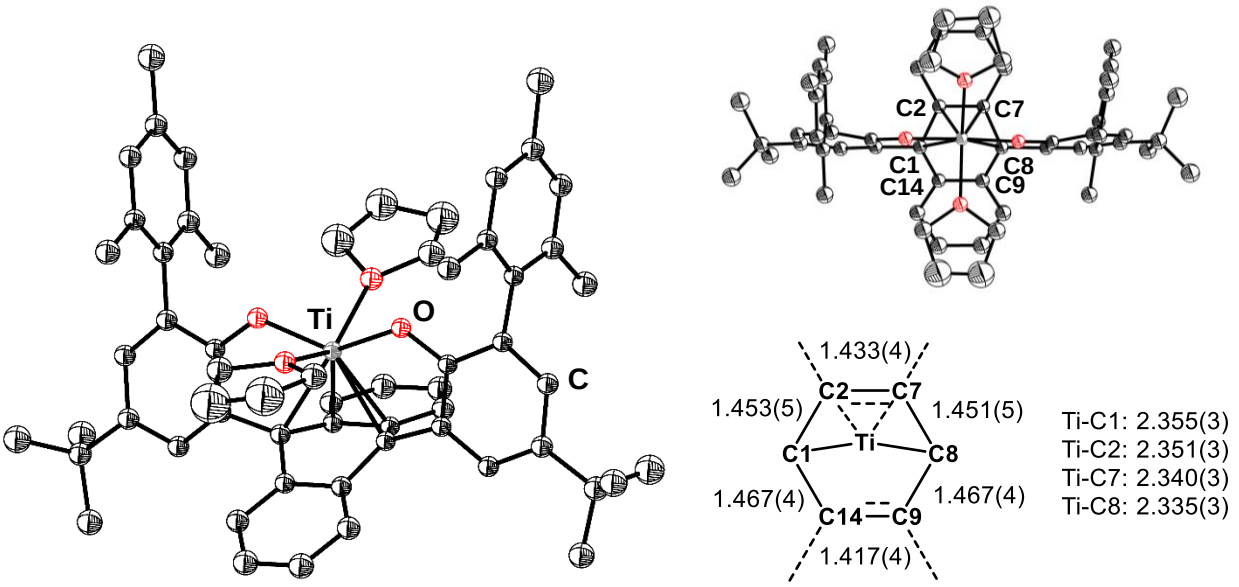

Figure 2.3. Solid-state structure of **2-[Ti]** and bond metrics of the central ring. Thermal ellipsoids shown at 50% probability. Hydrogen atoms and solvent molecules omitted for clarity.

state characterization of **2-[Ti]** (Figure 2.3) reveals coordination through the two phenoxide moieties, binding of two THF molecules, and coordination of the anthracene in an η^4 fashion. We observe two shorter C-C bonds within the central ring, C2-C7 and C9-C14 1.433(4) and 1.417(4) Å, and four longer bonds, C1-C2 (1.453(5)), C7-C8 (1.451(5)), C8-C9 (1.467(4)), and C1-C14

Table 2.1. Comparison of Ti system under various nitrile loading and optimized Zr system

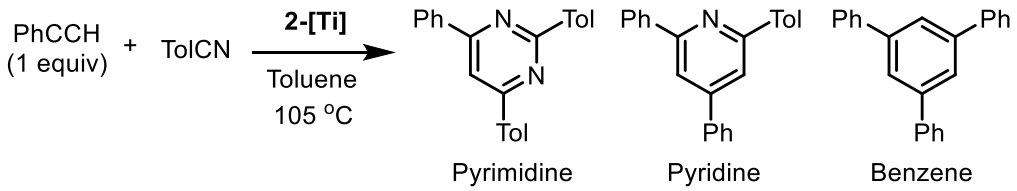

[a]Entry	Time (hr)	nitrile (equiv)	[b]PhCCH consumed (%)	[c]Selectivity for pyrimidine (%)
Zr	1	6	> 99	99
1	3	2	71	50
2	3	6	89	52
3	3	10	93	85

[a]catalyst loading 0.05 equiv [b]based on GC-MS [c]based on ^{1}H NMR integration

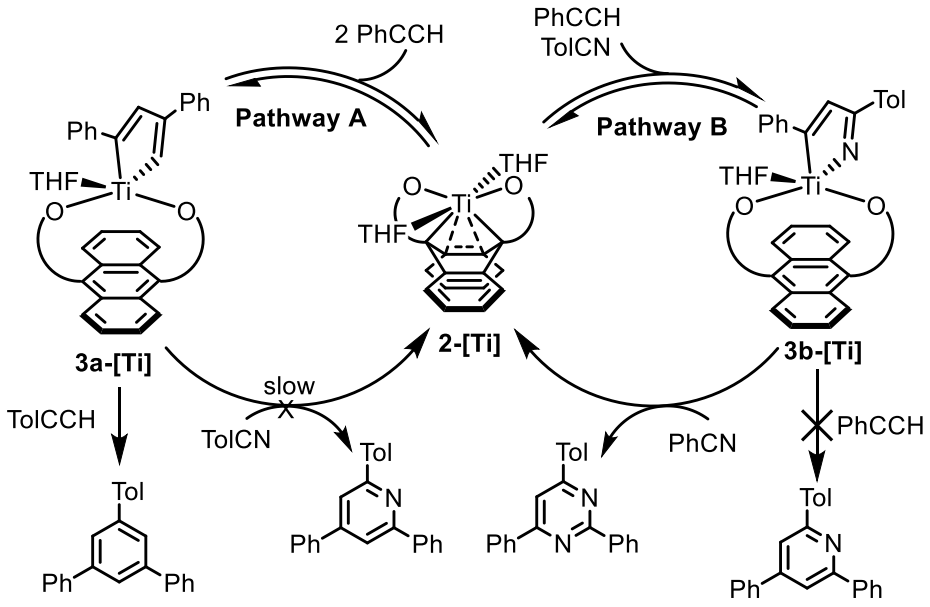

Scheme 2.2. Stoichiometric reactions involving catalytically relevant species.

(1.467(4)), consistent with loss of aromatization of the central ring and 2 electron reduction of the anthracene motif.[23-27] The changes in bond lengths and anthracene planarity are analogous to the previously characterized Zr species.[22]

Although the metal center is formally Ti(IV), the reduced anthracene stores two electrons, and the unique metal/ligand interaction affords a pathway to explore a new scope and range of reactivity with this pseudo "Ti(II)" species. The previously reported Zr system is competent for the [2+2+2] cotrimerization of alkynes and nitriles to afford the corresponding pyrimidines in the presence of excess nitrile. While pyrimidines are generated under catalytic conditions with **2-[Ti]** (Table 2.1), a decreased selectivity for pyrimidine is observed, with the formation of the substituted benzene product (from alkyne trimerization) which was not observed for the Zr system. The optimized conditions for the Zr-system afford the pyrimidine product with 99 % selectivity, yet the Ti system only achieves 52 % selectivity with the same catalyst loading and substrate equivalents (Table 2.1, entry Zr and 2). While an improvement in selectivity with **2-[Ti]** is

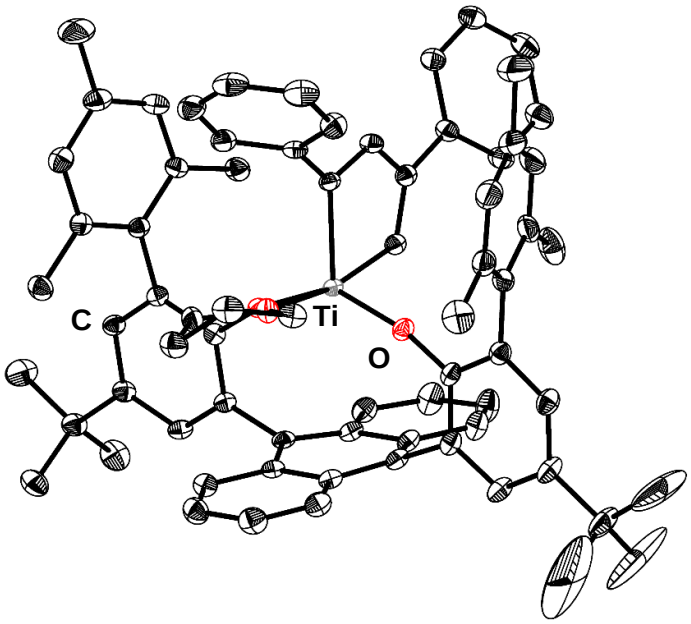

Figure 2.4. Solid-state structure of **3a-[Ti]**. Thermal ellipsoids shown at 50% probability Hydrogen atoms and solvent molecules omitted for clarity.

observed when the nitrile loading is increased to 10 equivalents (Entry 3), the observed selectivity is still attenuated compared to the Zr system.

To gain insight into the observed product selectivity, stoichiometric studies with alkynes and nitriles were conducted (Scheme 2.2). The addition of 2 equivalents of PhCCH to **2-[Ti]** results in the generation of **3a-[Ti]** (pathway A) which has been characterized by ^{1}H NMR and X-ray crystallography (Figure 2.4). Addition of one equivalent of TolCN and one equivalent of PhCCH to **2-[Ti]** affords the mixed metallacycle **3b-[Ti]** (pathway B). Stoichiometric reactions carried out from the isolated metallacyclyes (**3a-[Ti]** and **3b-[Ti]**) provide information about catalytically relevant pathways.

Exploring pathway A, reaction of **3a-[Ti]**, with 1 equivalent of TolCCH leads to the formation of substituted benzenes with mixed aryl substituents, with 1,3,5-triphenylbenzene and 5-phenyl-1,3-di(tolyl)benzene detected by GC-MS, indicating that initial coupling of the alkynes is reversible. Reaction of **3a-[Ti]** with TolCN results in some formation of the pyridine product, but

product formation is attenuated (by ^{1}H NMR), and substituted benzenes are also detected by GC-MS. This again confirms the reversibility of initial binding of the alkynes and the more favorable formation of the substitute benzene products, consistent with observed selectivity under catalytic conditions.

Exploring pathway B, treatment of **3b-[Ti]** with PhCN generates a distribution of the pyrimidine products, including 2,4,6-triphenylpyrimidine, 4,6-diphenyl-2-(*p*-tolyl)pyrimidine, and 4-phenyl-2,6-di-*p*-tolylpyrimidine, with minor formation of pyridine and benzene products, indicating the reversibility of the initial alkyne and nitrile coupling is on a similar timescale to pyrimidine formation. Treatment of **3b-[Ti]** with TolCCH generates a very wide distribution of mixed aryl products (including pyrimidines, pyridines, and benzenes), corresponding with more favorable reversibility of initial alkyne/nitrile coupling over pyridine formation, consistent with the observed catalytic results.

Interestingly, under catalytic conditions where alkyne trimerization is active, exclusive selectivity for 1,3,5 triphenylbenzene is observed over the more conventionally favored 1,2,4 triphenylbenzene.[28-29] In the absence of nitrile, the formation of both substituted benzenes is observed, but the selectivity for 1,3,5 triphenylbenzene can be dramatically increased by sub-stoichiometric addition of nitrile (0.05 equiv). In stoichiometric studies, generation of 1,3,5 triphenylbenzene is still favored with pre-generation of **3a-[Ti].** While not investigated further, the formation of substituted benzene products and the dominant selectivity for 1,3,5 triphenylbenzene is markedly different than the Zr system.

Additional chemical reactivity was explored for both the titanium (**2-[Ti]**) and zirconium systems (**2-[Zr]**). The reaction of the corresponding alkyne and oxime and subsequent dehydration generates stoichiometric pyridines. While pyridines have been generated from alkynes and oximes,

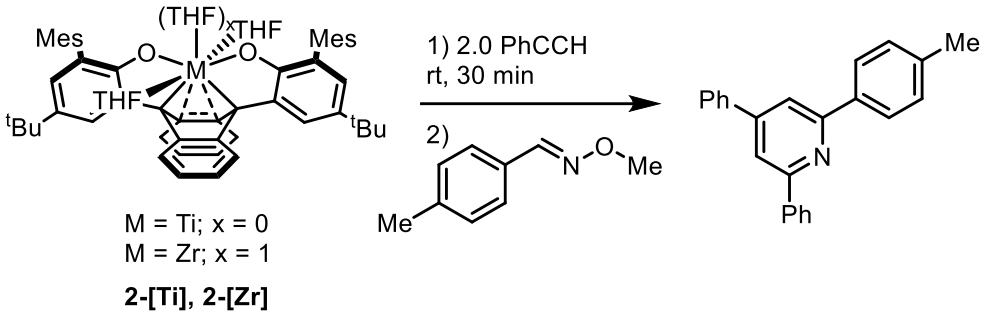

Scheme 2.3. Stiochiometric preparation of pyridines from alkynes and oximes.

they generally require metals including Rh[30-36], Ni[37], Cu[38] which are tolerant to dehydration byproducts.

While pyridine formation was detected by GC-MS for the **2-[Ti]** system, improved performance was observed with **2-[Zr]**, with a maximum observed oxime conversion of ~50 % detected by ^{1}H NMR. Given the non-catalytic performance, additional oxime substrates were not investigated further.

Given the reactivity observed *via supra* with a variety of unsaturated organic molecules, attempts were made to extend the coupling to other heteroatom-containing unsaturated small molecules, particularly CO_2. There is interest in utilizing CO_2 and a C1 feedstock, given it is abundant and nontoxic,[39] but incorporation of CO_2 into organic molecules remains challenging given the high thermodynamic and kinetic stability.[40-43] To explore reactivity, stoichiometric

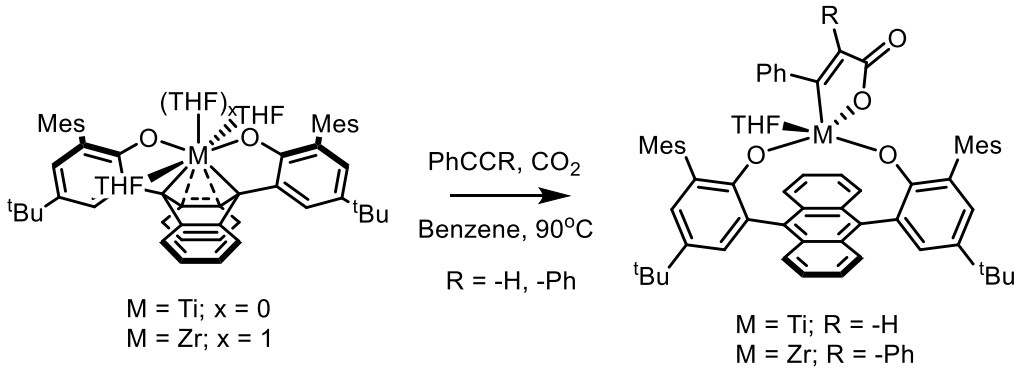

Scheme 2.4. Stoichiometric reactions alkynes and CO_2 with **2-[Ti]** and **2-[Zr]**.

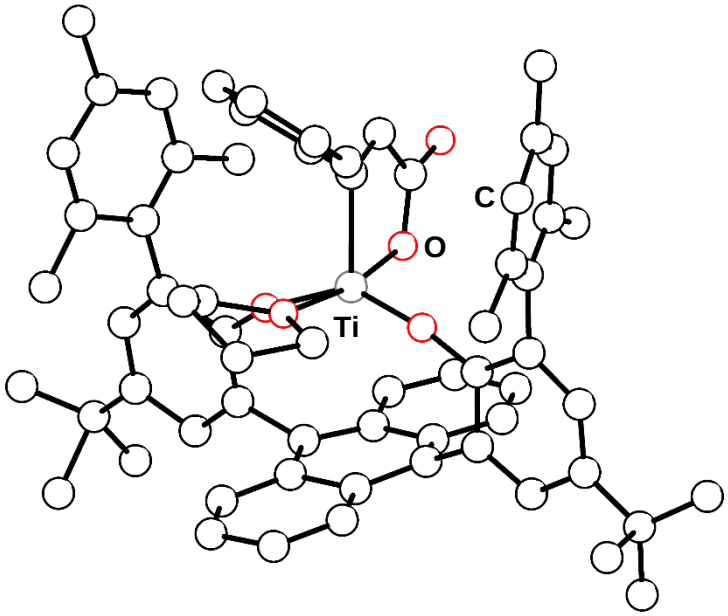

Figure 2.5. Preliminary structure of Ti(PhCCH)(CO_2)(O_2Anth). Due to data quality, only connectivity was determined.

reactions were carried out with **2-[Ti]** and **2-[Zr]** with alkynes under an atmosphere of CO_2 (Scheme 2.4). Coupling with CO_2 and alkynes was observed for both systems. The products were characterized by XRD, and solid-state characterization revealed the formation of a metallacycle formed from one equivalent of alkyne and one equivalent of CO_2. To facilitate turnover of the system, numerous attempts were made to remove the organic fragments from the metal center (Scheme 2.5). Due to the strong M-O bonds (M = Ti ~158 kcal/mol; M = Zr ~180 kcal/mol),[44] a variety of silane and borane reagents were screened due to the strength of the O-E bond (E = Si~191 kcal/mol; E = B~193 kcal/mol)[44] in the desired products. Unfortunately, no desired reactivity was observed, and the desired compounds were not observed by GC-MS.

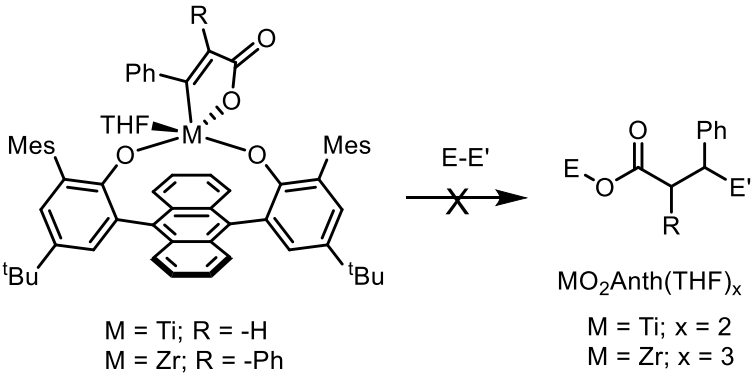

Scheme 2.5. Proposed reactivity for removal of organic fragment.

CONCLUSIONS

We have synthesized and characterized a series of titanium complexes supported by a redox non-innocent, hemilabile *bis*(phenoxide) ligand with a central 9,10-anthracenediyl motif. Analogous to the previously reported Zr system, two-electron chemistry at the Ti(IV) center is enabled by this ligand platform, including generation of the reduced complex by photolytic reductive elimination of bibenzyl from $Ti(O_2Anth)Bn_2$ and oxidative coupling of unsaturated organic substrates (including alkynes, nitriles). The Ti system is competent for the [2+2+2] cycloaddition of nitriles and alkynes to generate pyrimidines, albeit with lower selectivity than the Zr system due to the competing forming of the benzene derivative. Stoichiometric formation of pyridines is accessible with both the the Ti and Zr systems with appropriate alkyne and oxime substrates. Both the Ti and Zr systems are competent for the oxidative cycloaddition of alkynes and CO_2, although the coupled product remains bound to the metal center.

EXPERIMENTAL SECTION

General Considerations. Unless otherwise specified, all operations involving air- or water-sensitive reagents were carried out in an MBraun drybox under a nitrogen atmosphere or using standard Schlenk and vacuum line techniques. Solvents for air- and moisture-sensitive reactions were dried by the method of Grubbs.[45] Deuterated solvents were purchased from Cambridge Isotope Laboratories and C_6D_6 was vacuum transferred from sodium benzophenone ketyl before use. All solvents, once dried and degassed, were stored under a nitrogen atmosphere over 4 Å molecular sieves. LH_2[22] and tetrabenzyltitanium[46] were prepared according to literature procedures. Alkynes and nitriles used were either sublimed under reduced pressure or distilled from calcium hydride before use. All other reagents were used as received. ^1H and $^{13}C\{^1H\}$ spectra were recorded on Varian Mercury 300 MHz or Varian 400 MHz spectrometers at ambient temperatures, unless otherwise denoted. ^1H and $^{13}C\{^1H\}$ NMR spectra are reported referenced internally to residual solvent peaks reported relative to tetramethylsilane. Gas chromatography-mass spectrometry (GC-MS) was performed with on an Agilent 6890A instrument using a HP-5MS column (30 m length, 0.25 mm diameter, 0.50 μm film) and an Agilent 5973N mass-selective EI detector. Photolyses were conducted using an Oriel Instruments arc lamp housing and a Osram 75 W Xe arc lamp set to a current of 5.4 A.

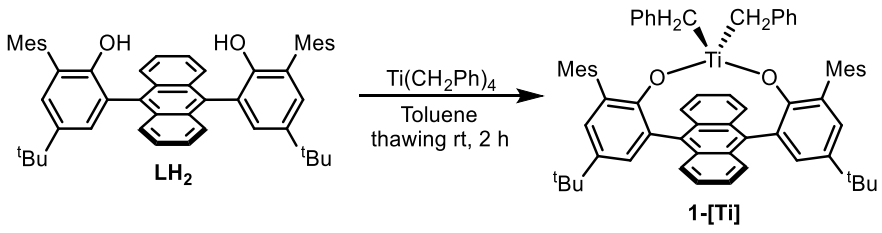

Synthesis of 1-[Ti]. This reaction was conducted under an inert atmosphere and with exclusion of light. To a thawing solution of tetrabenzyltitanium (290 mg, 0.703 mmol, 1 equiv) in toluene (20 mL), was added a thawing solution of LH_2 (500 mg, 0.703 mmol, 1 equiv) in toluene (10 mL)

with stirring. The reaction was allowed to warm up to room temperature and stirred an additional 2 h, followed by heating at 75 °C for 16 hr, forming a bright red solution. The solution was removed from the glovebox in a Schlenk tube and heated to 80 °C for 48 hr. Reaction progress was monitored by ^{1}H NMR. Upon completion, solvent was removed under reduced pressure. The solid was redissolved in pentane, filtered through a pad of diatomaceous earth, and volatiles were removed *in vacuo* to afford **1-[Ti]** as a red/brown solid. (620 mg, 94 %). ^{1}H NMR (400MHz, C_6D_6) 8.06 (dd, 4 H, Ar*H*), 8.03 (d, 2 H, Anth*H*), 7.33 (d, 2 H, Ar*H*), 7.04 (dd, 4 H, Anth*H*), 6.85 (s, 4 H, Mes*H*) 6.81-6.71 (m, 6 H, Ar*H*), 5.87 (d, 4 H, Ar*H*), 2.19 (s, 6 H, ArCH_3), 2.13 (s, 12 H, ArCH_3), 1.65 (s, 4 H, Ph-CH_2), 1.37 (s, 18 H, C(CH_3)$_3$). ^{13}C{^{1}H} NMR (101 MHz, C_6D_6): 161.25 (aryl-*C*), 144.81 (aryl-*C*), 142.51 (aryl-*C*), 137.06 (aryl-*C*), 136.88 (aryl-*C*), 134.76 (aryl-*C*), 133.29 (aryl-*C*), 132.09 (aryl-*C*), 131.17 (aryl-*C*), 129.02 (aryl-*C*), 128.62 (aryl-*C*), 128.59 (aryl-*C*), 126.40 (aryl-*C*), 126.10 (aryl-*C*), 124.52 (aryl-*C*), 123.77 (aryl-*C*), 88.84 (Ti*C*H$_2$Ph), 34.67 (*C*(CH$_3$)$_3$), 31.94 (C(*C*H$_3$)$_3$), 21.56 (Ar*C*H$_3$), 21.15 (Ar*C*H$_3$). Anal. Calcd. $C_{66}H_{66}O_2Ti$ (%): C, 84.41; H, 7.08. Found: C, 82.22; H, 6.85.

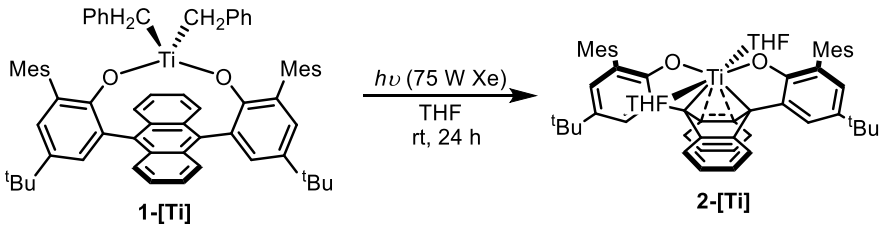

Synthesis of 2-[Ti]. A quartz Schlenk tube was charged with $TiO_2AnthBn_2$ (250 mg, 0.266 mmol) and dissolved in 30 mL THF. The reaction was stirred at RT under UV light for 16 hr. After complete conversion, the reaction mixture was pumped down to dryness and triturated 3x with 5 mL hexanes. The red-brown solid was rinsed with pentane to remove the bibenzyl side-product followed by extraction with benzene. A brown-red solid was obtained. (203 mg, 85%) ^{1}H NMR (400MHz, C_6D_6) 7.73 (d, 2 H, Ar*H*), 7.36 (dd, 4 H, Ar*H*), 7.34 (d, 2 H, Ar*H*), 6.94 (s, 4 H, Mes*H*),

6.73 (dd, 4 H, Ar*H*), 3.48 (br. m., 8 H, THF-OC*H*$_2$), 2.27 (s, 12 H, ArC*H*$_3$), 2.21 (s, 6 H, ArC*H*$_3$), 1.39 (s, 18 H, C(C*H*$_3$)$_3$), 1.27 (br. m., 8 H, THF-C*H*$_2$). ^{13}C{^{1}H} NMR (101 MHz, C_6D_6): 163.04 (aryl-*C*), 141.51 (aryl-*C*), 138.18 (aryl-*C*), 136.93 (aryl-*C*), 135.85 (aryl-*C*), 134.90 (aryl-*C*), 134.30 (aryl-*C*), 127.30 (aryl-*C*), 126.72 (aryl-*C*), 126.61 (aryl-*C*), 125.03 (aryl-*C*), 125.03 (2C, aryl-*C*), 118.80 (aryl-*C*), 73.40 (THF-O*C*H$_2$) 34.44 (*C*(CH$_3$)$_3$), 32.33 (C(*C*H$_3$)$_3$), 25.08 (THF-*C*H$_2$), 21.49 (Ar*C*H$_3$), 21.16 (Ar*C*H$_3$). Anal. Calcd. $C_{60}H_{66}O_4Ti$ (%): C, 80.16; H, 7.40. Found: C, 79.59; H, 7.62.

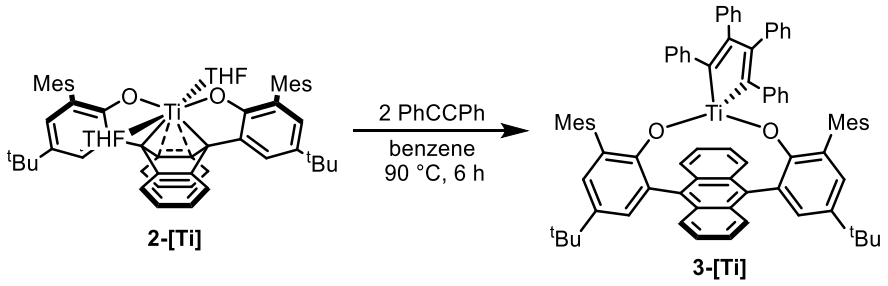

Synthesis of 3-[Ti]. A solution of **2-[Ti]** (50 mg, 0.0986 mmol) and diphenylacetylene (35.2 mg, 0.197 mmol) in benzene (5 mL) was heated to 90 °C with stirring for 6 hr. After cooling to room temperature, the volatiles were removed *in vacuo*. The residue was washed with cold pentane, extracted with benzene, and filtered through diatomaceous earth. Concentration under vacuum provided **3-[Ti]** as a brown solid (35.4 mg 70%). %) ^{1}H NMR (400MHz, C_6D_6): 8.08 (dd, 4 H, anth-*H*), 8.03 (d, 2 H, Ar*H*), 7.27 (d, 2 H, Ar*H*), 7.03 (dd, 4 H, anth-*H*), 6.91-6.66 (overlapping m, 18 H, Ar*H*), 6.50 (dd, 4H, Ar*H*), 5.69 (dd, 4H, Ar*H*), 2.25 (s, 6H, ArC*H*$_3$), 2.02 (s, 12H, ArC*H*$_3$), 1.42 (s, 18 H, C(C*H*$_3$)$_3$). ^{13}C{^{1}H} NMR (101 MHz, C_6D_6): 219.23 (Ti-*C*), 161.06 (aryl-*C*), 144.85 (aryl-*C*), 141.15 (aryl-*C*), 140.70 (aryl-*C*), 137.69 (aryl-*C*), 137.01 (aryl-*C*), 136.72 (aryl-*C*), 136.09 (aryl-*C*), 134.87 (aryl-*C*), 133.24 (aryl-*C*), 132.16 (aryl-*C*), 131.82 (aryl-*C*), 130.50 (aryl-*C*), 127.33 (aryl-*C*), 127.29 (aryl-*C*), 126.22 (aryl-*C*), 126.18 (aryl-*C*), 125.36 (aryl-*C*), 124.35

(aryl-*C*), 34.71 (*C*(CH_3)$_3$), 31.92 (C(*C*H_3)$_3$), 21.57 (Ar*C*H_3), 21.31 (Ar*C*H_3). Anal. Calcd. $C_{80}H_{72}O_2Ti$ (%): C, 86.31; H, 6.52. Found: C, 85.99; H, 6.67.

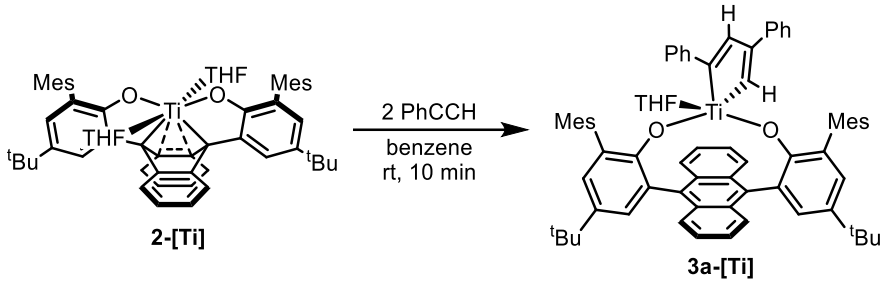

Synthesis of 3a-[Ti]. Phenylacetylene (13.3 mg, 0.13 mmol, 2 equiv) was dissolved in benzene (1 mL) and added dropwise to a stirred solution of **2-[Ti]** (58.4 mg, 0.065 mmol, 1 equiv) in benzene (5 mL) at room temperature. Upon addition, the solution changed from red-brown to yellow-brown. The reaction was stirred for 5 minutes, and volitates were concentrated *in vacuo.* The material was washed with cold pentane and extracted into benzene. After drying under reduced pressure, **3a-[Ti]** was isolated as a light brown powder (41.2 mg, 62 %). ^{1}H NMR (400 MHz, C_6D_6): 8.30 (dd, 4 H, anth-*H*), 8.04 (d, 2 H, Ar*H*), 7.99 (dd, 4 H, anth-*H*) 7.32 (d, 2 H, Ar*H*), 7.24-7.18 (overlapping m, 5 H, Ar-*H*), 7.08 (m, 1 H, Ar-*H*), 6.91-6.80 (overlapping m, 10 H, Ar*H*), 6.51 (br. s, 2 H, Ar*H*), 5.62 (d, 2 H, Ar*H*), 2.53 (br. t, 4 H, THF-OCH_2), 2.40 (s, 6 H, ArCH_3), 2.19 (s, 6 H, ArCH_3), 2.09 (s, 6 H, ArCH_3), 1.45 (s, 18 H, C(CH_3)$_3$), 0.49 (br. t, 4 H, THF-CH_2). ^{13}C{^{1}H} NMR (101 MHz, C_6D_6): 216.92 (Ti-*C*), 210.36 (Ti-*C*), 160.80 (aryl-*C*), 143.50 (aryl-*C*), 140.40 (aryl-*C*), 139.28 (aryl-*C*), 136.93 (aryl-*C*), 136.67 (aryl-*C*), 135.52 (aryl-*C*), 134.88 (aryl-*C*), 133.12 (aryl-*C*), 132.35 (aryl-*C*), 132.25 (aryl-*C*), 130.34 (aryl-*C*), 129.34 (aryl-*C*), 129.00 (aryl-*C*), 128.59 (aryl-*C*), 128.45 (aryl-*C*), 127.59 (aryl-*C*), 126.78 (aryl-*C*), 126.64 (aryl-*C*), 126.56 (aryl-*C*), 126.41 (aryl-*C*), 125.97 (aryl-*C*), 125.51 (aryl-*C*), 124.98 (aryl-*C*), 124.60 (aryl-*C*),124.18 (aryl-*C*), 69.59 (THF-OCH_2), 34.65 (*C*(CH_3)$_3$), 31.99 (C(*C*H_3)$_3$), 24.47 (THF-*C*H_2), 21.55 (Ar*C*H_3), 21.25 (Ar*C*H_3), 21.21 (Ar*C*H_3). Anal. Calc. for $C_{72}H_{72}O_3Ti$ (%): C, 83.70; H, 7.02. Found C, 83.93; H, 7.00.

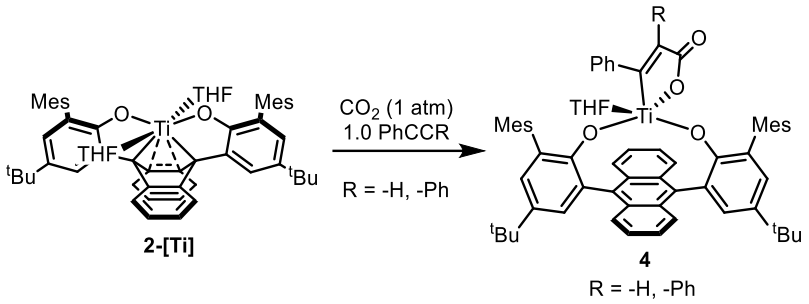

General procedure of stoichiometric coupling of alkynes and CO_2 with 2-[M]

A Schlenk tube was charged with 2-[M] (1 equiv) in benzene. The tube was then degassed by 3 freeze-pump-thaw cycles and CO_2 (1 atm) was introduced along with PhCCH *via* syringe (1 equiv) and stirred for 2 hours at 90 °C. Remove of volatiles yielded the corresponding complex.

General Setup for Catalytic Pyrimidine Synthesis. In the glovebox, stock solutions of nitrile, alkyne, and 2 in the appropriate solvent were measured with syringes and added in that order to a vial equipped with a Teflon-coated stir bar, additional solvent was added to ensure total volume of the reaction was 3 mL. The vial was capped with a PTFE-lined septum cap, taken out of the box, and placed into a preheated heating block at the appropriate temperature. After the reaction time, the reaction was cooled to room temperature and quenched by exposure to air with stirring. A small volume was taken, filtered through a pad of silica gel, and eluted with CH_2Cl_2 for GC-MS analysis. Conversion and selectivity detected by ^{1}H NMR. 1,3,5 trimethoxybenzene was added as an internal standard for quantification.

Substituted benzenes (1,3,5 triphenylbenzene and 1,2,4 triphenylbenzene) distinguished by ^{1}H NMR and GC-MS (by external comparison to authentic samples of 1,3,5 triphenylbenzene and 1,2,4 triphenylbenzene).

Representative GC-MS of Product Mixtures from Stoichiometric Studies

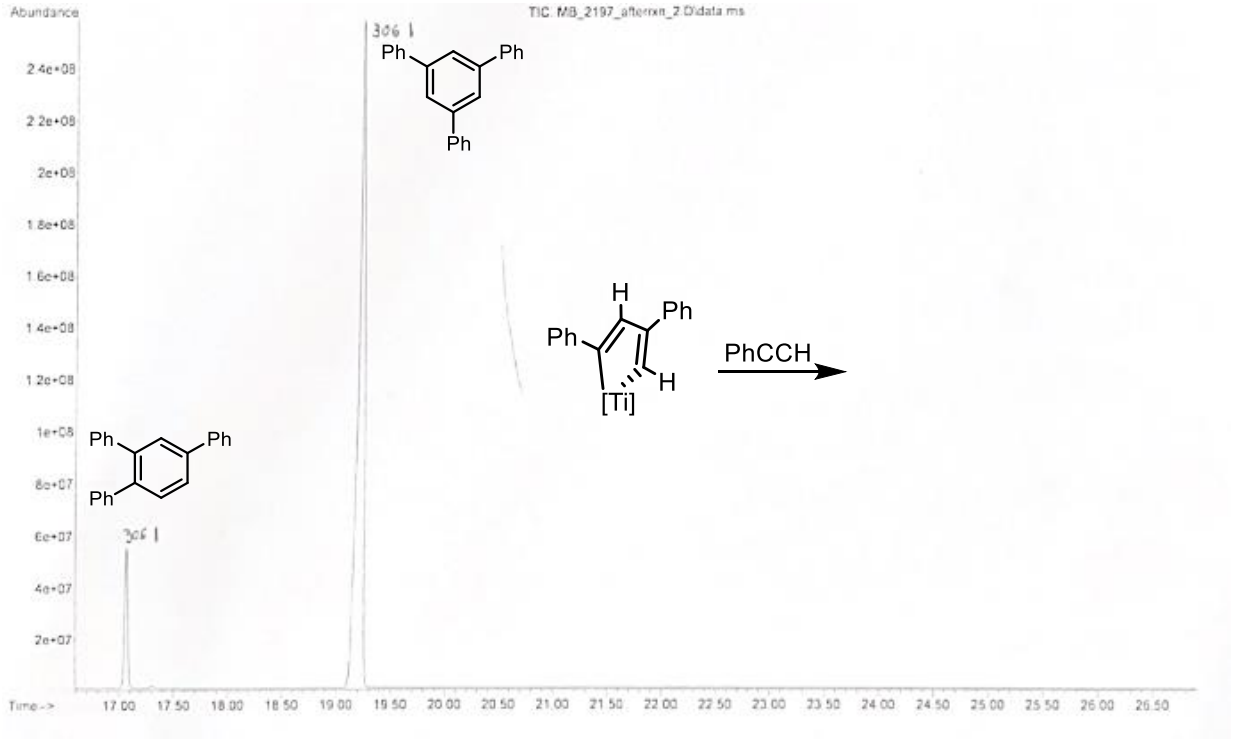

Figure 2.6. GC-MS chromatograph from reaction of **3a-[Ti]** with phenylacetylene.

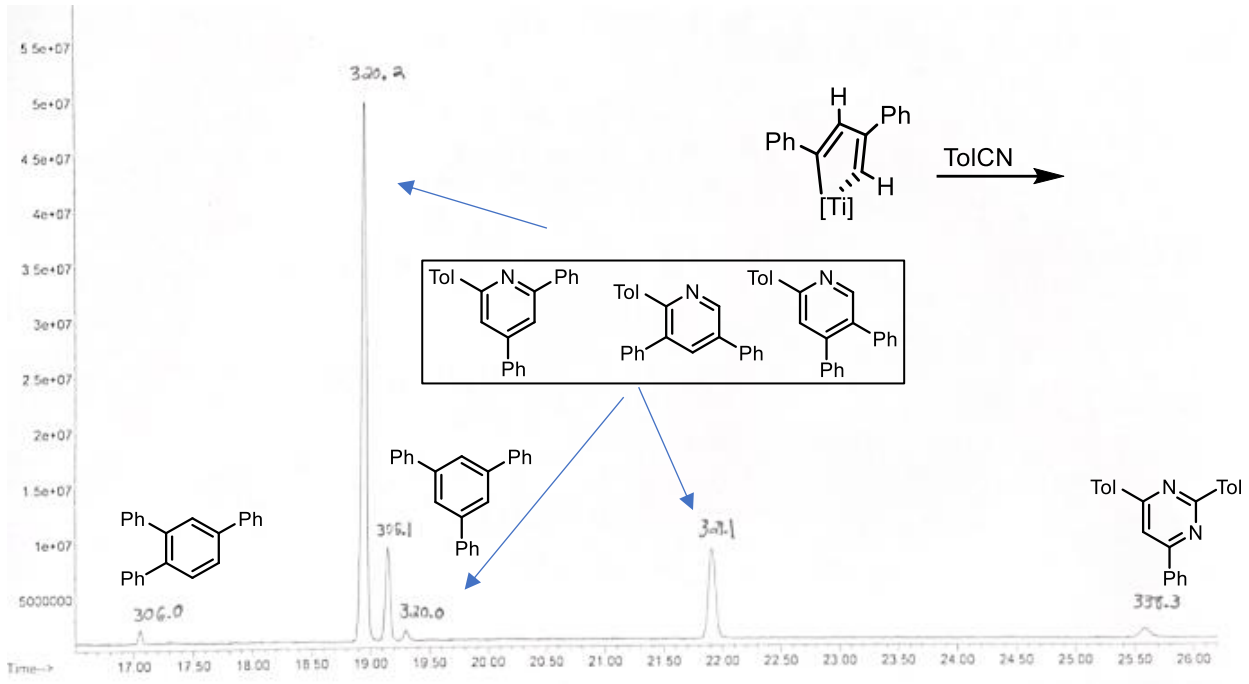

Figure 2.7. GC-MS chromatograph from reaction of **3a-[Ti]** with TolCN (specific assignments of pyridine products not distinguished.

Table 2.2. Crystal and refinement data

	2-[Ti]	3a-[Ti]
Empirical formula	$C_{65}H_{80}O_4Ti$	$C_{74.50}H_{78}O_3Ti$
Formula weight	973.19	1069.26
T (K)	100	100
a, Å	16.2834(9)	23.708(3)
b, Å	16.2834(9)	18.4392(13)
c, Å	41.577(4)	31.015(4)
α, °	90	60
β, °	90	101.304(10)
γ, °	120	90
Volume, $Å^3$	9547.2(14)	13295(3)
Z	6	8
Crystal system	Trigonal	Monoclinic
Space group	$P3_221$	$P2_1/n$
d_{calc}, g/cm^3	1.016	1.068
θ range, °	3.134 to 79.994	2.609 to 72.231
μ, mm^{-1}	1.446	1.418
Abs. Correction	Multi-scan	Multi Scan
GOF	1.031	1.068
R_1 ,[a] wR_2 [b] [I>2 σ(I)]	0.0482, 0.1052	0.0909,0.2668
Radiation Type	Cu K_α	Cu K_α

[a] $R_1 = \sum||F_o| - |F_c||/\sum|F_o|$. [b] $wR_2 = [\sum[w(F_o^2-F_c^2)^2]/\sum[w(F_o^2)^2]^{1/2}$.

NMR SPECTRA

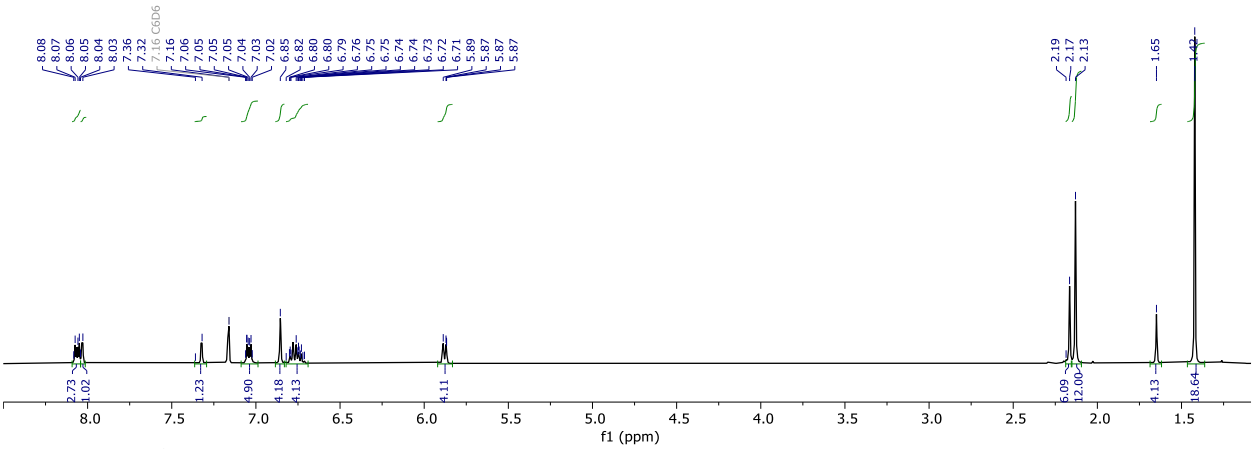

Figure 2.8. ^{1}H NMR of **1-[Ti]** in C_6D_6.

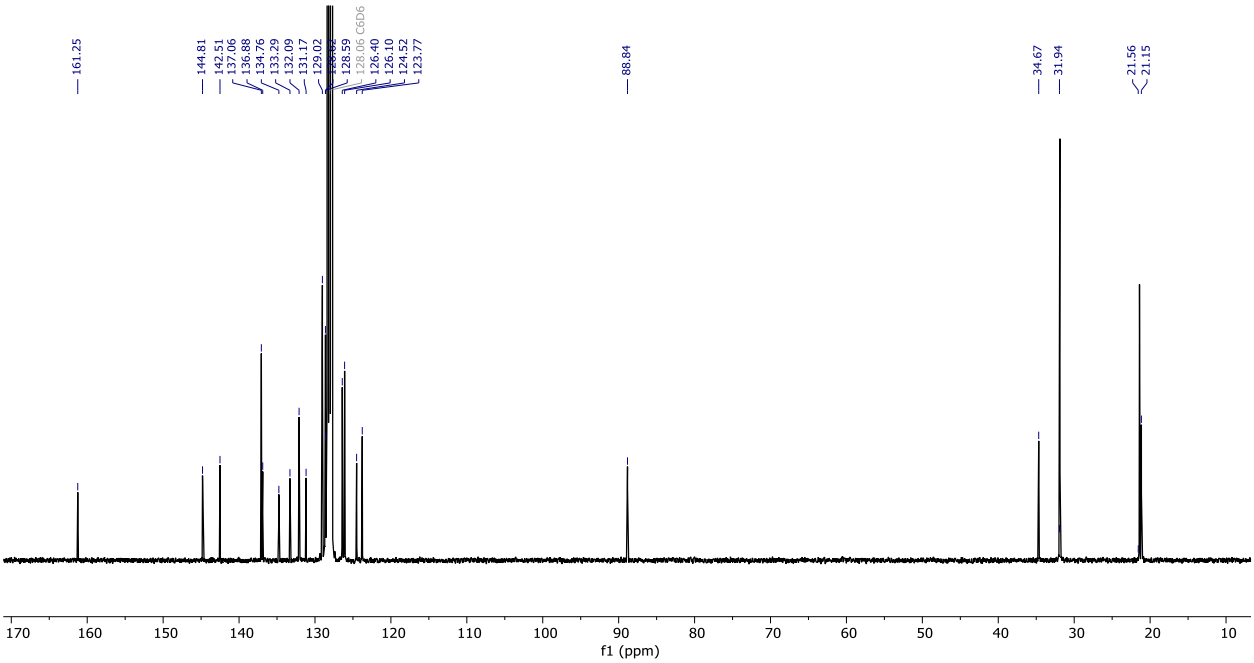

Figure 2.9. ^{13}C NMR of **1-[Ti]** in C_6D_6.

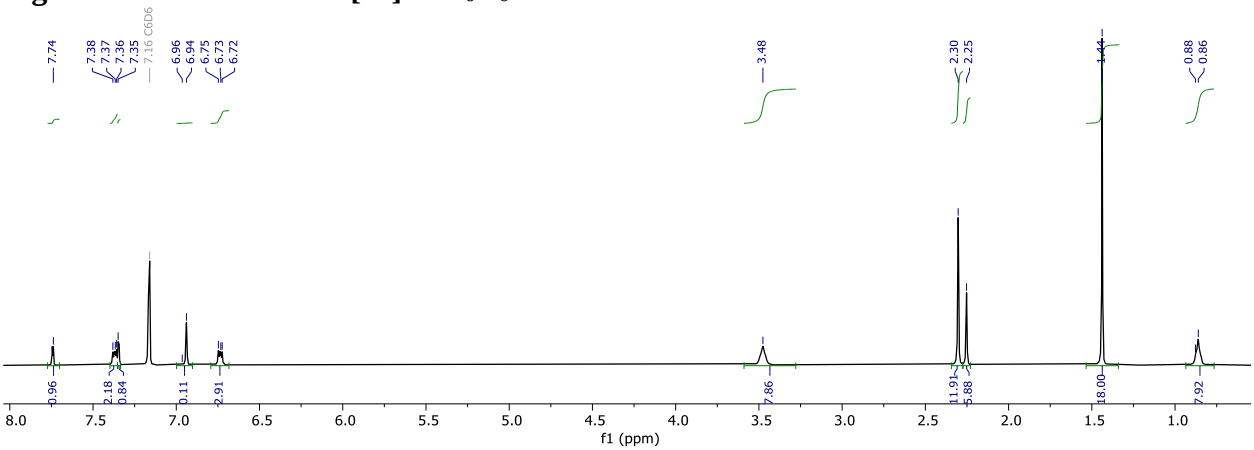

Figure 2.10. ^{1}H NMR of **2-[Ti]** in C_6D_6.

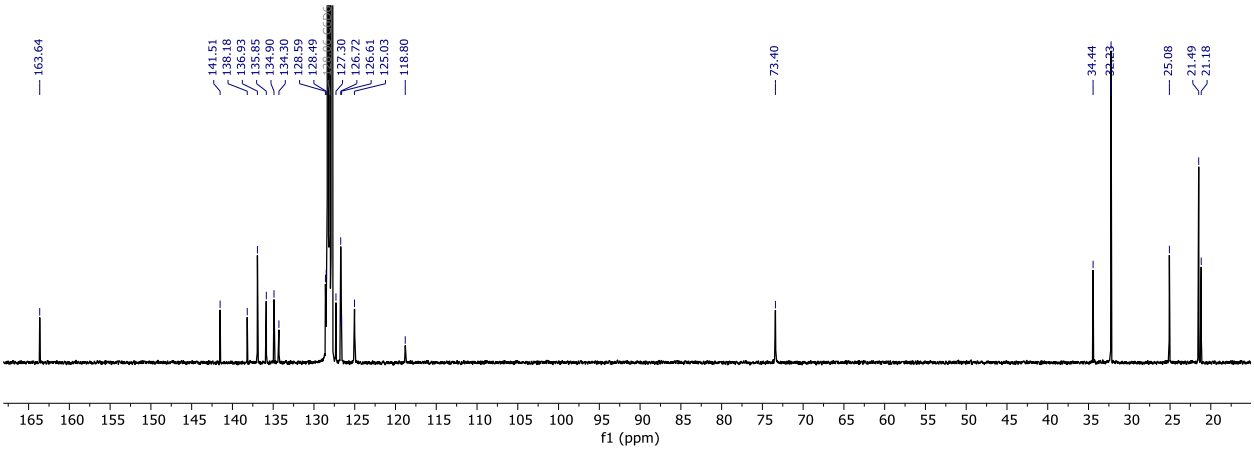

Figure 2.11. ^{13}C NMR of **2-[Ti]** in C_6D_6.

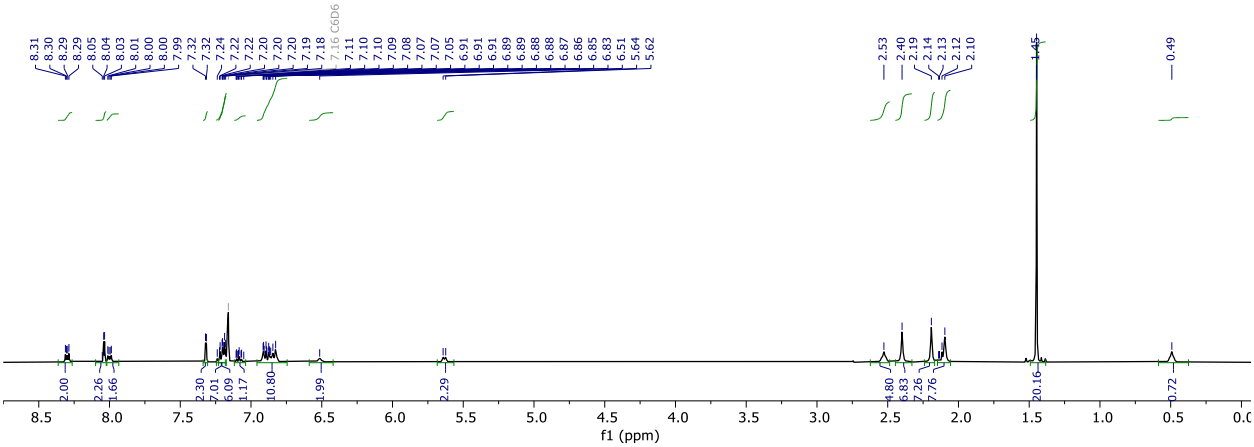

Figure 2.12. ^{1}H NMR of **3a-[Ti]** in C_6D_6.

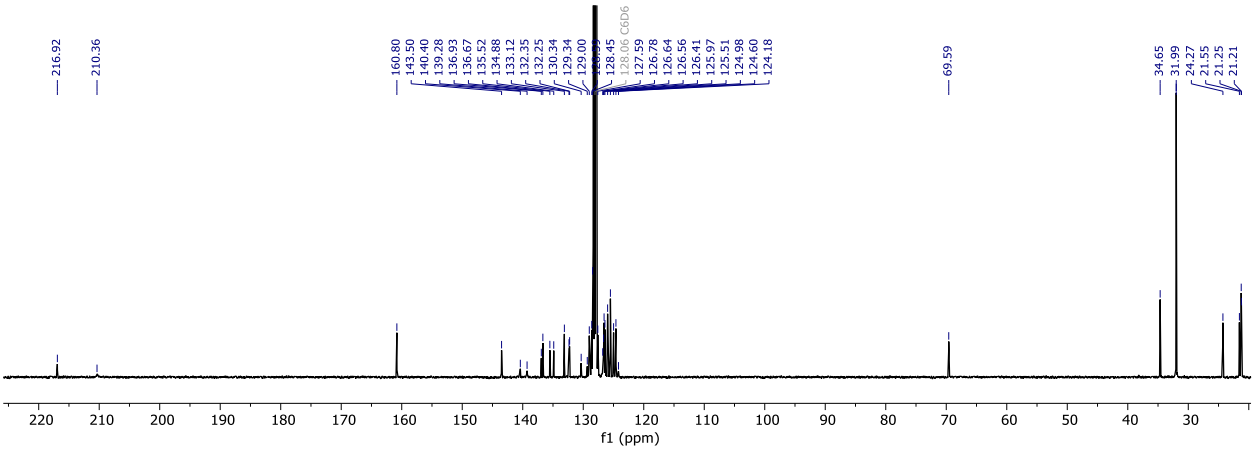

Figure 2.13. ^{13}C NMR of **3a-[Ti]** in C_6D_6.

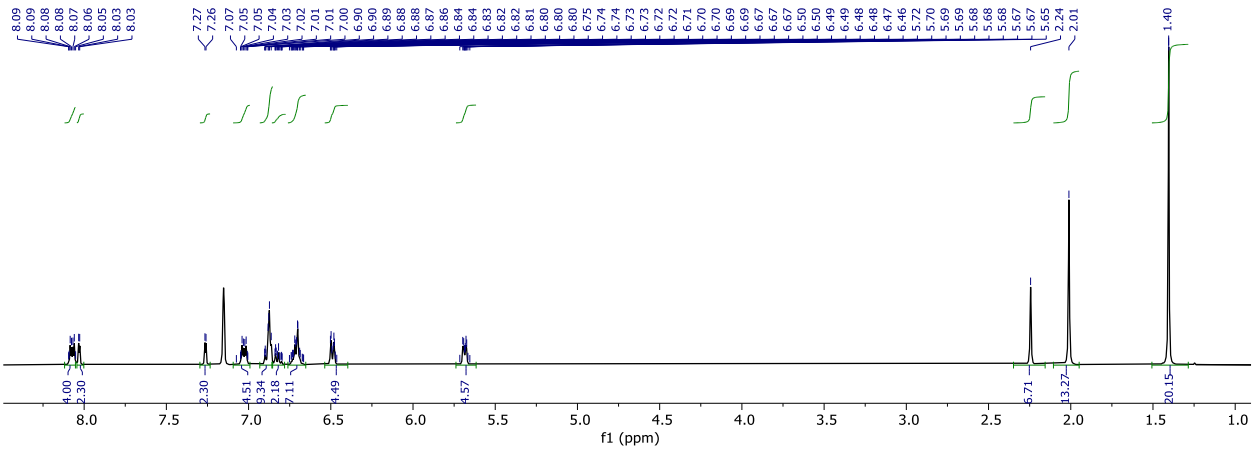

Figure 2.14. ^{1}H NMR of **3-[Ti]** in C_6D_6.

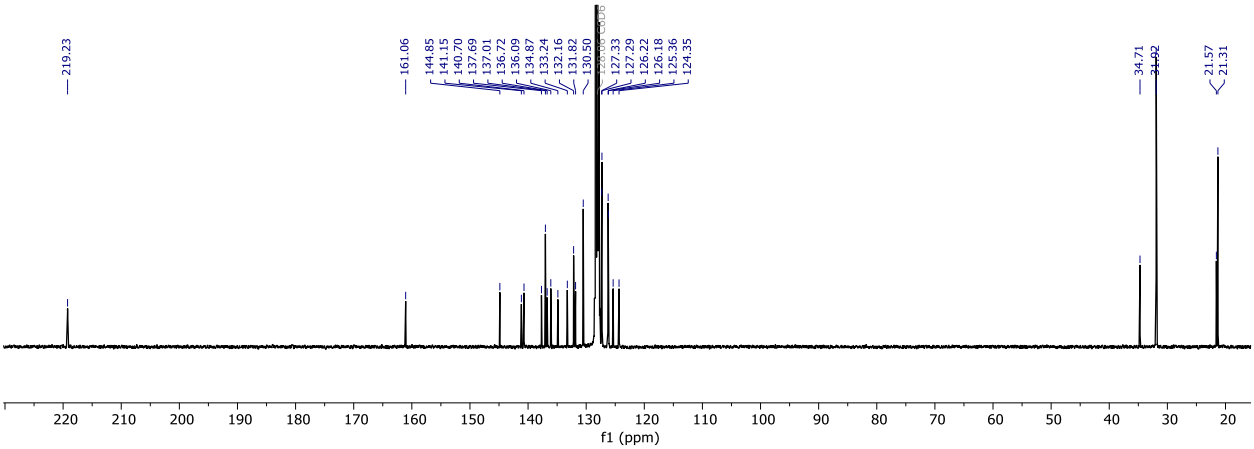

Figure 2.15. ^{13}C NMR of **3-[Ti]** in C_6D_6.

REFERENCES

1. Chirik, P. J.; Wieghardt, K., Radical Ligands Confer Nobility on Base-Metal Catalysts. *Science* **2010,** *327* (5967), 794-795. 10.1126/science.1183281
2. Luca, O. R.; Crabtree, R. H., Redox-active ligands in catalysis. *Chem. Soc. Rev.* **2013,** *42* (4), 1440-1459. 10.1039/C2CS35228A
3. Lyaskovskyy, V.; de Bruin, B., Redox Non-Innocent Ligands: Versatile New Tools to Control Catalytic Reactions. *ACS Catalysis* **2012,** *2* (2), 270-279. 10.1021/cs200660v
4. Nakada, A.; Matsumoto, T.; Chang, H.-C., Redox-active ligands for chemical, electrochemical, and photochemical molecular conversions. *Coord. Chem. Rev.* **2022,** *473*, 214804. 10.1016/j.ccr.2022.214804
5. Blackmore, K. J.; Lal, N.; Ziller, J. W.; Heyduk, A. F., Catalytic Reactivity of a Zirconium(IV) Redox-Active Ligand Complex with 1,2-Diphenylhydrazine. *J. Am. Chem. Soc.* **2008,** *130* (9), 2728-2729. 10.1021/ja710611v
6. Szigethy, G.; Heyduk, A. F., Steric and Electronic Consequences of Flexibility in a Tetradentate Redox-Active Ligand: Ti(IV) and Zr(IV) Complexes. *Inorg. Chem.* **2011,** *50* (1), 125-135. 10.1021/ic101468p
7. Blackmore, K. J.; Ziller, J. W.; Heyduk, A. F., "Oxidative Addition" to a Zirconium(IV) Redox-Active Ligand Complex. *Inorg. Chem.* **2005,** *44* (16), 5559-5561. 10.1021/ic050997c
8. Clark, K. M., Synthesis and Reactivity of Low-Coordinate Titanium Synthons Supported by a Reduced Redox-Active Ligand. *Inorg. Chem.* **2016,** *55* (13), 6443-6448. 10.1021/acs.inorgchem.6b00404
9. Heins, S. P.; Wolczanski, P. T.; Cundari, T. R.; MacMillan, S. N., Redox non-innocence permits catalytic nitrene carbonylation by (dadi)TiNAd (Ad = adamantyl). *Chem. Sci.* **2017,** *8* (5), 3410-3418. 10.1039/C6SC05610E
10. Lu, F.; Zarkesh, R. A.; Heyduk, A. F., A Redox-Active Ligand as a Reservoir for Protons and Electrons: O2 Reduction at Zirconium(IV). *Eur. J. Inorg. Chem.* **2012,** *2012* (3), 467-470. 10.1002/ejic.201100798
11. Kurogi, T.; Ishida, Y.; Kawaguchi, H., Synthesis of titanium and zirconium complexes supported by a *p*-terphenoxide ligand and their reactions with N_2, CO_2 and CS_2. *Chem. Commun.* **2013,** *49* (100), 11755-11757. 10.1039/C3CC47284A
12. Low, C. H.; Buss, J. A.; Agapie, T., Molybdenum-Mediated Coupling of Carbon Monoxide to a C_3 Product on a Single Metal Site. *Inorg. Chem.* **2022,** *61* (20), 7710-7714. 10.1021/acs.inorgchem.2c00266
13. Buss, J. A.; Bailey, G. A.; Oppenheim, J.; VanderVelde, D. G.; Goddard, W. A.; Agapie, T., CO Coupling Chemistry of a Terminal Mo Carbide: Sequential Addition of Proton, Hydride, and CO Releases Ethenone. *J. Am. Chem. Soc.* **2019,** *141* (39), 15664-15674. 10.1021/jacs.9b07743
14. Buss, J. A.; Oyala, P. H.; Agapie, T., Terminal Molybdenum Phosphides with d Electrons: Radical Character Promotes Coupling Chemistry. *Angew. Chem. Int. Ed.* **2017,** *56* (46), 14502-14506. 10.1002/anie.201707921
15. Buss, J. A.; Edouard, G. A.; Cheng, C.; Shi, J.; Agapie, T., Molybdenum Catalyzed Ammonia Borane Dehydrogenation: Oxidation State Specific Mechanisms. *J. Am. Chem. Soc.* **2014,** *136* (32), 11272-11275. 10.1021/ja5059923

16. Tsui, E. Y.; Agapie, T., Carbon dioxide cleavage by a Ni_2 complex supported by a binucleating bis(N-heterocyclic carbene) framework. *Polyhedron* **2014,** *84*, 103-110. 10.1016/j.poly.2014.06.041
17. Buss, J. A.; Agapie, T., Four-electron deoxygenative reductive coupling of carbon monoxide at a single metal site. *Nature* **2016,** *529* (7584), 72-75. 10.1038/nature16154
18. Horak, K. T.; Agapie, T., Dioxygen Reduction by a Pd(0)–Hydroquinone Diphosphine Complex. *J. Am. Chem. Soc.* **2016,** *138* (10), 3443-3452. 10.1021/jacs.5b12928
19. Horak, K. T.; Lin, S.; Rittle, J.; Agapie, T., Heterometallic Effects in Trinuclear Complexes Supported by p-Terphenyl Diphosphine Ligands. *Organometallics* **2015,** *34* (18), 4429-4432. 10.1021/acs.organomet.5b00579
20. Velian, A.; Lin, S.; Miller, A. J. M.; Day, M. W.; Agapie, T., Synthesis and C−C Coupling Reactivity of a Dinuclear Ni^{I}–Ni^{I} Complex Supported by a Terphenyl Diphosphine. *J. Am. Chem. Soc.* **2010,** *132* (18), 6296-6297. 10.1021/ja101699a
21. Connelly, N. G.; Geiger, W. E., Chemical Redox Agents for Organometallic Chemistry. *Chem. Rev.* **1996,** *96* (2), 877-910. 10.1021/cr940053x
22. Low, C. H.; Rosenberg, J. N.; Lopez, M. A.; Agapie, T., Oxidative Coupling with Zr(IV) Supported by a Noninnocent Anthracene-Based Ligand: Application to the Catalytic Cotrimerization of Alkynes and Nitriles to Pyrimidines. *J. Am. Chem. Soc.* **2018,** *140* (38), 11906-11910. 10.1021/jacs.8b07418
23. Roitershtein, D. M.; Rybakova, L. F.; Petrov, E. S.; Ellern, A. M.; Antipin, M. Y.; Struchkov, Y. T., Lutetium complexes with an anthracene dianion ligand. Molecular structure of $[(C_5H_5)_2Lu(C_{14}H_{10}^{2-})][Na^{+}(diglyme)_2]$. *J. Organomet. Chem.* **1993,** *460* (1), 39-45. 10.1016/0022-328X(93)80356-G
24. Bogdanovic, B., Magnesium anthracene systems and their application in synthesis and catalysis. *Acc. Chem. Res.* **1988,** *21* (7), 261-267.
25. Fedushkin, I. L.; Bochkarev, M. N.; Dechert, S.; Schumann, H., A Chemical Definition of the Effective Reducing Power of Thulium(II) Diiodide by Its Reactions with Cyclic Unsaturated Hydrocarbons. *Chemistry – A European Journal* **2001,** *7* (16), 3558-3563. 10.1002/1521-3765(20010817)7:16<3558::AID-CHEM3558>3.0.CO;2-H
26. Bogdanović, B.; Janke, N.; Krüger, C.; Mynott, R.; Schlichte, K.; Westeppe, U., Synthesis and Structure of 1,4-Dimethylanthracenemagnesium·3thf and μ-Trichlorodimagnesium·6thf(1^{+}) Anthracenide. *Angew. Chem. Int. Ed.* **1985,** *24* (11), 960-961. 10.1002/anie.198509601
27. Roitershtein, D. M.; Ellern, A. M.; Antipin, M. Y.; Rybakova, L. F.; Struchkov, Y. T.; Petrov, E. S., The First Structurally Characterized Organolanthanoid Compound with an Anthracene Dianion Ligand. Synthesis and Structure (at 143 K) of η^5-$(C_5H_5)LU(C_{14}H_{10}^{2-})$ 2thf (thf = tetrahydrofuran). *Mendeleev Commun.* **1992,** *2* (3), 118-120. 10.1070/MC1992v002n03ABEH000165
28. Okamoto, S.; Yamada, T.; Tanabe, Y.-k.; Sakai, M., Alkyne [2 + 2 + 2] Cyclotrimerization Catalyzed by a Low-Valent Titanium Reagent Derived from $CpTiX_3$ (X = Cl, O-i-Pr), Me_3SiCl, and Mg or Zn. *Organometallics* **2018,** *37* (23), 4431-4438. 10.1021/acs.organomet.8b00678
29. See, X. Y.; Beaumier, E. P.; Davis-Gilbert, Z. W.; Dunn, P. L.; Larsen, J. A.; Pearce, A. J.; Wheeler, T. A.; Tonks, I. A., Generation of Ti(II) Alkyne Trimerization Catalysts in the Absence of Strong Metal Reductants. *Organometallics* **2017,** *36* (7), 1383-1390. 10.1021/acs.organomet.7b00096

30. Xu, F.; Wang, C.; Wang, D.; Li, X.; Wan, B., Rhodium-Catalyzed [2+2+2] Cycloaddition of Oximes and Diynes To Give Pyridines. *Chem. Eur. J.* **2013,** *19* (7), 2252-2255. 10.1002/chem.201203909
31. Chen, S.; Bergman, R. G.; Ellman, J. A., Facile Rh(III)-Catalyzed Synthesis of Fluorinated Pyridines. *Org. Lett.* **2015,** *17* (11), 2567-2569. 10.1021/acs.orglett.5b00979
32. Parthasarathy, K.; Cheng, C.-H., Rhodium-catalyzed gram-scale synthesis of highly substituted pyridine derivatives. *Synthesis* **2009,** *2009* (08), 1400-1402.
33. Xu, F.; Wang, C.; Wang, H.; Li, X.; Wan, B., Eco-friendly synthesis of pyridines via rhodium-catalyzed cyclization of diynes with oximes. *Green Chem.* **2015,** *17* (2), 799-803. 10.1039/C4GC01756K
34. Martin, R. M.; Bergman, R. G.; Ellman, J. A., Synthesis of Pyridines from Ketoximes and Terminal Alkynes via C–H Bond Functionalization. *J. Org. Chem.* **2012,** *77* (5), 2501-2507. 10.1021/jo202280e
35. Hyster, T. K.; Rovis, T., Pyridine synthesis from oximes and alkynesviarhodium(iii) catalysis: Cp* and Cpt provide complementary selectivity. *Chem. Commun.* **2011,** *47* (43), 11846-11848. 10.1039/C1CC15248C
36. Too, P. C.; Noji, T.; Lim, Y. J.; Li, X.; Chiba, S., Rhodium(III)-Catalyzed Synthesis of Pyridines from α,β-Unsaturated Ketoximes and Internal Alkynes. *Synlett* **2011,** *2011* (19), 2789-2794. 10.1055/s-0031-1289556
37. Yoshida, Y.; Kurahashi, T.; Matsubara, S., Nickel-catalyzed Cycloaddition of α,β-Unsaturated Oximes with Alkynes: Synthesis of Highly Substituted Pyridine Derivatives. *Chem. Lett.* **2012,** *41* (11), 1498-1499. 10.1246/cl.2012.1498
38. Nakamura, I.; Zhang, D.; Terada, M., Copper-Catalyzed Tandem [2,3]-Rearrangement and 6π-3-Azatriene Electrocyclization in (E)-O-Propargylic α,β-Unsaturated Oximes. *J. Am. Chem. Soc.* **2010,** *132* (23), 7884-7886. 10.1021/ja102436z
39. Appel, A. M.; Bercaw, J. E.; Bocarsly, A. B.; Dobbek, H.; DuBois, D. L.; Dupuis, M.; Ferry, J. G.; Fujita, E.; Hille, R.; Kenis, P. J. A.; Kerfeld, C. A.; Morris, R. H.; Peden, C. H. F.; Portis, A. R.; Ragsdale, S. W.; Rauchfuss, T. B.; Reek, J. N. H.; Seefeldt, L. C.; Thauer, R. K.; Waldrop, G. L., Frontiers, Opportunities, and Challenges in Biochemical and Chemical Catalysis of CO_2 Fixation. *Chem. Rev.* **2013,** *113* (8), 6621-6658. 10.1021/cr300463y
40. Yu, D.; Teong, S. P.; Zhang, Y., Transition metal complex catalyzed carboxylation reactions with CO_2. *Coord. Chem. Rev.* **2015,** *293-294*, 279-291. 10.1016/j.ccr.2014.09.002
41. Tsuji, Y.; Fujihara, T., Carbon dioxide as a carbon source in organic transformation: carbon–carbon bond forming reactions by transition-metal catalysts. *Chem. Commun.* **2012,** *48* (80), 9956-9964. 10.1039/C2CC33848C
42. Liu, Q.; Wu, L.; Jackstell, R.; Beller, M., Using carbon dioxide as a building block in organic synthesis. *Nat. Commun.* **2015,** *6* (1), 5933. 10.1038/ncomms6933
43. Pinaka, A.; Vougioukalakis, G. C., Using sustainable metals to carry out "green" transformations: Fe- and Cu-catalyzed CO_2 monetization. *Coord. Chem. Rev.* **2015,** *288*, 69-97. 10.1016/j.ccr.2015.01.010
44. Luo, Y.-R., Comprehensive Handbook of Chemical Bond Energies. First ed.; 2007.
45. Pangborn, A. B.; Giardello, M. A.; Grubbs, R. H.; Rosen, R. K.; Timmers, F. J., Safe and Convenient Procedure for Solvent Purification. *Organometallics* **1996,** *15* (5), 1518-1520. 10.1021/om9503712
46. Hamaed, A.; Hoang, T. K. A.; Trudeau, M.; Antonelli, D. M., Optimization of hydrogen storage capacity in silica-supported low valent Ti systems exploiting Kubas binding of

hydrogen. *J. Organomet. Chem.* **2009,** *694* (17), 2793-2800. 10.1016/j.jorganchem.2009.02.034

CHAPTER 3. α,ω-Diene Generation from Ethylene and Butadiene by Copolymer Upcycling

This work was published in part as:

Bruening, M. A.; Xiong, S.; Agapie, T., α,ω-Diene Generation from Ethylene and Butadiene by Copolymer Upcycling. *ACS Sustainable Chem. Eng.* **2023,** *11* (27), 9918-9923. 10.1021/acssuschemeng.3c02569

For author contributions, see Page vii.

ABSTRACT

Linear α-olefins are accessed efficiently from ethylene in the Shell Higher Olefin Process (SHOP), an industrial process practiced on a million-ton scale that generates a statistical mixture of C_4-C_{30} products. An analogous general process for the preparation of a range of α,ω-dienes is lacking. We herein report a two-step method that generates industrially relevant α,ω-dienes. In the first step, ethylene and butadiene are copolymerized to generate copolymers with variable butadiene content. A titanium bisphenoxide bisthiolate catalyst activated with methylaluminumoxane (MAO) was selected for this step due to high selectivity for 1,4-butadiene incorporation. Ethenolysis of the copolymers results in a distribution of α,ω-dienes in the C_{10}-C_{20} range. Depending on conditions, linear trienes are also generated. The reported protocol provides a strategy for copolymer upcycling to value-added olefin products.

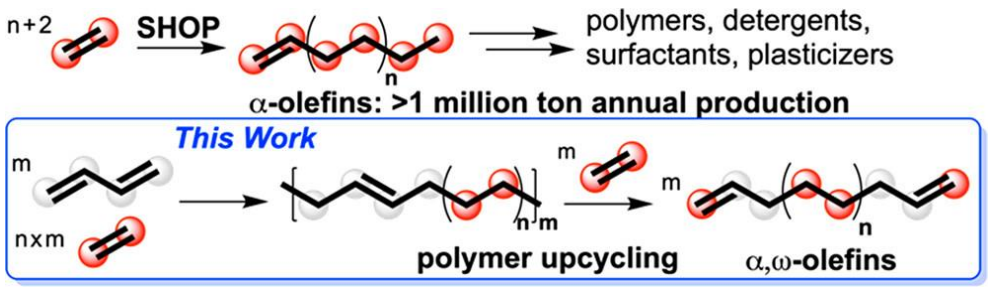

GENERAL INTRODUCTION

Linear α-olefins have a plethora of commercial applications with an annual production reaching million-ton scale.[1-4] They serve as lubricants (SHC oils), comonomers for low-density polyethylene (LDPE), and predominant commercial precursors to detergents.[2] Industrially, they are primarily produced in the Shell higher olefin process (SHOP, Figure 3.1a).[2] Under high pressure (100-110 bar), high temperature conditions (90-100 °C), a nickel phosphine complex serves as a catalyst for the synthesis of short oligomers.

α,ω-Dienes, analogs of α-olefins, are much less explored, potentially due to challenges in preparation. In addition to similar applications as α-olefins, they also serve as comonomers to prepare branched polyolefins and precursors for difunctionalized monomers for polymerization.[5-23] However, reported preparations of α,ω-dienes typically require multiple steps from cyclic olefinic precursors and are only applicable for several specific dienes.[4, 24-25] For example, dimerization and trimerization of butadiene affords a mixture of 1,5-cyclooctadiene and 1,5,7-cyclododecatriene. Partial hydrogenation of 1,5-cyclooctadiene followed by ethenolysis

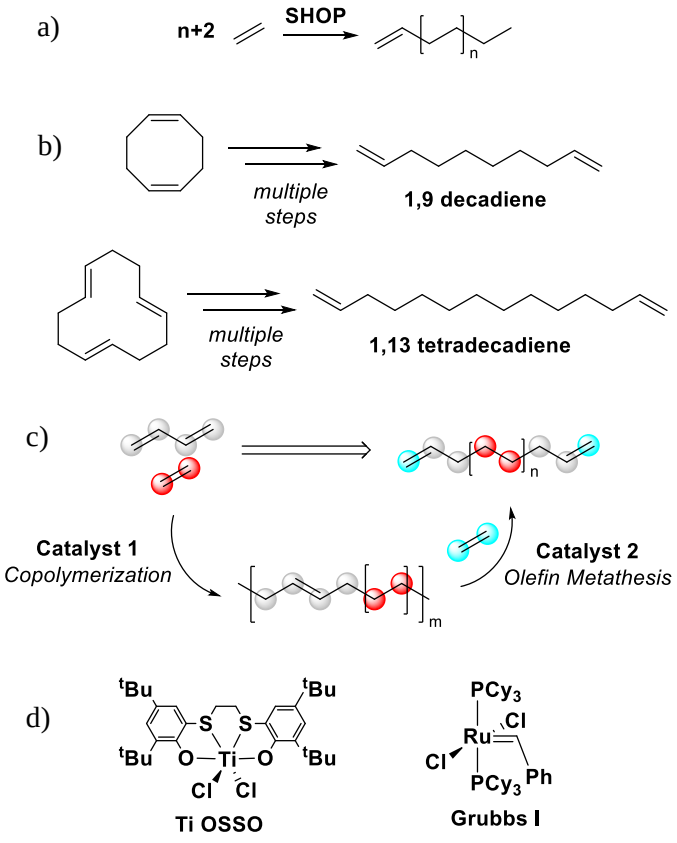

Figure 3.1. (a) Industrial preparation of α-olefins. (b) Examples of industrial synthesis of α,ω-dienes. (c) Depiction of two-step α,ω-diene generation in this work. (d) Key catalysts for optimized conditions (step 1: **Ti-OSSO**; step 2: **Grubbs I**)

affords the desired 1,9-decadiene.[26] Partial hydrogenation of 1,5,7- cyclododecatriene followed by ethenolysis affords 1,13-tetradecadiene (Figure 3.1b).[26] Ethenolysis of 1,5,7-cyclododecatriene generates 1,5-hexadiene.[27]

Aiming to increase the scope of α,ω-diene synthesis, we pursued an integrated two-step process involving the preparation of polyolefins featuring randomly distributed internal olefins followed by ethenolysis. Previously, ethenolysis has been utilized for polymer degradation,[24, 28-29] with products including lower MW oligomer/polymer fragments with α,ω divinyl tails. Examples include partially hydrogenated *cis*-1,4-polybutadiene and polyethylene,[30-31] copolymers prepared from ethylene, butadiene, and 1-octene,[32] butadiene/propylene copolymers[30, 33-34]and butadiene/styrene copolymers.[35] 1,5-Hexadiene has been generated from the ethenolysis of polybutadiene.[36] More recently, a combination of dehydrogenation, olefin isomerization, and olefin metathesis with ethylene has been employed to convert polyethylene to propylene.[37-38] However, a general strategy to target a distribution of chain lengths of α,ω-dienes resembling SHOP is not present. Herein we report the conversion of simple chemical feedstocks, butadiene and ethylene, into a statistical distribution of linear α,ω-dienes (C_{10}-C_{20}) in a two-step process.

RESULTS AND DISCUSSION

The preparation of linear α,ω-dienes from butadiene and ethylene via a copolymer intermediate requires control of polymer microstructure to generate linear olefins after the final step. Butadiene can insert into metal-alkyl bonds with 1,2, 1,4-*cis*, or 1,4-*trans* selectivity. Incorporation of butadiene in a 1,4 fashion is necessary to install the alkene functionality in the polymer backbone, a requirement for breakdown of the long hydrocarbyl chain through ethenolysis. Incorporation of butadiene in 1,2 fashion places the double bond in the side chain, which is undesirable because of lack of potential for cleavage of the main chain through ethenolysis and generation of branches in the cleaved products.

Catalysts for the copolymerization of ethylene and butadiene were selected based on their 1,4-selectivity. While copolymerization has been achieved with a variety of Sc, Y, Ti, Nb, Fe, Co catalyst systems, few examples feature high 1,4-selectivity, especially for earth-abundant catalysts.[39-44] A series of (bis(arylimino)pyridyl cobalt catalysts produce ethylene/butadiene copolymers with 1,4-selectivity up to 97% with MMAO as the activator.[41] We thus tested a relevant cobalt complex (**PDI-Co1**) under varying ethylene pressures and butadiene concentrations. Though **PDI-Co1** did produce ethylene/butadiene copolymers in the presence of MMAO, this system is not suitable for α,ω-diene generation since: 1) the catalytic activity and content of internal olefins (generated after 1,4-insertion of butadiene or elimination following chain walking) is relatively low (activity = 33 kg/(mol*h) for %Mol 1,4-BD = 2.6%, EXPERIMENTAL SECTION Table 3.6) and 2) subsequent metathesis with olefins (e.g., 4-octene) only yielded limited amounts of C9~C20 products, with a significant portion of polymer material remaining (>80% compared to starting copolymers, Table 3.7-3.8).

A titanium bisphenoxide bisthioether complex (Figure 3.1d), **Ti-OSSO**,[44] was investigated due to its reported ability to incorporate varying levels of butadiene with a strong preference for 1,4-

insertion. Activated with excess MAO, **Ti-OSSO** produces a variety of ethylene/butadiene copolymers with a relatively high activity around ~2,000-4,000 kg/(mol*h) and butadiene incorporation ranging from 4-27% (Sample A: 4.7%, B: 17.8%, C: 27.7%; Table 3.2).

Polymer microstructure was interrogated by ^{13}C NMR at elevated temperatures with specific arrangements of ethylene and butadiene ascertained based on characteristic peaks in $^{13}C\{^{1}H\}$ NMR spectra.[45] Even with low butadiene incorporation (sample A), the copolymer contains significant amounts of TET linkages (where T = *trans* butadiene and E = ethylene), suggesting the butadiene is not evenly distributed within the copolymer. For copolymers B and C, in addition to significant amounts of TET and TEE, some TT linkages are observed.

Table 3.1. Ethenolysis of Ethylene/Butadiene Copolymers

Entry	Polymer[b]	Polymer Mass (mg)	Ru (μmol)	C_2H_4 pressure (psi)	Time (hr)	Temp (^{o}C)	Remaining polymer mass (%)	1,4 Butadiene in remaining polymer (mol %)	Internal olefins in filtrate (%)
1	A	300	30	0	1	60	97	4.7	NA[g]
2	A	300	30	25	1	60	83	1.2	34
3	A	300	30	50	1	60	77	ND	29
4	A	300	30	100	1	60	82	0.9	23
5[c]	A^4	150	30	100	1	60	98	0.9	NA[g]
6	A	300	30	125	1	60	83	1.2	29
7	A	300	0	100	1	60	94	4.7	NA[g]
8	B	150	15	100	0.25	60	61	5.7	40
9	B	150	15	100	0.5	60	64	4.6	ND
10	B	900	30	100	1	60	55	3.7	49
11[d]	B^{10}	450	30	100	1	60	62 (34)[f]	1.5	23
12[e]	B^{11}	150	30	100	1	60	ND	ND	ND
13	B	300	30	100	2	60	58	5.3	43
14	B	300	30	100	16	60	52	4.5	42
15	C	300	30	100	1	60	39	10.8	49

[a] Solvent, toluene (10 mL). Following the ethenolysis trial, filtration was performed to remove remaining polymer. Solvent was concentrated under vacuum, and the olefin content of remaining filtrate (C_{14+}) was analyzed by ^{1}H NMR spectroscopy. [b] Polymers correspond to Polymer A (4.7% butadiene), Polymer B (17.8% butadiene), and Polymer C (27.7% butadiene); see Table 3.2. [c] Polymer residue from entry 4 was used as the precursor polymer. [d] Polymer residue from entry 10 was used as the precursor polymer. [e] Polymer residue from entry 11 was used as the precursor polymer. [f] Overall yield for two ethenolysis (entry 11). [g] Not applicable as no products from degradation were observed.

With copolymers having a range of butadiene content, the impact of ethenolysis conditions on the nature of α,ω-dienes produced was evaluated. Two commercially available ruthenium olefin metathesis catalysts, **Grubbs 1** (Figure 3.1d) and **Grubbs M202**, were tested.[24, 36] Ethenolysis conditions, including reaction time and ethylene pressure, were investigated first with a commercially available ruthenium metathesis catalyst, **Grubbs I**,[24, 36] to maximize polymer conversion to α, ω-dienes (Table 3.1). The mass of the remaining polymer, its remaining olefin content, and the content of internal olefin in the produced α,ω-dienes (after removal of solvent and C_{10}-C_{12} products) were determined. Increasing the ethylene pressure from 25 to 100 psi leads to higher conversion of polymer to dienes (Entry 2~4). However, this increase stops with higher ethylene pressure (entry 4 vs 5), a scenario that has been previously reported.[24, 36] A more thermally robust catalyst, **Grubbs M202**, was also employed for ethenolysis at higher temperatures. However, lower amounts of the desired α, ω-dienes were observed, with a wide distribution of species of both odd and even carbon numbers, potentially resulting from isomerization and cross-metathesis. (Figure 3.10, Table 3.4). Therefore, **Grubbs I** is preferred for this application, despite the temperature limitations.

^{1}H NMR and ^{13}C{^{1}H} NMR spectroscopy analysis of the remaining polymeric material revealed the presence of internal and terminal olefins (see EXPERIMENTAL SECTION). Notably, ^{13}C{^{1}H} NMR spectra also indicated that the TET units were significantly attenuated compared to TEE for all analyzed samples. The α, ω-dienes prepared from polymer degradation were examined by GC-MS and ^{1}H and ^{13}C NMR spectroscopy. Commercial 1,9-decadiene, 1-dodecene, 1-tetradecane, 1-hexadecene, and 1-octadecene were used as references in GC-MS (Table 3.5). Compared to the α-olefins, slightly different elution times were observed for α,ω-dienes generated in ethenolysis which are assigned to 1,11-dodecadiene, 1,13-tetradecadiene, 1,15-hexadecadiene,

and 1,17-octadecadiene, and 1,19-eicosadiene as the major species, in agreement with the MS assignment (Figure 3.2a). The nature of the products within each C_n set of isomers varies with the nature of the precursor polymers and ethenolysis conditions. In addition to the linear α,ω-dienes, more types of products were observed in the GC-MS spectra produced in entries 10 and 15 (Table 3.1) compared to entry 4 (Figure 3.2b and 3.2d vs 3.2a). Based on MS and NMR data, these peaks are assigned to α,ω-divinyl species with an additional internal olefin, arising from incomplete ethenolysis. Indeed, both internal and terminal olefins are observed by ^{1}H NMR after in-vacuo removal of the solvent and more volatile α,ω-dienes (C_{10}, C_{12}). Higher amounts of internal olefin are observed for trials where GC data are indicative of additional species. The presence of internal olefins has previously been observed for the incomplete ethenolysis of 1,4 *cis* polybutadiene.[36]

Ethenolysis was conducted again with polymer residues generated in entries 4 and 10 to determine if remaining internal olefins could be further cleaved. No reaction was observed with copolymers with low olefin content (entry 5). However, degradation was observed for copolymers with high butadiene incorporation (entry 11, Table 3.1), coupled with further attenuation of the content of internal olefins. Notably, the distribution of products generated from the second ethenolysis is different from initial ethenolysis. Only one major congener was observed for each of C_{10}, C_{12}, C_{14}, C_{16}, C_{18}, and C_{20} α,ω-dienes (Figure 3.2c) likely due to significant attenuation in the amount of TET linkages from the first ethenolysis trial. This distribution is reminiscent of statistical distributions observed in the oligomerization of ethylene with SHOP catalysts.[2-3] Unfortunately, no significant change was observed after a third ethenolysis trial, proposed to be caused by the low solubility of the polymer residue, limiting the overall generation of α,ω-dienes.

Analysis of possible products for the two-step procedure (Figure 3.2e) reveals that although multiple isomers can form for each carbon number, they are limited by the propensity of

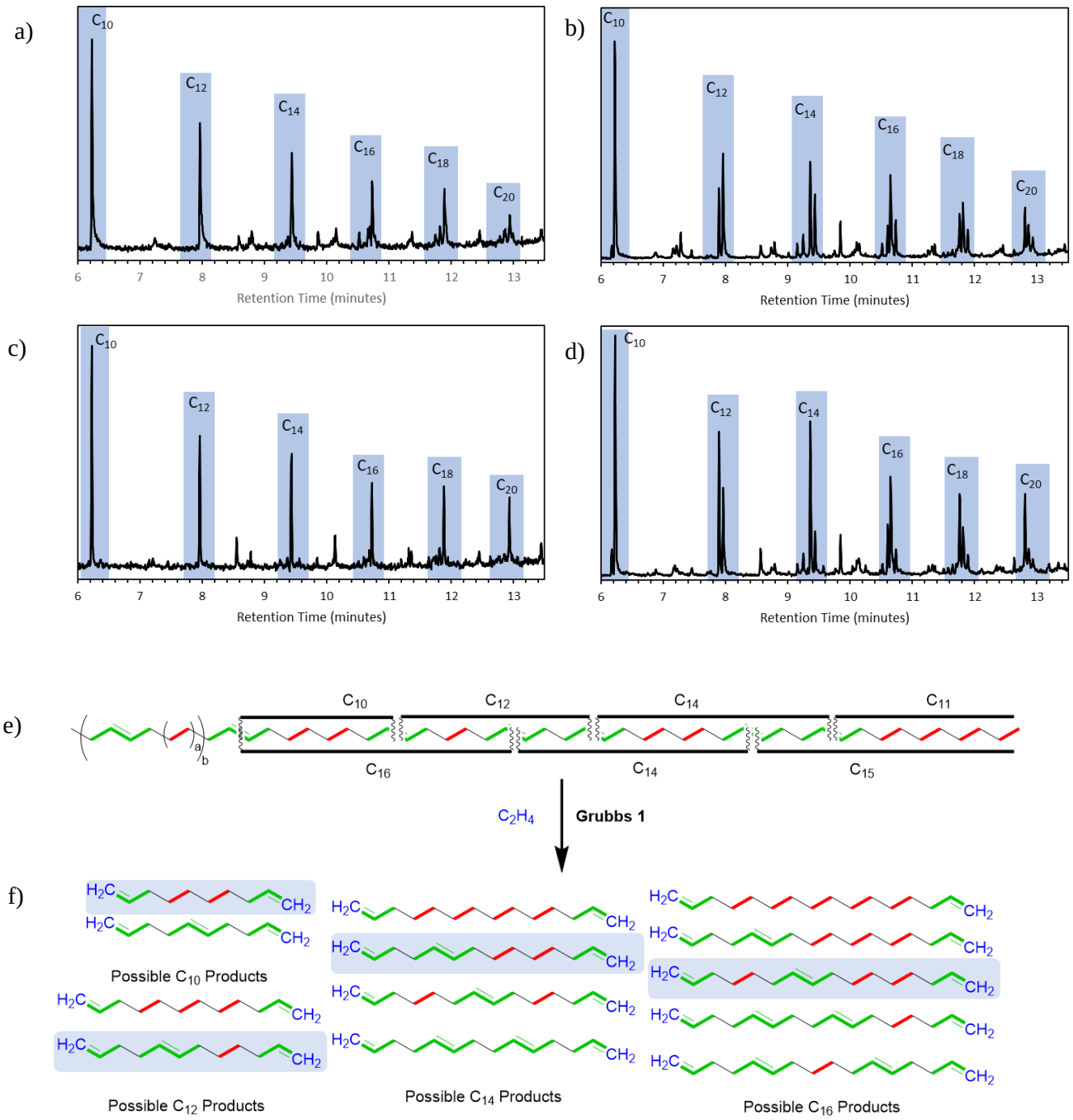

Figure 3.2. Gas chromatograms for filtrate samples derived from polymers with low initial content of butadiene (a, from entry 4, Table 1) and high initial content of butadiene (b, from entry 10; c, from entry 11; d, from entry 15, Table 1), schematic of possible polymer cleavage points labeled with corresponding C_n products after ethenolysis (e), comprehensive list of all possible products for C_{10}-C_{16} species resulting from an ethylene-butadiene copolymer upon ethenolysis (f). Notes: In e, number of butadiene insertions is not representative of the actual polymer composition. In f, internal double bonds represented in *trans* configuration, but corresponding cis isomers are also expected. Ethylene derived fragment, red; butadiene, green; ethylene derived from ethenolysis, blue. Light blue shading highlights products derived from the example polymer structure in e).

favored, as indicated by microstructural analysis of the copolymers with $^{13}C\{^{1}H\}$ NMR. Furthermore, ethenolysis products with an internal double bond are primarily the *trans* isomers, consistent with the more favored 1,4 *trans* insertions of butadiene vs. the 1,4 *cis* insertions during copolymerization. At higher carbon numbers, the complexity of the product mixture increases. While the products with different molecular weights are resolvable by GC-MS, it is not facile to distinguish between positional isomers of the same mass. Nevertheless, resonances for conjugated olefins are minor or virtually absent by ^{1}H NMR spectroscopy, indicating that double bond walking is limited. An example yield (Table 3.1, entry 4) for the generated mixture of α,ω-dienes was 76% of the converted polymer, or 13% of the initial polymer amount.

In addition to the targeted α, ω dienes, polyolefins with α,ω-divinyl ends and small amounts of odd carbon-number α-olefins are observed. Polyolefins with α,ω-divinyl ends, can serve as telechelic polymers for synthesis of polyethylene-like polyesters, polyethers, polyamides, and poly-α-olefin based lubricants or synthons for cross-linked polymers.[24, 30, 46] The odd-carbon α-olefins result from ethenolysis of polymer chain ends (Figure 3.2e). The commercial SHOP process produces only even-carbon α-olefins, making odd-carbon α-olefins less accessible and thus expensive for potential applications.[47] Current methods target these products via oxidative decarbonylation.[48-50] Modification of the polymerization and ethenolysis conditions presented here may offer an opportunity to access these types of products, though with low conversion. Although the present protocol is not practical due to the significant amount of polymer residue, it provides proof of principle for a concise two-step synthesis of a range of industrially relevant products via polyolefin conversion.

CONCLUSIONS

In summary, we have developed a two-step method for the generation of α,ω-dienes from ethylene and butadiene. This method consists of (1) ethylene/butadiene copolymerization with a **Ti-OSSO**/MAO catalyst system and (2) ethenolysis with a ruthenium catalyst. Careful catalyst selection for the initial copolymerization allows for good selectivity for 1,4 butadiene insertion, critical for installation of the alkene in the polymer backbone, and the butadiene content in the polymer can be controlled by modification of the polymerization conditions. Subsequent ethenolysis degrades the material to produce vinyl-terminated polymers and a distribution of α,ω-diolefins in an industrially relevant range.

EXPERIMENTAL SECTION

General Considerations

Unless otherwise specified, all operations involving air- or water-sensitive reagents were carried out in an MBraun drybox under a nitrogen atmosphere or using standard Schlenk and vacuum line techniques. Solvents for air- and moisture-sensitive reactions were dried by the method of Grubbs.[51] Deuterated solvents were purchased from Cambridge Isotope Laboratories and C_6D_6 was vacuum transferred from sodium benzophenone ketyl before use. All solvents, once dried and degassed, were stored under a nitrogen atmosphere over 4 Å molecular sieves. Ligand precursor 1[52] and Ti OSSO[44] and PDI-Co[41] were prepared according to literature procedures. Ligand 2 was prepared with modification to the published procedure. ^{1}H and ^{13}C{^{1}H} NMR spectra were recorded on Varian 400 MHz spectrometers at ambient temperatures, unless otherwise denoted. ^{1}H and ^{13}C{^{1}H} NMR spectra are reported referenced internally to residual solvent peaks reported relative to tetramethylsilane. Gas chromatography-mass spectrometry (GC-MS) were performed with on an Agilent 6890A instrument using a HP-5MS column (30 m length, 0.25 mm diameter, 0.50 μm film) and an Agilent 5973N mass-selective EI detector.

Scheme 3.1. Preparation of **3**.

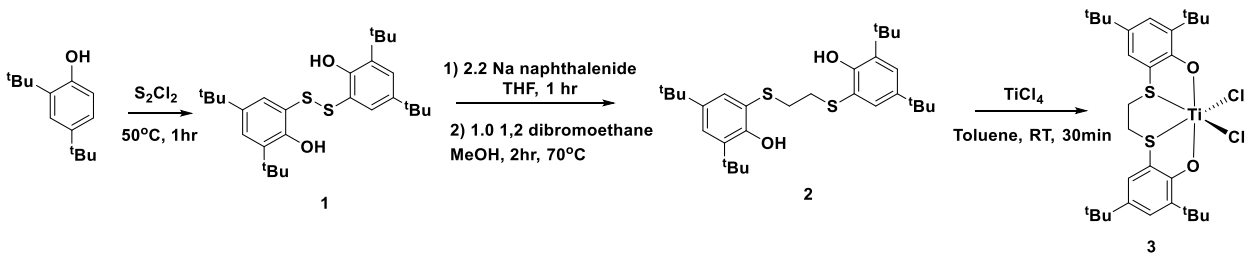

Compound 2 was prepared with modification to the published procedure.

To a solution of **1** (1.5 g, 3.1 mmol, 1.0 equiv) in THF was added dropwise a freshly prepared solution of sodium napthalenide (6.9 mmol, 2.2 equiv). The solution was stirred for 1hr at RT, before removal of all solvent *in vacuo*. The material was resuspended in dry MeOH (30 mL), and 1,2 dibromoethane (590 mg, 3.1 mmol, 1.0 equiv) was added under a counterflow of N_2. The reaction was heated to 70 ^oC for 1hr. Upon cooling to RT, the product precipitated and was filtered and washed with DCM. The product was redissolved in Et_2O and concentrated *in vacuo* to afford **2** as a white solid. (1.36 g, 86%) ^1H NMR (C_6D_6) 7.49 (d, 2 H, Ar-*H*), 7.02 (d, 2 H, Ar-*H*), 2.26 (m, 4 H, SCH_2CH_2S), 1.65 (s, 9 H, C(CH_3)$_3$), 1.17 (s, 9 H, C(CH_3)$_3$).

General Polymerization Conditions

A solution of butadiene (20 weight % in toluene, 1000-3000 equiv) and MAO (1000 equiv) were transferred to a Fisher Porter Vessel, and toluene was added to a final reaction volume of 14 mL. **3** (6.2 mg, 10 mmol, 1 equiv) was dissolved in toluene (1 mL) and transferred to a capped luer-lock syringe. The N_2 atmosphere was replaced with ethylene by pressurizing and venting the vessel. The catalyst was injected under 25 psi of ethylene before increasing the pressure to desired reaction conditions. The reaction was quenched by exposure to air, and the polymer was precipitated with MeOH and dried overnight under vacuum.

General Ethenolysis Conditions

Polymer sample (300 mg) and Grubbs Catalyst 1 (25 mg, 30 mmol) were dissolved in 10 mL of toluene and transferred to a Fisher Porter Vessel. The N_2 atmosphere was replaced with ethylene by pressurizing and venting the vessel. The vessel was heated to 60 ^oC for desired amount of time (0.25-16 hr). Ethyl vinyl ether (0.1 mL) was injected, and the vessel was stirred for an additional 30 minutes. The vessel was cooled to room temperature. The remaining polymer was precipitated with methanol (50 mL) and filtered. The filtrate was analyzed by GC-MS to detect the produced

α,ω dienes. The remaining polymeric material was dried under vacuum overnight, and the internal and terminal olefins were analyzed via ^{1}H NMR. The filtrate was concentrated under vacuum to remove solvent and products ≤ C_{12}, and the olefin content was analyzed by ^{1}H NMR .

Table 3.2: Ethylene/Butadiene Copolymers: Copolymers A, B, and C Prepared from Copolymerization of Butadiene and Ethylene

Entry[a]	[Ti] /μmol	[ethylene] /psi	[BD] /[Ti]	Temp. (°C)	time (min)	Yield (g)	Act. (kg/(mol·h))[b]	Mw /10^3	PDI	1,4-BD (mol %)[c]
A	10	100	1000	25	5	3.5	4542	7.1	3.45	4.6
B	10	50	3000	25	5	2.1	2505	7.16	3.76	17.8
C	10	25	3000	25	5	2.0	2345	ND	ND	27.8

[a] Polymerization conditions: Ti complex (10 μmol), Al/Ti = 1000, total volume = 25 mL [b] Activity = kg/(mol of Ti h) [c]Determined by ^{1}H NMR

Table 3.3: Ethenolysis Trials for Ethylene/Butadiene Copolymers A, B, and C[a]

Entry	Polymer	Polymer Mass (mg)	Ru (μmol)	C_2H_4 pressure (psi)	Time (hr)	Temp (°C)	Remaining polymer mass (%)	1,4 Butadiene in remaining polymer (mol %)	Internal olefins in filtrate (%)	Mw x10^3	PDI
Before	A							4.7		7.08	3.45
1	A	300	30	0	1	60	97	4.7	NA	ND	ND
2	A	300	30	25	1	60	83	1.2	34	6.95	3.79
3	A	300	30	50	1	60	77	ND	29	6.96	3.97
4	A	300	30	100	1	60	82	0.9	23	ND	ND
6	A	300	30	125	1	60	83	1.2	29	6.55	3.84
7	A	300	0	100	1	60	94	4.7	NA	6.31	3.81
5	A[b]	150	30	100	1	60	98	0.9	NA		
Before	B							17.8		7.16	3.76
8	B	150	15	100	0.25	60	61	5.7	40	3.11	2.99
9	B	150	15	100	0.5	60	64	4.6	ND	3.03	2.51
10	B	900	30	100	1	60	55	3.7	49	2.85	2.87
11	B[c]	450	30	100	1	60	62 (42)[e]	1.5	23	3.25	2.54
12	B[d]	150	30	100	1	60	ND	ND	ND	6.87	3.79

13	B	300	30	100	2	60	58	5.3	43	2.86	2.54
14	B	300	30	100	16	60	52	4.5	42	2.89	2.51
Before	C							27		ND	ND
15	C	300	30	100	1	60	39	10.8	49	ND	ND

[a] V = 10 mL, T= 60 °C, solvent: toluene. Following the ethenolysis trial, filtration was performed to remove remaining polymer. Solvent was concentrated under vacuum, and the olefin content of remaining filtrate (C_{14+}) was analyzed by ^{1}H NMR [b] Polymer residue from entry 4 was used as the precursor polymer. [c] Polymer residue from entry 10 was used as the precursor polymer. [d] Polymer residue from entry 11 was used as the precursor polymer. [e] Overall yield for two ethenolysis (entry 11).

Table 3.4: Ethenolysis Trials with M202 at Elevated Temperatures

Entry	Polymer	Polymer/ mg	Catalyst	Ru/ µmol	C_2H_4/ psi	t/h	Temp (°C)	1,4 butadiene in remaining polymer (mol %)	Remaining polymer mass (%)	Internal Olefins in Filtrate (%)
Before	**D**[a]							13.7		
1	**D**	300	M202	30	25	1	100	~5	64	80
2	**D**	300	M202	30	50	1	100	ND	59	85
3	**D**	300	M202	30	100	1	100	ND	62	94

[a]Polymer D prepared from copolymerization of ethylene (100psi) and butadiene (3000equiv) for 0.08h with 1000equiv MAO and 10µmol Ti-OSSO

Table 3.5: GC-MS Retention Times for commercially available standards

Compound	Retention Time (minutes)
1,5-hexadiene	2.008
1,7-octadiene	4.082
1,9-decadiene	6.231
1-decene	6.351
1-dodecene	8.042
1-tetradecene	9.517
1-hexadecene	10.780
1-octadecene	11.946

Figure 3.3: Calibration Curve for GC-FID Quantification of 1,9 decadiene

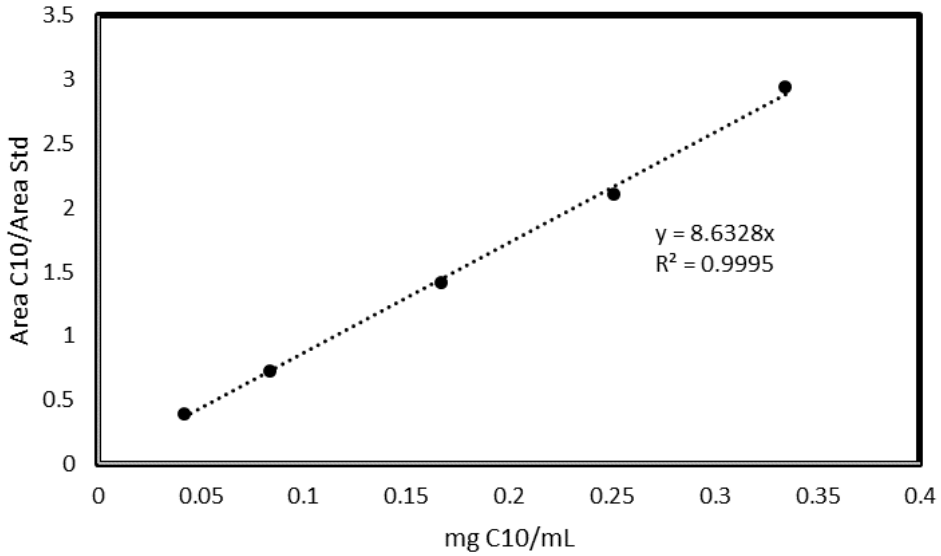

Calibration Curve for GC-FID Quantification of 1,9 decadiene; internal standard is 1,3,5 trimethoxybenzene

Yield calculation for α,ω-diene mixture

Due to the formation of a distribution of α,ω-dienes, product quantification is somewhat complicated. As an example, product quantification for Entry 4, Table 3.1 was accomplished using a combination of GC-FID, GC-MS, and residue mass upon removal of volatiles *in vacuo*. This ethenolysis trial provides a simple mixture for quantification given the formation of a primarily single α,ω-diene isomer for each C_n carbon number product. 1,9-decadiene was quantified by GC-FID upon calibration against an authentic commercial sample (8.6 mg produced upon ethenolysis). To account only for the mass derived from the degradation of polymer, a correction factor was applied (see Figure S2), with 6.8 mg of 1,9-decadiene produced from polymer degradation. 1,11-dodecadiene was quantified based on the GC-MS response relative to 1,9-decadiene (already quantified by GC-FID), and a correction factor was applied to account for product mass derived from the polymer (7.7 mg produced, with 6.4 mg corresponding to the polymer fragment). Due to

the more complex distributions observed for higher carbon number products, products C_{14} and higher were quantified by mass, upon complete removal of smaller dienes and solvent (C_{10}, C_{12}) under vacuum. A mass of 28 mg residue was isolated corresponding to products C_{14+}. Based on the decrease in mass of polymer after ethenolysis, an amount of 54 mg of α,ω-diene products is expected. The quantified amount is 41.2 mg (76%), indicating that the degraded polymeric material is primarily being converted to the desired α,ω-dienes.

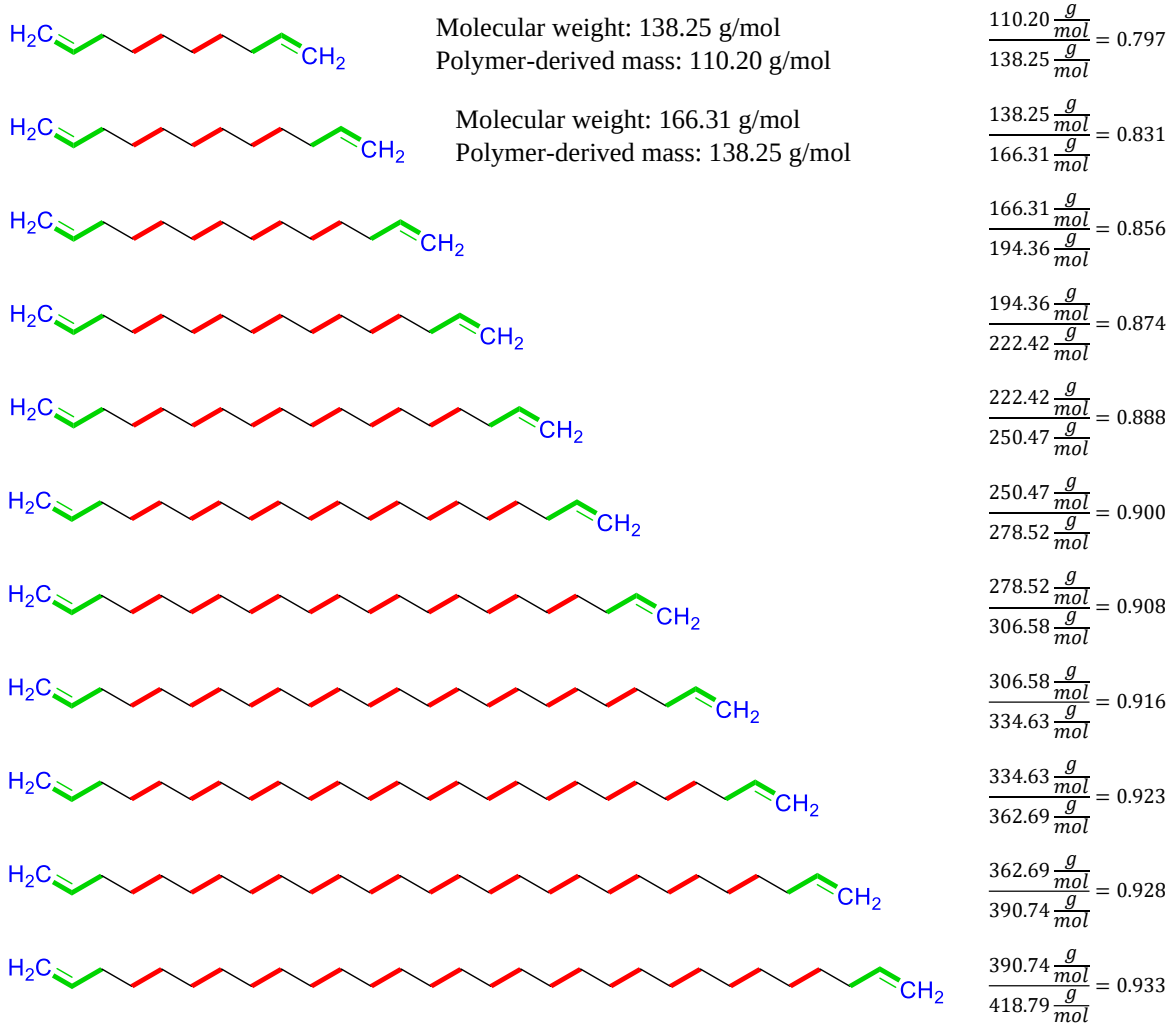

Figure 3.4. α,ω dienes C_{10}-C_{30} (left) with ethylene derived fragment, red; butadiene, green; ethylene derived from ethenolysis; blue. Representative molecular weights and polymer-derived

mass weights for C_{10} and C_{12} dienes (center). Correction factors (right) to account for mass derived only from degraded polymer.

Representative Gas Chromatograms

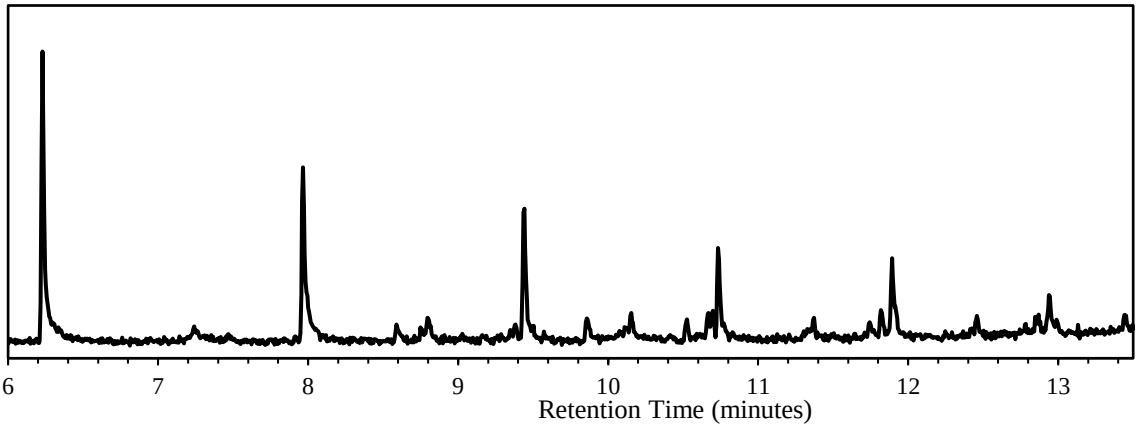

Figure 3.5. Gas Chromatogram of liquid products for Table 3.1, Entry 6.

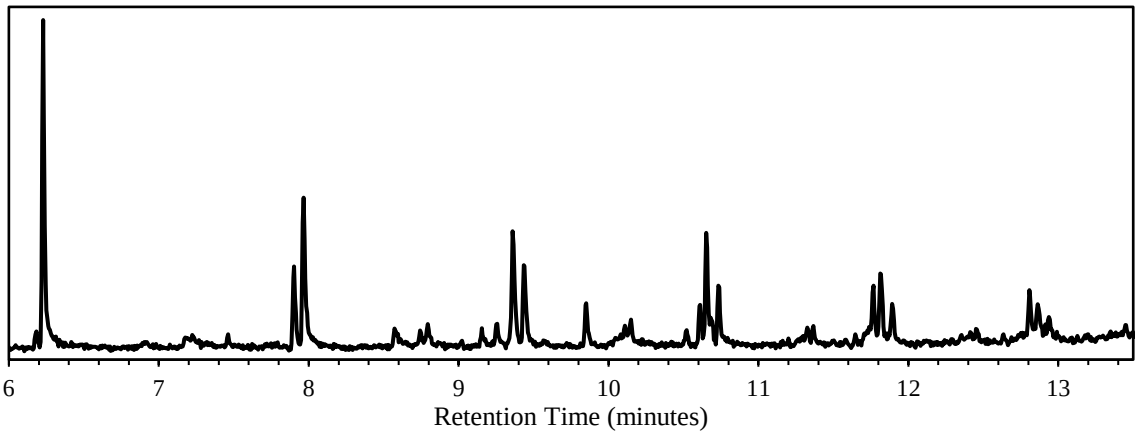

Figure 3.6. Gas Chromatogram of liquid products for Table 3.1, Entry 8.

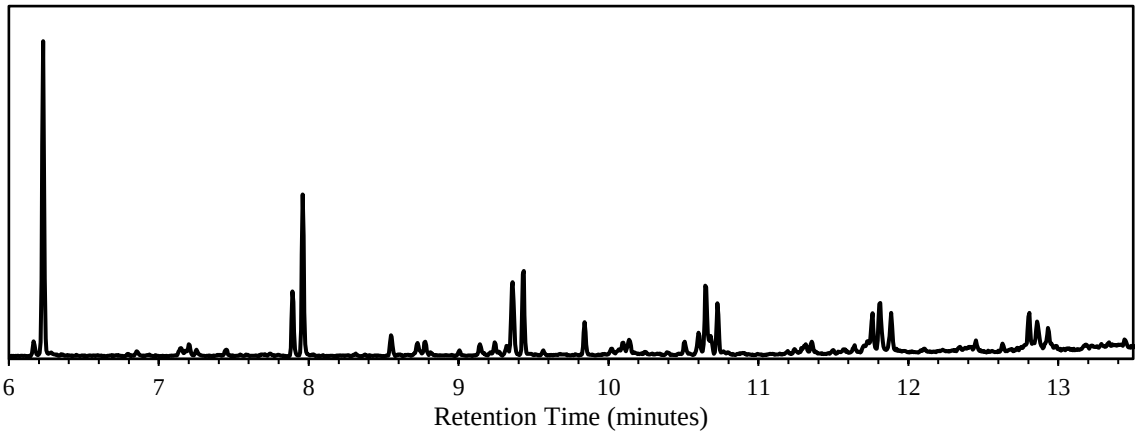

Figure 3.7. Gas Chromatogram of liquid products for Table 3.1, Entry 9.

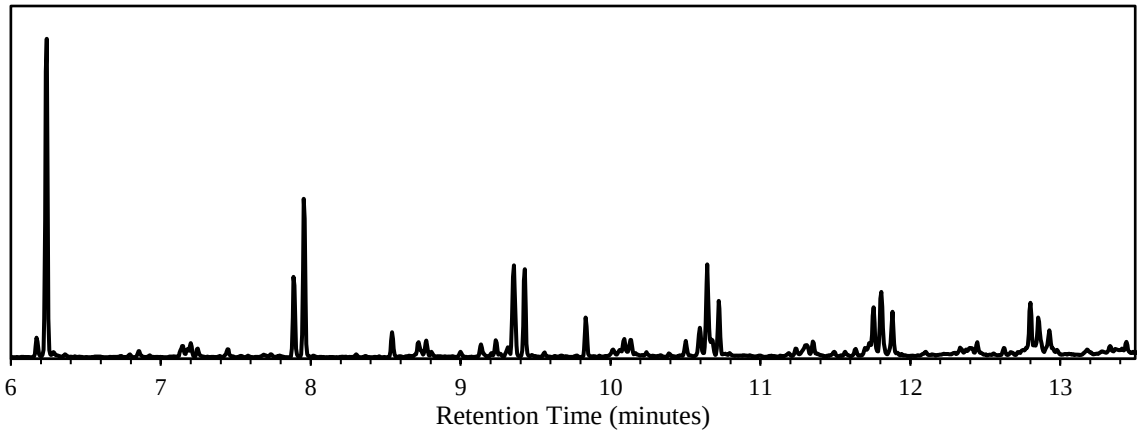

Figure 3.8. Gas Chromatogram of liquid products for Table 3.1, Entry 10.

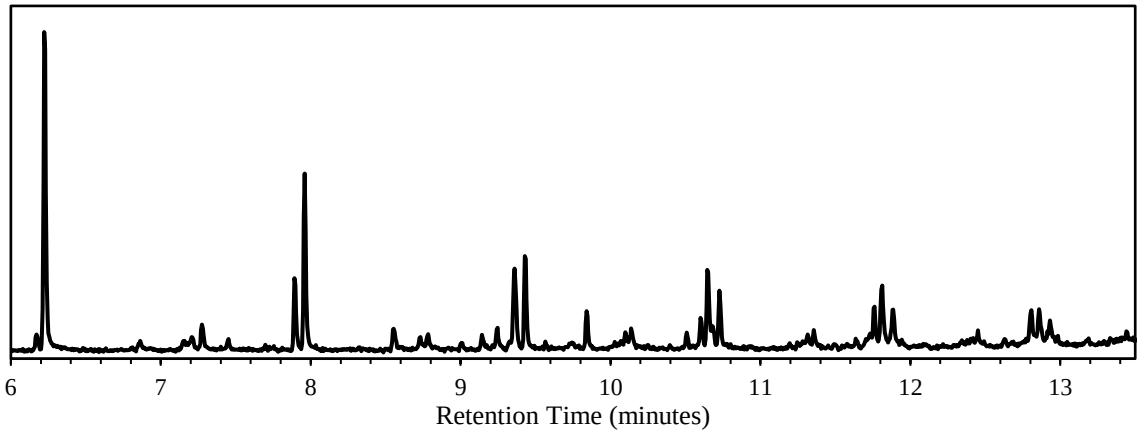

Figure 3.9. Gas Chromatogram of liquid products for Table 3.1, Entry 14.

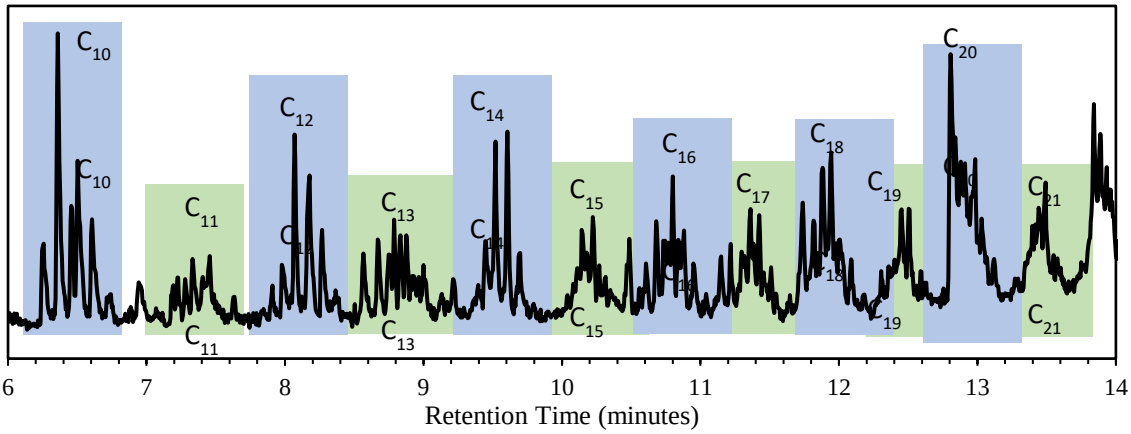

Figure 3.10. Gas Chromatogram of liquid products for Table 3.4, Entry 3.

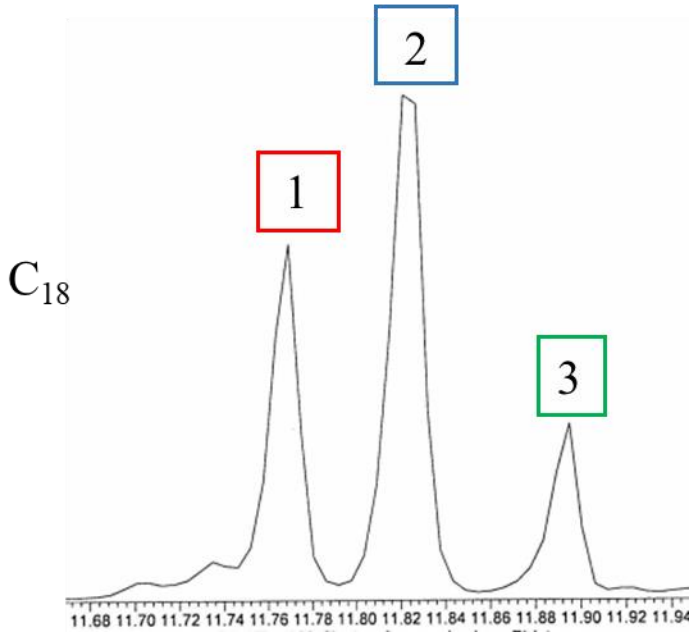

Figure 3.11. Mass Spectrum Analysis for C_{18} Products. GC Chromatogram of liquid products from Table 3.1, Entry 10 after concentration and removal of solvents, selected region shown only for C_{18} products.

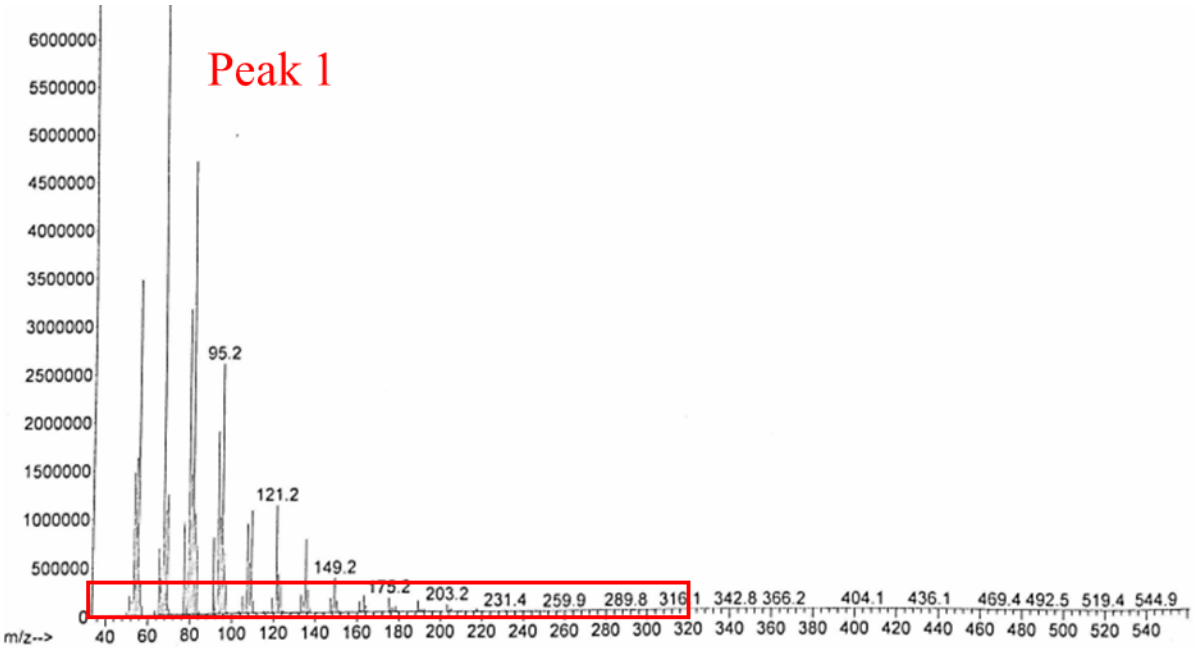

Figure 3.12. Full mass spectrum corresponding to Figure 3.11, peak 1. Zoom in for selected region indicated with red box and shown in Figure 3.15.

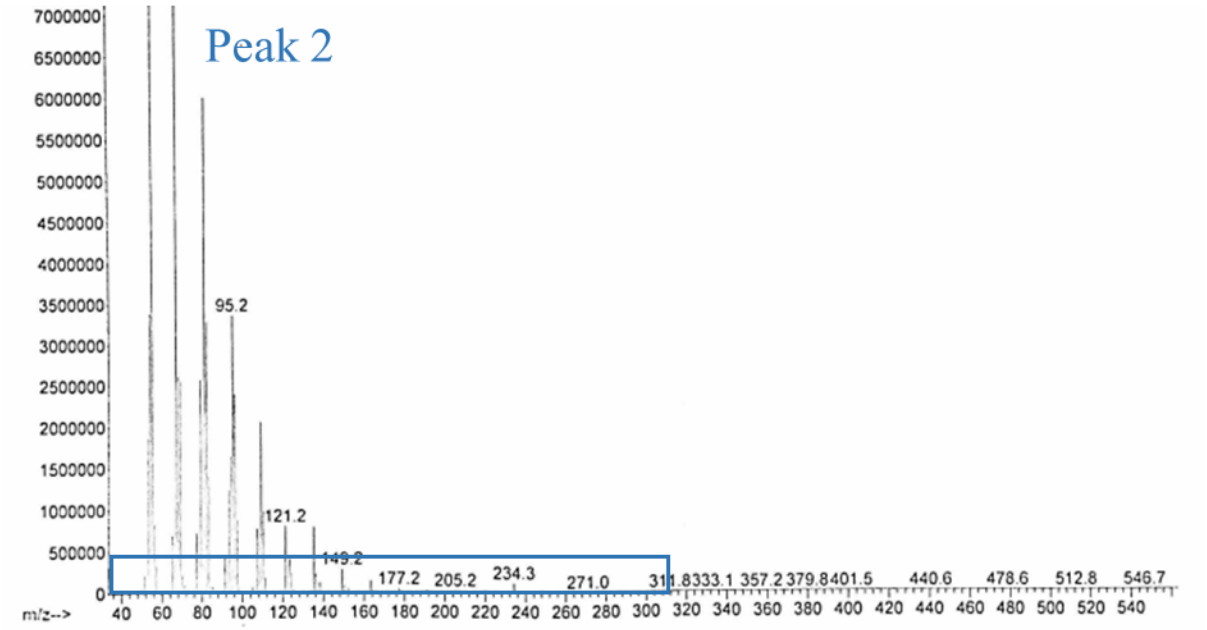

Figure 3.13. Full mass spectrum corresponding to Figure 3.11, peak 2. Zoom in for selected region indicated with blue box and shown in Figure 3.16.

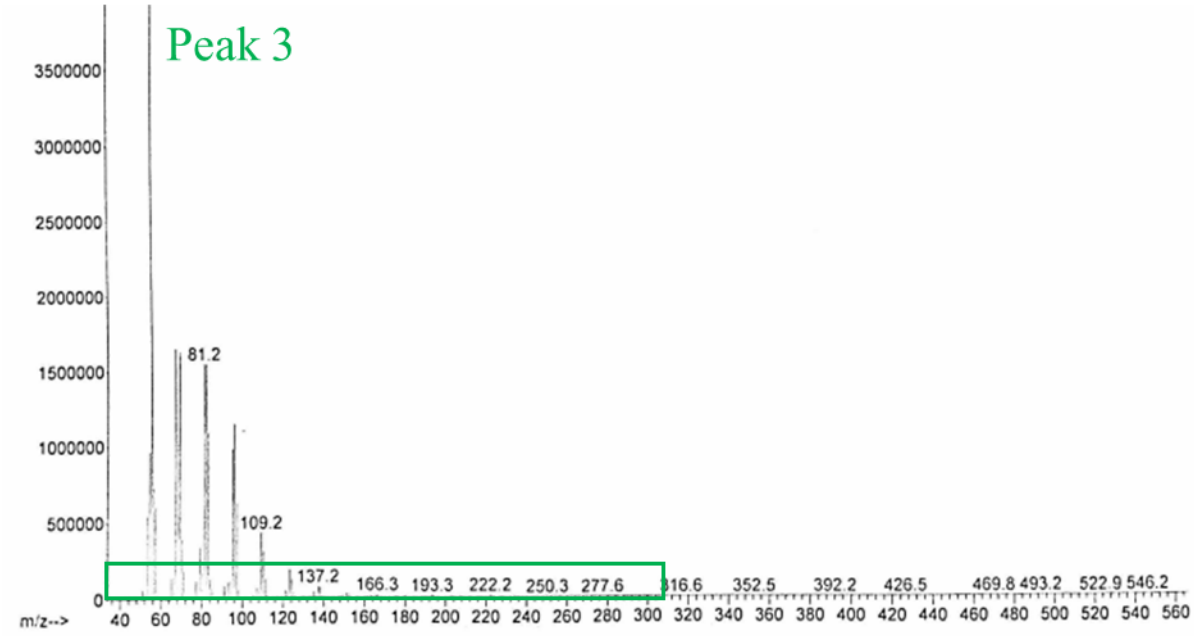

Figure 3.14. Full mass spectrum corresponding to Figure 3.11, peak 3. Zoom in for selected region indicated with red box and shown in Figure 3.17.

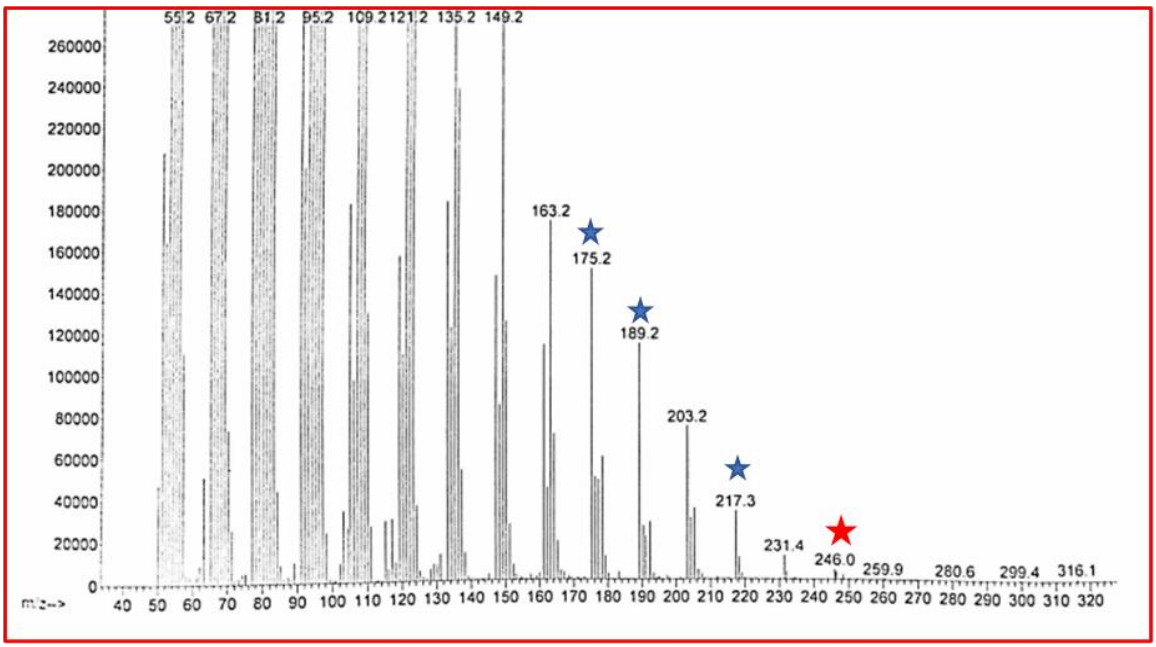

Figure 3.15. Selected region of mass corresponding to Figure 3.11, peak 1. Molecular ion peak indicated with red star. Molecular fragments which differ from molecular fragments in adjacent peak (Peak 2, Figure 3.16) by 2 mass units indicated with blue stars.

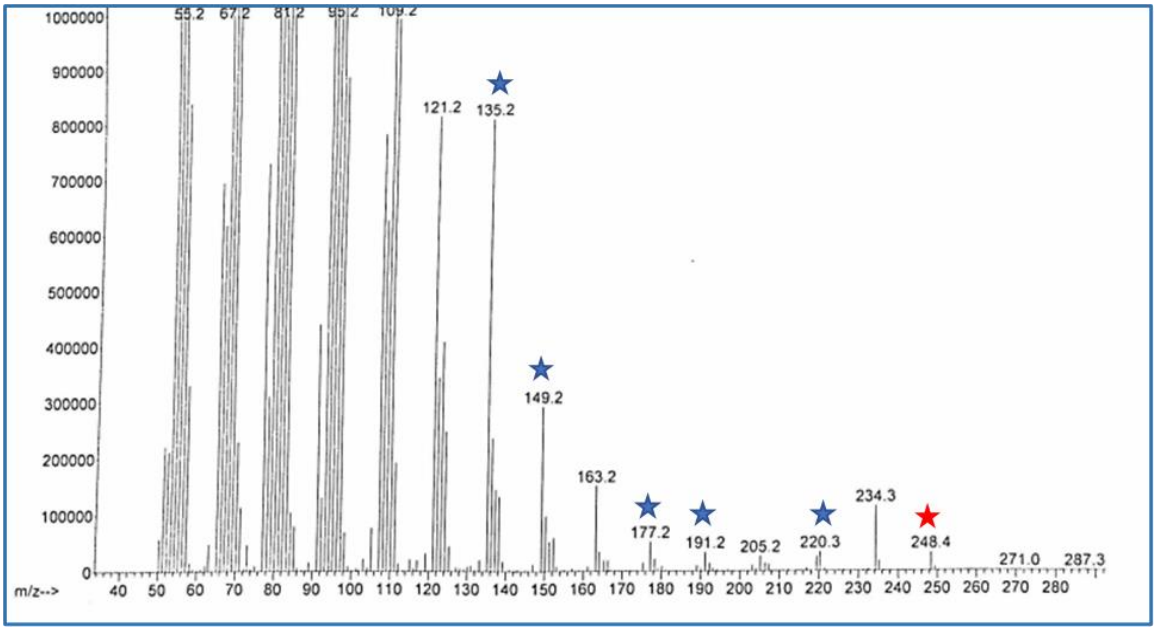

Figure 3.16. Selected region of mass corresponding to Figure 3.11, peak 2. Molecular ion peak indicated with red star. Molecular fragments which differ from molecular fragments in adjacent peaks (Peak 1, Figure 3.15 or Peak 3, Figure 3.17) by 2 mass units indicated with blue stars.

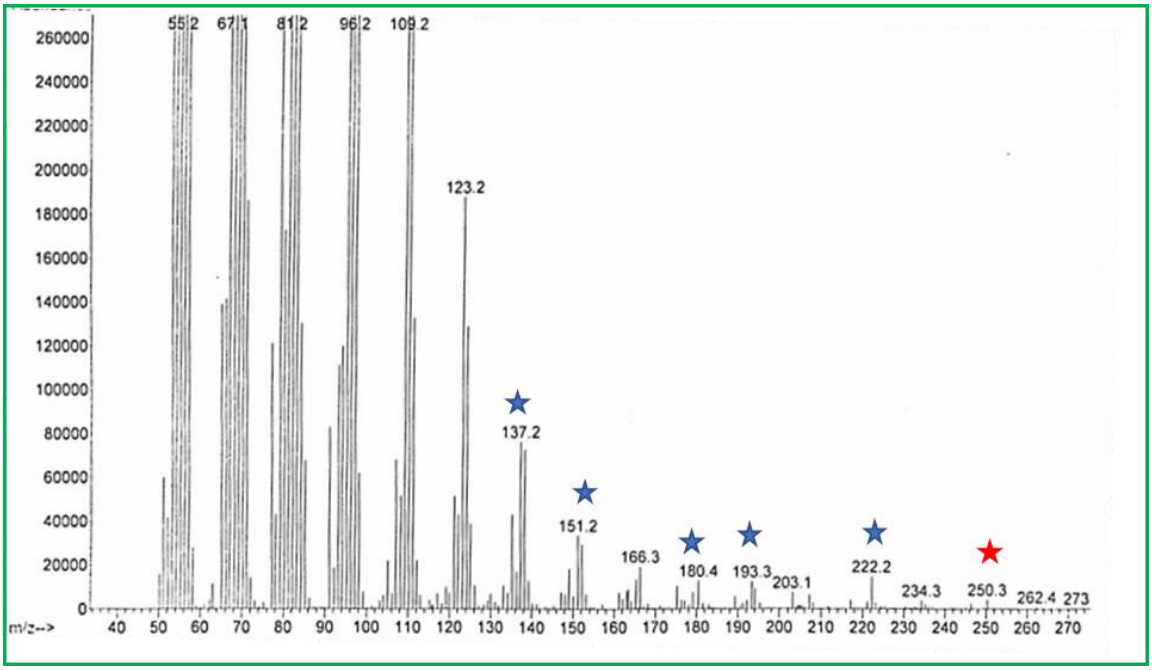

Figure 3.17. Selected region of mass corresponding to Figure 3.11, peak 3. Molecular ion peak indicated with red star. Molecular fragments which differ from molecular fragments in adjacent peak (Peak 2, Figure 3.16) by 2 mass units indicated with blue stars.

^{1}H and ^{13}C NMR Spectra of Copolymers A, B, and C

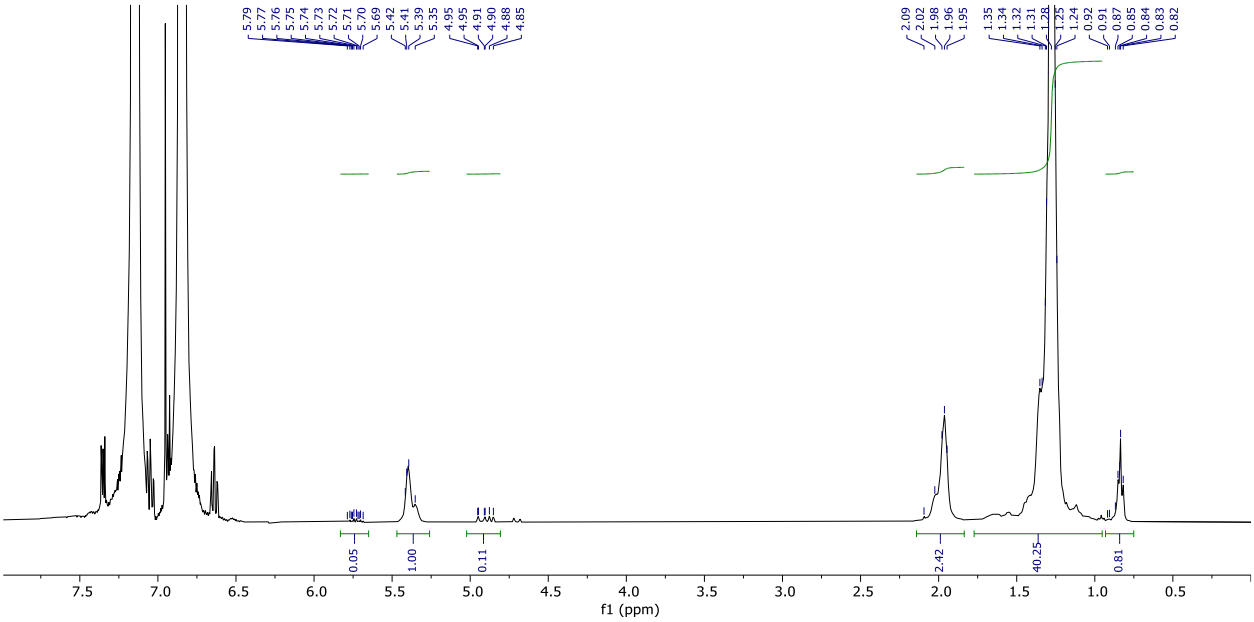

Figure 3.18. ^{1}H NMR analysis at 120 °C (80% 1,2 dichlorobenzene, 20% benzene-d_6) of ethylene/butadiene copolymer A.

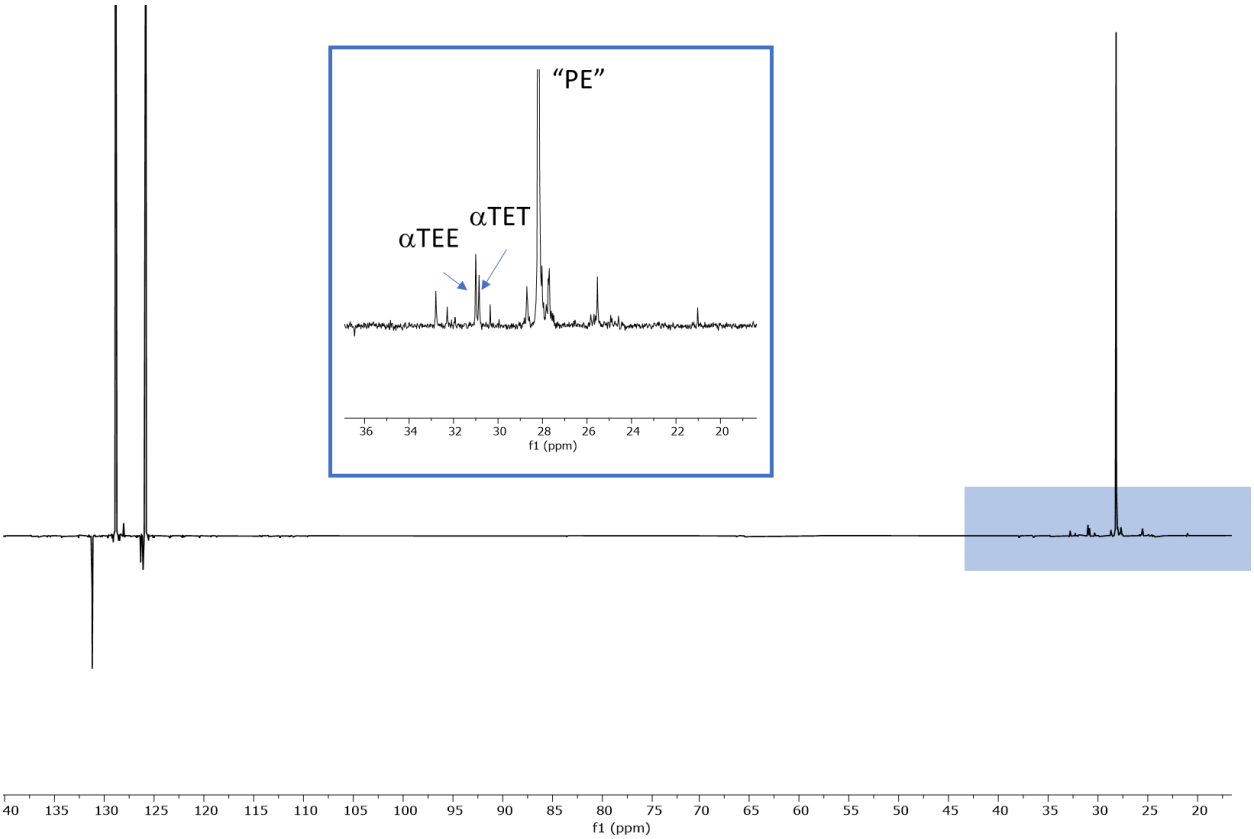

Figure 3.19. ^{13}C NMR (APT) analysis at 120 °C (80% 1,2 dichlorobenzene, 20% benzene-d_6) of ethylene/butadiene copolymer A.

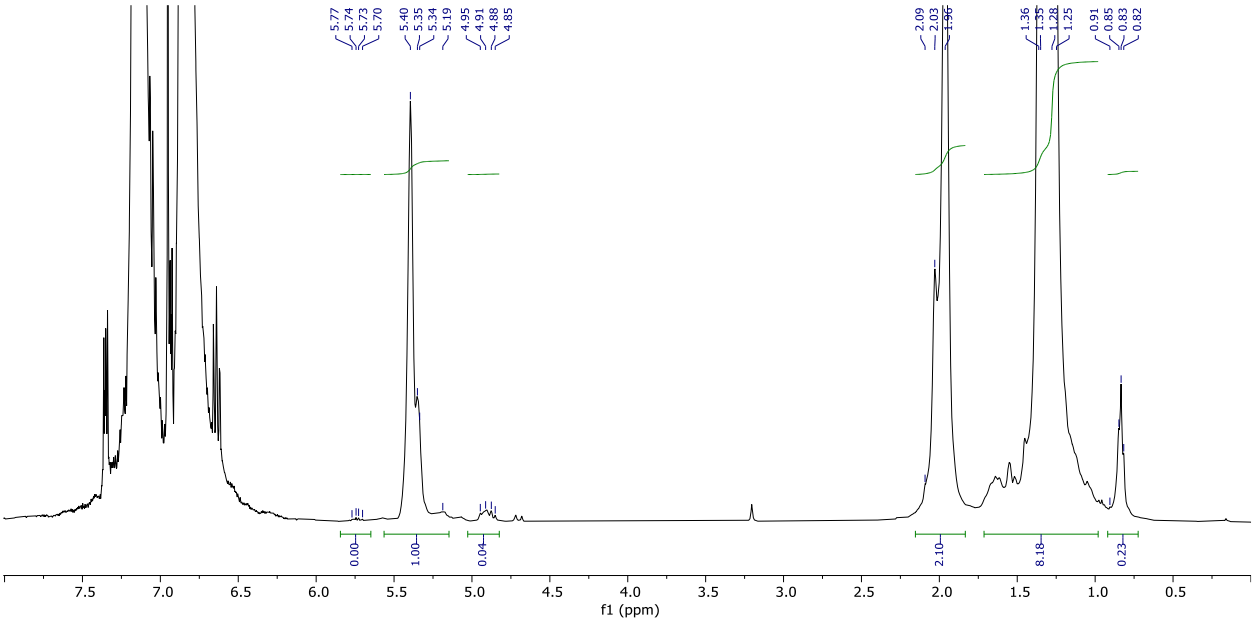

Figure 3.20. ^{1}H NMR analysis at 120 ºC (80% 1,2 dichlorobenzene, 20% benzene-d_6) of ethylene/butadiene copolymer B.

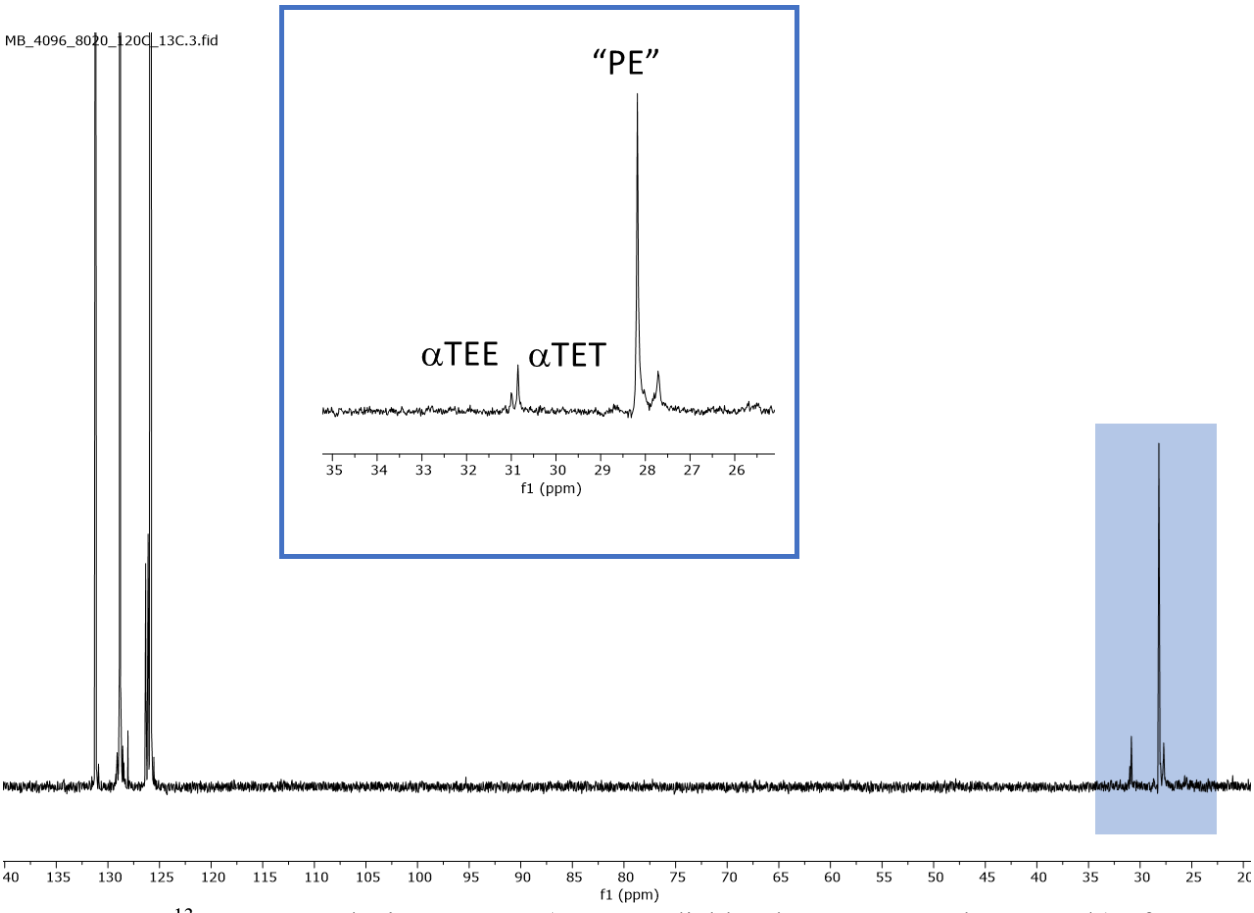

Figure 3.21. ^{13}C NMR analysis at 120 ºC (80% 1,2 dichlorobenzene, 20% benzene-d_6) of ethylene/butadiene copolymer B.

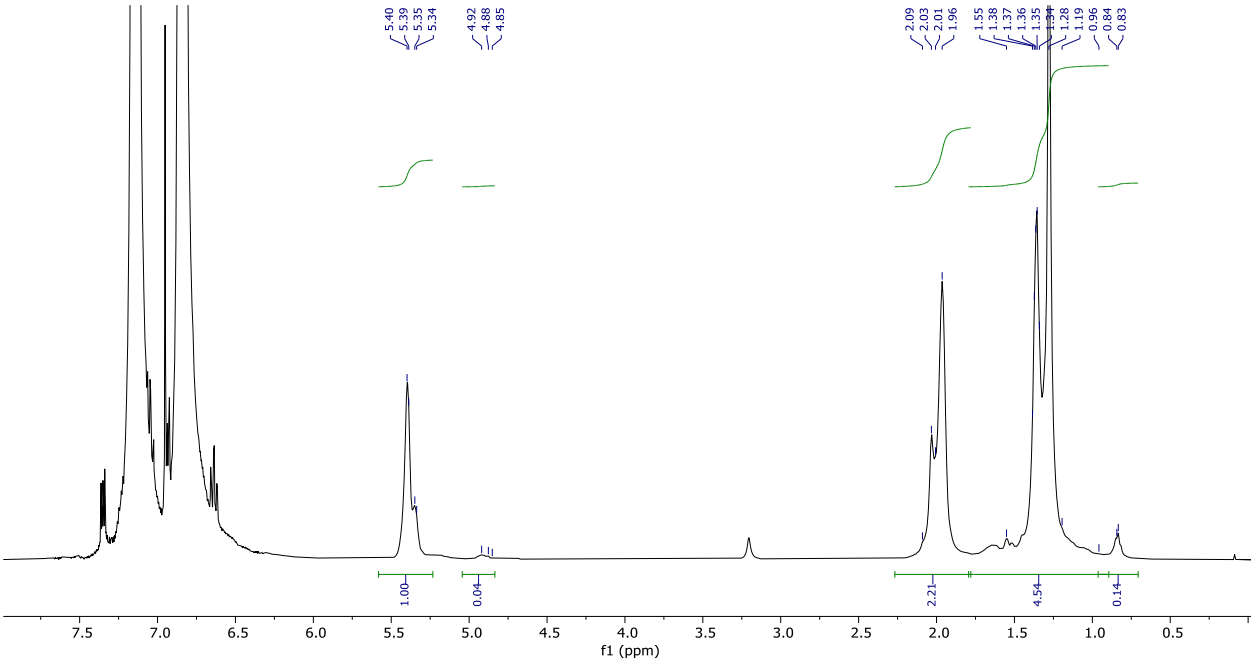

Figure 3.22. ^{1}H NMR analysis at 120 ºC (80% 1,2 dichlorobenzene, 20% benzene-d_6) of ethylene/butadiene copolymer C.

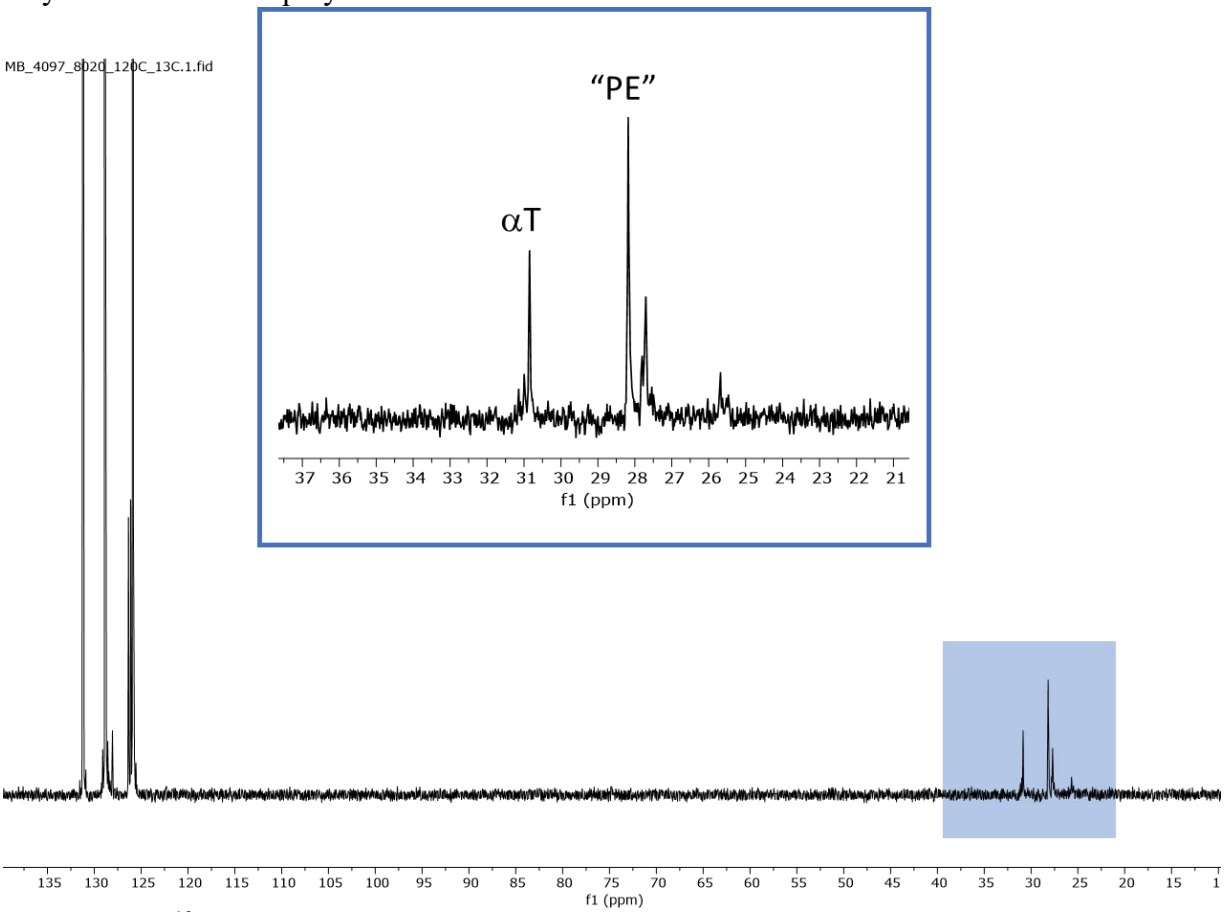

Figure 3.23. ^{13}C NMR analysis at 120 ºC (80% 1,2 dichlorobenzene, 20% benzene-d_6) of ethylene/butadiene copolymer C.

^{1}H NMR Spectra and selected ^{13}C NMR Spectra of Material after Ethenolysis

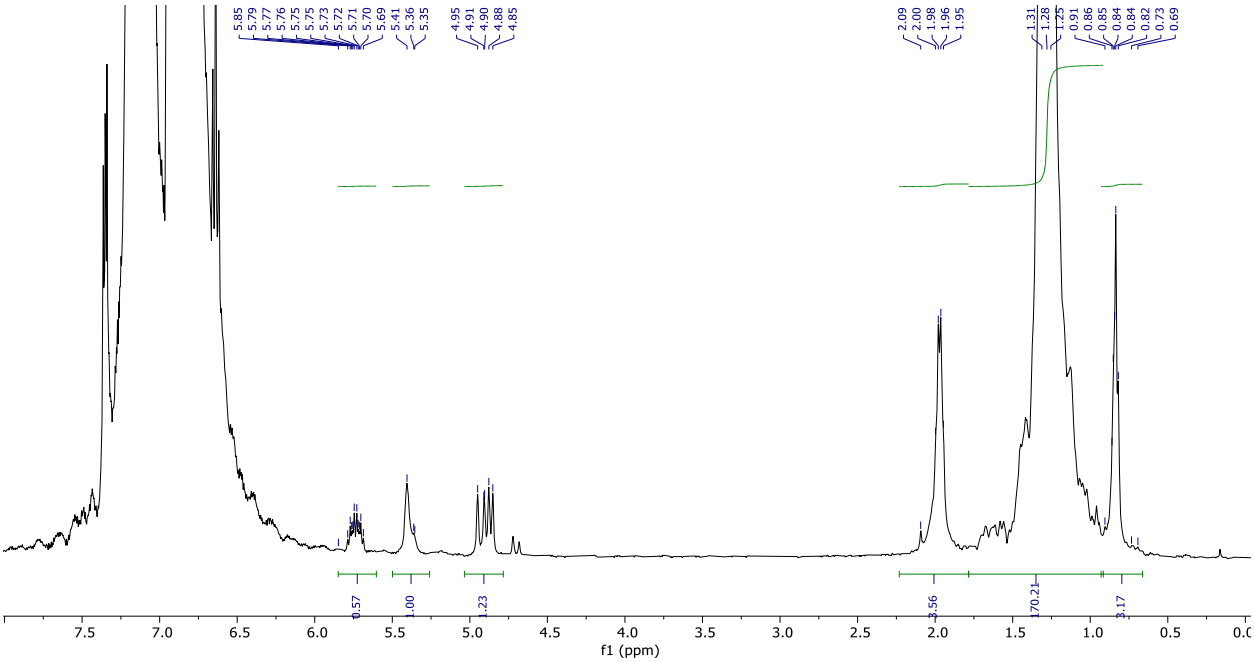

Figure 3.24. ^{1}H NMR analysis at 120 ºC (80% 1,2 dichlorobenzene, 20% benzene-d_6) of olefins in the insoluble fraction of the reaction mixture after ethenolysis (Table 3.1, Entry 2).

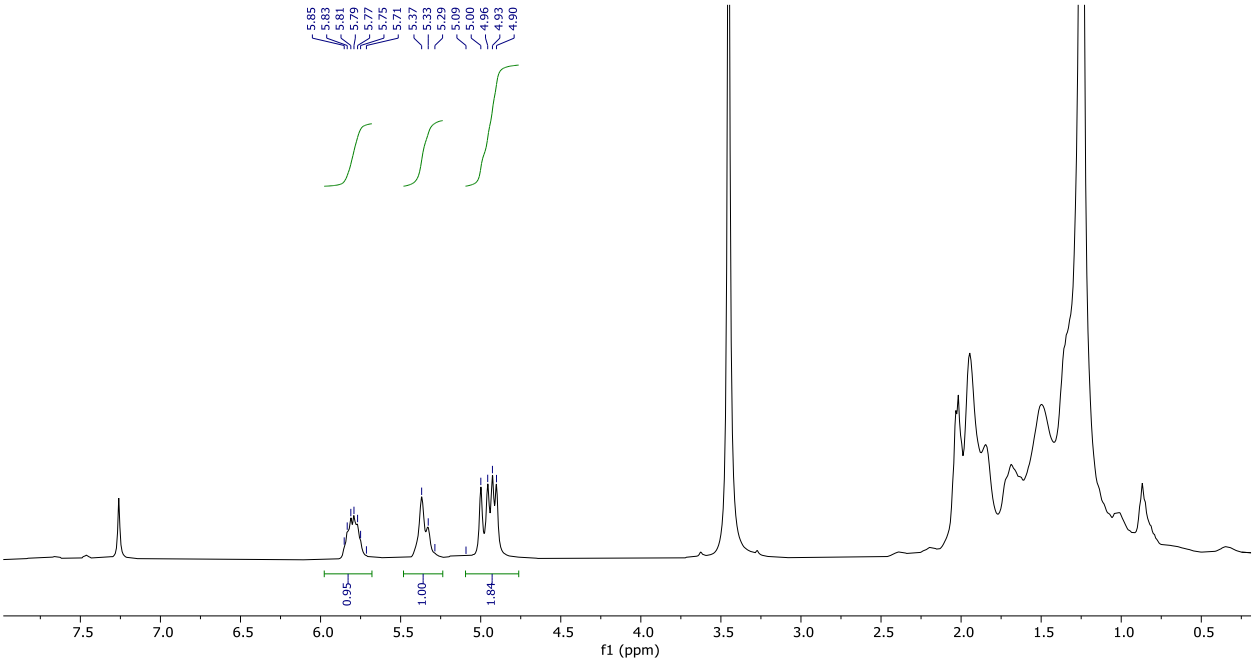

Figure 3.25. ^{1}H NMR analysis at RT ($CDCl_3$) of olefins concentrated *in vacuo* in the soluble fraction of the reaction mixture after ethenolysis (Table 3.1, Entry 2).

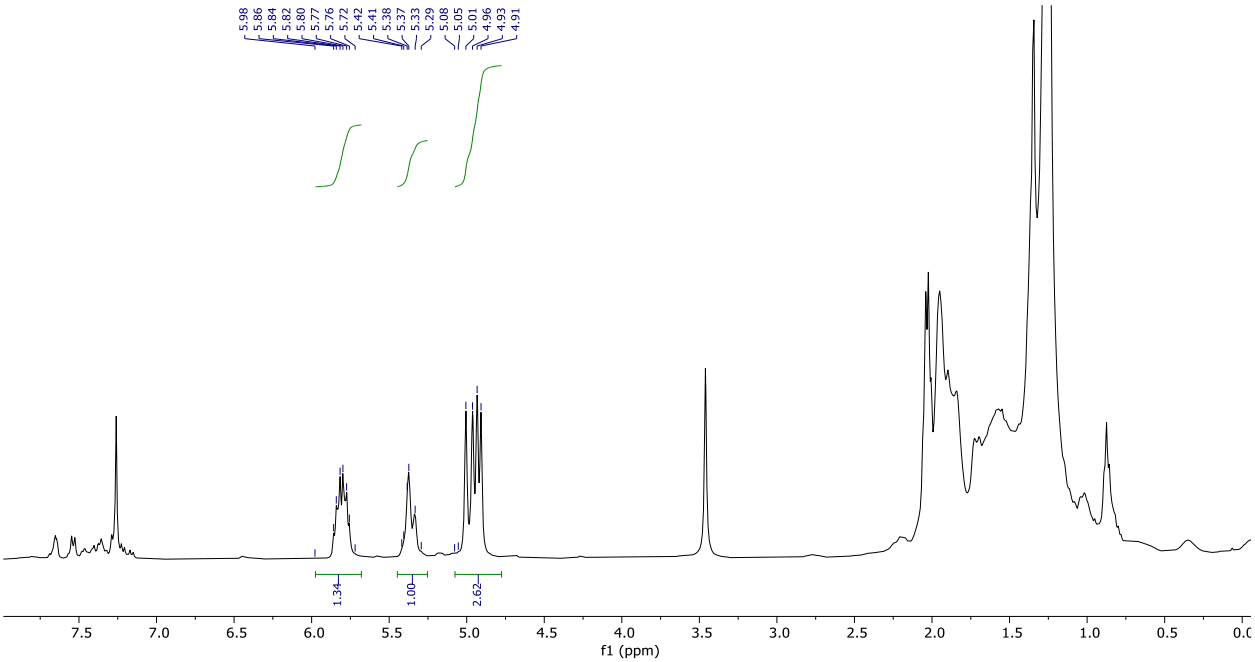

Figure 3.26. ^{1}H NMR analysis at RT ($CDCl_3$) of olefins concentrated *in vacuo* in the soluble fraction of the reaction mixture after ethenolysis (Table 1, Entry 3).

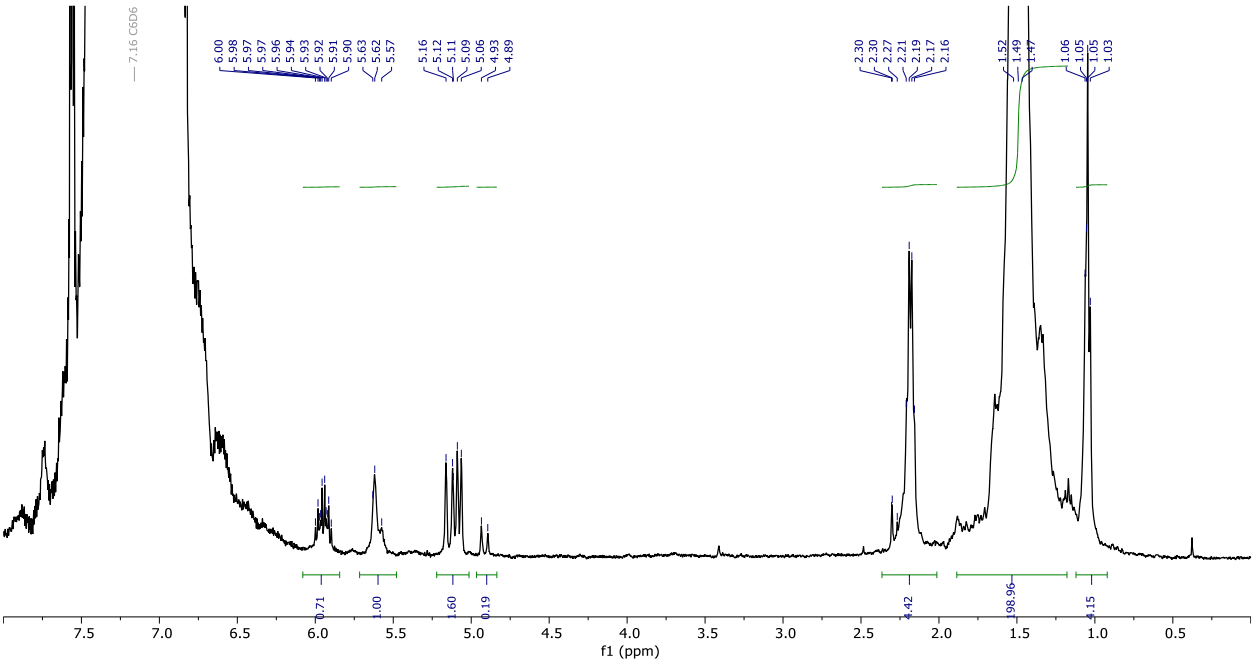

Figure 3.27. ^{1}H NMR analysis at 120 ºC (80% 1,2 dichlorobenzene, 20% benzene-d_6) of olefins in the insoluble fraction of the reaction mixture after ethenolysis (Table 3.1, Entry 4).

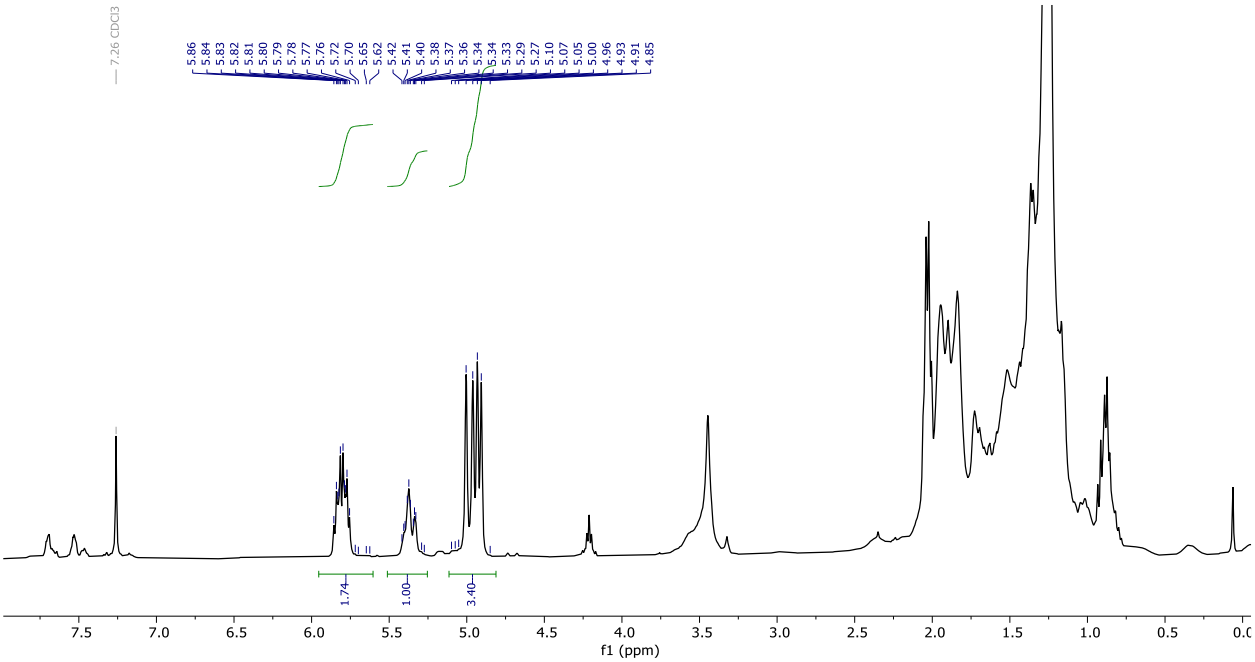

Figure 3.28. ^{1}H NMR analysis at RT ($CDCl_3$) of olefins concentrated *in vacuo* in the soluble fraction of the reaction mixture after ethenolysis (Table 3.1, Entry 4).

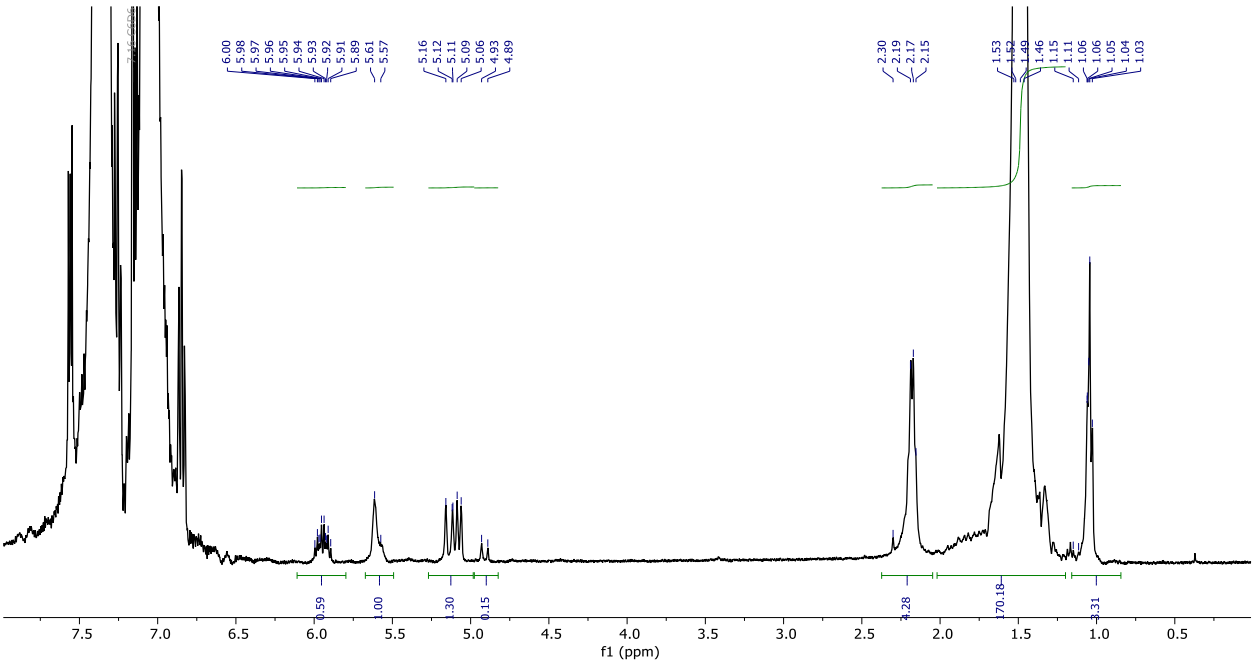

Figure 3.29. ^{1}H NMR analysis at 120 ºC (80% 1,2 dichlorobenzene, 20% benzene-d_6) of olefins in the insoluble fraction of the reaction mixture after ethenolysis (Table 3.1 , Entry 6).

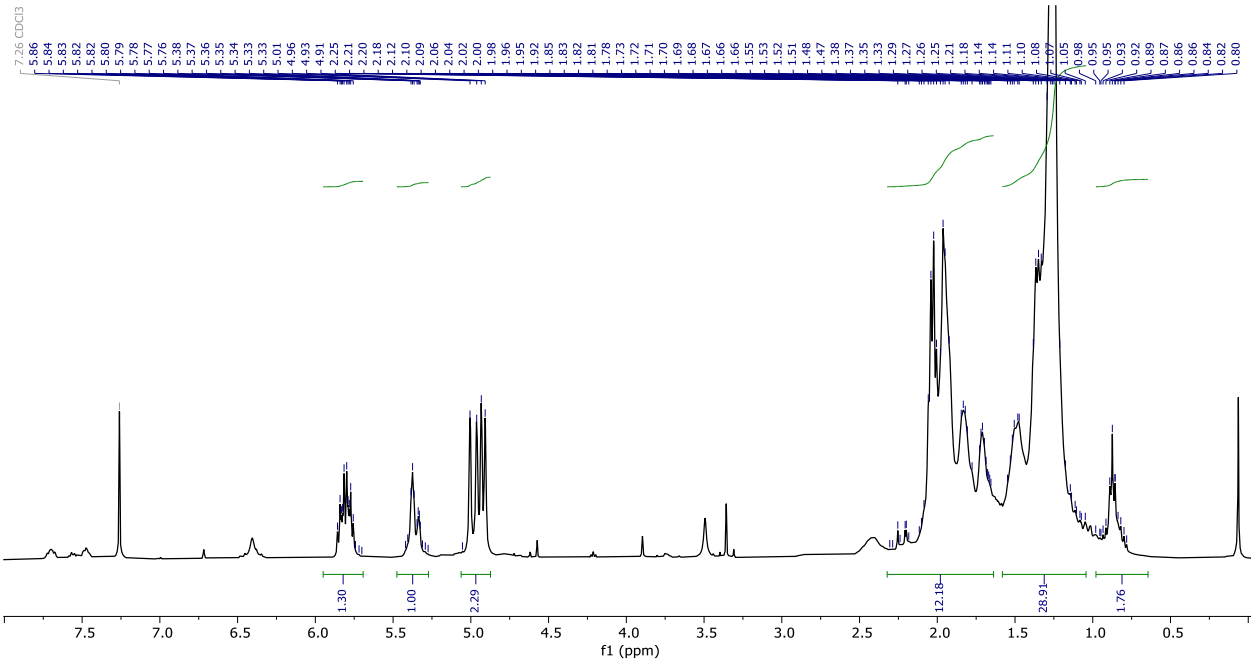

Figure 3.30. ^{1}H NMR analysis at RT ($CDCl_3$) of olefins concentrated *in vacuo* in the soluble fraction of the reaction mixture after ethenolysis (Table 3.1, Entry 6).

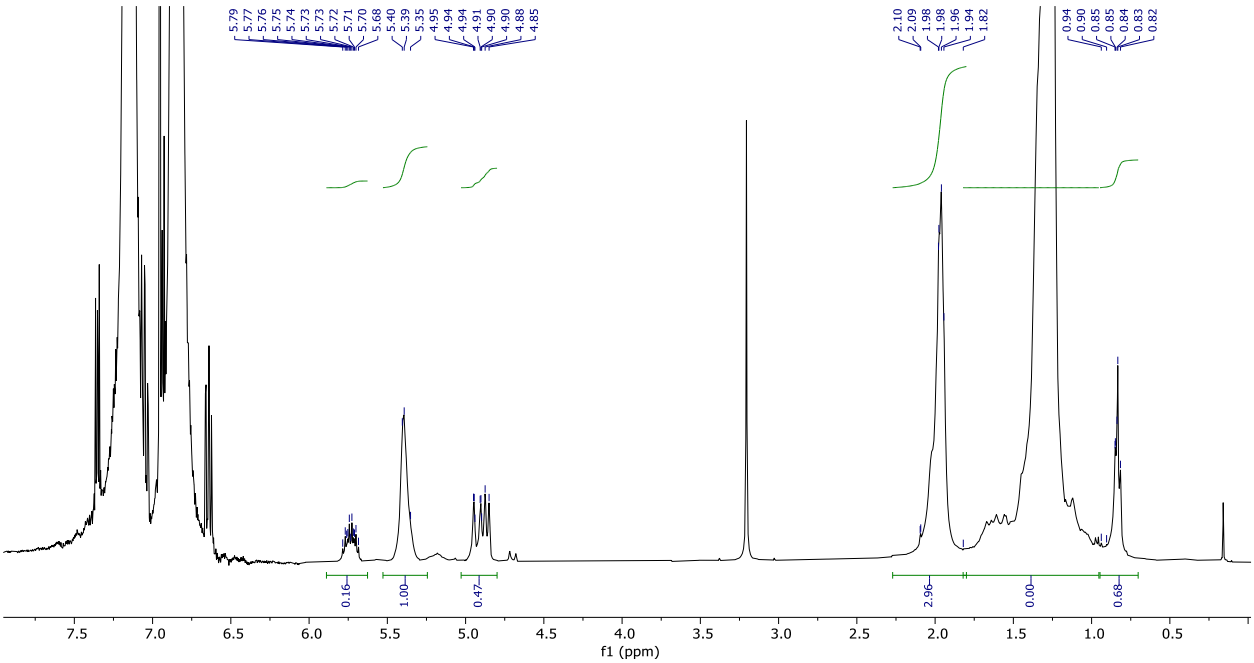

Figure 3.31. ^{1}H NMR analysis at 120 ºC (80% 1,2 dichlorobenzene, 20% benzene-d_6) of olefins in the insoluble fraction of the reaction mixture after ethenolysis (Table 3.1, Entry 8).

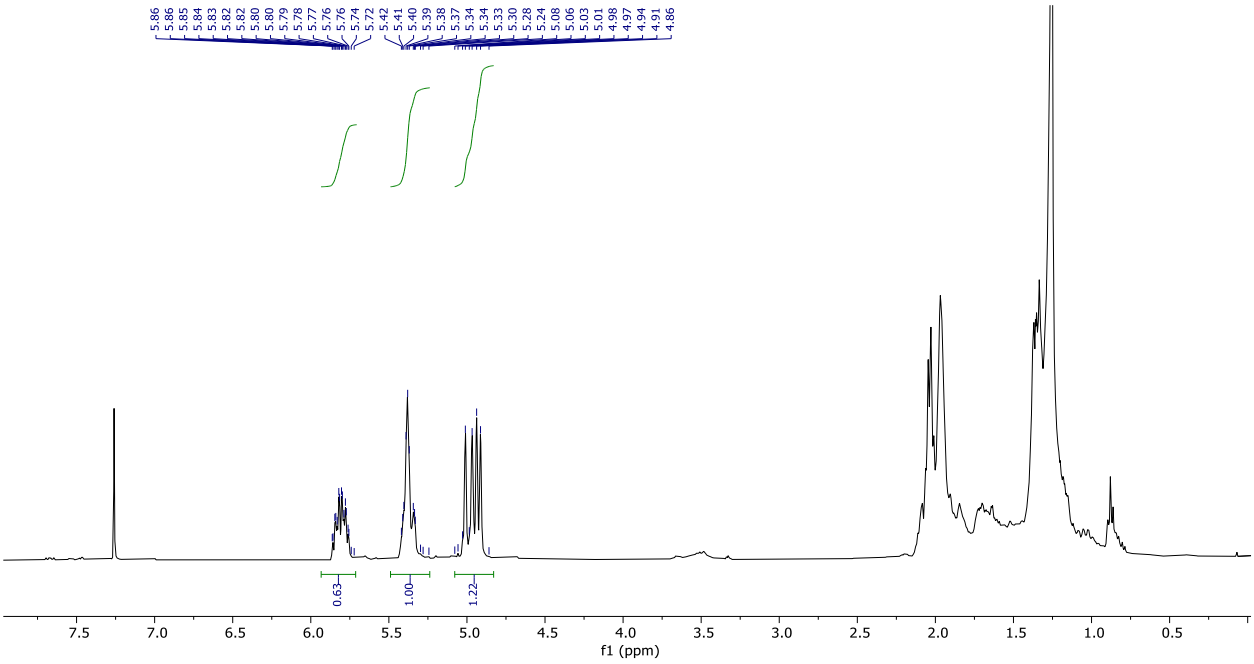

Figure 3.32. ^{1}H NMR analysis at RT ($CDCl_3$) of olefins concentrated in vacuo in the soluble fraction of the reaction mixture after ethenolysis (Table 3.1, Entry 8).

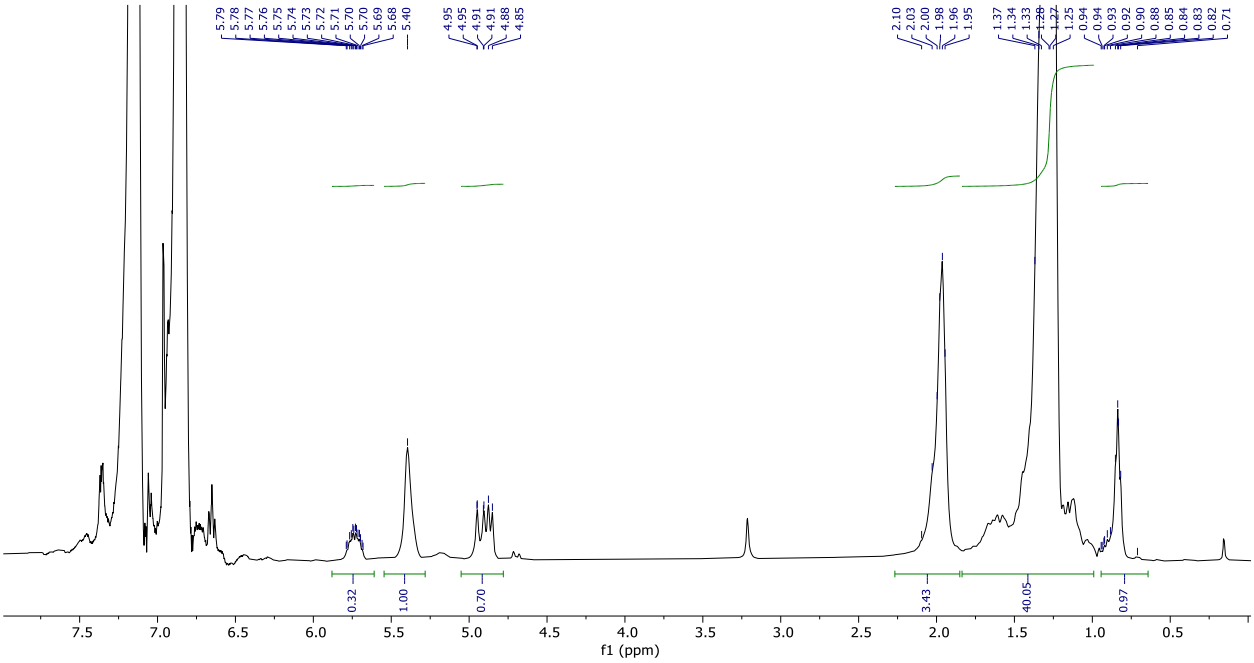

Figure 3.33. ^{1}H NMR analysis at 120 ºC (80% 1,2 dichlorobenzene, 20% benzene-d_6) of olefins in the insoluble fraction of the reaction mixture after ethenolysis (Table 3.1, Entry 9).

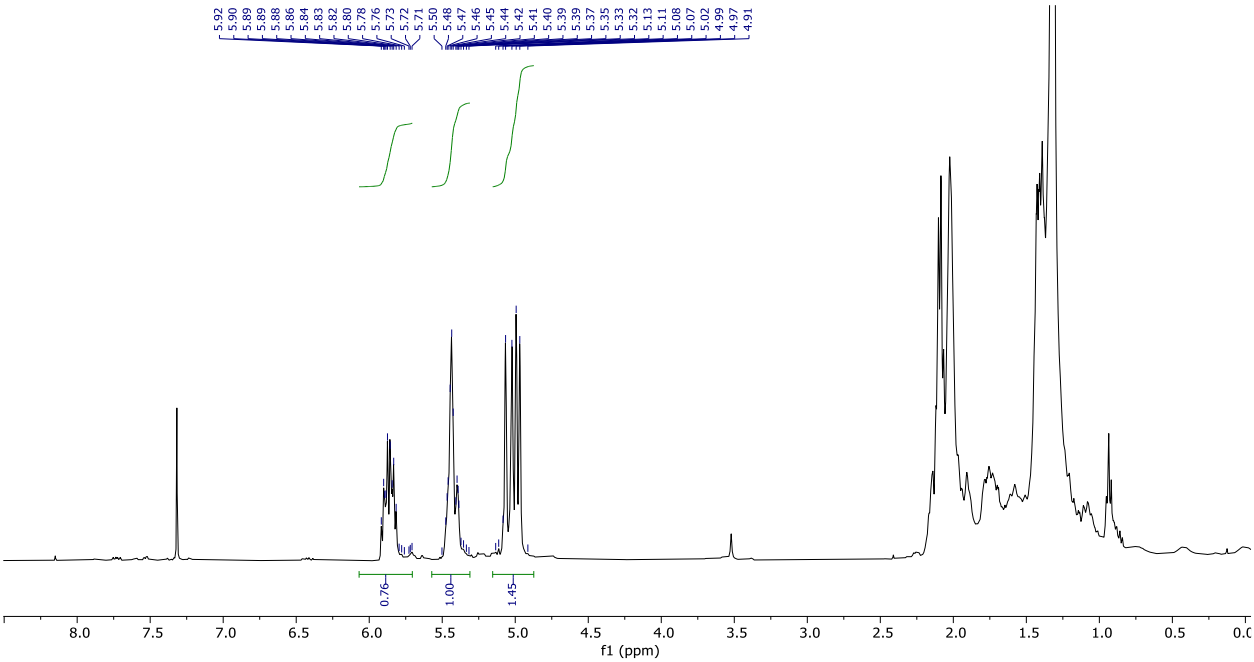

Figure 3.34. ^{1}H NMR analysis at RT ($CDCl_3$) of olefins concentrated in vacuo in the soluble fraction of the reaction mixture after ethenolysis (Table 3.1, Entry 9).

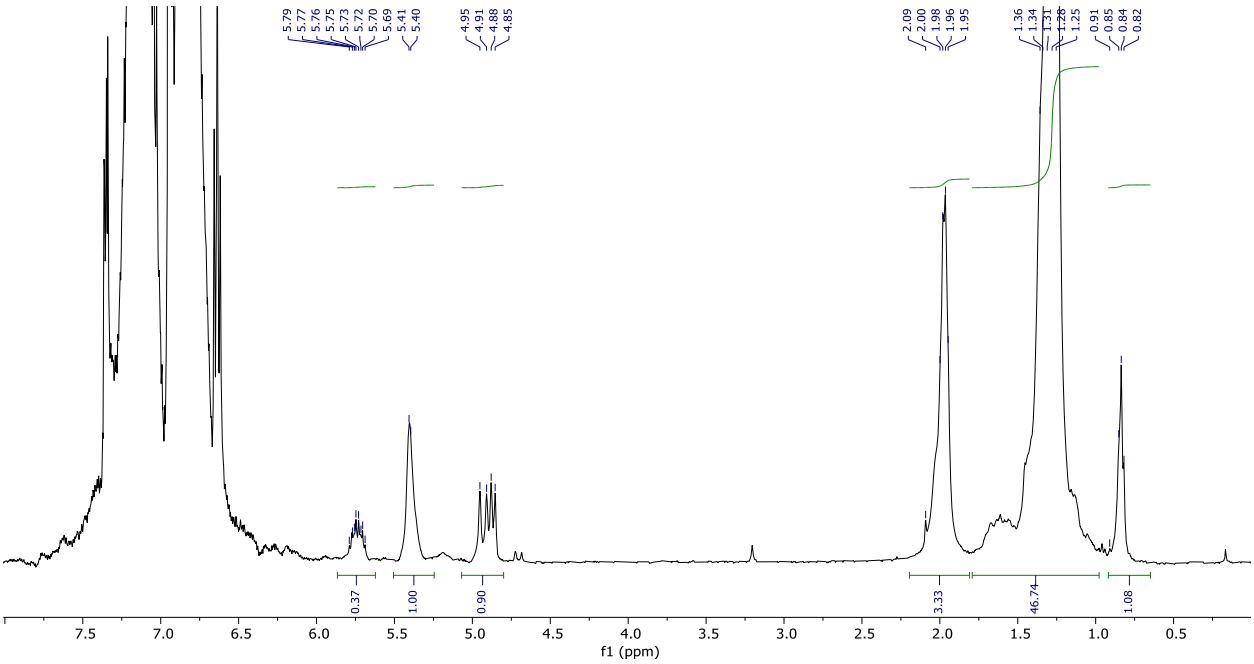

Figure 3.35. ^{1}H NMR analysis at 120 ºC (80% 1,2 dichlorobenzene, 20% benzene-d_6) of olefins in the insoluble fraction of the reaction mixture after ethenolysis (Table 3.1, Entry 10).

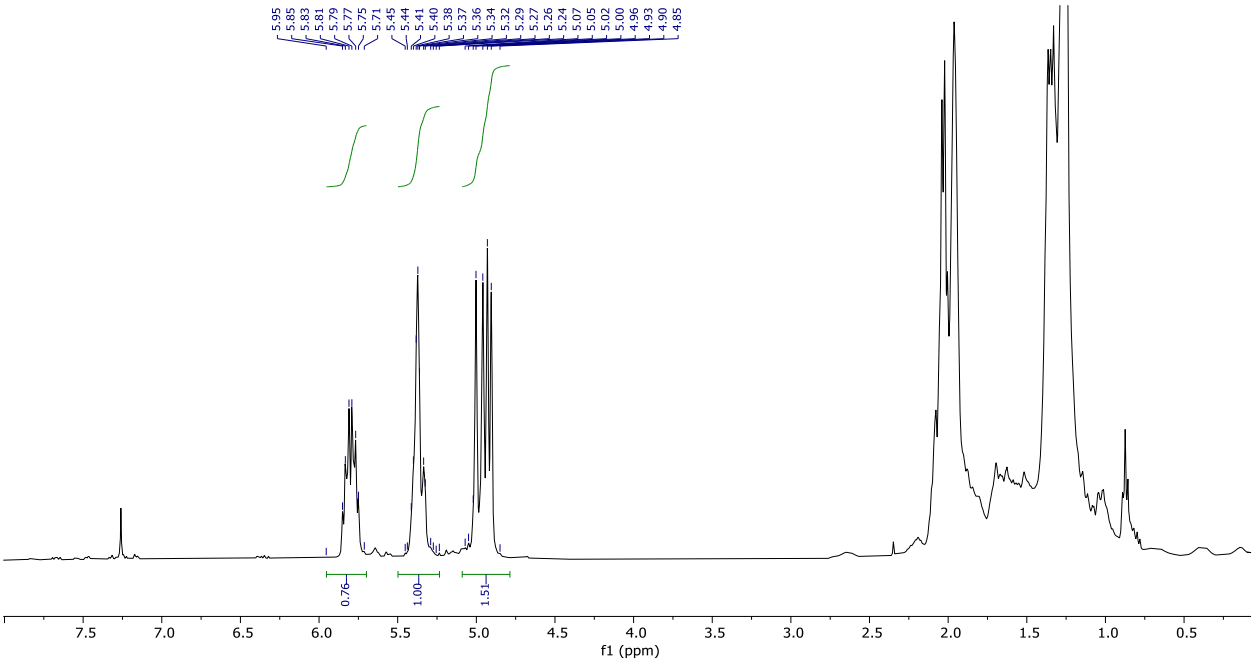

Figure 3.36. ^{1}H NMR analysis at RT ($CDCl_3$) of olefins concentrated in vacuo in the soluble fraction of the reaction mixture after ethenolysis (Table 3.1, Entry 10).

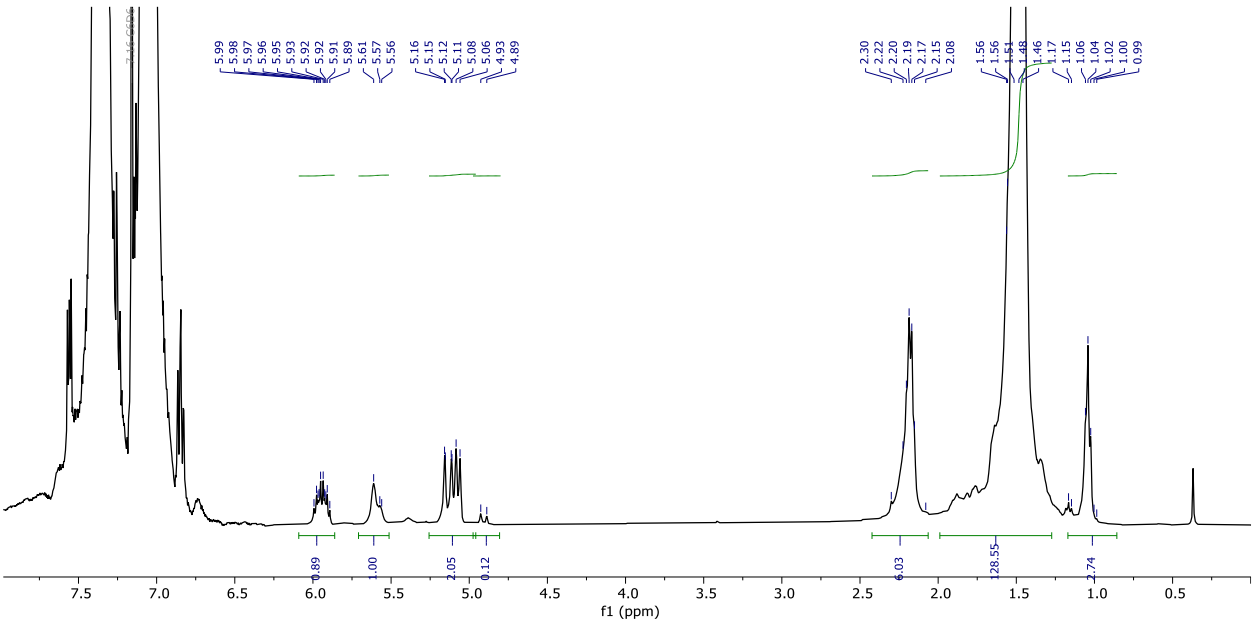

Figure 3.37. ^{1}H NMR analysis at 120 ºC (80% 1,2 dichlorobenzene, 20% benzene-d_6) of olefins in the insoluble fraction of the reaction mixture after ethenolysis (Table 3.1, Entry 11).

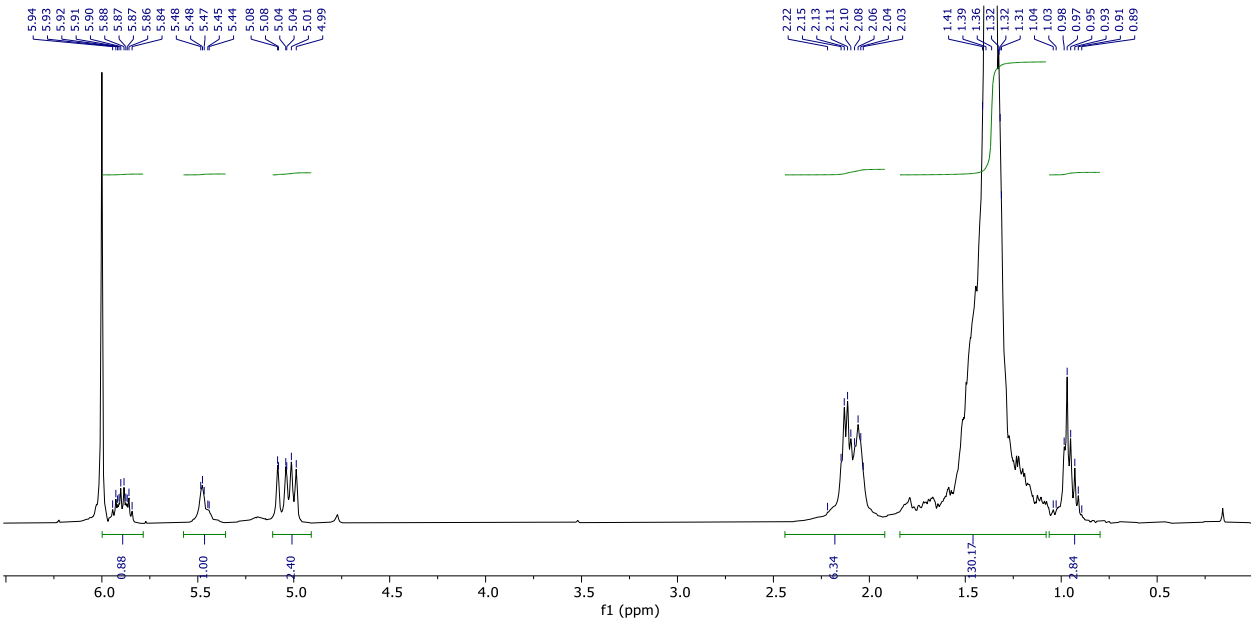

Figure 3.38. ^{1}H NMR analysis at 120 ºC (Tetrachloroethane-d_4) of olefins in the insoluble fraction of the reaction mixture after ethenolysis (Table 3.1, Entry 11).

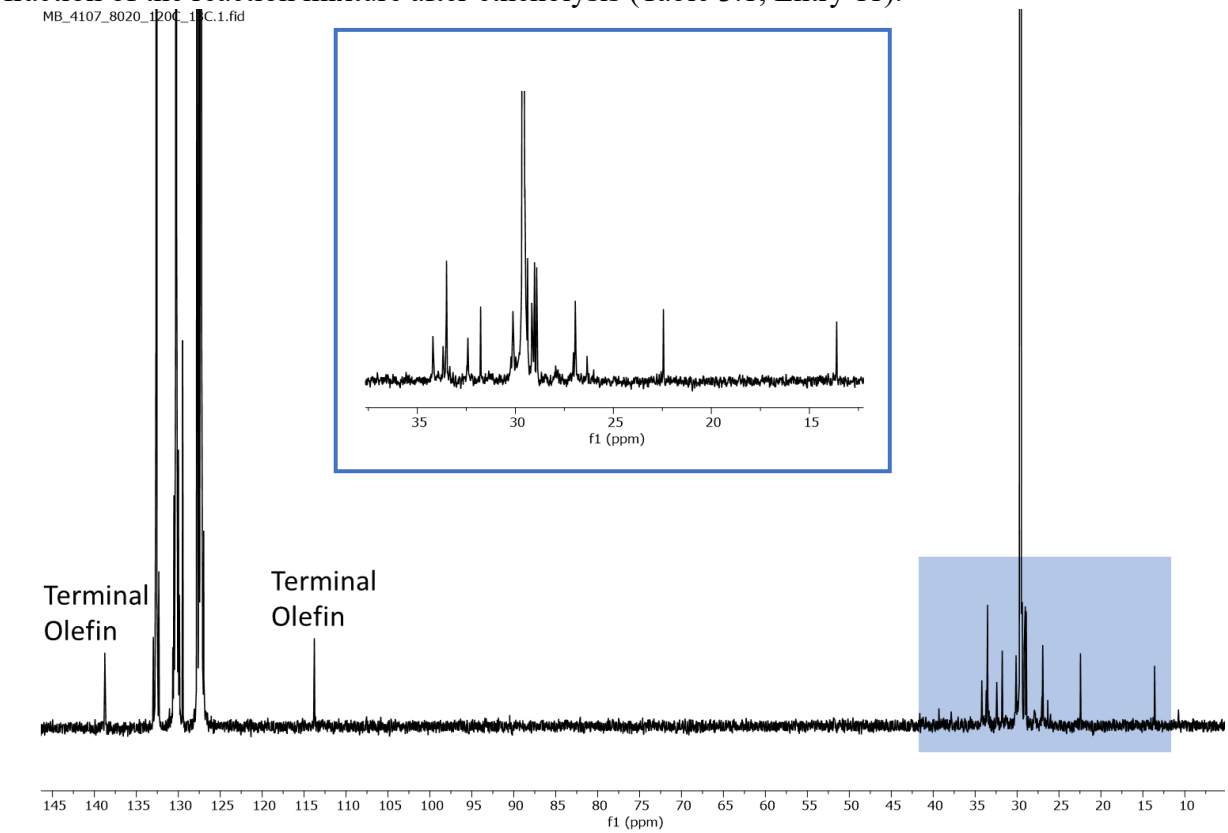

Figure 3.39. ^{13}C NMR analysis at 120 ºC (80% 1,2 dichlorobenzene, 20% benzene-d_6) of olefins in the insoluble fraction of the reaction mixture after ethenolysis (Table 3.1, Entry 11).

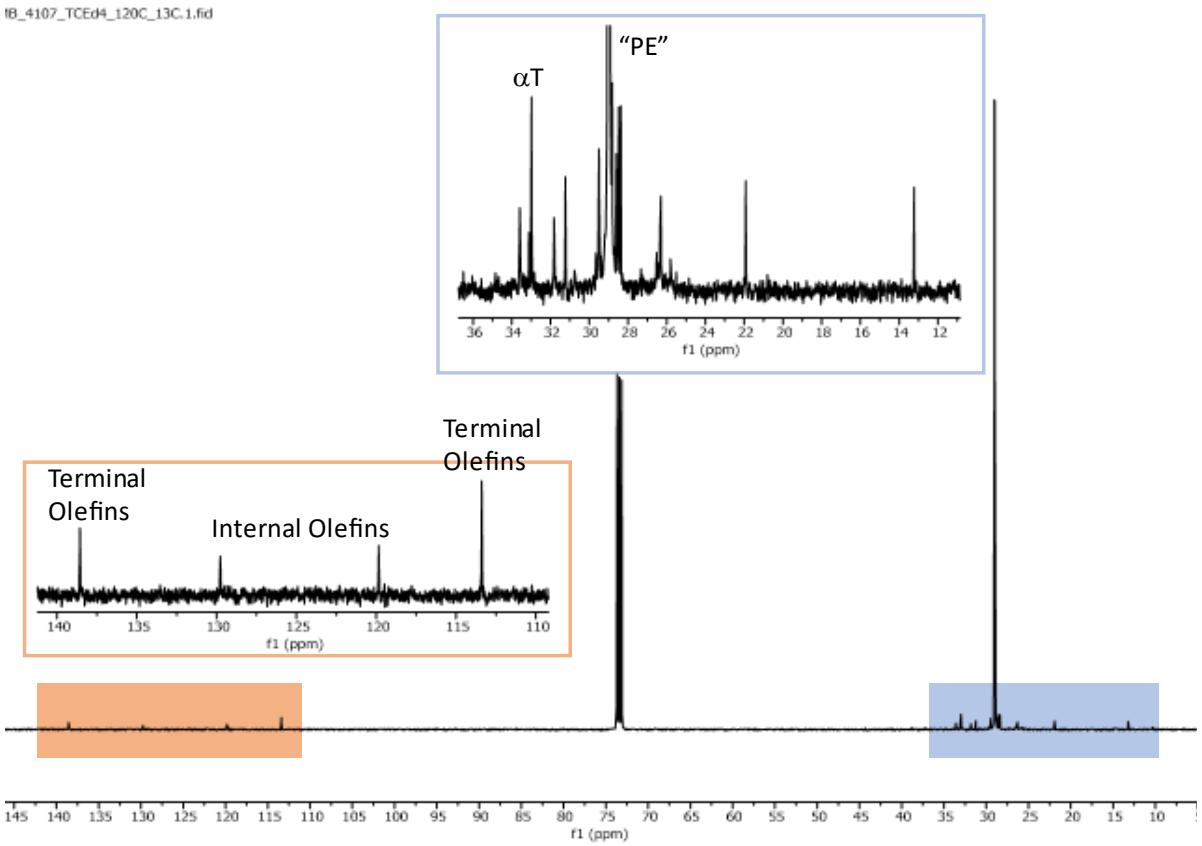

Figure 3.40. ^{13}C NMR analysis at 120 ºC (Tetrachloroethane-d_4) of olefins in the insoluble fraction of the reaction mixture after ethenolysis (Table 3.1, Entry 11).

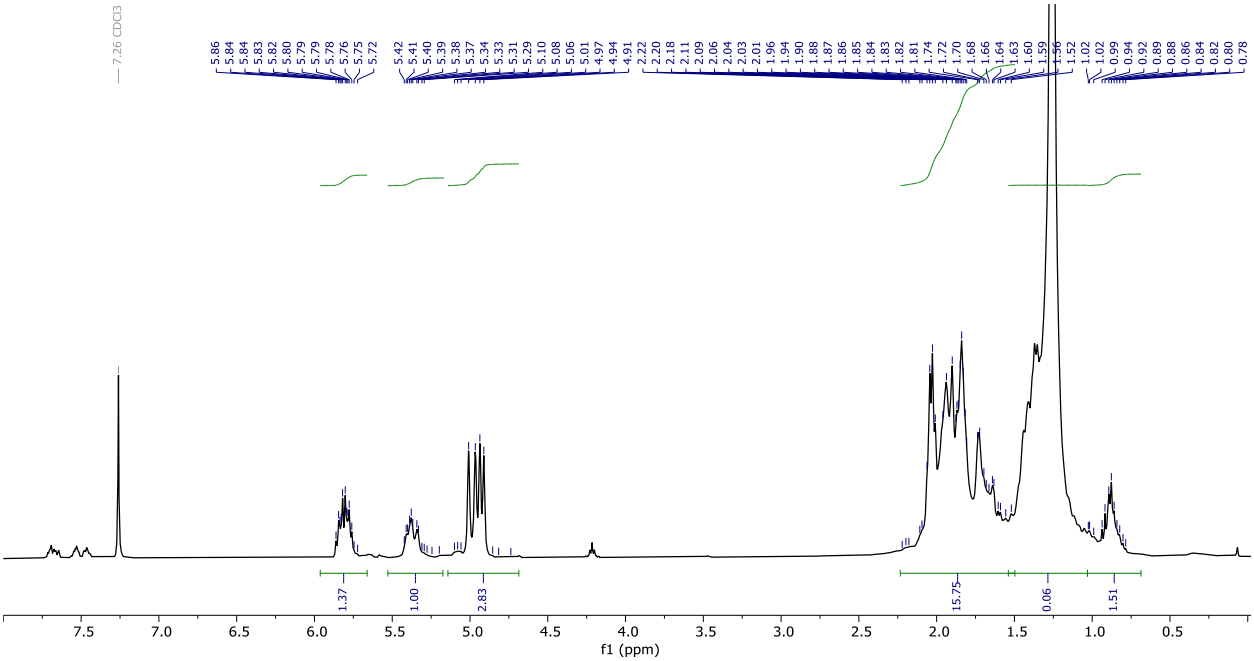

Figure 3.41. ^{1}H NMR analysis at RT ($CDCl_3$) of olefins concentrated in vacuo in the soluble fraction of the reaction mixture after ethenolysis (Table 3.1, Entry 11).

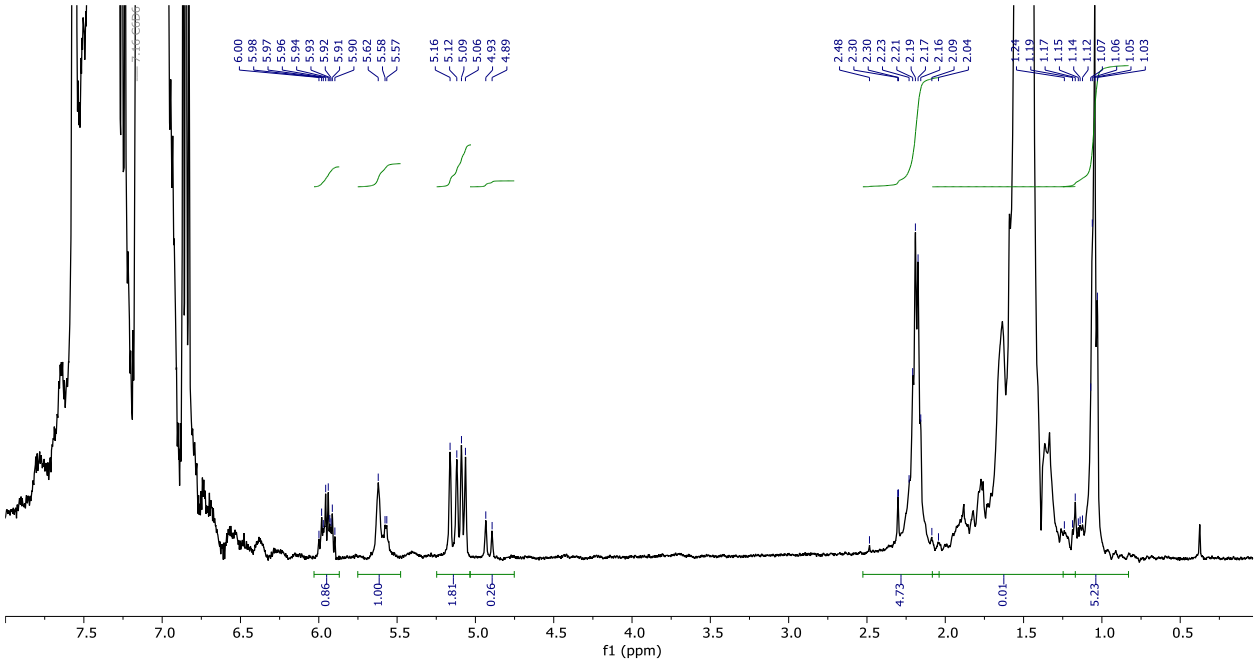

Figure 3.42. ^{1}H NMR analysis at 120 ºC (80% 1,2 dichlorobenzene, 20% benzene-d_6) of olefins in the insoluble fraction of the reaction mixture after ethenolysis (Table 3.1, Entry 12).

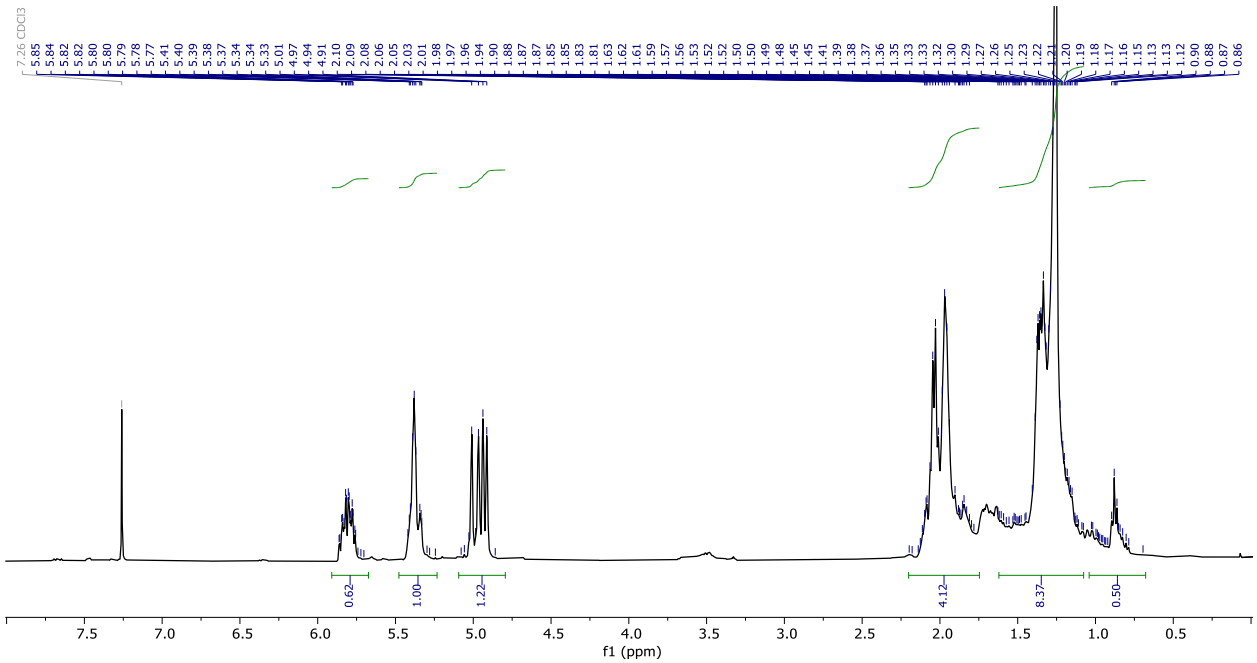

Figure 3.43. ^{1}H NMR analysis at RT ($CDCl_3$) of olefins concentrated in vacuo in the soluble fraction of the reaction mixture after ethenolysis (Table 3.1, Entry 12).

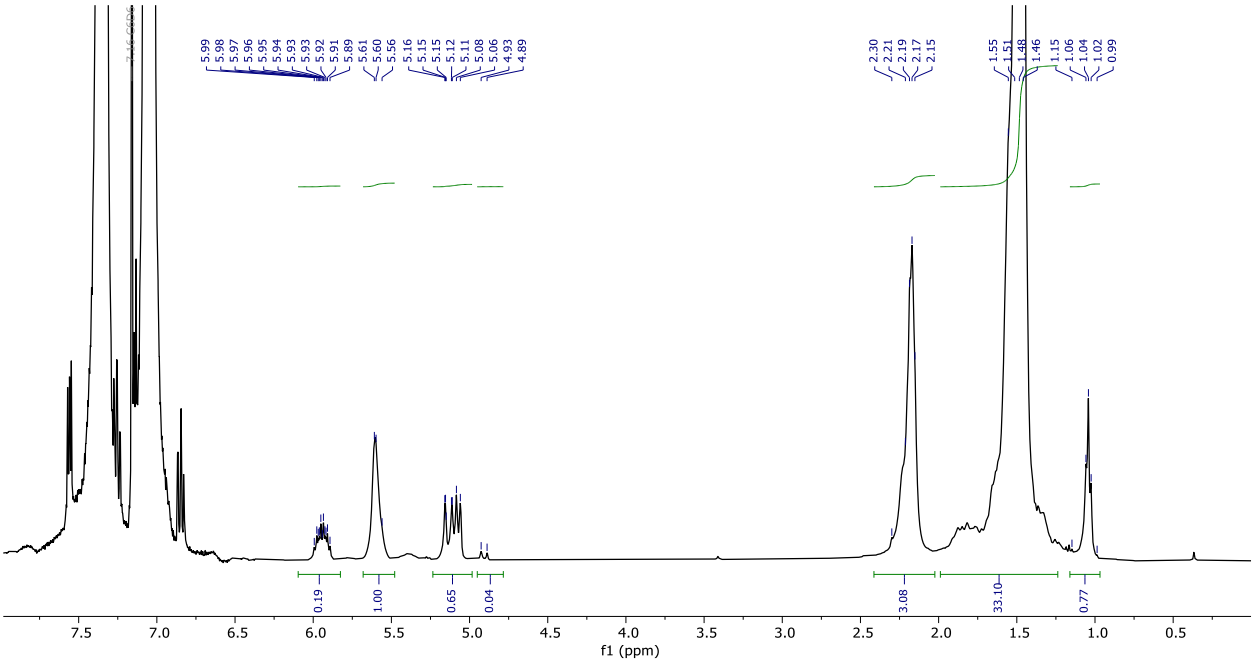

Figure 3.44. ^{1}H NMR analysis at 120 ºC (80% 1,2 dichlorobenzene, 20% benzene-d_6) of olefins in the insoluble fraction of the reaction mixture after ethenolysis (Table 3.1, Entry 13).

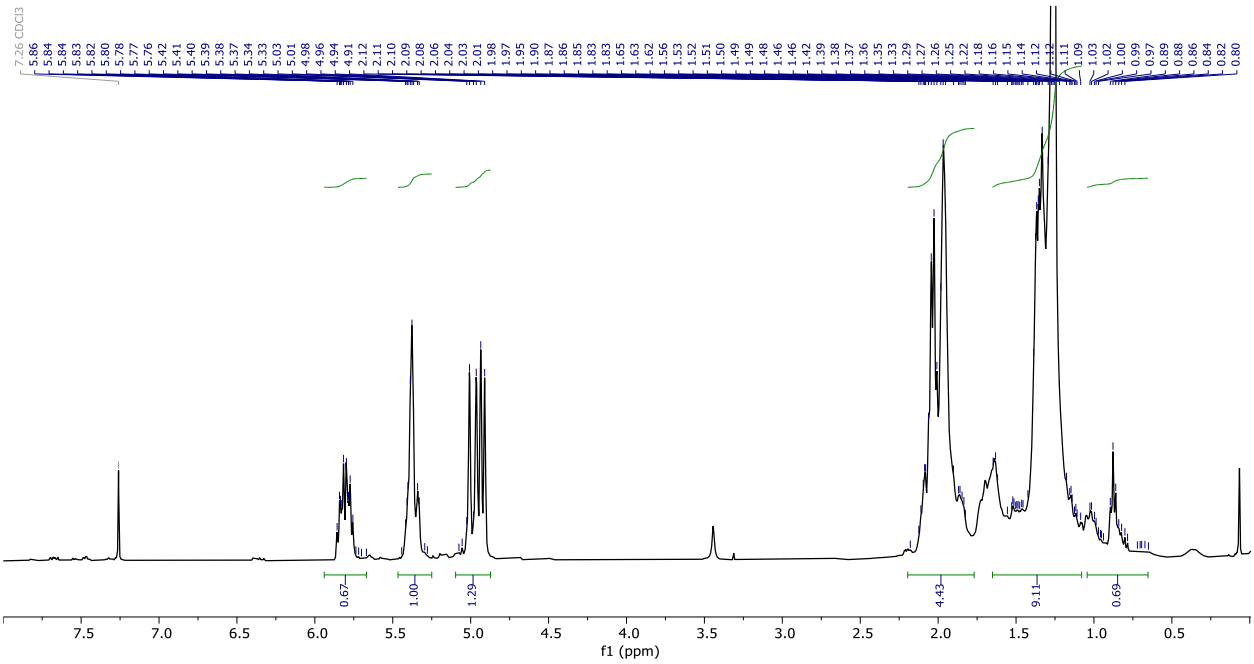

Figure 3.45. ^{1}H NMR analysis at RT ($CDCl_3$) of olefins concentrated in vacuo in the soluble fraction of the reaction mixture after ethenolysis (Table 3.1, Entry 13).

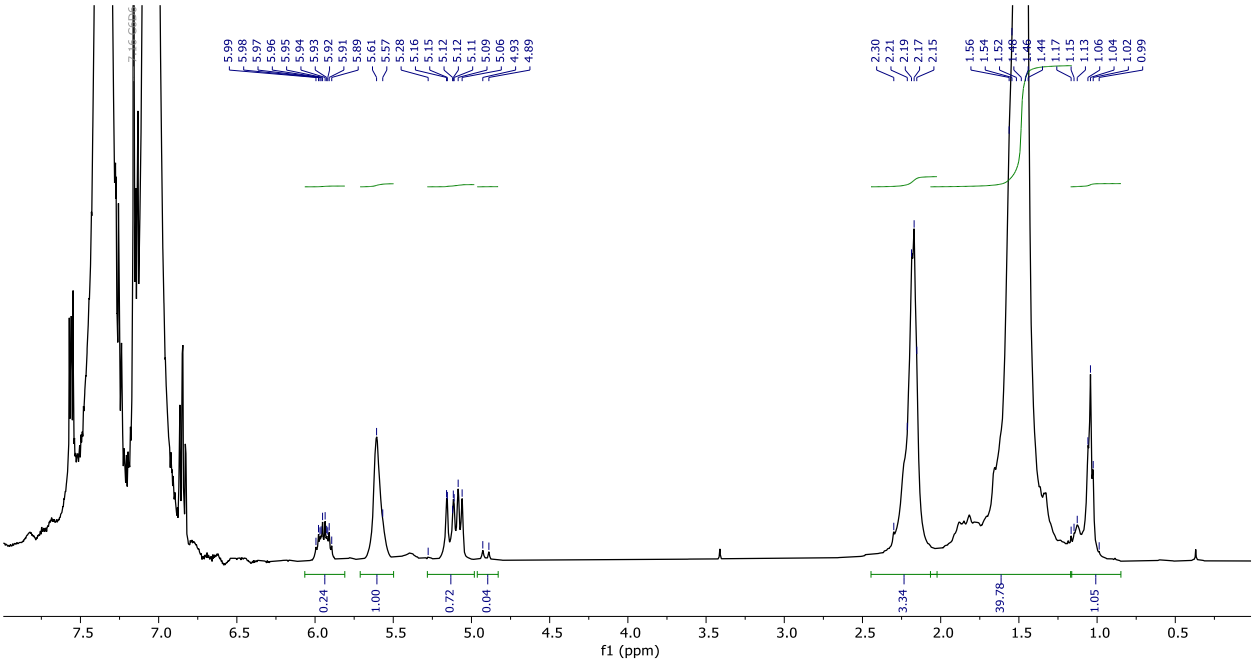

Figure 3.46. ^{1}H NMR analysis at 120 ºC (80% 1,2 dichlorobenzene, 20% benzene-d_6) of olefins in the insoluble fraction of the reaction mixture after ethenolysis (Table 3.1, Entry 14).

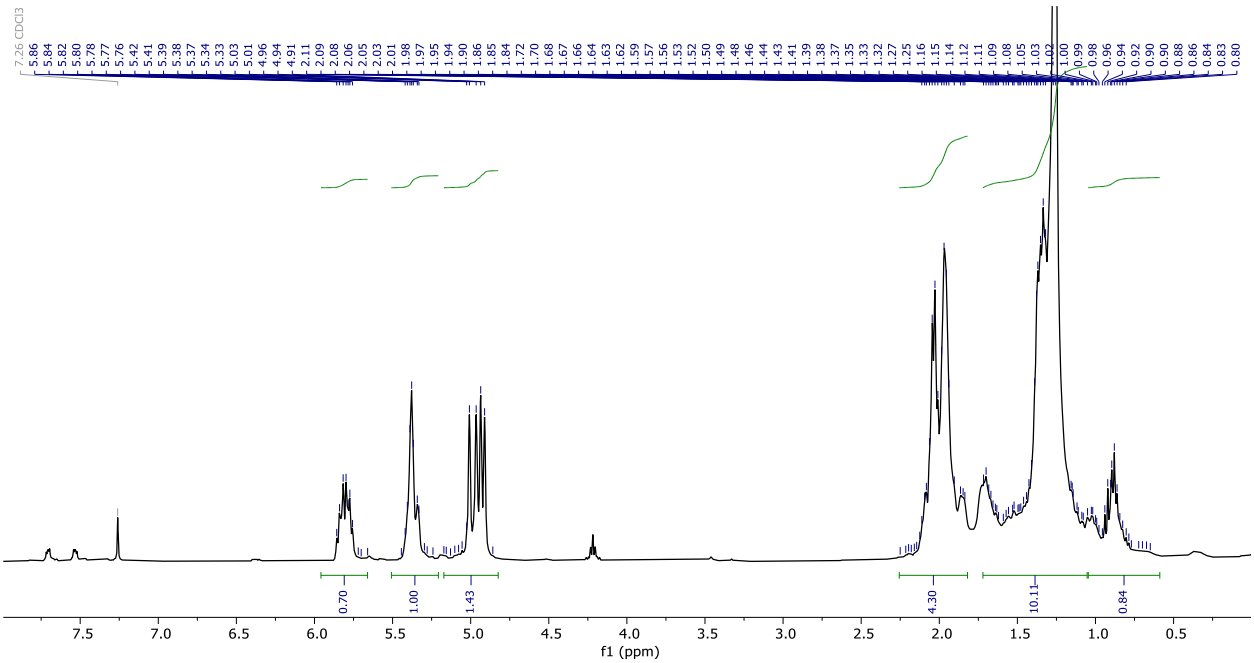

Figure 3.47. ^{1}H NMR analysis at RT ($CDCl_3$) of olefins concentrated in vacuo in the soluble fraction of the reaction mixture after ethenolysis (Table 3.1, Entry 14).

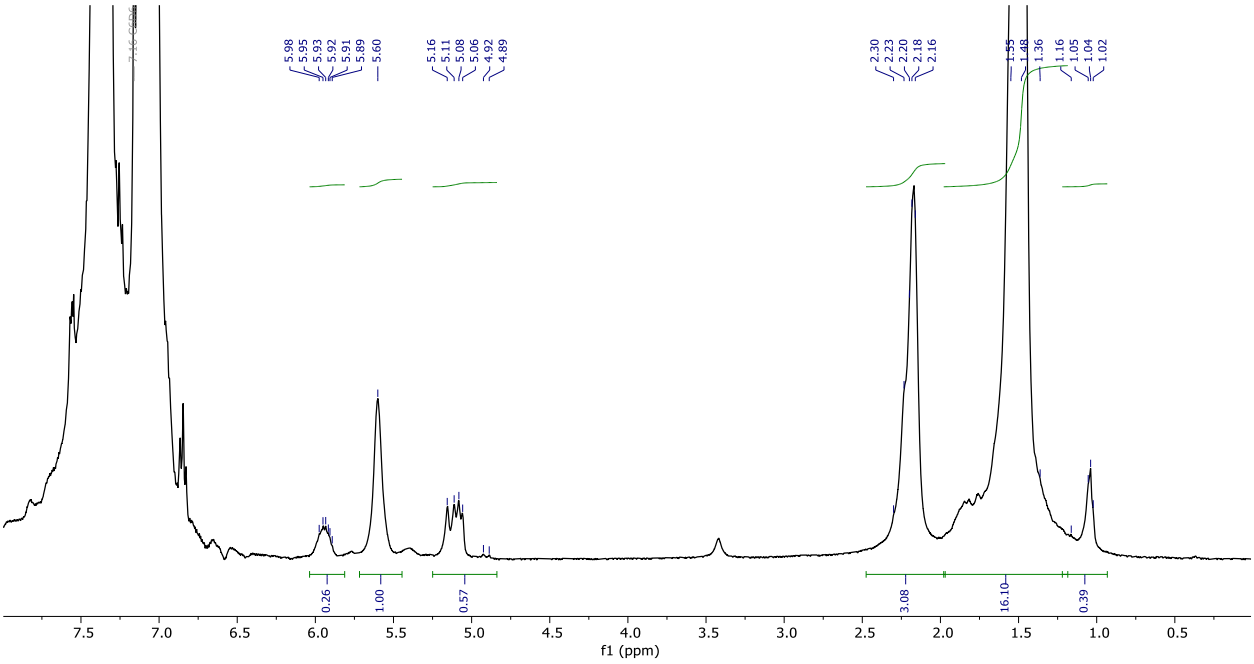

Figure 3.48. ^{1}H NMR analysis at 120 ºC (80% 1,2 dichlorobenzene, 20% benzene-d_6) of olefins in the insoluble fraction of the reaction mixture after ethenolysis (Table 3.1, Entry 15).

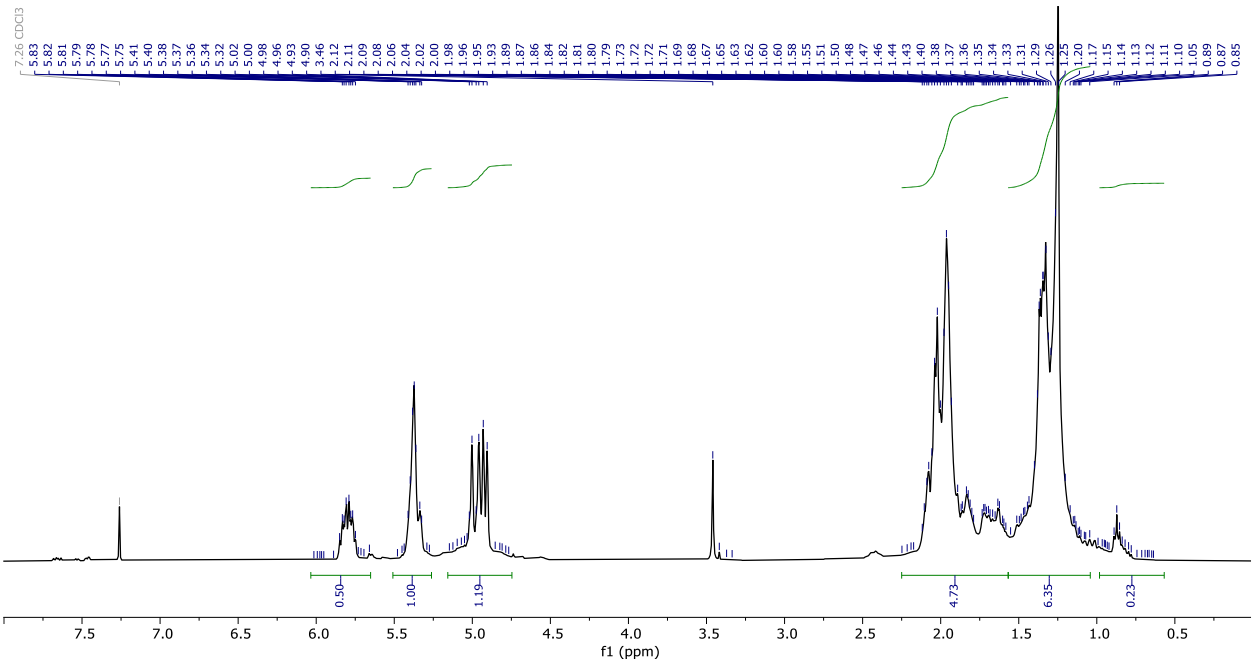

Figure 3.49. ^{1}H NMR analysis at RT ($CDCl_3$) of olefins concentrated in vacuo in the soluble fraction of the reaction mixture after ethenolysis (Table 3.1, Entry 15).

Ethylene/Butadiene Copolymerization by Cobalt Catalyst and Subsequent Metathesis

Experiments conducted by Shouyan Xiong

Table 3.6. Ethylene/butadiene copolymerization by **PDI-Co**/MAO

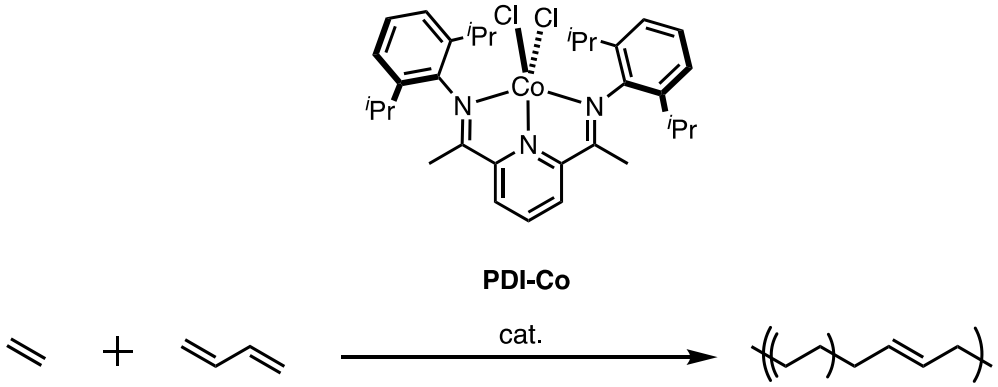

Entry[a,b]	[ethylene]/ psi	[BD]/ [Co]	Temp. (°C)	time (h)	Yield (g)	Act. (kg/(mol·h))	Mw/10^3	PDI	%Mol 1,4-BD	T_m (°C)
1	100	400	30	4	3.5	88	67.2	6.1	0.6	127.0
2	100	800	30	4	1.9	48	53.7	5.2	1.7	121.1
3	100	1600	30	4	1.3	33	42.6	4.8	2.6	117.6
4	60	1600	30	8	0.5	6	21.1	3.2	8.8	117.3

[a] Conditions unless specified: [Co] = 10 μmol, [MMAO]:[Co] = 200; V = 10 mL, toluene solvent; [b] Procedures: to the fisher-porter tube (filled with 3 mL toluene and corresponding BD) that have been purged and prefilled by ethylene (20 psi) was injected 2 mL toluene solution of PDI-Co

Table 3.7. Representative trials of metathesis of ethylene/butadiene copolymers produced by the Co system**.**

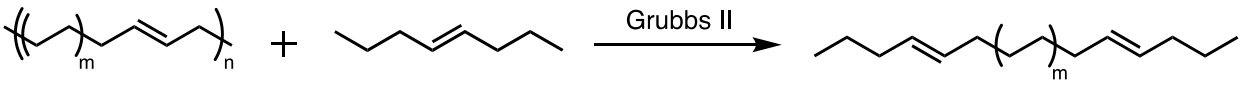

Entry[a]	Mw/10^3	Mn	PDI	%Mol 1,4-BD	T_m (°C)
Before	42.6	8.9	4.8	2.6	117.6
After	47.4	9.1	5.2	0.6	129.0

[a] Conditions: Copolymer: 50 mg, Grubbs II: 20 μmol, Cis-octene: 20 mmol, Toluene: 1.2 mL, T: 120 °C, time: 72 h.

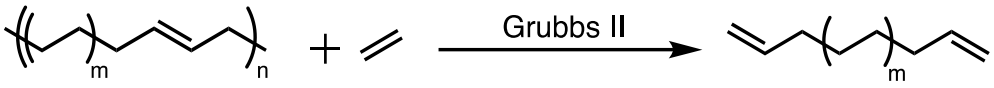

Entry[a]	Mw/10^3	Mn	PDI	%Mol 1,4-BD	T_m (°C)
Before	42.6	8.9	4.8	2.6	117.6
After	33.1	8.7	3.8	1.2	125.6

[a] Conditions: Copolymer: 50 mg, Grubbs II: 20 μmol, Cis-octene: 20 mmol, Toluene: 1.2 mL, T: 120 °C, time: 72 h.

REFERENCES

1. Mol, J. C., Industrial applications of olefin metathesis. *J. Mol. Catal. A: Chem.* **2004,** *213* (1), 39-45. 10.1016/j.molcata.2003.10.049
2. Keim, W., Oligomerization of Ethylene to α-Olefins: Discovery and Development of the Shell Higher Olefin Process (SHOP). *Angew. Chem. Int. Ed.* **2013,** *52* (48), 12492-12496. 10.1002/anie.201305308
3. Lutz, E. F., Shell higher olefins process. *J. Chem. Educ.* **1986,** *63* (3), 202. 10.1021/ed063p202
4. Keim, W., Nickel: An Element with Wide Application in Industrial Homogeneous Catalysis. *Angew. Chem. Int. Ed.* **1990,** *29* (3), 235-244. 10.1002/anie.199002351
5. Warwel, S.; Tillack, J.; Demes, C.; Kunz, M., Polyesters of ω-Unsaturated Fatty Acid Derivatives. *Macromol. Chem. Phys.* **2001,** *202* (7), 1114-1121. 10.1002/1521-3935(20010401)202:7<1114::AID-MACP1114>3.0.CO;2-T
6. Behr, A.; Toepell, S., Comparison of Reactivity in the Cross Metathesis of Allyl Acetate-Derivatives with Oleochemical Compounds. *J. Am. Oil Chem. Soc.* **2015,** *92* (4), 603-611. 10.1007/s11746-015-2614-7
7. Kolb, N.; Winkler, M.; Syldatk, C.; Meier, M. A. R., Long-chain polyesters and polyamides from biochemically derived fatty acids. *Eur. Polym. J.* **2014,** *51*, 159-166. 10.1016/j.eurpolymj.2013.11.007
8. Rybak, A.; Meier, M. A. R., Cross-metathesis of fatty acid derivatives with methyl acrylate: renewable raw materials for the chemical industry. *Green Chem.* **2007,** *9* (12), 1356-1361. S10.1039/B712293D
9. Behr, A.; Toepell, S.; Harmuth, S., Cross-metathesis of methyl 10-undecenoate with dimethyl maleate: an efficient protocol with nearly quantitative yields. *RSC Advances* **2014,** *4* (31), 16320-16326. 10.1039/C3RA47671E
10. Song, S.; Wu, A.; Yu, Y.; Yang, P.; Fu, Z.; Fan, Z., Nonconjugated diene homopolymerization and copolymerization with ethylene catalyzed by α-diimine Ni(II) complex/Et_2AlCl. *J. Polym. Sci., Part A: Polym. Chem.* **2017,** *55* (11), 1900-1909. 10.1002/pola.28561
11. Mehdiabadi, S.; Soares, J. B. P., Production of Ethylene/α-Olefin/1,9-Decadiene Copolymers with Complex Microstructures Using a Two-Stage Polymerization Process. *Macromolecules* **2011,** *44* (20), 7926-7939. 10.1021/ma201368c
12. Luo, L.; Liu, P.; Zhang, K.; Tang, G.; Hou, H.; Li, B.-G.; Wang, W.-J., Vinyl-Functionalized Polyolefins for Fast Photovoltaic Cell Encapsulation. *ACS Applied Polymer Materials* **2020,** *2* (7), 2571-2577. 10.1021/acsapm.0c00207
13. Inci, B.; Wagener, K. B., Decreasing the Alkyl Branch Frequency in Precision Polyethylene: Pushing the Limits toward Longer Run Lengths. *J. Am. Chem. Soc.* **2011,** *133* (31), 11872-11875. 10.1021/ja2040046
14. Watson, M. D.; Wagener, K. B., Ethylene/Vinyl Acetate Copolymers via Acyclic Diene Metathesis Polymerization. Examining the Effect of "Long" Precise Ethylene Run Lengths. *Macromolecules* **2000,** *33* (15), 5411-5417. 10.1021/ma9920689
15. Hoye, T. R.; Jeffrey, C. S.; Tennakoon, M. A.; Wang, J.; Zhao, H., Relay Ring-Closing Metathesis (RRCM): A Strategy for Directing Metal Movement Throughout Olefin Metathesis Sequences. *J. Am. Chem. Soc.* **2004,** *126* (33), 10210-10211. 10.1021/ja046385t
16. Schmidt, V. A.; Hoyt, J. M.; Margulieux, G. W.; Chirik, P. J., Cobalt-Catalyzed [2π + 2π] Cycloadditions of Alkenes: Scope, Mechanism, and Elucidation of Electronic Structure of Catalytic Intermediates. *J. Am. Chem. Soc.* **2015,** *137* (24), 7903-7914. 10.1021/jacs.5b04034

17. Bloodworth, A. J.; Curtis, R. J.; Mistry, N., 1,2-Dioxolane versus 1,2-dioxane formation in the cyclization of an α,ω-diene hydroperoxide under polar and free radical conditions. *J. Chem. Soc., Chem. Commun.* **1989,** (14), 954-955. 10.1039/C39890000954
18. Engl, P. S.; Santiago, C. B.; Gordon, C. P.; Liao, W.-C.; Fedorov, A.; Copéret, C.; Sigman, M. S.; Togni, A., Exploiting and Understanding the Selectivity of Ru-N-Heterocyclic Carbene Metathesis Catalysts for the Ethenolysis of Cyclic Olefins to α,ω-Dienes. *J. Am. Chem. Soc.* **2017,** *139* (37), 13117-13125. 10.1021/jacs.7b06947
19. Gao, Z.; You, Y.; Chen, Q.; North, M.; Xie, H., Vanillin-derived α,ω-diene monomer for thermosets preparation via thiol–ene click polymerization. *Green Chem.* **2023,** *25* (1), 172-182. 10.1039/D2GC02901D
20. Palucci, B.; Zanchin, G.; Ricci, G.; Vendier, L.; Lorber, C.; Leone, G., Vanadium-Catalyzed Terpolymerization of α,ω-Dienes with Ethylene and Cyclic Olefins: Ready Access to Polar-Functionalized Polyolefins. *Macromolecules* **2021,** *54* (23), 10700-10711. 10.1021/acs.macromol.1c02142
21. Nakamura, A.; Ito, S.; Nozaki, K., Coordination−Insertion Copolymerization of Fundamental Polar Monomers. *Chem. Rev.* **2009,** *109* (11), 5215-5244. 10.1021/cr900079r
22. Hou, W.; Zhang, D.; Camacho-Fernandez, M. A.; Zhang, Y.; Liu, G.; Tang, Y.; Guan, Z.; Huang, Z., Double-Linear Insertion Mode of α,ω-Dienes Enabled by Thio-imino-quinoline Iron Catalyst. *ACS Catalysis* **2020,** *10* (24), 15092-15103. 10.1021/acscatal.0c04567
23. Leone, G.; Palucci, B.; Zanchin, G.; Vignali, A.; Ricci, G.; Bertini, F., Dynamically Cross-Linked Polyolefins via Hydrogen Bonds: Tough yet Soft Thermoplastic Elastomers with High Elastic Recovery. *ACS Applied Polymer Materials* **2022,** *4* (5), 3770-3778. 10.1021/acsapm.2c00253
24. Bidange, J.; Fischmeister, C.; Bruneau, C., Ethenolysis: A Green Catalytic Tool to Cleave Carbon–Carbon Double Bonds. *Chem. Eur. J.* **2016,** *22* (35), 12226-12244. 10.1002/chem.201601052
25. Delaude, L.; Noels, A. F. Metathesis. In *Kirk-Othmer Encyclopedia of Chemical Technology*; Wiley: 2005; 10.1002/0471238961.metanoel.a01v
26. Zuech, E. A.; Hughes, W. B.; Kubicek, D.; Kittleman, E., Homogeneous catalysts for olefin disproportionations from nitrosyl molybdenum and tungsten compounds. *J. Am. Chem. Soc.* **1970,** *92* (3), 528-531. 10.1021/ja00706a018
27. Chaumont, P.; John, C. S., Olefin disproportionation technology (feast) - a challenge for process development. *J. Mol. Catal.* **1988,** *46* (1), 317-328. 10.1016/0304-5102(88)85104-6
28. Hummel, K.; Stelzer, F.; Heiling, P.; Wedam, O. A.; Griesser, H., Some new aspects of polymer degradation by olefin metathesis. *J. Mol. Catal.* **1980,** *8* (1), 253-262. 10.1016/0304-5102(80)87023-4
29. Wagener, K. B.; Puts, R. D.; Smith Jr., D. W., Acyclic diene metathesis depolymerization of elastomers. *Macromol. Rapid Commun.* **1991,** *12* (7), 419-425. 10.1002/marc.1991.030120708
30. Arroyave, A.; Cui, S.; Lopez, J. C.; Kocen, A. L.; LaPointe, A. M.; Delferro, M.; Coates, G. W., Catalytic Chemical Recycling of Post-Consumer Polyethylene. *J. Am. Chem. Soc.* **2022**. 10.1021/jacs.2c11949
31. Shiono, T.; Naga, N.; Soga, K., Synthesis of α,ω-divinylpolyethylene-like polymers from cis-1,4-polybutadiene using partial hydrogenation and metathesis degradation with ethylene. *Macromol. Rapid Commun.* **1993,** *14* (6), 323-327. 10.1002/marc.1993.030140601
32. Patil, V. B.; Saliu, K. O.; Jenkins, R. M.; Carnahan, E. M.; Kramer, E. J.; Fredrickson, G. H.; Bazan, G. C., Efficient Synthesis of α,ω-Divinyl-Functionalized Polyolefins. *Macromol. Chem. Phys.* **2014,** *215* (11), 1140-1145. 10.1002/macp.201400139

33. Ishihara, T.; Shiono, T., Synthesis of Poly(propylene-ran-1,3-butadiene) and Its Metathesis Degradation with Ethylene. *Macromolecules* **2003,** *36* (26), 9675-9677. 10.1021/ma0349480
34. Kocen, A. L.; Cui, S.; Lin, T.-W.; LaPointe, A. M.; Coates, G. W., Chemically Recyclable Ester-Linked Polypropylene. *J. Am. Chem. Soc.* **2022,** *144* (28), 12613-12618. 10.1021/jacs.2c04499
35. Craig, S. W.; Manzer, J. A.; Coughlin, E. B., Highly Efficient Acyclic Diene Metathesis Depolymerization Using a Ruthenium Catalyst Containing a N-Heterocyclic Carbene Ligand. *Macromolecules* **2001,** *34* (23), 7929-7931. 10.1021/ma011188p
36. Watson, M. D.; Wagener, K. B., Acyclic diene metathesis (ADMET) depolymerization: Ethenolysis of 1,4-polybutadiene using a ruthenium complex. *J. Polym. Sci., Part A: Polym. Chem.* **1999,** *37* (12), 1857-1861. 10.1002/(SICI)1099-0518(19990615)37:12<1857::AID-POLA15>3.0.CO;2-C
37. Conk, R. J.; Hanna, S.; Shi, J. X.; Yang, J.; Ciccia, N. R.; Qi, L.; Bloomer, B. J.; Heuvel, S.; Wills, T.; Su, J.; Bell, A. T.; Hartwig, J. F., Catalytic deconstruction of waste polyethylene with ethylene to form propylene. *Science* **2022,** *377* (6614), 1561-1566. 10.1126/science.add1088
38. Zeng, M.; Lee, Y.-H.; Strong, G.; LaPointe, A. M.; Kocen, A. L.; Qu, Z.; Coates, G. W.; Scott, S. L.; Abu-Omar, M. M., Chemical Upcycling of Polyethylene to Value-Added α,ω-Divinyl-Functionalized Oligomers. *ACS Sustainable Chemistry & Engineering* **2021,** *9* (41), 13926-13936. 10.1021/acssuschemeng.1c05272
39. Zhang, K.; Dou, Y.; Jiang, Y.; Zhang, Z.; Li, S.; Cui, D., High-Performance Elastomer from Trans-1,4 Copolymerization of Ethylene and Butadiene. *Macromolecules* **2021,** *54* (20), 9445-9451. 10.1021/acs.macromol.1c01384
40. Zhang, Y.; Xia, J.; Song, J.; Zhang, J.; Ni, X.; Jian, Z., Combination of Ethylene, 1,3-Butadiene, and Carbon Dioxide into Ester-Functionalized Polyethylenes via Palladium-Catalyzed Coupling and Insertion Polymerization. *Macromolecules* **2019,** *52* (6), 2504-2512. 10.1021/acs.macromol.9b00195
41. Železník, O.; Merna, J., Bis(arylimino)pyridyl cobalt catalysts for copolymerization of buta-1,3-diene with ethene. *Polymer* **2019,** *175*, 195-205. 10.1016/j.polymer.2019.05.025
42. Wu, C.; Liu, B.; Lin, F.; Wang, M.; Cui, D., cis-1,4-Selective Copolymerization of Ethylene and Butadiene: A Compromise between Two Mechanisms. *Angew. Chem. Int. Ed.* **2017,** *56* (24), 6975-6979. 10.1002/anie.201702128
43. Nsiri, H.; Belaid, I.; Larini, P.; Thuilliez, J.; Boisson, C.; Perrin, L., Ethylene–Butadiene Copolymerization by Neodymocene Complexes: A Ligand Structure/Activity/Polymer Microstructure Relationship Based on DFT Calculations. *ACS Catalysis* **2016,** *6* (2), 1028-1036. 10.1021/acscatal.5b02317
44. Capacchione, C.; Avagliano, A.; Proto, A., Ethylene−Butadiene Copolymerization Promoted by Titanium Complex Containing a Tetradentate [OSSO]-Type Bis(phenolato) Ligand. *Macromolecules* **2008,** *41* (13), 4573-4575. 10.1021/ma800864y
45. Llauro, M. F.; Monnet, C.; Barbotin, F.; Monteil, V.; Spitz, R.; Boisson, C., Investigation of Ethylene/Butadiene Copolymers Microstructure by ^{1}H and ^{13}C NMR. *Macromolecules* **2001,** *34* (18), 6304-6311. 10.1021/ma010421g
46. Ray, S.; Rao, P. V. C.; Choudary, N. V., Poly-α-olefin-based synthetic lubricants: a short review on various synthetic routes. *Lubr. Sci.* **2012,** *24* (1), 23-44. 10.1002/ls.166
47. Liu, Y.; Kim, K. E.; Herbert, M. B.; Fedorov, A.; Grubbs, R. H.; Stoltz, B. M., Palladium-Catalyzed Decarbonylative Dehydration of Fatty Acids for the Production of Linear Alpha Olefins. *Adv. Synth. Catal.* **2014,** *356* (1), 130-136. 10.1002/adsc.201301109

48. Zhang, Z.; Lin, W.; Li, Y.; Okejiri, F.; Lu, Y.; Liu, J.; Chen, H.; Lu, X.; Fu, J., Heterogeneous Non-noble Catalyst for Highly Selective Production of Linear α-Olefins from Fatty Acids: A Discovery of NiFe/C. *ChemSusChem* **2020,** *13* (18), 4922-4928. 10.1002/cssc.202001356
49. Yang, C.; Nie, R.; Fu, J.; Hou, Z.; Lu, X., Production of aviation fuel via catalytic hydrothermal decarboxylation of fatty acids in microalgae oil. *Bioresour. Technol.* **2013,** *146*, 569-573. 10.1016/j.biortech.2013.07.131
50. Zhang, X.; Jordan, F.; Szostak, M., Transition-metal-catalyzed decarbonylation of carboxylic acids to olefins: exploiting acyl C–O activation for the production of high value products. *Organic Chemistry Frontiers* **2018,** *5* (16), 2515-2521. 10.1039/C8QO00585K
51. Pangborn, A. B.; Giardello, M. A.; Grubbs, R. H.; Rosen, R. K.; Timmers, F. J., Safe and Convenient Procedure for Solvent Purification. *Organometallics* **1996,** *15* (5), 1518-1520. 10.1021/om9503712
52. Kanti Paine, T.; Sheet, D.; Weyhermüller, T.; Chaudhuri, P., Iron(II)-Mediated Reductive Cleavage of Disulfide and Diselenide Bonds: Iron(III) Complexes of Mixed O,X,O and O,X (X = S, Se) Donor Ligands. *Eur. J. Inorg. Chem.* **2011,** *2011* (34), 5250-5257. 10.1002/ejic.201100674

CHAPTER 4: Ionomers Modulate CO_2 Reduction: Potassium Ion Modulation of the Cu Electrode-Electrolyte Interface (Part A) and Structural Diversification of Ionomer Series (Part B)

Part A was published in part as:

Heim, G. P.;† **Bruening, M. A.**;† Musgrave, C. B.; Goddard, W. A.; Peters, J. C.; Agapie, T., Potassium ion modulation of the Cu electrode-electrolyte interface with ionomers enhances CO_2 reduction to C_{2+} products. *Joule* **2024**. 10.1016/j.joule.2024.03.019

†Denotes equal contribution

For author contributions, see Page vii.

Part A: Potassium Ion Modulation of the Cu Electrode-Electrolyte Interface with Ionomers Enhances CO_2 Reduction to C_{2+} Products

ABSTRACT

Ionomers have shown promise as organic coatings on Cu electrodes to increase the CO_2 reduction (CO_2R) selectivity towards multi-carbon (C_{2+}) products. However, effects of systematic polymer structure modification on electrocatalytic performance have been seldom reported. Herein, we report on a series of polystyrene-based ionomers to probe the effect of local [K^+] in the Cu electrode microenvironment on CO_2R performance. Partial current density towards C_{2+} products ($|j_{C2+}|$) increases with [K^+] in ionomer, up to 225 mA cm^{-2}. Replacing K^+ with $[Me_4N]^+$ lowers performance to the level of bare Cu, highlighting the crucial role of K^+ in improving C_{2+} product selectivity. Molecular dynamics simulations show that CO_2 diffusivity increases with [K^+], implicating CO_2 transport to the electrode as a potential mechanism for improved CO_2R performance. Our results highlight the intersection of synthetic polymer chemistry and electrocatalysis as a promising strategy in electrode modification towards achieving high selectivity of value-added chemicals.

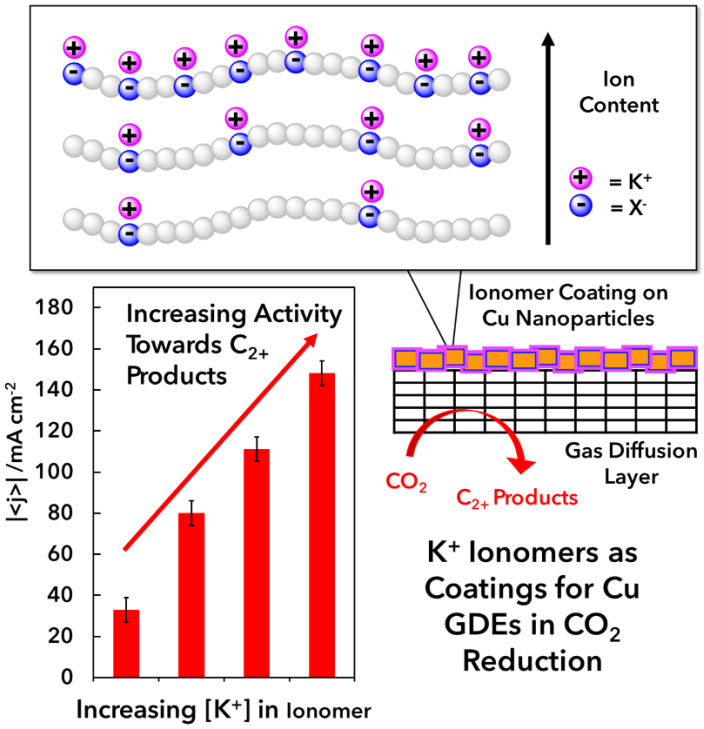

INTRODUCTION

Electrochemical conversion of CO_2 to value-added chemicals using renewable energy is a potential avenue toward achieving a net-zero carbon economy.[1] Cu is the only metallic electrode where multi-carbon (C_{2+}) products, including C_2H_4, C_2H_5OH, and C_3H_7OH are produced from electrochemical CO_2 reduction (CO_2R).[2] However, unmodified Cu suffers from poor selectivity towards C_{2+} products with significant generation of C_1 products and hydrogen.[2-4] Coating Cu electrodes with organic films is a strategy for steering CO_2R selectivity towards C_{2+} products. Organic coatings derived from molecular precursors such as pyridinium,[5-9] ionic liquids,[10-12] amines,[13-14] and aryl diazonium and iodonium species[15] have shown promise. Although the ease of precursor synthesis and *in situ* film generation are attractive features of a general approach, the physical properties of the coating and electrocatalyst microenvironment, including local pH, CO_2 concentration, hydrophobicity, and electric field strength, are not readily predicted. Ionomers are an alternative approach to organic films.[16-23] For example, Bell and co-workers recently examined a combination of ionomers to control local pH and hydrophobicity to achieve high C_{2+} product selectivity on Cu.[16] Also, Sargent and co-workers have demonstrated high current density electrolysis with Nafion on Cu.[17] These examples utilizing commercial polymers highlight the potential of this approach. However, a dearth of studies examining the effects of systematic changes in ionomer structure on CO_2R behavior limits fundamental understanding of the crucial features of electrochemical performance.[21, 23] Of note, Grubbs and co-workers synthesized and tested a library of ionomer coatings bearing imidazolium groups and observed high selectivity for C_{2+} products and low hydrogen evolution reaction (HER).[21] Computations suggested that high local [CO_2], as well as an induced electric field effect from the positively charged functional groups, drove high selectivity towards C_{2+} products. Alkali cations were found to facilitate CO_2R

on metallic electrodes.[19, 24-28] Their presence in the outer Helmholtz plane was hypothesized to suppress proton carrier mass transport and stabilize CO_2R intermediates.[19, 28-30]

With the concentration of alkali metal cations established to affect CO_2R, a systematic investigation of anionic polymers with alkali cations can provide a strategy to facilitate CO_2R and possibly shed light on their impact on the electrode-electrolyte interface. Herein we report the impact of a series of polystyrene-based ionomer films for CO_2R on Cu. A correlation is observed between the content of K^+ in the ionomer and $|j_{C2+}|$. The role of the ionomer has been probed experimentally and computationally.

RESULTS AND DISCUSSION

Ionomers containing variable K^+ content were prepared based on a polystyrene backbone using different ratios of 4-methoxystyrene and potassium (4-styrenesulfonyl)(trifluoromethanesulfonyl)imide (K-STFSI). A mixture of substituted styrene comonomers was treated with 10% azobisisobutyronitrile (AIBN) in MeCN and heated for 3 days at 70 °C (Figure 4.1A). Upon purification,[31] the resulting polymers were characterized by ^{1}H, ^{19}F, and ^{13}C nuclear magnetic resonance (NMR) spectroscopy. The percent of charged comonomer

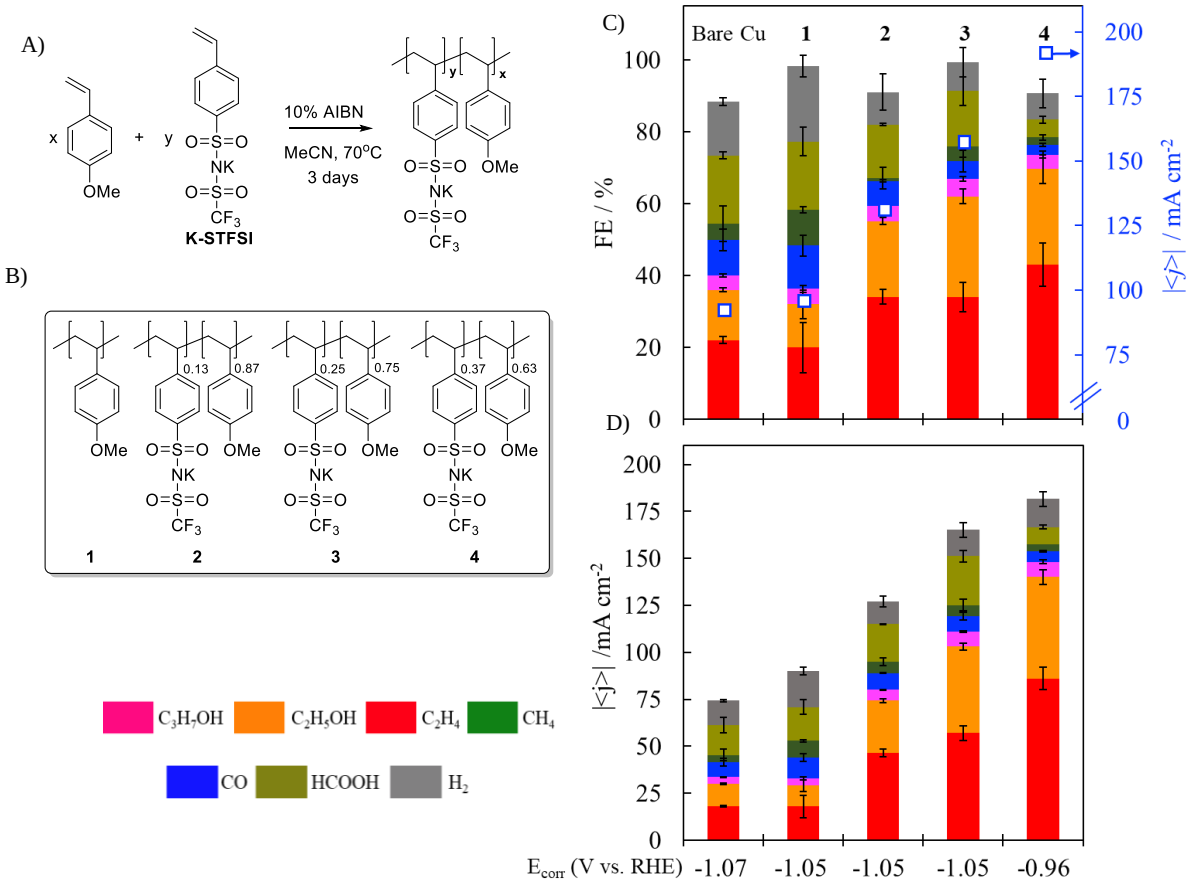

Figure 4.1: Polymers **1-4** and CO_2R performance on bare Cu. (A) Ionomer synthesis. (B) Series of prepared ionomers. (C) Faradaic efficiency (FE, columns) and current density (white squares) for CO_2R products on Cu/PTFE in the presence of ionomer films cast from solutions of **1**–**4**. Electrolysis performed in 1 M $KHCO_{3(aq)}$ for 30 min with $E_{applied}$ = -1.15 V vs. RHE. Corrected potentials (E_{corr}) determined from measured (uncompensated) resistance are reported. (D) Partial current densities for trials shown in (C).

incorporated was determined by ^{1}H NMR by integrating the OC*H*$_3$ peak for 4-methoxyphenyl at 3.7 ppm versus the protons *ortho* to the sulfonate moiety, centered at 7.6 ppm. Within this series in hand, copolymers were prepared with the content of the K-STFSI ranging from 0-37% (Figure 4.1B). While polymers with a higher content of charged monomer were accessed synthetically, they were soluble in the electrolyte solution (1 M $KHCO_{3(aq)}$), hindering further study as electrode coatings.

The ionomer film impact on CO_2R was studied in chronoamperometry experiments using a gas diffusion electrode (GDE),[7] at $E_{applied}$ = –1.15 V vs. RHE (1 M $KHCO_{3(aq)}$). The coated electrodes were prepared by drop casting stock solutions of ionomers in an alcohol mixture (50% v/v EtOH/^{i}PrOH) onto a Cu GDE, based on Cu sputtered onto PTFE (Cu/PTFE). All electrolysis experiments were carried out in a flow cell designed specifically for GDEs.[7, 9]

Ionomers **2**-**4** each increased C_{2+} product selectivity compared to both bare Cu and Cu coated with **1** (Figure 4.1C). Analysis of the partial current densities reveals that $|j_{C2+}|$ increases as a function of K^+ content in the ionomer (Figure 4.1D), where $|j_{C2+}|$ on Cu coated with **4** is greater than bare Cu (150 vs 34 mA cm^{-2}). The FE for C_{2+} products is improved using **4** relative to bare Cu (75% vs 40%). These results suggest that the charged polymer does not act as a physical barrier for the substrate. Rather, increased incorporation of K^+ within the microenvironment provided by ionomers at the electrode surface facilitates CO_2 reduction to C_{2+} products. While electric field effects can augment local cation concentration,[32-34] inductively coupled mass spectrometry (ICP-MS) measurements suggest that differences between the local [K^+] are established due to K^+ content provided by the ionomer (Table 4.6).[34-36] This effect is reminiscent of previous strategies for enhancing C_{2+} selectivity by increasing K^+ concentration in the bulk electrolyte, up to 4 M; in

the present approach, the K^+ concentration is increased at the electrode-electrolyte interface via the ionomer.[19, 30, 37]

CO_2R performance was further optimized by increasing the ionomer **3** loading from 4.5 µg to 13.5 µg, enabling FE_{C2+} = 82%, $|j_{C2+}|$ = 225 mA cm^{-2} (Figure 4.5, A-B). Notably, there appears to be no decrease of $|j_{H2}|$ (Figure 4.5C) suggesting that the improved selectivity for CO_2R is not solely a consequence of suppressed HER.[5, 8-9, 16] There is likely an insignificant local pH increase (*vide infra*).[16] Higher loadings of **4** were also attempted, leading to similarly high $|j_{C2+}|$ but also significantly greater $|j_{H2}|$ compared to **3** (Figure 4.6).

Next, CO_2R on a GDE catalyzed by Cu modified with organic films at high current densities ($|j_{C2+}|$ > 200 mA cm^{-2}) was compared (Tables 4.3, 4.4). Focusing on anionic ionomers, Nafion 1100 W tested under the CO_2R conditions reported herein (Figure 4.1) provided 36% FE_{C2+} at a $|j_{C2+}|$ = 25 mA cm^{-2}. In contrast, using ionomer **3** resulted in 82% FE_{C2+} at $|j_{C2+}|$ = 225 mA cm^{-2} (Figure 4.5). This result highlights that potential designer ionomers can offer improved CO_2R. For comparison, the best-in-class performance using Nafion-coated electrodes has been previously reported in highly basic, high [K^+] conditions (7 M KOH), resulting in FE_{C2+} = 79.5 %, $|j_{C2+}|$ at 1232 mA cm^{-2}.[7] Similar FEs are obtained with ionomer **3** in 1 M $KHCO_{3(aq)}$, despite the much lower [K^+] in the electrolyte.

To address the critical role of the K^+ ionomer, CO_2R was performed in the absence of any alkali metal. Previous work examining ionomers suggested a critical role of the anionic species in limiting hydroxide diffusion away from the microenvironment, thus facilitating C–C coupling.[16-17] In addition, a bis(sulfonyl)imide anion was found to promote bulk CO_2 solubility.[38] Such a species alone could enhance local CO_2 concentration in the ionomers, leading to enhanced CO_2R performance.[21] Therefore, $[Me_4N]^+$ was introduced in both the ionomer and the electrolyte (1 M

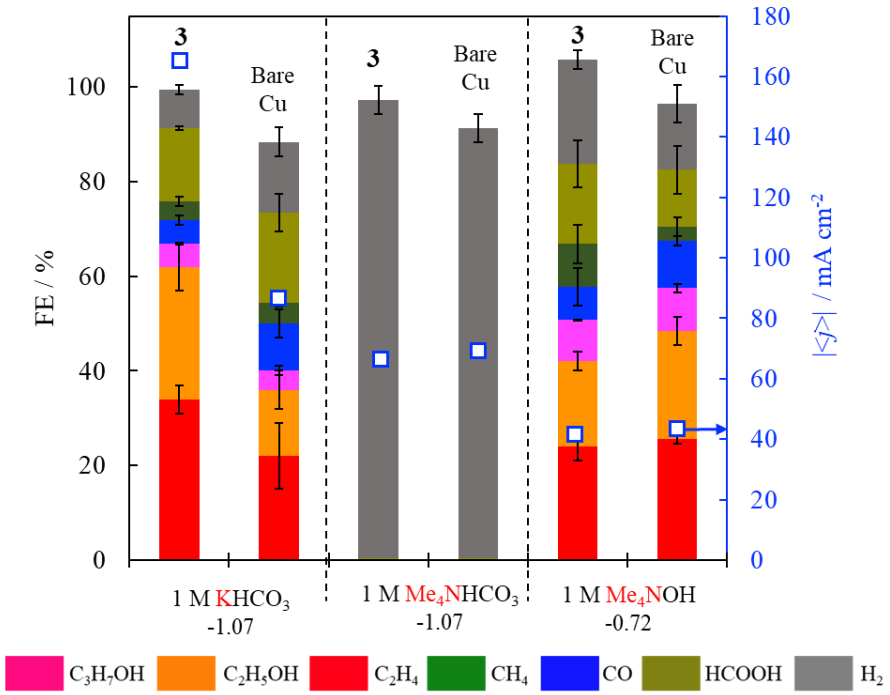

Figure 4.2. Replacing K^+ with Me_4N^+ Selectivity profile from CO_2R on Cu/PTFE in the presence of ionomer film **3** (4.5 mg) tested in various electrolyte solutions. $E_{applied}$ = -1.6 V vs. SHE. For 1 M $KHCO_{3(aq)}$ and 1 M $Me_4NHCO_{3(aq)}$, $E_{applied}$ = -1.15 V vs. RHE. For 1 M Me_4NOH, $E_{applied}$ = -0.80 V vs. RHE.

$Me_4NHCO_{3(aq)}$, pH = 7.8). With 1 M $Me_4NHCO_{3(aq)}$, H_2 was the exclusive product observed in each experiment, both with bare Cu and **3**-coated Cu (Figure 4.2). Despite the consumption of proton carriers, we do not expect local pH to increase significantly at relatively low current densities (~–60 mA cm^{-2}), as previously demonstrated.[19, 39] While CO_2R was observed with N-aryl pyridinium films in the absence of alkali cations,[9] the results with Me_4N^+ indicate that the ionomer coating alone is not sufficient to compensate for the detrimental effect of the absence of K^+ in the electrolyte.[26-27] Additionally, no improvement in CO_2R selectivity was observed in the presence of **3** compared to bare Cu in 1 M $Me_4NOH_{(aq)}$, pH = 14. These results underscore the importance of local K^+ content in the electrode microenvironment in improving CO_2R performance as the ionomer in the absence of K^+ is insufficient. Moreover, a pH effect alone, stemming from the ionomer accumulating hydroxide in the microenvironment, is inconsistent with these observations.

The impact of K^+ was also probed at lower concentrations of electrolyte. High selectivity towards C_{2+} products was still observed in 0.1 M $KHCO_{3(aq)}$, albeit at lower current densities (Figure 4.9), further demonstrating that high [K^+] in the electrolyte is not necessary to obtain good selectivity from K^+ ionomer-modified electrodes.

Varying the partial pressure of CO_2 (P_{CO2}) provides additional insight into the impact of the ionomer. On bare Cu, a non-linear relationship between P_{CO2} and $|j_{C2+}|$ is observed such that $|j_{C2+}|$ is greatest at 0.4 atm (Figure 4.3; see Figure 4.10 for FEs), consistent with previous observations.[40-42] A rationalization of this phenomenon has pointed to surface saturation with *CO, thereby excluding *H and preventing the formation of C_{2+} products.[40, 42] Another explanation has also been proposed:[41] greater local CO_2 concentration lowers the local pH, thereby promoting HER. This behavior limits CO_2R at higher P_{CO2}. However, in the presence of **3** on Cu, a monotonic increase in $|j_{C2+}|$ as a function of P_{CO2} is observed, effectively overcoming the volcano relationship observed on bare Cu. A log-log plot of P_{CO2} and $|j_{C2+}|$ reveals a first-order relationship between C_{2+} product

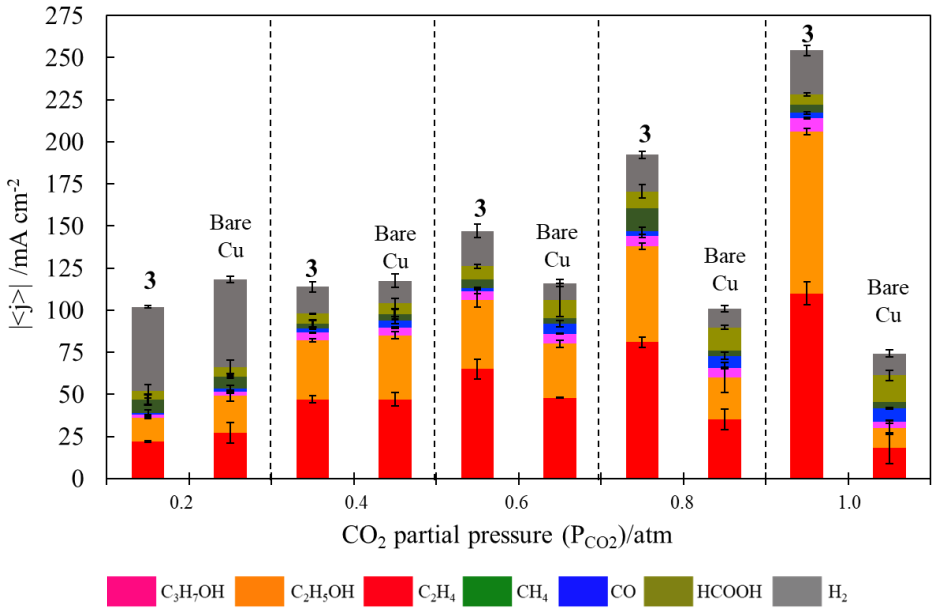

Figure 4.3. Variable partial pressure CO_2 electrolysis. Partial current densities from CO_2R in the presence of the ionomer **3** (ionomer loading: 13.5 mg) tested in 1 M $KHCO_{3(aq)}$ at various CO_2 partial pressures (Ar balance gas). $E_{applied}$ = -1.15 V vs. RHE.

formation and CO_2 in the presence of **3** (Figure 4.11), suggesting efficient mass transport through the ionomer film (*vide infra*).[5, 43-44] In our previous work with pyridinium-derived films on Ag,[5] the relationship between P_{CO2} and j_{CO2R} was unchanged relative to bare Ag, suggesting no effect of the film on CO_2 mass transport. In the present work, the increase in $|j_{C2+}|$ with P_{CO2} is in stark contrast to the relationship on bare Cu, highlighting the ionomers' ability to enhance reactivity with CO_2. While the ionomer films could be providing other effects not evident from these experiments (including increasing local pH[16, 19, 28] and modulating the local electric field[28, 37, 45]) our data points towards an elevation of CO_2 mass transport.

We employed molecular dynamics (MD) calculations to examine thermodynamic and mass transport behavior of CO_2 molecules in each polymer **1–4**. While the model could be constructed differently, it is crucial that the $[K^+]$ content be varied as consistent with charged comonomer incorporation determined by ^{1}H NMR. From the Fourier transform of the velocity autocorrelation function, we calculated molecular entropies (S), Helmholtz free energies (A_q), and diffusion coefficients (D) via the 2-Phase Thermodynamics (2PT) method.[46] This methodology was previously employed to understand CO transport with pyridinium-derived films.[47] The calculations suggest that increasing the amount of charged monomer in the polymer enhances CO_2 mass transport within the bulk polymer environment. For instance, 2PT predicts that the CO_2 entropy increases from **1** to **4** (Table 4.9).

2PT predicts a decrease in CO_2 free energy from **1** to **4**. The enhanced CO_2 stabilization in **4**, relative to **1**-**3**, is related to the increase in favorable coulomb interactions between CO_2 and nearby K^+,[21, 48] which is a result of increased content of the K-STFSI comonomer. CO_2 evidently possesses

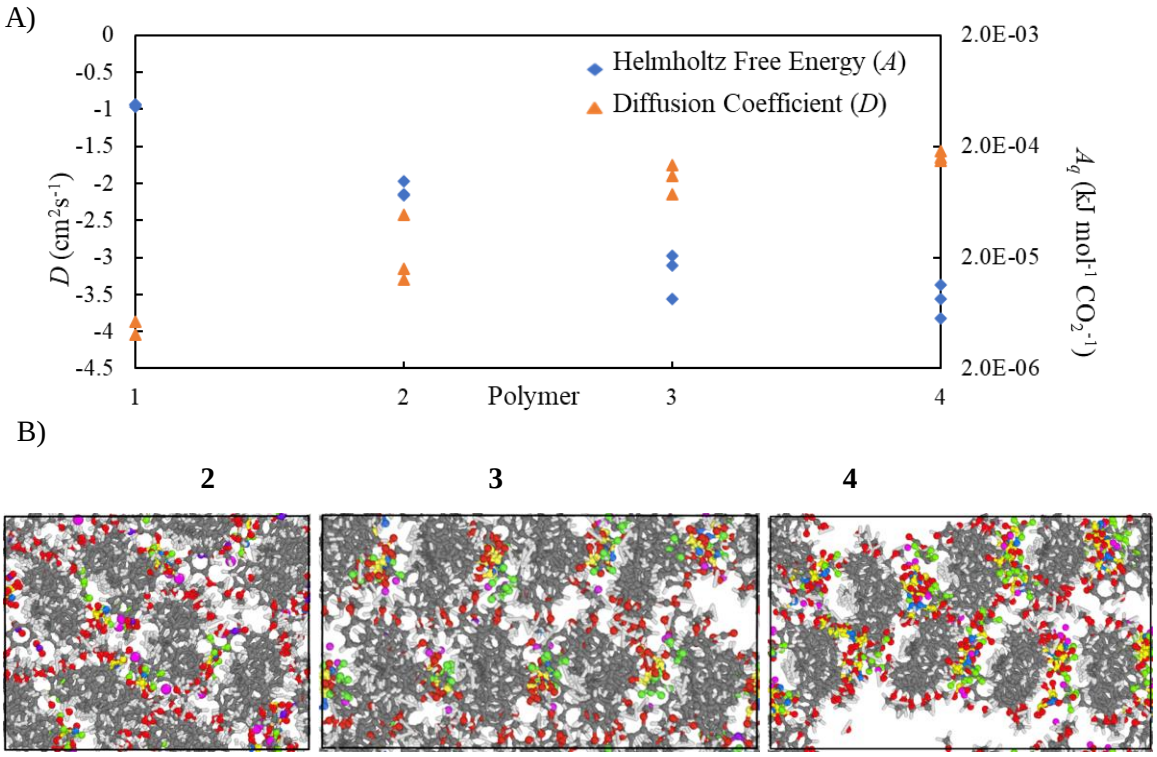

Figure 4.4. Results from two-phase thermodynamics calculations.(A) Helmholtz free energy (A) and diffusion coefficient (D) for **1** through **4** calculated from molecular dynamics calculations. A is normalized by the number of CO_2 molecules in the simulation box. (B) Top view of simulation box (looking down polymer backbone) of **2** through **4**. Atom color legend: gray, carbon; white, hydrogen; red, oxygen; green, fluorine; yellow, sulfur; purple, potassium.

the most favorable mass transport in the polymer matrix created by **4**, giving rise to the largest D_{CO2} among all the polymers. The correlation of D_{CO2} with K^+ concentration trends with an increased $|j_{C2+}|$ observed in the CO_2R experiments (Figure 4.1D). This suggests that improved CO_2R is due to more facile mass transport of CO_2 to the electrode. This agrees with previous claims that improved CO_2 diffusion leads to higher performance CO_2R towards C_{2+} products.[21, 24, 49-50] Inspection of the simulation boxes provides insight as to how increasing the amount of charged monomer units may increase interactions with CO_2 to improve mass transport (Figure 4.4B and Figure 4.14). Specifically, as the concentration of K-STFSI is increased, we observe increased interactions between CO_2 and K^+. In polymer **2**, only 6% of the CO_2 molecules have a K^+ within

5 Å, whereas in polymer **3**, 44% do, and in polymer **4**, 56% of the CO_2 molecules interact with nearby K^+ (Table 4.10).

These interactions lower the energy of the CO_2 molecule, shown by the decrease in $A_{q,CO2}$, effectively improving solubility in the ionomer. Despite lower $A_{q,CO2}$ with increasing K^+ content, reaction with CO_2 is not less favorable.[51-52] Rather, this gives rise to an enhanced local CO_2 concentration at the ionomer film-electrode interface, providing a possible explanation for improved CO_2R performance with increasing K^+ in the ionomer film. The porosity of the ionomer correlates with the amount of K-STFSI in the polymer due to repulsion from like charges. Figure 4.4B illustrates a top view (looking down the polymer backbone) of **2** through **4**, showing that **4** has the most substantial porosity derived from larger channels. To quantify porosity, we evaluated the open volume for polymers **1** through **4**, which is the total cell volume minus the volume occupied by the polymer backbone (see Computations in **EXPERIMENTAL SECTION** for calculation details). At equilibrium, polymers **1** through **4** have open volumes of 2324, 2442, 2575, and 2744 $Å^3$, respectively (Table 4.9). Hence polymer **1** has the lowest porosity while polymer **4** has the highest. CO_2 mass transport to the Cu surface is improved due to favorable interactions with K^+, and greater K^+ content leads to greater polymer porosity.[16, 21, 24, 53-55]

To further understand how cation identity affects CO_2, K^+ was replaced with $[NMe_4]^+$ in polymer **4** (Table 4.9). Despite increasing the polymer porosity in **4**-NMe_4 relative to **4** (3066 vs. 2744 $Å^3$), CO_2 possesses a weakened interaction between CO_2 and $[Me_4N]^+$ (compared to K^+), leading to less favorable mass transport and substantially less cation-induced stabilization. CO_2 diffusion decreases for **4**-NMe_4 as $A_{q,CO2}$ is raised. These calculations, in addition to the experimental results displaying lack of improved CO_2R in the ionomer films devoid of K^+, (Figure 4.2) demonstrate the crucial role of the alkali cation in driving CO_2R performance.

CONCLUSIONS

In summary, we demonstrated a novel strategy for modulating local [K^+] at the electrode-electrolyte interface via systematic variation of ionomer structure. We observed that $|j_{C2+}|$ trends with the amount of K^+-containing comonomer, reaching $|j_{C2+}|$ = 225 mA cm^{-2} for the ionomer featuring the highest K^+ content. Replacing the cation with $[Me_4N]^+$ eliminates any improvement in selectivity compared to bare Cu, highlighting the indispensable role of K^+ in these polymers for enhanced CO_2R. MD simulations suggest that increased entropy, diffusivity, and lower free energy of CO_2 in the polymer matrix facilitate CO_2 reactivity at the electrode interface. The combined results from electrochemistry and MD simulations highlight a crucial effect of K^+ within ionomers **2**-**4**, in which the reaction of CO_2R is favored due to enhanced mass transport and stabilization in the ionomer microenvironment. Finally, this study highlights a promising strategy for preparing film-modified electrodes for higher performance CO_2R.

EXPERIMENTAL SECTION

General Considerations All solvents and reagents were obtained from commercial sources (Aldrich, Merck, and Combi Blocks) and used as received, unless stated otherwise. 4-Methoxystyrene was dried with CaH_2 and filtered under an inert atmosphere. **K-STFSI** was prepared based on a previously reported synthesis.[56] Acetonitrile was dried by passing over activated alumina by the method of Grubbs[57] and stored over 3 Å molecular sieves in an N_2-filled glovebox. Nafion 1100 W was purchased from Sigma-Aldrich (Product #274704, 5 wt% in 1-propanol/2-propanol).

Copper nanoparticles, potassium carbonate (99.995%), trimethylammonium hydroxide (semiconductor grade, 99.99% trace metals basis), 4-methoxystyrene, and 1 M aqueous trimethylammonium bicarbonate solution (99%), isopropanol (HPLC grade), and ethanol (HPLC grade) were purchased from Sigma Aldrich. Polytetrafluoroethylene (PTFE) was purchased from McMaster-Carr. The leakless Ag/AgCl reference electrode was purchased from Innovative Instruments. Platinum mesh (99.99% Pt, 25 mm × 25 mm × 0.05 mm) was purchased from Alfa Aesar. CO_2 (research grade) was purchased from Airgas. Deuterium oxide (D, 99.96%), CD_3CN (D, 99.8%), and $CDCl_3$ (D, 99.8% were purchased from Cambridge Isotope Laboratories. The ^1H and ^{19}F NMR spectra were recorded on a Bruker 400 MHz with broadband auto-tune OneProbe. ^{13}C NMR spectra were recorded on a Bruker 400 MHz instrument with a prodigy broadband cryoprobe. Shifts were reported relative to the residual solvent peak. Inductively coupled plasma-mass spectrometry (ICP-MS) was performed on a Thermo Fisher Scientific iCAP^{TM} RQ instrument. Each sample was digested/diluted by a factor of 10 with 2% v/v $HNO_{3(aq)}$.

Water was purified by a Nanopure Analytical Ultrapure Water System (Thermo Scientific) or a Milli-Q Advantage A10 Water Purification System (Millipore) with specific resistance of 18.2

MΩ·cm at 25 °C. A VWR sympHony™ pH meter (calibrated with a pH = 1.68 standard) was used to determine the pH of the electrolytes before experiments.

Synthesis of Methoxystyrene Homopolymer: The reaction was conducted under an inert atmosphere. Methoxystyrene (208 mg, 1.55 mmol, 1.0 equiv) was dissolved in MeCN (4 mL). AIBN (26 mg, 0.1 equiv) was added and rinsed with MeCN (1 mL). The vial was sealed, removed from the glovebox, and heated at 70 ^{o}C for 3 days. The reaction was quenched by exposure to air. The crude material was concentrated, redissolved in THF, and precipitated into MeOH (100 mL). The polymer was isolated as a fine white solid. Isolated yield: 108 mg. ^{1}H NMR CD_3CN: 7.0-6.5 (br., 4 H), 3.71 (br., 3 H), 1.8-0.8 (br., multiple peaks, 3 H).

General Procedure for Copolymer Synthesis: The reaction was conducted under an inert atmosphere. Methoxystyrene was added to a 20-mL scintillation vial and dissolved in MeCN (2 mL) followed by addition of K-STFSI dissolved in MeCN (2 mL). AIBN (0.1 equiv) was added and rinsed with MeCN (1mL). The vial was sealed, removed from the glovebox, and heated at 70 ^{o}C for 3 days. The reaction was quenched by exposure to air. The crude polymer was precipitated into Et_2O (100 mL) and filtered. The precipitate was stirred with 20 mL of an aqueous solution of 1 M $KHCO_3$ at 90 ^{o}C for a minimum of 30 minutes. The mixture was filtered hot over a glass frit. An additional 2 washes with 1 M $KHCO_{3(aq)}$ were necessary for most purifications. The solid material was extracted with MeCN, concentrated under reduced vacuum, redissolved in MeCN and filtered. The filtrate was precipitated with Et_2O (100 mL) and filtered. The polymer was isolated as a fine white solid.

Polymer 2: Methoxystyrene (189 mg, 1.416 mmol, 0.9 equiv), K-STFSI (50mg, 0.1416 mmol, 0.1 equiv), AIBN (26 mg, 0.157 mmol, 0.1 equiv). Isolated Yield: 146 mg ^{1}H NMR CD_3CN: 7.60, 6.63, 3.72, 1.8-0.8. ^{19}F NMR -79.22.

Polymer 3: Methoxystyrene (456 mg, 3.40 mmol, 0.8 equiv), K-STFSI (300 mg, 0.8499 mmol, 0.2 equiv), AIBN (69.8 mg, 0.423 mmol, 0.1 equiv). Isolated yield: 357 mg ^{1}H NMR CD_3CN: 7.63, 6.63, 3.72, 1.8-0.8. ^{19}F NMR -79.22.

Polymer 4: Methoxystyrene (399.2 mg, 2.97 mmol, 0.7 equiv), K-STFSI (450 mg, 1.27 mmol, 0.3 equiv), AIBN (69.8 mg, 0.423 mmol, 0.1 equiv). Isolated yield: 318 mg ^{1}H NMR CD_3CN: 7.60, 6.63, 3.72, 1.8-0.8. ^{19}F NMR -79.22.

All polymer representations here and in the main text express the ratio of the monomers as determined by ^{1}H NMR spectroscopy. However, the comonomers are considered to be ordered randomly.

Electrolyte Preparation

Potassium bicarbonate electrolyte (1 M $KHCO_{3(aq)}$) was prepared by sparging an aqueous solution of potassium carbonate (0.5 M $K_2CO_{3(aq)}$) with CO_2 for at least 1 hour prior to electrolysis. This process converts K_2CO_3 into $KHCO_3$ and saturates the electrolyte solution with CO_2. A similar preparation was carried out for 0.1 M $KHCO_{3(aq)}$. Before electrolysis with $CO_{(g)}$ or $Ar_{(g)}$, the electrolyte was sparged with $Ar_{(g)}$ to remove any residual $CO_{2(g)}$. Trimethylammonium hydroxide electrolyte (1 M Me_4NOH) was prepared by dissolving solid Me_4NOH into water and sparging for at least 30 minutes prior to electrolysis under CO_2.

Electrode Preparation

The gas diffusion electrodes (GDEs) were prepared by sputtering 300 nm Cu onto a 5 cm x 5 cm portion of polytetrafluoroethylene membrane (pore size of 450 nm, with polypropylene support on backside) using a pure Cu target (99.99%) at a sputtering rate of 1 Å s^{-1}.

A 0.3 mg mL^{-1} stock solution of the ionomer was prepared in 50% v/v EtOH/^{i}PrOH and sonicated for 30 minutes to ensure complete dissolution. For a standard loading, 15 µL were drop casted (4.5 µg) onto a 2.5 cm^2 electrode, ensuring complete coverage of the Cu nanoparticles, and allowed to dry under ambient conditions for 1 hour.

To test Nafion 1100 W, 60 µL of the stock solution (5 wt% in propanol mixture) was drop casted onto a 2.5 cm^2 electrode to match the loading that was reported by Bell and co-workers.[16]

For experiments involving Me_4N^+, 15 µL of the standard 0.3 mg mL^{-1} ionomer solution were drop casted onto Cu/PTFE, and the electrode was dried for 1 hour. The cell was assembled and 1 M $Me_4NHCO_{3(aq)}$ (or 1 M $Me_4NOH_{(aq)}$) was circulated using a peristaltic pump at 10 mL min^{-1} with 30 sccm CO_2 flowing for 30 minutes. Before electrolysis under CO_2, the electrolyte was replaced with fresh electrolyte.

Electrochemical Measurements in the GDE (Flow) Cell

CO_2R and COR measurements were conducted in a gas-tight liquid-electrolyte flow cell. Chronoamperometry experiments were carried out in a custom-made PEEK liquid-electrolyte cell similar to the one reported by Sargent and co-workers.[58] The liquid-electrolyte flow cell consists of three compartments: gas chamber, catholyte chamber, and anolyte chamber. The PTFE electrode was sandwiched between CO_2 gas chamber and catholyte chamber with an exposure area of 0.5 cm^{-2}. Catholyte and anolyte chambers were separated by a Selemion AMV anion-exchange membrane (AGC Engineering Co.). The reference electrode was calibrated against H^+/H_2 on Pt in a 0.5 M sulfuric acid solution (0 V vs. RHE) and saturated calomel electrode (SCE) (+0.241 V saturated vs. RHE). An Autolab PGSTAT204 in a potentiostatic mode was used as the electrochemical workstation. The PTFE electrode, leakless Ag/AgCl electrode (Innovative Instruments), and Pt mesh (rinsed with water and annealed with a butane torch) were employed as

working, reference, and counter electrodes, respectively. The applied potentials were converted to the reversible hydrogen electrode (RHE) scale with *i*R correction through the following equation:

$$E_{corrected}\ (\text{vs. RHE}) = E\ (\text{vs. Ag/AgCl}) + (0.059 \times \text{pH}) + 0.210 + iR \qquad (1)$$

$E_{applied}$ in this report is the applied potential without *i*R compensation. In order to convert from potential vs. Ag/AgCl, we use the following relationship:

$$E_{applied}\ (\text{vs. RHE}) = E\ (\text{vs. Ag/AgCl}) + (0.059 \times \text{pH}) + 0.210 \qquad (2)$$

where *i* is the current at each applied potential and R is the equivalent series resistance measured via potentioelectrochemical impedance spectroscopy (PEIS) in the frequency range of 10^5 – 0.1 Hz with an amplitude of 10 mV. The appropriate gas-saturated electrolyte was used as both catholyte and anolyte and was circulated through the flow cell using peristaltic pumps with a silicone Shore A50 tubing. The electrolyte was bubbled with the desired gas during the entire electrolysis process. The electrolyte flow rate was kept at 10 mL min^{-1}. The flow rate of the gas flowing into the gas chamber was kept at 30 sccm by a digital mass flow controller.

Ohmic resistance values were determined with procedures described elsewhere[59-60] and employed in our prior work[8-9, 58] PEIS measurements were carried out prior to and after each electrolysis experiment to determine the Ohmic resistance of the flow cell and ensure it is unchanged during the experiment.[61-62] The impedance measurements were carried out at frequencies ranging from 200 kHz to 100 MHz. A Nyquist plot was obtained, and in the low-frequency region (containing a Warburg element) a line was plotted to determine the value of the intersection with the x-axis, representing the Ohmic resistance (Figure 4.12).[59] An average of 3 measurements was taken to calculate the value of R. Typically, small resistances were measured, ranging from 4 to 7 Ω. The

potentiostat was set to compensate for 85 % of the Ohmic drop, with the remaining 15 % being compensated for after the measurements.[59-60]

All chronoamperometric experiments were performed for 30 min at 25 °C. Before each electrolysis experiment, the ionomer was drop casted onto a 2.5 cm^2 Cu/PTFE electrode. The entire Ohmic drop was compensated before and after the measurement. The effluent gas stream coming from the cell (30 mL min^{-1}) was flowed into the sample loops of a gas chromatograph (GC-FID/TCD, SRI 8610C, in Multi Gas 5 configuration) equipped with HayeSep D and Molsieve 5A columns. Methane, ethylene, ethane, and carbon monoxide were detected by a methanizer-flame ionization detector (FID) and the hydrogen was detected by a thermal conductivity detector (TCD). Every 15 minutes, 2 mL of gas was sampled to determine the concentration of gaseous products. After electrolysis, the liquid products in the catholytes were quantified by both HPLC (Thermo Scientific Ultimate 3000) and ^{1}H NMR spectroscopy (Bruker 400 MHz Spectrometer). For ^{1}H NMR analysis, 630 µL of the electrolyte sample was combined with 30 µL of internal standard solution (10 mM DMSO and 50 mM phenol) and 70 µL of D_2O. Water suppression was achieved with a presaturation sequence.[8, 62]

The Faradaic efficiencies for gaseous products were calculated from the following equations:

$$F_m = \frac{pF_v}{RT} \qquad (3)$$

$$FE_{prod} = \frac{n_{prod}Fx_{prod}F_m}{i} \qquad (4)$$

$F_m$is the molar flow, defined by the pressure p, the volume flow F_v, the gas constant R, and temperature T. FE_{prod} is the Faradaic efficiency of a gaseous product $prod$, defined by the

electron transfer coefficient of the product n_{prod}, Faraday's constant F, the fraction of the product x_{prod}, the molar flow F_m, and the current i.

Error bars shown in all figures and tables represent standard deviations from at least three replicate measurements.

For variable partial pressure $CO_{2(g)}$ (P_{CO2}) experiments, $Ar_{(g)}$ was utilized as the balance gas such that the total flow rate remained at 30 sccm. For example, in the case where pCO_2 = 0.8 atm, the flow rate of $CO_{2(g)}$ was 24 sccm and that of $Ar_{(g)}$ was 6 sccm.

To compare local K^+ between ionomers **2** and **4** each in the presence and absence of applied potential, extraction with 0.1 M $LiHCO_{3(aq)}$ was carried out[34] to exchange K^+ in the ionomer with Li^+, as was carried out in the cation exchange experiments described above.

No applied potential: 45 µL of each ionomer solution was drop casted onto a separate 2.5 cm^2 electrode. Each electrode was placed in a 1 mL solution of 0.1 M $LiHCO_{3(aq)}$ and stirred for 72 hours. The electrodes were rinsed with their extraction solution to ensure complete removal of K^+. The solutions were submitted for ICP-MS.

With applied potential: 45 µL of each ionomer solution was drop casted onto a separate 2.5 cm^2 electrode, and each was submitted for electrolysis in 1 M $KHCO_{3(aq)}$ with $CO_{2(g)}$ in the GDE cell for 30 minutes. Each electrode was rinsed with 500 µL of nanopure water to remove excess K^+ from the electrolyte. Each electrode was placed in a 1 mL solution of 0.1 M $LiHCO_{3(aq)}$ and stirred for 72 hours. The electrodes were rinsed with their extraction solution to ensure complete removal of K^+. The solutions were submitted for ICP-MS.

Computations

All molecular dynamics calculations were performed using the LAMMPS software package. The Universal Force Field (UFF) was used, along with the qEq charge scheme, which has been shown to accurately capture atomic charges calculated from quantum mechanics. All K^+ charges were fixed at +0.6 and all N^- charges were fixed at -0.6. Polymer chains are bound to themselves at the periodic boundaries, such that the polymers are infinite in length. When adding the charged monomer units to polymers **2** through **4**, spacing was chosen to maximize the distance between charged groups.

Calculations were initiated by energy minimization. Minimization was followed by heating via Nose-Hoover NVT molecular dynamics (MD) from 1.0 to 300.0 K over 10 ps. Following heating, the temperature was held at 300 K (still with Nose-Hoover NVT) while the box was deformed to an energy minima. Finally, the simulation box was equilibrated at 300 K at the new cell volume for 220 ps; the last 120 ps were used for analysis.

The periodic simulation boxes for polymers **1-4** each contain 8 polymer chains propagating parallel to each other; the polymer chains are each made of 20 explicit monomeric units. However, the ends of the polymer chains are bound together at the periodic boundary such that the polymers are infinite in length. The simulation boxes also include 16 CO_2 molecules and 16 water molecules.

The 2 Phase Thermodynamics (2PT) method was used to calculate entropies, free energies, and diffusion coefficients from our MD simulations. 2PT tracks atom velocities in order to calculate the velocity autocorrelation function, which in turn can undergo a Fourier transform to yield the density of state function. Entropy and free energy are calculated via weighted integrals over the density of states, and diffusion coefficient is calculated via the density of states at zero

frequency. We perform 3 calculations based on the velocity autocorrelation function, which we have found requires 40 ps to converge and yield reasonable statistics (120 ps total).

The polymer open volumes (V_{open}, Equation 3) are defined as the total cell volumes (V_{total}) minus the volumes occupied by the polymer backbone. The polymer backbone volume is computed assuming that all atoms are spheres with radii equivalent to their covalent atomic radius (r_i), as computed from first principles by Clementi et al.[63] n_i in Equation 3 is the number of atoms of type i.

$$V_{open} = V_{total} - \sum_i n_i \frac{4}{3}\pi r_i^3 \qquad (5)$$

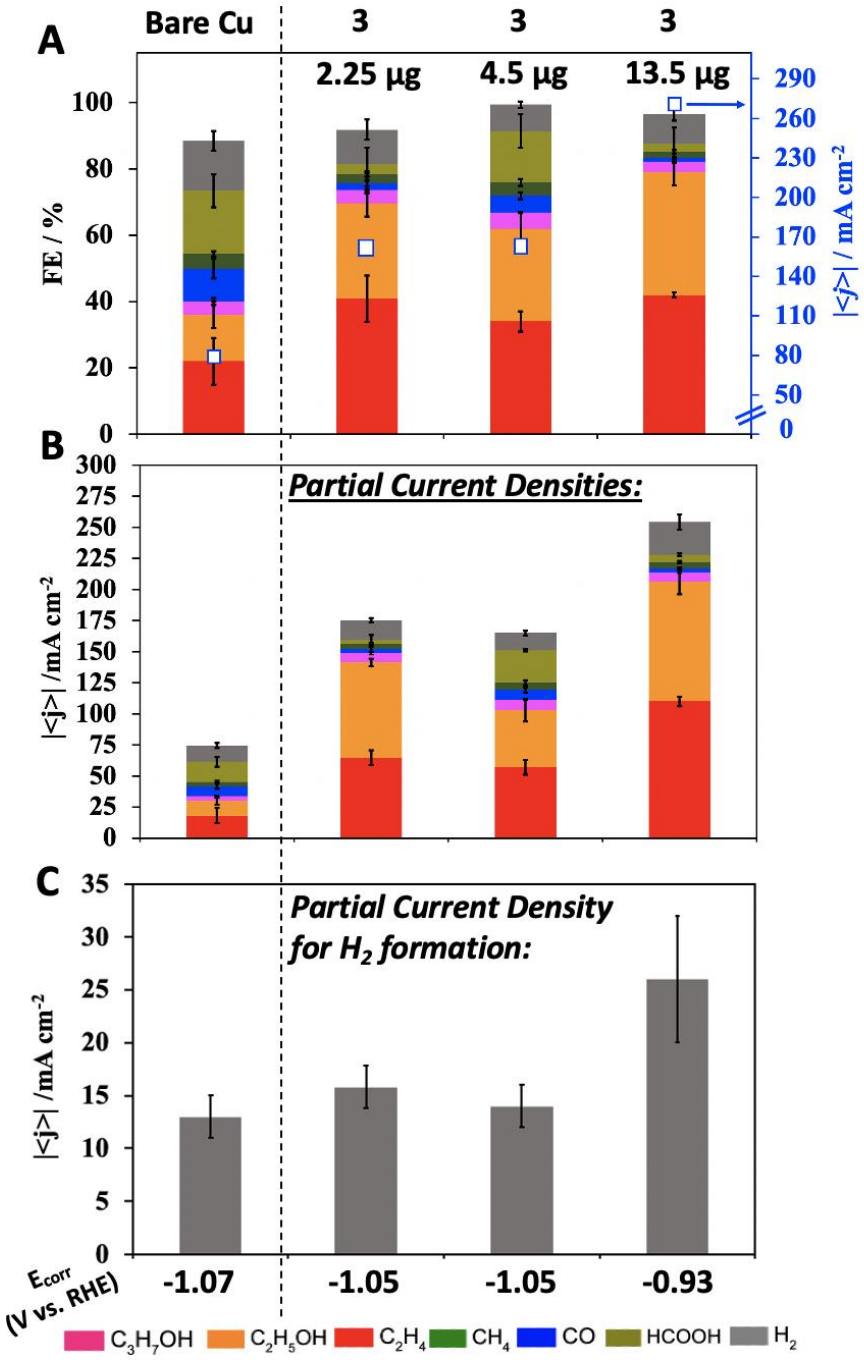

Figure 4.5 Selectivity profile with 3 at different ionomer loadings. A. Faradaic efficiencies (FEs, columns) and current densities (white squares) and **B.** partial current densities from CO_2R on 3-coated Cu at different loadings. **C.** Partial current density for hydrogen formation. Chronoamperometry performed in 1 M $KHCO_3$ at –1.15 V vs. RHE. E_{corr} represents potentials corrected after compensating for ohmic losses.

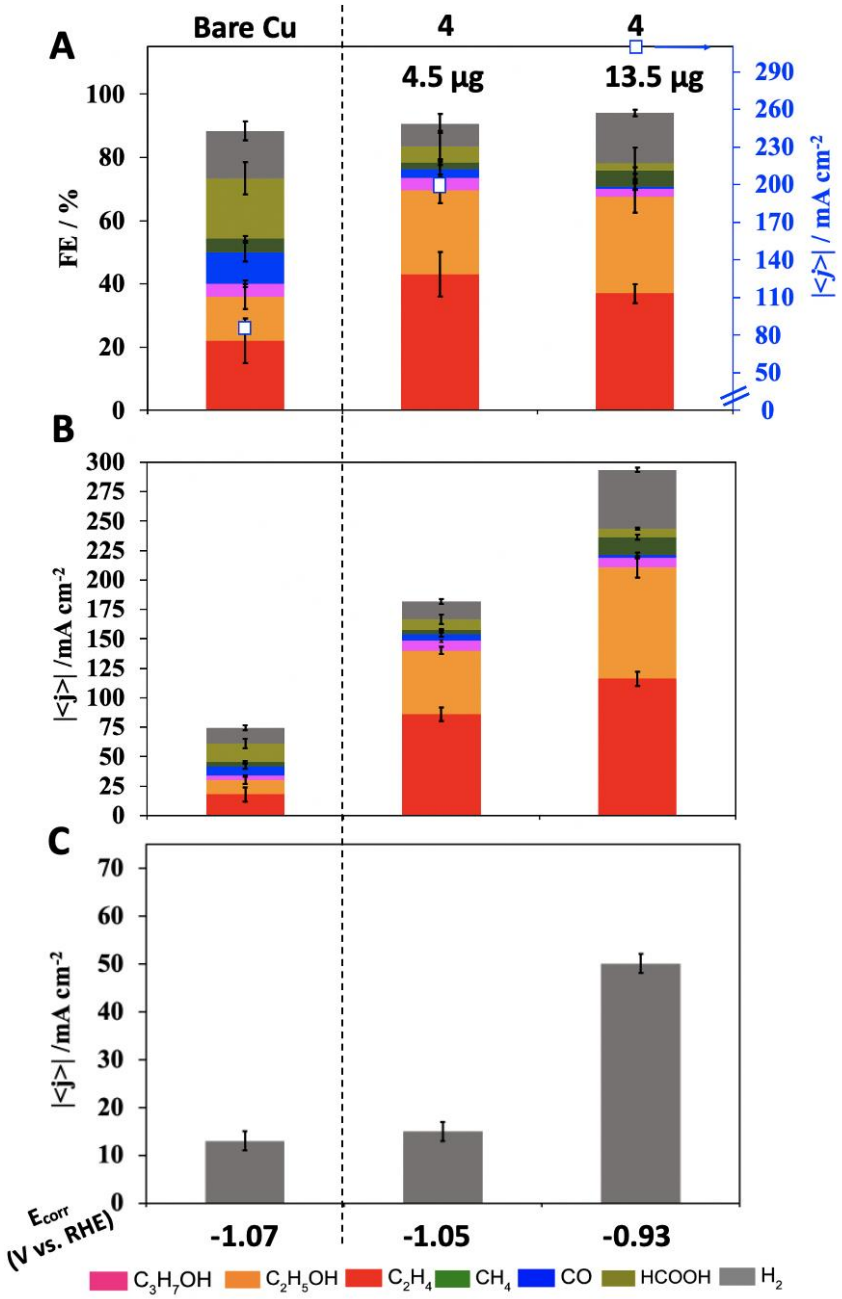

Figure 4.6. Selectivity profile with 4 at different ionomer loadings. A. Faradaic efficiencies (Fes, columns) and current densities (white squares) and **B.** partial current densities from CO_2R on **4**-coated Cu at different loadings. **C.** Partial current density for hydrogen formation. Chronoamperometry performed in 1 M $KHCO_3$ at –1.15 V vs. RHE.

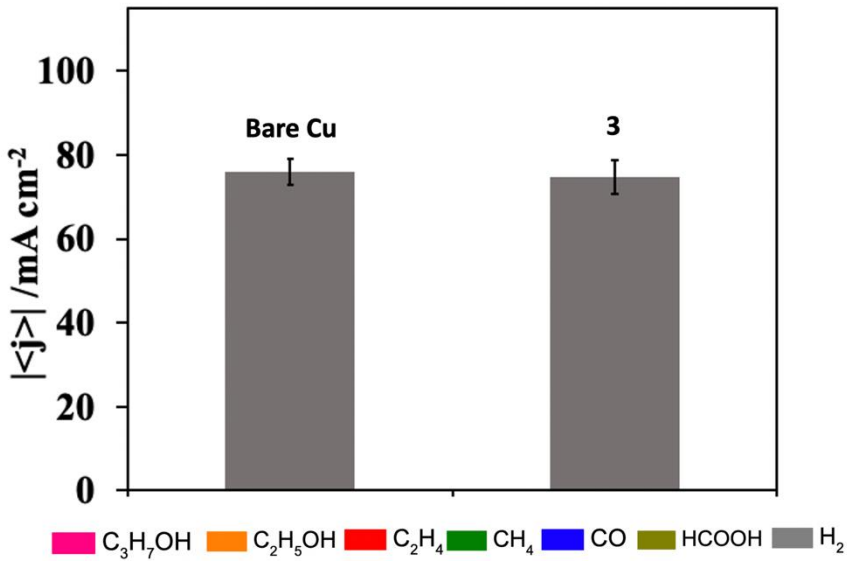

Figure 4.7. Partial current densities from chronoamperometry in 1 M $KHCO_3$ at –1.16 V vs. RHE in the presence of $Ar_{(g)}$ comparing bare Cu/PTFE with **3**-coated Cu.

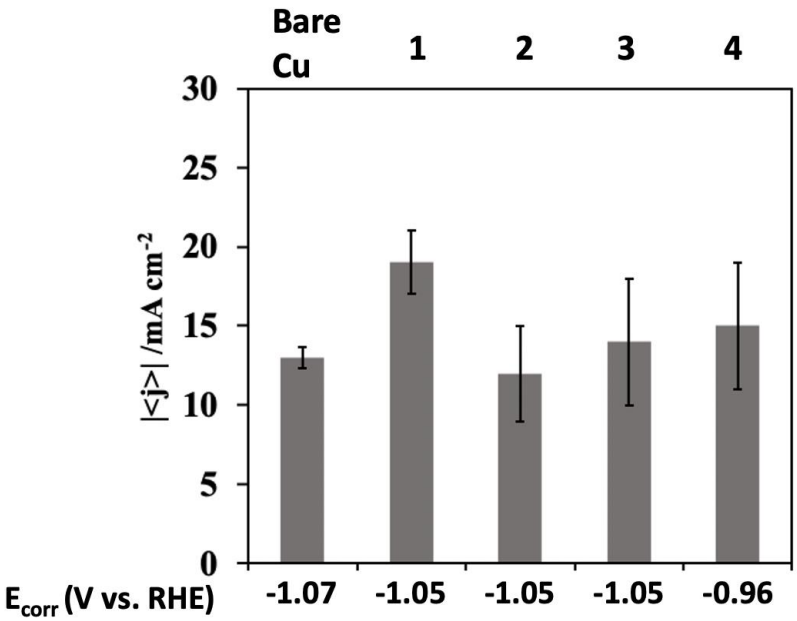

Figure 4.8. Partial current density for H_2 for each ionomer-coated Cu from electrolysis in 1 M $KHCO_3$ with $CO_{2(g)}$. $E_{applied}$ = –1.15 V vs. RHE.

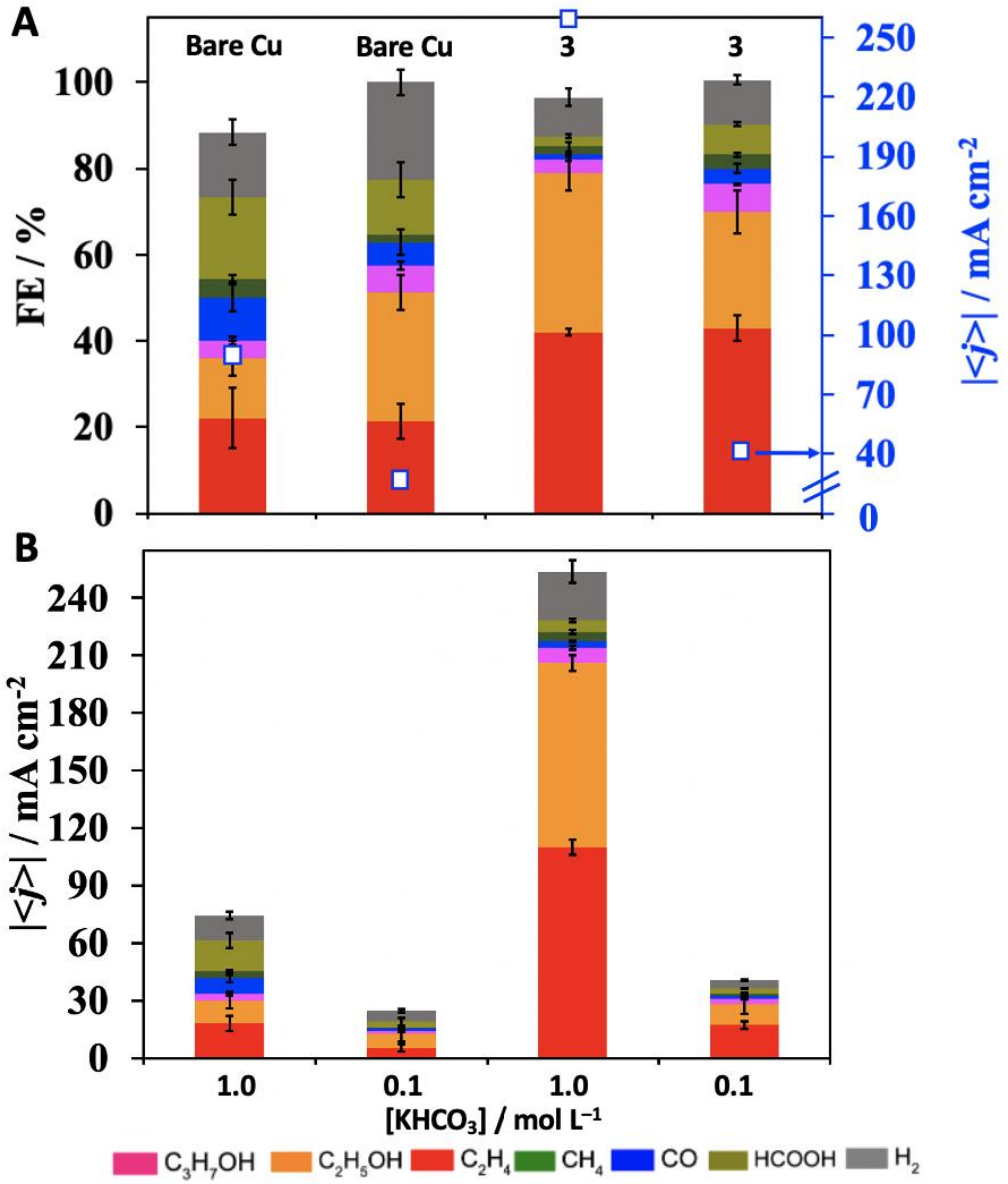

Figure 4.9. CO_2R chronoamperometry in 1 M $KHCO_3$ at –1.15 V vs. RHE in 0.1 M $KHCO_3$ and 1 M $KHCO_3$ comparing bare Cu/PTFE with 3-coated Cu **A.** Faradaic efficiencies (FEs) and current densities (white squares) from CO_2R on bare Cu/PTFE and **3**-coated Cu comparing 0.1 M $KHCO_{3(aq)}$ and 1 M $KHCO_{3(aq)}$ Chronoamperometry performed in 1 M $KHCO_{3(aq)}$ at –1.15 V vs. RHE and 0.1 M $KHCO_{3(aq)}$ at –1.05 V vs. RHE. **B.** Partial current densities of each product.

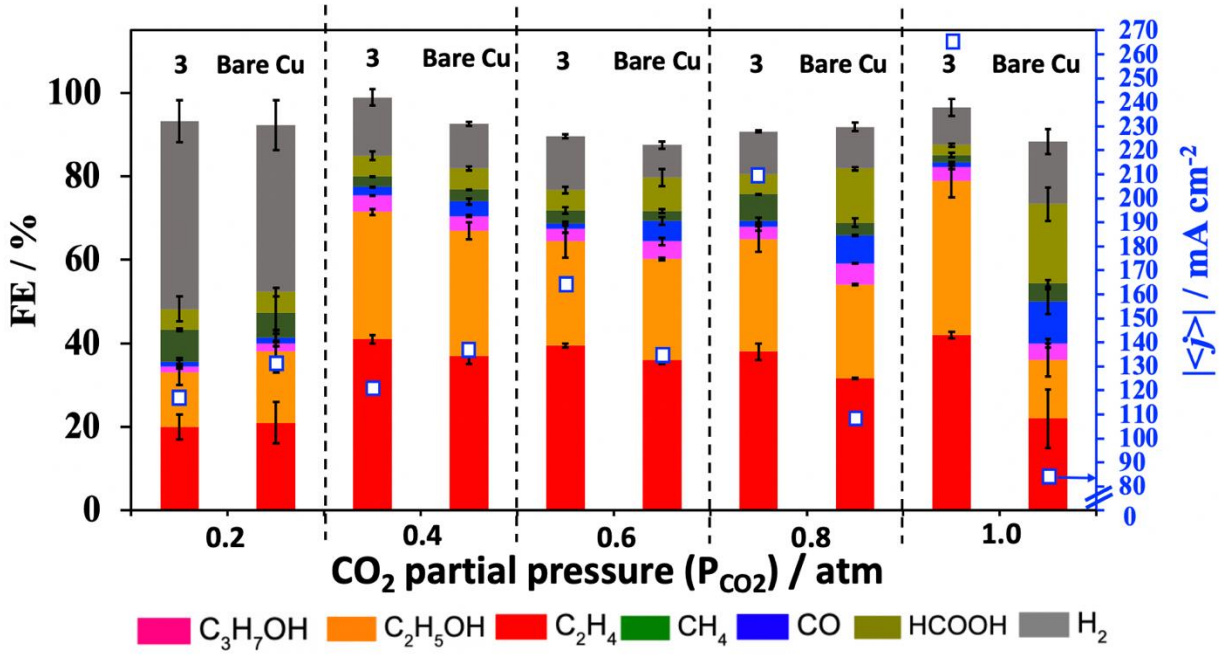

Figure 4.10. Faradaic efficiencies (FEs) and current densities (white squares) from CO_2R on Cu/PTFE in the presence of film drop casted from **3** (ionomer loading: 13.5 µg) tested in 1 M $KHCO_{3(aq)}$ at various CO_2 partial pressures ($Ar_{(g)}$ balance gas).

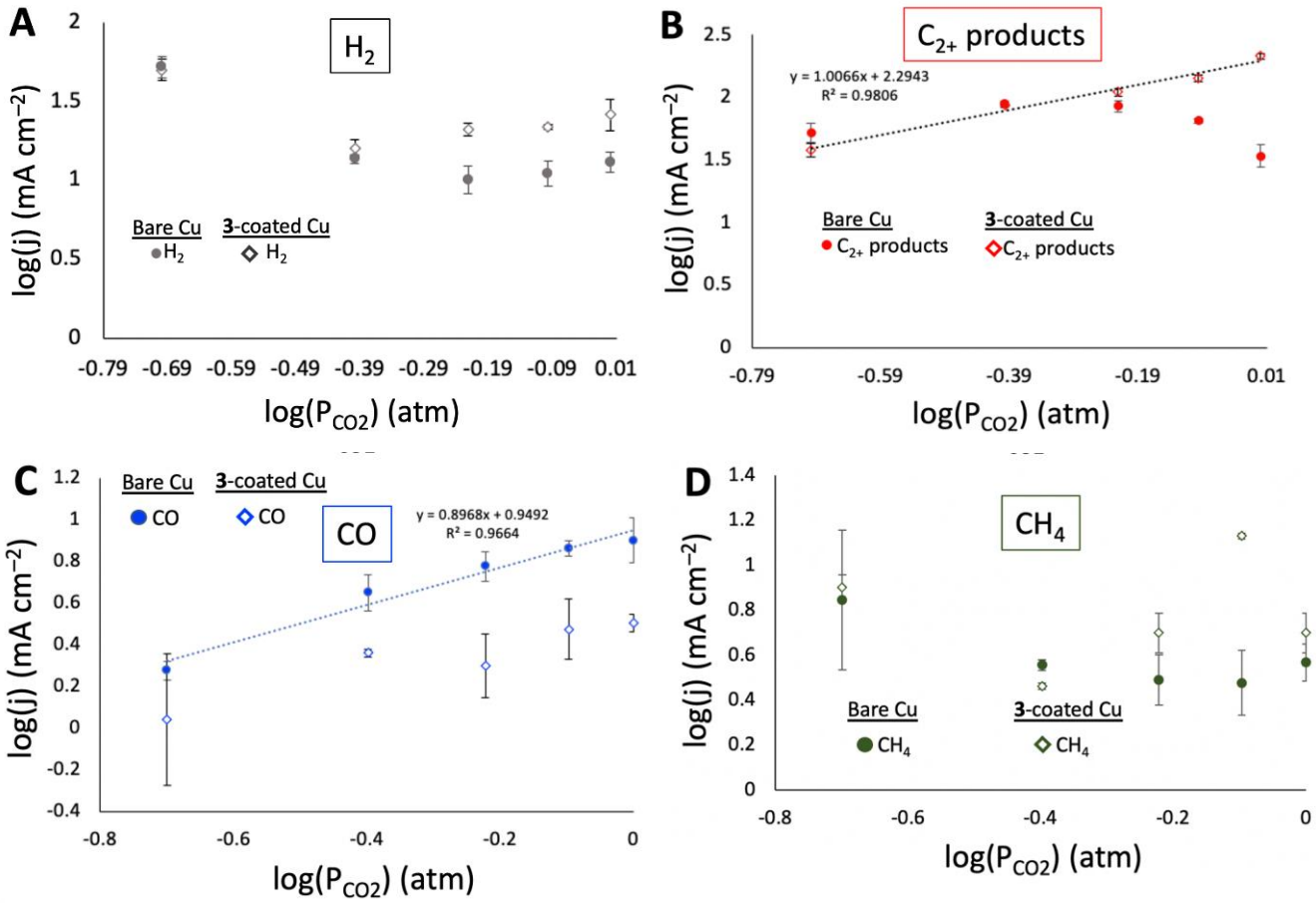

Figure 4.11. Plots of log(j_{prod}) vs. log(P_{CO2}) from variable partial pressure CO_2 experiments.

Plots of log(j_{prod}) vs. log(P_{CO2}) from variable partial pressure CO_2 experiments for H_2 (panel A), C_{2+} products (panel B), CO (panel C)**,** CH_4 (panel D). Filled circles represent bare Cu data and hollow diamonds represent **3**-coated Cu.

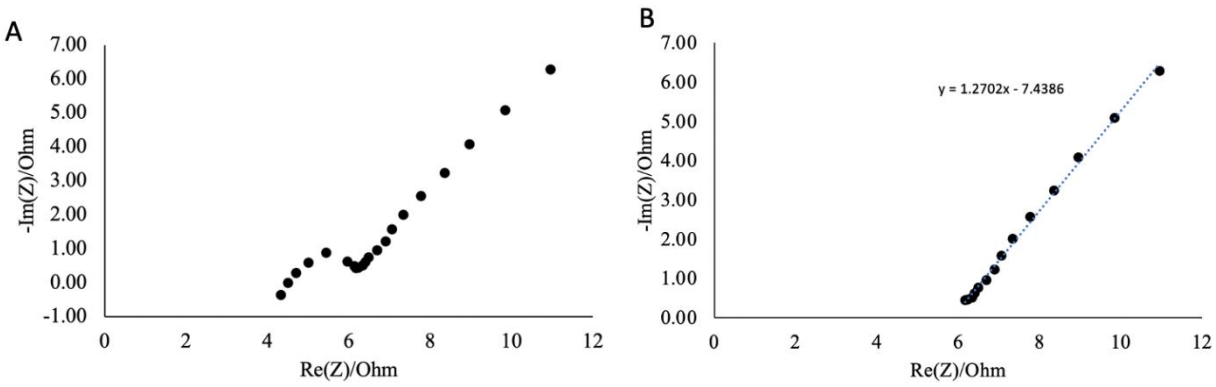

Figure 4.12. **Impedance spectroscopy. A.** Example Nyquist plot from CO_2R electrolysis with **3**-coated Cu (13.5 µg). **B.** Linear fit of Warburg region.

Table 4.1. Partial current densities from CO_2R with different alkali cations (Li^+, K^+, and Cs^+) in the ionomer (4.5 µg) and electrolyte.

Ionomer	Electrolyte	$E_{applied}$ (V vs. RHE)	$E_{corrected}$ (V vs. RHE)	$\|j\|$ (mA/cm^2)							
				H_2	CH_4	CO	C_2H_4	$HCOO^-$	C_2H_5OH	C_3H_7OH	$\|j_{C2+}\|$
Bare Cu	0.1 M $LiHCO_{3(aq)}$	-1.10	-0.98	11.2 ± 0.5	2.4 ± 0.6	0.12 ± 0.03	0.31±0.03	0.6 ± 0.1	0	0	0.31±0.03
4	0.1 M $LiHCO_{3(aq)}$	-1.10	-0.98	2.2 ± 0.2	0.11± 0.09	2.8 ± 0.7	1.9 ± 0.3	3 ± 1	1.3 ± 0.6	1.1 ± 0.6	4.2 ± 0.9
Bare Cu	0.1 M $KHCO_{3(aq)}$	-1.10	-0.92	5.6 ± 0.6	0.4 ± 0.2	1.3 ± 0.3	5 ± 1	3 ± 1	7 ± 1	1.5 ± 0.5	14 ± 2
4	0.1 M $KHCO_{3(aq)}$	-1.10	-0.93	4.2 ± 0.4	1.3 ± 0.4	1.5 ± 0.5	24 ± 1	2.82 ± 0.03	15 ± 2	5.0 ± 0.4	44 ± 3
Bare Cu	0.1 M $CsHCO_{3(aq)}$	-1.10	-0.75	11 ± 2	0	12 ± 1	12.5 ± 0.5	7 ± 2	10 ± 3	5 ± 1	30 ± 3
4	0.1 M $CsHCO_{3(aq)}$	-1.10	-0.5	10 ± 2	0	14.5 ± 0.7	22 ± 1	12 ± 1	23 ± 2	4.9 ± 0.3	50 ± 2

Table 4.2. Selectivity profile from CO_2R on Cu GDE modified by 1-4; $E_{applied}$ = –0.95 V vs. RHE. 1 M $KHCO_{3(aq)}$.

Ionomer	$E_{corrected}$ (V vs. RHE)	Faradaic Efficiency (%)									
		H_2	CO	HCOOH	CH_4	C_2H_4	C_2H_5OH	C_3H_7OH	Total	FE_{C2+}/FE_{C1}	j (mA/cm^2)
Bare Cu	-0.89	22 ± 4	6.7 ± 0.2	17 ± 0.4	17 ± 2	19 ± 4	10 ± 1	3.0 ± 0.4	95 ± 6	1.2 ± 0.5	-45 ± 1
1	-0.88	23 ± 1	9 ± 1	20 ± 1	4 ± 1	18 ± 2	11 ± 1	3 ± 1	98 ± 4	1.0 ± 0.1	-46 ± 1
2	-0.87	20 ± 4	6 ± 1	15 ± 1	4 ± 1	25 ± 6	17 ± 4	2 ± 1	90 ± 4	1.8 ± 0.8	–55 ± 5
3	-0.78	18 ± 2	8 ± 2	19 ± 5	4 ± 3	30 ± 3	15 ± 2	3 ± 1	97 ± 6	1.5 ± 0.7	–65 ± 3
4	-0.85	18 ± 2	4.0 ± 0.7	8 ± 1	2 ± 1	34 ± 3	15 ± 5	4 ± 1	85 ± 4	4.1 ± 0.8	–80 ± 8
Nafion 1100W	-0.92	32 ± 2	15.6 ± 0.7	27 ± 5	4.4 ± 0.7	5 ± 3	19 ± 6	7 ± 1	110 ± 8	1.1 ± 0.5	–17 ± 4

Table 4.3. Selectivity profile from CO_2R on Cu GDE modified by 1-4; $E_{applied}$ = –1.05 V vs. RHE. 1 M $KHCO_{3(aq)}$.

Ionomer	$E_{corrected}$ (V vs. RHE)	Faradaic Efficiency (%)									
		H_2	CO	HCOOH	CH_4	C_2H_4	C_2H_5OH	C_3H_7OH	Total	FE_{C2+}/FE_{C1}	*j* (mA/cm^2)
Bare Cu	-0.99	27 ± 1	13 ± 3	27 ± 1	4 ± 2	17 ± 1	10.6 ± 0.5	4.5 ± 0.4	103 ± 6	0.7 ± 0.1	–65 ± 1
1	-0.98	23 ± 5	13 ± 3	19.7 ± 0.3	9 ± 3	18 ± 2	12 ± 1	4.30 ± 0.05	99 ± 6	0.82 ± 0.08	–65 ± 1
2	-0.94	13 ± 4	6.2 ± 0.4	11 ± 1	4.5 ± 0.7	40 ± 6	22 ± 4	5 ± 1	102 ± 8	3.1 ± 0.4	–99 ± 5
3	-0.96	14 ± 2	6 ± 2	12 ± 5	4 ± 2	34 ± 3	25 ± 2	4 ± 1	99 ± 7	2.9 ± 0.9	–105 ± 7
4	-0.87	11 ± 2	3.3 ± 0.7	8.4 ± 0.3	2.1 ± 0.2	34 ± 3	20.3 ± 0.2	5.6 ± 0.1	85 ± 6	4.3 ± 0.8	–111 ± 8
Nafion 1100 W	-0.96	22 ± 2	6 ± 1	30 ± 2	2.5 ± 0.5	18 ± 3	18 ± 2	5 ± 1	102 ± 5	1.1 ± 0.5	–58 ± 2

Table 4.4. Selectivity profile from CO_2R on Cu GDE modified by 1-4; $E_{applied}$ = –1.15 V vs. RHE. 1 M $KHCO_{3(aq)}$.

Ionomer	$E_{corrected}$ (V vs. RHE)	Faradaic Efficiency (%)									
		H_2	CO	HCOOH	CH_4	C_2H_4	C_2H_5OH	C_3H_7OH	Total	FE_{C2+}/FE_{C1}	*j* (mA/cm^2)
Bare Cu	-1.07	15 ± 3	10 ± 3	19 ± 4	4.4 ± 0.8	22 ± 2	14 ± 4	4 ± 1	90 ± 8	1.2 ± 0.3	–84 ± 5
1	-1.05	21 ± 4	12 ± 3	19 ± 3	10 ± 3	20 ± 2	12 ± 2	4.3 ± 0.6	98 ± 8	0.9 ± 0.2	–90 ± 1
2	-1.05	9 ± 1	7 ± 1	15 ± 8	1 ± 1	34.1 ± 0.2	21 ± 1	4.23 ± 0.03	92 ± 6	2.6 ± 0.9	–135 ± 5
3	-1.05	8 ± 1	5 ± 1	15.5 ± 0.5	2 ± 1	34 ± 3	25 ± 2	4 ± 1	97 ± 6	3.0 ± 0.3	–166 ± 8
4	-0.96	7.3 ± 8	2.7 ± 0.1	8.4 ± 0.3	2.7 ± 0.5	43 ± 5	28 ± 5	4.86 ± 0.05	90 ± 5	7.5 ± 0.8	–202 ± 9
Nafion 1100 W	-1.07	25 ± 2	3 ± 1	30 ± 1	1.0 ± 0.5	22 ± 1	11 ± 2	4 ± 1	96 ± 4	1.1 ± 0.5	-69 ± 2

Table 4.5. Selectivity profile from CO_2R on Cu GDE modified by 4 with Me_4N^+-containing electrolyte. $E_{applied}$ = –1.6 V vs. SHE.

Ionomer	Electrolyte	$E_{corrected}$ (V vs. RHE)	Faradaic Efficiency (%)								
			H_2	CH_4	CO	C_2H_4	$HCOO^-$	C_2H_5OH	C_3H_7OH	Total	*j* (mA/cm^2)
Bare Cu	1 M $Me_4NHCO_{3\,(aq)}$	-1.07	91 ± 3	0	0	0	0	0	0	91 ± 3	-65 ± 1
4	1 M $Me_4NHCO_{3\,(aq)}$	-1.07	95 ± 3	0	0	0	0	0	0	95 ± 3	-67 ± 1
4-Me_4N[a]	1 M $Me_4NHCO_{3\,(aq)}$	-1.07	97 ± 1	0	0	0	0	0	0	97 ± 3	-67 ± 1
Bare Cu	1 M $Me_4NOH_{(aq)}$	-0.72	14 ± 4	3 ± 2	10 ± 1	26 ± 1	12 ± 3	23 ± 3	9 ± 1	97 ± 8	-40 ± 3
4	1 M $Me_4NOH_{(aq)}$	-0.72	22 ± 4	9 ± 4	7 ± 4	24 ± 3	17 ± 5	18 ± 2	8.8 ± 0.1	106 ± 8	-40 ± 5

[a]Performed cation exchange with **4** or **3** in 1 M $Me_4NHCO_{3(aq)}$, then drop casted onto Cu GDE.

Table 4.6. ICP-MS data to determine K^+ concentration from each ionomer with and without electrolysis.

Sample	$[K^+]$ (μg mL^{-1}) [a]	$[K^+]$ (μg mL^{-1}) with background subtraction
Water	20 ± 1	N/A
0.1 M $LiHCO_{3(aq)}$	20 ± 1	N/A
4, no electrolysis	53 ± 6	33 ± 6
4, with electrolysis	360 ± 10	340 ± 10
2, no electrolysis	41 ± 2	21 ± 2
2, with electrolysis	210 ± 10	190 ± 10

[a]Standard deviations represent error from triplicate measurements.

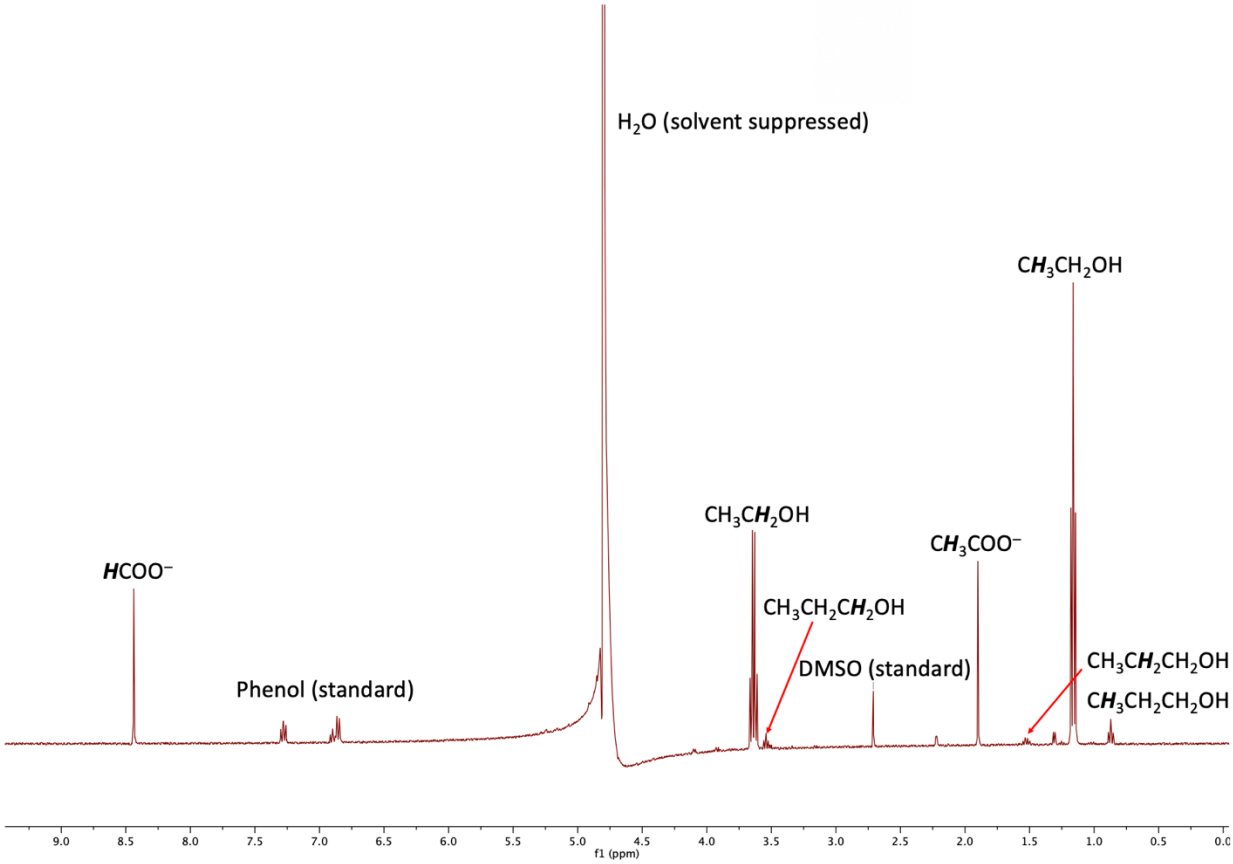

Figure 4.13. Sample ^{1}H NMR spectrum (400 MHz, 10% v/v D_2O) of catholyte after 30-minute CO_2R chronoamperometry ($E_{applied}$ = –1.15 V vs. RHE) with **3**-coated Cu (4.5 µg). DMSO and phenol were used as standards.

Table 4.7. Comparing CO_2R performance between Cu electrodes with coated with ionomer films.

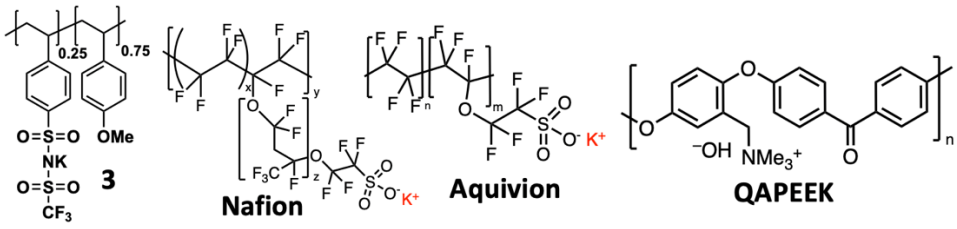

Authors	Ionomer	Electrolyte	$E_{corrected}$ (V vs. RHE)	FE_{C2+}	$\|j_{C2+}\|$ (mA cm^{-2})	FE_{H2}
This work	**3**	1 M $KHCO_3$	–0.96	82%	225	8%
	Nafion 1100 W	1 M $KHCO_3$	–1.07	36%	25	25%
Sinton, Sargent, and co-workers[17]	**Nafion 1000 W**	7 M KOH	–0.91	79.5%	1232.3	6.8%
	Nafion 1000 W	7 M KOH	–1.43	82.5%	420.8	13%
Bell and co-workers[16]	**Nafion 1100 W**	0.1 M $CsHCO_3$	–1.15	64%	6.5	12.1%
Sinton, Sargent, and co-workers[19]	**Aquivion**	3 M KCl/1 M H_3PO_4	*Not reported*	~48%	576	35%
Agapie, Peters, Sargent, and co-workers[18]	**Aquivion**	*None* (MEA)	*Not reported*	45%	68	10%
Zhuang, L., et al.[23]	**QAPEEK**	*None* (MEA)	*Not reported*	73.4%	587	10.6%
				65.3%	653	16.4%

Table 4.8. Comparing CO_2R performance between Cu electrodes with various coatings that impart high performance towards C_{2+} products.

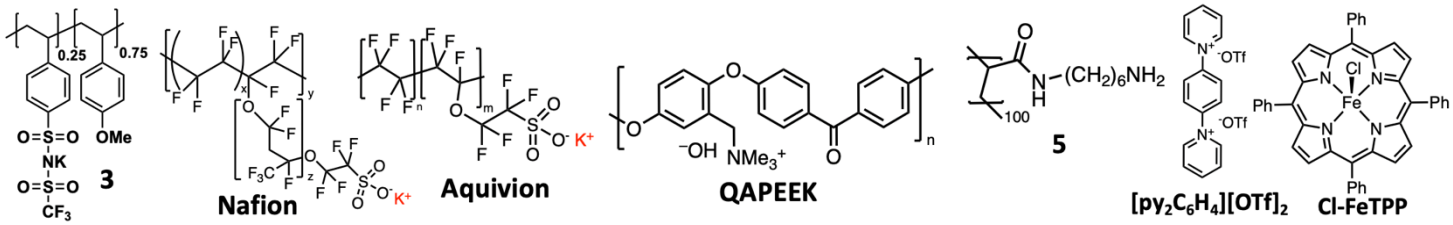

Authors	Ionomer	Electrolyte	$E_{corrected}$ (V vs. RHE)	FE_{C2+}	$\lvert j_{C2+} \rvert$ (mA cm^{-2})	FE_{H2}
This work	**3**	1 M $KHCO_3$	–0.96	82%	225	8%
	Nafion 1100 W	1 M $KHCO_3$	–1.07	36%	25	25%
Sinton, Sargent, and co-workers[17]	**Nafion 1000 W**	7 M KOH	–0.91	79.5%	1232.3	6.8%
	Nafion 1000 W	7 M KOH	–1.43	82.5%	420.8	13%
Bell and co-workers[16]	**Nafion 1100 W**	0.1 M $CsHCO_3$	–1.15	64%	6.5	12.1%
Sinton, Sargent, and co-workers[19]	**Aquivion**	3 M KCl/1 M H_3PO_4	*Not reported*	~48%	576	35%
Agapie, Peters, Sargent, and co-workers[18]	**Aquivion**	*None* (MEA)	*Not reported*	45%	68	10%
Zhuang, L., et al.[23]	**QAPEEK**	*None* (MEA)	*Not reported*	73.4%	587	10.6%
				65.3%	653	16.4%

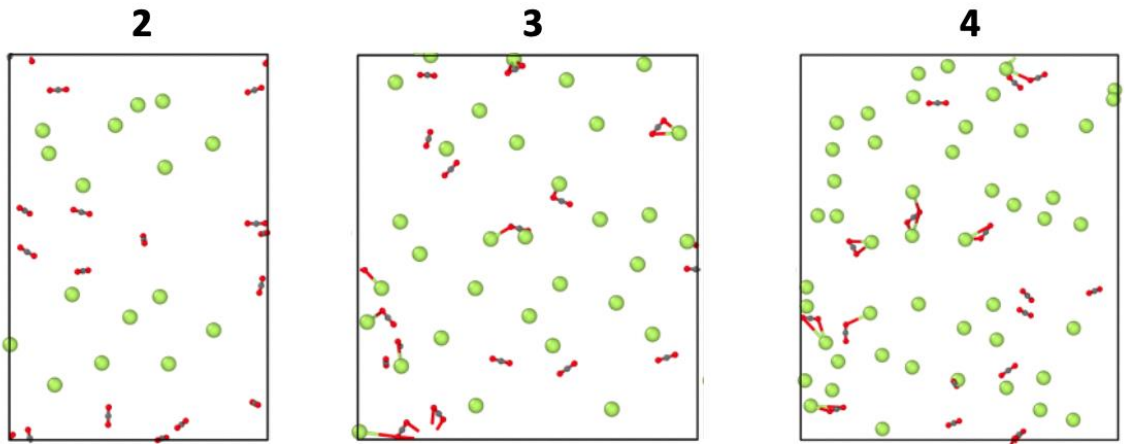

Figure 4.14. Computational model representing CO_2 and K^+ in polymers **2** through **4**. The O–K distance cutoff is set to 5 Å.

Table 4.9. Thermodynamic values computed from 2PT method.

Polymer	Entropy (*S*, J/mol/K/CO_2)	Helmholtz Free Energy (*A*, kJ/mol/K/CO_2)	Diffusion coefficient (*D*, cm^2/s)	Total number of K^+ [a]	Total volume ($Å^3$)	Polymer volume ($Å^3$)	Open volume ($Å^3$)[b]
1	3.26	-0.95	$3.6*10^{-6}$	0	2504	180.4	2324
2	4.96	-2.09	$2.6*10^{-5}$	16	2629	187.3	2442
3	5.91	-3.22	$1.07*10^{-4}$	32	2769	194.2	2575
4	6.26	-3.58	$1.6*10^{-4}$	48	2945	201.1	2744
4-NMe_4	3.73	-1.13	$1.92*10^{-5}$	0	3267	201	3066
4 (remove charges)[c]	3.33	-0.98	$3.7*10^{-6}$	0	2451	180	2271

[a]160 total monomeric units; one K^+ per monomer

[b](Open volume) = (Total volume) – (Polymer volume)

[c]From the optimized structure of polymer **4**, the charged comonomer units were removed and the structure and parameters recalculated.

Table 4.10. Coordination of CO_2 molecules to ionomers derived from simulations.

Polymer	Average number of CO_2 molecules within 5 Å	% CO_2 molecules within 5 Å of K^+
2	1	6
3	7	44
4	9	56

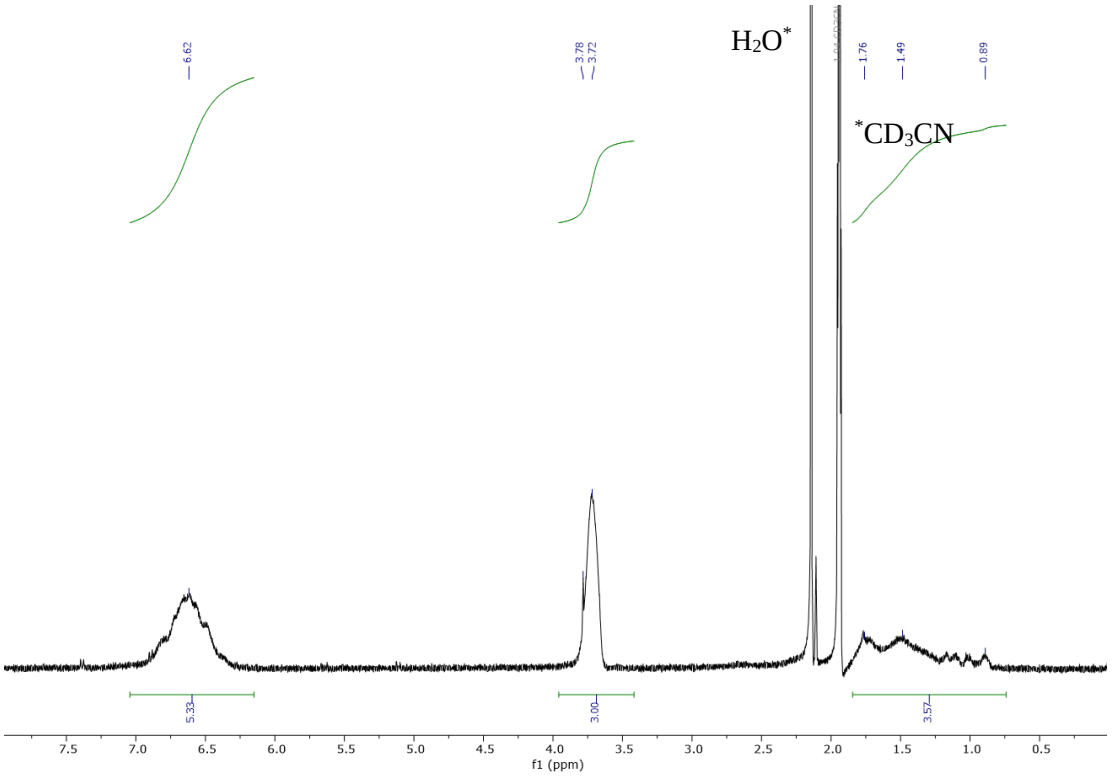

Figure 4.15. ^{1}H NMR of polymer **1** in CD_3CN.

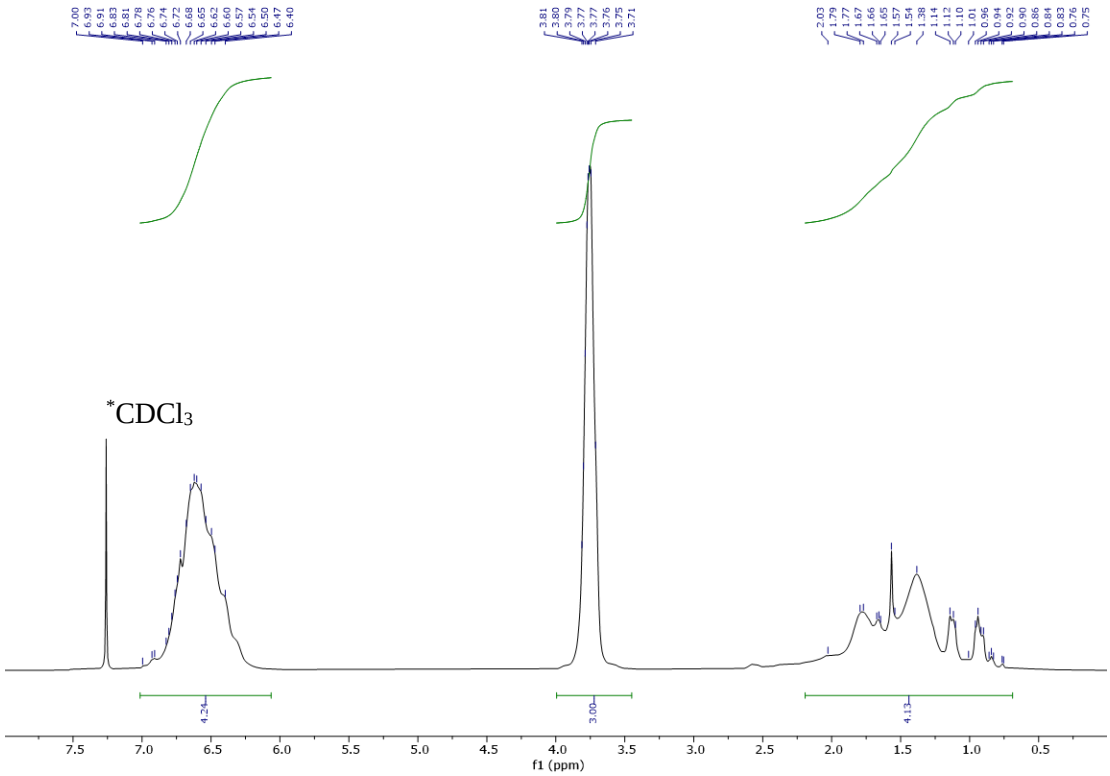

Figure 4.16. ^{1}H NMR of polymer **1** in $CDCl_3$.

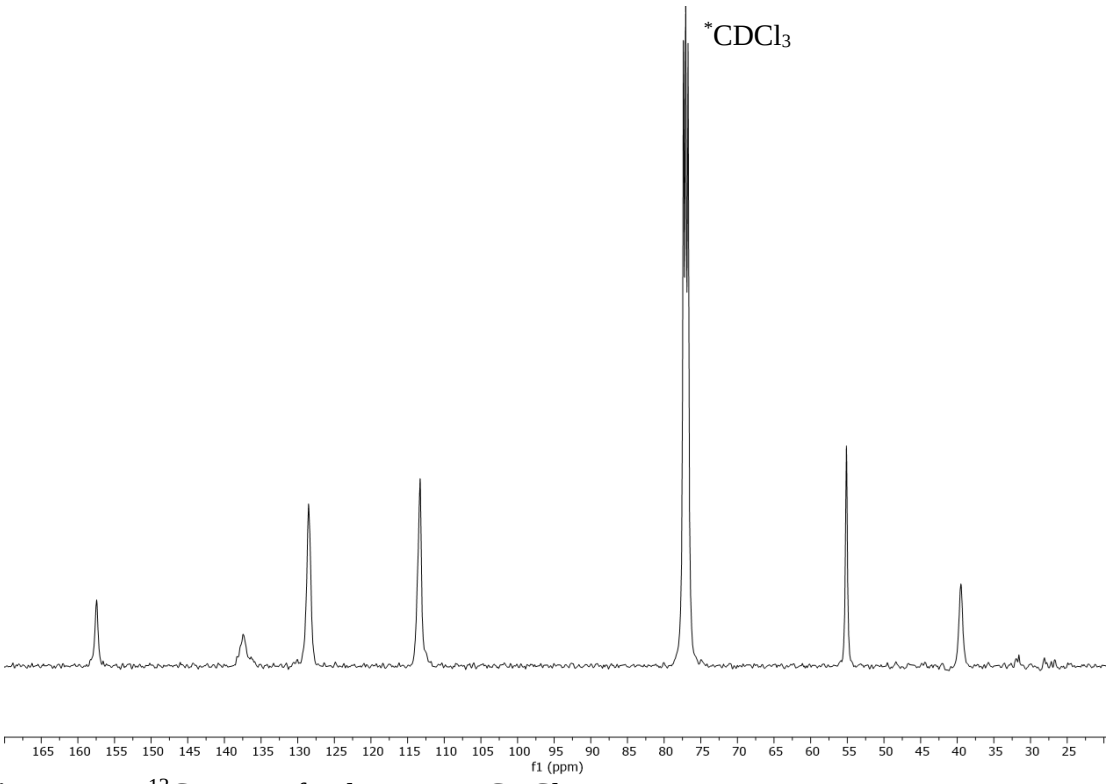

Figure 4.17. ^{13}C NMR of polymer **1** in $CDCl_3$.

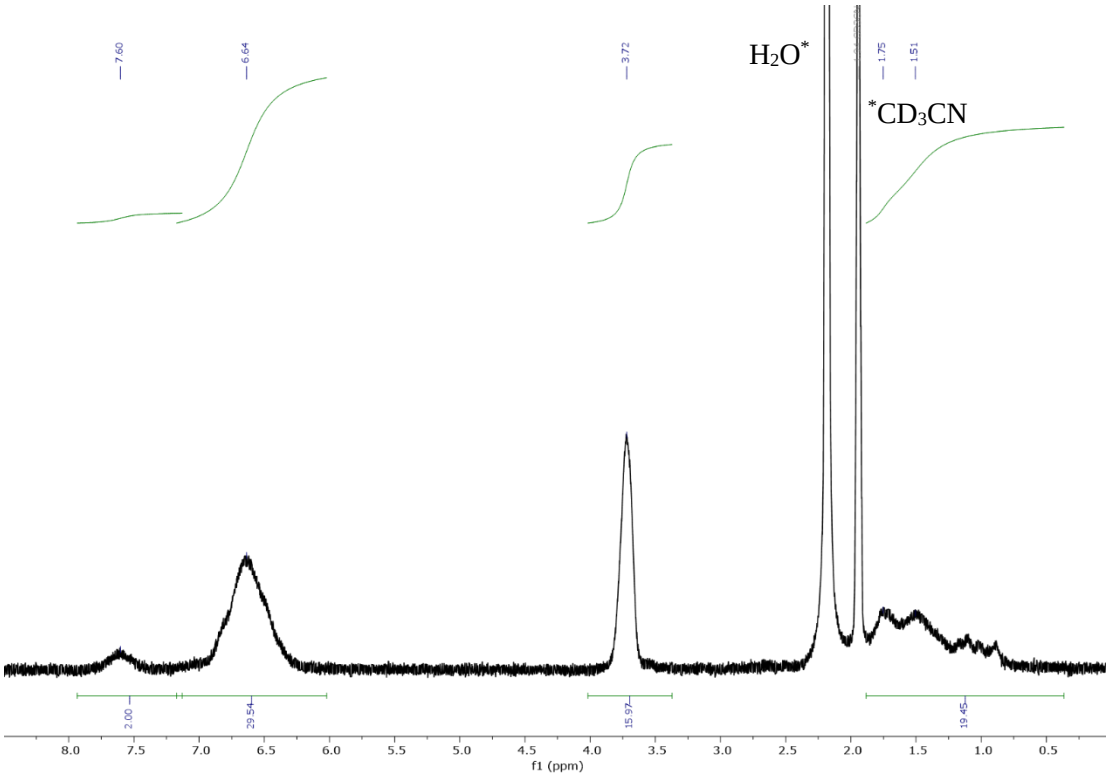

Figure 4.18. ^{1}H NMR of polymer **2** in CD_3CN.

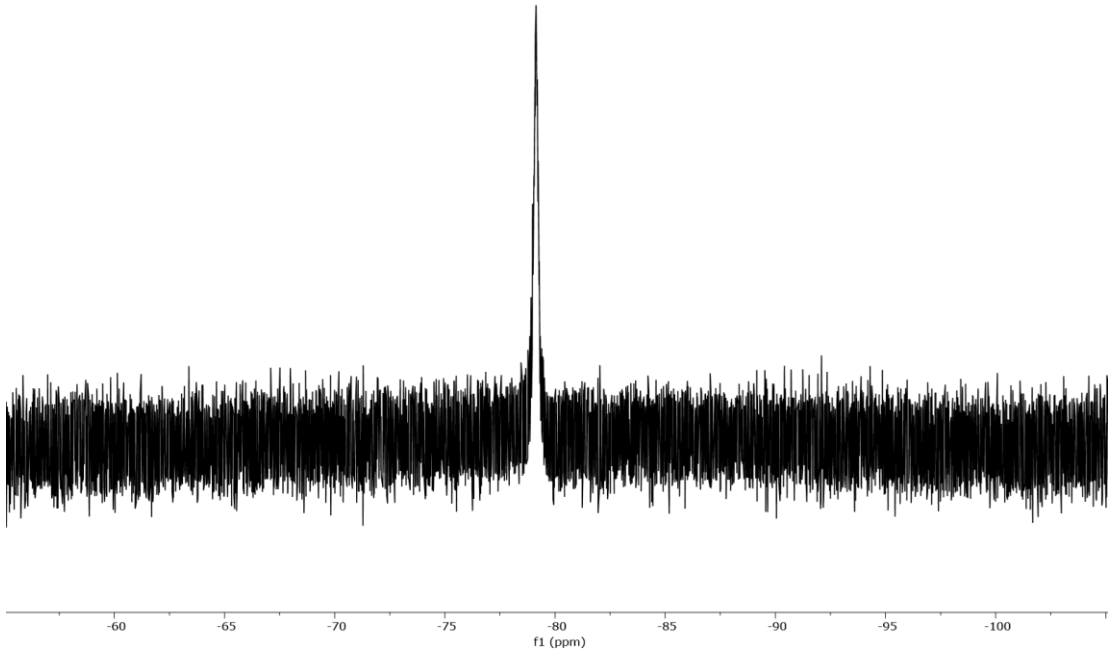

Figure 4.19. ^{19}F NMR of polymer **2** in CD_3CN.

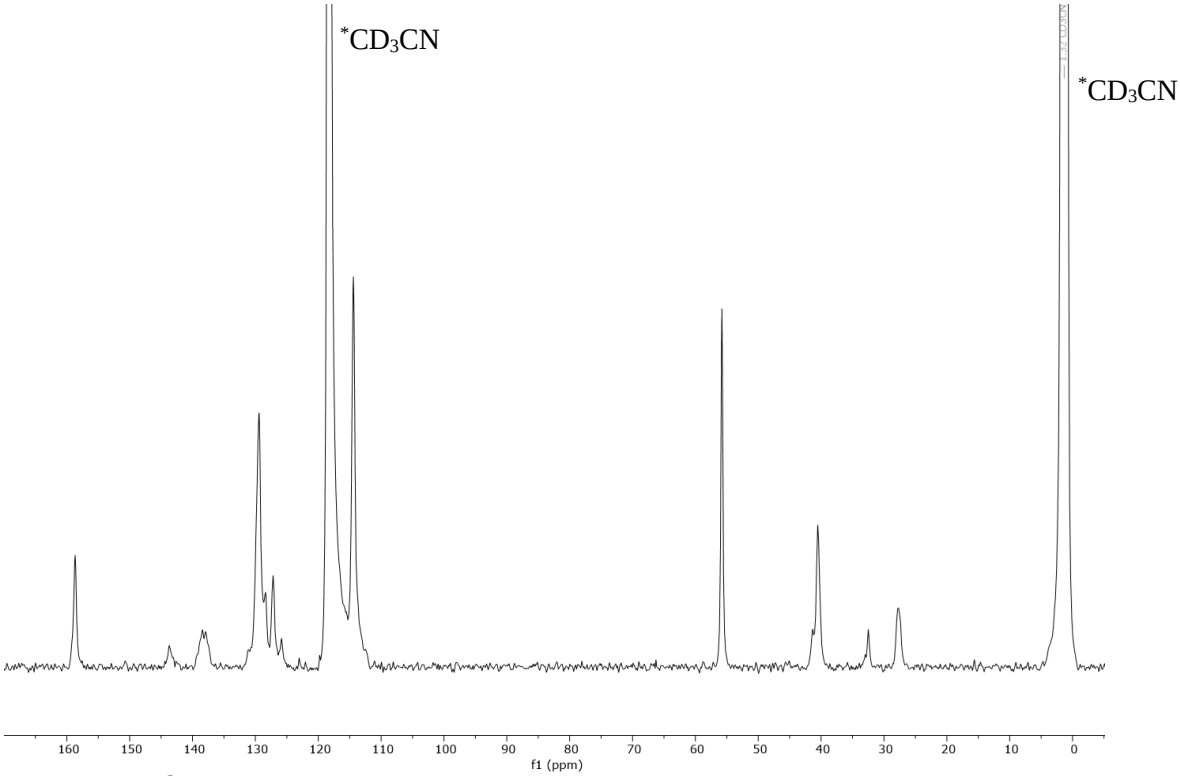

Figure 4.20. ^{13}C NMR of polymer **2** in CD_3CN.

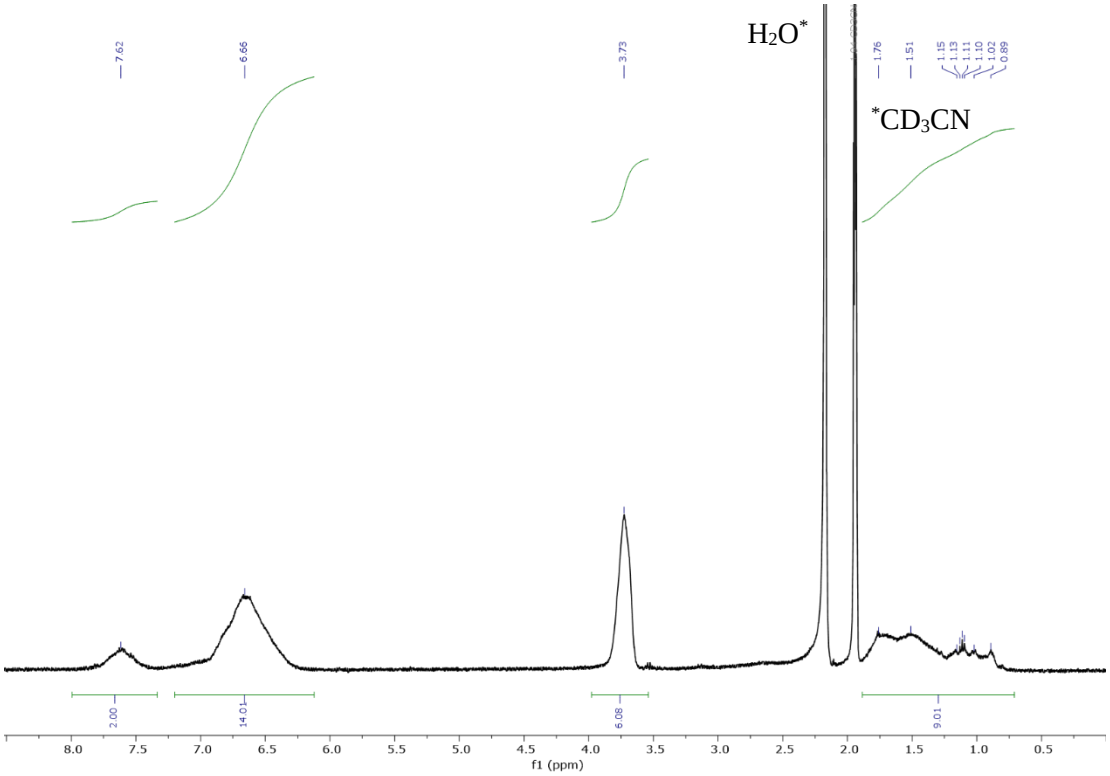

Figure 4.21. ^{1}H NMR of polymer **3** in CD_3CN.

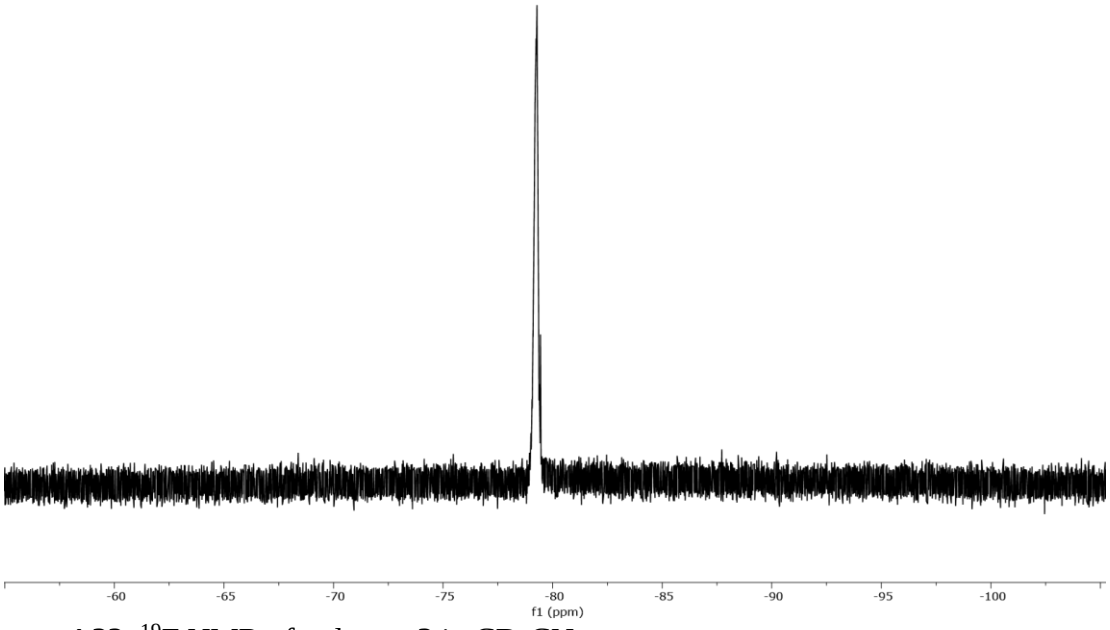

Figure 4.22. ^{19}F NMR of polymer **3** in CD_3CN.

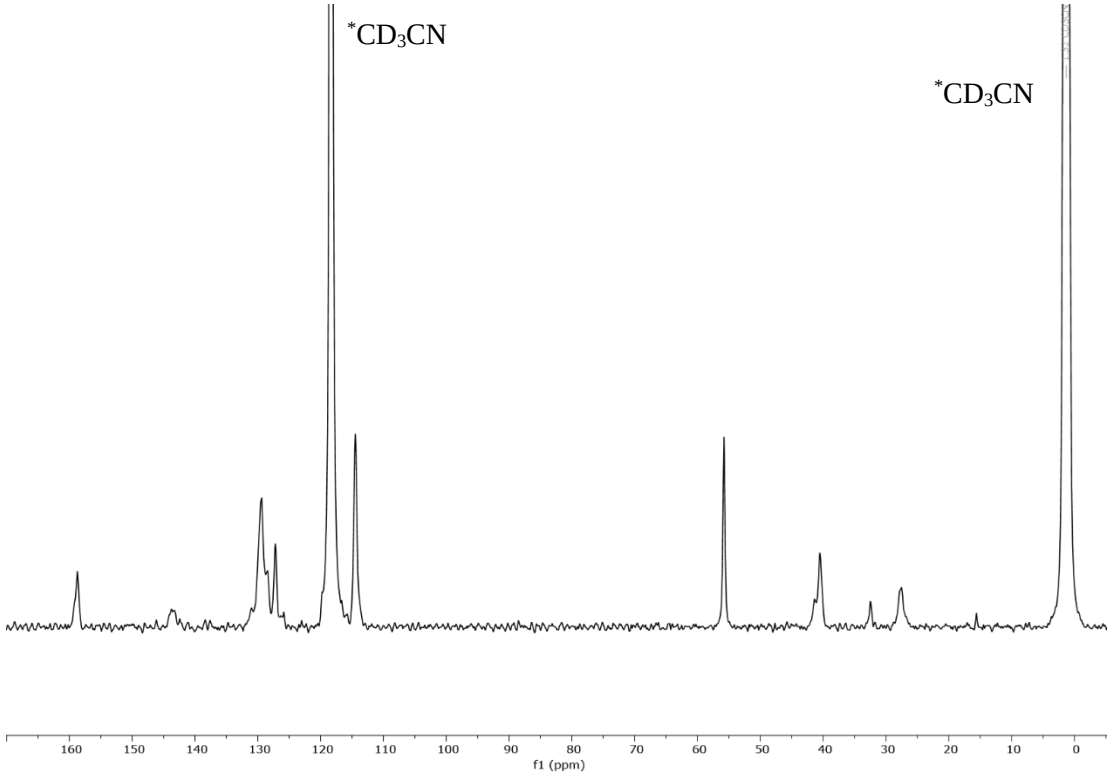

Figure 4.23. ^{13}C NMR of polymer **3** in CD_3CN.

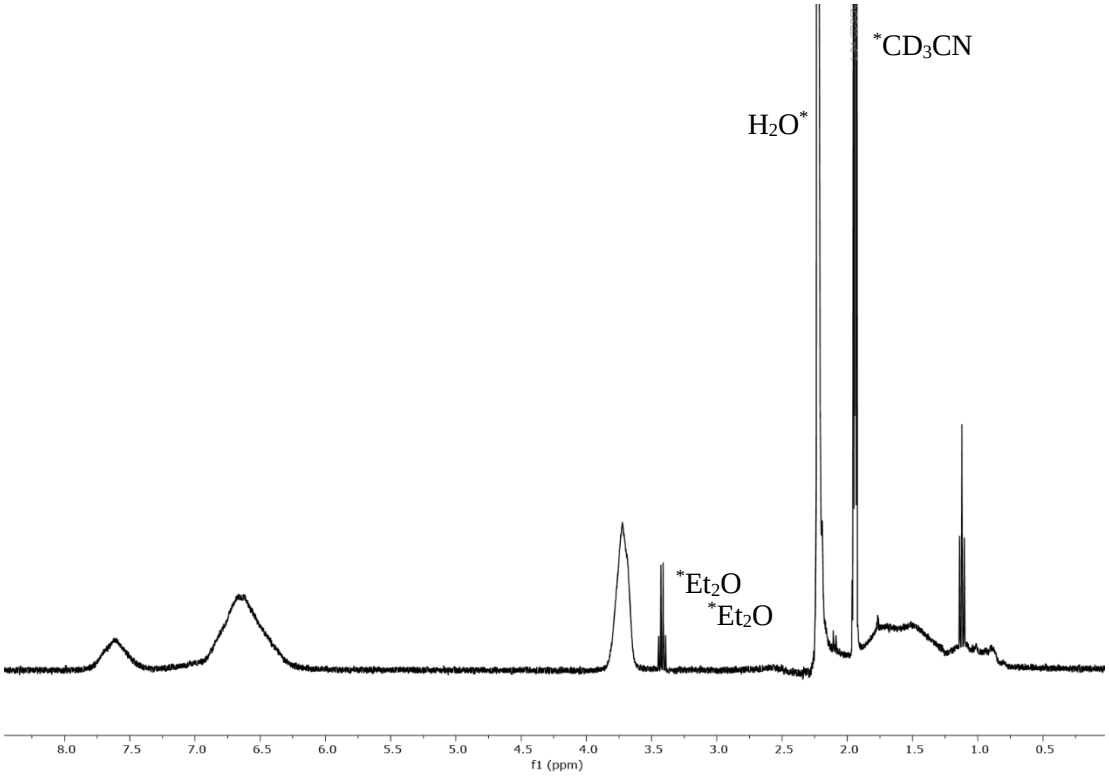

Figure 4.24. ^{1}H NMR of polymer **4** in CD_3CN.

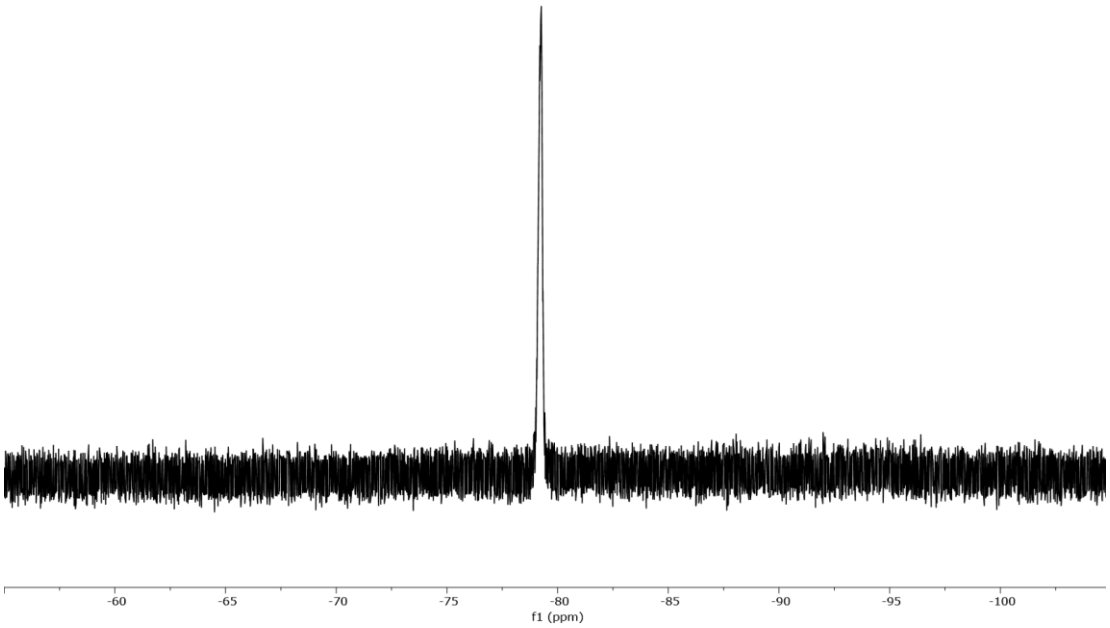

Figure 4.25. ^{19}F NMR of polymer **4** in CD_3CN.

Part B: Structural Diversification of Ionomer Series

ABSTRACT

As discussed in Part A, we observed a correlation between [K^+] in the ionomer coating and |j_{C2+}|. Experimental and computational results were consistent with elevated CO_2 mass transport at the electrode surface. To expand upon the results discussed in Part A, a diversified series of ionomers was prepared to explore the impact of a larger, more extensive series of ionomer coating on CO_2R.

Within this section, we additional (charged and neutral) polymer coatings. While many of the coatings exhibit good performance (current density > 200 mA cm^{-2}, Faradaic Efficiency (FE) > 70% for multi-carbon products) with significant improvement over bare Cu, the trends observed with the methoxystyrene series (Part A) do not extend to series with other neutral comonomers (vinyl biphenyl) or cross-linked polymers. In some cases, the analogous K^+-free polymer exhibits similar performance to the K^+-containing congener, suggesting a non-innocent role of neutral monomers.

RESULTS AND DISCUSSION

One of the main challenges encountered in Part A was the solubility of the prepared ionomers. Because a correlation was observed between an increase in $[K^+]$ and an increase in CO_2R performance, obtaining ionomers with higher $[K^+]$ was hypothesized to further improve CO_2R. However, within the initial series, $[K^+]$ was limited to ~37%; ionomers with a higher $[K^+]$ were soluble in the electrolyte solution (1 M $KHCO_{3(aq)}$), prohibiting their use as electrode coatings. Therefore, modification of the ionomer components was necessary to probe the impact of higher cation concentrations. Several design strategies are discussed below, including (1) a vinyl biphenyl monomer and (2) ionomer variants with cross-linking comonomers.

Seeking a less soluble comonomer than the previously utilized methoxystyrene, a series of polymers were prepared and studied based on a vinyl-biphenyl monomer. $[K^+]$ ranged from 0 to ~30 %.[64] A comparison of performance across the series is shown in Figure 4.26. Notably, unlike the methoxystyrene series discussed in Part A, an obvious correlation between $[K^+]$ and performance is not observed. While an increase in current density is observed for **8** (the higher $[K^+]$), this is accompanied by a decrease in selectivity for C_{2+} products. While the same type of trend is not observed, these results are notable in that *all* of the polymers have improved performance over bare Cu, including the vinyl biphenyl homopolymer. The observation suggests that the modified performance for CO_2RR is complicated by varying a number of parameters including porosity, solubility, polymer structure, etc. While additional electrochemical and computational studies would be necessary to probe further, the improved performance with the biphenyl comonomer is reminiscent of the increased performance with electrodeposition of bis(aryl)iodonium triflate salts to generate poly(aryl) films.[15]

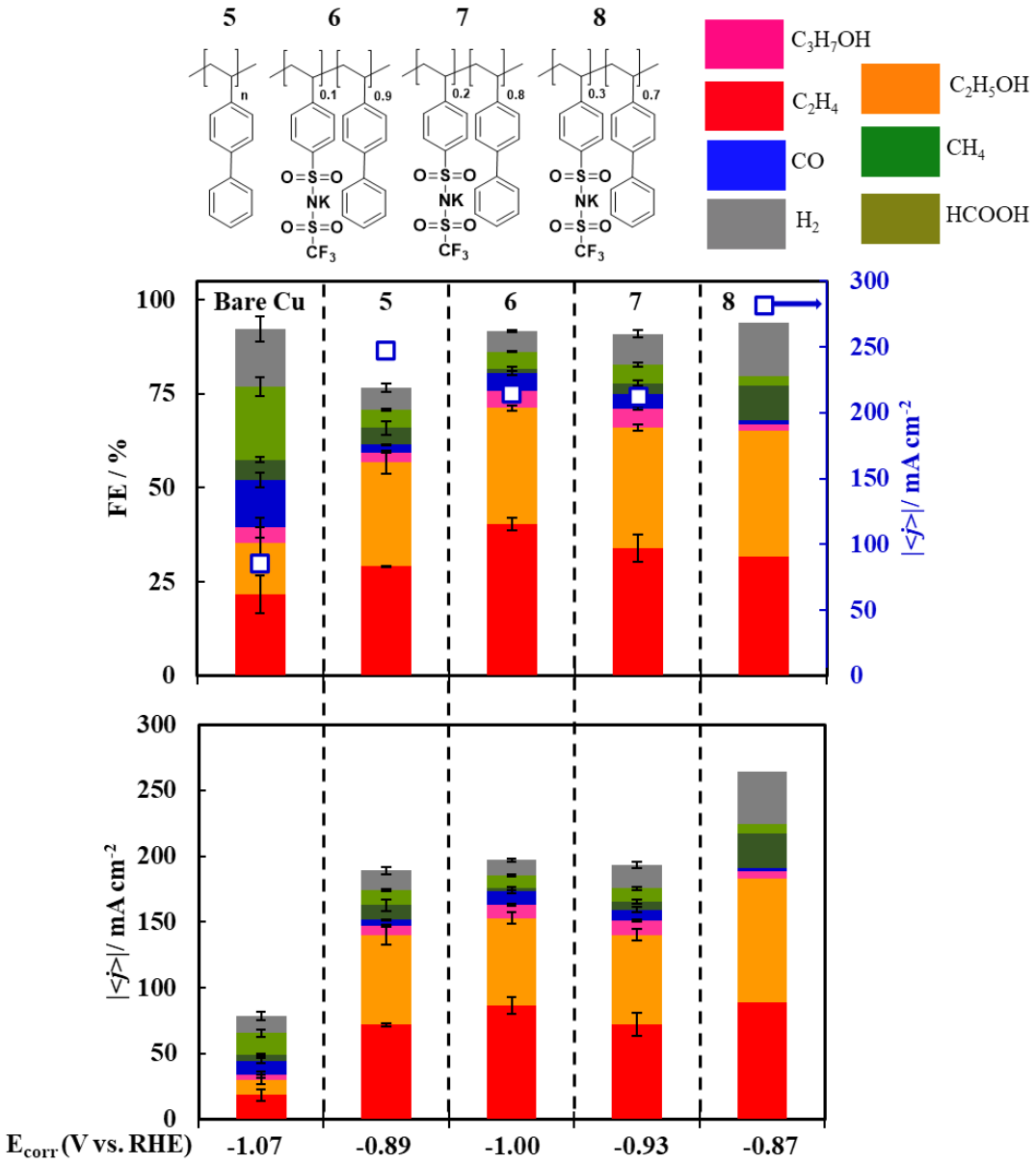

Figure 4.26. Polymers **5-8** and CO_2R performance on bare Cu. **Top.** Faradaic efficiency (FE, columns) and current density (white squares) for CO_2R products on Cu/PTFE in the presence of ionomer films casted from solutions of **5-8**. Electrolysis performed in 1 M $KHCO_{3(aq)}$ for 30 minutes with $E_{applied}$ = –1.15 V vs. RHE. Corrected potentials (E_{corr}) determined from measured (uncompensated) resistance are reported. **Bottom.** Partial current densities for trials shown in top panel. Where present, error bars represent standard deviations from multiple measurements.

Alternative strategies to decrease the ionomer solubility were targeted, including the use of cross-linking monomers, with the hypothesis that ionomers with a higher $[K^+]$ would be accessible (while remaining insoluble in the electrolyte solution). This is indeed possible, with heavily cross-

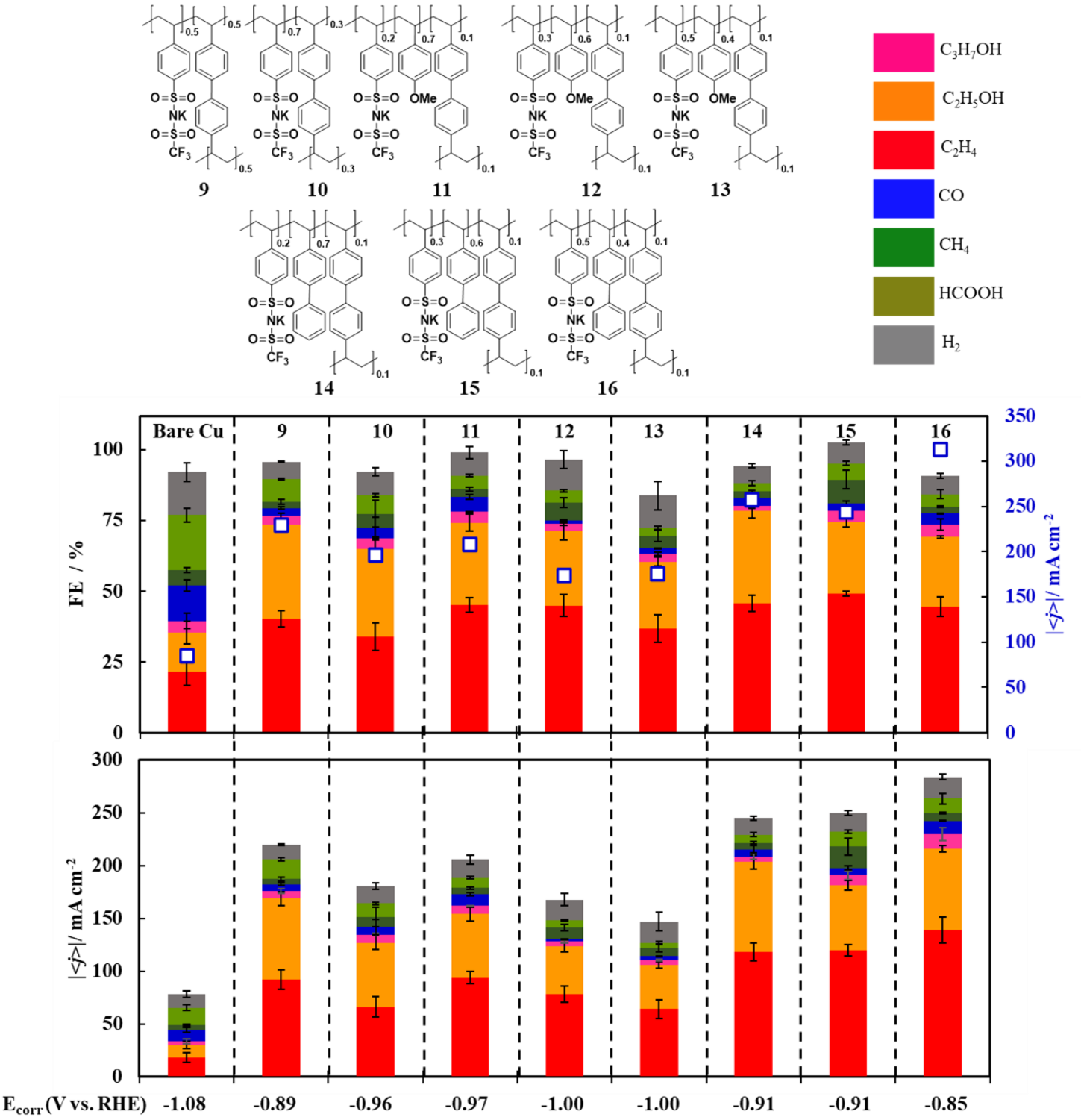

Figure 4.27. Polymers **9-15** and CO_2R performance on bare Cu. **Top.** Faradaic efficiency (FE, columns) and current density (white squares) for CO_2R products on Cu/PTFE in the presence of ionomer films casted from solutions of **9-15**. Electrolysis performed in 1 M $KHCO_{3(aq)}$ for 30 minutes with $E_{applied}$ = –1.15 V vs. RHE. Corrected potentials (E_{corr}) determined from measured (uncompensated) resistance are reported. **Bottom.** Partial current densities for trials shown in top panel. Error bars represent standard deviations from multiple measurements.

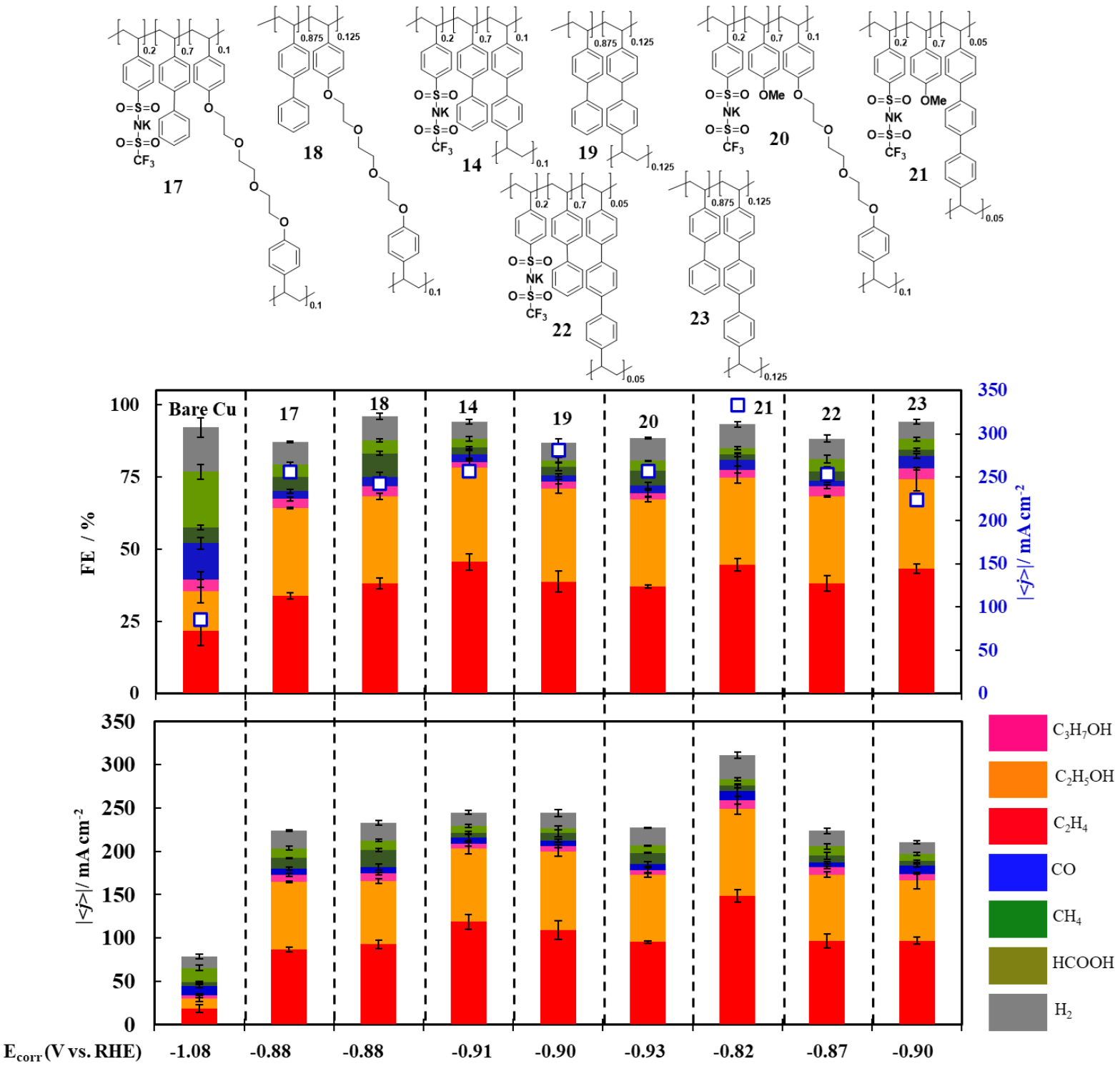

Figure 4.28. Polymers **17-23** and CO_2R performance on bare Cu.**Top.** Faradaic efficiency (FE, columns) and current density (white squares) for CO_2R products on Cu/PTFE in the presence of ionomer films casted from solutions of **17-23**. Electrolysis performed in 1 M $KHCO_{3(aq)}$ for 30 minutes with $E_{applied}$ = –1.15 V vs. RHE. Corrected potentials (E_{corr}) determined from measured (uncompensated) resistance are reported. **Bottom.** Partial current densities for trials shown in top panel. Error bars represent standard deviations from multiple measurements.

linked polymers reaching 50% and 70% mol K-STFSI with a 4,4'-divinyl-1,1'-biphenyl cross-linking monomer (polymers **9** and **10**, respectively). Unfortunately, these ionomers do not exhibit the desired performance, with **10** (the higher [K^+] ionomer) displaying a notably worse CO_2R performance ($|<j>|$ = ~200 vs ~230 mA cm^{-2} and FE_{C2+} = ~65% vs. ~75%). Similar to the vinyl biphenyl series of ionomers (**5-8**) where the neutral comonomer impacts performance, **9** and **10** suggest that polymer structure and degree of cross-linking (and therefore, the degree of porosity) impact performance. This is consistent with the computations discussed in Part A where porosity, open volume, and [K^+] impacted performance.

To minimize the negative impacts of very high content of the cross-linking monomer (while still decreasing solubility in the electrolyte solution), tricomponent ionomers were prepared with methoxystyrene and vinylbiphenyl as the major neutral monomer. The electrochemical performance of the methoxystyrene series (**11-13**) and the vinylbiphenyl series (**14-16**) is shown in Figure 4.27. For both sets of compounds, high performance is observed without an obvious trend in $[K]^+$ and increased performance.

Any overall conclusions remain quite speculative without additional studies, but an interesting comparison is the performance of **9** and **16**. While both ionomers have the same [K^+], **9** has a large ratio of cross-linking comonomer (50 %) and **16** has a modest content (10 %) and additional vinyl biphenyl monomer (40 %). As coatings on Cu, **16** has a similar selectivity to **9** but a much higher overall current density, resulting in a higher $|<j_{C2+}>|$. This again suggests that the overall flexibility and porosity (enforced by the extent of cross-linking) of the polymer may be crucial. Additional cross-linking monomers were investigated, including terphenyl and poly(ethylene glycol)-based linkers. Due to the detrimental impact of a high amount of cross-linking monomer observed previously (**9** and **10**), tricomponent polymers were prepared, with methoxystyrene and

vinylbiphenyl as the major neutral monomer. In an effort to partially deconvolute the impact [K^+] and polymer structure, neutral polymers with the same relative ratio of cross-linking monomer:neutral monomer.[65] The performance of polymers **17-23** is shown in Figure 4.28. Notably, polymer **21** demonstrates the record performance (across all polymers discussed), with $|<j_{C2+}>|$ of 260 mA cm^{-2} (9-fold increase vs. bare Cu). However, it is interesting to observe that each K^+-free variant demonstrates quite similar high performance for CO_2R. Again, this demonstrates the non-innocent impact of the neutral components. The polyaromatic motifs may improve CO_2R by increasing local [K^+] by a cation-π effect[66] or improved CO_2 mass transport. However, additional experiments are necessary to more accurately understand the observed performance.

CONCLUSIONS

In summary, an expanded series of ionomers was investigated as coatings on Cu electrodes for CO_2R. Modification of the neutral comonomer and use of aryl (biphenyl, terphenyl) and poly(ethylene glycol)-based cross-linkers enabled access to a diverse range of polymer coatings. While significant increases in product selectivity and current density were observed for all of the tested materials, a direct trend between $[K^+]$ and performance was not observed, indicating a more complicated balance of factors to drive the modification in selectivity, including the identity of the neutral comonomer, the degree of cross-linking, and the $[K^+]$. Future work will facilitate an improved understanding of how these polymers impact CO_2R on Cu. Scattered angle X-ray spectroscopy measurements (SAXS) will be carried out to rule out morphological changes to Cu, and electrochemical measurements will also be performed to determine CO_2 diffusion coefficients. Complimentary MD simulations (similar to those discussed in Part A) can help elucidate the films' effects on CO_2R performance.

EXPERIMENTAL SECTION

For details related to electrochemistry experiments, please see Part A (page 88).

General Considerations. All solvents and reagents were obtained from commercial sources (Aldrich, Merck, and Combi Blocks) and used as received, unless stated otherwise. 4-Methoxystyrene was dried with CaH_2 and filtered under inert atmosphere. Azobisisobutyronitrile (AIBN) was dried under vacuum for 16 hr. 4-vinylbiphenyl was dried under vacuum for 16 hr. **K-STFSI** was prepared based on a previously reported synthesis.[56] Acetonitrile was dried by passing over activated alumina by the method of Grubbs[57] and stored over 3 Å molecular sieves in a N_2-filled glovebox. Anhydrous dimethylformamide (DMF) was degassed and stored over 3 Å molecular sieves in a N_2-filled glovebox. $KHCO_3$ (grade) for polymer purification was purchased from Sigma Aldrich.

Preparation of Cross-Linking Monomers:

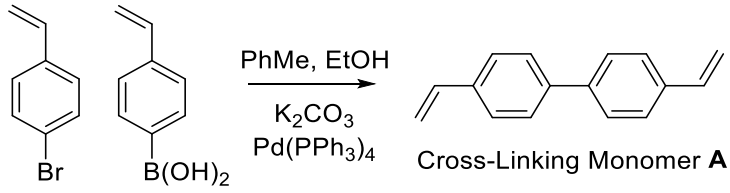

4-Bromostyrene (3.36 g, 18.35 mmol, 1.0 equiv) and 4-vinylphenylboronic acid (2.72 g, 18.35 mmol, 1.0 equiv) were added as solids to a Schlenk tube and suspended in toluene (20 mL), ethanol (20 mL) and 2 M aqueous K_2CO_3 (10 mL). The reaction mixture was thoroughly degassed 3x before addition of $Pd(PPh_3)_4$ (5 mol%), and the reaction was heated to 70 ^oC for 16 hr. The reaction was quenched with exposure to air, and the reaction was filtered over a silica plug and extracted with DCM. The volatiles were concentrated *in vacuo*, dissolved in DCM, and the mixture was washed 3x with water. The organic layer was dried with $MgSO_4$, and the volatiles were removed

in vacuo. The product was purified by column chromatography. The product was isolated as a light yellow solid. Characterization is consistent with previous reports.[67]

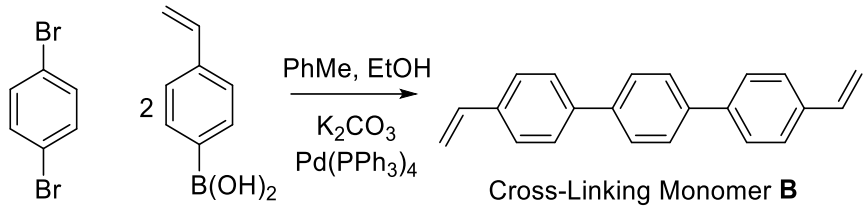

1,4 dibromobenzene (3.98 g, 16.89 mmol, 1.0 equiv) and 4-vinylphenylboronic acid (5 g, 33.79 mmol) were added as solids to a Schlenk tube and suspended in toluene (120 mL), ethanol (40 mL), and 2 M aqueous K_2CO_3 (66 mL). The reaction mixture was thoroughly degassed 3x before addition of $Pd(PPh_3)_4$ (400 mg, 0.3379 mmol, 0.02 equiv), and the reaction was heated to 70 ^oC for 16 hr. The reaction was quenched with exposure to air, and the reaction was filtered over a silica plug and extracted with DCM. The volatiles were concentrated *in vacuo*, dissolved in DCM, and the mixture was washed 3x with water. The organic layer was dried with $MgSO_4$, and the volatiles were removed *in vacuo*. The product was purified by column chromatography. The product was isolated as a light yellow solid. Characterization is consistent with previous reports.[67]

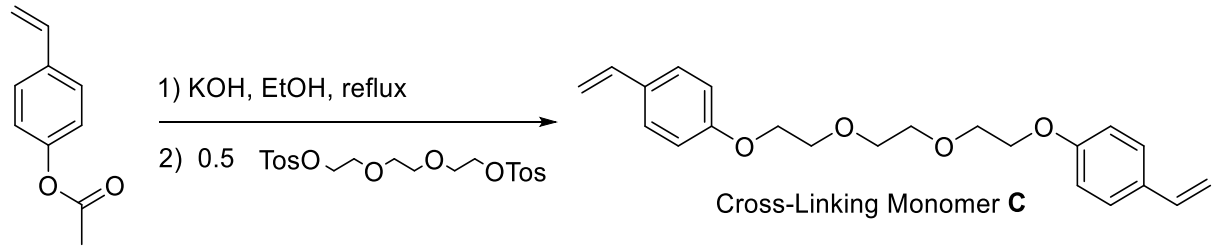

4-Acetoxystyrene (1.965 g, 12.12 mmol, 2.0 equiv) was dissolved in EtOH followed by addition of KOH (0.85 g, 15.15 mmol, 2.5 equiv). The reaction was heated to 70 ^oC for 1.5 hr, followed by addition of triethylene glycol di(*p*-toluenesulfonate) (2.77 g, 6.05 mmol, 1.0 equiv). The

reaction was stirred for 16 hr at RT. The volatiles were concentrated *in vacuo*, dissolved in DCM, and the mixture was washed 3x with water. The product was purified by column chromatography. The product was isolated as a white solid. Characterization is consistent with previous reports.

General Procedure for Synthesis of Neutral Homopolymer: The reaction was conducted under an inert atmosphere. The neutral monomer (methoxystyrene or vinylbiphenyl) was dissolved in MeCN (4 mL). AIBN (26 mg, 0.1 equiv) was added and rinsed with MeCN (1 mL). The vial was sealed, removed from the glovebox, and heated at 70 ^{o}C for 3 days. The reaction was quenched by exposure to air. The crude material was concentrated, redissolved in THF, and precipitated into MeOH (100 mL). The polymer was isolated as a fine white solid.

General Procedure for Copolymer Synthesis: The reaction was conducted under an inert atmosphere. The neutral monomer (methoxystyrene or vinylbiphenyl) was added to a 20-mL scintillation vial and dissolved in MeCN (2 mL) followed by addition of K-STFSI dissolved in MeCN (2 mL). AIBN (0.1 equiv) was added and rinsed with MeCN (1 mL). The vial was sealed, removed from the glovebox, and heated at 70 ^{o}C for 3 days. The reaction was quenched by exposure to air. The crude polymer was precipitated into Et_2O (100 mL) and filtered. The precipitate was stirred with 20 mL of an aqueous solution of 1 M $KHCO_3$ at 90 ^{o}C for a minimum of 30 minutes. The mixture was filtered hot over a glass frit. An additional 2 washes with 1 M $KHCO_{3(aq)}$ were necessary for most purifications. The solid material was extracted with MeCN, concentrated under reduced vacuum, redissolved in MeCN, and filtered. The filtrate was precipitated with Et_2O (100 mL) and filtered. The polymer dried under vacuum and was isolated as a fine white solid.

General Procedure for Cross-Linking Copolymers Synthesis with Cross-Linking Monomer A: The reaction was conducted under an inert atmosphere. The neutral monomer (methoxystyrene or vinylbiphenyl) was added to a 20-mL scintillation vial and dissolved in MeCN (2 mL) followed by addition of cross-linking comonomer and K-STFSI dissolved in MeCN (1 mL, each). AIBN (0.1 equiv) was added and rinsed with MeCN (1 mL). The vial was sealed, removed from the glovebox, and heated at 70 ^{o}C for 3 days. The reaction was quenched by exposure to air. The polymer was precipitated into Et_2O (100 mL) and filtered. The precipitate was stirred with 20 mL of an aqueous solution of 1 M $KHCO_3$ at 90 ^{o}C for a minimum of 30 minutes. The mixture was filtered hot over a glass frit. An additional 2 washes with 1 M $KHCO_{3(aq)}$ were necessary for most purifications. The solid material was extracted with MeCN, concentrated under reduced vacuum, redissolved in MeCN, and filtered. The filtrate was precipitated with Et_2O (100 mL) and filtered. The polymer dried under vacuum and was isolated as a fine white solid.

General Procedure for Cross-Linking Copolymers Synthesis with Cross-Linking Monomers B and C: The reaction was conducted under an inert atmosphere. The neutral monomer (methoxystyrene or vinylbiphenyl) was added to a 20-mL scintillation vial and dissolved in DMF (2 mL) followed by addition of cross-linking comonomer and K-STFSI dissolved in DMF (1 mL, each). AIBN (0.1 equiv) was added and rinsed with DMF (1 mL). The vial was sealed, removed from the glovebox, and heated at 70 ^{o}C for 3 days. The reaction was quenched by exposure to air. DMF was removed *in vacuo*, and the crude polymer was redissolved in minimal MeCN (~5 mL). The polymer was precipitated into Et_2O (100 mL) and filtered. The precipitate was stirred with 20 mL of an aqueous solution of 1 M $KHCO_3$ at 90 ^{o}C for a minimum of 30 minutes. The mixture was filtered hot over a glass frit. An additional 2 washes with 1 M $KHCO_{3(aq)}$ were necessary for

most purifications. The solid material was extracted with MeCN, concentrated under reduced vacuum, redissolved in MeCN, and filtered. The filtrate was precipitated with Et_2O (100 mL) and filtered. The polymer dried under vacuum and was isolated as a fine white solid.

Note about Polymer Purification: For some copolymers with a higher content of charged comonomer where some moderate solubility in 90 ^oC 1 M $KHCO_3$ is observed, an alternative purification was used to remove unreacted K-STFSI. The crude polymer was dissolved in minimal MeCN (< 5 mL) and precipitated by addition to 1 M aqueous $KHCO_3$ (25 mL). The purification was repeated until residual unreacted monomer was removed (generally 3-5 washes). The polymer was then further purified with the same procedure described above (redissolved in MeCN, filtered, and precipitated with Et_2O).

NMR Spectra of Prepared Polymers

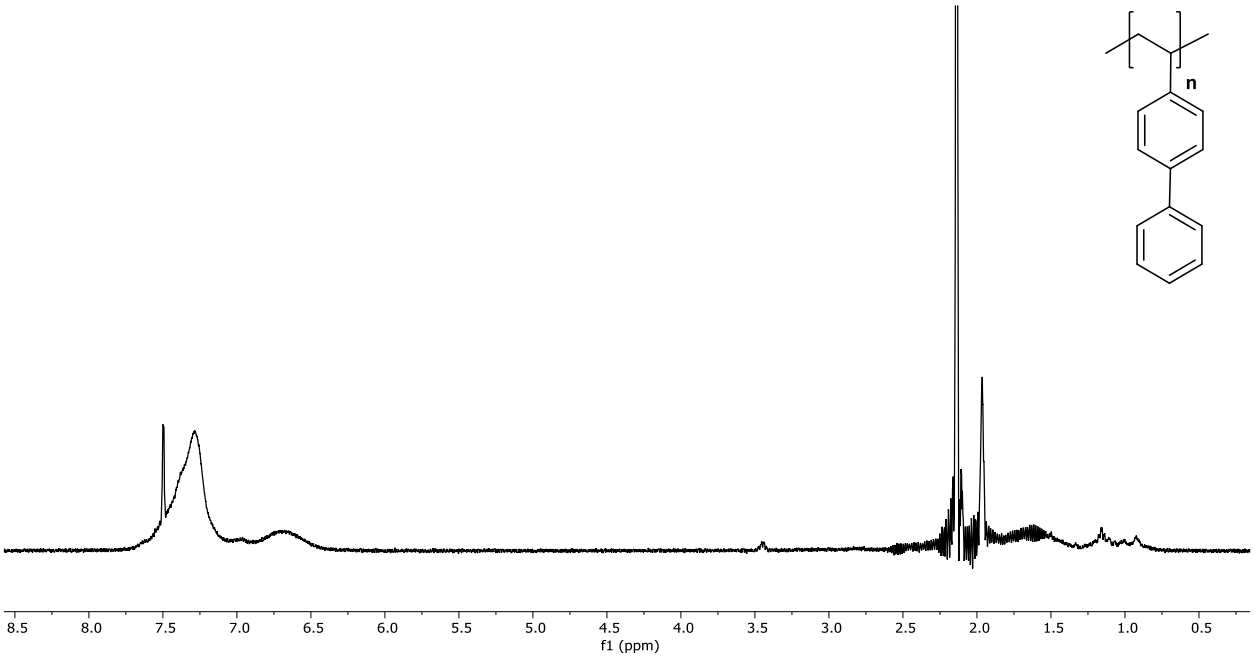

Figure 4.29. ^{1}H NMR of **5** in CD_3CN.

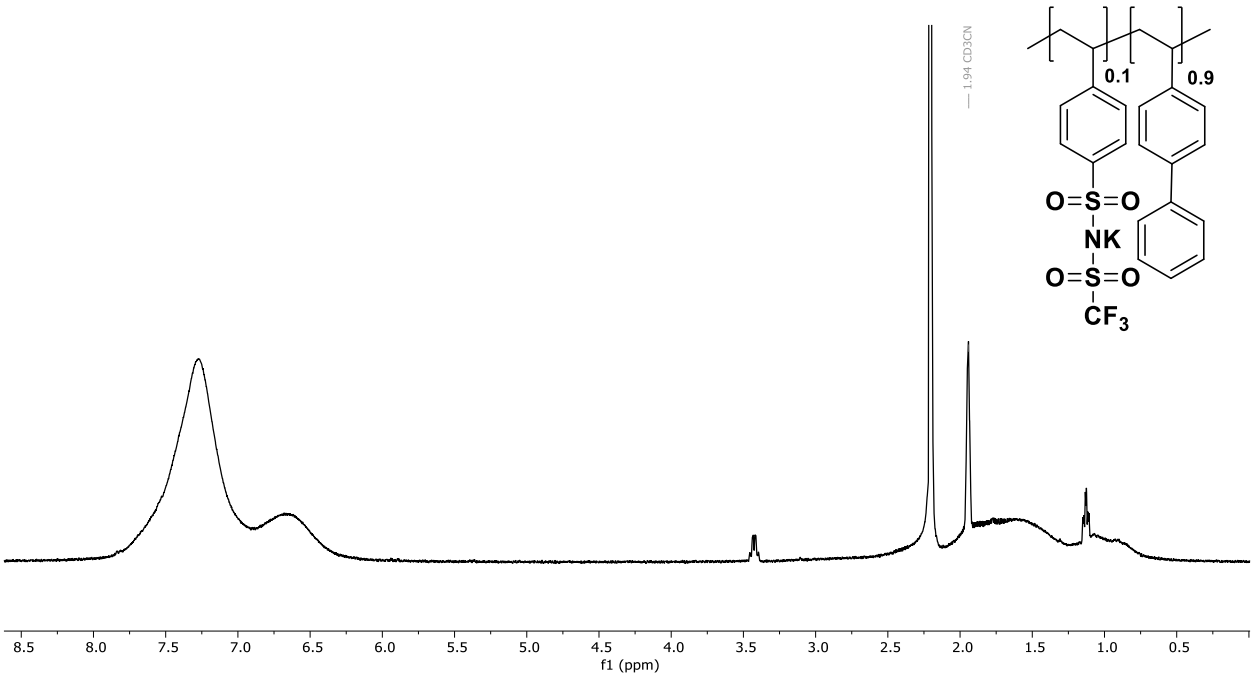

Figure 4.30. ^{1}H NMR of **6** in CD_3CN.

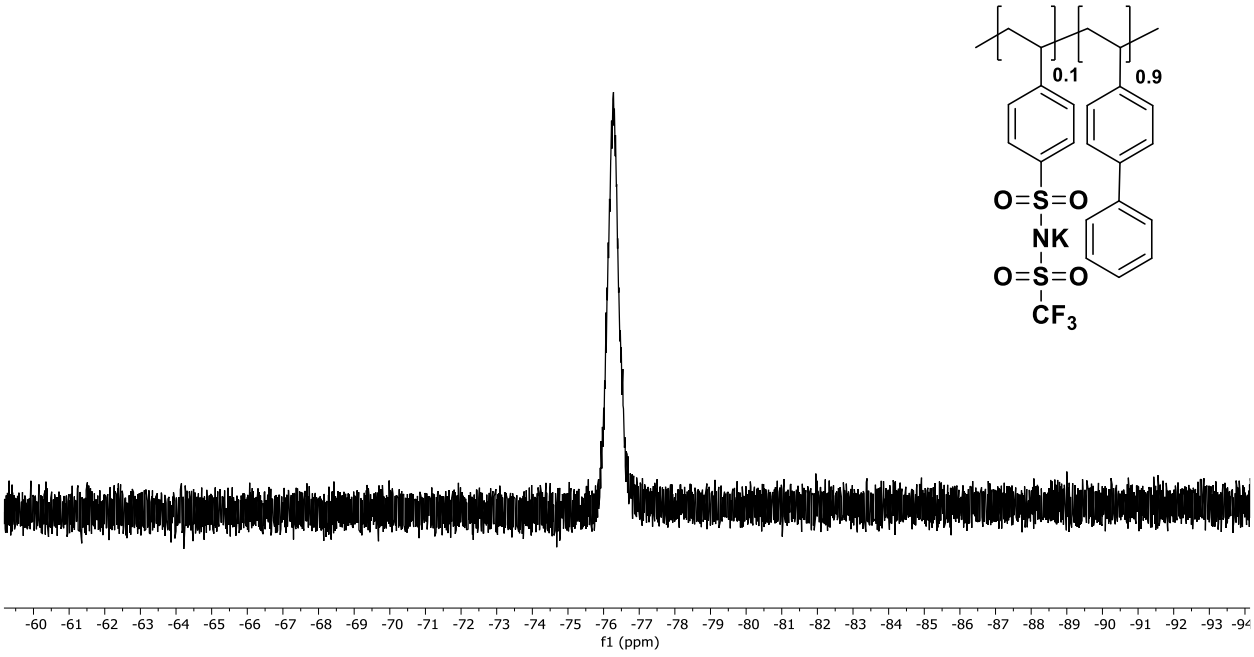

Figure 4.31. ^{19}F NMR of **6** in CD_3CN.

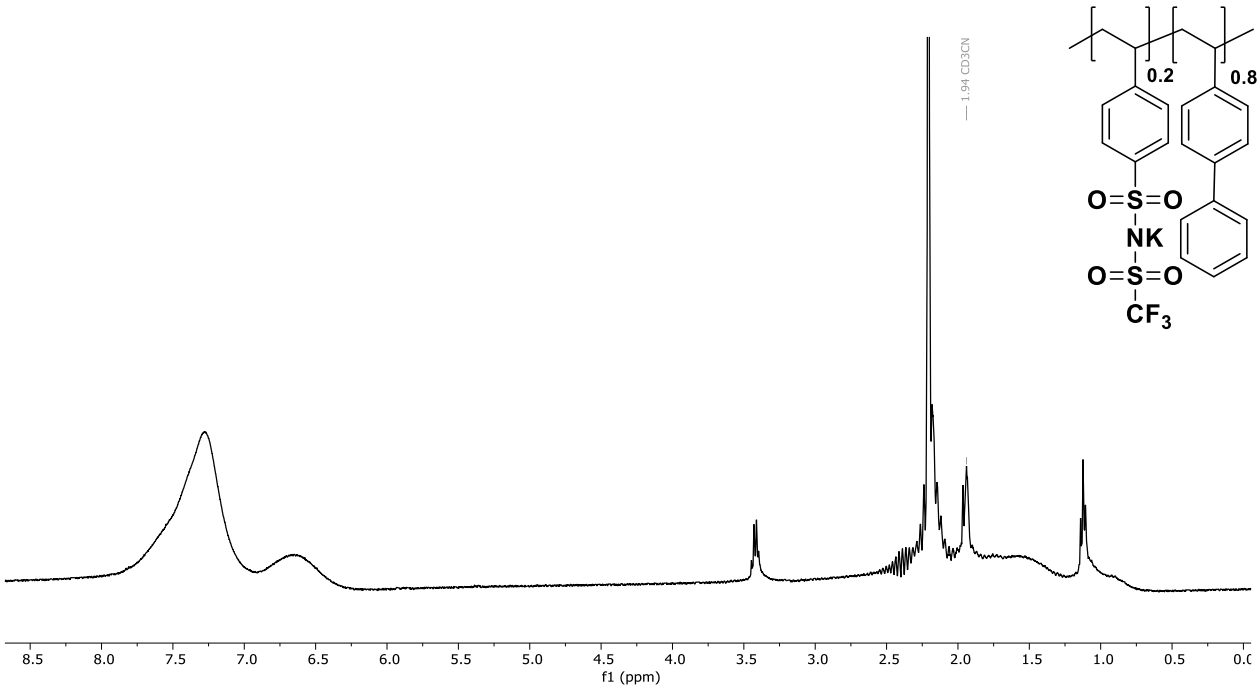

Figure 4.32. ^{1}H NMR of **7** in CD_3CN.

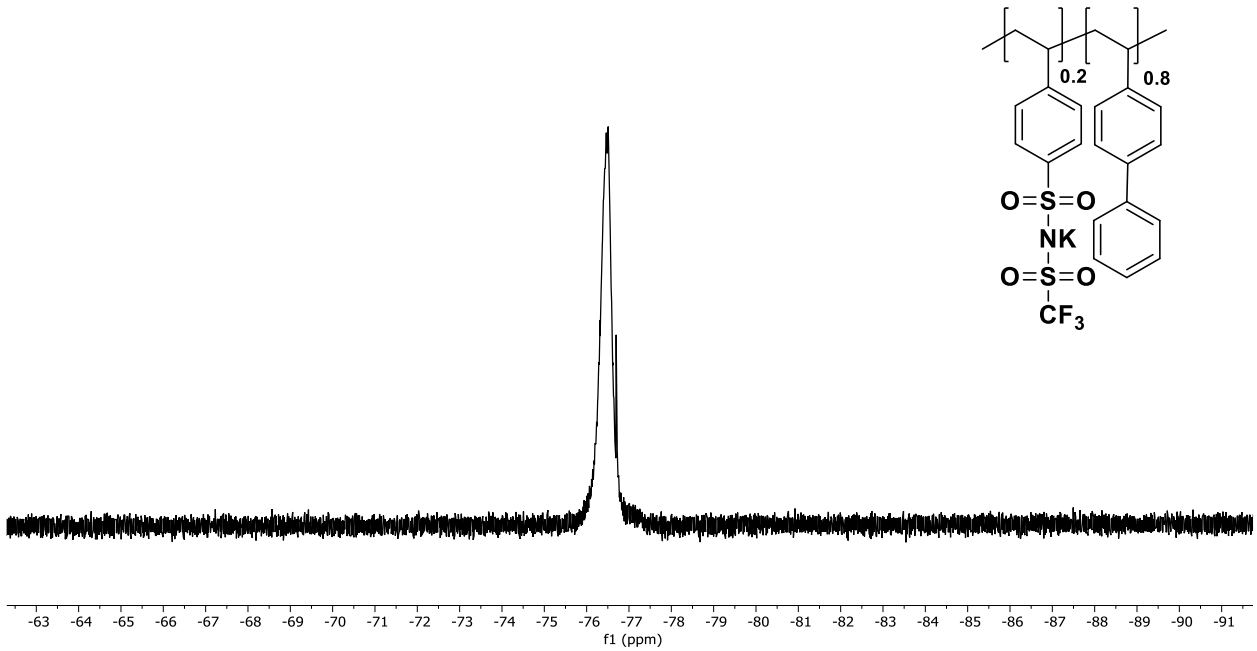

Figure 4.33. ^{19}F NMR of **7** in CD_3CN.

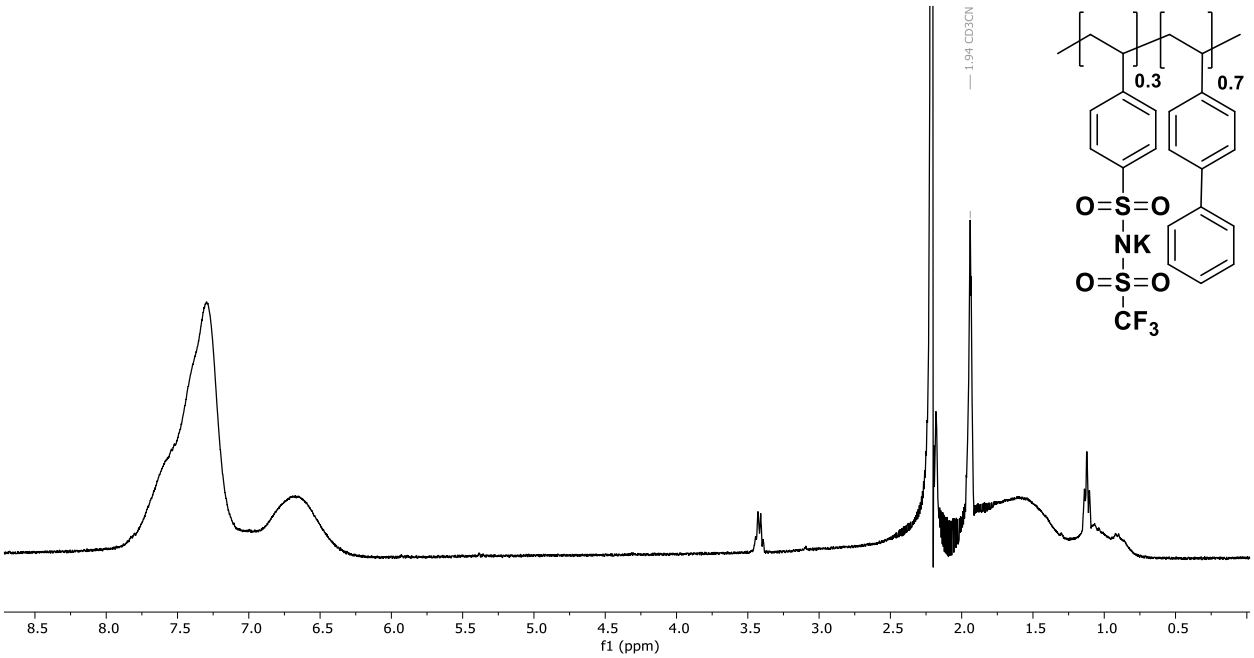

Figure 4.34. ^{1}H NMR of **8** in CD_3CN.

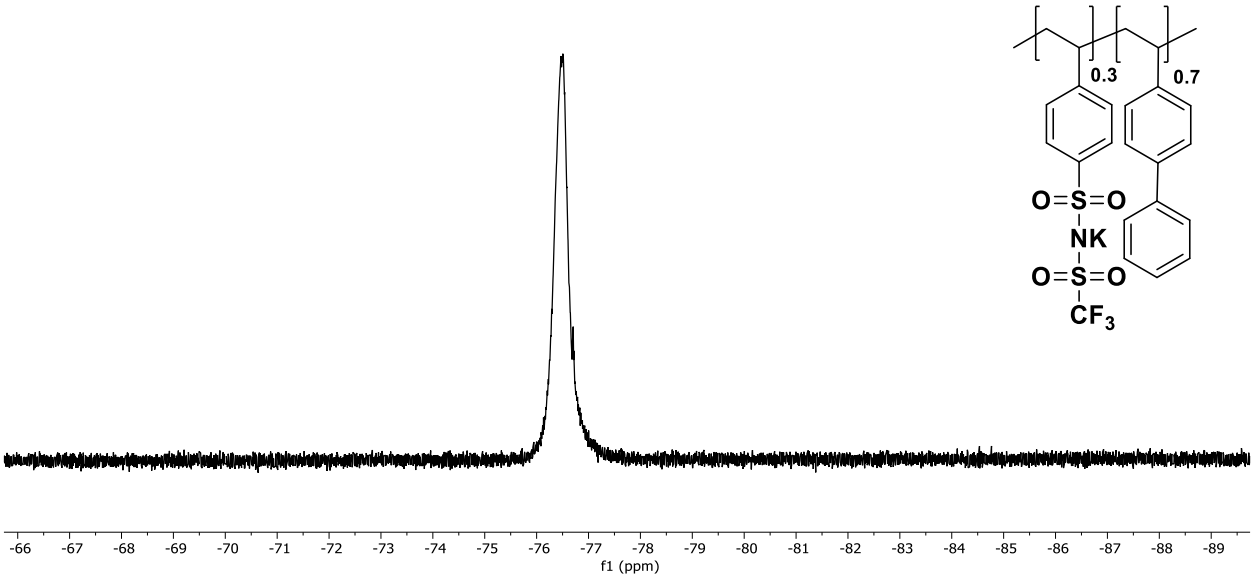

Figure 4.35. ^{19}F NMR of **8** in CD_3CN.

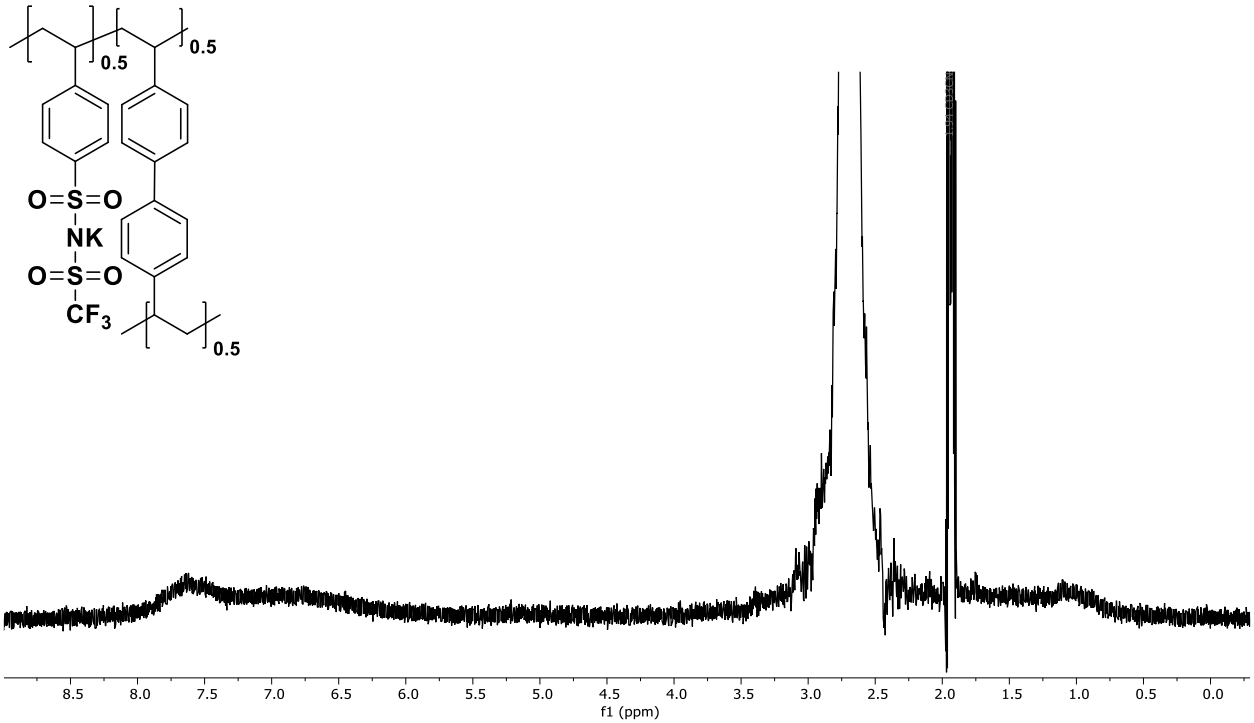

Figure 4.36. ^{1}H NMR of **9** in CD_3CN.

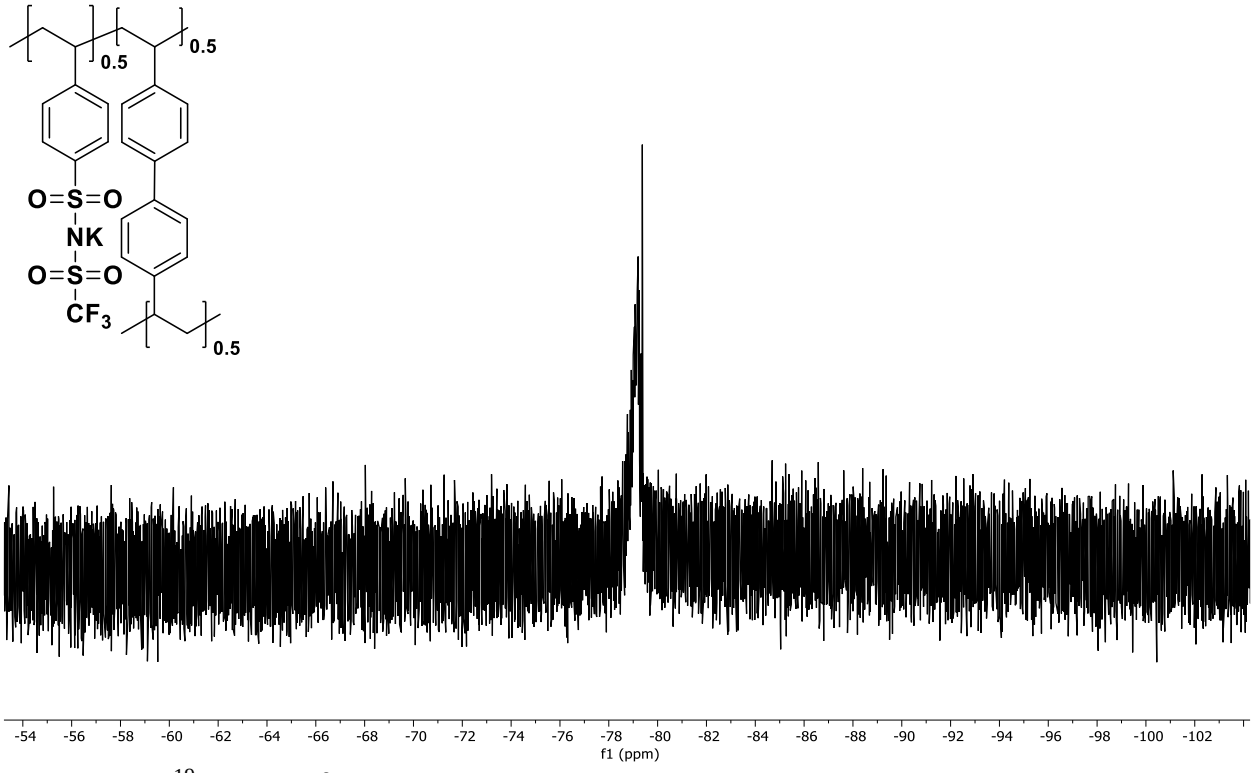

Figure 4.37. ^{19}F NMR of **9** in CD_3CN.

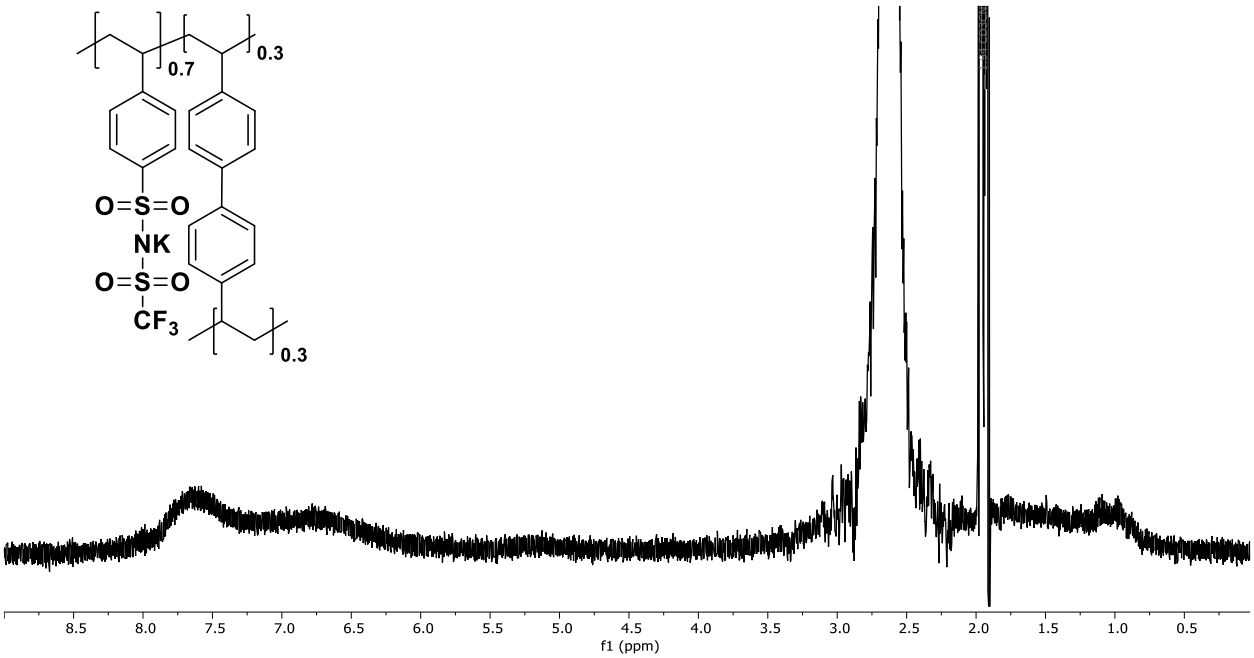

Figure 4.38. ^{1}H NMR of **10** in CD_3CN.

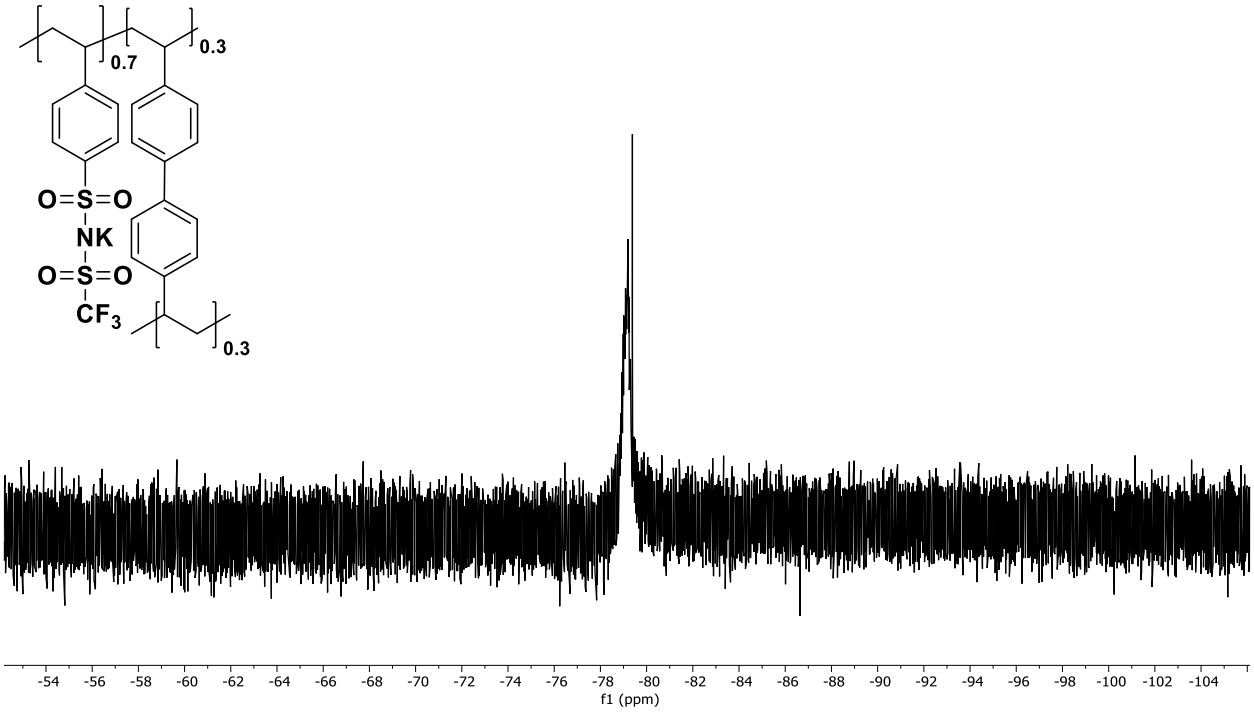

Figure 4.39. ^{19}F NMR of **10** in CD_3CN.

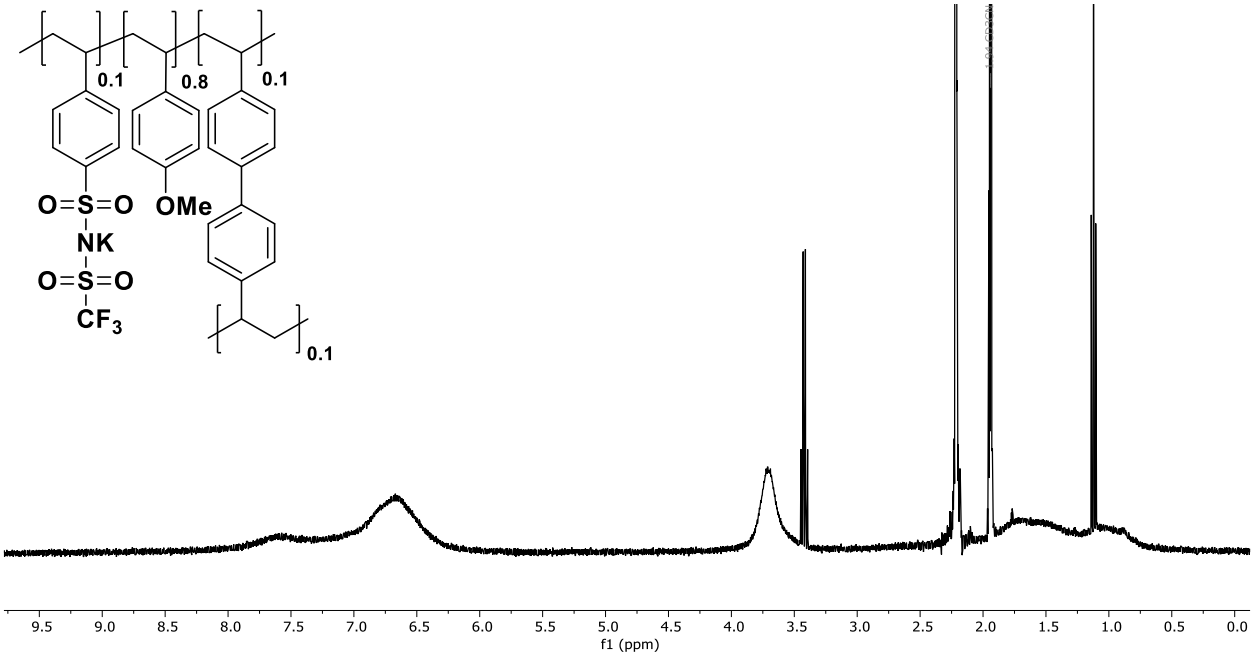

Figure 4.40. ^{1}H NMR of 10/80/10 K-STFSI/methoxystyrene/biphenyl cross-linker polymer in CD_3CN (not tested for CO_2R performance).

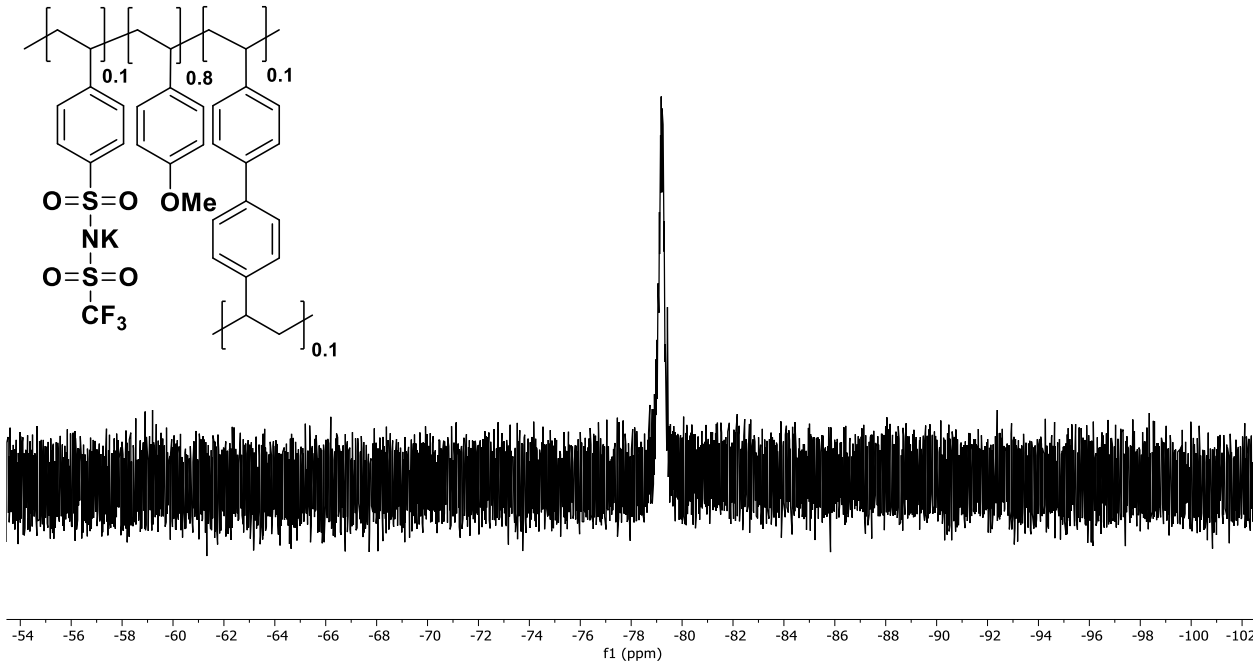

Figure 4.41. ^{19}F NMR of 10/80/10 K-STFSI/methoxystyrene/biphenyl cross-linker polymer in CD_3CN (not tested for CO_2R performance).

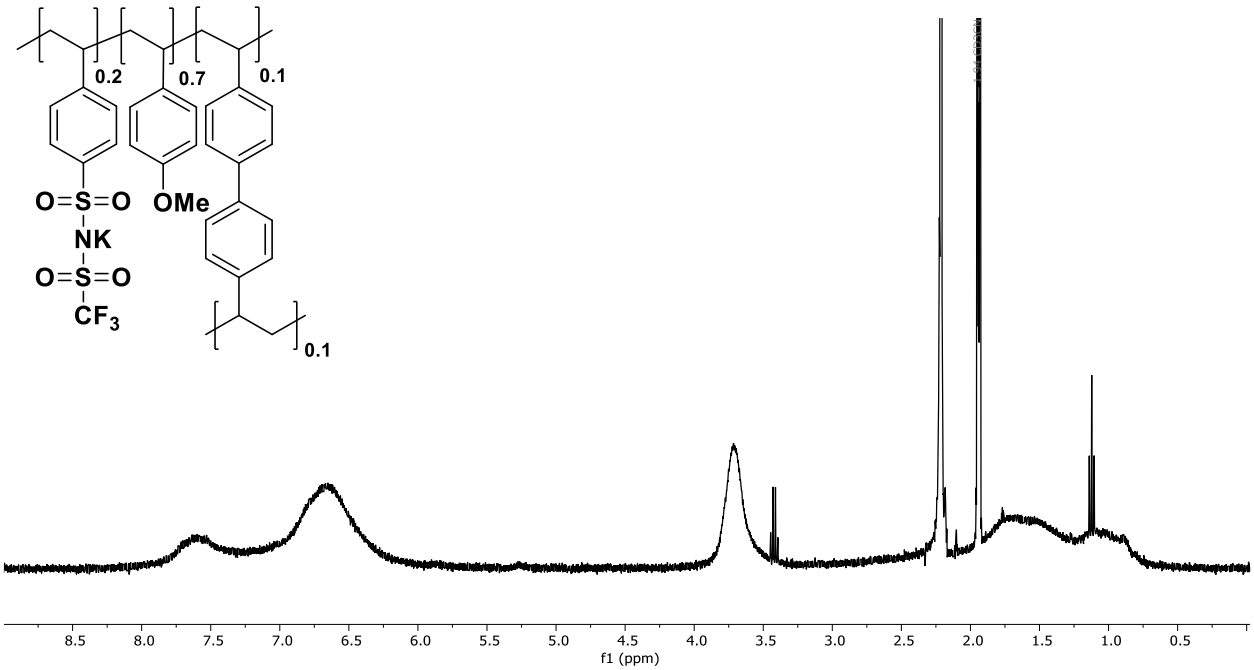

Figure 4.42. ^{1}H NMR of **11** in CD_3CN.

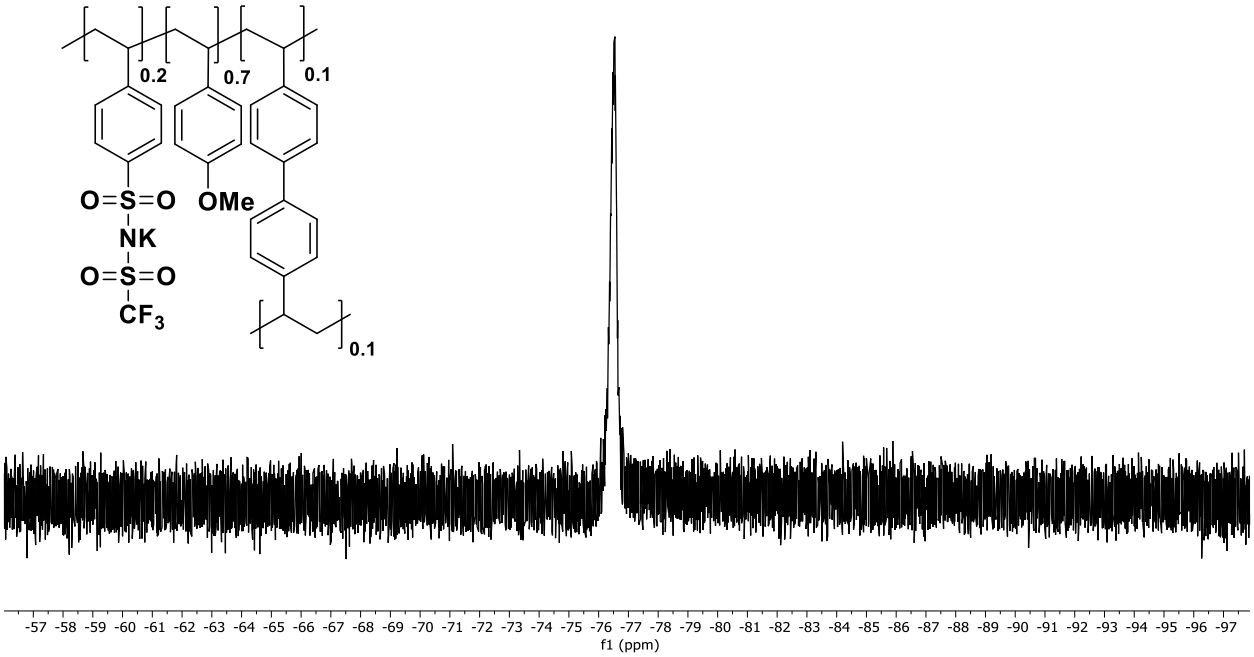

Figure 4.43. ^{19}F NMR of **11** in CD_3CN.

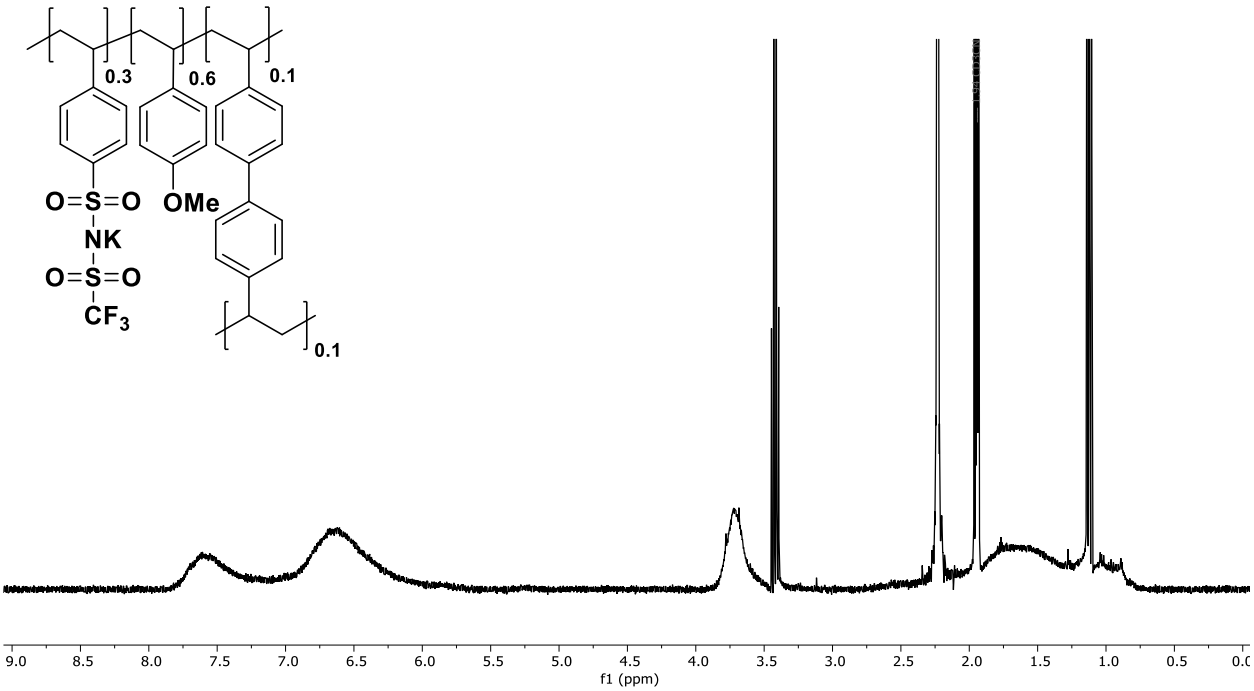

Figure 4.44. ^{1}H NMR of **12** in CD_3CN.

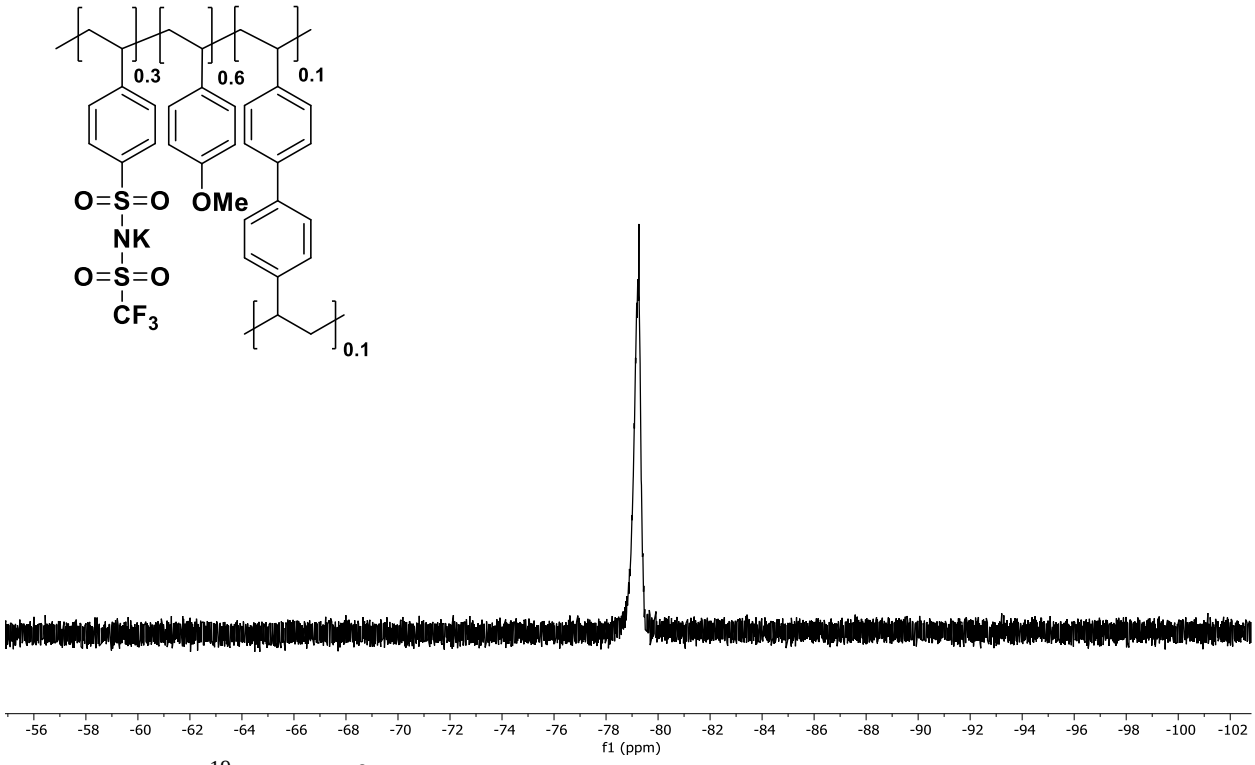

Figure 4.45. ^{19}F NMR of **12** in CD_3CN.

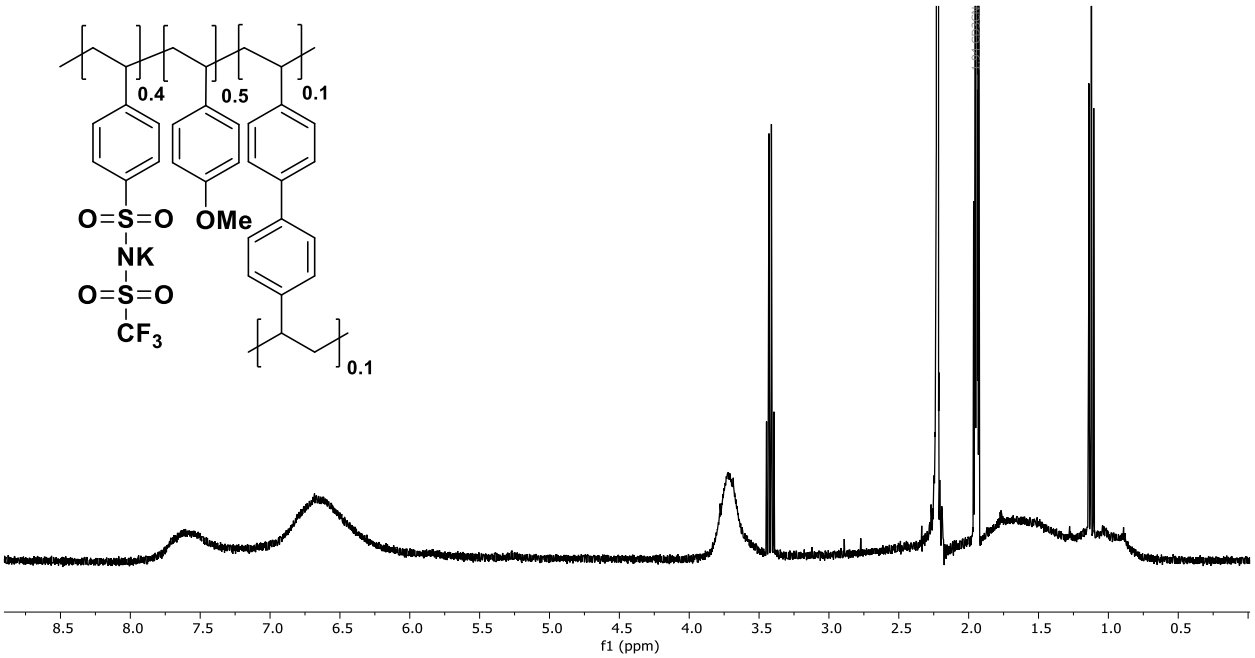

Figure 4.46. ^{1}H NMR of 40/50/10 (K-STFSI/methoxystyrene/biphenyl cross-linker) polymer in CD_3CN (not tested for CO_2R performance).

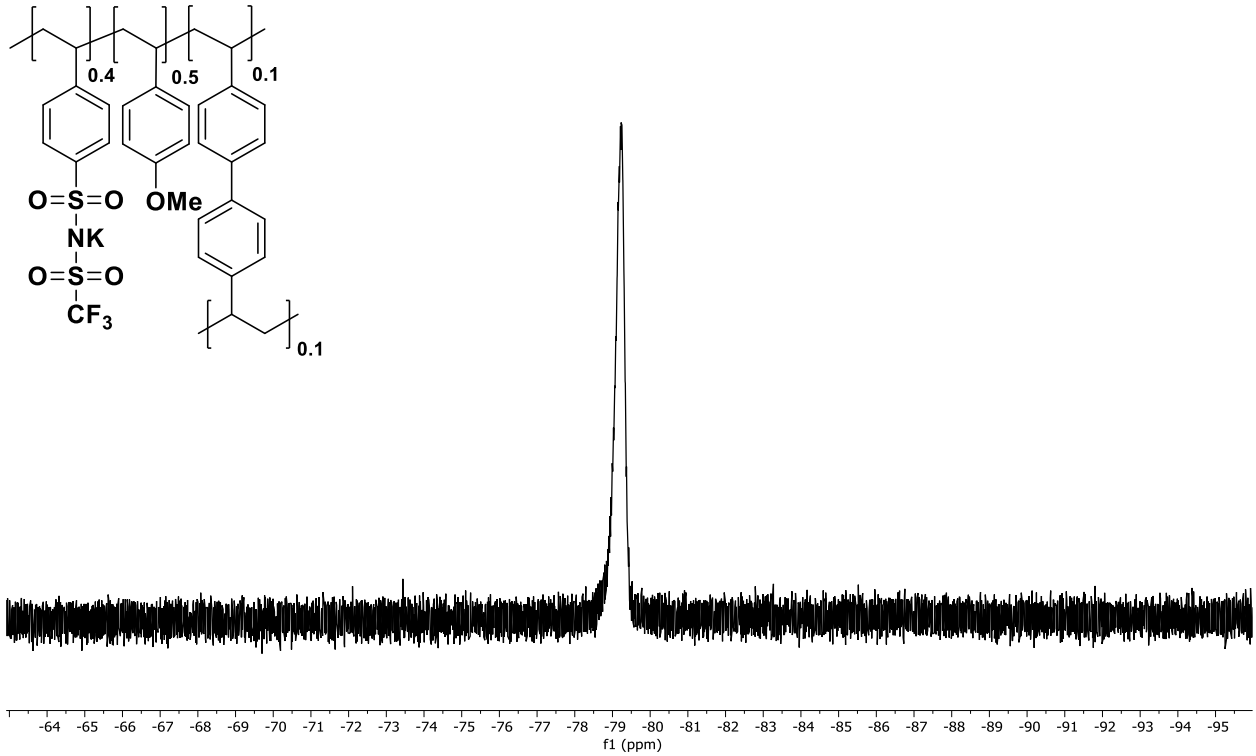

Figure 4.47. ^{19}F NMR of 40/50/10 (K-STFSI/methoxystyrene/biphenyl cross-linker) polymer in CD_3CN (not tested for CO_2R performance).

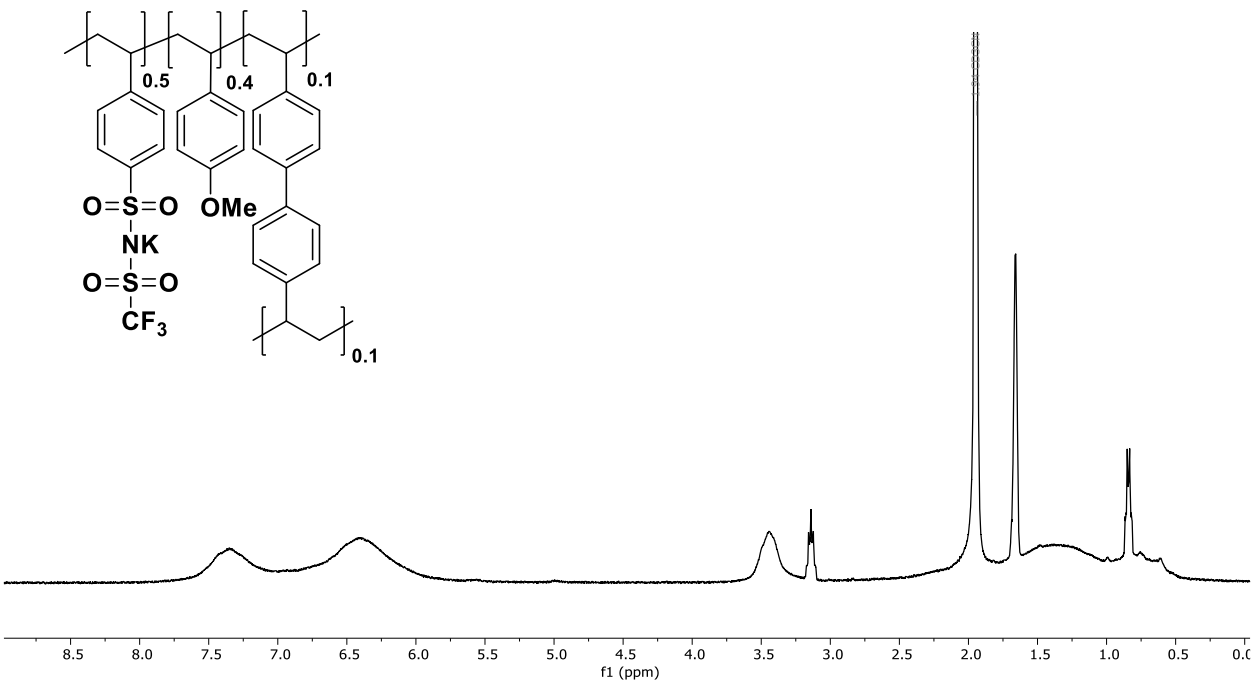

Figure 4.48. ^{1}H NMR of **13** in CD_3CN.

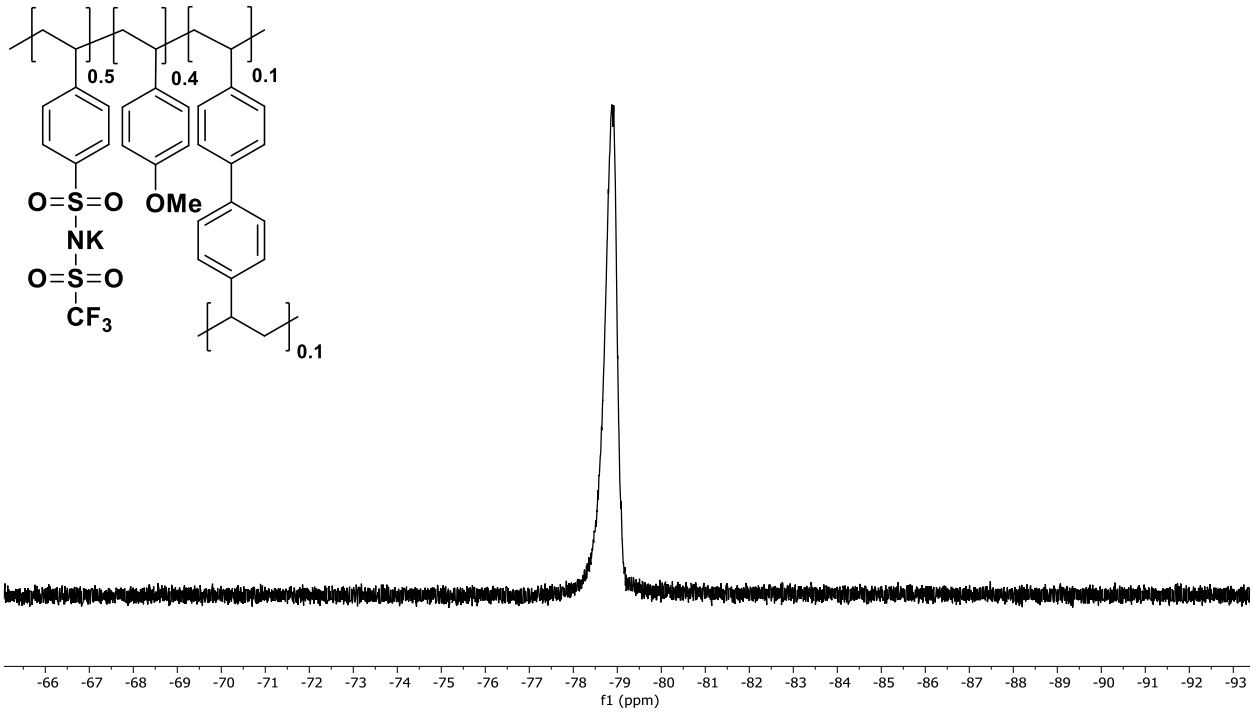

Figure 4.49. ^{19}F NMR of **13** in CD_3CN.

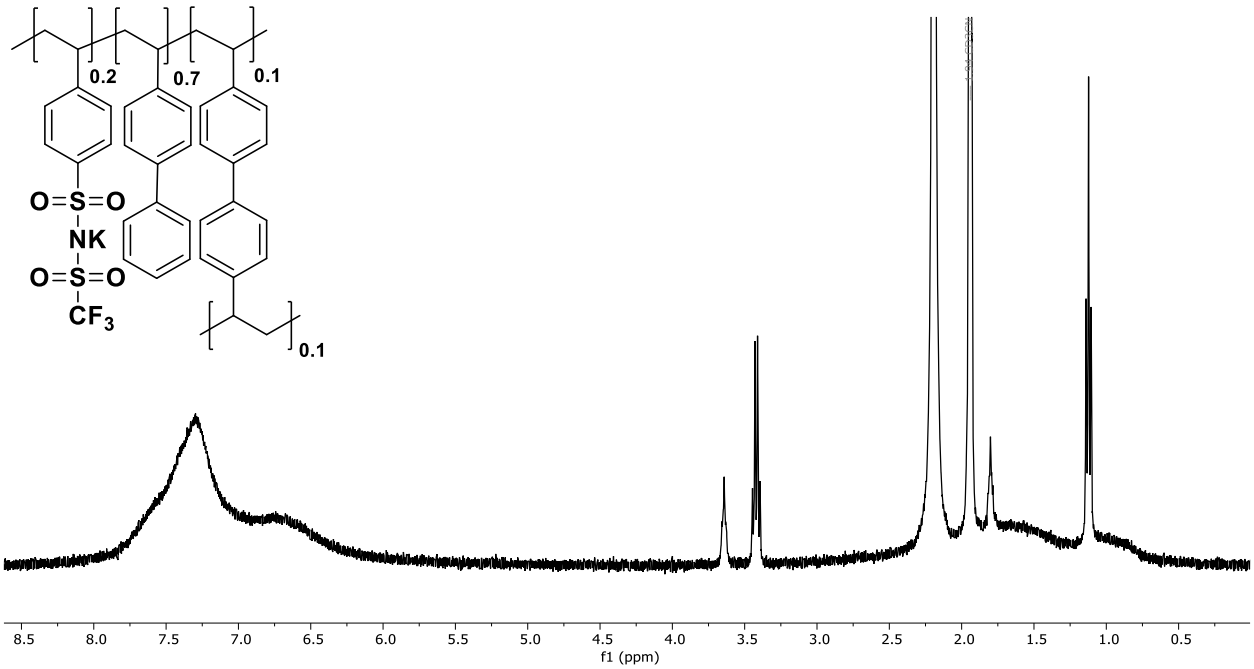

Figure 4.50. ^{1}H NMR of **14** in CD_3CN.

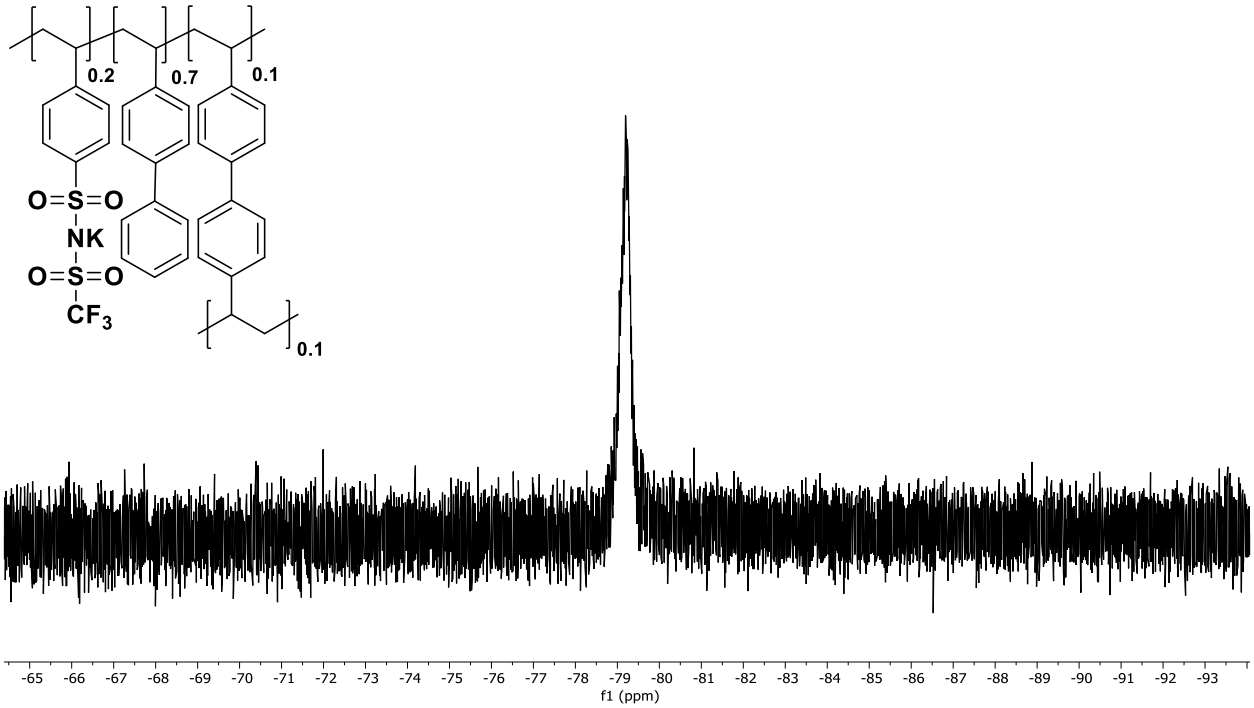

Figure 4.51. ^{19}F NMR of **14** in CD_3CN.

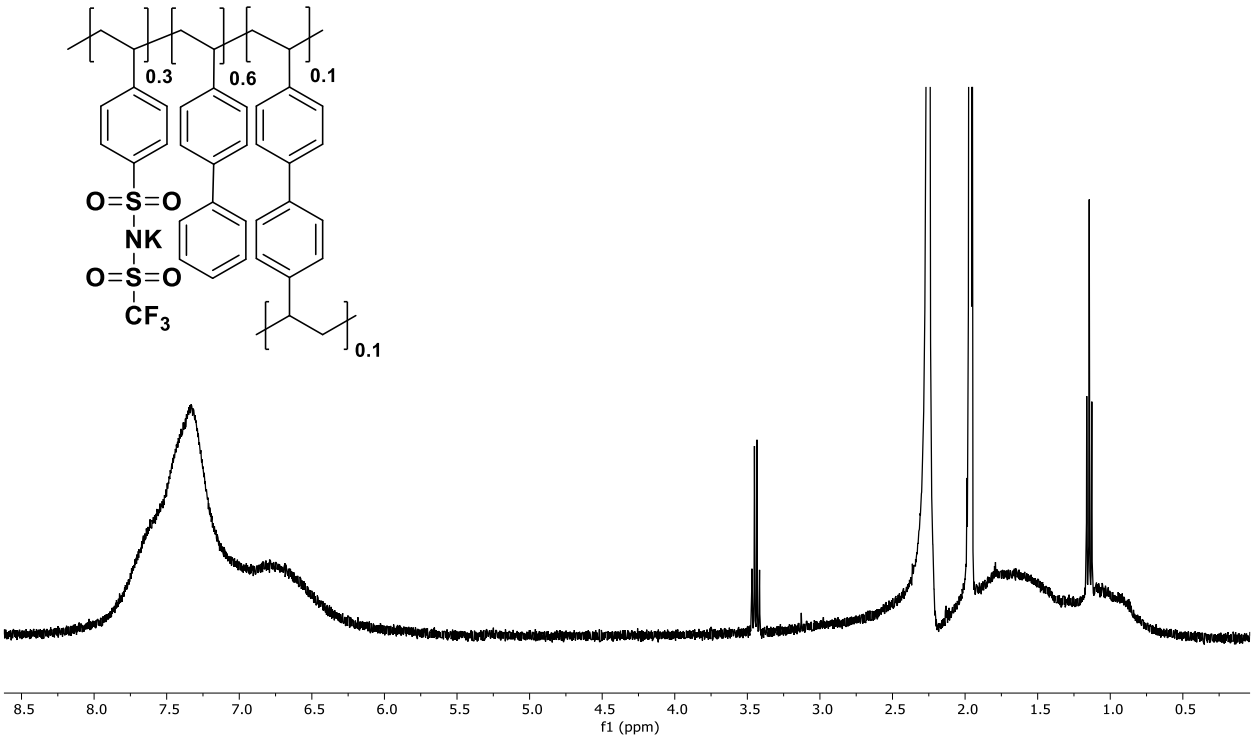

Figure 4.52. ^{1}H NMR of **15** in CD_3CN.

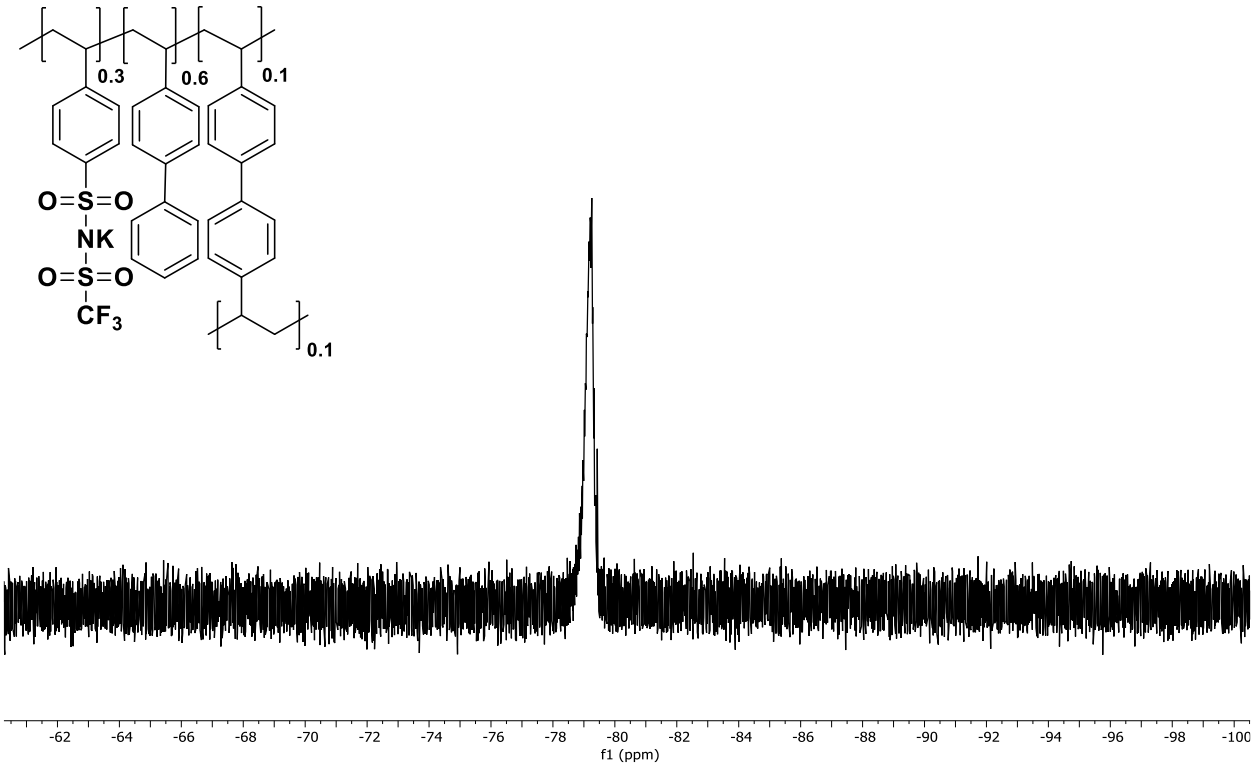

Figure 4.53. ^{19}F NMR of **15** in CD_3CN.

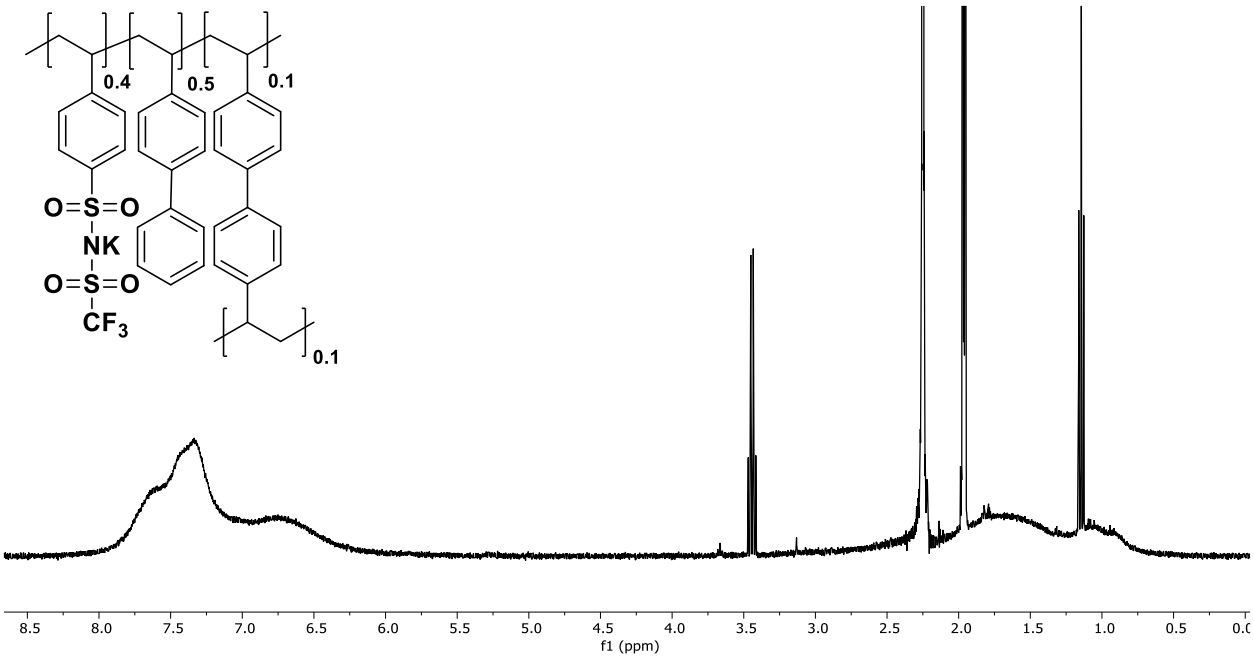

Figure 4.54. ^{1}H NMR of 40/50/10 (K-STFSI/vinylbiphenyl/biphenyl cross-linker) polymer in CD_3CN (not tested for CO_2R performance).

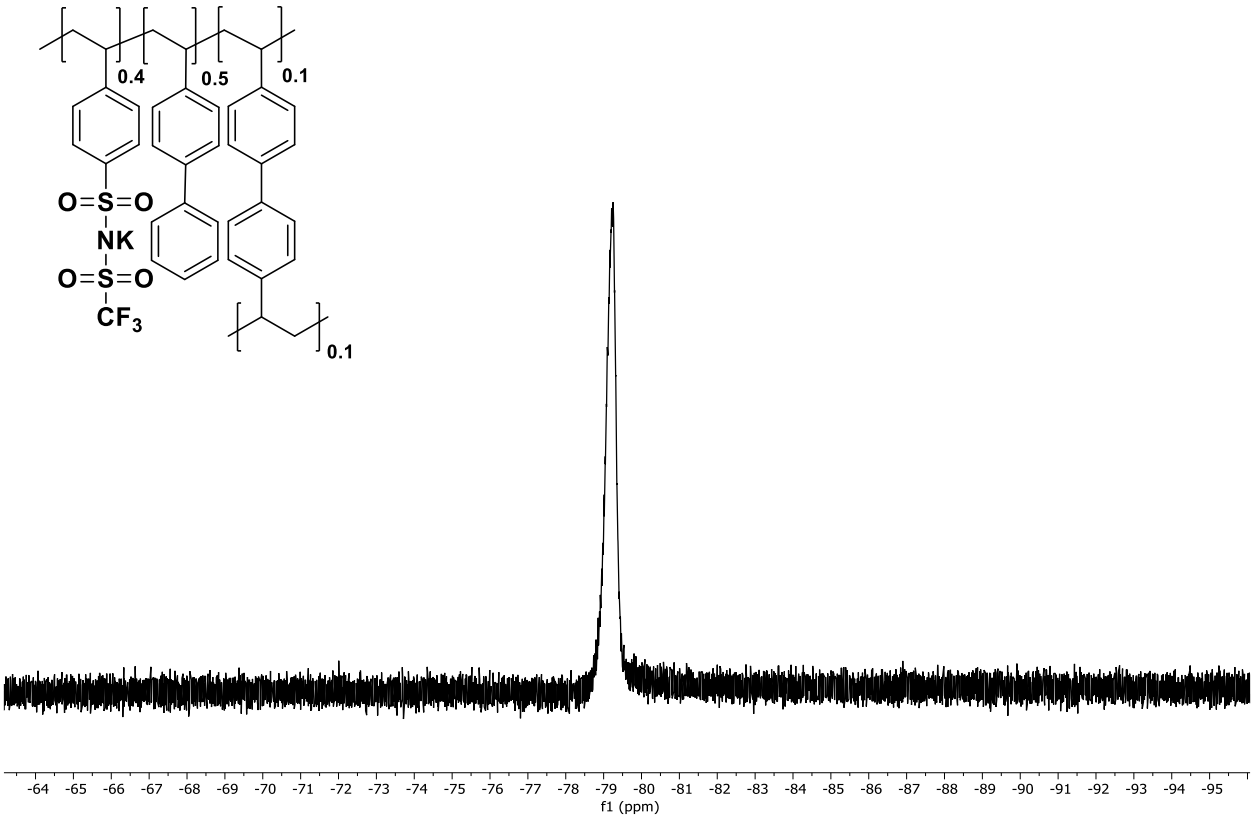

Figure 4.55. ^{19}F NMR of 40/50/10 (K-STFSI/vinylbiphenyl/biphenyl cross-linker) polymer in CD_3CN (not tested for CO_2R performance).

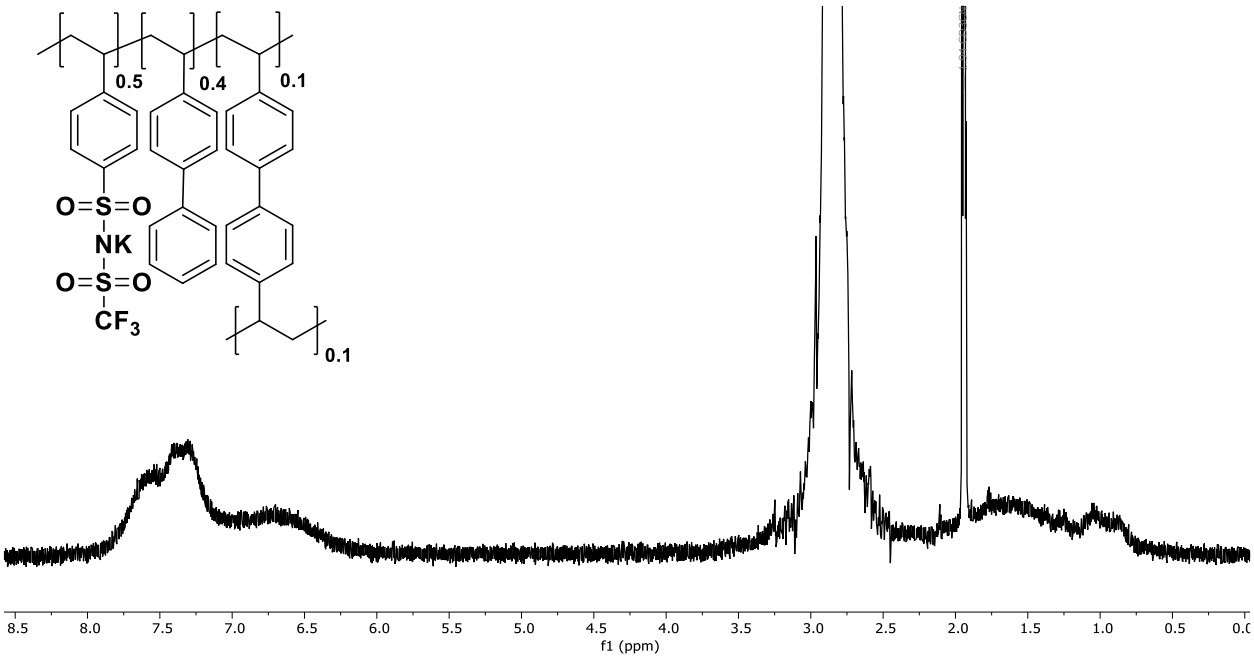

Figure 4.56. ^{1}H NMR of **16** in CD_3CN.

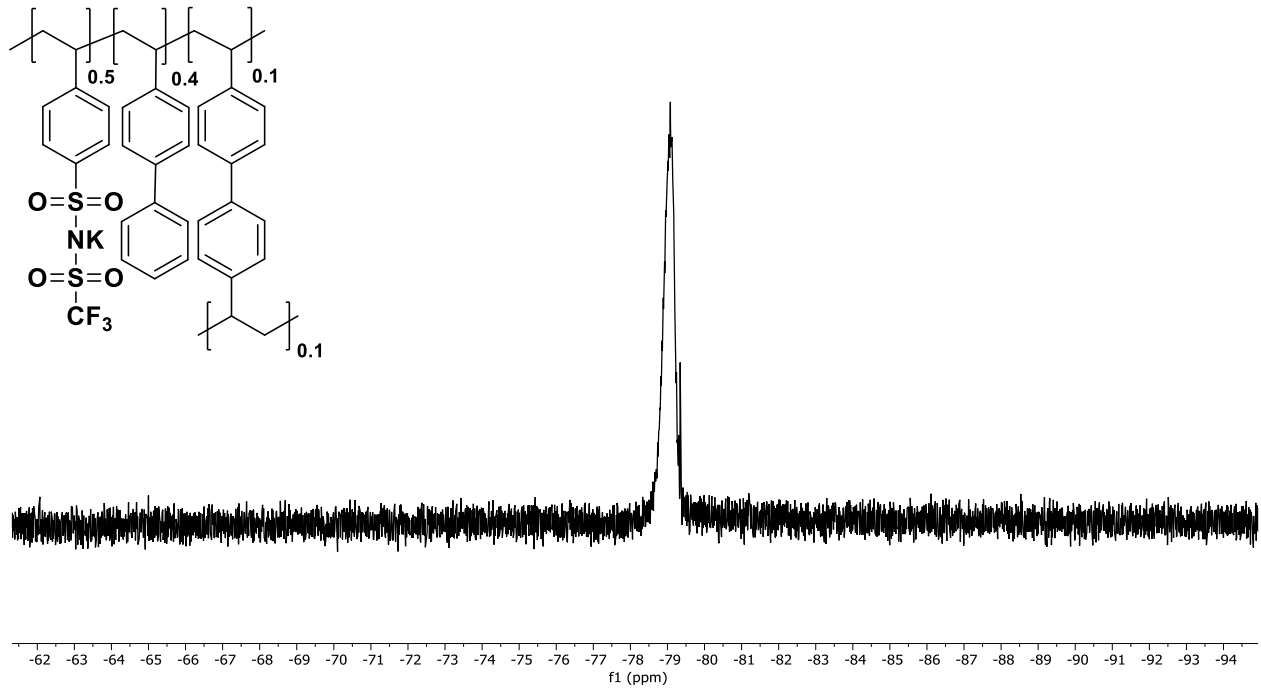

Figure 4.57. ^{19}F NMR of **16** in CD_3CN.

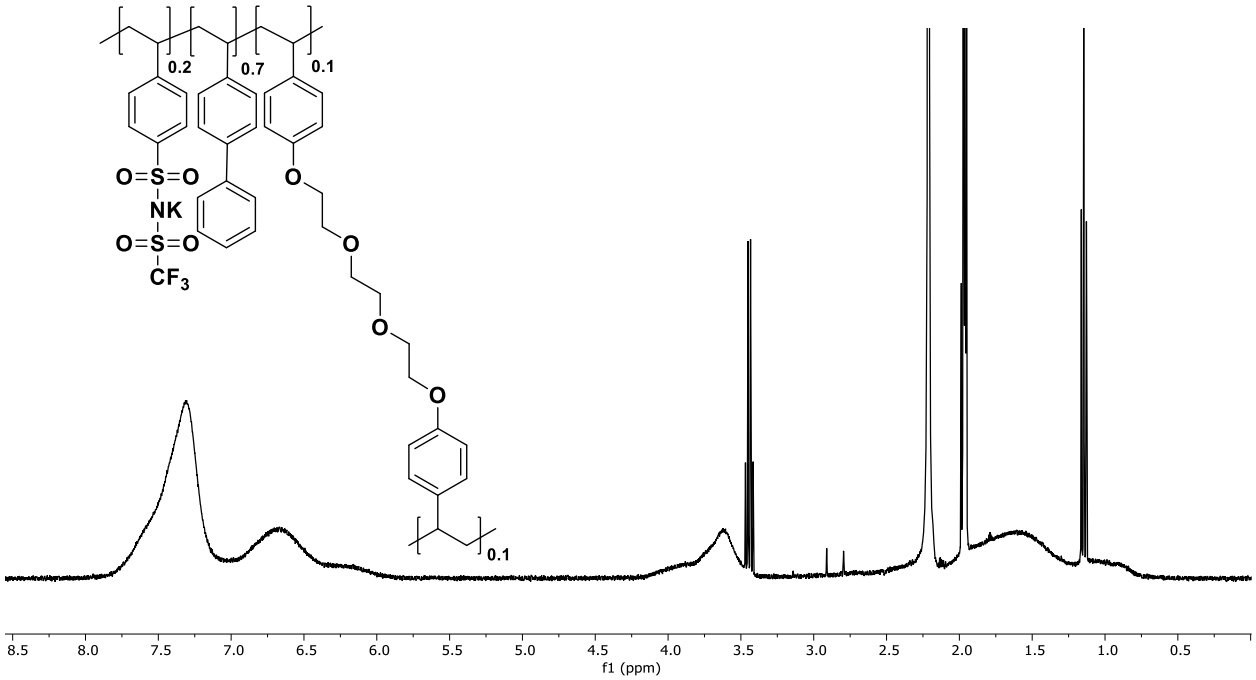

Figure 4.58. ^{1}H NMR of **17** in CD_3CN.

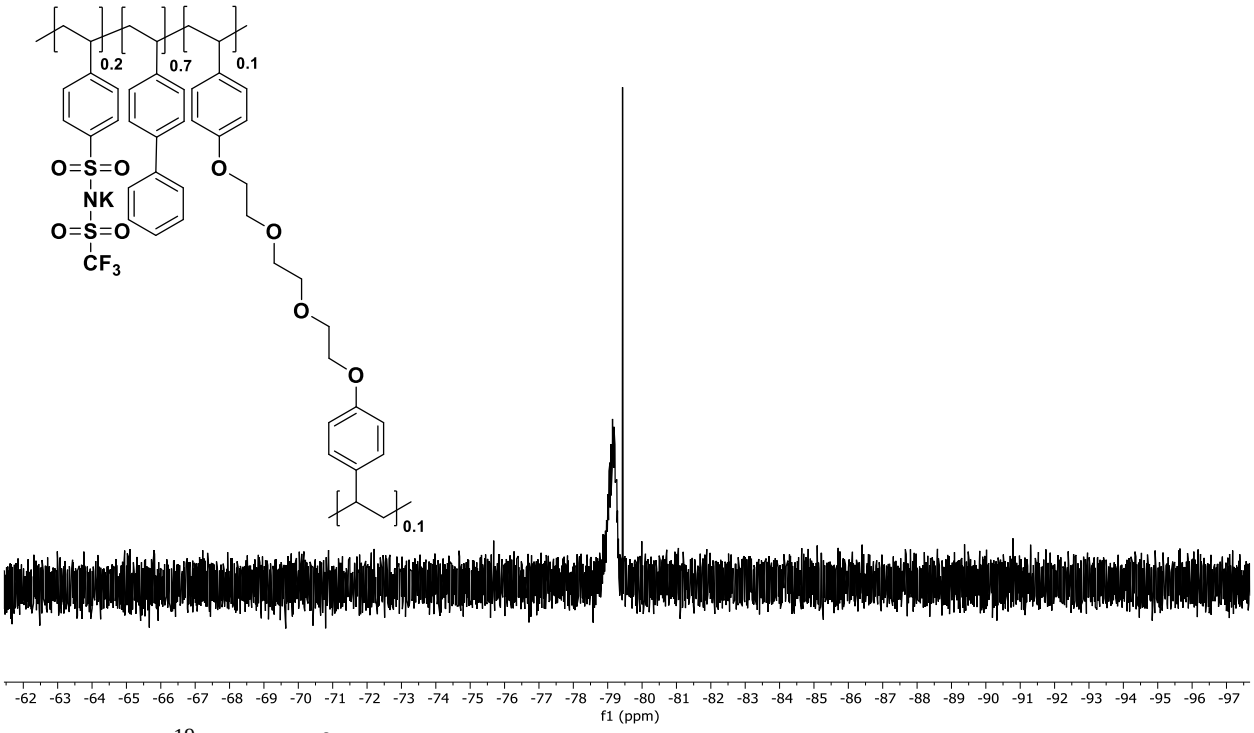

Figure 4.59. ^{19}F NMR of **17** in CD_3CN.

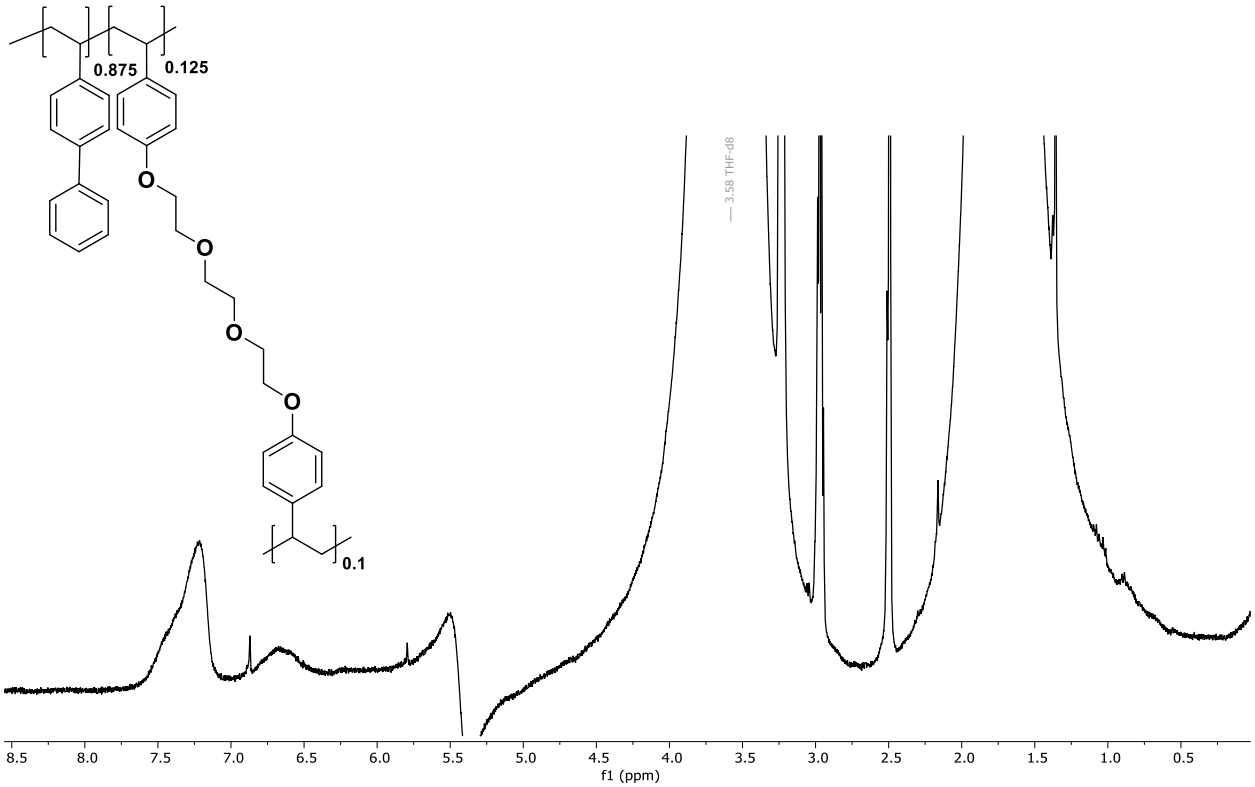

Figure 4.60. ^{1}H NMR of **18** in THF-h_8.

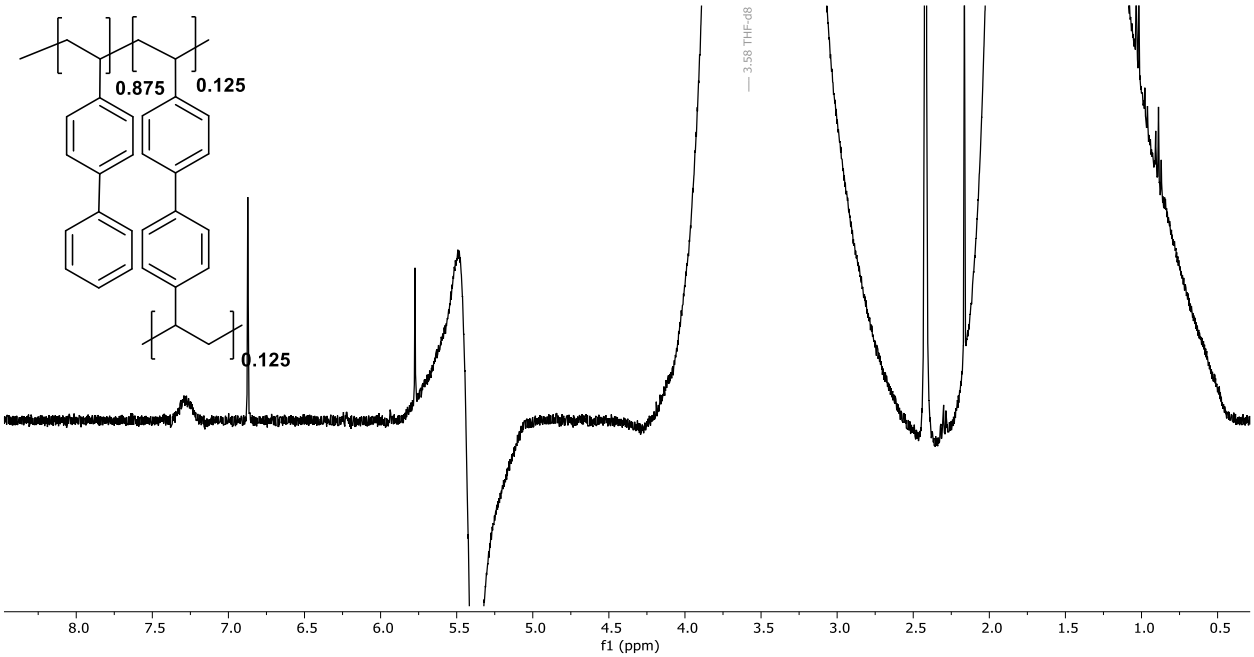

Figure 4.61. ^{1}H NMR of **19** in THF-h_8.

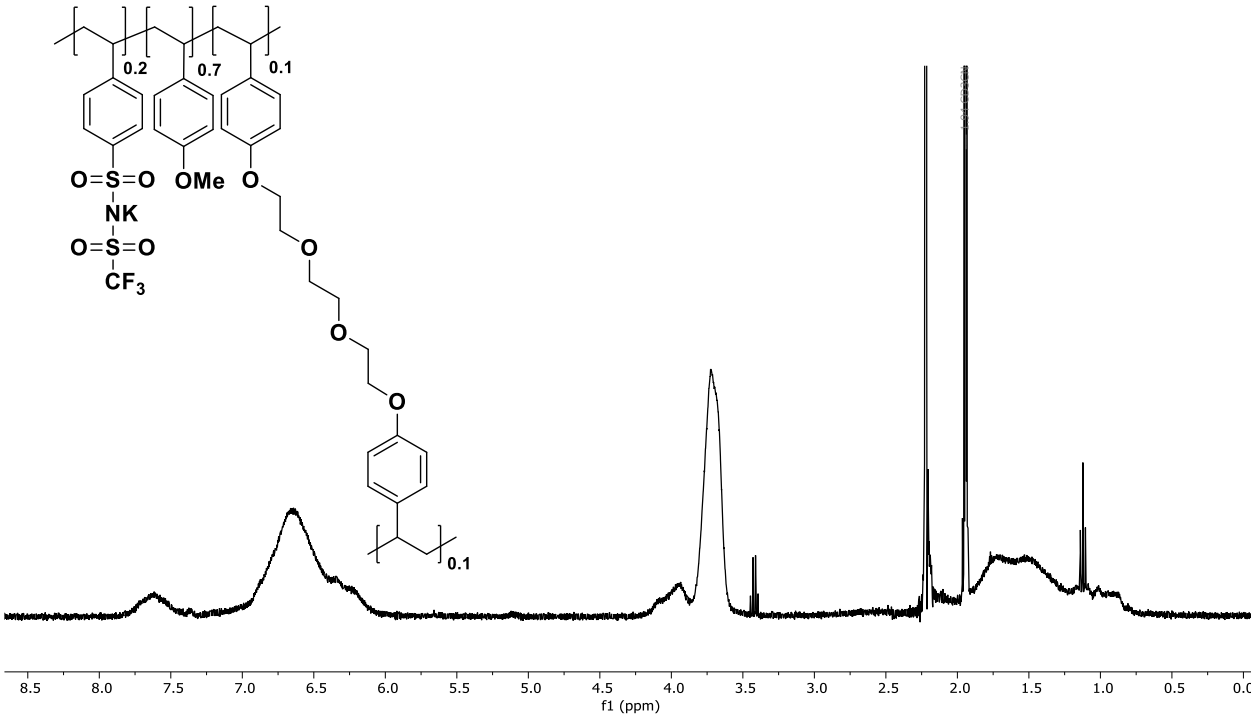

Figure 4.62. ^{1}H NMR of **20** in CD_3CN.

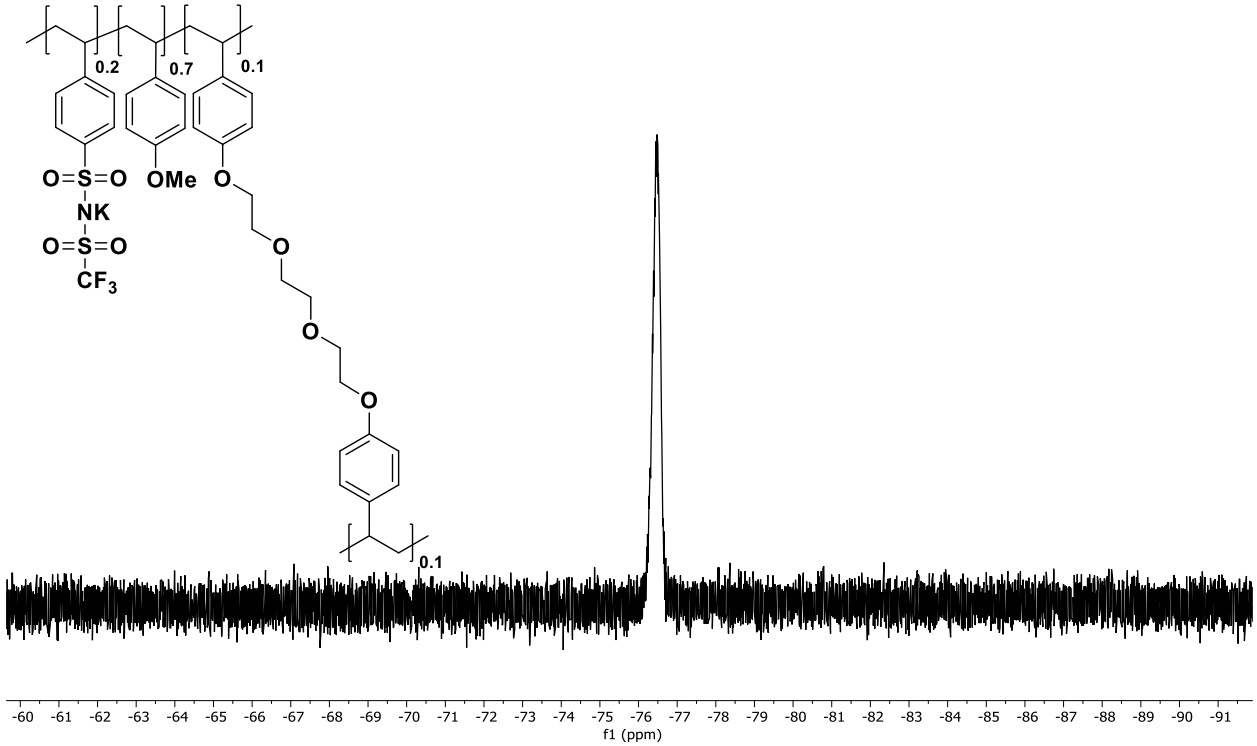

Figure 4.63. ^{19}F NMR of **20** in CD_3CN.

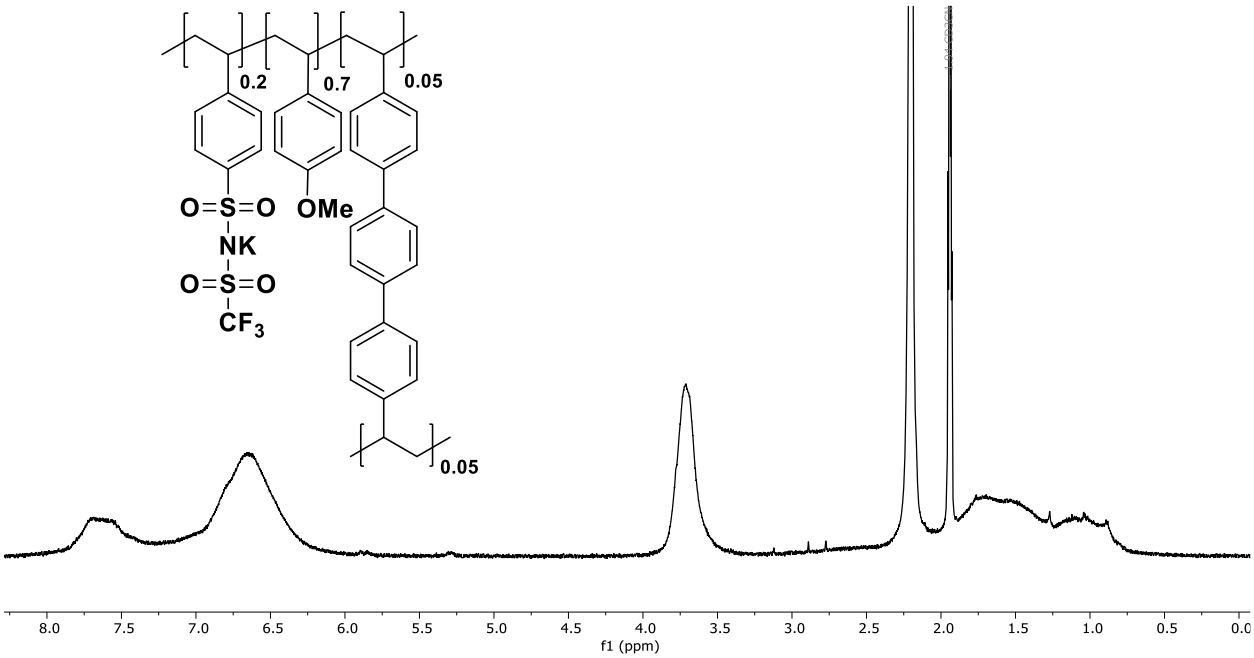

Figure 4.64. ^{1}H NMR of **21** in CD_3CN.

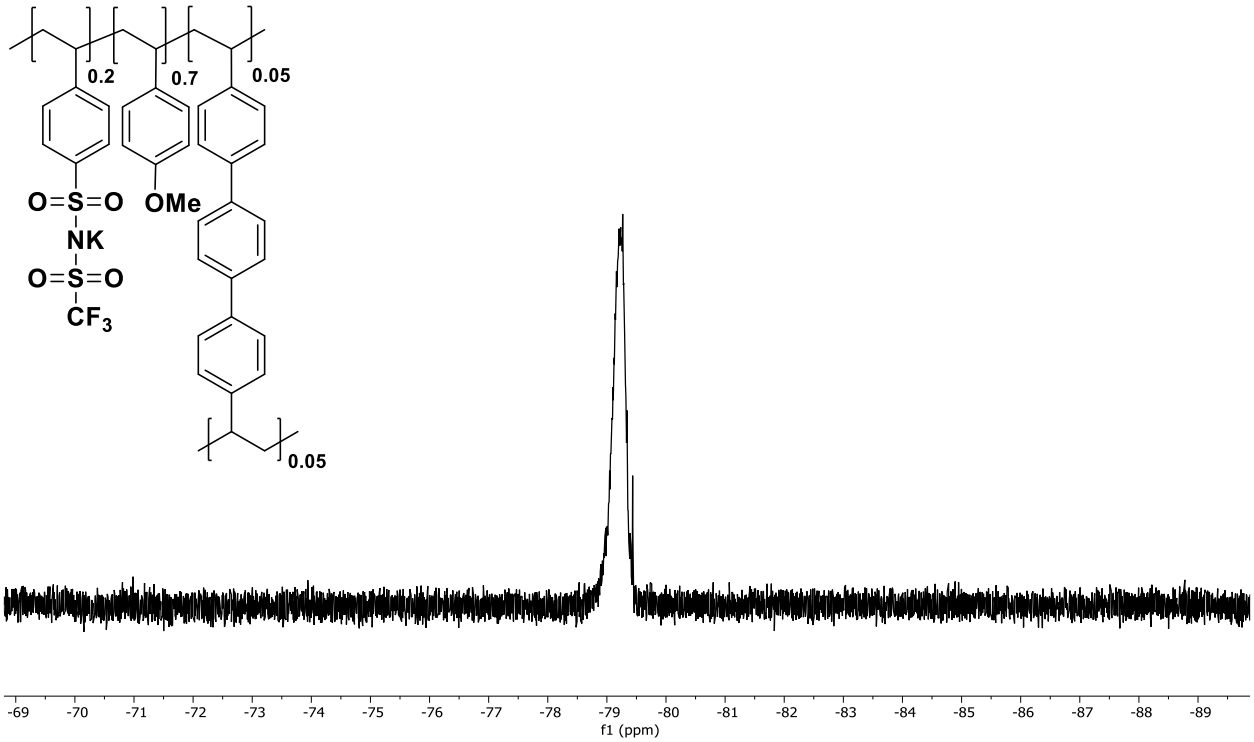

Figure 4.65. ^{19}F NMR of **21** in CD_3CN.

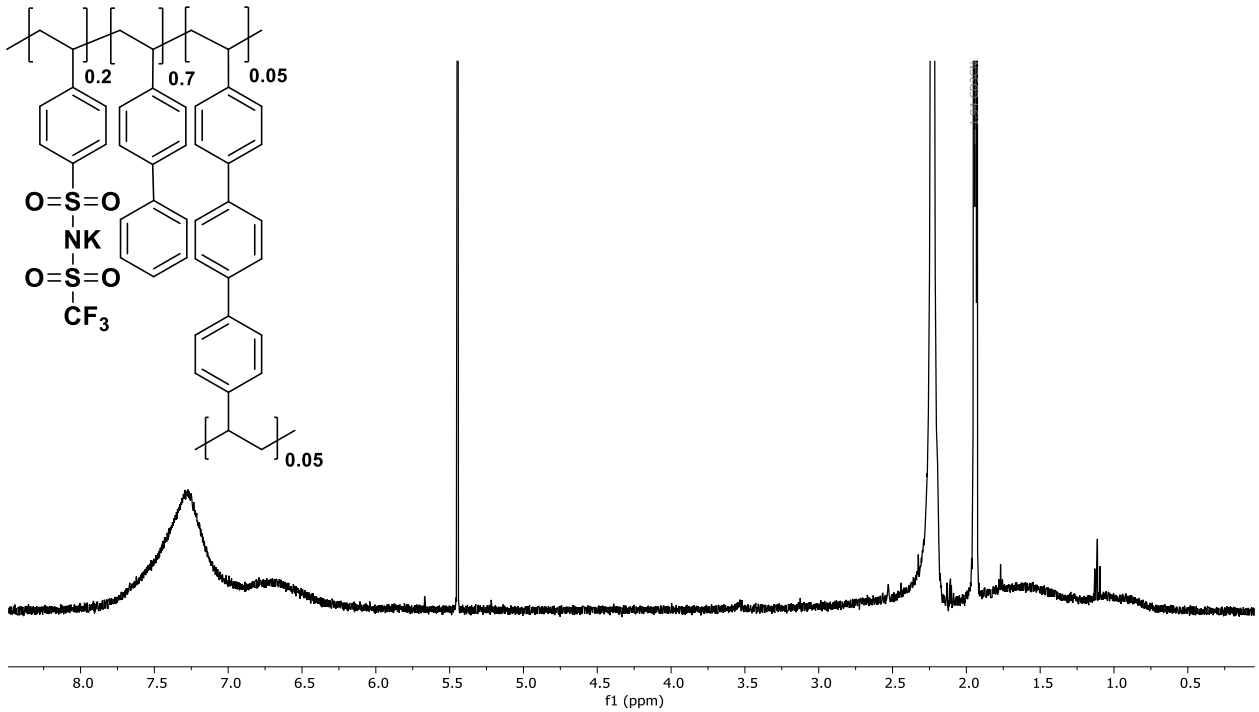

Figure 4.66. ^{1}H NMR of **22** in CD_3CN.

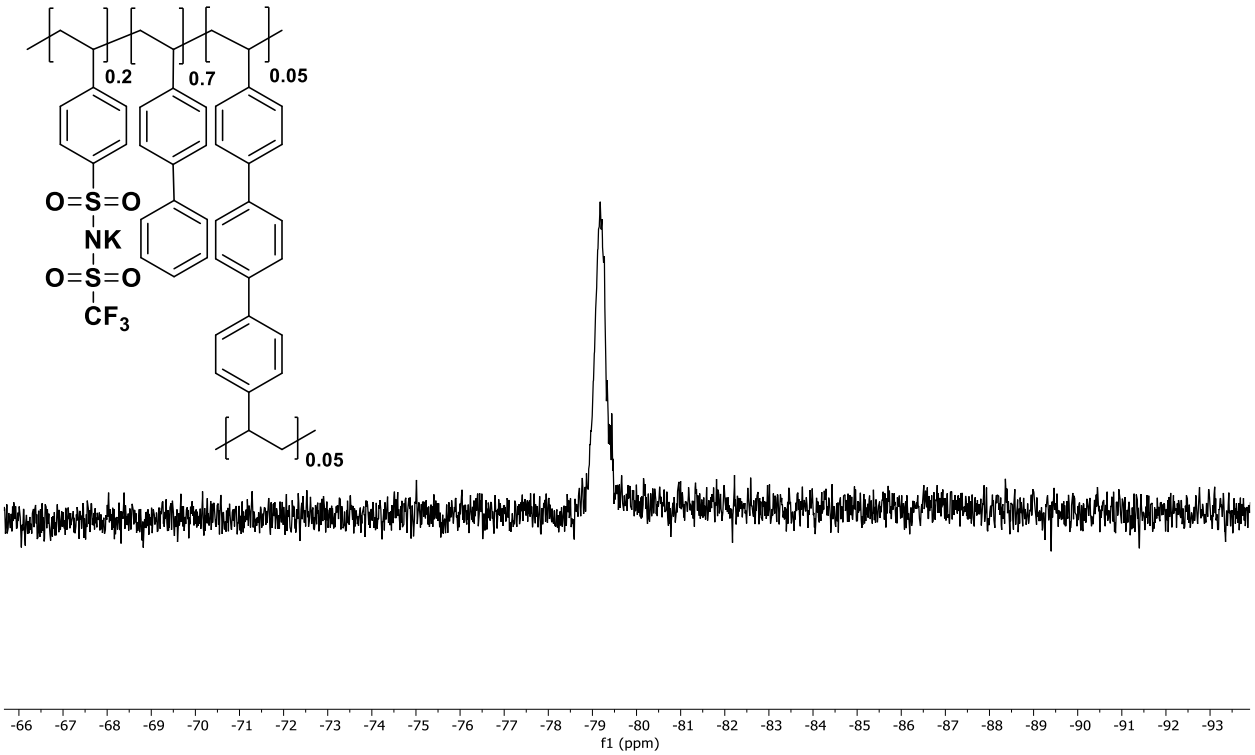

Figure 4.67. ^{19}F NMR of **22** in CD_3CN.

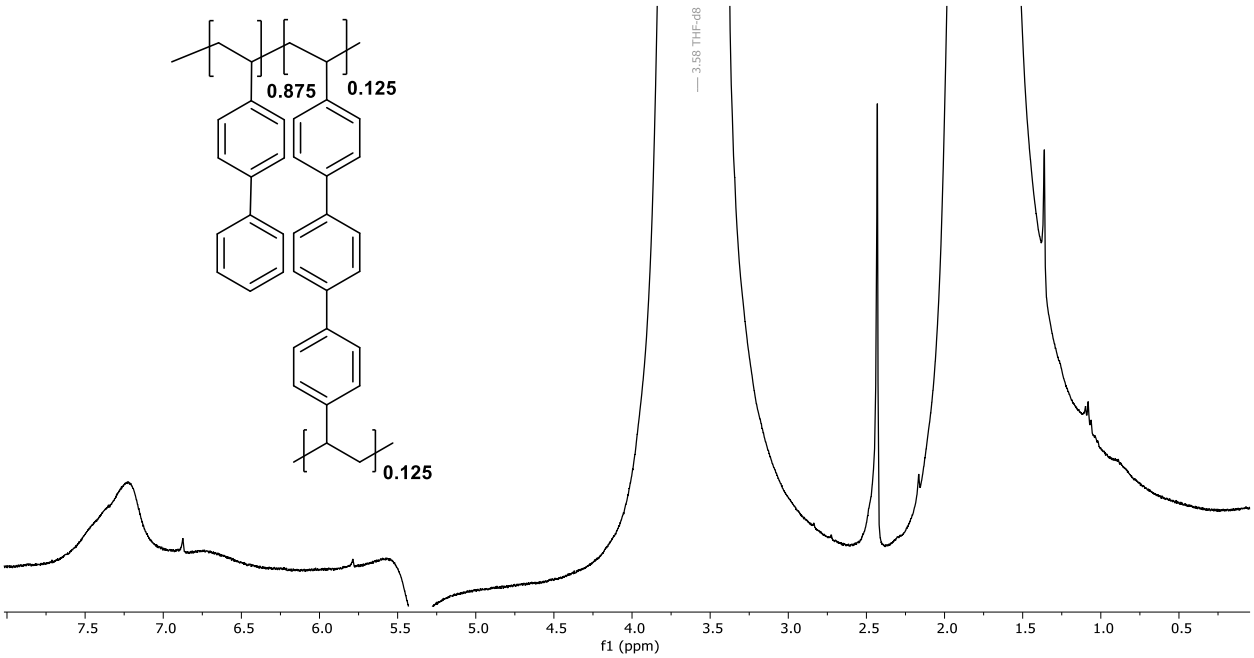

Figure 4.68. ^{1}H NMR of **23** in THF-h_8.

REFERENCES

1. Nitopi, S.; Bertheussen, E.; Scott, S. B.; Liu, X.; Engstfeld, A. K.; Horch, S.; Seger, B.; Stephens, I. E. L.; Chan, K.; Hahn, C.; Nørskov, J. K.; Jaramillo, T. F.; Chorkendorff, I., Progress and Perspectives of Electrochemical CO_2 Reduction on Copper in Aqueous Electrolyte. *Chem. Rev.* **2019,** *119* (12), 7610-7672. 10.1021/acs.chemrev.8b00705
2. Hori, Y.; Kikuchi, K.; Suzuki, S., Production of CO and CH_4 in Electrochemical Reduction of CO_2 at Metal Electrodes in Aqueous Hydrogencarbonate Solution. *Chem. Lett.* **2006,** *14* (11), 1695-1698. 10.1246/cl.1985.1695
3. Kuhl, K. P.; Cave, E. R.; Abram, D. N.; Jaramillo, T. F., New insights into the electrochemical reduction of carbon dioxide on metallic copper surfaces. *Energy & Environmental Science* **2012,** *5* (5), 7050-7059. 10.1039/C2EE21234J
4. Murata, A.; Hori, Y., Product Selectivity Affected by Cationic Species in Electrochemical Reduction of CO_2 and CO at a Cu Electrode. *Bull. Chem. Soc. Jpn.* **2006,** *64* (1), 123-127. 10.1246/bcsj.64.123
5. Thevenon, A.; Rosas-Hernández, A.; Fontani Herreros, A. M.; Agapie, T.; Peters, J. C., Dramatic HER Suppression on Ag Electrodes via Molecular Films for Highly Selective CO_2 to CO Reduction. *ACS Catalysis* **2021,** *11* (8), 4530-4537. 10.1021/acscatal.1c00338
6. Thevenon, A.; Rosas-Hernández, A.; Peters, J. C.; Agapie, T., In-Situ Nanostructuring and Stabilization of Polycrystalline Copper by an Organic Salt Additive Promotes Electrocatalytic CO_2 Reduction to Ethylene. *Angew. Chem. Int. Ed.* **2019,** *58* (47), 16952-16958. 10.1002/anie.201907935
7. Li, F.; Thevenon, A.; Rosas-Hernández, A.; Wang, Z.; Li, Y.; Gabardo, C. M.; Ozden, A.; Dinh, C. T.; Li, J.; Wang, Y.; Edwards, J. P.; Xu, Y.; McCallum, C.; Tao, L.; Liang, Z.-Q.; Luo, M.; Wang, X.; Li, H.; O'Brien, C. P.; Tan, C.-S.; Nam, D.-H.; Quintero-Bermudez, R.; Zhuang, T.-T.; Li, Y. C.; Han, Z.; Britt, R. D.; Sinton, D.; Agapie, T.; Peters, J. C.; Sargent, E. H., Molecular tuning of CO2-to-ethylene conversion. *Nature* **2020,** *577* (7791), 509-513. 10.1038/s41586-019-1782-2
8. Han, Z.; Kortlever, R.; Chen, H.-Y.; Peters, J. C.; Agapie, T., CO_2 Reduction Selective for $C_{\geq 2}$ Products on Polycrystalline Copper with N-Substituted Pyridinium Additives. *ACS Central Science* **2017,** *3* (8), 853-859. 10.1021/acscentsci.7b00180
9. Nie, W.; Heim, G. P.; Watkins, N. B.; Agapie, T.; Peters, J. C., Organic Additive-derived Films on Cu Electrodes Promote Electrochemical CO_2 Reduction to C_{2+} Products Under Strongly Acidic Conditions. *Angew. Chem. Int. Ed.* **2023,** *62* (12), e202216102. 10.1002/anie.202216102
10. Cheng, B.; Du, J.; Yuan, H.; Tao, Y.; Chen, Y.; Lei, J.; Han, Z., Selective CO_2 Reduction to Ethylene Using Imidazolium-Functionalized Copper. *ACS Applied Materials & Interfaces* **2022,** *14* (24), 27823-27832. 10.1021/acsami.2c03748
11. Buckley, A. K.; Cheng, T.; Oh, M. H.; Su, G. M.; Garrison, J.; Utan, S. W.; Zhu, C.; Toste, F. D.; Goddard, W. A., III; Toma, F. M., Approaching 100% Selectivity at Low Potential on Ag for Electrochemical CO_2 Reduction to CO Using a Surface Additive. *ACS Catalysis* **2021,** *11* (15), 9034-9042. 10.1021/acscatal.1c00830
12. Rosen, B. A.; Salehi-Khojin, A.; Thorson, M. R.; Zhu, W.; Whipple, D. T.; Kenis, P. J. A.; Masel, R. I., Ionic Liquid; Mediated Selective Conversion of CO_2 to CO at Low Overpotentials. *Science* **2011,** *334* (6056), 643-644. 10.1126/science.1209786
13. Chen, X.; Chen, J.; Alghoraibi, N. M.; Henckel, D. A.; Zhang, R.; Nwabara, U. O.; Madsen, K. E.; Kenis, P. J. A.; Zimmerman, S. C.; Gewirth, A. A., Electrochemical CO_2-to-ethylene conversion

on polyamine-incorporated Cu electrodes. *Nature Catalysis* **2021,** *4* (1), 20-27. 10.1038/s41929-020-00547-0

14. Wei, X.; Yin, Z.; Lyu, K.; Li, Z.; Gong, J.; Wang, G.; Xiao, L.; Lu, J.; Zhuang, L., Highly Selective Reduction of CO_2 to C_{2+} Hydrocarbons at Copper/Polyaniline Interfaces. *ACS Catalysis* **2020,** *10* (7), 4103-4111. 10.1021/acscatal.0c00049
15. Watkins, N. B.; Wu, Y.; Nie, W.; Peters, J. C.; Agapie, T., In Situ Deposited Polyaromatic Layer Generates Robust Copper Catalyst for Selective Electrochemical CO_2 Reduction at Variable pH. *ACS Energy Letters* **2023,** *8* (1), 189-195. 10.1021/acsenergylett.2c02002
16. Kim, C.; Bui, J. C.; Luo, X.; Cooper, J. K.; Kusoglu, A.; Weber, A. Z.; Bell, A. T., Tailored catalyst microenvironments for CO_2 electroreduction to multicarbon products on copper using bilayer ionomer coatings. *Nature Energy* **2021,** *6* (11), 1026-1034. 10.1038/s41560-021-00920-8
17. García de Arquer, F. P.; Dinh, C.-T.; Ozden, A.; Wicks, J.; McCallum, C.; Kirmani, A. R.; Nam, D.-H.; Gabardo, C.; Seifitokaldani, A.; Wang, X.; Li, Y. C.; Li, F.; Edwards, J.; Richter, L. J.; Thorpe, S. J.; Sinton, D.; Sargent, E. H., CO_2 electrolysis to multicarbon products at activities greater than 1 A cm^{-2}. *Science* **2020,** *367* (6478), 661-666. 10.1126/science.aay4217
18. Ozden, A.; Li, F.; García de Arquer, F. P.; Rosas-Hernández, A.; Thevenon, A.; Wang, Y.; Hung, S.-F.; Wang, X.; Chen, B.; Li, J.; Wicks, J.; Luo, M.; Wang, Z.; Agapie, T.; Peters, J. C.; Sargent, E. H.; Sinton, D., High-Rate and Efficient Ethylene Electrosynthesis Using a Catalyst/Promoter/Transport Layer. *ACS Energy Letters* **2020,** *5* (9), 2811-2818. 10.1021/acsenergylett.0c01266
19. Huang, J. E.; Li, F.; Ozden, A.; Sedighian Rasouli, A.; García de Arquer, F. P.; Liu, S.; Zhang, S.; Luo, M.; Wang, X.; Lum, Y.; Xu, Y.; Bertens, K.; Miao, R. K.; Dinh, C.-T.; Sinton, D.; Sargent, E. H., CO_2 electrolysis to multicarbon products in strong acid. *Science* **2021,** *372* (6546), 1074-1078. 10.1126/science.abg6582
20. Pan, H.; Barile, C. J., Electrochemical CO_2 reduction to methane with remarkably high Faradaic efficiency in the presence of a proton permeable membrane. *Energy & Environmental Science* **2020,** *13* (10), 3567-3578. 10.1039/D0EE02189J
21. Wang, J.; Cheng, T.; Fenwick, A. Q.; Baroud, T. N.; Rosas-Hernández, A.; Ko, J. H.; Gan, Q.; Goddard Iii, W. A.; Grubbs, R. H., Selective CO_2 Electrochemical Reduction Enabled by a Tricomponent Copolymer Modifier on a Copper Surface. *J. Am. Chem. Soc.* **2021,** *143* (7), 2857-2865. 10.1021/jacs.0c12478
22. Chang, M.; Ren, W.; Ni, W.; Lee, S.; Hu, X., Ionomers Modify the Selectivity of Cu-Catalyzed Electrochemical CO_2 Reduction. *ChemSusChem* **2023,** *16* (5), e202201687. 10.1002/cssc.202201687
23. Li, W.; Yin, Z.; Gao, Z.; Wang, G.; Li, Z.; Wei, F.; Wei, X.; Peng, H.; Hu, X.; Xiao, L.; Lu, J.; Zhuang, L., Bifunctional ionomers for efficient co-electrolysis of CO_2 and pure water towards ethylene production at industrial-scale current densities. *Nature Energy* **2022,** *7* (9), 835-843. 10.1038/s41560-022-01092-9
24. Shin, S.-J.; Choi, H.; Ringe, S.; Won, D. H.; Oh, H.-S.; Kim, D. H.; Lee, T.; Nam, D.-H.; Kim, H.; Choi, C. H., A unifying mechanism for cation effect modulating C_1 and C_2 productions from CO_2 electroreduction. *Nature Communications* **2022,** *13* (1), 5482. 10.1038/s41467-022-33199-8
25. Ringe, S.; Clark, E. L.; Resasco, J.; Walton, A.; Seger, B.; Bell, A. T.; Chan, K., Understanding cation effects in electrochemical CO_2 reduction. *Energy & Environmental Science* **2019,** *12* (10), 3001-3014. 10.1039/C9EE01341E

26. Resasco, J.; Chen, L. D.; Clark, E.; Tsai, C.; Hahn, C.; Jaramillo, T. F.; Chan, K.; Bell, A. T., Promoter Effects of Alkali Metal Cations on the Electrochemical Reduction of Carbon Dioxide. *J. Am. Chem. Soc.* **2017,** *139* (32), 11277-11287. 10.1021/jacs.7b06765
27. Monteiro, M. C. O.; Dattila, F.; Hagedoorn, B.; García-Muelas, R.; López, N.; Koper, M. T. M., Absence of CO_2 electroreduction on copper, gold and silver electrodes without metal cations in solution. *Nature Catalysis* **2021,** *4* (8), 654-662. 10.1038/s41929-021-00655-5
28. Gu, J.; Liu, S.; Ni, W.; Ren, W.; Haussener, S.; Hu, X., Modulating electric field distribution by alkali cations for CO_2 electroreduction in strongly acidic medium. *Nature Catalysis* **2022,** *5* (4), 268-276. 10.1038/s41929-022-00761-y
29. Qin, H.-G.; Li, F.-Z.; Du, Y.-F.; Yang, L.-F.; Wang, H.; Bai, Y.-Y.; Lin, M.; Gu, J., Quantitative Understanding of Cation Effects on the Electrochemical Reduction of CO_2 and H^+ in Acidic Solution. *ACS Catalysis* **2023,** *13* (2), 916-926. 10.1021/acscatal.2c04875
30. Waegele, M. M.; Gunathunge, C. M.; Li, J.; Li, X., How cations affect the electric double layer and the rates and selectivity of electrocatalytic processes. *The Journal of Chemical Physics* **2019,** *151* (16), 160902. 10.1063/1.5124878
31. Residual styrene starting materials were removed from the ionomers by precipitation of polymer from a concentrated MeCN solution with Et_2O, washing with hot 1 M $KHCO_{3(aq)}$, and followed by reprecipitation with MeCN and Et_2O. Due to the difference in solubility, a modified purification procedure was employed for the methoxystyrene homopolymer, with residual starting material removed by precipitation of a concentrated THF solution into MeOH.
32. Weitzner, S. E.; Akhade, S. A.; Varley, J. B.; Wood, B. C.; Otani, M.; Baker, S. E.; Duoss, E. B., Toward Engineering of Solution Microenvironments for the CO_2 Reduction Reaction: Unraveling pH and Voltage Effects from a Combined Density-Functional–Continuum Theory. *The Journal of Physical Chemistry Letters* **2020,** *11* (10), 4113-4118. 10.1021/acs.jpclett.0c00957
33. Zhao, Y.; Hao, L.; Ozden, A.; Liu, S.; Miao, R. K.; Ou, P.; Alkayyali, T.; Zhang, S.; Ning, J.; Liang, Y.; Xu, Y.; Fan, M.; Chen, Y.; Huang, J. E.; Xie, K.; Zhang, J.; O'Brien, C. P.; Li, F.; Sargent, E. H.; Sinton, D., Conversion of CO_2 to multicarbon products in strong acid by controlling the catalyst microenvironment. *Nature Synthesis* **2023,** *2* (5), 403-412. 10.1038/s44160-022-00234-x
34. Zi, X.; Zhou, Y.; Zhu, L.; Chen, Q.; Tan, Y.; Wang, X.; Sayed, M.; Pensa, E.; Geioushy, R. A.; Liu, K.; Fu, J.; Cortés, E.; Liu, M., Breaking K^+ Concentration Limit on Cu Nanoneedles for Acidic Electrocatalytic CO_2 Reduction to Multi-Carbon Products. *Angew. Chem. Int. Ed.* **2023,** *62* (42), e202309351. 10.1002/anie.202309351
35. Liu, M.; Pang, Y.; Zhang, B.; De Luna, P.; Voznyy, O.; Xu, J.; Zheng, X.; Dinh, C. T.; Fan, F.; Cao, C.; de Arquer, F. P. G.; Safaei, T. S.; Mepham, A.; Klinkova, A.; Kumacheva, E.; Filleter, T.; Sinton, D.; Kelley, S. O.; Sargent, E. H., Enhanced electrocatalytic CO_2 reduction via field-induced reagent concentration. *Nature* **2016,** *537* (7620), 382-386. 10.1038/nature19060
36. While ICP-MS measurements might not exactly match K^+ content as measured by integration in ^1H NMR of the material, ionomer **4** provides 57% and 79% greater local [K^+] than **2** in the absence of applied potential and after electrolysis, respectively. Exact measurements of local [K^+] are limited by the ability of K^+ to exchange with Li^+ in the mother liquor (see Experimental Information, Electrochemical Measurments. in GDE. (Flow) Cell).
37. Ren, W.; Xu, A.; Chan, K.; Hu, X., A Cation Concentration Gradient Approach to Tune the Selectivity and Activity of CO_2 Electroreduction. *Angew. Chem. Int. Ed.* **2022,** *61* (49), e202214173. 10.1002/anie.202214173
38. Ramdin, M.; de Loos, T. W.; Vlugt, T. J. H., State-of-the-Art of CO_2 Capture with Ionic Liquids. *Industrial & Engineering Chemistry Research* **2012,** *51* (24), 8149-8177. 10.1021/ie3003705

39. Li, L.; Liu, Z.; Yu, X.; Zhong, M., Achieving High Single-Pass Carbon Conversion Efficiencies in Durable CO_2 Electroreduction in Strong Acids via Electrode Structure Engineering. *Angew. Chem. Int. Ed.* **2023,** *62* (21), e202300226. 10.1002/anie.202300226
40. Song, H.; Song, J. T.; Kim, B.; Tan, Y. C.; Oh, J., Activation of C_2H_4 reaction pathways in electrochemical CO_2 reduction under low CO_2 partial pressure. *Applied Catalysis B: Environmental* **2020,** *272*, 119049. 10.1016/j.apcatb.2020.119049
41. Moradzaman, M.; Martínez, C. S.; Mul, G., Effect of partial pressure on product selectivity in Cu-catalyzed electrochemical reduction of CO_2. *Sustainable Energy & Fuels* **2020,** *4* (10), 5195-5202. 10.1039/D0SE00865F
42. Moradzaman, M.; Mul, G., Optimizing CO Coverage on Rough Copper Electrodes: Effect of the Partial Pressure of CO and Electrolyte Anions (pH) on Selectivity toward Ethylene. *The Journal of Physical Chemistry C* **2021,** *125* (12), 6546-6554. 10.1021/acs.jpcc.0c10792
43. Lu, S.; Wang, Y.; Xiang, H.; Lei, H.; Xu, B. B.; Xing, L.; Yu, E. H.; Liu, T. X., Mass transfer effect to electrochemical reduction of CO2: Electrode, electrocatalyst and electrolyte. *Journal of Energy Storage* **2022,** *52*, 104764. 10.1016/j.est.2022.104764
44. Yano, H.; Tanaka, T.; Nakayama, M.; Ogura, K., Selective electrochemical reduction of CO_2 to ethylene at a three-phase interface on copper(I) halide-confined Cu-mesh electrodes in acidic solutions of potassium halides. *J. Electroanal. Chem.* **2004,** *565* (2), 287-293. 10.1016/j.jelechem.2003.10.021
45. Chen, L. D.; Urushihara, M.; Chan, K.; Nørskov, J. K., Electric Field Effects in Electrochemical CO_2 Reduction. *ACS Catalysis* **2016,** *6* (10), 7133-7139. 10.1021/acscatal.6b02299
46. Lin, S.-T.; Blanco, M.; Goddard, W. A., III, The two-phase model for calculating thermodynamic properties of liquids from molecular dynamics: Validation for the phase diagram of Lennard-Jones fluids. *The Journal of Chemical Physics* **2003,** *119* (22), 11792-11805. 10.1063/1.1624057
47. Watkins, N. B.; Schiffer, Z. J.; Lai, Y.; Musgrave, C. B., III; Atwater, H. A.; Goddard, W. A., III; Agapie, T.; Peters, J. C.; Gregoire, J. M., Hydrodynamics Change Tafel Slopes in Electrochemical CO_2 Reduction on Copper. *ACS Energy Letters* **2023,** *8* (5), 2185-2192. 10.1021/acsenergylett.3c00442
48. Prasetyo, N.; Hofer, T. S., Structure, Dynamics, and Hydration Free Energy of Carbon Dioxide in Aqueous Solution: A Quantum Mechanical/Molecular Mechanics Molecular Dynamics Thermodynamic Integration (QM/MM MD TI) Simulation Study. *Journal of Chemical Theory and Computation* **2018,** *14* (12), 6472-6483. 10.1021/acs.jctc.8b00557
49. Goyal, A.; Marcandalli, G.; Mints, V. A.; Koper, M. T. M., Competition between CO_2 Reduction and Hydrogen Evolution on a Gold Electrode under Well-Defined Mass Transport Conditions. *J. Am. Chem. Soc.* **2020,** *142* (9), 4154-4161. 10.1021/jacs.9b10061
50. Richard, D.; Tom, M.; Jang, J.; Yun, S.; Christofides, P. D.; Morales-Guio, C. G., Quantifying transport and electrocatalytic reaction processes in a gastight rotating cylinder electrode reactor via integration of Computational Fluid Dynamics modeling and experiments. *Electrochim. Acta* **2023,** *440*, 141698. 10.1016/j.electacta.2022.141698
51. Qiao, Y.; Lai, W.; Huang, K.; Yu, T.; Wang, Q.; Gao, L.; Yang, Z.; Ma, Z.; Sun, T.; Liu, M.; Lian, C.; Huang, H., Engineering the Local Microenvironment over Bi Nanosheets for Highly Selective Electrocatalytic Conversion of CO_2 to HCOOH in Strong Acid. *ACS Catalysis* **2022,** *12* (4), 2357-2364. 10.1021/acscatal.1c05135
52. Liang, Y.; Zhao, J.; Yang, Y.; Hung, S.-F.; Li, J.; Zhang, S.; Zhao, Y.; Zhang, A.; Wang, C.; Appadoo, D.; Zhang, L.; Geng, Z.; Li, F.; Zeng, J., Stabilizing copper sites in coordination

polymers toward efficient electrochemical C-C coupling. *Nature Communications* **2023,** *14* (1), 474. 10.1038/s41467-023-35993-4

53. Sato, Y.; Takikawa, T.; Sorakubo, A.; Takishima, S.; Masuoka, H.; Imaizumi, M., Solubility and Diffusion Coefficient of Carbon Dioxide in Biodegradable Polymers. *Industrial & Engineering Chemistry Research* **2000,** *39* (12), 4813-4819. 10.1021/ie0001220
54. We acknowledge the complicated relationship between gas solubility and diffusivity as models have previously highlighted an inverse relationship when comparing ionomers (ref. 16) while others have experimentally observed direct correlations (ref. 53) Other models have invoked both improved mass transport and greater local CO_2 concentration as phenomena to explain greater FE_{C2+} and $|j_{C2+}|$ with Cu electrodes (ref. 21). In our system, minimization of Helmholtz free energy is attributed to increased CO_2 entropy (S_{CO2}, Table 4.9) which is a result of increased diffusion, as well as decreased internal energy due to enhanced K^+-related coulomb stabilization.
55. Soniat, M.; Tesfaye, M.; Brooks, D.; Merinov, B.; Goddard, W. A.; Weber, A. Z.; Houle, F. A., Predictive simulation of non-steady-state transport of gases through rubbery polymer membranes. *Polymer* **2018,** *134*, 125-142. 10.1016/j.polymer.2017.11.055
56. Luo, G.; Yuan, B.; Guan, T.; Cheng, F.; Zhang, W.; Chen, J., Synthesis of Single Lithium-Ion Conducting Polymer Electrolyte Membrane for Solid-State Lithium Metal Batteries. *ACS Applied Energy Materials* **2019,** *2* (5), 3028-3034. 10.1021/acsaem.9b00440
57. Pangborn, A. B.; Giardello, M. A.; Grubbs, R. H.; Rosen, R. K.; Timmers, F. J., Safe and Convenient Procedure for Solvent Purification. *Organometallics* **1996,** *15* (5), 1518-1520. 10.1021/om9503712
58. Li, F.; Thevenon, A.; Rosas-Hernández, A.; Wang, Z.; Li, Y.; Gabardo, C. M.; Ozden, A.; Dinh, C. T.; Li, J.; Wang, Y.; Edwards, J. P.; Xu, Y.; McCallum, C.; Tao, L.; Liang, Z.-Q.; Luo, M.; Wang, X.; Li, H.; O'Brien, C. P.; Tan, C.-S.; Nam, D.-H.; Quintero-Bermudez, R.; Zhuang, T.-T.; Li, Y. C.; Han, Z.; Britt, R. D.; Sinton, D.; Agapie, T.; Peters, J. C.; Sargent, E. H., Molecular tuning of CO_2 -to-ethylene conversion. *Nature* **2019**, 1-1. 10.1038/s41586-019-1782-2
59. Lazanas, A. C.; Prodromidis, M. I., Electrochemical Impedance Spectroscopy─A Tutorial. *ACS Measurement Science Au* **2023,** *3* (3), 162-193. 10.1021/acsmeasuresciau.2c00070
60. Zheng, W., iR Compensation for Electrocatalysis Studies: Considerations and Recommendations. *ACS Energy Letters* **2023,** *8* (4), 1952-1958. 10.1021/acsenergylett.3c00366
61. Heenan, A. R.; Hamonnet, J.; Marshall, A. T., Why Careful iR Compensation and Reporting of Electrode Potentials Are Critical for the CO_2 Reduction Reaction. *ACS Energy Letters* **2022,** *7* (7), 2357-2361. 10.1021/acsenergylett.2c00800
62. Ma, M.; Zheng, Z.; Yan, W.; Hu, C.; Seger, B., Rigorous Evaluation of Liquid Products in High-Rate CO_2/CO Electrolysis. *ACS Energy Letters* **2022,** *7* (8), 2595-2601. 10.1021/acsenergylett.2c01288
63. Clementi, E.; Raimondi, D. L.; Reinhardt, W. P., Atomic Screening Constants from SCF Functions. II. Atoms with 37 to 86 Electrons. *The Journal of Chemical Physics* **1967,** *47* (4), 1300-1307. 10.1063/1.1712084
64. Quantification of monomer ratio is not easily measured by ^{1}H NMR due to the overlapping peaks of the biphenyl and STFSI moieties.
65. It is acknowledged that the neutral "control" polymers do not have the STFSI moiety, and, therefore, are not a completely faithful comparison.
66. Dougherty, D. A., The Cation−π Interaction. *Acc. Chem. Res.* **2013,** *46* (4), 885-893. 10.1021/ar300265y

67. Majchrzak, M.; Kostera, S.; Kubicki, M.; Kownacki, I., Synthesis of new styrylarenes via Suzuki–Miyaura coupling catalysed by highly active, well-defined palladium catalysts. *Dalton Transactions* **2013,** *42* (44), 15535-15539. 10.1039/C3DT52063C

CHAPTER 5. Novel Silicate Platform as Weakly-Coordinating Anions for Organometallic and Electrochemical Applications

For author contributions, see Page vii.

ABSTRACT

Weakly-coordinating anions (WCAs) are employed in a wide range of applications, but limitations remain, including high reactivity, limited redox window, complicated synthesis, high cost, low solubility, and low structural tunability. Herein, we report a new class of WCA based on alkyl or aryl (**R**) substituted ***si***licates bearing ***f***luorinated pinacolate ligands, **"[^{R}SiF]$^{-}$".** Anions bearing a variety of R groups were prepared, enabling facile tuning of sterics and solubility. A range of cations employed in chemical reactivity has been supported by these anions, including ether-free alkali cations (useful for subsequent salt metathesis reactions), Ph_3C^+, and an ethylene/CO copolymerization catalyst $[Pd(dppe)(NCMe)Me]^+$ (generated by salt metathesis or protonation of a metal-alkyl bond). These examples showcase the ability of the $^{R}SiF^-$ anions to support applications in coordination chemistry. Electrochemical studies on the $[Bu_4N]^+$ variant show an exceptionally wide stability window for the $^{Me}SiF^-$ anion of 7.5 V in MeCN. The $[^{C6F5}SiF]^-$ variant can be readily further modified to access diverse and/or dianionic variants.

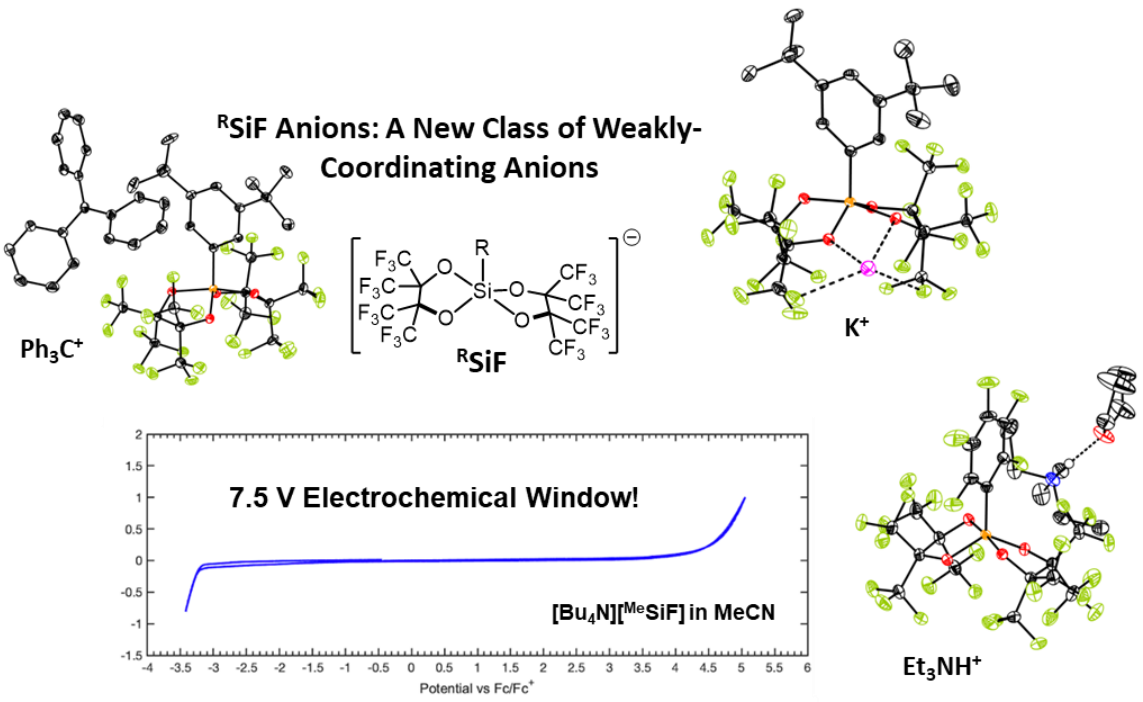

INTRODUCTION

Weakly-coordinating anions[1] (WCAs) facilitate diverse chemistry from access to highly electrophilic centers for olefin polymerization or C-H bond activation, to redox stability for battery electrolytes and electron transfer reactions, to Bronsted superacidity.[2-4] Typically, a WCA features: (1) Weak cation-anion interaction, (2) Low propensity to undergo oxidation/reduction, and (3) Low reactivity towards highly electrophilic fragments.[5] Early examples of WCA include $[PF_6]^-$, $[BF_4]^-$, $[O_3SCF_3]^-$ and $[N(SO_2CF_3)_2]$.[1-9] These species typically feature wide redox stability windows and they are frequently employed as supporting electrolytes for electrochemical studies of organometallic compounds because of their stability and commercial availability.[7] However, in the presence of highly electrophilic cations, these anions decompose *via* fluoride abstraction.[5, 8, 10] Less nucleophilic anions, less susceptible to decomposition have been developed for a variety of transformations, including borates, carboranes, and aluminates. Borates that feature multiple electron-withdrawing aryl substituents, including tetrakis (pentafluorophenyl)borate ($[B(C_6F_5)_4]^-$) and tetrakis-[3,5-(bistrifluoromethyl)phenyl] borate ($[BAr^F{}_{24}]^-$), are commercially available.[4, 8, 11] The electron-deficient aryl substituents impart high stability, high solubility, and low propensity to coordinate. While less soluble than $[BAr^F{}_{24}]^-$ the performance of $[B(C_6F_5)_4]^-$ as a WCA is highlighted by its tolerance towards highly electrophilic cations such as zirconocene and silylium because of its robust C_{sp2}-F bonds.[9, 12] Halogenated carborane anions, such as $[HCB_{12}H_5Cl_6]$ and $[HCB_{12}H_5Br_6]$, support Et_3Si^+-catalyzed hydrodefluorination reactions with higher turnover numbers (TON) and conversion compared to $[B(C_6F_5)_4]^-$.[9] Weakly-coordinating aluminates with highly-fluorinated, bulky alkoxide ligands support unusual, reactive motifs such as cationic binary P-X species (X = halogen), $CS_2Br_3^+$, CX_3^+ (X = Br, I) that are otherwise unknown in the condensed

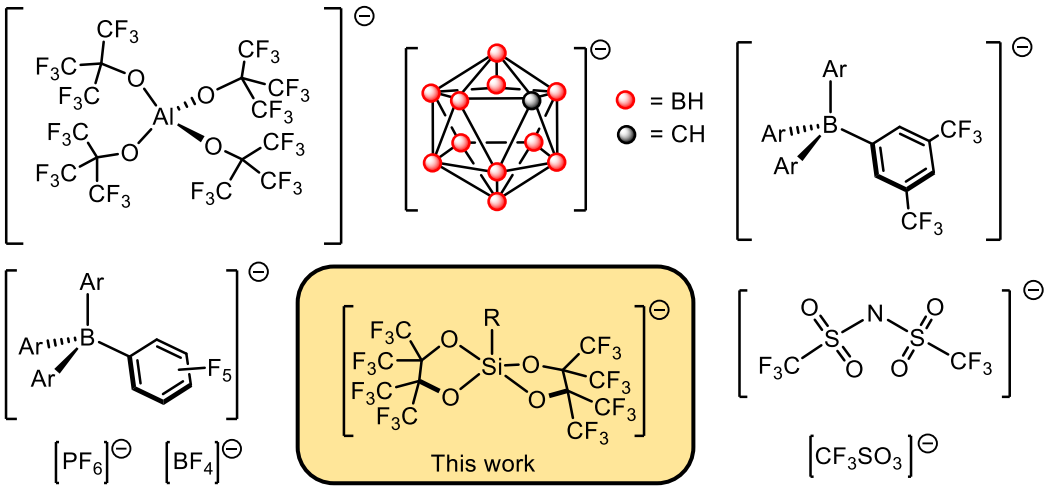

Figure 5.1. Common weakly coordinating anions with application in coordination chemistry

phase. In addition to supporting challenging, reactive cations, these more modern WCAs also support cations commonly used as reagents in coordination chemistry such as $[H(OEt_2)_2]^+$, $[Ph_3C]^+$, $[Ag]^+$.[5, 8, 10]

The development of new weakly-coordinating anions including the following properties is of particular interest: 1) facile preparation and functionalization; 2) support of coordination chemistry applications, and 3) wide redox window. Herein, we report the design and synthesis of a new class of WCA based on silicon ("^{R}SiF anions") and their applications in coordination chemistry, organometallic catalysis, and electrochemistry.

RESULTS AND DISCUSSION

Our design for a WCA is inspired by weakly-coordinating borates, $[BAr^{F}{}_{24}]^-$ and $[B(C_6F_5)_4]^-$. Charge delocalization over several electron-deficient substituents imparts low nucleophilicity, basicity, and propensity to oxidize.[8] Conceptually, a highly Lewis acidic fragment (e.g., neutral borane, such as $B(C_6F_5)_3$) results in a WCA (e.g., $[B(C_6F_5)_4]^-$) upon incorporation of an aryl, $(C_6F_5)^-$, or other anionic groups.[8] Lewis acids based on Si were identified as potential candidates given their synthetic accessibility and high Lewis acidity.[13-17] Recently, Si-based Lewis acids have been shown to possess fluoride ion affinities (FIA) higher or comparable to that of SbF_5,[13-17] the baseline for Lewis superacidity.[18] For example, Si supported by two perfluoropinacolato ligands, $(MeCN)Si(O_2C_6F_{12})_2$ (Figure 5.2), was calculated to have a fluoride affinity of 474 kJ/mol, closer to SbF_5 (501 kJ/mol) than $B(C_6F_5)_3$ (435 kJ/mol), suggesting that it may serve as the basis for a five-coordinate Si WCA.[17] Indeed, $(MeCN)Si(O_2C_6F_{12})_2$ is highly reactive and activates the Si-F bond of Et_3SiF.[17] Although little is known about the ability of pentacoordinate silicates to act as WCAs, some simple variants have been known since the 1960s.[19-21]

We targeted pentacoordinate silicates of the form $[^{R}Si(O_2C_6F_{12})_2]^-$ (**^{R}SiF$^-$**), with the perfluoropinacolato ligands imparting steric protection and oxidative stability, and the alkyl/aryl

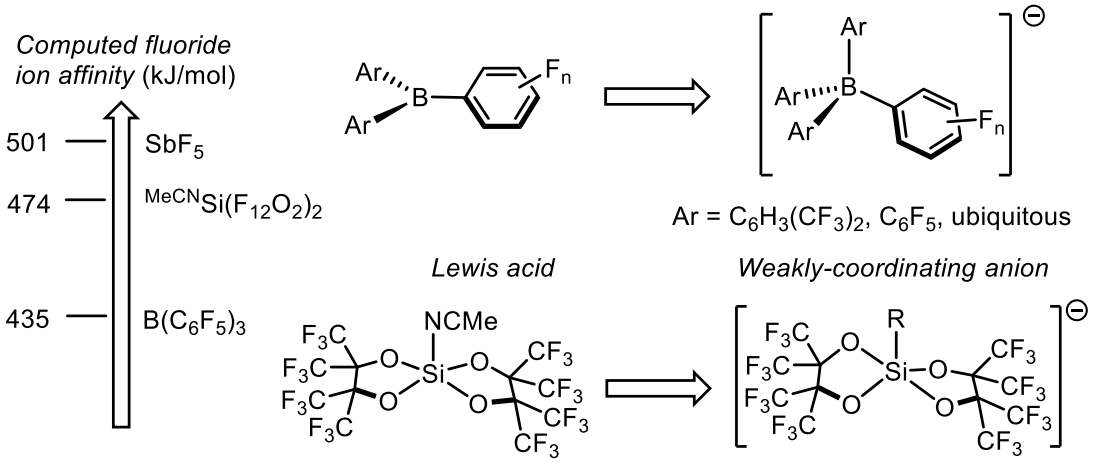

Figure 5.2. Design principle of a pentacoordinate silicate anion.

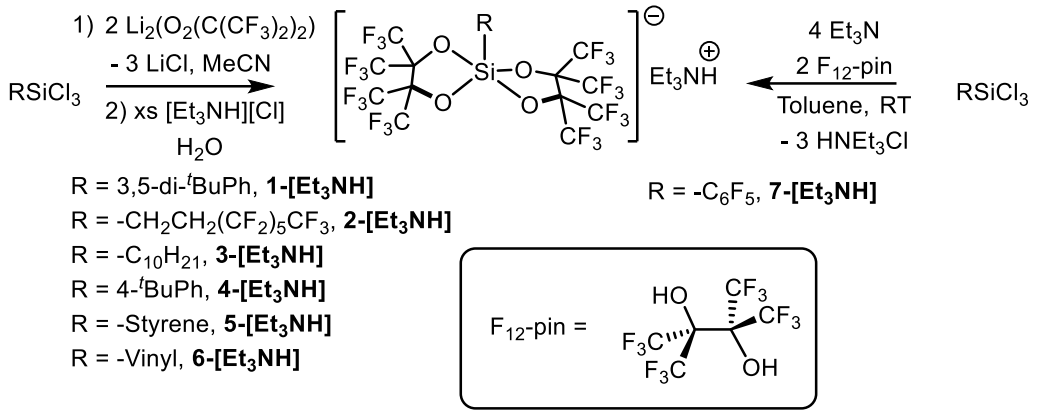

Scheme 5.1. Preparation of $[Et_3NH][^RSiF]$.

substituent R imparting structural and electronic tunability. With the precedent to access pentacoordinate silicate anions from $RSiCl_3$ precursors (R = H or Cl),[17] stoichiometric treatment of $RSiCl_3$ (R = 3,5-di-*tert*-butylphenyl) with 2 equivalents of $Li_2(O_2(C(CF_3)_2)_2$ (Li_2F_{12}-pin) in acetonitrile results in LiCl precipitation and generates $[Li(NCMe)_n][^RSiF]$. Cation exchange with excess $[Et_3NH][Cl]$ in water affords $[Et_3NH][^RSiF]$ **(1-[Et$_3$NH])**. The ^{1}H NMR spectrum of **1-[Et$_3$NH]** displays six peaks, corresponding to the aryl protons and the ^{t}Bu groups as well as the peaks corresponding to the $[Et_3NH]^+$ motif. The ^{19}F NMR of **1-[Et$_3$NH]** displays two multiplets centered δ -69.2 ppm and δ -69.8 ppm, and the ^{29}Si spectrum displays a single peak at -88.9 ppm, consistent with previously reported silicates bearing two perfluoropinacolato motifs.[17]

As indicated by a single crystal X-ray diffraction study (Figure 5.3), in the solid state, the anionic silicate motif was found to be *pseudo*-trigonal bipyramidal, with the aryl group in the equatorial plane. A hydrogen bonding interaction is observed with a fluoride, reminiscent of hydrogen bonding interactions observed in borates.[22-24] The structural tunability of $[^RSiF]^-$ anions was explored with a variety of alkyl and aryl substituents (**2-[Et$_3$NH] - 6-[Et$_3$NH])** to tune the solubility and sterics of the anion**.**

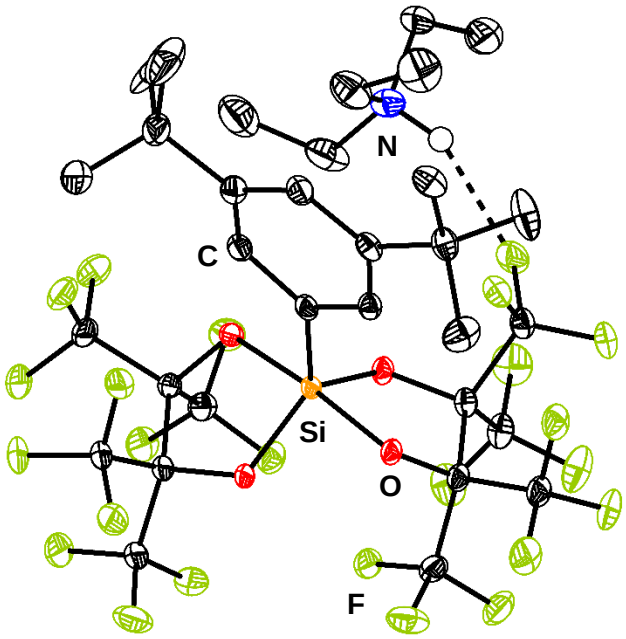

Figure 5.3. Crystal structure of **1-[Et$_3$NH]**. Thermal ellipsoids shown at 50% probability. Hydrogen atoms omitted for clarity.

To target a more fully fluorinated version of the [^{R}SiF] anion with R = C_6F_5, the same preparation route used for **1-[Et$_3$NH]** – **6-[Et$_3$NH]** was attempted. However, no formation of the desired product was observed, with only formation of many unidentified species by ^{19}F NMR. Use of more forcing conditions (extended reaction time, heating) did not improve the reaction. Due to the formation of many new Aryl-F peaks, concern of nucleophilic attack from the (Li_2F_{12}-pin) resulted in development of different reaction conditions (Scheme 5.1, right), where **7-[Et$_3$NH]** is formed directly from $C_6F_5SiCl_3$ by treatment with 2 equivalents of perfluoropinacol (F_{12}-pin) and 4 equivalents of NEt_3 in toluene. Following purification to remove the generated [Et_3NH]Cl, **7-[Et$_3$NH]** can be isolated. While this route can be applied to other variants, the initial 2-step method is preferred when possible. The solid-state structure of **7-[Et$_3$NH]** is shown in Figure 5.4, with the same *pseudo*-trigonal bipyramidal seen in Figure 5.3. The triethylammonium cation is hydrogen-bonded to a molecule of co-crystallized THF.

All [Et_3NH][^{R}SiF] variants have been prepared on multi-gram batches, enabling extensive

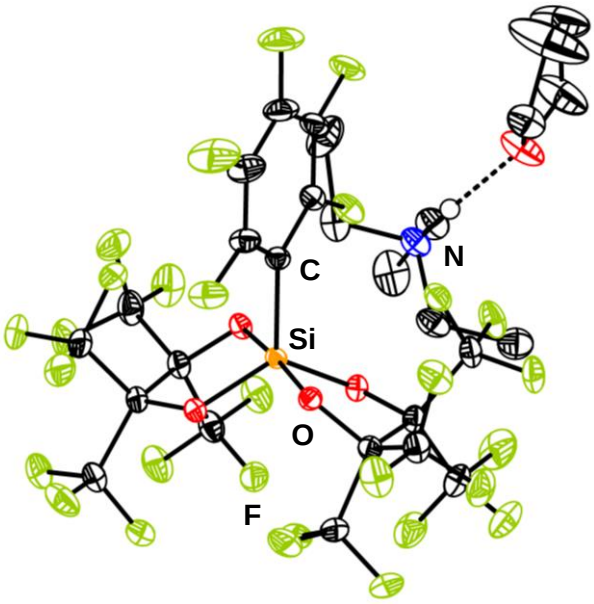

Figure 5.4. Crystal structure of **7-[Et$_3$NH].** Thermal ellipsoids shown at 50% probability. Hydrogen atoms omitted for clarity.

further study of cations supported by this new class of WCA. Due to the improved solubility and useful NMR handles (aromatic and alkyl signals), **1-[Et$_3$NH]** was the representative variant used for further exploration. Inspired by synthetic approaches in borate chemistry, where NaBAr$^F{}_{24}$ is a versatile intermediate,[3-5, 7-8] variants displaying alkaline metal cations were targeted. **1-[M]** (M = Na^+, K^+) can be directly prepared from **1-[Et$_3$NH]** by treatment with the corresponding hexamethyldisilazide regents (M(N(SiMe$_3$)) in aromatic solvents (Scheme 5.2). Notably, **1-[Na]** and **1-[K]** are free of coordinated ethereal solvents and do not require prolonged heating under vacuum. **1-[K]** displays mild solubility in benzene and dichloromethane (0.1 mmol/L in benzene, 0.4 mmol/L in dichloromethane) with improved solubility with **1-[Na]** (2 mmol/L in benzene, 1.3

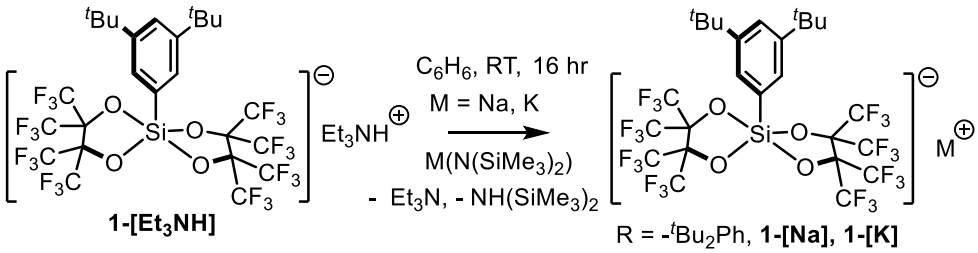

Scheme 5.2. Preparation of [alkali metal][^{R}SiF] compounds.

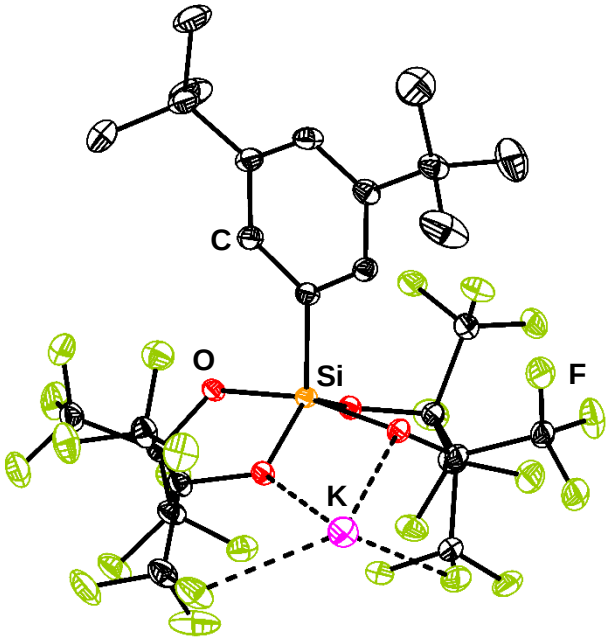

Figure 5.5. Crystal structure of **1-[K].** Thermal ellipsoids shown at 50% probability. Hydrogen atoms omitted for clarity.

mmol/L in dichloromethane). The solid-state structure of **1-[K]** is shown in Figure 5.5, where the compound forms a polymeric structure, where each potassium cation has close interactions with two O and two F atoms on each SiF anion. These short interactions are very reminiscent of solid-state structures of solvent-free K[BArF$_{24}$][25] and K[B(C$_6$F$_5$)$_4$].[26]

The [Ph$_3$C]$^+$ cation is a versatile reagent for both hydride abstraction and chemical oxidation.[2, 9, 27-28] Conveniently, the high solubility of **1-[K]** in CH_2Cl_2 and lack of coordinated ether ligands allowed facile preparation of **1-[Ph$_3$C]** (Scheme 5.3). The solid-state structure of **1-[Ph$_3$C]** (Figure 5.6) is consistent with formation of the desired compound.

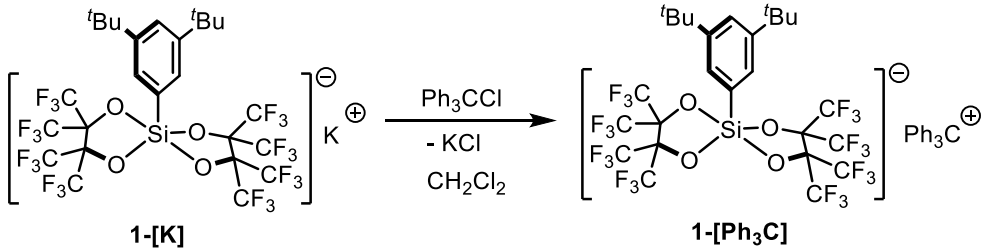

Scheme 5.3. Preparation of **1-[Ph$_3$C].**

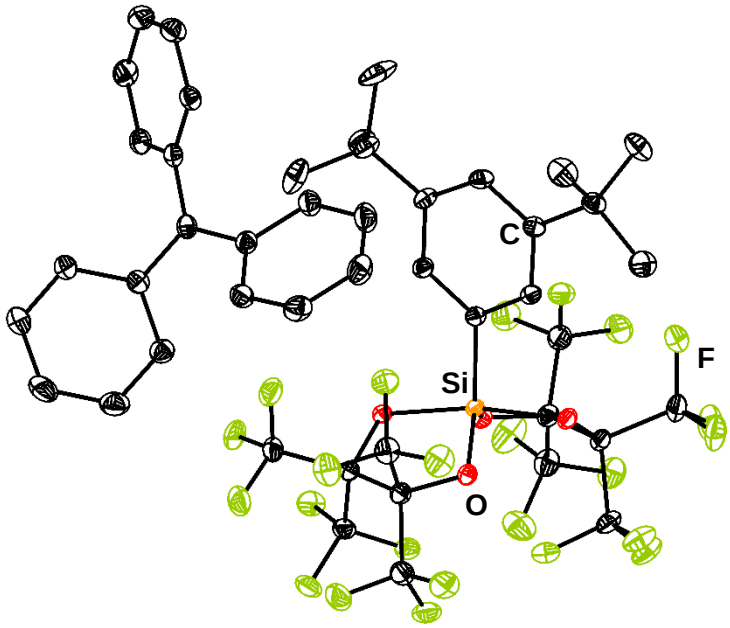

Figure 5.6. Crystal structure of **1-[Ph$_3$C].** Thermal ellipsoids shown at 50% probability. Hydrogen atoms omitted for clarity.

The $[Ph_3C]^+$ cation is also the common precursor used to generate $[R_3Si]^+$ cations.[29] Due to the reactive nature of $[R_3Si]^+$ cations, they are only stable with a small sub-set of weakly coordinating anions including $B(C_6F_5)_4$ and carboranes.[29] Attempts were made to access $[R_3Si][^RSiF]$ from Ph_3SiH or Et_3SiH, but only anion decomposition was observed.

To explore application in a catalytic organometallic system, we studied the generation of $[Pd(dppe)(solvent)Me]^+[^RSiF]^-$ from precatalysts Pd(dppe)MeCl and $Pd(dppe)Me_2$ by halide

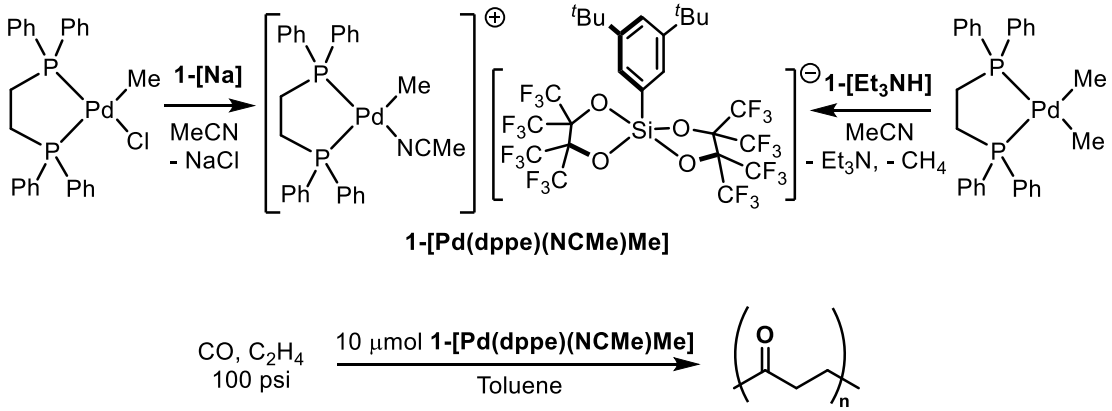

Scheme 5.4. Preparation of **1-[Pd(dppe)(NCMe)Me]** by salt metathesis (left) or protonlysis (right).

abstraction and protonation of a metal-alkyl bond, respectively. The cationic Pd-Me species has been reported to be competent for the alternating copolymerization of ethylene and carbon monoxide to generate polyketones.[30-31] Under typical activation conditions, $[Pd(dppe)(solvent)Me]^+[BAr^F{}_{24}]^-$, is prepared from reaction with $NaBAr^F{}_{24}$. Generation of the cationic active species was probed with **1-[Na]** (Scheme 5.4, left). The salt metathesis proceeds cleanly, forming the cationic Pd compound by precipitation of NaCl. Analysis of the product by ^1H and ^{31}P NMR in $CDCl_3$ revealed full conversion to the desired product, with a diagnostic pair of inequivalent, coupled ^{31}P resonances at δ 60.7 ppm and δ 38.6 ppm, shifted from those of the starting material (δ 59.1 ppm and δ 30.7 ppm). The same cationic species has also been accessed by protonation of $Pd(dppe)Me_2$ with $[(Et_2O)_2H][BAr^F{}_{24}]$.[32-33] Conveniently, analogous reactivity was observed with **1-[Et$_3$NH]** (Scheme 5.4, right). Under polymerization conditions, **1-[Pd(dppe)(NCMe)Me]** is catalytically active (activity = 1.7 g $mmol^{-1}$ hr^{-1}) and exhibits activity similar to the system with the $BArF_{24}$ anion ($[Pd(dppe)(NCMe)Me][BAr^F{}_{24}]$, activity = 2.3 g $mmol^{-1}$ hr^{-1}).

The electrochemical stability window of this novel class of WCAs is of interest. Therefore, the electrochemistry of **[Bu$_4$N][^{Me}SiF]** (a related variant that can be prepared on 60^+ gram scales) was evaluated with cyclic voltammetry (CV) and linear sweep voltammetry (LSV) (Figure 5.7). The performance was compared to $[Bu_4N][PF_6]$, a common electrolyte employed in electrochemical characterization of coordination compounds. While $^{Me}SiF^-$ and PF_6^- anions have effectively the same reductive stability in MeCN of ca. -3.1 V vs. Fc/Fc^+, the $^{Me}SiF^-$ anion displayed increased oxidative stability up to 4.5 V vs. Fc/Fc^+, surpassing the oxidative stability of PF_6^- by *ca.* 1 V. Together, **[Bu$_4$N][^{Me}SiF]** has a wide stability window of ca. 7.5 V in MeCN, highlighting its potential for supporting highly oxidizing, electrophilic cations in both chemical

and electrochemical oxidation reactions.

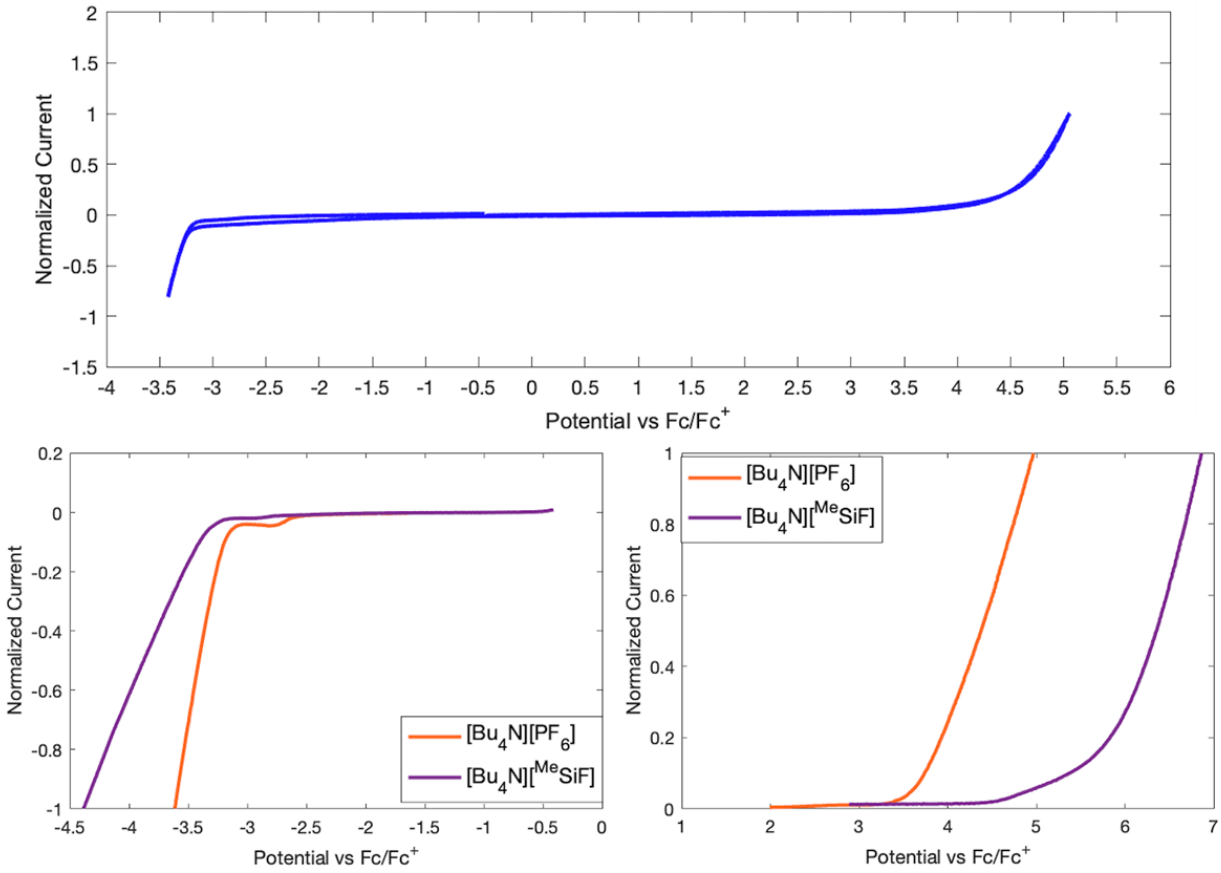

Figure 5.7. Cyclic voltammetry and linear sweep voltammetry experiments of 0.1 M **[Bu$_4$N][^{Me}SiF]** and [Bu$_4$N][PF$_6$] in MeCN; Current shown were normalized to the highest current in each experiment; Top: Cyclic voltammogram of **[Bu$_4$N][^{Me}SiF]** in MeCN; WE: Glassy carbon; CE: Pt wire; RE: Ag wire; scan rate = 100 mVs^{-1}; Bottom: Linear sweep voltammograms of 0.1 M **[Bu$_4$N][^{Me}SiF]** and [Bu$_4$N][PF$_6$] in MeCN; WE: Glassy carbon; CE: Pt wire; RE: Ag wire; scan rate = 50 mVs^{-1}.

The R = -C$_6$F$_5$ variant provides unique access to a readily modifiable [^{R}SiF]$^{-}$ anion, where aromatic nucleophilic substitution in the *para* position[34] facilitates formation of a functionalized SiF anion (Scheme 5.5). In all cases, the formation of the desired product was confirmed by ^{1}H and ^{19}F NMR, with additional confirmation by ESI-MS, as needed. In ^{19}F NMR, the disappearance of the *para*-fluorine and formation of two new sets of doublets of doublets is consistent with the expected transformation. Due to the bulky nature of the SiF anion, substitution in the *ortho*-

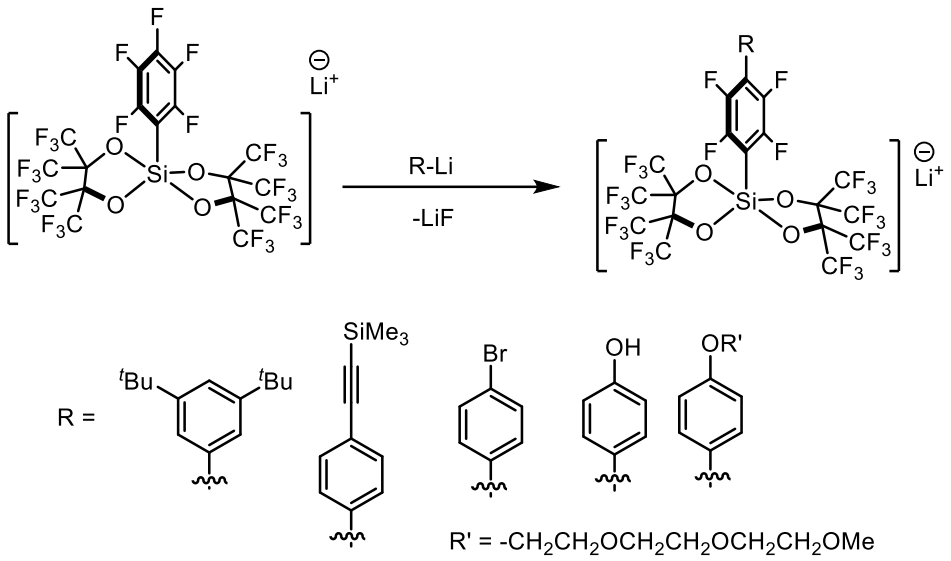

Scheme 5.5: Preparation of variants from **[^{C6F5}SiF]$^-$**

position is sterically hindered. Notably, in cases where a complex product mixture is obtained, neither formation of di-/tri- substituted species nor *ortho*- or *meta*- substitution is observed (by ^{19}F NMR or ESI-MS). Trace amounts of these species may form, but they have not been observed in a detectable amount. Many differentiated SiF anions have been accessed (some selected examples shown in Scheme 5.5). Using the corresponding Ar-Li reagent, a variety of chemical functionalities can be installed on the SiF including a protected alkyne (which has been subsequently deprotected to access the terminal alkyne), aryl halides (useful synthons for subsequent Li/halogen exchange and/or cross-coupling reactions), phenols, and aryls with alkyl ethers. Beyond monoanionic [^{R}SiF]$^-$ anions, a dianionic version can be prepared by treating the [^{C6F5}SiF] anion with 1,4 di-lithium aryl (Scheme 5.6).

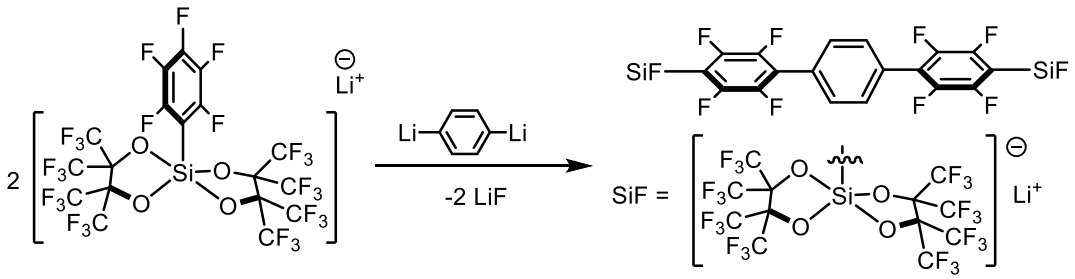

Scheme 5.6: Preparation of dianionic silicate (**[SiF]-Ar-[SiF])**

Due to the reliable and tolerant nature of this reaction, it is currently being investigated as a straightforward method to install [^{R}SiF] anions on complex/difficult to functionalize ligands.

CONCLUSIONS

In summary, we have developed a new class of WCAs featuring a *pseudo*-trigonal bipyramidal silicate. The synthetic routes reported have allowed access to a variety of $[^{R}SiF]^-$ structures. Cations relevant to coordination chemistry and catalysis were supported by these novel anions. The electrochemical stability window of the $[^{Me}SiF]^-$ anion was found to be 7.5 V in MeCN, surpassing that of $[Bu_4N][PF_6]$ by *ca.* 1 V oxidatively. The $[^{C6F5}SiF]^-$ variant provides a unique strategy for further modification of a $[^{R}SiF]^-$ anion. Together, these results demonstrate that the $[^{R}SiF]^-$ anion platform is readily diversified and supports coordination chemistry applications. The tunability of this platform allows for development of anions with tailored performance.

EXPERIMENTAL SECTION

General Considerations

Unless otherwise specified, all operations were carried out in an MBraun drybox under a nitrogen atmosphere or using standard Schlenk line or high vacuum techniques. Solvents for air- and moisture-sensitive reactions were dried with sodium mirror (1,4 dioxane), sodium benzophenone ketyl (DME), or by the method of Grubbs[35] (THF, Et_2O, toluene, pentane, benzene). Solvents, once dried and degassed, were vacuum transferred directly and stored under inert atmosphere over 3 Å molecular sieves. C_6D_6, C_7D_8, CD_3CN, CD_2Cl_2 were purchased from Cambridge Isotope Laboratories and vacuum transferred from sodium benzophenone ketyl (C_6D_6, C_7D_8) or CaH_2 (CD_3CN, CD_2Cl_2) after three freeze-pump-thaw cycles. Et_3N was dried over CaH_2, degassed, and vacuum transferred prior to use. Perfluoropinacol was purchased from TCI America and used as received. $Li_2(O_2(C(CF_3)_2)_2)$ was prepared according to literature procedures.[17] For the preparation of $Li_2(O_2(C(CF_3)_2)_2)$, perfluoropinacol was dried over 3 Å molecular sieves at 40 °C for at least 16 hours and vacuum transferred. $SiCl_4$ was purchased from Sigma-Aldrich, dried over CaH_2, and distilled immediately before use. Unless otherwise noted, $RSiCl_3$ precursors were purchased from commercial vendors, freeze-pump-thawed thrice, and bump-degassed before use.

Unless otherwise noted, all other chemicals were purchased from commercial vendors and used as received. ^1H, ^{13}C, ^{19}F, and ^{29}Si NMR spectra were either recorded on a Varian 400 MHz spectrometer or a Bruker 400 MHz spectrometer with chemical shifts reported in parts per million (ppm). ^1H NMR spectra were referenced to residual solvent peaks. [1] Multiplicities are abbreviated as follows: s = singlet, d = doublet, t = triplet, dd = doublet of doublets, dt = doublet of triplets, td = triplet of doublets, m = multiplet, br = broad, and app = apparent.

Electrochemical characterization: Linear sweep voltammetry experiments of **1-[Bu_4N]** and **[Bu_4N][PF_6]** were performed under an N_2 atmosphere using a Pine Instrument Company AFCBP1 potentiostat using the AfterMath software package. Linear sweep voltammograms were recorded in the glovebox at 25 °C with an auxiliary Pt-coil counter electrode, Ag-wire reference electrode, and 3.0 mm glassy carbon working electrode (BASI). The electrolyte solution was 0.1 M of the corresponding tetra-n-butylammonium salt in MeCN. All reported values are referenced to an internal ferrocene/ferrocenium couple.

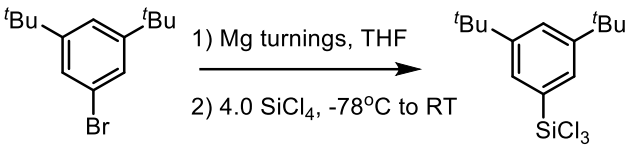

Synthesis of trichloro(3,5-di-tert-butylphenyl)silane: In an N_2-filled glovebox, Mg turnings (5 equiv) were transferred to a Schlenk tube and suspended in 200 mL of THF. 1-Bromo-3,5-di-*tert*-butylbenzene (11.5 g, 1 equiv) was dissolved in 50 mL of THF and added dropwise while maintaining vigorous stirring. Upon complete addition of the aryl bromide, the Grignard was stirred for 30 min at RT. A separate Schlenk tube was filled with 200 mL of THF and cycled onto the Schlenk tube before transferring 15 mL $SiCl_4$ (21.73 g, 4 equiv). The flask was then cooled to -78 ^oC, and the Schlenk tube containing the Grignard was cycled onto the line. The Grignard solution was transferred dropwise (1 drop/second) via cannula to the chilled $SiCl_4$ solution. After complete addition, the reaction continued to stir in the chilled bath for 16 hr, slowly warming to RT. The volatiles were concentrated *in vacuo*, and the desired product was extracted with pentane and filtration to remove the salts. The product was isolated as clear, colorless oil and used in subsequent steps without further purification.

(4-(*tert*-butyl)phenyl)trichlorosilane and $C_6F_5SiCl_3$ can be prepared analogously beginning from 1-bromo-4-*tert*-butylbenzene and pentafluorobromobenzene, respectively, and used without further purification.

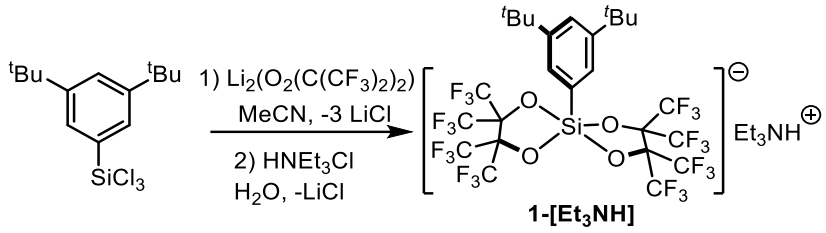

Synthesis of [Et$_3$H][^{tBu2Ph}SiF]/1-[Et$_3$NH]: In an N_2-filled glovebox, $Li_2(O_2(C(CF_3)_2)_2)$ (16.7 g, 48.2 mmol, 2.0 equiv) was dissolved in MeCN (100 mL). (3,5-di^{t}BuPh)$SiCl_3$ (7.8 g, 24.1 mmol, 1.0 equiv) was dissolved in MeCN and added to the stirring solution, with precipitation of LiCl within 5 minutes. The reaction was stirred for an additional 30 min at RT, and the LiCl was subsequently removed by filtration. The solvent was removed in vacuo, and the thick oil was suspended in DI H_2O with excess $HNEt_3Cl$. The suspension was stirred at RT for 1 hr, and the solids were subsequently collected by filtration. The solid was washed extensively with DI water to remove excess $HNEt_3Cl$. The solid was dried for 16 hr under vacuum before being transferred to an N_2-filled and washed with anhydrous toluene. **1-[HNEt$_3$]** was isolated as a fine white powder. Yield: (15.8 g, 66 %).

[Et$_3$NH][^{tBu2Ph}SiF]/1-[Et$_3$NH]

^{1}H (CD_3CN, 400 MHz): 7.77 (d, 2 H, Ar-*H*), 7.38 (t, 1 H, Ar-*H*), 6.51 (br s, 1 H, N-H), 3.14 (q, 6 H, NC*H*$_2$CH$_3$), 1.28 (s, 18 H, C(C*H*$_3$)$_3$), 1.24 (t, 9 H, NCH$_2$C*H*$_3$). ^{19}F (CD_3CN, 376 MHz,): -69.24 (app m, 12 F, C*F*$_3$), -69.83 (app m, 12 F, C*F*$_3$). ^{13}C{^{1}H} (CD_3CN, 101 MHz): 148.81 (s, Ar-*C*), 137.86 (s, Ar-*C*), 132.57 (s, Ar-*C*), 123.12 (s, Ar-*C*), 123.12 (q app m, *C*F$_3$), 84.36 (br s, O*C*(CF$_3$)$_2$), 48.08 (s, N*C*H$_2$CH$_3$), 35.31 (s, *C*(CH$_3$)$_3$), 31.80 (s, C(*C*H$_3$)$_3$), 9.20 (s, NCH$_2$*C*H$_3$). ^{29}Si

(CD_3CN, 80 MHz): -88.91 (s). Anal. Calcd. for $C_{32}H_{37}F_{24}NO_4Si$ (%): C, 39.07; H, 3.79; N, 1.42. Found: C, 39.04; H, 3.83; N, 1.23.

[Et$_3$NH][$^{CH2CH2(CF2)5CF33}$SiF]/2-[Et$_3$NH], [Et$_3$NH][^{Decyl}SiF]/3-[Et$_3$NH], **[Et$_3$NH][^{tBu}PhSiF]/4-[Et$_3$NH], [Et$_3$NH][^{Sty}SiF]/5-[Et$_3$NH], [Et$_3$NH][^{Vinyl}SiF]/6-[Et$_3$NH],** and can be prepared analogously using the corresponding $RSiCl_3$ reagent.

[Et$_3$NH][$^{CH2CH2(CF2)5CF3}$SiF]/2-[Et$_3$NH]

^{1}H (CD_3CN, 400 MHz): 6.52 (br app. t, 1 H, N-H), 3.14 (q, 6 H, NC*H*$_2$CH$_3$), 2.21 (m, 2H, SiCH$_2$C*H*$_2$(CF$_2$)$_5$CF$_3$), 1.24 (t, 9 H, NCH$_2$C*H*$_3$), 1.02 (m, 2H, SiC*H*$_2$CH$_2$(CF$_2$)$_5$CF$_3$). ^{19}F (CD_3CN, 376 MHz,): -69.84 (app m, 12 F, C*F*$_3$), -70.13 (app m, 12 F, C*F*$_3$), -81.68 (tt, 3 F, SiCH$_2$CH$_2$(CF$_2$)$_5$C*F*$_3$), -116.99 (m, 2 F, SiCH$_2$CH$_2$(C*F*$_2$)$_5$CF$_3$), -122.53 (m, 2 F, SiCH$_2$CH$_2$(C*F*$_2$)$_5$CF$_3$), -123.46 (m, 2 F, SiCH$_2$CH$_2$(C*F*$_2$)$_5$CF$_3$), -124.51 (m, 2 F, SiCH$_2$CH$_2$(C*F*$_2$)$_5$CF$_3$), -126.71 (m, 2 F, SiCH$_2$CH$_2$(C*F*$_2$)$_5$CF$_3$). ^{13}C{^{1}H} (CD_3CN, 101 MHz): 122.03 (q app m, *C*F$_3$), 117.19 (indirectly detected by ^{19}F-^{13}C HSQC, SiCH$_2$CH$_2$(CF$_2$)$_5$C*F*$_3$), 118.95 (indirectly detected by ^{19}F-^{13}C HSQC, SiCH$_2$CH$_2$(C*F*$_2$)$_5$CF$_3$), 111.45 (indirectly detected by ^{19}F-^{13}C HSQC, SiCH$_2$CH$_2$(C*F*$_2$)$_5$CF$_3$), 111.09 (indirectly detected by ^{19}F-^{13}C HSQC, SiCH$_2$CH$_2$(C*F*$_2$)$_5$CF$_3$), 110.31 (indirectly detected by ^{19}F-^{13}C HSQC, SiCH$_2$CH$_2$(C*F*$_2$)$_5$CF$_3$), 108.52 (indirectly detected by ^{19}F-^{13}C HSQC, SiCH$_2$CH$_2$(C*F*$_2$)$_5$CF$_3$) 84.50 (br s, O*C*(CF$_3$)$_2$), 48.10 (s, N*C*H$_2$CH$_3$), 27.30 (t, Si*C*H$_2$CH$_2$(CF$_2$)$_5$CF$_3$), 9.19 (s, NCH$_2$*C*H$_3$), 7.36 (s, SiCH$_2$*C*H$_2$(CF$_2$)$_5$CF$_3$). ^{29}Si (CD_3CN, 80 MHz): -78.01 (s). Anal. Calcd. for $C_{26}H_{20}F_{37}NO_4Si$ (%): C, 27.36; H, 1.77; N, 1.23. Found: C, 27.46; H, 1.72; N, 1.46.

[Et$_3$NH][^{Decyl}SiF]/3-[Et$_3$NH]

^{1}H (CD_3CN, 400 MHz): 6.59 (br s, 1 H, N-H), 3.14 (q, 6 H, NC*H*$_2$CH$_3$), 1.38 (m, 2 H, alkyl-*H*), 1.30 (br. app. s, 14 H, alkyl-*H*), 1.27 (t, 9 H, NCH$_2$C*H*$_3$), 0.91 (t, 3 H, alkyl-*H*), 0.79 (t, 2 H, alkyl-

H). ^{19}F (CD_3CN, 376 MHz,): -69.75 (app s, 12 F, C*F*$_3$), -69.86 (app s, 12 F, C*F*$_3$). ^{13}C{^{1}H} (CD_3CN, 101 MHz): 123.25 (q app m, *C*F_3), 84.56 (br s, O*C*$(CF_3)_2$), 48.12 (s, N*C*H_2CH_3), 34.04 (s, alkyl-*C*), 32.70 (s, alkyl-*C*), 30.42 (s, alkyl-*C*), 30.32 (s, alkyl-*C*), 30.16 (s, alkyl-*C*), 30.14 (s, alkyl-*C*) 25.07 (s, alkyl-*C*), 23.45 (s, alkyl-*C*), 18.39 (s, alkyl-*C*), 14.42 (s, alkyl-*C*), 9.20 (s, NCH_2*C*H_3). ^{29}Si (CD_3CN, 80 MHz): -75.44 (s). Anal. Calcd. for $C_{28}H_{37}F_{24}NO_4Si$ (%): C, 35.94; H, 3.99; N, 1.50. Found: C, 36.05; H, 3.96; N, 1.27.

[Et$_3$NH][^{tBu}PhSiF]/4-[Et$_3$NH]

^{1}H (CD_3CN, 400 MHz): 7.74 (dt, 2 H, Ar-H), 7.27 (dt, 2 H, Ar-H), 6.53 (br s, 1 H, N-*H*), 3.14 (q, 6 H, NC*H*$_2$$CH_3$), 1.29 (s, 9 H, -^{t}Bu), 1.27 (t, 9 H, NCH_2C*H*$_3$). ^{19}F (CD_3CN, 376 MHz,): -69.48 (app m, 12 F, C*F*$_3$), -69.81 (app m, 12 F, C*F*$_3$). ^{13}C{^{1}H} (CD_3CN, 101 MHz): 152.02 (s, Ar-*C*), 137.42 (s, Ar-*C*), 136.45 (s, Ar-*C*), 124.21 (s, Ar-*C*), 123.26 (q app m, *C*F_3), 84.29 (br s, O*C*$(CF_3)_2$), 48.09 (s, N*C*H_2CH_3), 35.07 (s, *C*$(CH_3)_3$), 31.60 (s, C(*C*$H_3)_3$), 9.19 (s, NCH_2*C*H_3). ^{29}Si (CD_3CN, 80 MHz): -89.08 (s). Anal. Calcd. for $C_{28}H_{29}F_{24}NO_4Si$·0.38 THF (based on residual solvent in NMR) (%): C, 37.18; H, 3.23; N, 1.47. Found: 37.17, 3.35, 1.83.

[Et$_3$NH][^{Sty}SiF]/5-[Et$_3$NH]

^{1}H (CD_3CN, 400 MHz): 7.75 (d, 2 H, Ar-*H*), 7.31 (d, 2 H, Ar-*H*), 6.73 (dd, 1 H, Ar-C*H*=CH_2), 6.54 (br s, 1 H, N-H), 5.80 (dd, 1 H, Ar-CH=C*H*,H), 5.22 (dd, 1 H, Ar-CH=CH,*H*), 3.13 (q, 6 H, NC*H*$_2$$CH_3$), 1.23 (t, 9 H, NCH_2C*H*$_3$). ^{19}F (CD_3CN, 376 MHz,): -69.47 (app m, 12 F, C*F*$_3$), -69.91 (app m, 12 F, C*F*$_3$). ^{13}C{^{1}H} (CD_3CN, 101 MHz): 140.01 (s, Ar-*C*), 138.35 (s, Ar-*C*), 138.06 (s, Ar-*C*H=CH_2), 137.58 (s, Ar-*C*), 125.20 (s, Ar-*C*), 123.09 (q app m, *C*F_3), 114.26 (s, Ar-CH=*C*H_2), 48.08 (s, N*C*H_2CH_3), 9.19 (s, NCH_2*C*H_3). ^{29}Si (CD_3CN, 80 MHz): -89.54 (s). Anal. Calcd. for $C_{26}H_{23}F_{24}NO_4Si$·0.12 THF (based on residual solvent in NMR) (%): C, 35.12; H, 2.61; N, 1.55. Found: C, 35.42; H, 2.60; N, 1.46.

[Et$_3$NH][^{Vinyl}SiF]/6-[Et$_3$NH]

^{1}H (CD_3CN, 400 MHz): 6.60 (br s, 1 H, N-*H*), 5.88 (m, 3 H, vinyl-*H*) 3.13 (q, 6 H, NCH_2CH_3), l1.24 (t, 9 H, NCH_2CH_3). ^{19}F (CD_3CN, 376 MHz,): -69.59 (app m, 12 F, CF_3), -69.79 (app m, 12 F, CF_3). ^{13}C{^{1}H} (CD_3CN, 101 MHz): 138.55 (s, vinyl-*C*), 135.76 (s, vinyl-*C*), 123.16 (q app m, CF_3), 84.42 (br s, $OC(CF_3)_2$), 48.07 (s, NCH_2CH_3), 9.19 (s, NCH_2CH_3). ^{29}Si (CD_3CN, 80 MHz): -90.39 (s). Anal. Calcd. for $C_{20}H_{19}F_{24}NO_4Si$ (%): C, 29.24; H, 2.33; N, 1.71. Found: C, 29.36; H, 2.23; N, 1.57.

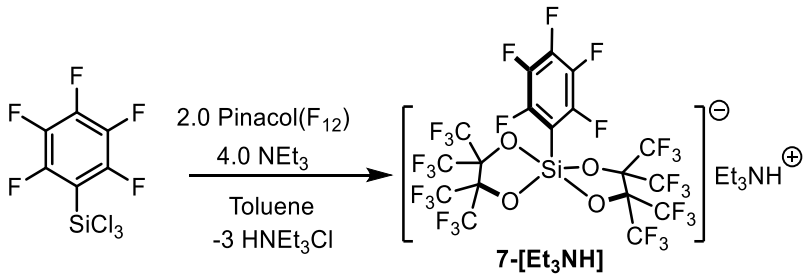

Synthesis of **[Et$_3$H][^{C6F5}SiF]/7-[Et$_3$NH]**: In an N_2-filled glovebox, $C_6F_5SiCl_3$ (11.98 g, 39.7 mmol, 1 equiv) was dissolved in toluene (100 mL) and transferred to a Schlenk tube. Pinacol(F_{12}) (26.76 g, 79.45 mmol, 2 equiv) and NEt_3 (11.21 g, 158.94 mmol, 4 equiv) were added, resulting in rapid precipitation of $HNEt_3Cl$ and the desired product. The reaction was stirred an additional 30 minutes at RT before volatiles were removed *in vacuo*. The solid was washed extensively with pentane and extracted with THF. After removal of the solvents, the thick brown oil was washed with toluene, resulting in precipitation of the product as a white solid. The solid was washed with additional toluene (50 mL) and extracted with THF (50 mL). The solvents were removed, and **7-[Et$_3$NH]** was isolated as a white solid. Yield: 13.2 g (14 %).

[Et$_3$NH][^{C6F5}SiF]/7-[Et$_3$NH]: ^{1}H NMR (CD_3CN, 400MHz): 6.60 (s, 1 H, N-*H*) 3.14 (q, 6H, NCH_2CH_3), 1.24 (t, 9H, NCH_2CH_3). ^{19}F (CD_3CN, 376 MHz): -69.96 (app. br. s, 24 F, CF_3), -129.21 (dd, 2 F, Ar-*F*), -157.08 (tt, 1 F, Ar-*F*), -165.95 (m, 2 F, , Ar-*F*). ^{13}C{^{1}H}: (CD_3CN, 101

MHz): 148.05 (d app, m, Ar-*F*), 141.91 (d app. m, Ar-*F*), 137.39 (d app. m, Ar-*F*), 122.83 (q app m, *C*F_3), 84.04 (br s, O*C*$(CF_3)_2$), 48.09 (s, N*C*H_2CH_3), 9.19 (s, NCH_2*C*H_3). ^{29}Si: (CD_3CN, 80 MHz): -92.14 (s)

Anal. Calcd. for $C_{24}H_{16}F_{29}NO_4Si$·0.55 THF (based on residual solvent in NMR) (%): C, 31.52; H, 1.84; N, 1.40. Found: C, 32.33; H, 2.34; N, 1.60.

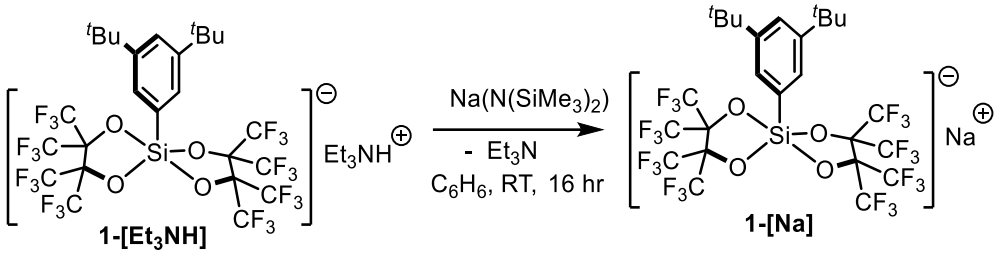

Synthesis of [Na][^{tBu2Ph}SiF]/1-[Na]: In an N_2-filled glovebox, **1-[HNEt$_3$]** (1 g, 1.016 mmol, 1 equiv) was suspended in C_6H_6 (30 mL) and KHMDS (243.3 mg, 1.22 mmol, 1.2 equiv) was added as a solid. The solution was stirred for 16 hr at RT before collecting the product by filtration. The solid was further washed with additional C_6H_6 and dried under vacuum. The product was isolated as a white solid.

Note: The alkali cation readily coordinates trace ethereal solvents (THF, Et_2O), so all compounds must be handled appropriately to avoid unwanted solvent coordination.

1-[K] can be prepared analogously using KHMDS.

[Na][^{tBu2Ph}SiF]/1-[Na]

^{1}H (CD_3CN, 400 MHz): 7.77 (d, 2 H, Ar-*H*), 7.38 (t, 1 H, Ar-*H*), 1.28 (s, 18 H, , C(C*H*$_3$)$_3$). ^{19}F (CD_3CN, 376 MHz,): -69.26 (app m, 12 F, C*F*$_3$), -69.83 (app m, 12 F, C*F*$_3$). ^{13}C{^{1}H} (CD_3CN, 101 MHz): 148.81 (s, Ar-*C*), 137.86 (s, Ar-*C*), 132.56 (s, Ar-*C*), 123.11 (s, Ar-*C*), 123.11 (q app m, *C*F_3), 84.36 (br s, O*C*$(CF_3)_2$), 35.31 (s, *C*$(CH_3)_3$), 31.79 (s, C(*C*H_3)$_3$). ^{29}Si (CD_3CN, 80 MHz):

-88.82 (s, indirectly detected by ^{1}H-^{29}Si HMBC). Anal. Calcd. For $C_{26}H_{21}F_{24}NaO_4Si$ (%): C, 34.53; H, 2.34. Found: C, 35.55; H, 2.31.

[K][^{tBu2Ph}SiF]/1-[K]

^{1}H (CD_3CN, 400 MHz): 7.77 (d, 2 H, Ar-*H*), 7.38 (t, 1 H, Ar-*H*), 1.28 (s, 18 H, , C(C*H*$_3$)$_3$). ^{19}F (CD_3CN, 376 MHz,): -69.25 (app m, 12 F, C*F*$_3$), -69.83 (app m, 12 F, C*F*$_3$). $^{13}C\{^{1}H\}$ (CD_3CN, 101 MHz): 148.81 (s, Ar-*C*), 137.86 (s, Ar-*C*), 132.57 (s, Ar-*C*), 123.12 (s, Ar-*C*), 123.12 (q app m, *C*F_3), 84.36 (br s, O*C*$(CF_3)_2$), 35.31 (s, *C*$(CH_3)_3$), 31.79 (s, C(*C*$H_3)_3$). ^{29}Si (CD_3CN, 80 MHz): -88.82 (s). Anal. Calcd. For $C_{26}H_{21}F_{24}KO_4Si$ (%): C, 33.92; H, 2.30. Found: C, 33.90; H, 2.31.

Prepared by Tianyi He

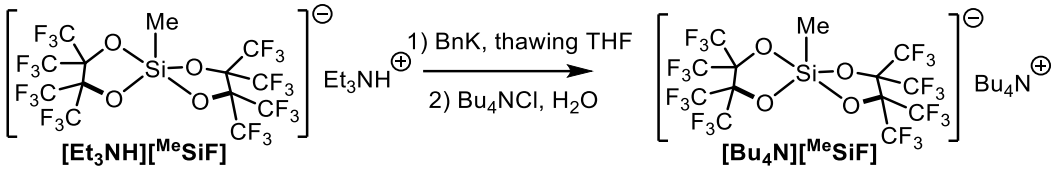

Synthesis of [Bu$_4$N][^{Me}SiF]: In an N_2-filled glovebox, **[Et$_3$NH][^{Me}SiF]** (6.14 g, 7.60 mmol) and BnK (1.19 g, 9.14 mmol) were combined in a 250 mL Schlenk tube with a Teflon stir bar. The Schlenk tube was cycled onto a high vacuum line manifold, and *ca.* 60 mL of THF from a Na/benzophenone pot was condensed directly onto the solid reactants at -196 °C. The Schlenk tube was allowed to thaw and stirring was initiated. After the reaction mixture was warmed to room temperature, the mixture was dried *in vacuo*. [Bu$_4$N][Cl] (*ca.* 15 g, ~54 mmol) was dissolved in *ca.* 200 mL of H_2O and poured into the Schlenk tube on the bench. The suspension was stirred under air for 16 hours and the solids were collected on a medium porosity sintered glass frit. The solids were washed with *ca.* 2 L of H_2O and dried over $CaSO_4$ under high vacuum for 16 hours. The resulting off-white solids were redissolved in CH_2Cl_2, filtered over a glass fiber filter paper, and layered with pentane. The resulting microcrystalline solids were collected on a medium

porosity sintered glass frit and washed with 50 mL of pentane. The solids were once again dried under high vacuum for 16 hours to yield analytically pure **[Bu$_4$N][^{Me}SiF]** (4.3 g, 60 %).

^{1}H (CD_3CN, 400 MHz): 3.07 (m, 8 H, NC*H*$_2$CH$_2$CH$_2$CH$_3$), 1.60 (m, 8 H, NCH$_2$C*H*$_2$CH$_2$CH$_3$), 1.35 (m, 8 H, NCH$_2$CH$_2$C*H*$_2$CH$_3$), 0.97 (t, 12 H, NCH$_2$CH$_2$CH$_2$C*H*$_3$), 0.19 (s, 3 H, SiC*H*$_3$). ^{19}F (CD_3CN, 376 MHz): -69.79 (overlapping app br s, 12 F, -C*F*$_3$), -69.83 (overlapping app br s, 12 F, -C*F*$_3$). ^{13}C{^{1}H} (CD_3CN, 101 MHz): 123.7 (q app m, *C*F$_3$), 84.5 (br s, O*C*(CF$_3$)$_2$), 59.3 (t, NC*H*$_2$CH$_2$CH$_2$CH$_3$), 24.3 (s, NCH$_2$*C*H$_2$CH$_2$CH$_3$), 20.3 (t, NCH$_2$CH$_2$*C*H$_2$CH$_3$), 13.7 (s, NCH$_2$CH$_2$CH$_2$*C*H$_3$), 1.0 (s, Si*C*H$_3$). ^{29}Si (CD_3CN, 80 MHz): -73.8 (s). Anal. Calcd. for $C_{29}H_{39}F_{24}NO_4Si$ (%): C, 36.68; H, 4.14; N, 1.47. Found: C, 36.64; H, 4.08; N, 1.20.

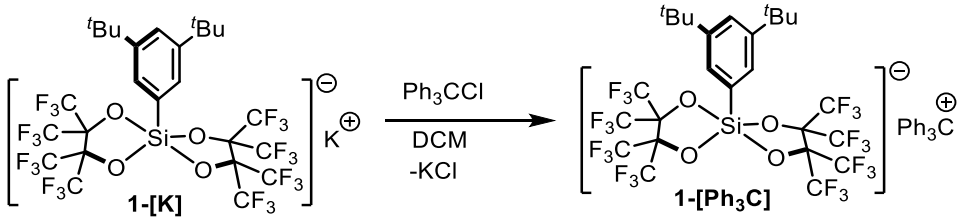

Synthesis of [Ph$_3$C][^{tBu2Ph}SiF]/1-[Ph$_3$C]: In an N_2-filled glovebox, **1-[K]** (400 mg, 0.434 mmol, 1 equiv) and Ph_3CCl (157.5 mg, 1.26 mmol, 2.9 equiv) were transferred to a 100 mL round bottom flask connected to a swivel frit. *Note:* **1-[K]** *must not have coordinated Et$_2$O or THF*. The glassware was cycled onto a high vacuum line, and anhydrous DCM (10 mL) was vacuum transferred onto the reactants at -196^{o}C. The reaction was warmed to RT and stirred for 16 hr. Upon completion, the mixture was filtered to remove KCl; the product was extracted 3x with DCM. Volatiles were removed *in vacuo*, and the product was washed thoroughly with pentane. The product was dried and transferred to a glovebox. Recrystallization from layered DCM and pentane afforded a dark orange solid.

^{1}H (CD_2Cl_2, 400 MHz): 8.29 (t, 3 H, Ar-*H*), 7.90 (t, 6 H, Ar-*H*), 7.78 (d, 2 H, ^{t}Bu$_2$Ar-*H*), 7.67 (d, 6 H, Ar-*H*), 7.30 (t, 1 H, ^{t}Bu$_2$Ar-*H*), 1.27 (s, 18 H, C(C*H*$_3$)$_3$). ^{19}F (CD_2Cl_2, 376 MHz): -68.83 (m,

12 F, C*F*$_3$), -69.63 (m, 12 F, C*F*$_3$). ^{13}C{^{1}H} (CD_2Cl_2, 101 MHz): 211.20 (s, Ph_3C^+), 147.88 (s, ^{t}Bu$_2$Ph-*C*), 144.11 (s, Ph-*C*), 143.05 (s, Ph-*C*), 140.29 (s, Ph-*C*), 137.38 (^{t}Bu$_2$Ph-*C*), 132.10 (s, ^{t}Bu$_2$Ph-*C*), 131.11 (s, Ph-*C*), 128.23 (s, ^{t}Bu$_2$Ph-*C*), 122.42 q app m, *C*F$_3$), 121.87 (^{t}Bu$_2$Ph-*C*), 83.30 (s, O*C*(CF$_3$)$_2$), 34.95 (s, *C*(CH$_3$)$_3$), 31.65 (C(*C*H$_3$)$_3$). ^{29}Si (CD_2Cl_2, 80 MHz): -88.59 (s). Anal. Calcd. for $C_{45}H_{36}F_{24}O_4Si$ (%): C, 48.05; H, 3.23. Found: C: 47.97; H, 2.92.

7-[Ph$_3$C] can be prepared analogously using **7-[Na]**.

[Ph$_3$C][^{C6F5}SiF]/7-[Ph$_3$C]

^{1}H (CD_2Cl_2, 400 MHz): 8.29 (t, 3 H, Ar-*H*), 7.90 (t, 6 H, Ar-*H*), 7.68 (d, 6 H, Ar-*H*). ^{19}F NMR (CD_2Cl_2, 376 MHz): -69.64 (m, 12 F, C*F*$_3$), -69.69 (m, 12 F, C*F*$_3$), -128.41 (dd, 2 F, Ar-*F*), -157.28 (t, 1 F, Ar-*F*), -165.28 (m, 2 F, Ar-*F*). Anal. Calcd. for $C_{37}H_{15}F_{29}O_4Si$ (%): C, 40.31; H, 1.37. Found: C: 40.14; H, 1.30.

Polymerization Trials

In a N_2 glovebox, Pd catalyst (10 μmol) was dissolved in toluene (10 mL) was transferred to a Fisher-Porter vessel. The reactor was removed from the glovebox and connected to a C_2H_4/CO gas feed. The N_2 atmosphere was replaced with a 1:1 mixture of C_2H_4/CO (flow rate 300 sccm for each gas) by pressurizing the vessel to 100 psi and venting 3x. After pressurizing to 100 psi, polymerization was run for 3 hr at RT. The reaction was quenched upon exposure to air, and the polymer was precipitated by stirring with acidic methanol (0.6 mL HCl/10 mL MeOH). The polymer was collected and dried under vacuum overnight.

NMRs were recorded in a mixture of 1, 1, 1, 3, 3, 3-hexafluoro-2-propanol and C_6D_6 (4:1) at RT.

Catalyst	Polymer Yield	Activity (g mol^{-1} hr^{-1})
[Pd(dppe)(NCMe)Me]$^+$[BAr$^F{}_{24}$]$^-$	68.6	2.28
[Pd(dppe)(NCMe)Me]$^+$[^{tBu2Ph}SiF]	50.2	1.67

Table 5.1. Ethylene/CO Copolymerization Performance

Procedure for Determining Solubility

1-[Na] and **1-[K]** (~50 mg each) were suspended in C_6D_6 and stirred vigorously for 16 hr. Each sample was filtered, and 600 mL was transferred to a new vial. Fluorobenzene (5 mL) was added as an internal standard to the filtered solution and mixed thoroughly via pipette. Concentration was determined by ^{19}F NMR by integrating the flurobenzene peak (1 F) at -112.9 ppm (in benzene) or -114.0 ppm (in dichloromethane) vs. the silicate (24 F) at ~68-70 ppm.

Determination of Trigonal Bipyramidal vs. Square Pyramidal Geometry

As a representative example, bond angles for 1-[$HNEt_3$] were examined to determine geometry.

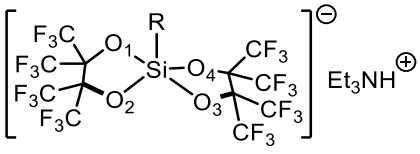

Et_3NH $^{tBu2Ph}SiF$		
O1-Si-O3	171.06(9)	t = 0.84-0.86
O2-Si-O4	120.13(9)	
O2-Si-R	120.4(1)	
O4-Si-R	119.5(1)	

Table 5.2. Bond Angles of [Et_3NH][$^{tBu2Ph}SiF$]

An index parameter was previously developed to calculate the distorted geometry,[36] where t = 0 for perfectly square pyramidal and t = 1 for perfectly trigonal bipyramidal.

$$\tau = \frac{(\beta - \alpha)}{60}$$

For our complexes, β is the O_1-Si-O_3 angle and α is the O_2-Si-O_4, O_2-Si-R, O_4-Si-R angles. For **1-[$HNEt_3$]**, the geometry is trigonal bipyramidal.

General Procedure for Treatment of [Et_3NH][^{C6F5}SiF] (7-[Et_3NH]) with Aryl-Li

[Et_3NH][^{C6F5}SiF] was dissolved in THF and treated with $LiCH_2SiMe_3$ (1 equiv). Within 5 minutes, the solution turned bright yellow. A solution of aryl-Li in THF was added dropwise, and the reaction was stirred for 15 minutes. Upon completion, the reaction was quenched by exposure to air. The volatiles were removed *in vacuo*. If necessary, the product was purified by recrystallization. Due to the complexity of the ^{13}C NMR and low signal intensity of ^{29}Si, only ^{1}H and ^{19}F are reported for most of the compounds below.

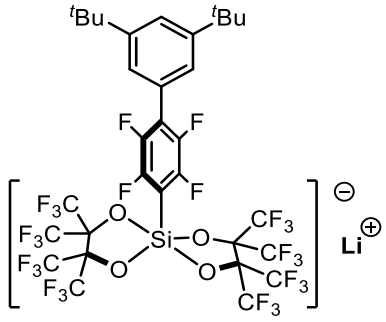

[Li][^{R}SiF] R = 3',5'-di-tert-butyl-2,3,5,6-tetrafluoro-1,1'-biphenyl

Product not isolated ^{19}F (THF h_8, 376 MHz): -68.08 (m, 12 F), -68.47 (m, 12 F), -126.93 (m, 2 F), -146.59 (m, 2 F).

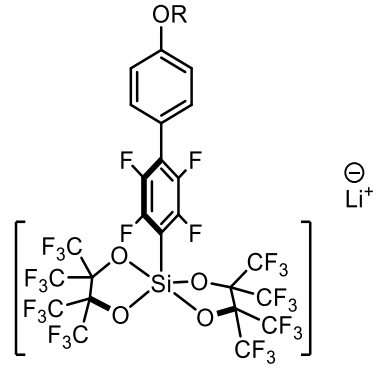

R = -$CH_2CH_2OCH_2CH_2OCH_2CH_2OMe$

[Li][^{R}SiF] R = 2,3,5,6-tetrafluoro-4'-(2-(2-(2-methoxyethoxy)ethoxy)ethoxy)-1,1'-biphenyl

Purified by washing with Et_2O and extracting product into acetone. Product isolated as a white solid.

^{1}H (Acetone-d_6, 400 MHz): 7.46 (d, 2 H, Ar-*H*), 7.10 (d, 2 H, Ar-*H*), 4.22 (m, 2 H, Peg-*H*), 3.86 (m, 2 H, Peg-*H*), 3.67 (m, 2 H, Peg-*H*), 3.62-3.57 (overlapping peaks, 4 H, Peg-*H*), 3.47 (m, 2 H, Peg-*H*), 3.28 (s, 3 H, Peg-*H*). ^{19}F (Acetone-d_6, 376 MHz): -69.67 (m, 12 F, C*F*$_3$), -69.89 (m, 12 F, C*F*$_3$), -128.77 (dd, 2 F, Ar-*F*), -148.39 (dd, 2 F, Ar-*F*). ^{13}C{^{1}H} (Acetone-d_6, 101 MHz): 160.36 (s, Ar-*C*), 132.38 (s, Ar-*C*), 115.48 (s, Ar-*C*), 72.63 (s, Peg-*C*), 71.43 (s, Peg-*C*), 71.25 (s, Peg-*C*), 71.09 (s, Peg-*C*), 70.28 (s, Peg-*C*), 68.45 (s, Peg-*C*), 58.77 (s, Peg-*C*).

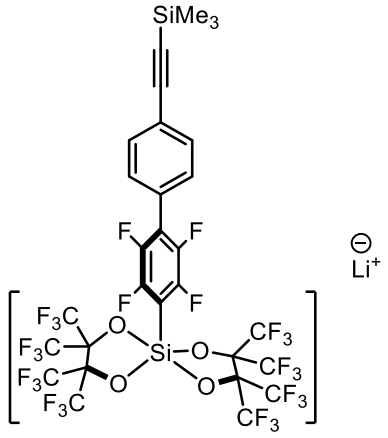

[Li][^{R}SiF] R = trimethyl((2',3',5',6'-tetrafluoro-[1,1'-biphenyl]-4-yl)ethynyl)silane. Product isolated as a white solid.

^{1}H (THF-h_8, 400 MHz): 8.09 (d, 2 H, Ar-*H*), 8.04 (d, 2 H, Ar-*H*). ^{19}F (THF-h_8, 376 MHz): -69.26 (m, 12 F, C*F*$_3$), -69.51 (m, 12 F, C*F*$_3$), -127.52 (dd, 2 F, Ar-*F*), -147.96 (dd, 2 F, Ar-*F*).

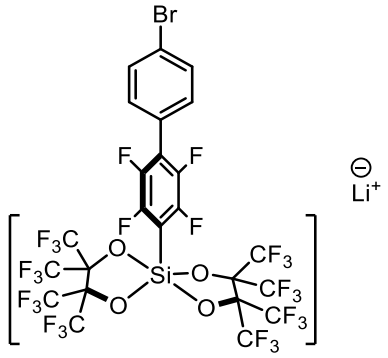

[Li][^{R}SiF] R = 4'-bromo-2,3,5,6-tetrafluoro-1,1'-biphenyl. Purified by washing extensively with hexanes and extracting product into Et_2O. Isolated as a white solid. ^{1}H (THF-h_8, 400 MHz): 8.19 (d, 2 H, Ar-*H*), 8.00 (d, 2 H, Ar-*H*) ^{19}F (THF-h_8, 376 MHz): -69.29 (m, 12 F, C*F*$_3$), -69.50 (m, 12 F, C*F*$_3$), -127.70 (m, 2 F, Ar-*F*), -147.93 (m, 2 F, Ar-*F*).

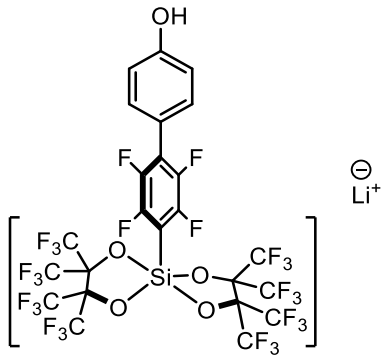

[Li][^{R}SiF] R = 2',3',5',6'-tetrafluoro-[1,1'-biphenyl]-4-ol. Recrystallized by layering THF/pentane. Isolated as a pale pink solid. ^{1}H (Acetone-d$_6$, 400 MHz): 7.14 (d, 2 H, Ar-*H*), 6.72 (d, 2 H, Ar-*H*), 3.62 (m, 16 H, THF-*H*), 1.78 (m, 16 H, THF-*H*). ^{19}F (Acetone-d$_6$, 376 MHz): -69.65 (m, 12 F, C*F*$_3$), -69.83 (m, 12 F, C*F*$_3$), -129.57 (dd, 2 F, Ar-*F*), -148.72 (dd, 2 F, Ar-*F*). ^{29}Si (Acetone-d$_6$, 80 MHz): -91.25 (s).

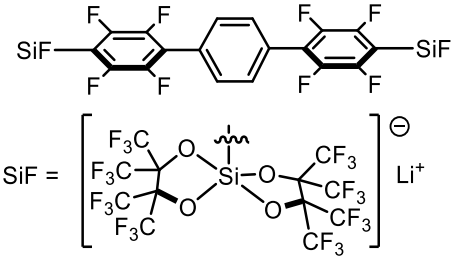

Dianionic ^{R}SiF. Purified by washing with Et_2O and extracting product into THF. Isolated as a white solid.

^{1}H (THF-h_8, 400 MHz): 7.59 (s, 4 H, Ar-*H*). ^{19}F (THF-h_8, 376 MHz): -70.55 (m, 12 F, C*F*$_3$), -70.84 (m, 12 F, C*F*$_3$), -128.88 (dd, 2 F, Ar-*F*), -149.08 (dd, 2 F, Ar-F).

Crystallography refinement details

Refinement Details—In each case, crystals were mounted on a glass fiber or MiTeGen loop using Paratone oil, then placed on the diffractometer under a nitrogen stream. Low temperature (100 K or 200 K) X-ray data were obtained on a Bruker KAPPA APEXII CCD-based diffractometer (Mo fine-focus sealed X-ray tube, K_α = 0.71073 Å) or a Bruker D8 VENTURE Kappa Duo PHOTON 100 CMOS based diffractometer (Mo $I_\mu S$ HB micro-focus sealed X-ray tube, K_α = 0.71073 Å). All diffractometer manipulations, including data collection, integration, and scaling were carried out using the Bruker APEXIII software. Absorption corrections were applied using SADABS. Space groups were determined on the basis of systematic absences and intensity statistics and the structures were solved in the Olex 2 software interface by intrinsic phasing using XT (incorporated into SHELXTL) and refined by full-matrix least-squares on F^2. All non-hydrogen atoms were refined using anisotropic displacement parameters. Hydrogen atoms were placed in the idealized positions and refined using a riding model, unless noted otherwise. The structure was refined (weighed least-squares refinement on F^2) to convergence. Graphical representation of structures with 50% probability thermal ellipsoids were generated using the Diamond3 visualization software.

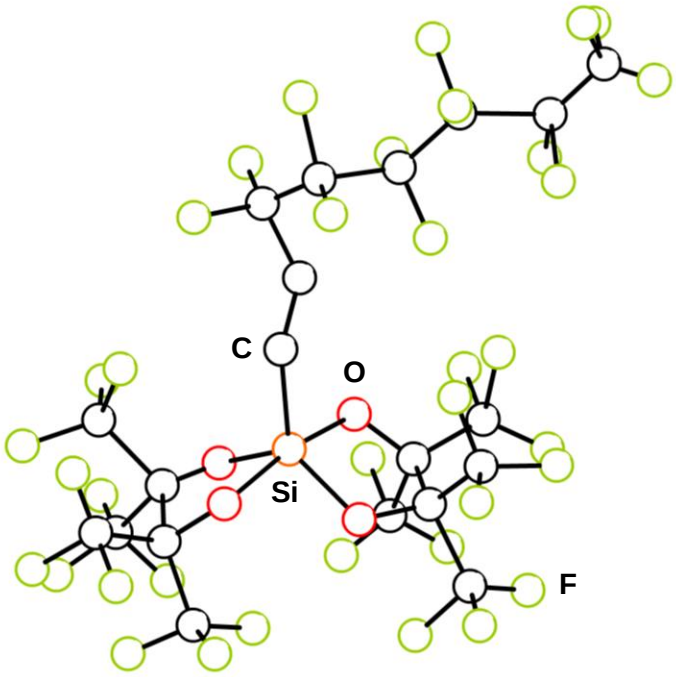

Figure 5.8. Preliminary solid-state structure of **2-[Et$_3$NH]**. Hydrogen atoms and Et$_3$NH cation omitted for clarity.

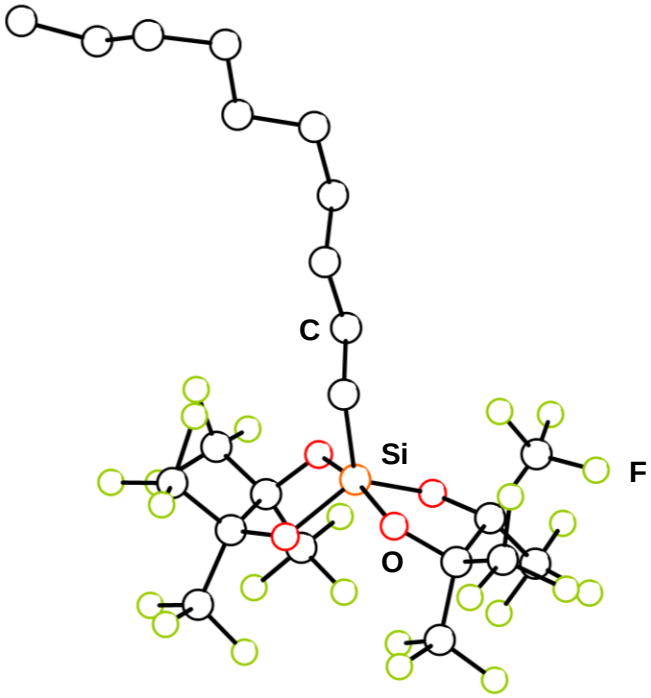

Figure 5.9. Preliminary solid-state structure of **3-[Et$_3$NH]**. Hydrogen atoms and Et$_3$NH cation omitted for clarity.

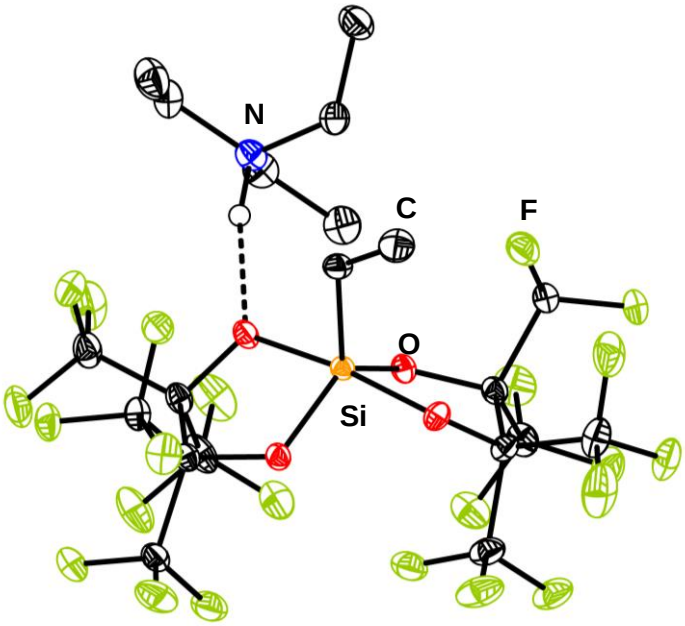

Figure 5.10. Solid-state structure of **5-[Et$_3$NH]**. Thermal ellipsoids shown at 50% probability. Hydrogen atoms omitted for clarity.

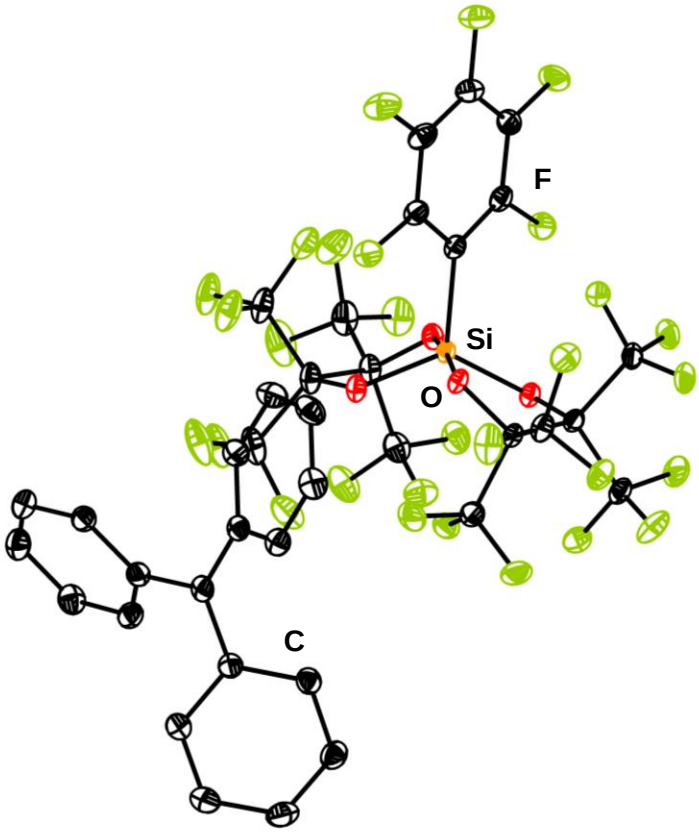

Figure 5.11. Solid-state structure of **7-[Ph$_3$C]**. Thermal ellipsoids shown at 50% probability. Hydrogen atoms omitted for clarity.

Table 5.3. Crystal and refinement data

	[Et_3NH][^{C6F5}SiF]	**[Et_3NH][^{tBu2}PhSiF]**	**[Et_3NH][^{vinyl}SiF]**	**[K][^{tBu2}PhSiF]**
	7-[Et_3NH]	**1-[Et_3NH]**	**5-[Et_3NH]**	**1-[K]**
Empirical formula	$C_{28}H_{24}F_{29}NO_5Si$	$C_{32}H_{37}F_{24}NO_4Si$	$C_{20}H_{19}F_{24}NO_4Si$	$C_{61}H_{50}F_{48}K_2O_8Si_2$
Formula weight	1033.57	983.70	821.45	1957.39
T (K)	100	100	100	100
a, Å	10.0337(9)	27.756(3)	12.2552(10)	12.5486(8)
b, Å	30.638(3)	19.1647(17)	18.553(2)	14.7156(12)
c, Å	11.9905(12)	19.0790(17)	12.8226(15)	22.537(2)
α, °	90	90	90	74.584(6)
β, °	91.423(5)	130.208(2)	95.263(7)	87.270(4)
γ, °	90	90	90	68.875(4)
Volume, $Å^3$	3684.9(6)	7750.7(12)	2903.2(5)	3736.9(6)
Z	4	8	4	2
Crystal system	Monoclinic	Monoclinic	Monoclinic	Triclinic
Space group	$P2_1/n$	C2/c	$P2_1/n$	$P\bar{1}$
d_{calc}, g/cm^3	1.863	1.686	1.879	1.945
θ range, °	2.885 to 72.372	3.109 to 67.679	4.203 to 72.135	2.036 to 74.686
μ, mm^{-1}	2.349	1.983	2.497	13.486
Abs. Correction	Multi-scan	Multi-scan	Multi-scan	Multi-scan
GOF	1.051	1.082	0.958	0.913
R_1 ,[a] wR_2 [b] [I>2 σ(I)]	0.0353, 0.0891	0.0521,0.1493	0.0325, 0.1093	0.0361, 0.1087
Radiation Type	Cu K_α	Cu K_α	Cu K_α	Cu K_α

[a] $R_1 = \sum||F_o| - |F_c||/\sum|F_o|$. [b] $wR_2 = [\sum[w(F_o^2-F_c^2)^2]/\sum[w(F_o^2)^2]^{1/2}$.

Table 5.3. Crystal and refinement data (continued)

	[Ph$_3$C][^{tBu2}PhSiF]	**[Ph$_3$C][^{C6F5}PhSiF]**
	1-[Ph$_3$C]	**7-[Ph$_3$C]**
Empirical formula	$C_{45}H_{36}F_{24}O_4Si$	$C_{37}H_{15}F_{29}O_4Si$
Formula weight	1124.83	1102.58
T (K)	100	100
a, Å	12.0592(9)	10.8407(9)
b, Å	12.4407(10)	12.1087(12)
c, Å	16.2264(11)	16.775(2)
α, °	89.738(7)	93.315(6)
β, °	88.738(7)	94.008(4)
γ, °	78.830(6)	115.671
Volume, Å^3	2387.6(3)	1970.2(4)
Z	2	2
Crystal system	Triclinic	Triclinic
Space group	$P\bar{1}$	$P\bar{1}$
d_{calc}, g/cm^3	1.565	1.859
θ range, °	2.724 to 72.156	2.653 to 72.441
μ, mm^{-1}	1.693	2.230
Abs. Correction	Multi-scan	Multi-scan
GOF	1.037	1.067
R_1 ,^{a} wR_2 ^{b} [I>2 σ(I)]	0.0287, 0.0719	0.0372, 0.1024
Radiation Type	Cu K$_\alpha$	Cu K$_\alpha$

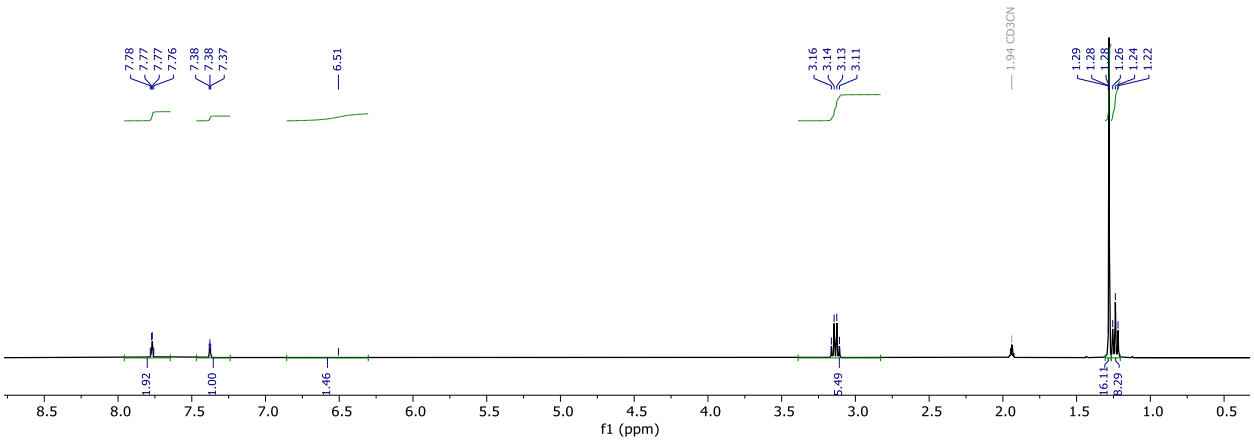

Figure 5.12. ^{1}H NMR of **1-[Et$_3$NH]** in CD_3CN.

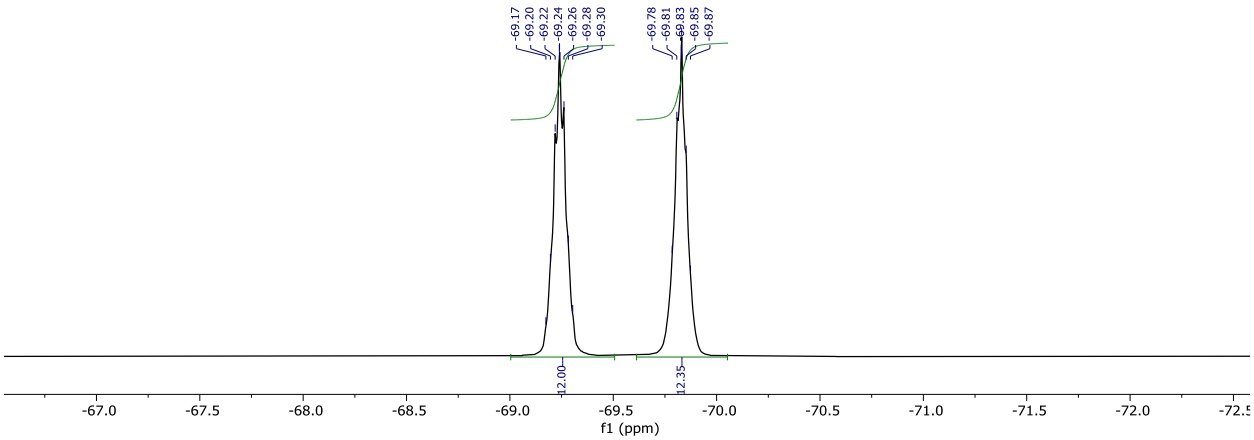

Figure 5.13. ^{19}F NMR of **1-[Et$_3$NH]** in CD_3CN.

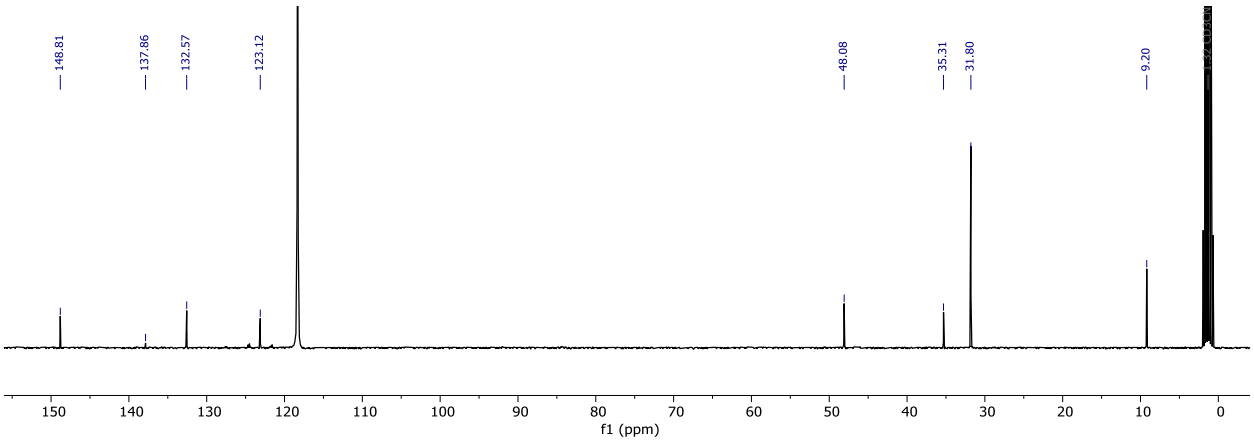

Figure 5.14. ^{13}C NMR of **1-[Et$_3$NH]** in CD_3CN.

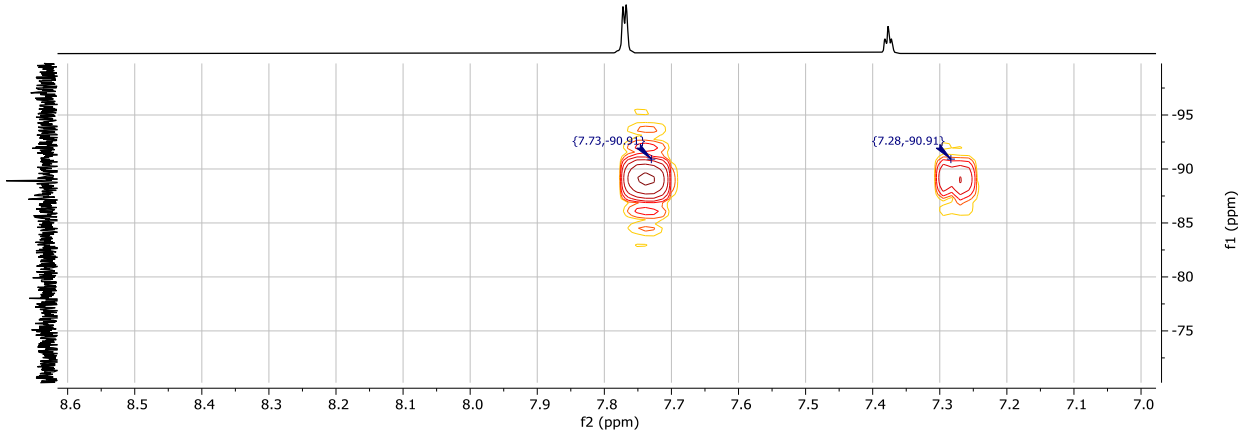

Figure 5.15. $^{1}H/^{29}Si$ HMBC NMR of **1-[Et$_3$NH]** in CD_3CN.

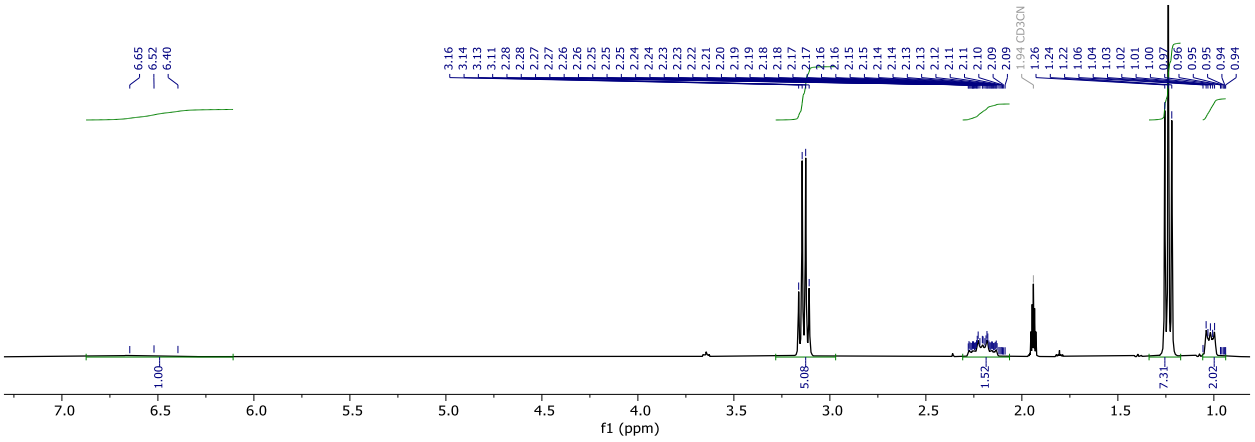

Figure 5.16. ^{1}H NMR of **2-[Et$_3$NH]** in CD_3CN.

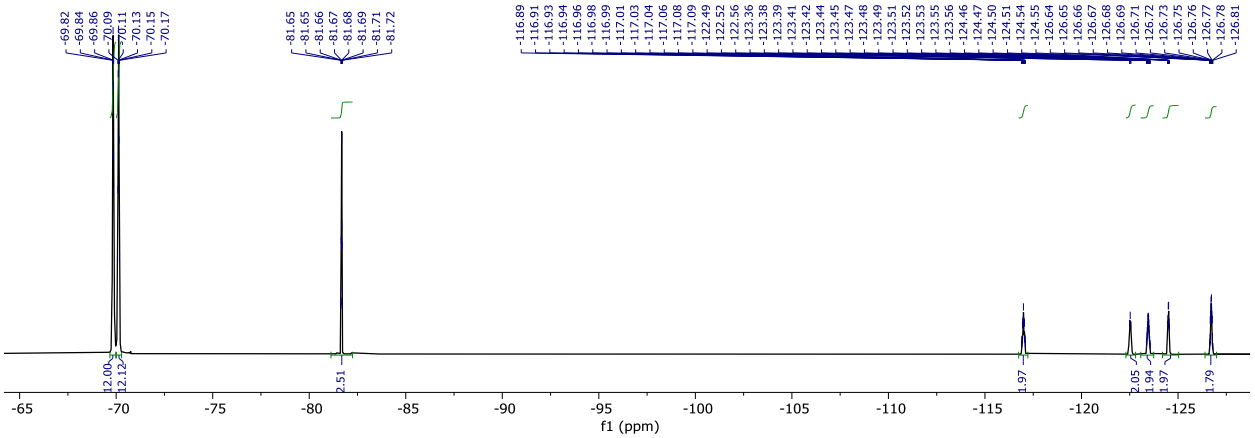

Figure 5.17. ^{19}F NMR of **2-[Et$_3$NH]** in CD_3CN.

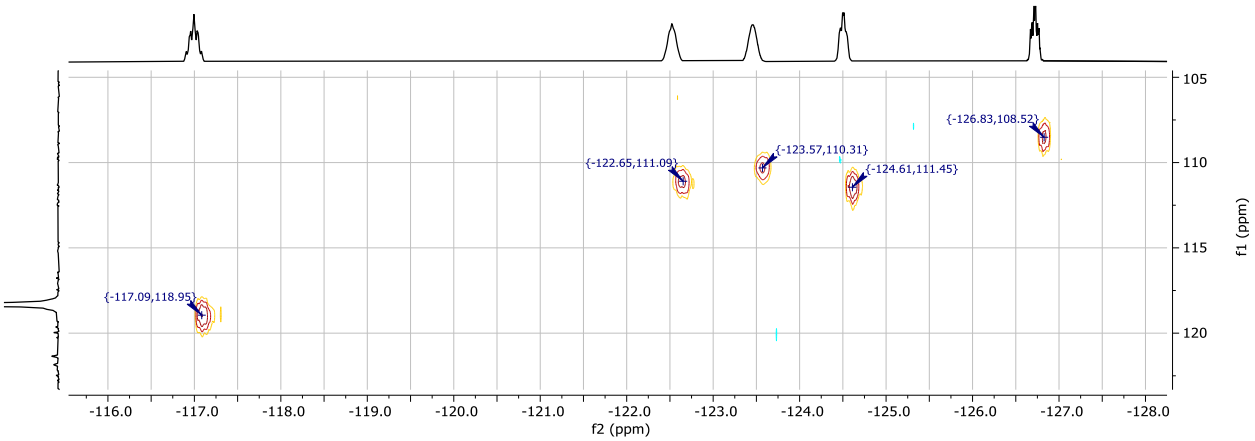

Figure 5.18. $^{19}F/^{13}C$ HSQC of **2-[Et$_3$NH]** in CD_3CN.

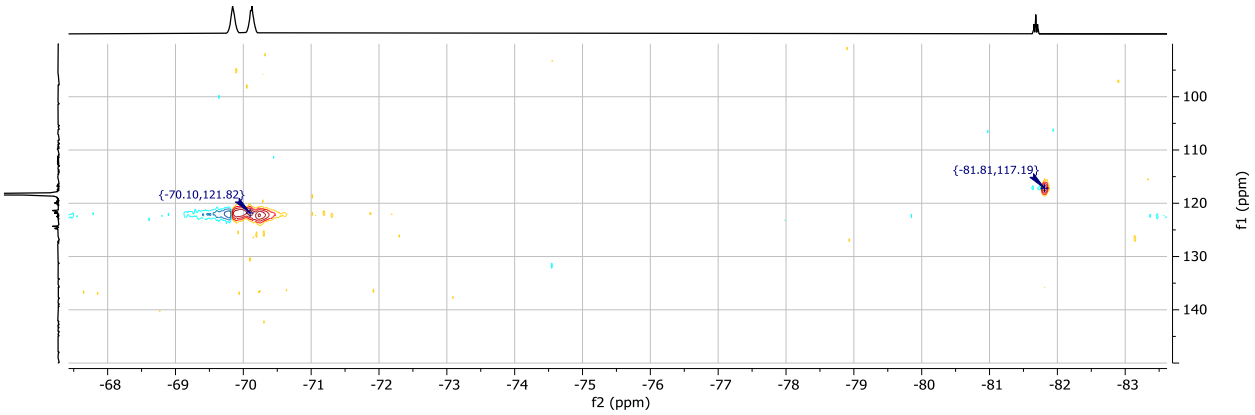

Figure 5.19. $^{19}F/^{13}C$ HSQC of **2-[Et$_3$NH]** in CD_3CN.

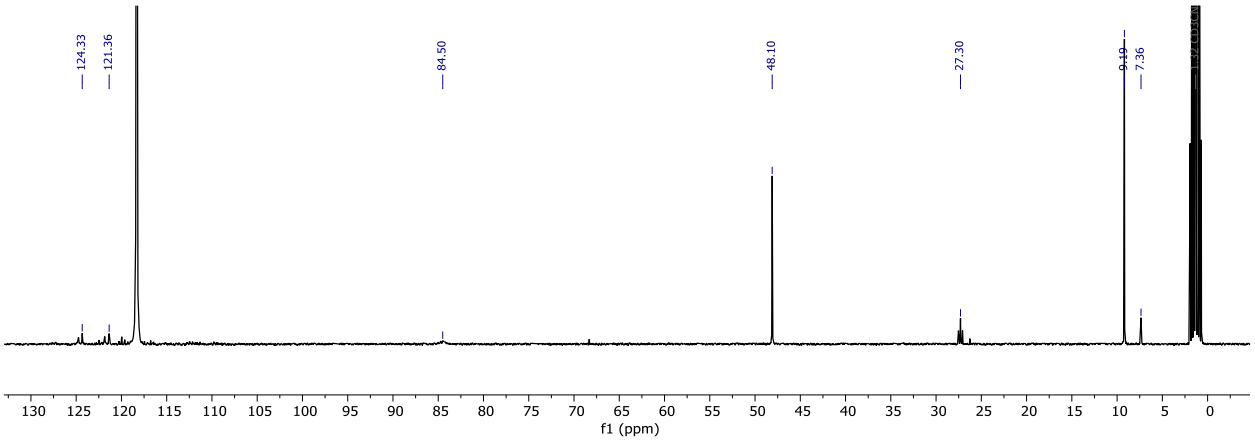

Figure 5.20. ^{13}C NMR of **2-[Et$_3$NH]** in CD_3CN.

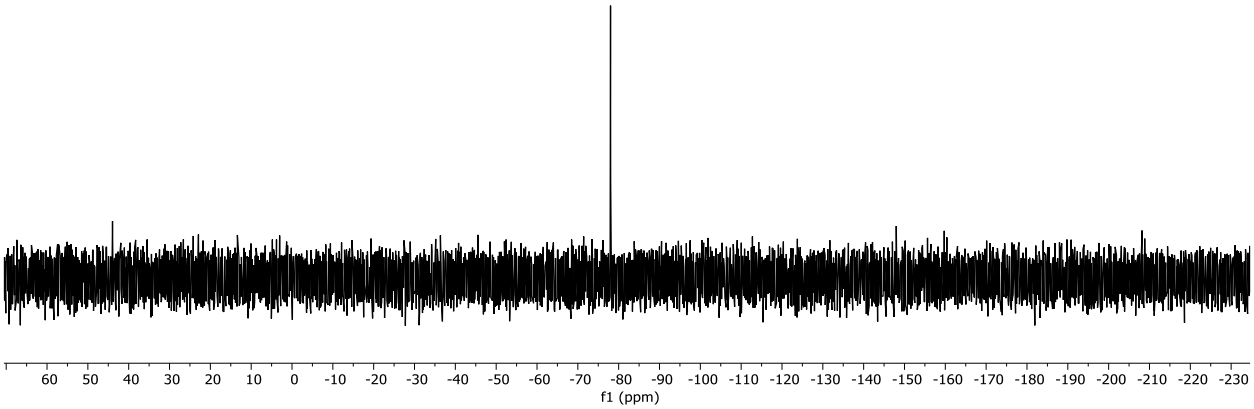

Figure 5.21. ^{29}Si NMR of **2-[Et$_3$NH]** in CD_3CN.

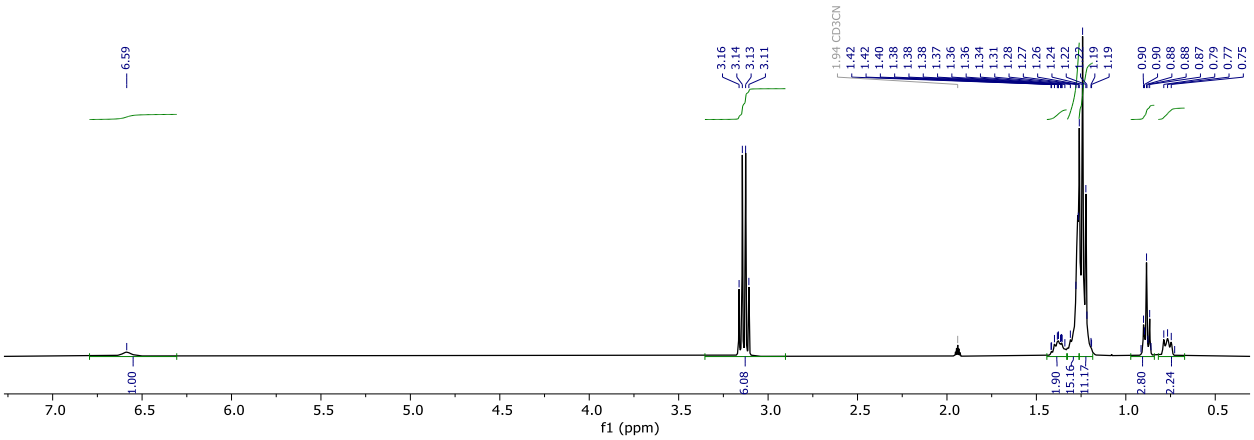

Figure 5.22. ^{1}H NMR of **3-[Et$_3$NH]** in CD_3CN.

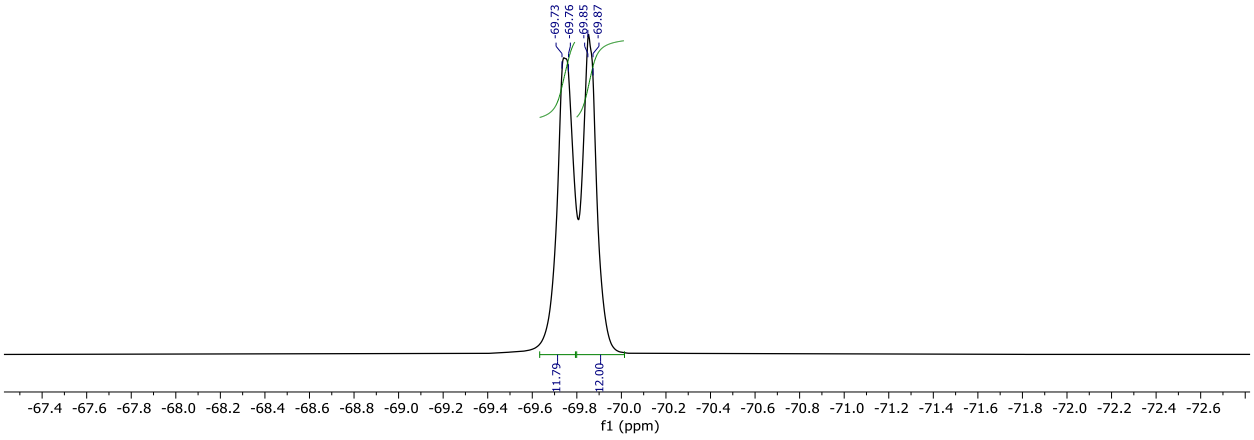

Figure 5.23. ^{19}F NMR of **3-[Et$_3$NH]** in CD_3CN.

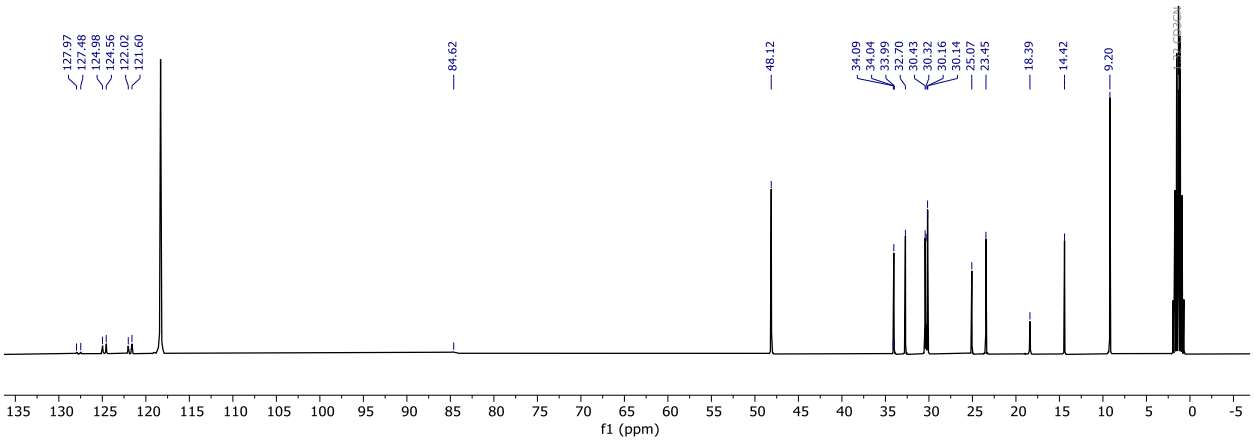

Figure 5.24. ^{13}C NMR of **3-[Et$_3$NH]** in CD_3CN.

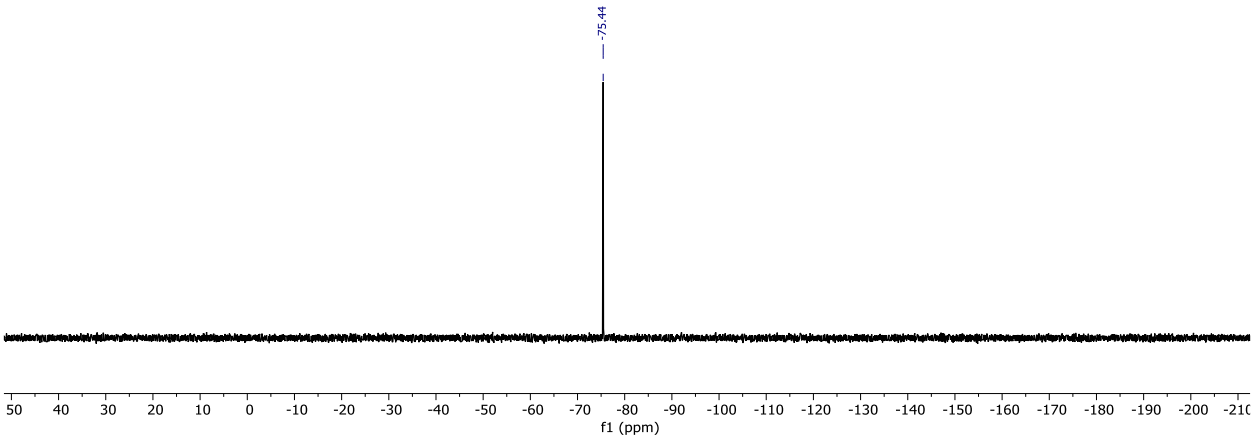

Figure 5.25. ^{29}Si NMR of **3-[Et$_3$NH]** in CD_3CN.

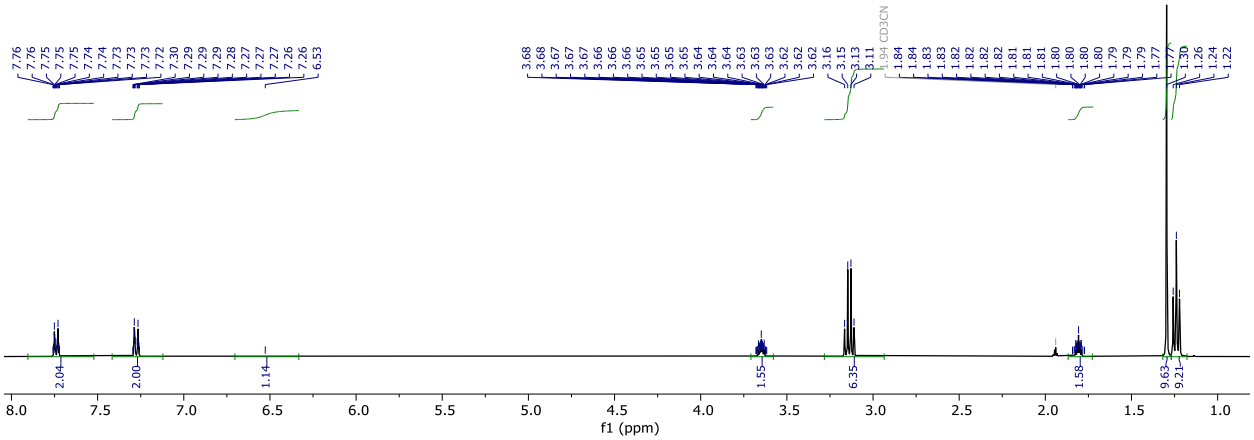

Figure 5.26. ^{1}H NMR of **4-[Et$_3$NH]** in CD_3CN.

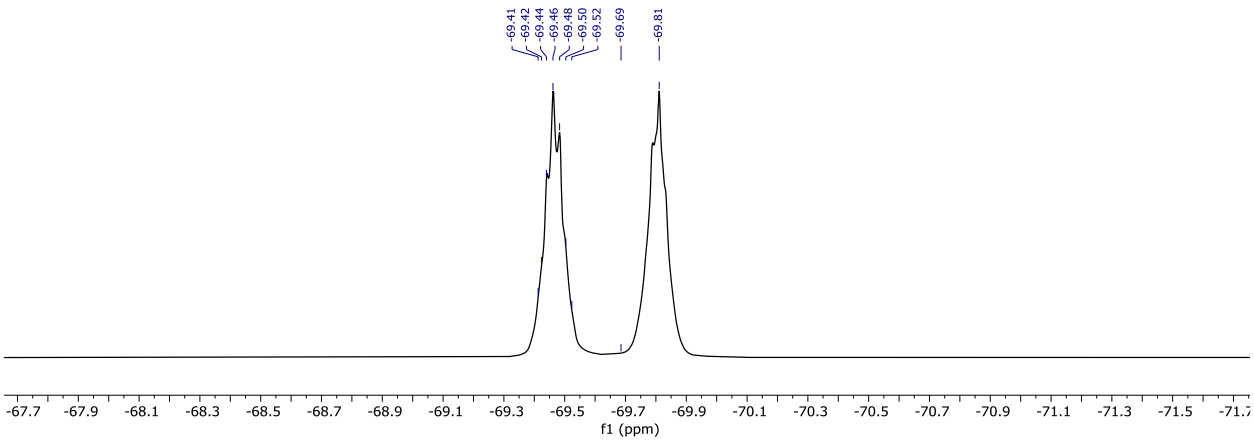

Figure 5.27. ^{19}F NMR of **4-[Et$_3$NH]** in CD_3CN.

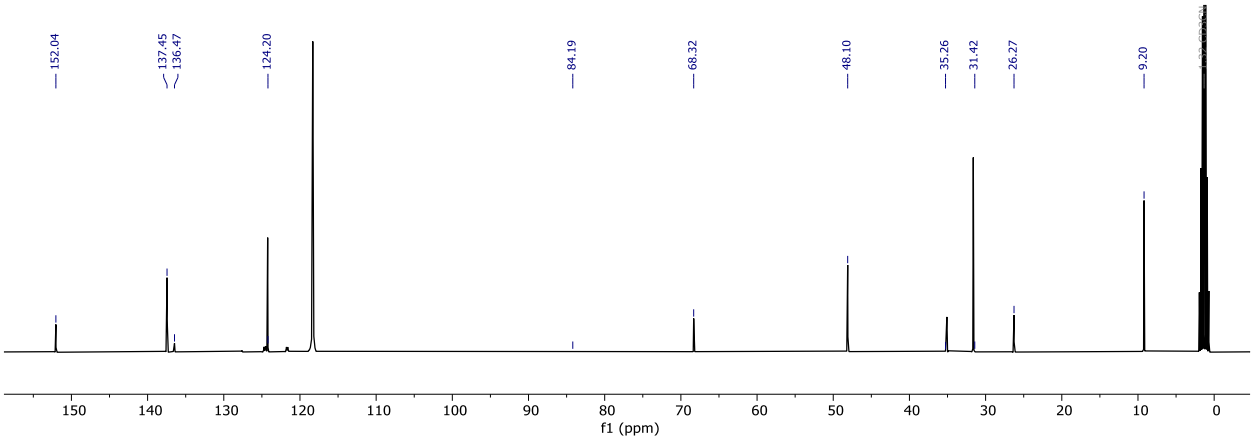

Figure 5.28. ^{13}C NMR of **4-[Et$_3$NH]** in CD_3CN.

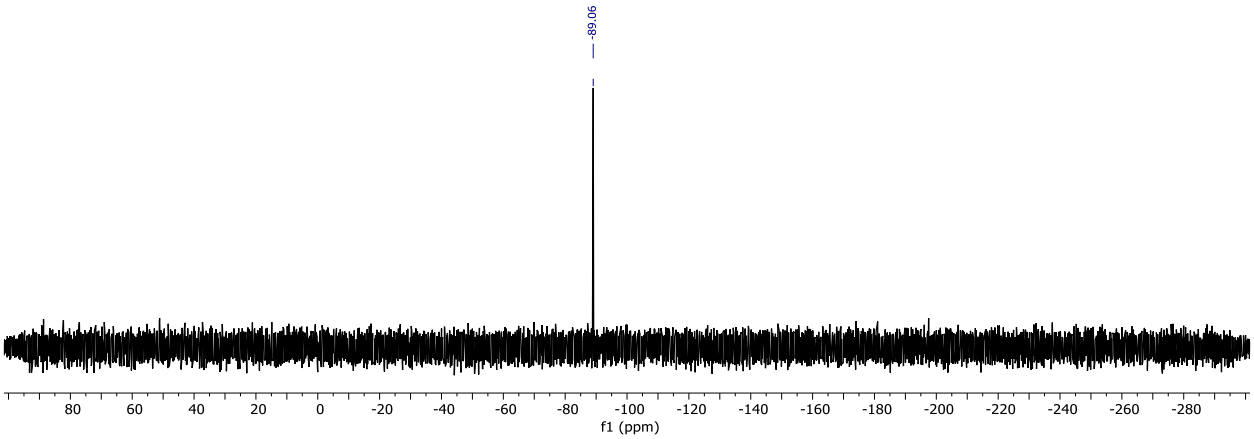

Figure 5.29. ^{29}Si NMR of **4-[Et$_3$NH]** in CD_3CN.

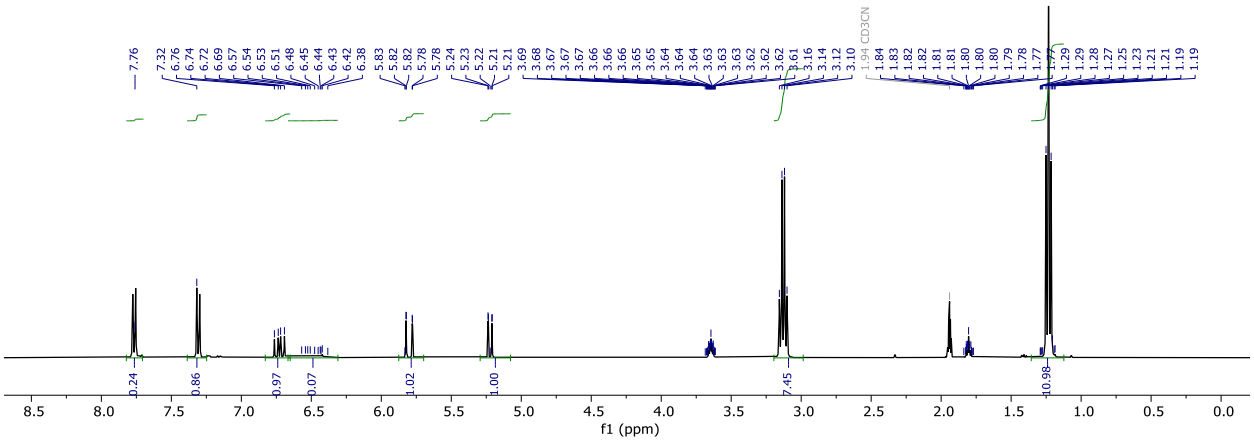

Figure 5.30. ^{1}H NMR of **5-[Et$_3$NH]** in CD_3CN.

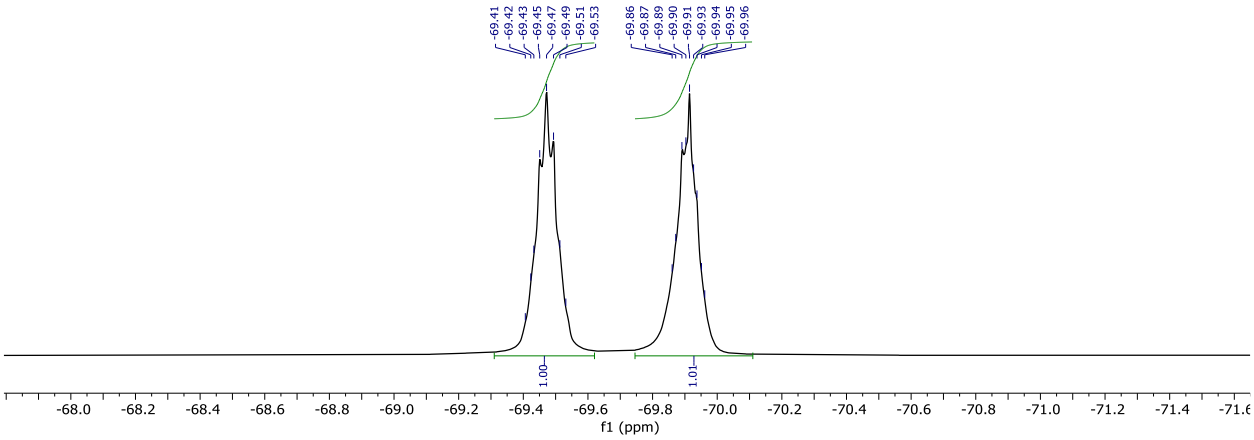

Figure 5.31. ^{19}F NMR of **5-[Et$_3$NH]** in CD_3CN.

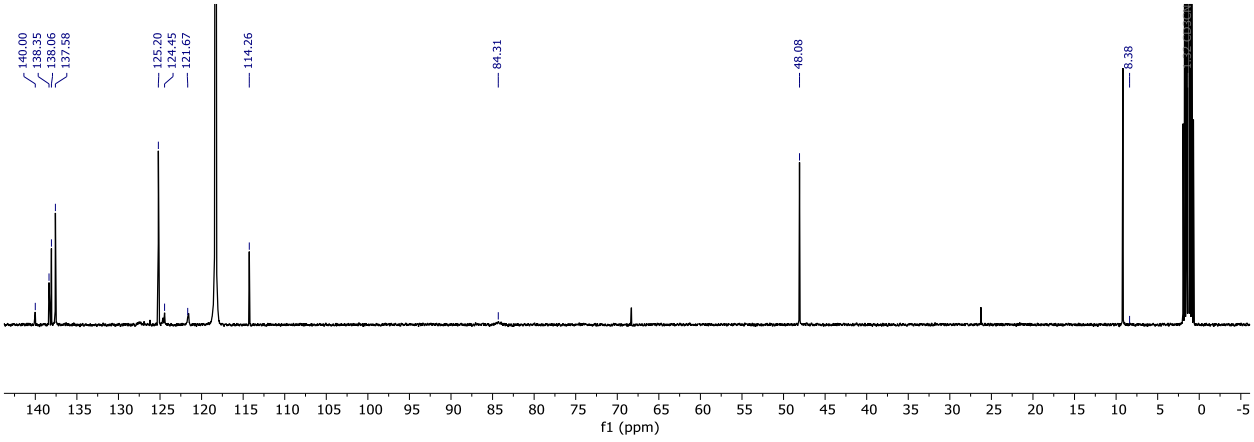

Figure 5.32. ^{13}C NMR of **5-[Et$_3$NH]** in CD_3CN.

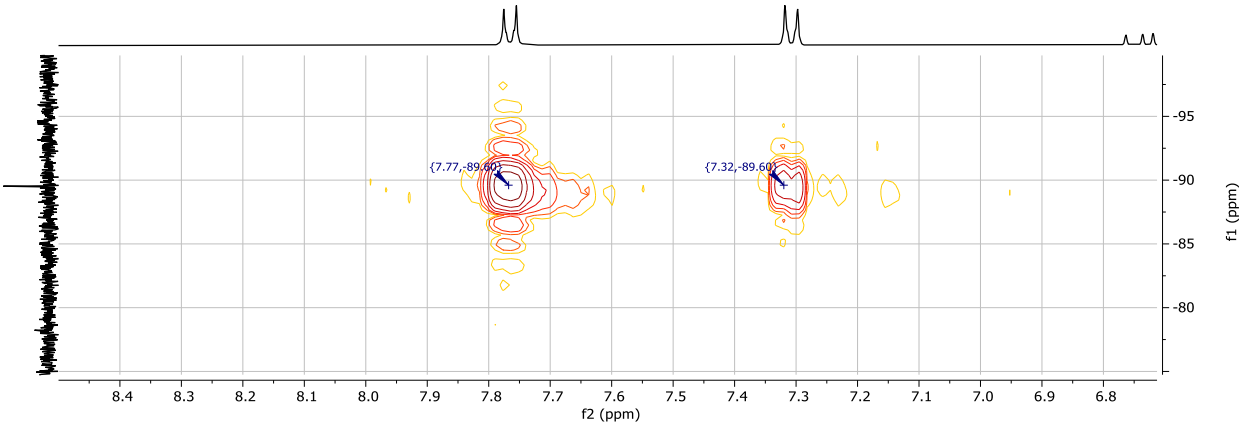

Figure 5.33. $^{1}H/^{29}Si$ HMBC of **5-[Et$_3$NH]** in CD_3CN.

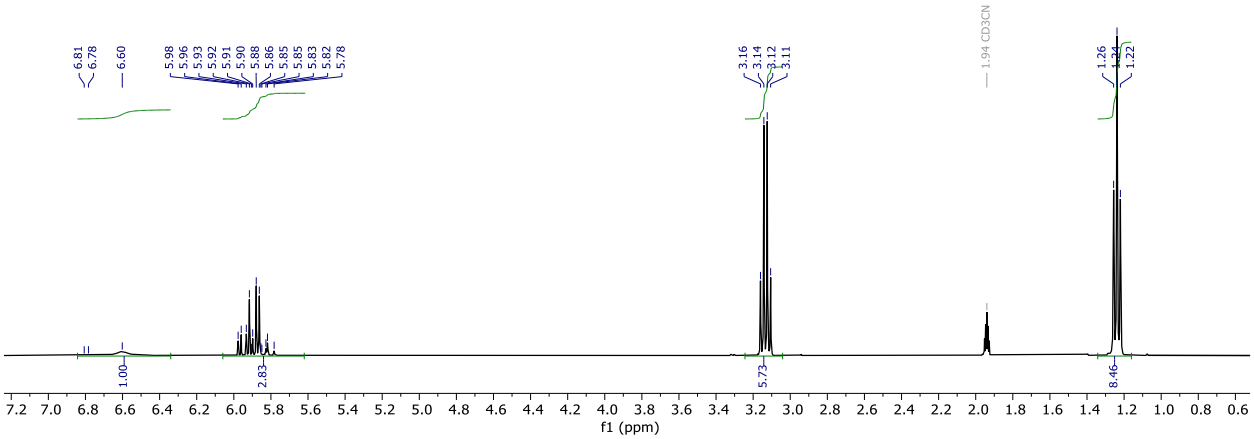

Figure 5.34. ^{1}H NMR of **6-[Et$_3$NH]** in CD_3CN.

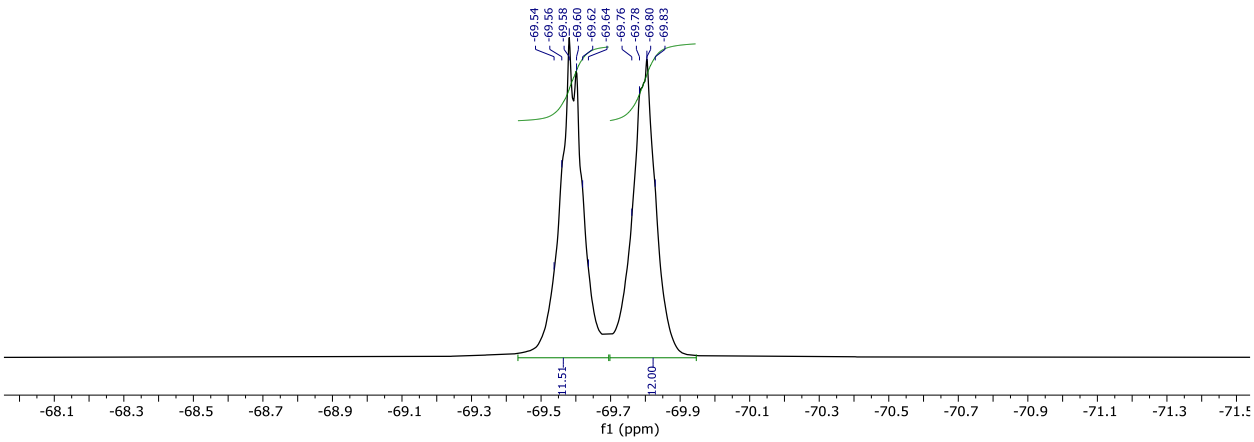

Figure 5.35. ^{19}F NMR of **6-[Et$_3$NH]** in CD_3CN.

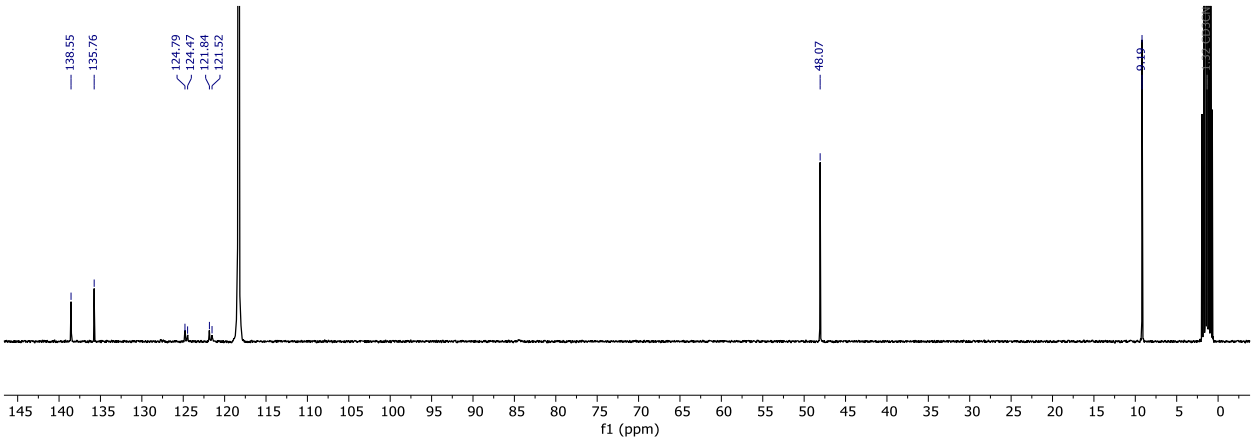

Figure 5.36. ^{13}C NMR of **6-[Et$_3$NH]** in CD_3CN.

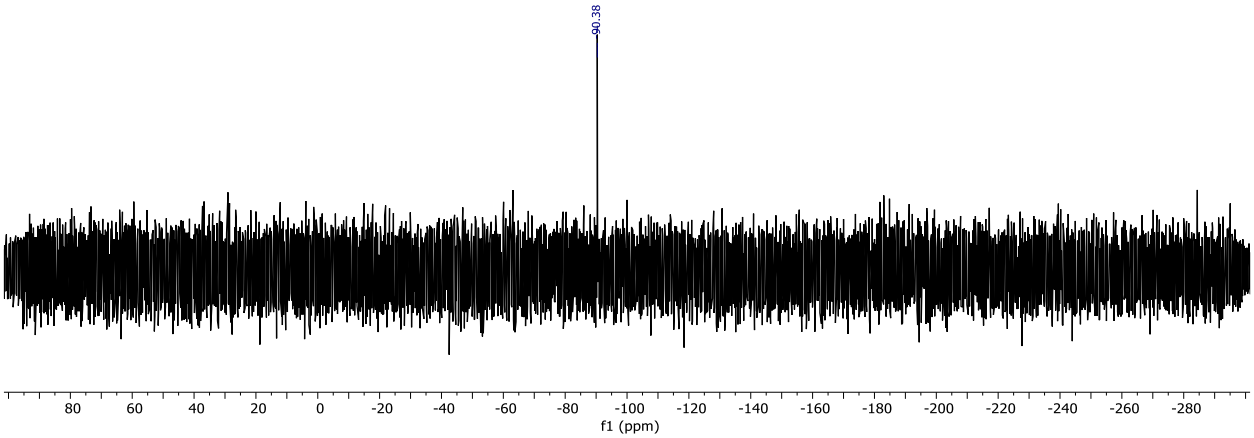

Figure 5.37. ^{29}Si NMR of **6-[Et$_3$NH]** in CD_3CN.

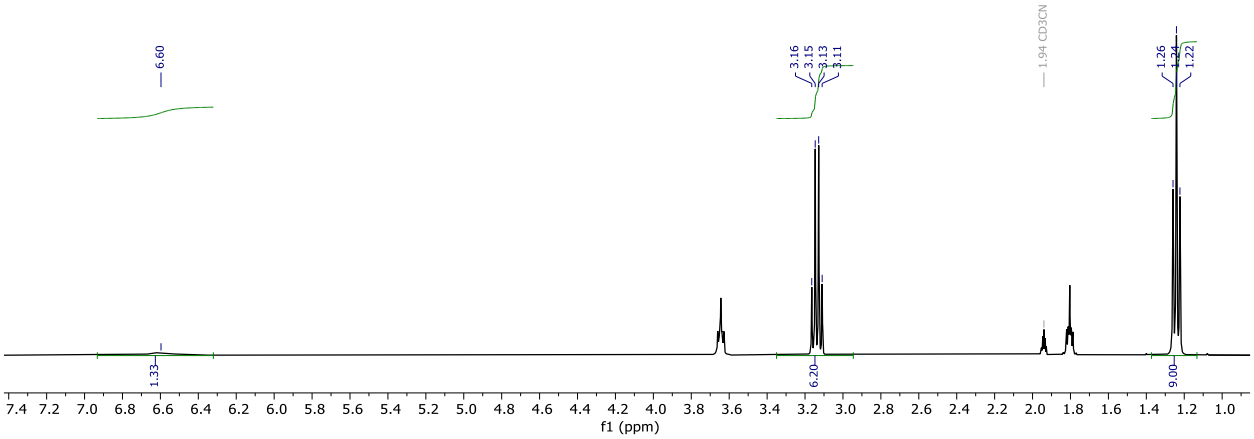

Figure 5.38. ^{1}H NMR of **7-[Et$_3$NH]** in CD_3CN.

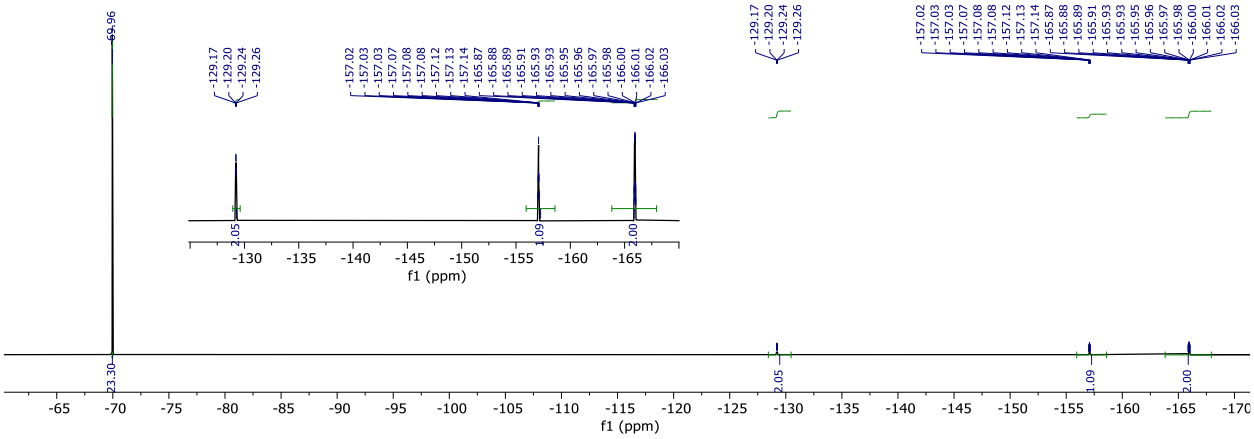

Figure 5.39. ^{19}F NMR of **7-[Et$_3$NH]** in CD_3CN.

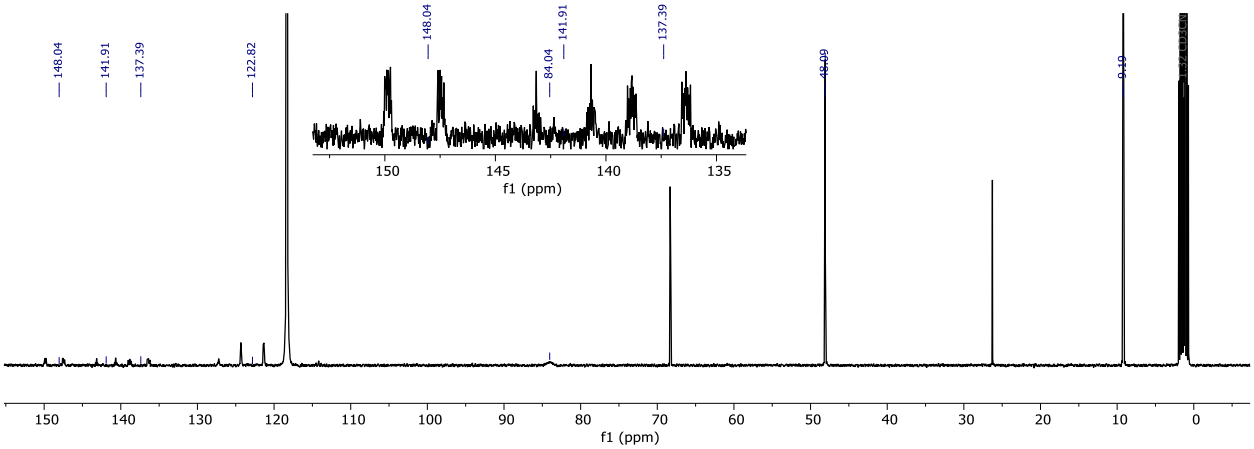

Figure 5.40. ^{13}C NMR of **7-[Et$_3$NH]** in CD_3CN.

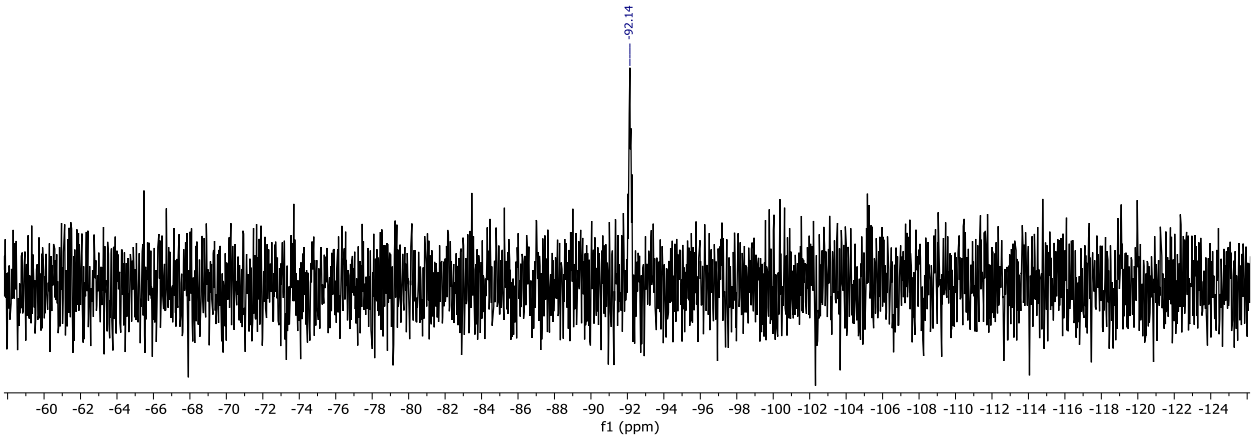

Figure 5.41. ^{29}Si NMR of **7-[Et$_3$NH]** in CD_3CN.

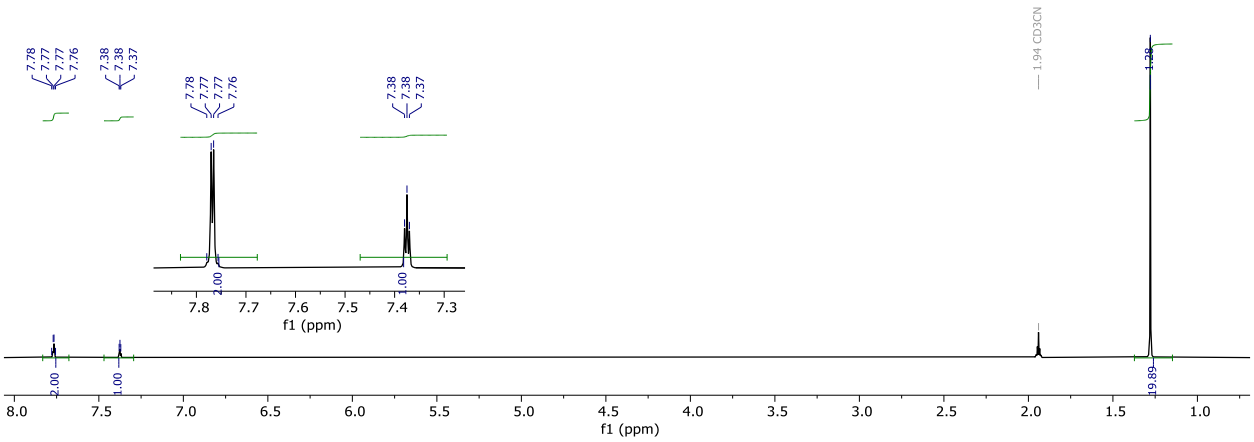

Figure 5.42. ^{1}H NMR of **1-[Na]** in CD_3CN.

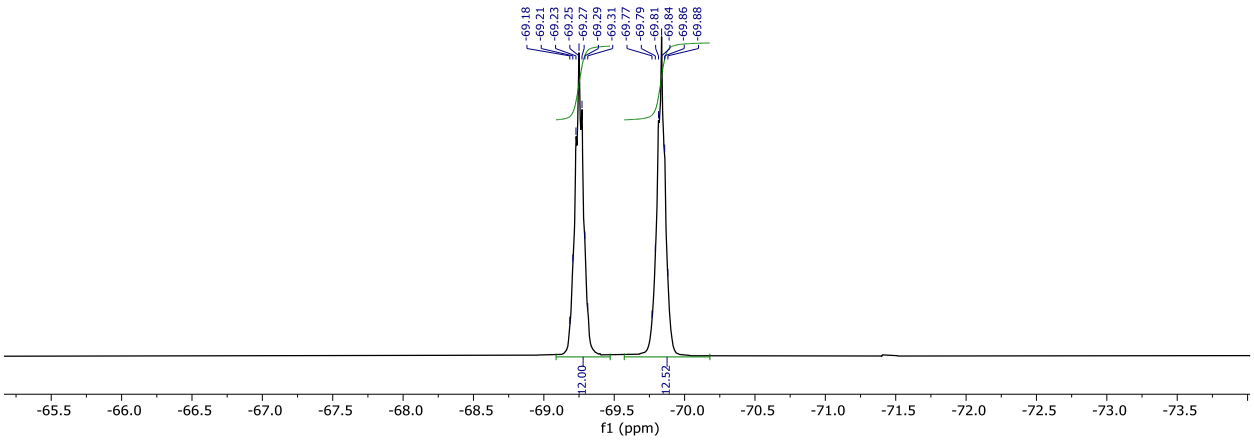

Figure 5.43. ^{19}F NMR of **1-[Na]** in CD_3CN.

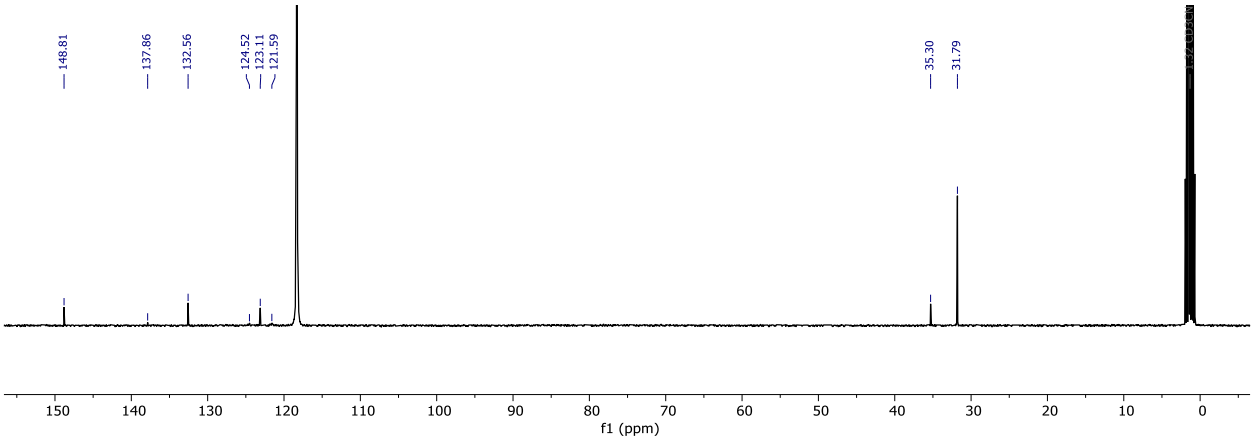

Figure 5.44. ^{13}C NMR of **1-[Na]** in CD_3CN.

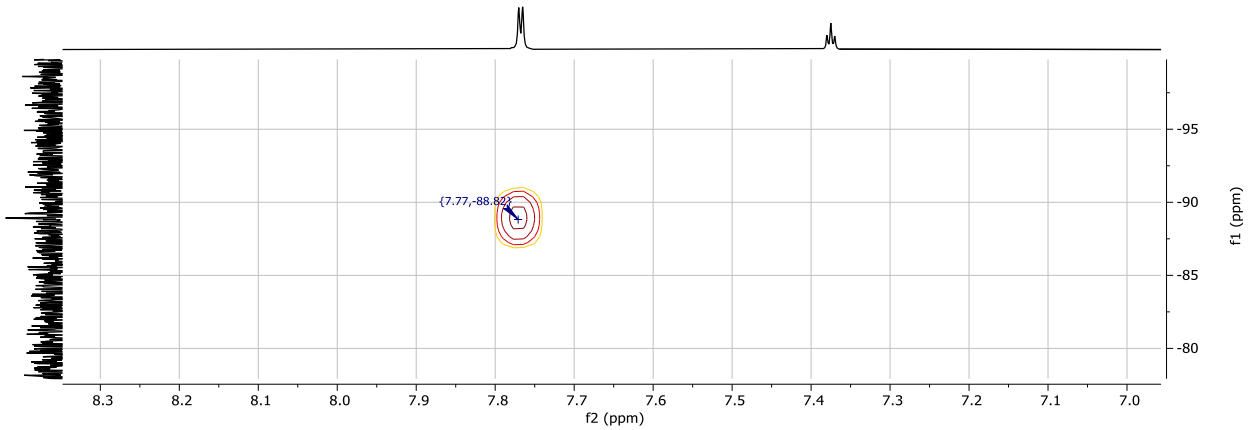

Figure 5.45. $^{1}H/^{29}Si$ HMBC NMR of **1-[Na]** in CD_3CN.

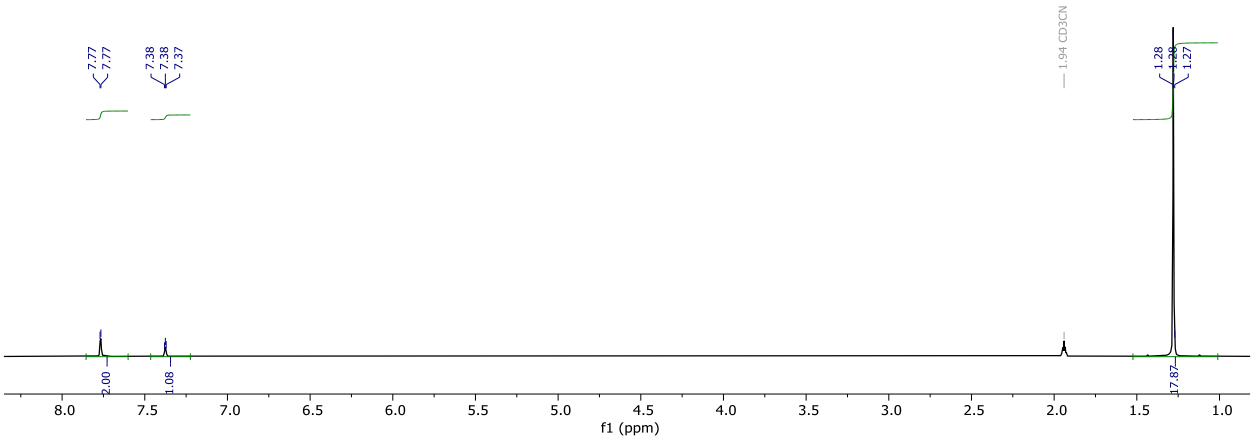

Figure 5.46. ^{1}H NMR of **1-[K]** in CD_3CN.

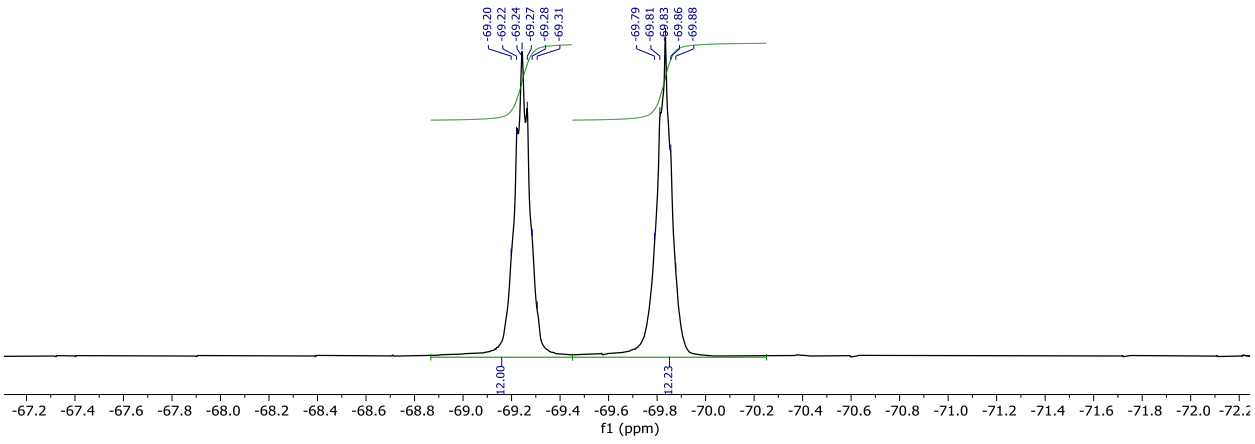

Figure 5.47. ^{19}F NMR of **1-[K]** in CD_3CN.

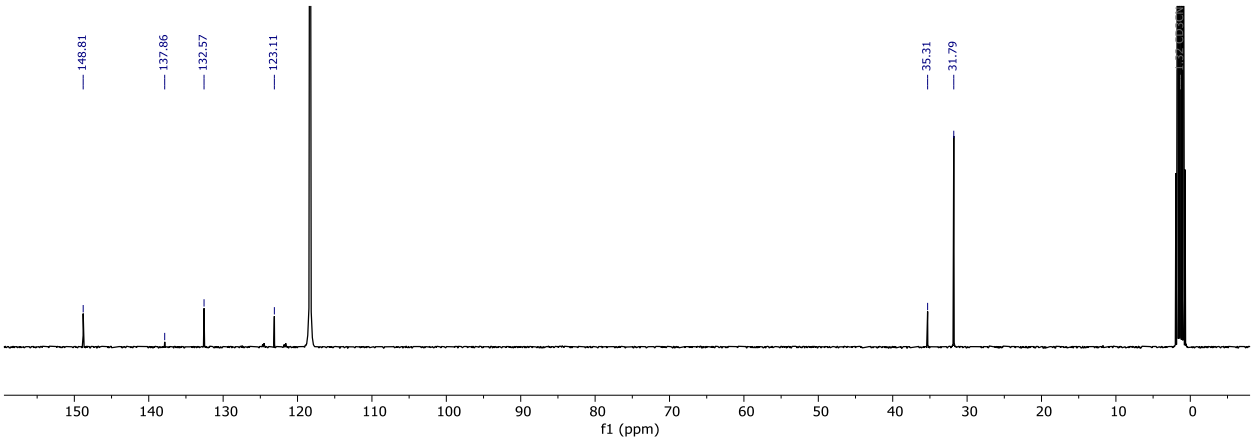

Figure 5.48. ^{13}C NMR of **1-[K]** in CD_3CN.

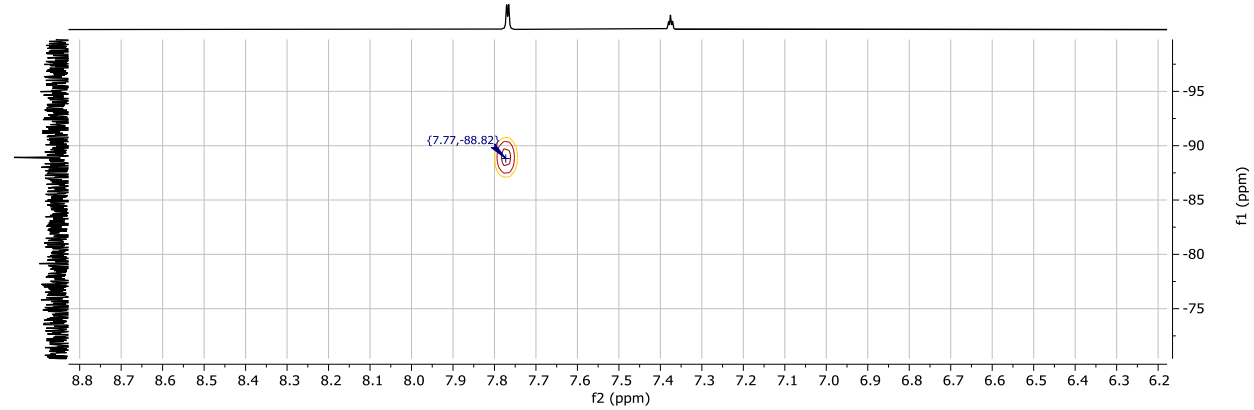

Figure 5.49. $^{1}H/^{29}Si$ NMR of **1-[K]** in CD_3CN.

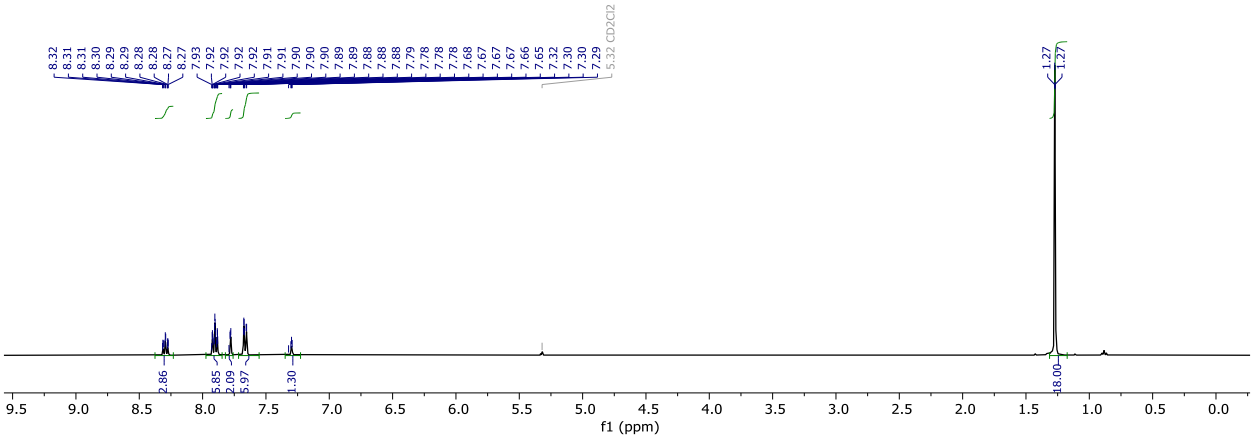

Figure 5.50. ^{1}H NMR of **1-[Ph$_3$C]** in CD_3CN.

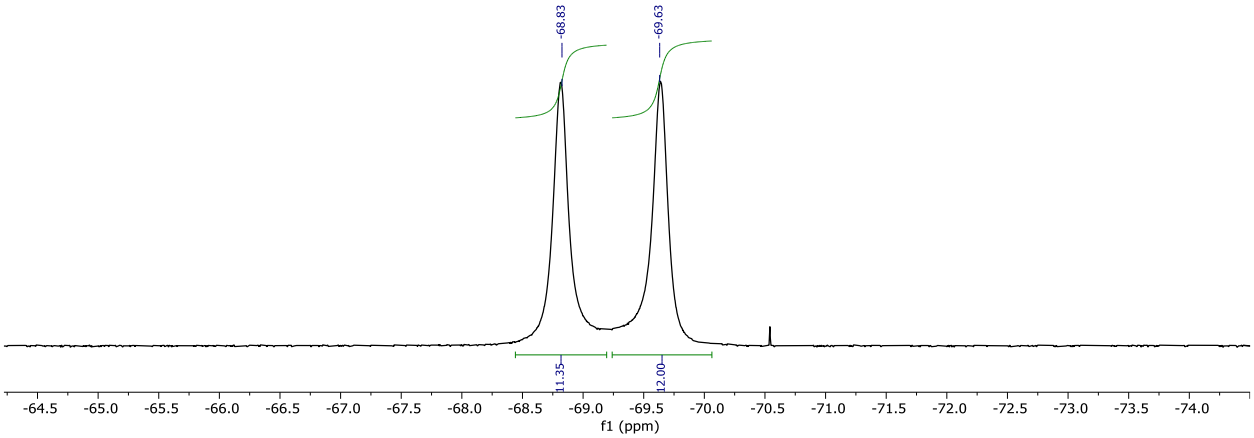

Figure 5.51. ^{19}F NMR of **1-[Ph$_3$C]** in CD_3CN.

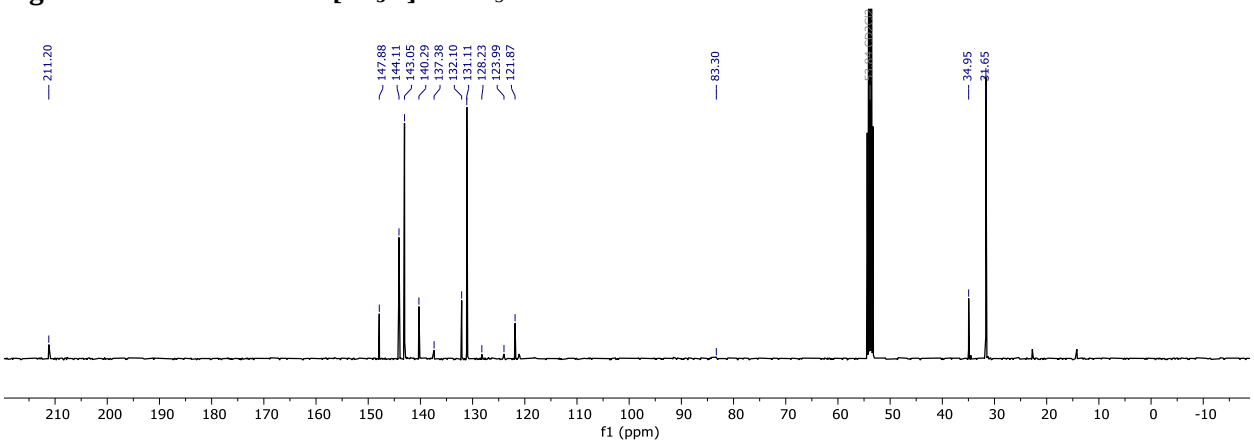

Figure 5.52. ^{13}C NMR of **1-[Ph$_3$C]** in CD_3CN.

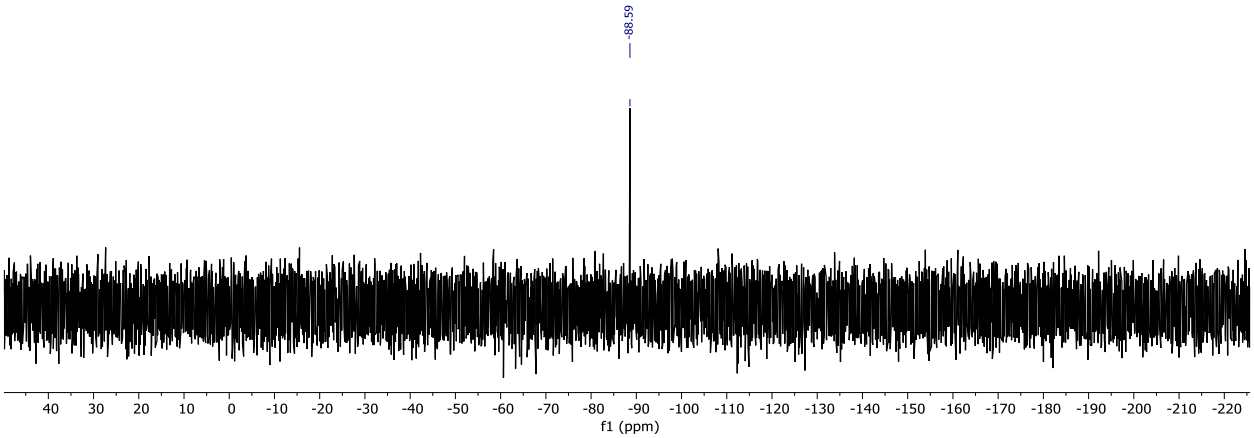

Figure 5.53. ^{29}Si NMR of **1-[Ph$_3$C]** in CD_3CN.

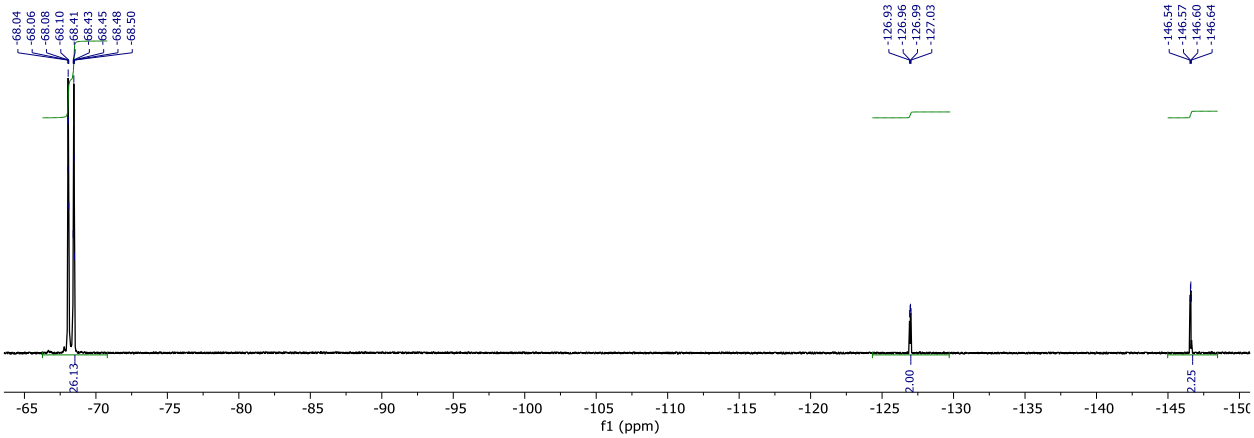

Figure 5.54. ^{19}F NMR of **[Li][^{R}SiF] R = 3',5'-di-tert-butyl-2,3,5,6-tetrafluoro-1,1'-biphenyl** in THF-h_8.

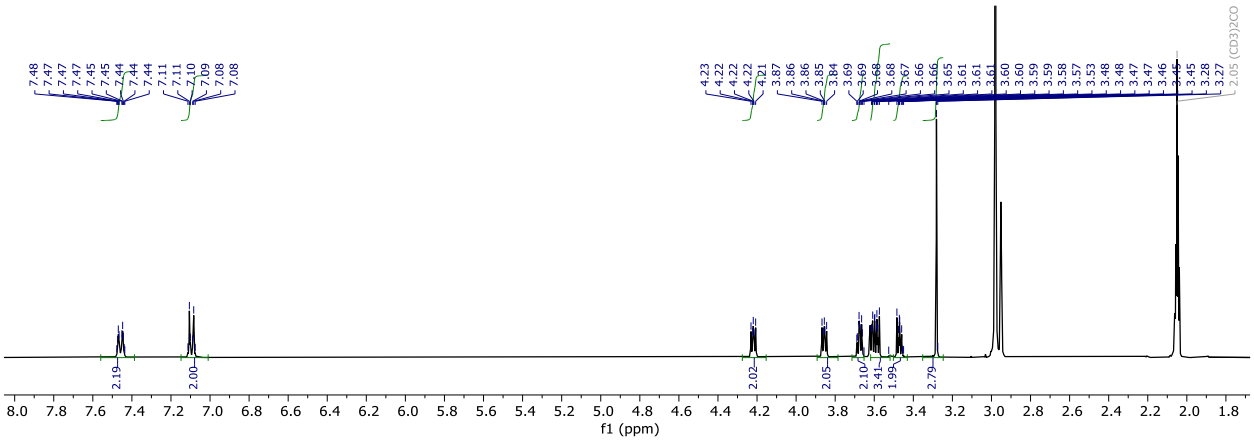

Figure 5.55. ^{1}H NMR of **[Li][^{R}SiF] R = 2,3,5,6-tetrafluoro-4'-(2-(2-(2-methoxyethoxy)ethoxy)ethoxy)-1,1'-biphenyl** in Acetone-d_6.

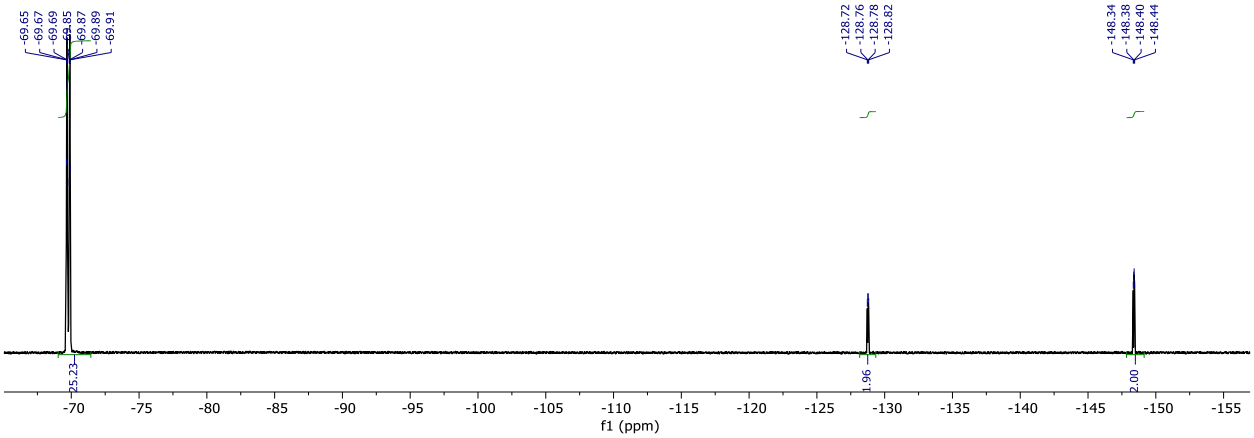

Figure 5.56. ^{19}F NMR of **[Li][^{R}SiF] R = 2,3,5,6-tetrafluoro-4'-(2-(2-(2-methoxyethoxy)ethoxy)ethoxy)-1,1'-biphenyl** in Acetone-d_6.

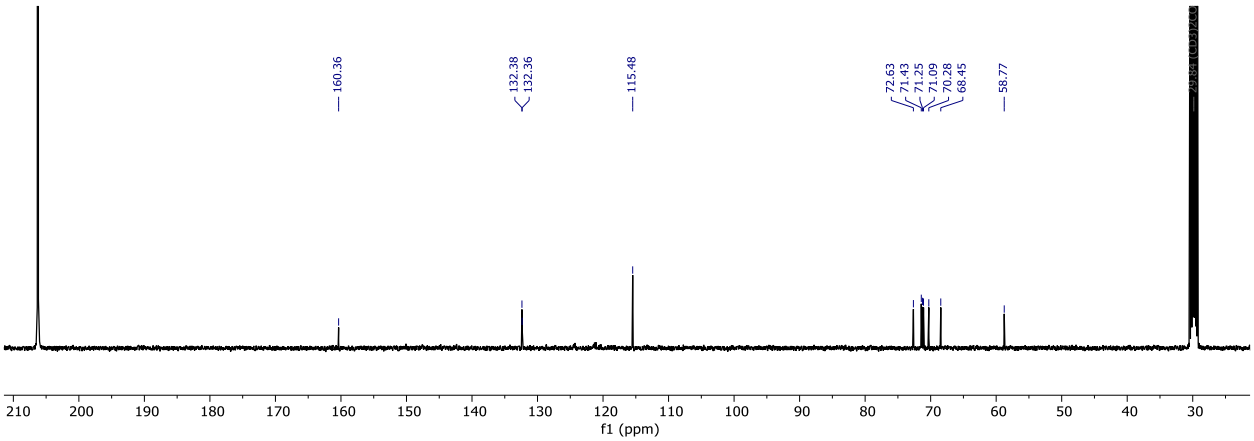

Figure 5.57. ^{13}C NMR of **[Li][^{R}SiF] R = 2,3,5,6-tetrafluoro-4'-(2-(2-(2-methoxyethoxy)ethoxy)ethoxy)-1,1'-biphenyl** in Acetone-d_6.

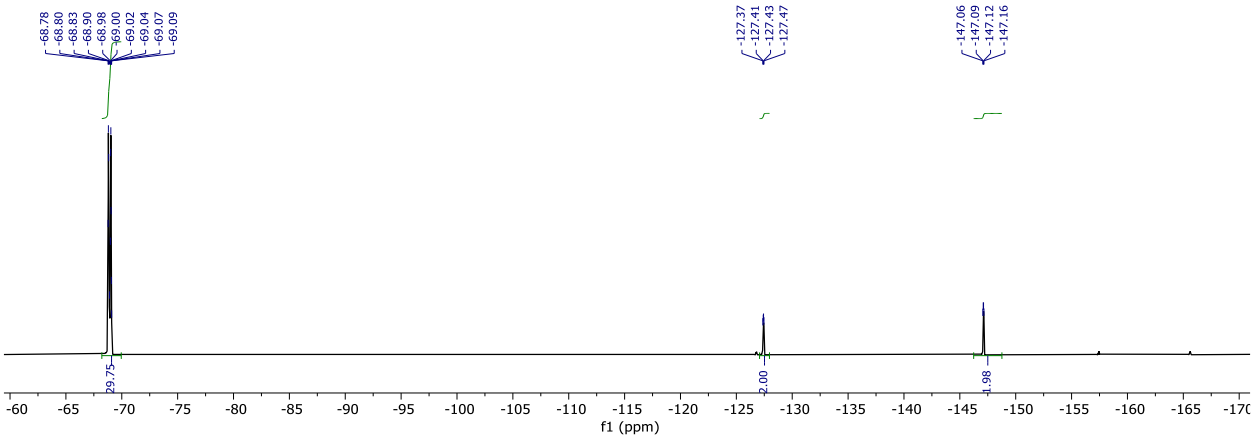

Figure 5.58. ^{19}F NMR of **[Li][^{R}SiF] R = trimethyl((2',3',5',6'-tetrafluoro-[1,1'-biphenyl]-4-yl)ethynyl)silane** in THF-h_8.

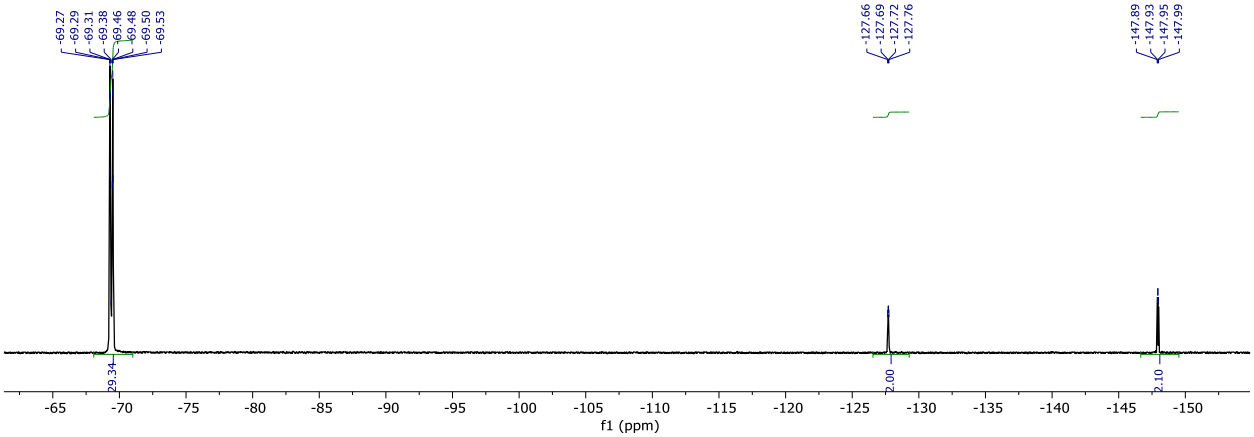

Figure 5.59. ^{19}F NMR of **[Li][^{R}SiF] R = 4'-bromo-2,3,5,6-tetrafluoro-1,1'-biphenyl** in Acetone-d_6.

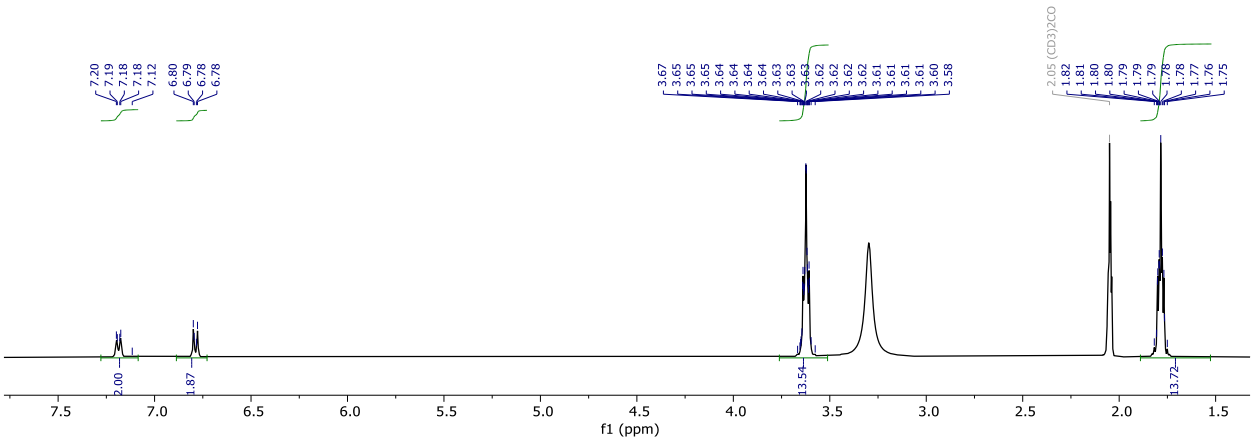

Figure 5.60. ^{1}H NMR of **[Li][^{R}SiF] R = 2',3',5',6'-tetrafluoro-[1,1'-biphenyl]-4-ol** in Acetone-d_6.

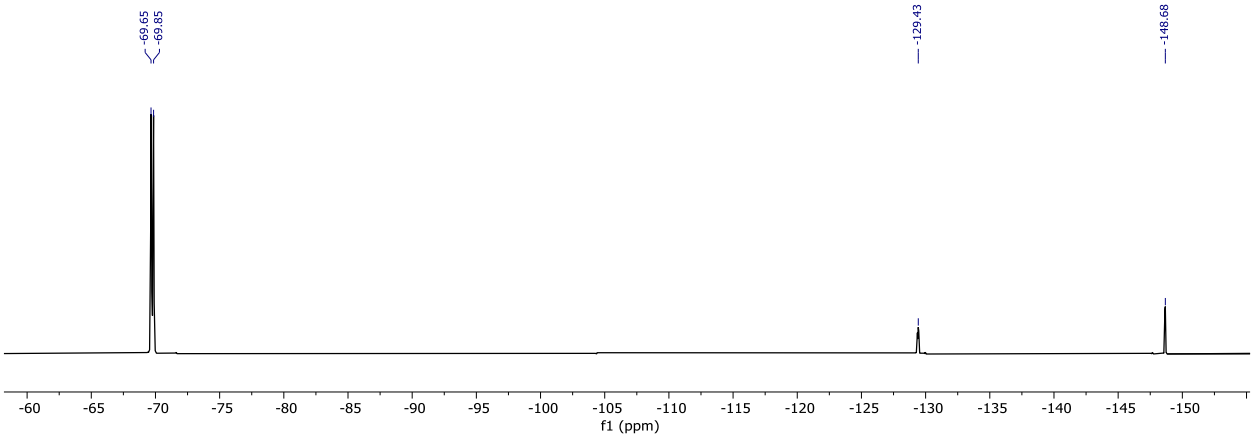

Figure 5.61. ^{19}F NMR of **[Li][^{R}SiF] R = 2',3',5',6'-tetrafluoro-[1,1'-biphenyl]-4-ol** in Acetone-d_6.

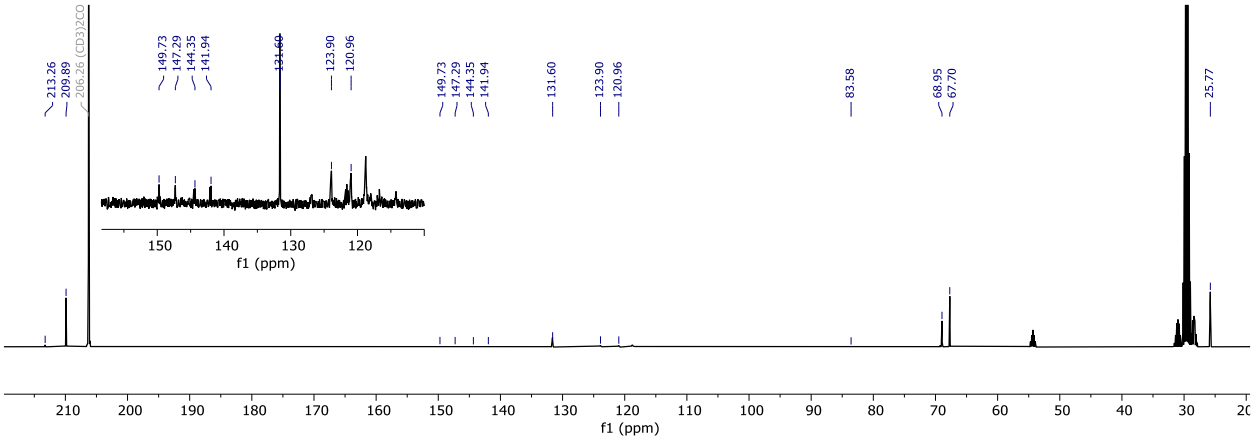

Figure 5.62. ^{13}C NMR of **[Li][^{R}SiF] R = 2',3',5',6'-tetrafluoro-[1,1'-biphenyl]-4-ol** in Acetone-d_6.

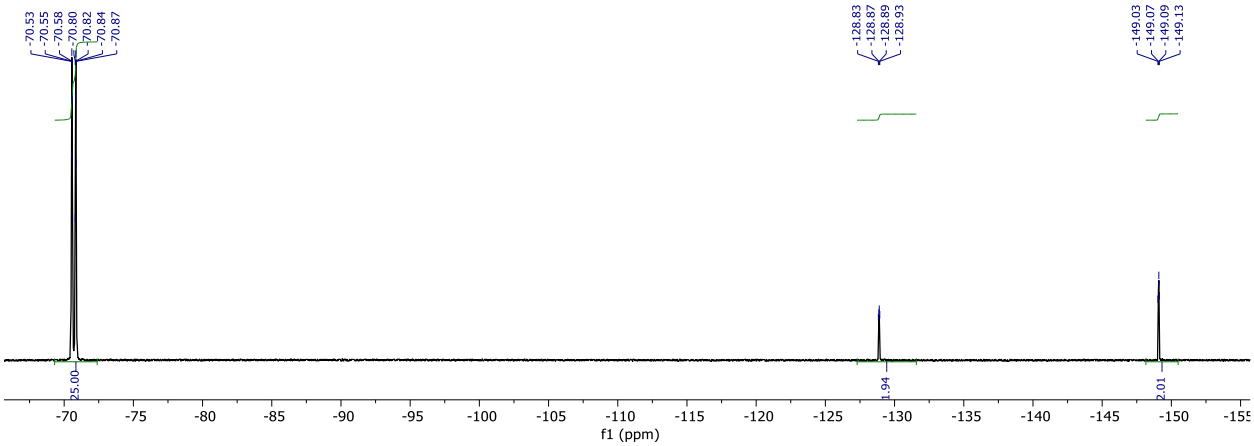

Figure 5.63. ^{19}F NMR of **Dianionic ^{R}SiF** in THF-h_8.

REFERENCES:

1. Beck, W.; Suenkel, K., Metal complexes of weakly coordinating anions. Precursors of strong cationic organometallic Lewis acids. *Chem. Rev.* **1988,** *88* (7), 1405-1421. 10.1021/cr00089a017
2. Chen, E. Y.-X.; Marks, T. J., Cocatalysts for Metal-Catalyzed Olefin Polymerization: Activators, Activation Processes, and Structure−Activity Relationships. *Chem. Rev.* **2000,** *100* (4), 1391-1434. 10.1021/cr980462j
3. Reed, C. A., Carboranes: A New Class of Weakly Coordinating Anions for Strong Electrophiles, Oxidants, and Superacids. *Acc. Chem. Res.* **1998,** *31* (3), 133-139. 10.1021/ar970230r
4. Strauss, S. H., The search for larger and more weakly coordinating anions. *Chem. Rev.* **1993,** *93* (3), 927-942. 10.1021/cr00019a005
5. Riddlestone, I. M.; Kraft, A.; Schaefer, J.; Krossing, I., Taming the Cationic Beast: Novel Developments in the Synthesis and Application of Weakly Coordinating Anions. *Angew. Chem. Int. Ed.* **2018,** *57* (43), 13982-14024. 10.1002/anie.201710782
6. Rosenthal, M. R., The myth of the non-coordinating anion. *J. Chem. Educ.* **1973,** *50* (5), 331. 10.1021/ed050p331
7. Connelly, N. G.; Geiger, W. E., Chemical Redox Agents for Organometallic Chemistry. *Chem. Rev.* **1996,** *96* (2), 877-910. 10.1021/cr940053x
8. Krossing, I.; Raabe, I., Noncoordinating Anions—Fact or Fiction? A Survey of Likely Candidates. *Angew. Chem. Int. Ed.* **2004,** *43* (16), 2066-2090. 10.1002/anie.200300620
9. Fisher, S. P.; Tomich, A. W.; Lovera, S. O.; Kleinsasser, J. F.; Guo, J.; Asay, M. J.; Nelson, H. M.; Lavallo, V., Nonclassical Applications of closo-Carborane Anions: From Main Group Chemistry and Catalysis to Energy Storage. *Chem. Rev.* **2019,** *119* (14), 8262-8290. 10.1021/acs.chemrev.8b00551
10. Krossing, I.; Reisinger, A., Chemistry with weakly-coordinating fluorinated alkoxyaluminate anions: Gas phase cations in condensed phases? *Coord. Chem. Rev.* **2006,** *250* (21), 2721-2744. 10.1016/j.ccr.2005.10.023
11. Barrière, F.; Geiger, W. E., Use of Weakly Coordinating Anions to Develop an Integrated Approach to the Tuning of $\Delta E_{1/2}$ Values by Medium Effects. *J. Am. Chem. Soc.* **2006,** *128* (12), 3980-3989. 10.1021/ja058171x
12. Bahr, S. R.; Boudjouk, P., Trityl tetrakis[3,5-bis(trifluoromethyl)phenyl]borate: a new hydride abstraction reagent. *J. Org. Chem.* **1992,** *57* (20), 5545-5547. 10.1021/jo00046a048
13. Liberman-Martin, A. L.; Bergman, R. G.; Tilley, T. D., Lewis Acidity of Bis(perfluorocatecholato)silane: Aldehyde Hydrosilylation Catalyzed by a Neutral Silicon Compound. *J. Am. Chem. Soc.* **2015,** *137* (16), 5328-5331. 10.1021/jacs.5b02807
14. Maskey, R.; Schädler, M.; Legler, C.; Greb, L., Bis(perchlorocatecholato)silane—A Neutral Silicon Lewis Super Acid. *Angew. Chem. Int. Ed.* **2018,** *57* (6), 1717-1720. 10.1002/anie.201712155
15. Hartmann, D.; Schädler, M.; Greb, L., Bis(catecholato)silanes: assessing, rationalizing and increasing silicon's Lewis superacidity. *Chemical Science* **2019,** *10* (31), 7379-7388. 10.1039/C9SC02167A
16. Thorwart, T.; Roth, D.; Greb, L., Bis(pertrifluoromethylcatecholato)silane: Extreme Lewis Acidity Broadens the Catalytic Portfolio of Silicon. *Chem. Eur. J.* **2021,** *27* (40), 10422-10427. 10.1002/chem.202101138

17. Tschernuth, F. S.; Thorwart, T.; Greb, L.; Hanusch, F.; Inoue, S., Bis(perfluoropinacolato)silane: A Neutral Silane Lewis Superacid Activates Si−F Bonds. *Angew. Chem. Int. Ed.* **2021,** *60* (49), 25799-25803. 10.1002/anie.202110980
18. Müller, L. O.; Himmel, D.; Stauffer, J.; Steinfeld, G.; Slattery, J.; Santiso-Quiñones, G.; Brecht, V.; Krossing, I., Simple Access to the Non-Oxidizing Lewis Superacid $PhF{\rightarrow}Al(OR^F)_3$ (R^F=$C(CF_3)_3$). *Angew. Chem. Int. Ed.* **2008,** *47* (40), 7659-7663. 10.1002/anie.200800783
19. Frye, C. L., Pentacoordinate Silicon Derivatives. II.1 Salts of Bis(o-arylenedioxy) organosiliconic Acids. *J. Am. Chem. Soc.* **1964,** *86* (15), 3170-3171. 10.1021/ja01069a054
20. Frye, C. L., Pentacoordinate silicon derivatives. IV. Alkylammonium siliconate salts derived from aliphatic 1,2-diols. *J. Am. Chem. Soc.* **1970,** *92* (5), 1205-1210. 10.1021/ja00708a016
21. Chuit, C.; Corriu, R. J. P.; Reye, C.; Young, J. C., Reactivity of penta- and hexacoordinate silicon compounds and their role as reaction intermediates. *Chem. Rev.* **1993,** *93* (4), 1371-1448. 10.1021/cr00020a003
22. Kays, D. L.; Rossin, A.; Day, J. K.; Ooi, L.-L.; Aldridge, S., Synthetic and reaction chemistry of heteroatom stabilized boryl and cationic borylene complexes. *Dalton Transactions* **2006,** (2), 399-410. 10.1039/B512275A
23. Scerba, M. T.; Leavitt, C. M.; Diener, M. E.; DeBlase, A. F.; Guasco, T. L.; Siegler, M. A.; Bair, N.; Johnson, M. A.; Lectka, T., NH^+–F Hydrogen Bonding in a Fluorinated "Proton Sponge" Derivative: Integration of Solution, Solid-State, Gas-Phase, and Computational Studies. *J. Org. Chem.* **2011,** *76* (19), 7975-7984. 10.1021/jo2015328
24. Carreras, L.; Rovira, L.; Vaquero, M.; Mon, I.; Martin, E.; Benet-Buchholz, J.; Vidal-Ferran, A., Syntheses, characterisation and solid-state study of alkali and ammonium BArF salts. *RSC Advances* **2017,** *7* (52), 32833-32841. 10.1039/C7RA05928K
25. Martínez-Martínez, A. J.; Weller, A. S., Solvent-free anhydrous Li^+, Na^+ and K^+ salts of $[B(3,5\text{-}(CF_3)_2C_6H_3)_4]^-$, $[BArF_4]^-$. Improved synthesis and solid-state structures. *Dalton Transactions* **2019,** *48* (11), 3551-3554. 10.1039/C9DT00235A
26. Protchenko, A. V.; Bates, J. I.; Saleh, L. M. A.; Blake, M. P.; Schwarz, A. D.; Kolychev, E. L.; Thompson, A. L.; Jones, C.; Mountford, P.; Aldridge, S., Enabling and Probing Oxidative Addition and Reductive Elimination at a Group 14 Metal Center: Cleavage and Functionalization of E–H Bonds by a Bis(boryl)stannylene. *J. Am. Chem. Soc.* **2016,** *138* (13), 4555-4564. 10.1021/jacs.6b00710
27. Dong, Z.; Pezzato, C.; Sienkiewicz, A.; Scopelliti, R.; Fadaei-Tirani, F.; Severin, K., SET processes in Lewis acid–base reactions: the tritylation of N-heterocyclic carbenes. *Chemical Science* **2020,** *11* (29), 7615-7618. 10.1039/D0SC01278E
28. Dasgupta, A.; Richards, E.; Melen, R. L., Frustrated Radical Pairs: Insights from EPR Spectroscopy. *Angew. Chem. Int. Ed.* **2021,** *60* (1), 53-65. 10.1002/anie.202010633
29. Klare, H. F. T.; Albers, L.; Süsse, L.; Keess, S.; Müller, T.; Oestreich, M., Silylium Ions: From Elusive Reactive Intermediates to Potent Catalysts. *Chem. Rev.* **2021,** *121* (10), 5889-5985. 10.1021/acs.chemrev.0c00855
30. Drent, E.; Van Broekhoven, J. A. M.; Doyle, M. J., Efficient palladium catalysts for the copolymerization of carbon monoxide with olefins to produce perfectly alternating polyketones. *J. Organomet. Chem.* **1991,** *417* (1), 235-251. 10.1016/0022-328X(91)80176-K
31. Drent, E.; Budzelaar, P. H. M., Palladium-Catalyzed Alternating Copolymerization of Alkenes and Carbon Monoxide. *Chem. Rev.* **1996,** *96* (2), 663-682. 10.1021/cr940282j

32. Ledford, J.; Shultz, C. S.; Gates, D. P.; White, P. S.; DeSimone, J. M.; Brookhart, M., Bond Angle Effects on the Migratory Insertion of Ethylene and Carbon Monoxide into Palladium(II)−Methyl Bonds in Complexes Bearing Bidentate Phosphine Ligands. *Organometallics* **2001,** *20* (25), 5266-5276. 10.1021/om010489k
33. Shultz, C. S.; Ledford, J.; DeSimone, J. M.; Brookhart, M., Kinetic Studies of Migratory Insertion Reactions at the (1,3-Bis(diphenylphosphino)propane)Pd(II) Center and Their Relationship to the Alternating Copolymerization of Ethylene and Carbon Monoxide. *J. Am. Chem. Soc.* **2000,** *122* (27), 6351-6356. 10.1021/ja994251n
34. Rohrbach, S.; Smith, A. J.; Pang, J. H.; Poole, D. L.; Tuttle, T.; Chiba, S.; Murphy, J. A., Concerted Nucleophilic Aromatic Substitution Reactions. *Angew. Chem. Int. Ed.* **2019,** *58* (46), 16368-16388. 10.1002/anie.201902216
35. Pangborn, A. B.; Giardello, M. A.; Grubbs, R. H.; Rosen, R. K.; Timmers, F. J., Safe and Convenient Procedure for Solvent Purification. *Organometallics* **1996,** *15* (5), 1518-1520. 10.1021/om9503712
36. Crans, D. C.; Tarlton, M. L.; McLauchlan, C. C., Trigonal Bipyramidal or Square Pyramidal Coordination Geometry? Investigating the Most Potent Geometry for Vanadium Phosphatase Inhibitors. *Eur. J. Inorg. Chem.* **2014,** *2014* (27), 4450-4468. 10.1002/ejic.201402306

CHAPTER 6. Magnesium Silicates as Electrolytes for Next-Generation Mg Batteries

For author contributions, see Page vii.

ABSTRACT

We report the synthesis and electrochemical performance of a new class of magnesium electrolytes for next-generation batteries. The electrolytes are based on weakly-coordinating anions with alkyl or aryl (**R**) substituted ***si***licates bearing ***f***luorinated pinacolate ligands, **"[^{R}SiF]$^{-}$"**. $[Mg(DME)_3][^{Me}SiF]_2$ demonstrates remarkable performance with good stability with moderate conditioning, coulumbic efficiency (> 96%), and current density (~100 $mAcm^{-2}$). However, the electrochemical performance is intrinsically sensitive, requiring careful study of many parameters including the impact of MgR_2 additives (identity and concentration), cycling protocol, synthetic route, Pt working electrode, etc. to understand how the electrochemical performance is impacted. While addition of $MgMe_2$ improves electrochemical performance, it is not inherently required for reversible Mg deposition and stripping. Following an extensive investigation of the cyclic voltammetry (CV) performance of $[Mg(DME)_3][^{Me}SiF]_2$, preliminary screening of additional $Mg(DME)_3[^{R}SiF]_2$ variants was conducted.

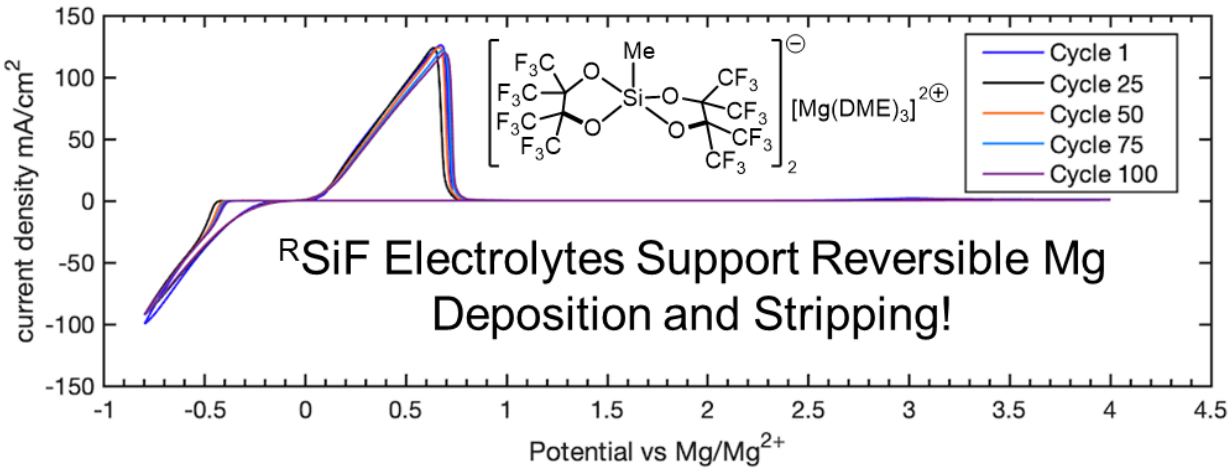

INTRODUCTION

As the use of renewable energy continually grows to replace fossil fuels and coal, there is a paramount need for energy storage to compensate for the intermittent nature of these greener energy sources.[2-3] Li-ion batteries (LIBs) are the current industry standard, and their use continues to climb rapidly.[4-7] Demand for LIBs is expected to increase more than 10x between 2020 and 2030 to an astonishing ~2000 GWh.[4] However, there are rising concerns over (1) the price, availability, and uneven global distribution of Li,[8-9] (2) the availability of Co and Ni (key components of LIB cathodes),[12-13] (3) the safety hazard of LIBs with a combustible material and oxidizing agent,[14-15] and (4) volumetric energy density.[16] As modern LIBs approach their theoretical capacity limits (dictated by the density of available crystallographic sites in intercalation cathodes), research has shifted to focus on anode development—use of Li-metal anodes or Li-Si anodes—but these are both challenging due to the formation of Li dendrites or large volume changes, respectively. To accommodate the energy storage requirements of the future, research has shifted to focus on development of alternative battery technologies.

Many next-generation batteries have been explored as viable candidates to replace Li, including systems based on monovalents (Na^+ and K^+),[17-18] divalents (Mg^{2+}, Ca^{2+}, and Zn^{2+})[19-21] and trivalents (Al^{3+}).[22-24] A comparison of the atomic radii, energy densities (gravimetric and volumetric), abundance in the earth's crust, and standard reduction potentials for Li and next-generation systems is shown in Figure 6.1.

Compared to other next-generation systems and existing Li-based technologies, Mg-based systems have clear logistical and technical advantages. Mg (1) is significantly more abundant than Li (2.6 wt. % in Earth's crust vs. 0.0065 %),[25] (2) has a theoretical volumetric capacity 2x greater

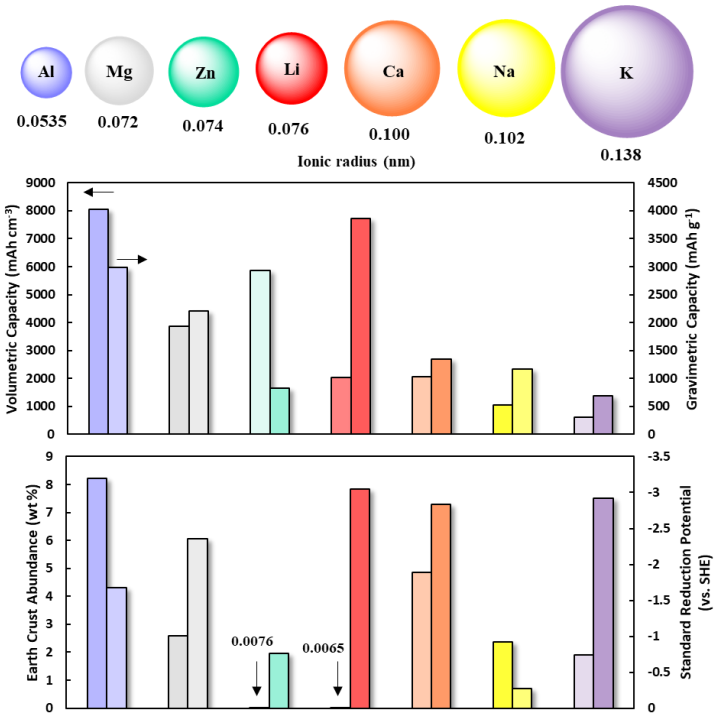

Figure 6.1: Comparison of ionic radius, volumetric capacity, gravimetric capacity, abundance in the earth's crust, and standard reduction potential in candidates for next-generation batteries. Figure adapted from Ref.[24]

than Li (due to the similar ionic radii, 0.072 and 0.076 nm for Mg^{2+} and Li^{+}, respectively and divalent charge of Mg^{2+}), and (3) Mg is much less prone to dendrite formation, enabling the use of Mg metal anodes for high energy density. The increased abundance alleviates concerns about limited resources; the increased volumetric density is particularly attractive for the development of small energy storage devices, and the less dendritic Mg anodes address the safety concerns posed by the reactivity and dendritic behavior of Li anodes.

One of the main challenges of Mg batteries is electrolyte compatibility. General design strategies for electrolytes prioritize ionic conductivity, chemical and electrochemical stability (within a large electrochemical window to enable use with high-voltage cathodes), and moderate interactions between the active ion and solvent molecules (to facilitate sufficient solubility and reasonable desolvation energy).[26] While LIBs electrolytes achieve excellent performance with simple fluorinated salts (PF_6^-, BF_4^-, etc.), balancing these criteria is inherently more challenging

for Mg^{2+}. Anion decomposition and formation of MgF_2 results in surface passivation.[27-28] Formation of passivation films can be attenuated by the use of (corrosive) chloride-containing electrolytes. This is exemplified by the success of early Mg electrolytes including the magnesium aluminum chloride complex (MACC)[29-31] and the all-phenyl complex (APC).[32] However, the necessity of Cl^- is not ideal—the oxidative stability of these electrolytes is limited to < 3.5 V (vs. Mg/Mg^{2+}) due to oxidative formation of chlorine gas, and these electrolytes are corrosive, rendering them incompatible with materials of many common cell components (including stainless steel).[28]

Research has shifted focus towards the use of halide-free electrolyte systems to increase the compatibility with cell components. Beyond $Mg(PF_6)_2$, systems based on $Mg(BH_4)_2$,[33-35] $Mg(BPh_2R_2)_2$ (R = ^{n}Bu or Ph),[28, 36] and $Mg(TFSI)_2$[37-41] have been shown to reversibly plate and strip Mg. However, each of these systems have inherent limitations: $Mg(BH_4)_2$ is water-sensitive, poorly conductive (without additional added salts), and has limited oxidative stability (1.7 V vs. Mg/Mg^{2+}).[33] $Mg(BPh_2R_2)_2$ (R = ^{n}Bu or Ph) electrolytes also suffer from limited oxidative stability (due to the electron-rich alkyl and aryl substituents), limiting practical use with high-voltage cathode materials.[28] $Mg(TFSI)_2$, while more oxidatively stable, suffers from high reductive overpotentials and is prone to significant decomposition of the TFSI anion.[42-43]

Current research on electrolyte design for Mg-batteries focuses on designer weakly-coordinating anions (WCAs). Use of bulkier, less nucleophilic WCA-supported electrolytes imparts higher ionic conductivity, stability, and reversibility. Aluminates and borates featuring bulky and electron-withdrawing fluorinated alkoxide ligands such as $[B(O(CH(CF_3)_2))_4]^-$,[44] $[Al(O(CH(CF_3)_2))_4]^-$[1, 45-46] and $[B(O_2C_2(CF_3)_4)_2]^-$[47] have been shown to support reversible Mg

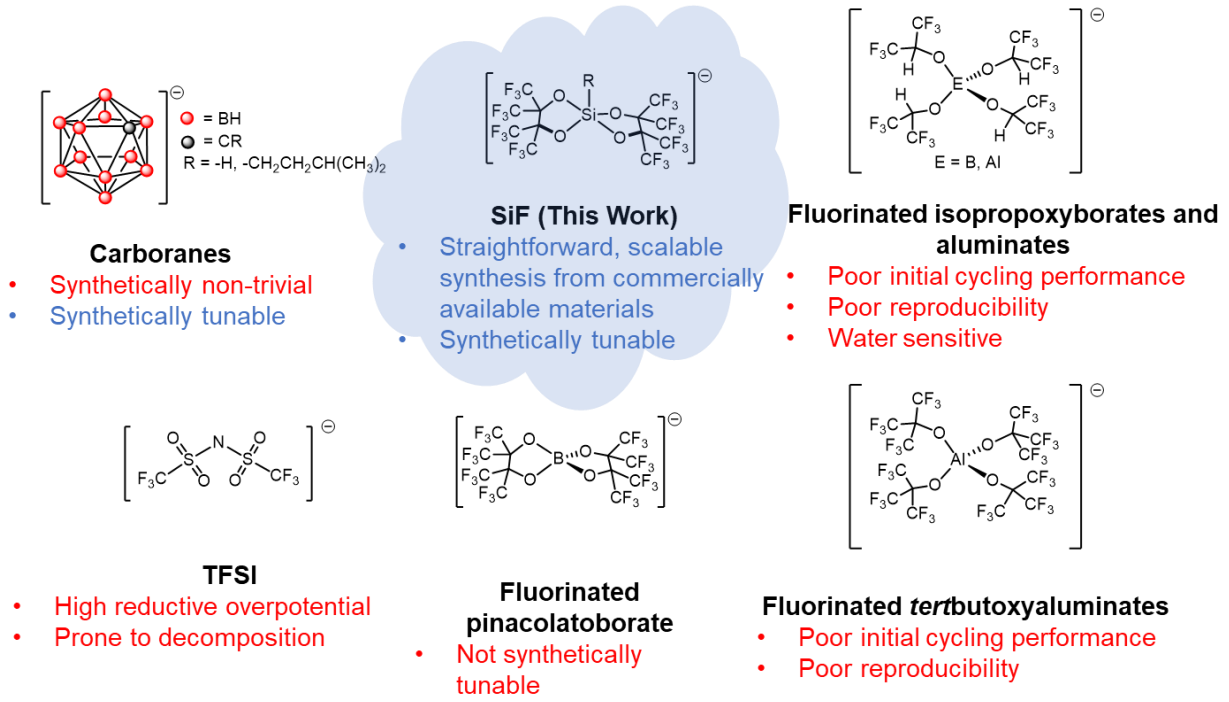

Figure 6.2: Fluorinated, halide-free Mg electrolytes with associated challenges

deposition and stripping. Monocarborane electrolytes have also demonstrated remarkable electrochemical performance,[41,48-51,52] and alkylation can significantly improve the solubility of carboranes,[48] (enabling the use of DME instead of requiring longer chained, more solubilizing glymes). While many of these systems have shown promise, there are many challenges which remain (see discussion below)

Batch Dependence

Magnesium electrochemistry is intrinsically sensitive, where minor impurities can be reduced on the Mg surface to form insulating surface films.[27, 53] This is inherently different than Li systems where surface films on Li anodes form a solid-electrode interphase (SEI) which conducts Li, retaining electrochemical performance. Because the majority of Mg electrolytes are not commercially available, they require synthetic preparation, with consideration of potential impurities arising from each step. Minor impurities in the commercially available starting materials must also be considered as they may carry through the synthesis and may dictate observed

electrochemical performance. While WCA-supported Mg electrolytes have seen considerable success, the field remains challenged by irreproducible, inconsistent electrolyte performance between published reports likely due, in part, to the sensitivity of Mg electrochemistry. To examine these challenges in depth, particularly the aspects of synthesis, the various preparations and performances of two electrolytes, $Mg[B(O(CH(CF_3)_2))_4]_2$ and $Mg[Al(O(CF_3)_3))_4]_2$, will be discussed.

$Mg[B(O(CH(CF_3)_2))_4]_2$, (commonly referred to in the literature as $Mg[B(HFIP)_4]_2$, demonstrated remarkable performance in the initial report, with a low deposition overpotential (~200 mV) and high columbic efficiency (98 %).[54] However, this performance (and reproducibility of performance) has been found to be dependent on the synthetic route (Scheme 6.1). $Mg[B(O(CH(CF_3)_2))_4]_2$ is prepared by protonlysis or transmetalation. When generated from direct protonolysis of $Mg(BH_4)_2$ by $(CF_3)_2CHOH$ (Scheme 6.1, left), different batches of $Mg[B(O(CH(CF_3)_2))_4]_2$ showed distinct electrochemical performance, ranging from reversible Mg deposition/stripping to no reversible performance.[45] $Mg[B(O(CH(CF_3)_2))_4]_2$ prepared by transmetalation from $B[OCH(CF_3)_2]_3$ and $Mg(OCH(CF_3)_2)_2$ generated *in situ* (Scheme 6.1, right) were found to have better electrochemical performance and consistency across different batches.[45] This improved performance and reproducibility was attributed to the presence of fewer inorganic impurities.

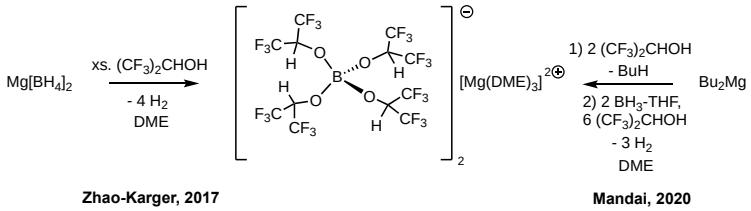

Scheme 6.1. Synthetic preparations of $Mg[B(O(CH(CF_3)_2))_4]_2$ with protonolysis (left) and transmetalation (right).

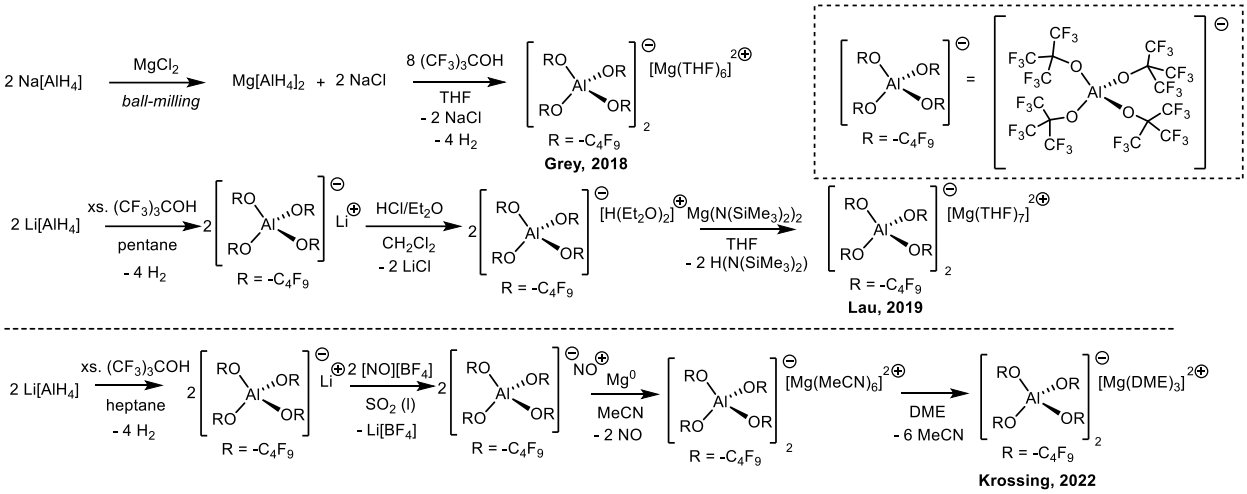

Scheme 6.2. Synthetic routes towards $[Mg(solvent)_n][Al(OC(CF_3)_4)]_2$ reported by Grey *et al*. (top)[1], Lau *et al* (middle).[10] and Krossing *et al.* (bottom)[11] that resulted in materials with different Mg deposition/stripping performance.

Similarly, the performance of $Mg[Al(O(CF_3)_3))_4]_2$ is dependent on the preparation (Scheme 6.2). Grey *et al.* reported a synthesis that starts from $NaAlH_4$ (Scheme 6.2, top), where the product, $[Mg(THF)_6][Al(O(CF_3)_3))_4]_2$, exhibited some reversible electrochemical performance. However, this synthetic route led to known chloride contamination of the final product (2.64 % by weight, lowered by 0.11 % by extraction into CH_2Cl_2).[1] Reversible performance was also observed for Lau *et. al.* (Scheme 6.2, middle),[10] when preparing $[Mg(solvent)_n][Al(OC(CF_3)_4)]_2$ beginning from $LiAlH_4$. Krossing *et al.*[11] developed a multi-step route, less susceptible to trace inorganic impurities, beginning from $LiAlH_4$. However, they were unable to obtain reversible Mg electrochemistry with the cleaner $[Mg(solvent)_n][Al(OC(CF_3)_4)]_2$ material, and subsequent addition of inorganic salts as additives did not result in reversible Mg electrochemistry.[11] Again, the reported differences in performance were attributed to different impurities in the electrolyte.

In a discussion about inconsistent performance in extensively studied Mg electrolytes, it is notable that carborane-based Mg electrolytes do not seem to exhibit the severe degree of batch/route dependence seen with aluminates and borates. While somewhat speculative, it is

important to note that carboranes require either (1) significant financial investment to purchase the $Cs^+[HCB_{11}H_{11}]$ precursor (~$1000/g)[55] or (2) advanced synthetic technique to access the materials, limiting the general use. Additionally, preparations of carborane electrolytes frequently involve recrystallization of the electrolytes prior to use, affording cleaner (and therefore more reproducible) material.

Possible contamination from synthetic routes

To understand the different impurities that can carry through a synthesis (which may explain the batch/route-dependent electrochemical performance discussed above), it helps to consider some general protocols used for electrolyte preparation, particularly synthetic protocols for alkoxyborate and aluminate WCA-based electrolytes. For many electrolytes, a salt metathesis reaction is necessary to exchange the cation to the desired Mg^{2+}. However, cation exchange without a strong thermodynamic driving force is not 100% effective (especially salt metathesis of magnesium halides with alkali metal cations).[56] The polarity of the solvent can dictate (1) the completion of the reaction and (2) the purity of the material. In addition, complete removal of all byproducts and/or starting materials is challenging in both hydrocarbon *and* ethereal solvents given the similar solubilities of the materials. Incomplete removal of reactants and byproducts cannot be detected by ^{1}H NMR spectroscopy, and detection instead requires inductively coupled plasma mass spectrometry (ICP-MS) or related analysis methods.

Protonlysis as a means of cation exchange (with R_2Mg (where R = alkyl or aryl groups) and/or $Mg(N(SiMe_3)_2)$) is generally more effective due to the difference in solubility of the starting materials (allowing for more effective removal of unreacted starting material), and the resulting byproducts are readily removed by drying *in vacuo* or washing. Incomplete removal of starting materials can be detected by ^{1}H NMR spectroscopy.

However, beyond the considerations discussed above, the purity of commercially available materials must also be considered (Mg^nBu_2 can contain varying minor amounts of THF and $AlEt_3$,[57] $LiAlH_4$,[58] $Mg(N(SiMe_3)_2)_2$,[59] etc are typically available at purities ~95-97 %). Depending on the route of preparation, the starting material ([BH][WCA]) could carry salt or halide impurities from earlier steps in the synthesis.

Solvent purity

Mg electrochemistry requires compatible solvents which are not reduced by metallic magnesium, commonly ethereal solvents (including THF and glymes).[60-61] The solvent is used in a large excess compared to the Mg salt, rendering even minor contaminants potentially problematic. For example, a 0.25 M solution of $Mg[WCA]_2$ in DME with 20 ppm of water present in the solvent would amount to *ca.* 0.08 mol % of water vs. the electrolyte in the electrolyte solution. However, commercial "anhydrous" grade solvents typically have a water content >> 1 ppm (~ 30-50 ppm for DME) if used *as received* (Sigma), and it is well-documented in the literature that additional solvent drying is necessary for reversible electrochemical performance.[62-63] Trace O_2 contamination is possible if the solvent is not degassed prior to use. Mg electrochemistry is sensitive to trace water and oxygen in the electrolyte solution, as formation of passivating $Mg(OH)_2$ and MgO layers on the electrode surface can alter Mg deposition/stripping behaviors. To ensure electrochemical analysis of the electrolyte solution is not convoluted with water or oxygen effects, additional purification of commercial solvents is necessary.

However, additional purification itself can introduce different forms of contamination. While likely less problematic than residual water and oxygen, even minor potential contaminants warrant consideration. For example, distillation from Na/benzophenone is effective for drying, but decomposition of the Na ketyl radical can yield a variety of aromatic by-products (including

benzene, which can transfer over during distillation). Additionally, glymes are more acidic than THF, and heating a Na/benzophenone-glyme mixture can result in deprotonation of the solvent. For DME, a formal E2 reaction generates methyl vinyl ether and sodium methoxide. While these potential contaminants (benzene, methyl vinyl ether, etc) are quite minor, given the sensitivity of Mg electrochemistry, a thorough consideration of all possible contaminants is worthwhile. In many cases, a thorough analysis may explain many of the observed differences in electrochemical performance.

Herein, we discuss efforts towards reproducible/reliable Mg electrochemistry with a new silicon-based WCA electrolyte, $[Mg(DME)_3][^{Me}SiF]_2$. Reversible Mg deposition and stripping (with minimal conditioning) and stable CE requires consideration of the quality of Pt wire working electrode (WE), batch dependence of different synthetic routes, presence of basic and acidic/protic additives in electrolyte solutions, and the quality of glovebox atmosphere. Following the extensive characterization of $Mg(DME)_3[^{Me}SiF]_2$, some preliminary experiments with additional $Mg(DME)_3[^{R}SiF]_2$ variants are discussed.

RESTULS AND DISCUSSION:

Leveraging the wide electrochemical window of $[Bu_4N][^{Me}SiF]$ previously explored (see Chapter 5), a Mg^{2+} salt was targeted to serve as a potential Mg battery electrolyte with high oxidative stability. Treating $[Et_3NH][^{Me}SiF]$ with a slight excess of $MgMe_2$ affords the corresponding $[Mg(DME)_3][^{Me}SiF]_2$ (Scheme 6.3). The ^1H NMR is consistent with three DME molecules coordinated to the Mg^{2+} cation.

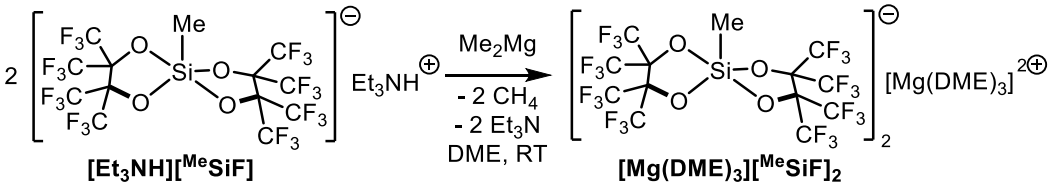

Scheme 6.3. Synthesis of $[Mg(DME)_3][^{Me}SiF]_2$

Preliminary electrochemical studies (*Notes about preliminary electrochemical studies* (in **EXPERIMENTAL SECTION**), suggested intriguing electrochemical performance, but independent electrochemical investigation was necessary to obtain meaningful results.

Within in this work, the cyclic voltammograms of $Mg(DME)_3[^{Me}SiF]_2$ are reported (*Notes about preliminary electrochemical studies* (in **EXPERIMENTAL SECTION**). While $Mg(DME)_3[^{Me}SiF]_2$ exhibits remarkable performance for a Mg electrolyte (average CE > 96 %, oxidative stability > 4 V vs. Mg/Mg^{2+}, and conditioning-free), reproducible Mg electrochemistry is very sensitive. Herein, we consider the following parameters and impacts on stability, reproducibility, and/or performance:

1) Additives (identity and concentration)—Impact on *Performance*
2) Pt wire—Impact on *Stability*
3) Batch dependence—Impact on *Reproducibility*

4) Synthetic route—Impact on *Reproducibility*
5) Cycling protocol and scan rate—Impact on *Performance*
6) Addition of $[Et_3NH][^{Me}SiF]$—Impact on *Performance*
7) Use of 3-methoxypropylamine as a cosolvent—Impact on *Performance*
8) Impact of glovebox atmosphere—Impact on *Reproducibility* and *Stability*

Statement on general reproducibility

Unless otherwise specified, all CV experiments were run pairwise with two separate batches of $[Mg(DME)_3][^{Me}SiF]_2$. The batches were prepared independently by two researchers by the same synthetic protocol. This ensures changes observed in electrochemical performance are not due to "batch-dependent" (unknown impurities) differences in a specific batch. Synthetic protocol and additional information are described in the **EXPERIMENTAL SECTION**.

Impact of additives (identity and concentration) on *Performance*

As mentioned in *Notes about preliminary electrochemical studies* (in **EXPERIMENTAL SECTION**), it was initially hypothesized that the presence of excess dialkylmagnesium was *necessary* for reversible Mg deposition and stripping. However, with careful optimization of synthesis and electrochemical conditions, it was found that $[Mg(DME)_3][^{Me}SiF]_2$ supports reversible Mg deposition/stripping in the absence of dialkylmagnesium additive. While not required, the addition of Me_2Mg does improve performance with a reduction in the number of cycles before optimal electrochemical performance was observed (termed "conditioning" in battery literature). This is reminiscent of the performance improvements observed with other types of additives.[64-65] Within this section, the effect of additive concentration on Mg

deposition/stripping supported by $[Mg(DME)_3][^{Me}SiF]_2$ is discussed. Discussion of $MgMe_2$ concentration is limited to 10, 0.1, and 0 mM; while reversible electrochemical performance was obtained at intermediate $MgMe_2$ concentrations, other parameters (Pt wire, etc) were not yet optimized.

We began an investigation of the cycling behavior of $[Mg(DME)_3][^{Me}SiF]_2$ in the absence of any additive (Figure 6.3). Gratifyingly, reversible Mg plating and stripping was observed from cycle 1 and persisted throughout all 200 cycles of the experiment, although initial cycles displayed high deposition overpotential (> 600 mV vs. Mg/Mg^{2+}) and lower coulombic efficiencies (Figure 6.3, bottom right). Electrochemical performance, however, improves with cycling and stabilizes past cycle 100 with CE ~97%. The conditioning behavior was attributed to the gradual formation of a favorable SEI on the working electrode that facilitates deposition/stripping of Mg.

To explore strategies to decrease the conditioning, CV experiments were performed in the presence of 0.1 mM of Me_2Mg (Figure 6.4). Similar to that of 0.26 M $[Mg(DME)_3][^{Me}SiF]_2$ without Me_2Mg, cycle 1 of the electrolyte solution with 0.1 mM Me_2Mg showed high deposition

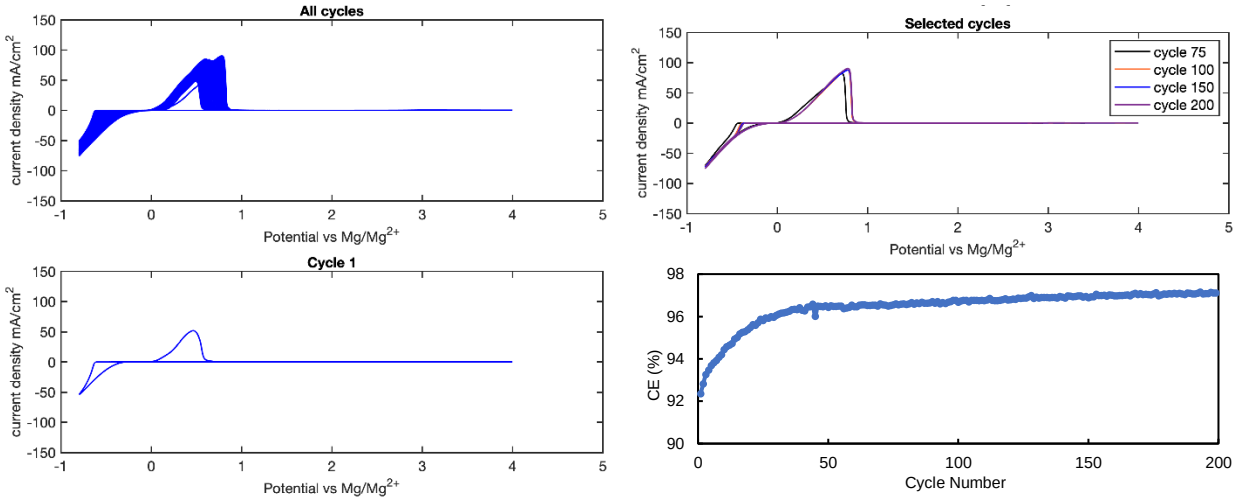

Figure 6.3. Representative cycling performance of 0.26 M $[Mg(DME)_3][^{Me}SiF]_2$ in DME. Cycling protocol: WE: Pt wire; CE: Mg strip; RE: Mg strip; cycling protocol: -0.8 V to 4.0 V; scan rate = 25 mVs^{-1}.

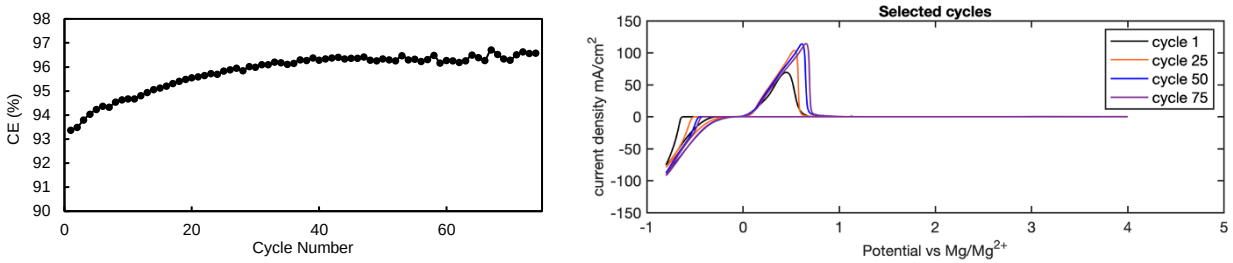

Figure 6.4. Selected CV traces of 0.26 M $[Mg(DME)_3][\,^{Me}SiF]_2$ + 0.1 mM Me_2Mg in DME; WE: Pt wire; CE: Mg strip; RE: Mg strip; cycling protocol: -0.8 V to 4.0 V; scan rate = 25 mVs^{-1}.

overpotential (>600 mV vs. Mg/Mg^{2+}) and low current density. The performance improved with prolonged cycling, and the conditioning process with 0.1 mM Me_2Mg (less than 50 cycles) is significantly shorter than that with no Me_2Mg (*ca.* 100 cycles).

Additional incremental increases in $MgMe_2$ were investigated, with optimal performance achieved with 10 mM $MgMe_2$. All experiments in subsequent sections utilize the optimized $MgMe_2$ conditions. Comparison of CE and deposition stripping curves for 0 mM and 10 mM $MgMe_2$ are shown in Figure 6.5, where higher CE is observed in the presence of $MgMe_2$, beginning

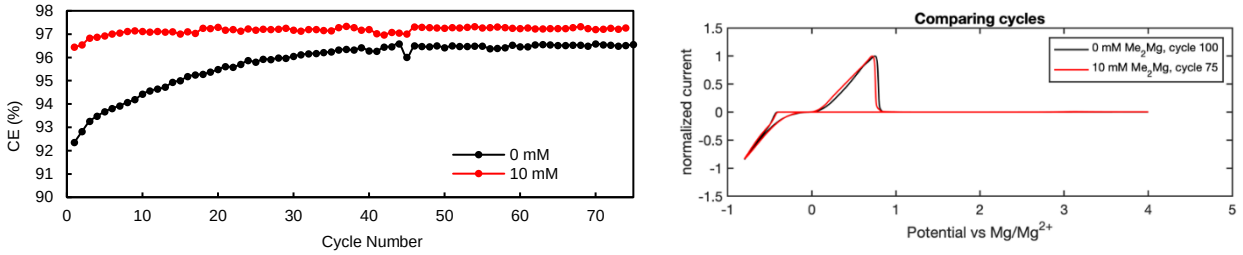

Figure 6.5. Comparison of cycling performances of 0.26 M $[Mg(DME)_3][\,^{Me}SiF]_2$ with 0 mM (cycle 100 shown) and 10 mM (cycle 75 shown) of Me_2Mg additive. Cycling protocol: -0.8 V to 4.0 V; scan rate = 25 mVs^{-1}.

from cycle 1.

While not visible on the typical scale for CV experiments, experiments run with 10 mM Me_2Mg invariably showed an irreversible oxidation wave between 3 to 4 V with E_p ~3.1 V vs. Mg/Mg^{2+} that was attributed to oxidation of Me_2Mg (Figure 6.6). Intriguingly, in the absence of Me_2Mg, the same irreversible oxidation was observed after the Mg oxidation wave, albeit at much lower current density (Figure 6.6). The current density of the irreversible oxidation feature increased

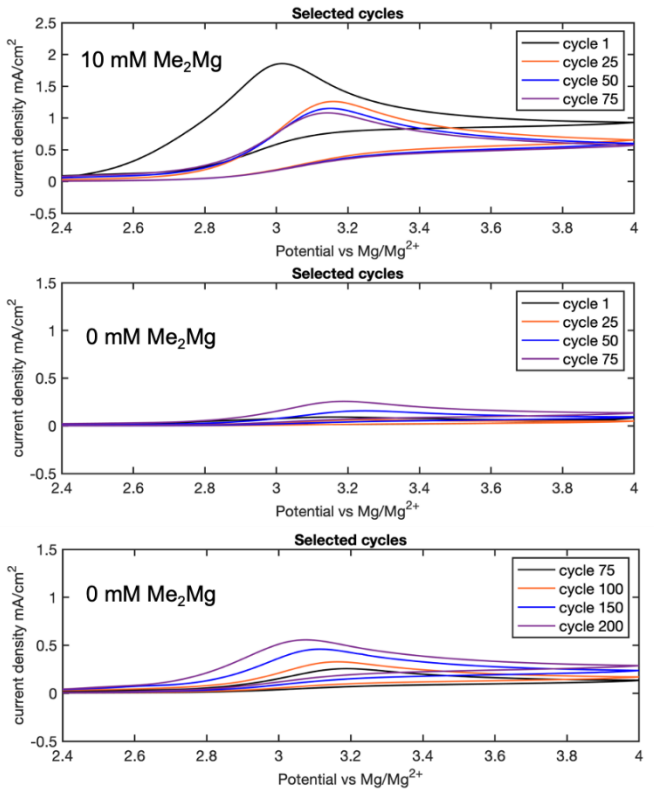

Figure 6.6. Zoomed-in view of experiments run with 10 mM and 0 mM of Me_2Mg between 2.4 V to 4.0 V vs. Mg/Mg^{2+}.

with cycling, concomitant with improvement in cycling performance (including decreasing deposition overpotential and improved oxidation kinetics, cf. Figure 6.3). Therefore, it was proposed that in the absence of bulk Me_2Mg, this oxidation wave corresponded to the electrochemical oxidation of the favorable SEI that facilitated Mg deposition and stripping. While the exact composition of the SEI is unknown, it is likely a mixture of HMgX or MeMgX species formed during Mg deposition, because of the similarity of E_p with that of Me_2Mg. Indeed, ^{1}H NMR spectra of the electrolyte solution (with no Me_2Mg additive) after cycling in DME-h_{12} revealed up-field signals near δ -1.7 ppm, further suggesting the presence of HMgX or MeMgX in solution (Figure 6.21).

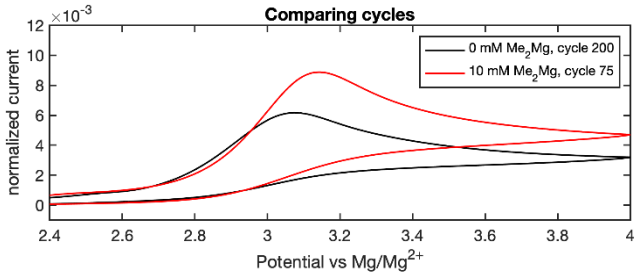

Figure 6.7. Zoomed-in view of experiments run with 10 mM and 0 mM of Me_2Mg between 2.4 V to 4.0 V vs. Mg/Mg^{2+}. Current normalized to largest current within each cycle for comparison.

During optimization of electrochemical conditions, $Mg(N(SiMe_3)_2)_2$ was also investigated as an electrolyte additive as an alternative to $MgMe_2$. To rule out effects from different impurities across different commercial batches, $Mg(N(SiMe_3)_2)_2$ was prepared from Me_2Mg and $H(N(SiMe_3)_2)_2$. Aside from the initial high deposition overpotential (>600 mV), cycling did not improve deposition overpotential beyond 500 mV, suggesting an SEI that is distinct from those formed with cycling with or without Me_2Mg. Indeed, the irreversible oxidation waves between 3

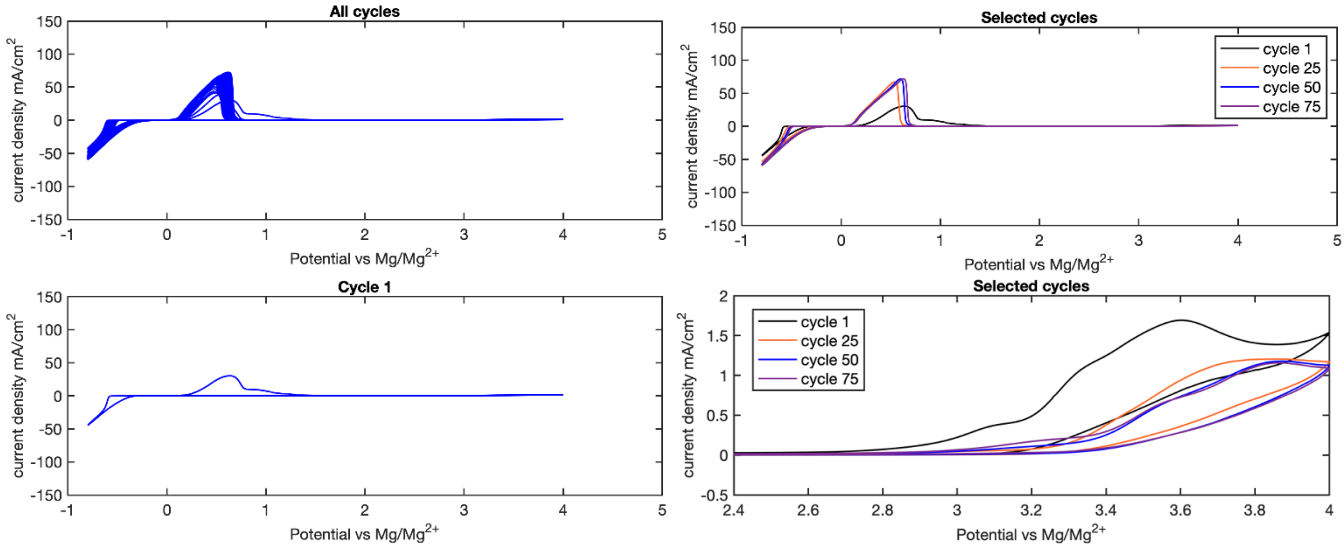

Figure 6.8. CV traces of 0.26 M $[Mg(DME)_3][^{Me}SiF]_2$ + 10 mM $Mg(N(SiMe_3)_2)_2$. The Pt wire used was one of the wires that showed abnormal shapes of the initial Mg oxidation wave (*vide supra*). Cycling protocol: WE: Pt wire; CE: Mg strip; RE: Mg strip; cycling protocol: -0.8 V to 4.0 V; scan rate = 25 mVs^{-1}. Bottom right: Selected cycles highlighting the region where minor oxidation features that likely correspond to SEI/additive oxidation typically show up.

to 4 V vs. Mg/Mg^{2+} when $Mg(N(SiMe_3)_2)_2$ was used as the additive (Figure 6.8, bottom right) was found to be distinct from that with or without Me_2Mg (Figure 6.6).

While the role of $^{n}Bu_2Mg$[40, 66-67] and $Mg(N(SiMe_3)_2)_2$ as an Mg electrolyte additive is frequently summarized as water/impurity scavengers, the actual effect of these additives is likely more complicated. For example, comproportionation between solvated Mg^{2+} and Ph_2Mg is known to generate the $PhMg(solvent)_n^+$ cation, which can be the active species for Mg plating/stripping.[51] While experiments to probe comproportionation between $[Mg(DME)_3]^{2+}$ and Me_2Mg have thus far been unsuccessful, it was proposed that formations of species such as $MeMg(solvent)_n^+$ could be responsible for lowering the overpotential of initial Mg deposition/stripping on cycle 1 and/or forming the favorable SEI for facile Mg deposition/stripping. In the absence of Me_2Mg, generation of such species and/or such an SEI would necessitate reductive decomposition of either the $^{Me}SiF^-$ anion or coordinated DME molecules on Mg;[54] this is a topic of ongoing investigation.

Impact of Pt wire on *Stability*

The Pt wires used in initial CV experiments had visibly "rough" surfaces after cleaning in concentrated HNO_3. When annealed in with an H_2/air flame, the wires did not glow evenly (due to the roughness of the surface). Reversible Mg deposition and stripping was observed, but the systems were very unstable, with erratic cycling performance and unstable CE (Figure 6.9, left and Figure 6.10, left). While some stable cycling behavior was observed before cycle 10, large fluctuations are observed on later cycles (>10).

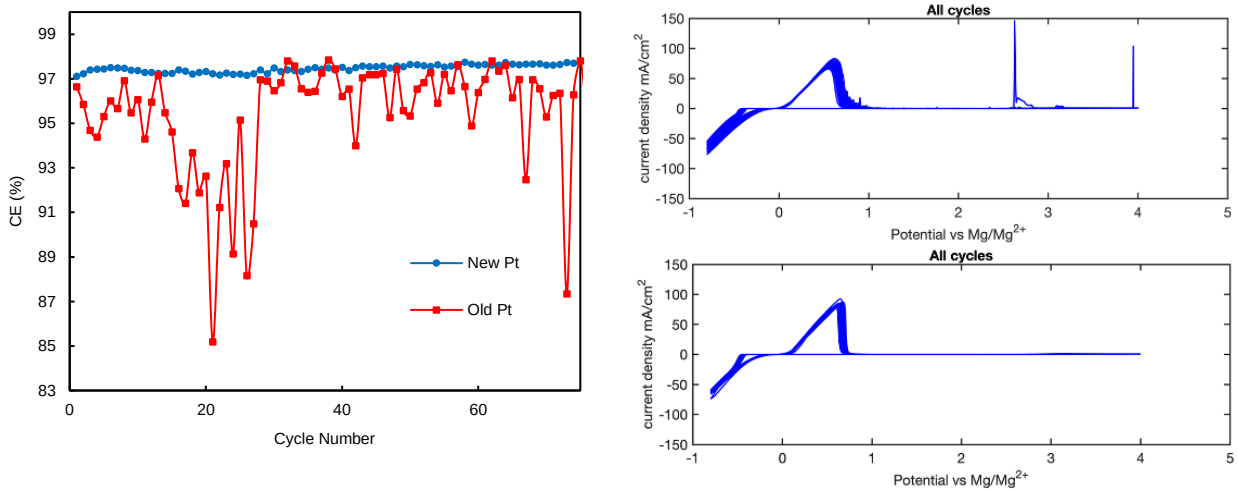

Figure 6.9. Representative comparisons between electrochemical performances of the same batch of 0.26 M $[Mg(DME)_3][^{Me}SiF]_2$ + 10 mM Me_2Mg with two different Pt wires under the same cycling conditions (TH-III-189 vs. TH-III-173). Left: Pristine (new, unused) Pt wire, cycles 1 – 75. Right: old (with jagged surface) Pt wire, cycles 1-75. WE: Pt wire; CE: Mg strip; RE: Mg strip; cycling protocol: -0.8 V to 4.0 V; scan rate = 25 mVs^{-1}.

The instability in cycling performance can be resolved with the use of new Pt wires that were (visually) much smoother. When cleaned and annealed by the same method, the new wires glowed evenly in the H_2 flame. Comparison of the cycling performance and CE are shown in Figure 6.9,

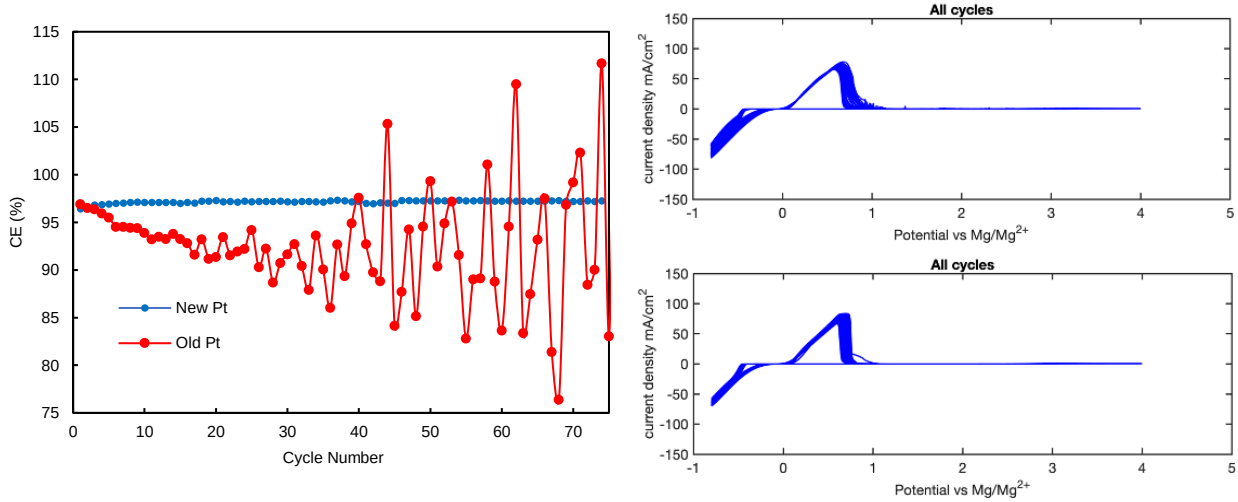

Figure 6.10. Representative comparisons between electrochemical performances of the same batch of 0.25 M $[Mg(DME)_3][^{Me}SiF]_2$ + 10 mM Me_2Mg with two different Pt wires under the same cycling conditions (MB5140 vs. MB5117). Left: Pristine (new, unused) Pt wire, cycles 1 – 75. Right: old (with jagged surface) Pt wire, cycles 1-75. WE: Pt wire; CE: Mg strip; RE: Mg strip; cycling protocol: -0.8 V to 4.0 V; scan rate = 25 mVs^{-1}.

right and 6.10, right. The Pt wire was the only variable that changed, and this profound difference in performance stability was observed across multiple batches of $Mg(DME)_3[^{Me}SiF]_2$. It has been explored in the literature that the roughness and curvature of the electrode surface can impact growth behavior of metal deposition for Li[68-69] and Na[70] batteries. It is hypothesized that the new (smooth) Pt wires facilitated more even deposition and stripping of Mg.

Impact of batch dependence on *Reproducibility*

As discussed at length in the introduction, batch-dependent electrochemistry behavior, "*batch dependence*," is a challenge with many Mg electrolytes. There are several key considerations about the preparation of $[Mg(DME)_3][^{Me}SiF]_2$ which minimize potential "batch dependent" performance. $[Mg(DME)_3][^{Me}SiF]_2$ is synthesized from $[Et_3NH][^{Me}SiF]$ and Me_2Mg, where Me_2Mg is prepared by the dioxane precipitation method, beginning from commercially available MeMgBr in Et_2O.[71] While Cl^- contamination has been reported to alter the electrochemical behavior of Mg deposition/stripping, the possible presence of trace Br^- attenuates concern. A slight excess of Me_2Mg (at least 1.2 equiv) is used to ensure complete protonlysis $[Et_3NH][^{Me}SiF]$, and the excess Me_2Mg is removed by recrystallization of a concentrated DME solution with Et_2O. The recrystallization step also removes the coordinated dioxane carried over from Me_2Mg. In all instances, complete removal of Me_2Mg was confirmed *via* ^1H NMR spectroscopy.

To demonstrate the remarkable reproducibility of $[Mg(DME)_3][^{Me}SiF]_2$, 4 cycling experiments (2 electrolyte batches with 2 replicates each) were collected under the same conditions (Figure 6.12). The small degree of variation between each experiment is more pronounced than the differences between the batches. In all experiments, similar deposition/stripping curves, reductive and oxidative overpotentials, and stable CE were observed.

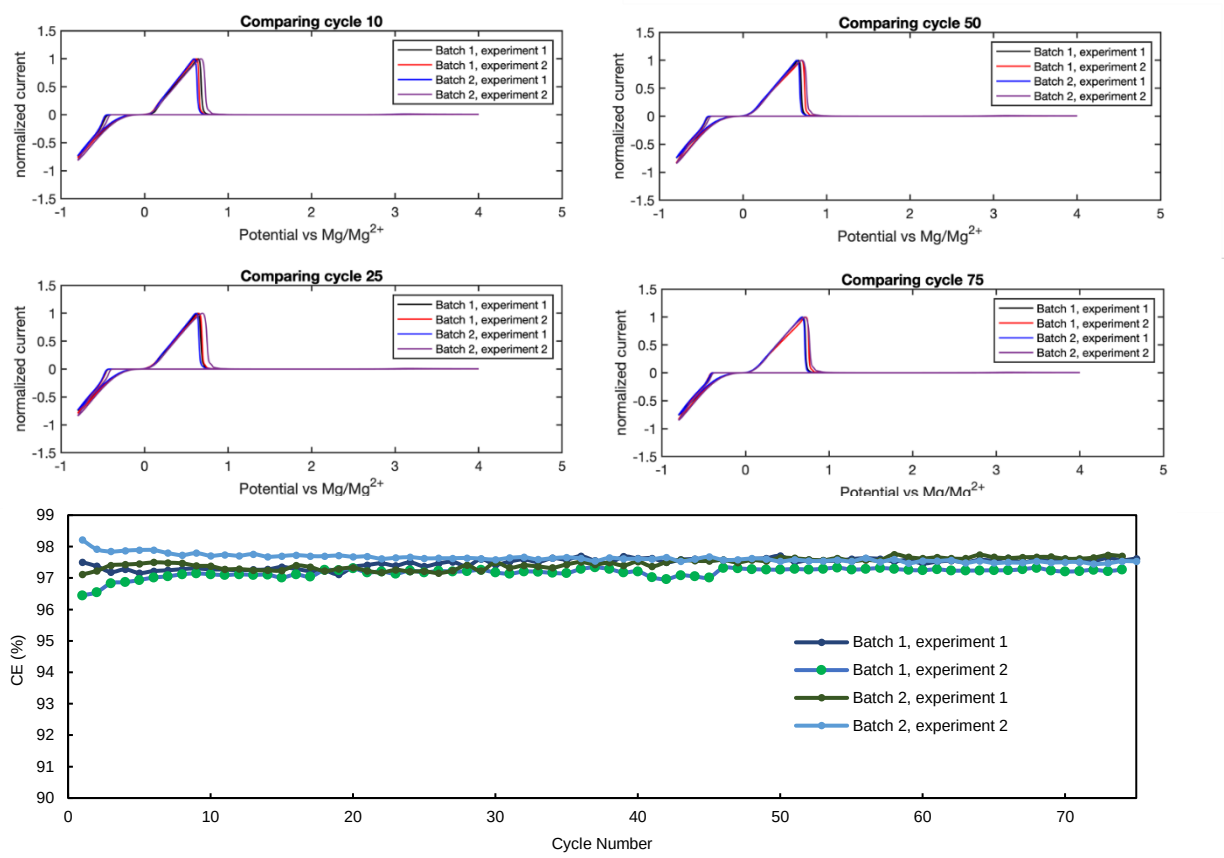

Figure 6.11. Comparison of cycle 10, 25, 50, 75 across four experiments run with two batches (batch 1 and batch 2) prepared by *two* researchers *independently* from the same synthetic procedure. Current normalized to largest current within each cycle for comparison. WE: Pt wire; CE: Mg strip; RE: Mg strip; cycling protocol: -0.8 V to 4.0 V; scan rate = 25 mVs^{-1}. Me_2Mg loading: 10 mM.

Impact of synthetic route on *Reproducibility*

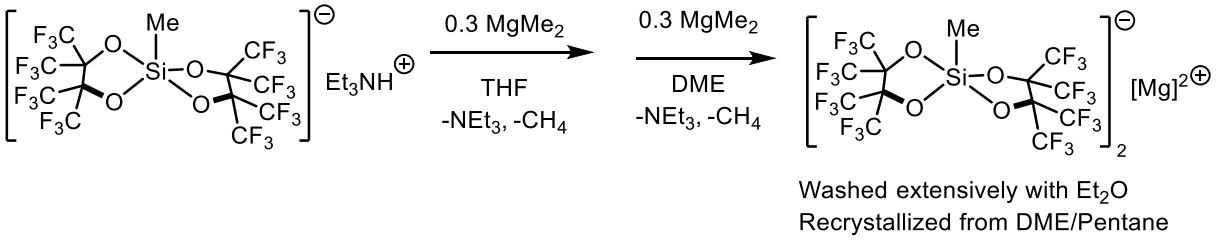

Scheme 6.4. Synthesis of $[Mg(DME)_3][^{Me}SiF]_2$ by modified protocol (Protocol 2)

To begin probing the impact of the synthetic route (and solvent) on $[Mg(DME)_3][^{Me}SiF]_2$, materials were prepared by a two-step method (Scheme 6.2). Notably, the reaction solvents (THF/DME vs. DME), purification (washing extensively with Et_2O vs. no washing), and crystallization conditions (DME/Pentane vs. DME/Et_2O) were modified. Prior to electrochemical experiments, the material was examined by ^{1}H and ^{19}F NMR, and the material was spectroscopically identical to previous batches.

Gratifyingly, the electrochemical performance was identical to the results of previous batches (within previously observed minor experiment-to-experiment variations) (Figure 6.12). Notably,

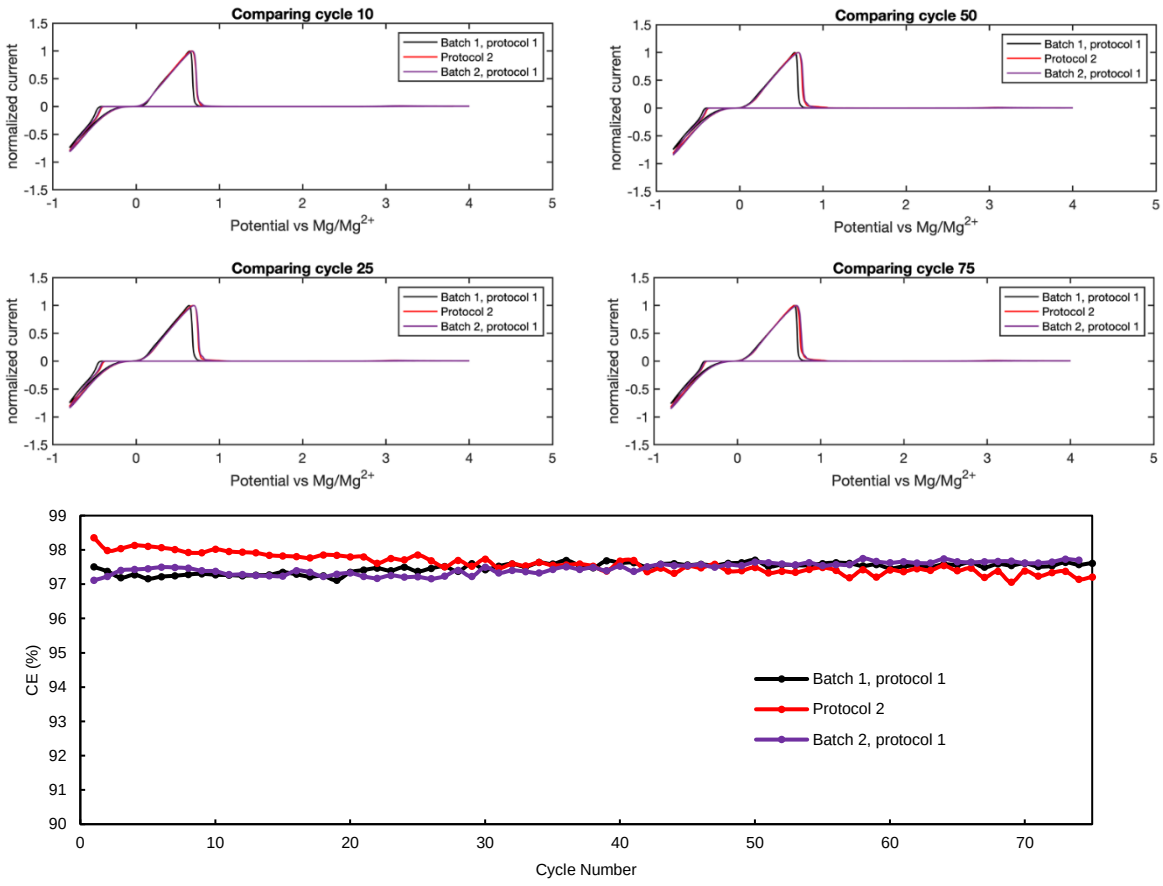

Figure 6.12. Comparisons across electrochemical performances of electrolytes prepared *via* two synthetic protocols. Batch 1 and 2 were prepared *via* protocol 1 by two researchers independently. Current normalized to largest current within each cycle for comparison. WE: Pt wire; CE: Mg strip; RE: Mg strip; cycling protocol: -0.8 V to 4.0 V; scan rate = 25 mVs^{-1}. Me_2Mg loading: 10 mM.

CV traces of electrolyte prepared *via* protocol 2 was found to be very similar, *if not identical*, to those of batch 2, protocol 1. Within different protocols (and different batches within the same synthetic protocol), the performance metrics of $[Mg(DME)_3][^{Me}SiF]_2$, including the shape of Mg deposition/stripping features, reductive and oxidative overpotentials, and coulombic efficiencies, were found to be identical within experiment-to-experiment variation. It is important to note that while the difference between the two protocols was minute, the electrochemical performance demonstrates that electrochemical performances could be free of batch/protocol differences (with sufficient care taken in synthetic protocols). The consistency of the performance of $[Mg(DME)_3][^{Me}SiF]_2$ was also a testament to its reliability and potential as an Mg electrolyte. If necessary, $[Mg(DME)_3][^{Me}SiF]_2$ could be prepared beginning from alternative silicon starting materials ($MeSiCl_3$). However, this is not an area of ongoing investigation.

Cycling protocol and scan rate—Impact on *Performance*

All of the discussed results were collected with the same cycling parameters (scan rate = 25 mV/s, -0.8 to 4 V vs. Mg/Mg^{2+}). To examine how cycling protocol and scan rate impacts performance, CVs were collected with a different cycling window (-0.8 to 2 V vs. Mg/Mg^{2+}) or a slower scan rate (5 mV/s).

While the bulk of the electrochemical studies were done with a wide cycling window of -0.8 V to 4.0 V, preliminary electrochemical characterizations (as mentioned in *Note about preliminary electrochemical studies* in the Experimental Section) were done with a smaller cycling window of

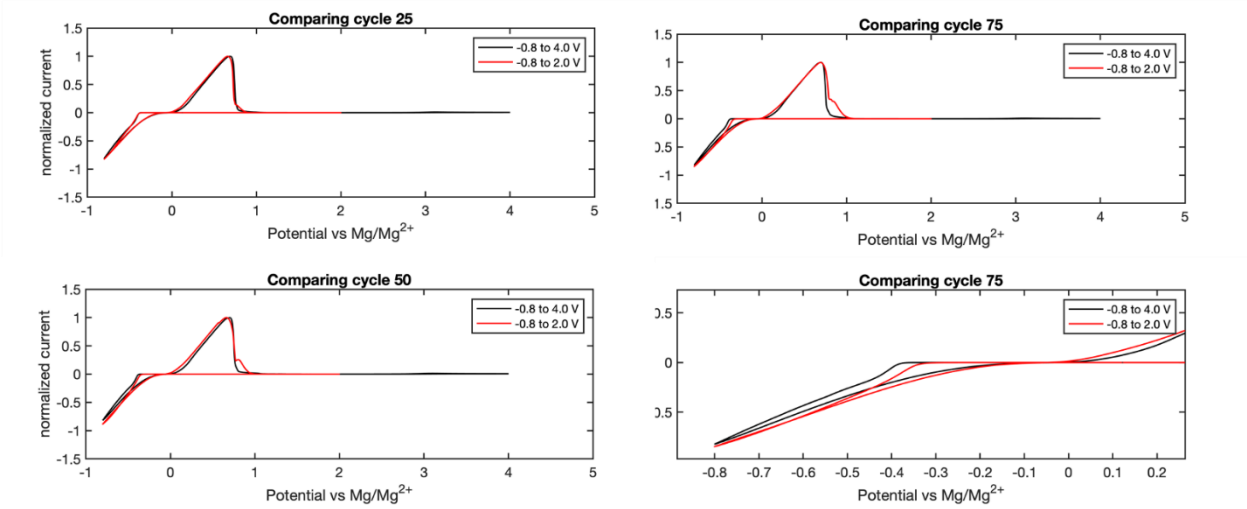

Figure 6.13. Comparison of cycling performances across two cycling protocols. WE: Pt wire; CE: Mg strip; RE: Mg strip; cycling protocol: -0.8 V to 4.0 V (black), -0.8 V to 2.0 V (red) ; scan rate = 25 mVs^{-1}. Me_2Mg loading: 10 mM.

-0.8 V to 2.0 V, where stable cycling performances were observed. To examine how cycling protocol, CVs were collected with a different cycling window of -0.8 V to 2.0 V (Figure 6.13).

As shown in Figure 6.13, while the deposition/stripping waves were identical across the two protocols, cycle 50 and cycle 75 of the narrower window showed the growth of a second feature in the Mg oxidation wave, suggesting speciation of the plated Mg (such as formation of MgO), likely unrelated to the cycling protocol. Notably, the narrower window showed diminishing plating overpotential from *ca.* 400 mV (-0.8 V to 4.0 V) to *ca.* 320 mV (-0.8 V to 2.0 V). It was hypothesized that the higher overpotential for the wider cycling window was from the continual oxidation of a favorable SEI (solid-electrolyte-interphase) between 3.0 to 4.0 V vs. Mg/Mg^{2+}.

Cycling with a slower scan rate (5 mVs^{-1}) was also attempted. While scan rate dependence of Mg electrolyte performances has not been extensively discussed/studied and prior examples of WCA-based electrolytes were reported with varying scan rates, ranging from (50 mVs^{-1} to 5 mVs^{-1}).[41, 50, 54] To probe the stability and reversibility of $[Mg(DME)_3][^{Me}SiF]_2$, CV traces were recorded with 5 mVs^{-1} scan rate (Figure 4.14).

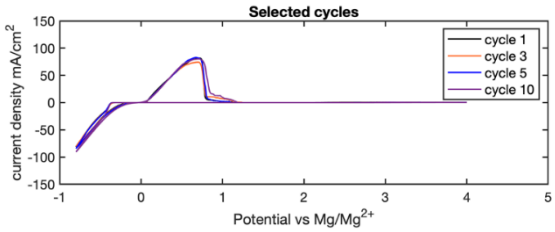

Figure 6.14. Representative CV traces of 0.26 M $[Mg(DME)_3][^{Me}SiF]_2$ + 10 mM Me_2Mg in DME. Cycling protocol: WE: Pt wire; CE: Mg strip; RE: Mg strip; cycling protocol: -0.8 V to 4.0 V; scan rate = 5 mVs^{-1}.

The electrochemical performance of $[Mg(DME)_3][^{Me}SiF]_2$ was very unstable when cycled at 5 mVs^{-1}. Starting from cycle 1, the deposition/stripping waves were visibly "jagged", indicating unstable deposition/stripping behavior. In addition, experiments run with a 5 mVs^{-1} scan rate were found to short-circuit around cycle 15 due to an accumulation of Mg^0, limiting evaluation of further cycling behavior. While the exact causes of the unstable cycling behavior at 5 mVs^{-1} remained elusive, it was hypothesized that the slower scan rate resulted in a much greater amount of Mg^0 during deposition because of the long time spent at potentials negative of Mg^{2+}/Mg. Because Mg was deposited on a thin Pt wire, it is conceivable that the deposited Mg could "break off" of the Pt surface, resulting in the observed unstable cycling behavior. Notably, the carborane electrolytes with 5 mVs^{-1} scan rates have notably lower current densities,[49] resulting in less Mg^0 deposition at slow scan rates, possibly explaining the reported stable performance.

Use of 3-methoxypropylamine as a cosolvent (Impact on *Performance*)

Previous studies on the solvent effect of Mg deposition overpotential have suggested that incorporating 3-methoxypropylamine (3-MPA) as a co-solvent of Mg can decrease de-solvation energy, translating as a decrease in Mg deposition overpotential. It was also proposed that incorporation of 3-MPA in the electrolyte renders a higher tolerance to trace levels of water, with the N-H protons able to hydrogen-bond to water. To examine the impact of 3-methoxypropylamine (3MPA) on $Mg(DME)_3[^{Me}SiF]_2$ electrochemistry, several CV preliminary experiments were conducted. While the ionic conductivity of 3-methoxypropylamine is greater than DME (0.94 vs.

0.34 mS cm^{-1}, respectively),[72] it is significantly more viscous (1.27 vs. 0.5 mpa s).[72] CVs were conducted in varying 3MPA:DME conditions including 100:0 (neat 3MPA, Figure 6.15) and 1:9 v/v (Figure 6.15). In all experiments, the Mg deposition overpotential was dramatically lower than the previously optimized conditions (discussed above. Significantly more electrochemical conditioning was observed at early cycles, and the shape of the Mg stripping feature is broader, with a tail that beyond 1 V (vs. Mg/Mg^{2+}). In all cases, electrochemical performance was less ideal than performances observed with 0.26 M $[Mg(DME)_3][^{Me}SiF]_2$ + 10 mM Me_2Mg.

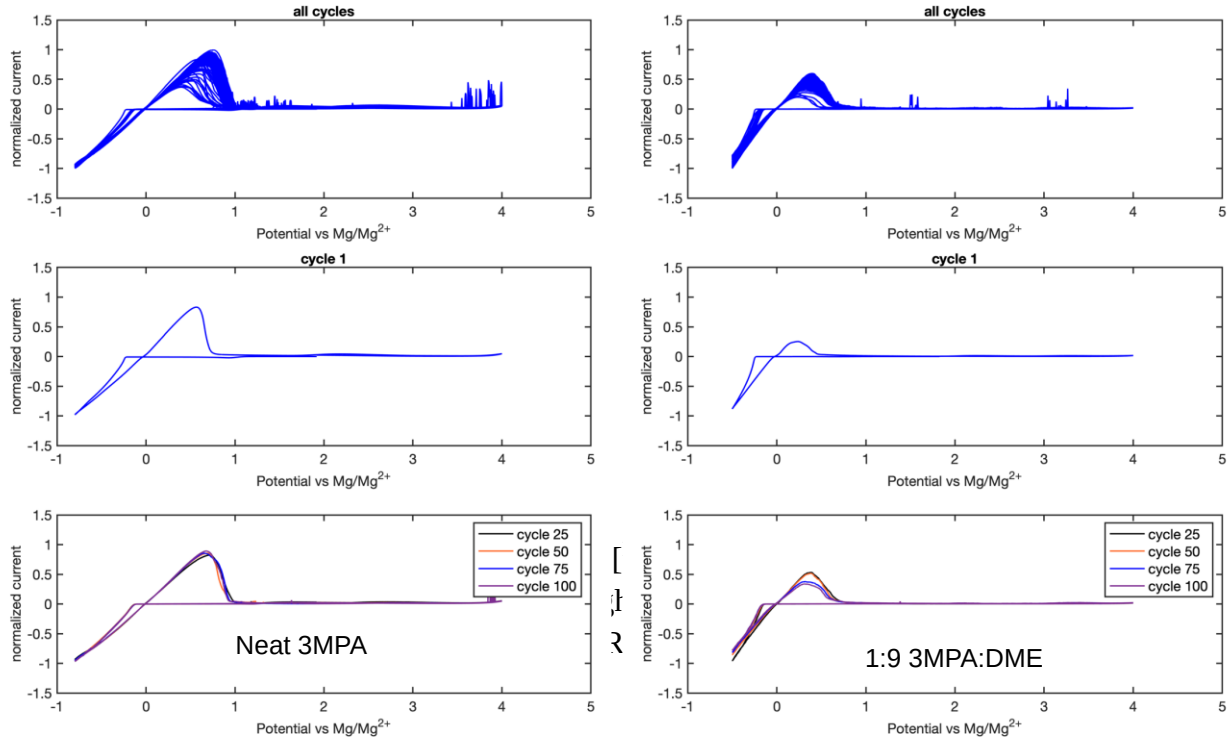

Figure 6.15. CV traces of 0.26 M $[Mg(DME)_3][^{Me}SiF]_2$ in 3-methoxypropylamine (left) and 1:9 3-methoxypropylamine:DME. Current normalized to highest current for the duration of the experiment; Cycling protocol: WE: Pt wire; CE: Mg strip; RE: Mg strip; cycling protocol: -0.8 V to 4.0 V; scan rate = 25 mVs^{-1}. Irregular "spikes" at oxidative potentials observed even with "new" Pt wires (see section: Impact of Pt Wire on Stability)

Addition of $Et_3NH[^{Me}SiF]$ (Impact on *Performance*)

Based on the observed (but not well-understood) decrease in reductive overpotential in mixed 3MPA:DME solvent mixtures, it was hypothesized that addition of $Et_3NH[^{Me}SiF]$ may serve a similar role to 3MPA with N-H protons, where the proton of $[Et_3NH]^+$ is significantly more acidic. To test this hypothesis, 20 mM $Et_3NH[^{Me}SiF]$ was introduced as an additive (Figure 6.16). Unfortunately, addition of $Et_3NH[^{Me}SiF]$ does not decrease the Mg deposition overpotential. On cycle 1, the reductive overpotential is ~380 mV which further decreases to ~280 mV with cycling. There is a significant increase in current density and change in Mg stripping peak shape from cycle 1 to cycle 2, somewhat reminiscent of the conditioning observed with 3MPA. However, unlike

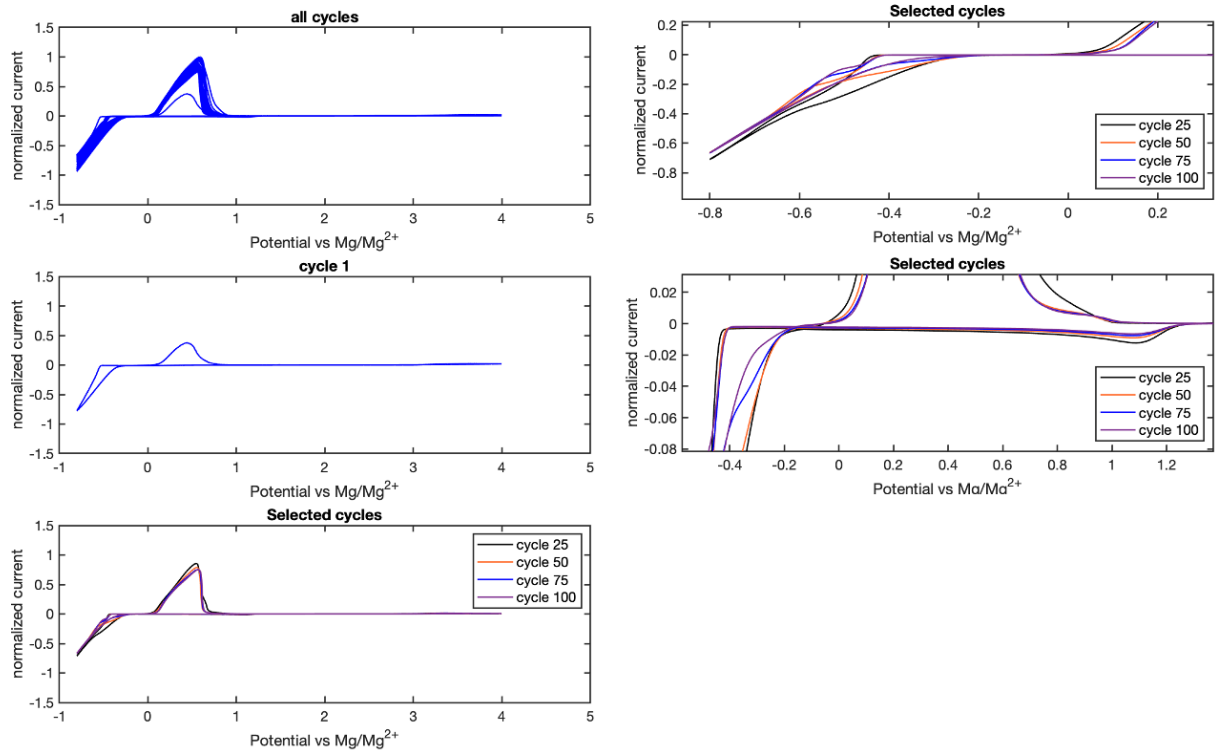

Figure 6.16. CV traces of 0.26 M $[Mg(DME)_3][^{Me}SiF]_2$ + 20 mM $[Et_3NH][^{Me}SiF]$; Zoomed in view of CV traces highlight jagged Mg deposition and HER. Current normalized to highest current for the duration of the experiment; Cycling protocol: WE: Pt wire; CE: Mg strip; RE: Mg strip; cycling protocol: -0.8 V to 4.0 V; scan rate = 25 mVs^{-1}.

electrolyte mixtures containing 3MPA, the shape of the reductive and oxidative features is significantly different.

Unfortunately, $[Et_3NH][^{Me}SiF]$ does not engender the desired decrease in Mg deposition overpotential. On cycle 1, the reductive overpotential was 550 mV which further decreases to *ca.* 450 mV with cycling. The increase in current density and change in Mg stripping peak shape from cycle 1 to cycle 2 was reminiscent of the electrochemical conditioning observed with 3MPA. However, unlike electrolyte mixtures containing 3MPA, the shape of the reductive and oxidative features was significantly different from that in the presence of 3MPA: a) From cycle 50 onwards, the Mg deposition waves were visibly "jagged", suggesting markedly different charge-transfer kinetics; b) For every cycle, there was a catalytic reduction wave at *ca.* 1.2 V vs. Mg/Mg^{2+}, which was assigned to the Hydrogen Evolution Reaction (HER) *via* electroreduction of the N-H proton.

Impact of glovebox atmosphere on *Reproducibility/Performance*

All CVs were conducted in an empty glovebox (no chemical or solvent storage) without exposure to the catalyst bed (to prevent atmospheric contamination from trace impurities in the catalyst bed). The glovebox atmosphere was monitored with $ZnEt_2$ (< low ppm O_2)[73] and titanocene (< 5 ppm O_2),[73] and the atmosphere was purged for an additional 20 minutes with a nitrogen pressure > 3.0 mbar before each CV. Oxygen and moisture sensors were not used due to (1) cost and (2) need for frequent and regular recalibration for accurate measurement.

However, this strict purification procedure is insufficient for cycling experiments. As shown in Figure 6.17, CVs were run with the same batch of material. For both experiments, no changes in glovebox atmosphere (with $ZnEt_2$ and/or titanocene) were detected over the course of the experiment. However, without rigorous drying of the glovebox interior, a shoulder develops on

the Mg oxidative peak, with the shoulder increasing over time. This feature is tentatively assigned to MgO or $Mg(OH)_2$ formation.

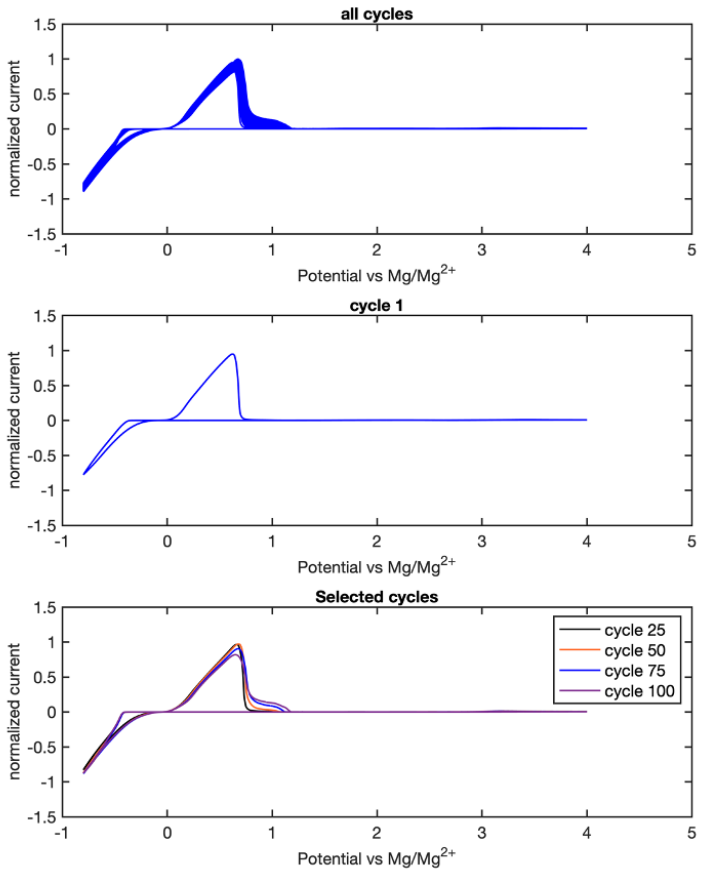

Figure 6.17. CV traces of 0.26 M $[Mg(DME)_3][^{Me}SiF]_2$ + 10 mM Me_2Mg run in a glove box where the interior has not been rigorously dried. Current normalized to highest current for the duration of the experiment; Cycling protocol: WE: Pt wire; CE: Mg strip; RE: Mg strip; cycling protocol: -0.8 V to 4.0 V; scan rate = 25 mVs^{-1}.

Preliminary Exploration of Additional Variants

To begin a structure/function study of $[^{R}SiF]^-$ anions, preliminary experiments were conducted with several $Mg(DME)_3[^{R}SiF]_2$ variants, including R = Ph, $C_{10}H_{21}$, 3,5 di^{t}BuPh, and C_6F_5. All $Mg(DME)_3[^{R}SiF]_2$ electrolytes were prepared by the same procedure as previously discussed $Mg(DME)_3[^{R}SiF]_2$ (Scheme 6.1). For additional synthetic information for each variant, see **EXPERIMENTAL SECTION.** The electrochemical performance of each variant was only tested

once, so the discussion below is very preliminary.

All $[Mg(DME)_3][^{R}SiF]_2$ variants displayed reversible Mg deposition and stripping was observed, albeit with significant differences in (1) reductive and oxidative overpotentials and (2) performance stability. The CVs are shown in Figure 6.18-6.19. Due to concerns about decreased oxidative stability, arising from the more electron-rich R-groups, the CVs were collected with slightly modified protocols. Each electrolyte was tested from -0.8 to 3.5 V (vs. Mg/Mg^{2+}) for 100 cycles at 25 mV/s.

For R = Ph, very stable, consistent performance is observed, with a decrease in reductive overpotential with cycling. Smooth and stable performance is observed for the full 100 cycles.

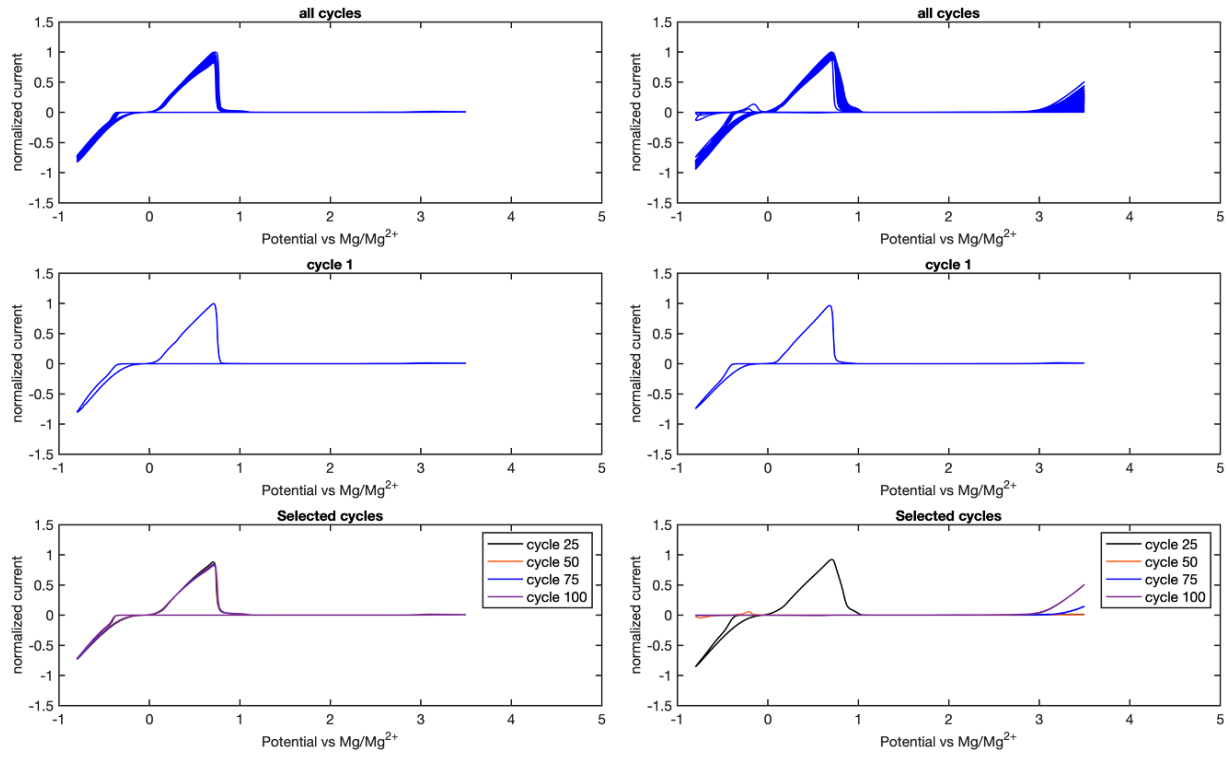

Figure 6.18. CV traces of 0.25 M $[Mg(DME)_3][^{Ph}SiF]_2$ + 10.75 mM Me_2Mg (left) and 0.25 M $[Mg(DME)_3][^{decyl}SiF]_2$ + 10 mM Me_2Mg. Current normalized to highest current for the duration of the experiment; Cycling protocol: WE: Pt wire; CE: Mg strip; RE: Mg strip; cycling protocol: -0.8 V to 4.0 V; scan rate = 25 mVs^{-1}.

Similar performance is observed for R = $C_{10}H_{21}$ during early cycles. Unfortunately, a dramatic loss of reversible performance is observed in cycle 49; additional runs are necessary to determine if the loss of reversible performance is reproducible.

The R = C_6F_5 variant was targeted to further increase the oxidative stability by addition of the electron-withdrawing aryl group. However, this variant exhibited a dramatically decreased solubility in DME compared to other $[^{R}SiF]^-$ variants, with solution saturation at ~56 mM (by ^{19}F NMR). As this concentration is too low for sufficient ion concentration and conductivity, $Mg(DME)_3[^{C6F5}SiF]_2$ (0.01 M) was combined with the thoroughly studied $Mg(DME)_3[^{Me}SiF]_2$ (0.24 M) to prepare an electrolyte mixture where $[Mg^{2+}]$ = 0.25 M. The CV is shown in Figure

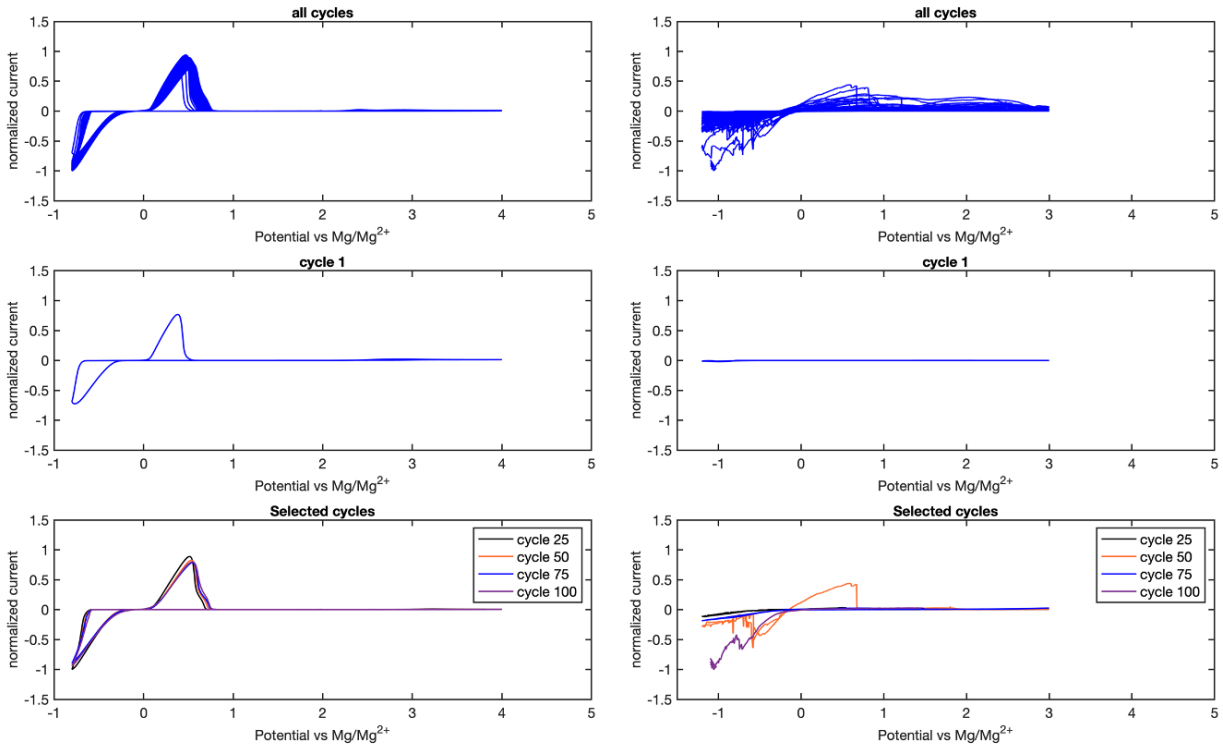

Figure 6.19. CV traces of 0.24 M $[Mg(DME)_3][^{Me}SiF]_2$ + 0.01 M $[Mg(DME)_3][^{C6F5}SiF]$ + 10 mM Me_2Mg (left) and 0.25 M $[Mg(DME)_3][^{3,5ditBuAr}SiF]_2$ + 10 mM Me_2Mg. Current normalized to highest current for the duration of the experiment; Cycling protocol: WE: Pt wire; CE: Mg strip; RE: Mg strip; cycling protocol: -0.8 V to 4.0 V; scan rate = 25 mVs^{-1}.

6.19 (right). Reversible Mg deposition and stripping is observed from cycle 1, albeit with a dramatic increase in deposition and stripping overpotentials compared to the $Mg(DME)_3[^{Me}SiF]_2$ (0.25 M) electrochemistry discussed above, likely due to reductive decomposition of the $[^{C6F5}SiF]$ anion. For the R = 3,5 di^{t}BuPh variant, the voltage window was modified to -1.2 V to 3 V (vs. Mg/Mg^{2+}) as no reversible performance was observed when sweeping only to -0.8 V, and the oxidative limit was further reduced due to additional concern over oxidative decomposition. While this variant was prepared to target a more soluble SiF variant to examine the performance at higher concentrations (> 0.25 M), the electrochemical performance was markedly inferior to the other variants. No reversible performance was observed even in early cycles, with anomalous features growing in throughout cycling. With this electrolyte variant, a dramatic increase in viscosity was qualitatively observed during preparation of the electrolyte solution. Solution viscosity can impact ion mobility,[74] and may explain the poor electrochemical performance.

While preliminary, these experiments of additional variants begin a possible structure/function study of how the anion structure impacts electrochemical performance, a type of study that is not possible with most other Mg electrolytes.

CONCLUSIONS

In summary, we extensively examined parameters required for reproducible/reliable Mg electrochemistry with a new silicon-based WCA electrolyte, $[Mg(DME)_3][^{Me}SiF]_2$. While not inherently necessary for reversible Mg deposition and stripping, addition of 10 mM $MgMe_2$ minimizes electrochemical conditioning. The stability of performance is dictated by the quality of the working electrode (Pt wire), and the addition of co-solvents (3MPA) or other proton sources $[Et_3NH][^{Me}SiF]$ does not improve performance. Preliminary exploration of additional $[^{R}SiF]$ variants demonstrates significant differences in electrochemical performance, allowing access to a future electrolyte structure/function study.

EXPERIMENTAL SECTION

General Considerations - Synthesis Unless otherwise specified, all operations were carried out in an MBraun drybox under a nitrogen atmosphere or using standard Schlenk line or high vacuum techniques. Solvents for air- and moisture-sensitive reactions were dried with sodium mirror (1,4 dioxane), sodium benzophenone ketyl (DME), or by the method of Grubbs[75] (THF, Et_2O, toluene, pentane, benzene). Solvents, once dried and degassed, were vacuum transferred directly and stored under inert atmosphere over 3 Å molecular sieves. C_6D_6, C_7D_8, CD_3CN, CD_2Cl_2 were purchased from Cambridge Isotope Laboratories and vacuum transferred from CaH_2 (CD_3CN) after three freeze-pump-thaw cycles. $[Et_3NH][^{R}SiF]$ were prepared according to modified literature procedures[76] or by routes discussed in Chapter 5. Unless otherwise noted, all other chemicals were purchased from commercial vendors and used as received. ^{1}H, ^{13}C, ^{19}F, and ^{29}Si NMR spectra were either recorded on a Varian 400 MHz spectrometer or a Bruker 400 MHz spectrometer with chemical shifts reported in parts per million (ppm). ^{1}H NMR spectra were referenced to residual solvent peaks. [1] Multiplicities are abbreviated as follows: s = singlet, d = doublet, t = triplet, dd = doublet of doublets, dt = doublet of triplets, td = triplet of doublets, m = multiplet, br = broad, and app = apparent.

Special considerations for electrochemistry:

DME and **$[Mg(DME)_3][^{R}SiF]_2$** were only used with the glovebox circulation purifier turned off after extensive purging of the glovebox atmosphere (minimum 20 minutes at 4.0 bar above atmospheric pressure to ensure full atmosphere exchange) to avoid cross-contamination with other atmospheric solvents. Cyclic voltammetry experiments of **$[Mg(DME)_3][^{R}SiF]$** were run in an empty N_2-filled glovebox where no solvent or chemicals were stored. Electrolyte

solutions were prepared in a separate glovebox by dissolving **[Mg(DME)$_3$][^{R}SiF]** in 0.5 mL of DME and stirred with a new Teflon stir bar until complete dissolution, sealed, and transported to the electrochemistry glovebox immediately before electrochemical experiments were performed.

Mg electrodes (99.9%, MTI) were polished with a razor blade immediately before use. Pt electrodes (wire, 0.5 mm diameter, 99.999%, Thermo Scientific) were soaked in concentrated HNO_3 for at least 72 hours, rinsed with deionized water at least thrice, annealed with an H_2 torch, and immediately brought into the glovebox in a flame-dried 20 mL scintillation vial while hot. Cyclic voltammetry experiments of **[Mg(DME)$_3$][^{R}SiF]** were performed in 3-neck glass cells with 0.5 mL of electrolyte. A Pt wire served as the working electrode, and Mg foils were the counter and reference electrodes. Electrodes were secured with Li BMC 1.5 mm Substrate Holders (Gamry). Experiments of **[Mg(DME)$_3$][^{R}SiF]** were conducted on either a Biologic SP150 potentiostat or a Biologic VSP-300 potentiostat.

Note about preliminary electrochemical studies (not shown)

Preliminary electrochemical conditions were investigated collaboratively with the See group. Initial preparation of Mg(DME)$_3$[^{Me}SiF]$_2$ contained residual unreacted Mg(^{n}Bu)$_2$. This material demonstrated reversible Mg deposition and stripping with high current densities, but decomposition above ~2.4 V (from Mg(^{n}Bu)$_2$) severely hindered oxidative stability. Unfortunately, with complete removal of Mg(^{n}Bu)$_2$, Mg(DME)$_3$[^{Me}SiF]$_2$ did not exhibit reversible Mg electrochemistry. Based on previous literature where addition of Mg(^{n}Bu)$_2$ to electrolytes can facilitate removal of water, oxygen, and protic impurities;[40] it was hypothesized that Mg(^{n}Bu)$_2$ may be performing a similar role in this system. Indeed, with introduction of small, quantified

amounts of $Mg(^{n}Bu)_2$, reversible Mg electrochemistry was observed again (with minimal decomposition above 2.4 V).

$Mg(^{n}Bu)_2$ was replaced with $MgMe_2$ which did not negatively impact the electrochemistry. This change of MgR_2 additive was done to (1) improve the purity of the MgR_2 (by avoiding direct use of commercially available material without purification), (2) improve ease-of-use (fine solid powder vs. viscous oily solid). and (3) avoid supply-chain challenges.

However, due to inconsistent glovebox practices, reproducible electrochemical results could not be obtained within this preliminary investigation. Independent study in the Agapie group was performed resulting in the reproducible data reported here.

Additional impact of Pt wire:

Beyond the observed impacts on cycling stability and CE, a subset of new Pt wires displayed an oxidative feature on the end of the Mg stripping trace (hereinafter termed "oxtail"), regardless of whether the wire has been previously used (Figure 6.20). This oxtail was only observed at low cycle numbers (< cycle 3) and did not impact later cycles *or* the overall stability of the system. This feature was observed across different batches of $[Mg(DME)_3][^{Me}SiF]_2$ and with different Pt wires; even within the same electrolyte batch, certain Pt wires displayed different Mg stripping behavior on cycle 1 (Figure 6.20). This suggests that the presence of this oxidation feature is solely dependent on the Pt wire. It is hypothesized that certain Pt wires may have more impurities or contaminants on the surface than others, resulting in different Mg stripping traces.

Aside from the "oxtail" behavior, use of new Pt wires resulted in stable electrochemical performance. For the additional parameters discussed below, all data was collected with newer Pt

wires. In the subset of cases where the data set had an oxidative tail on early cycles, this behavior was noted but does not impact the overall conclusions about the impact of each parameter.

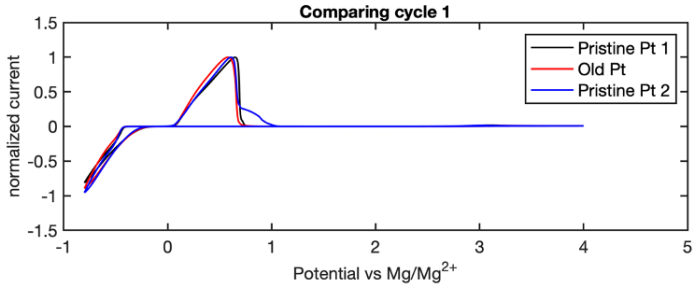

Figure 6.20. Comparison across the first cycles for three experiments (0.26 M $[Mg(DME)_3][^{Me}SiF]_2$ + 10 mM Me_2Mg) run with three different Pt wires. Pristine Pt wire electrodes 1 and 2 were cut from the same Pt wire purchased from Thermo Fischer Scientific. The old Pt wire used in this experiment was visibly jagged (cf. Figure 6.X, experiment MB5117). Current normalized to largest current within each cycle for comparison. WE: Pt wire; CE: Mg strip; RE: Mg strip; cycling protocol: -0.8 V to 4.0 V; scan rate = 25 mVs^{-1}. Me_2Mg loading: 10 mM.

Synthesis of $[Mg(DME)_3][^{Me}SiF]_2$ *Synthesis developed by Tianyi He. $[Mg(DME)_3][^{Me}SiF]_2$ prepared by Meaghan Bruening and Tianyi He*

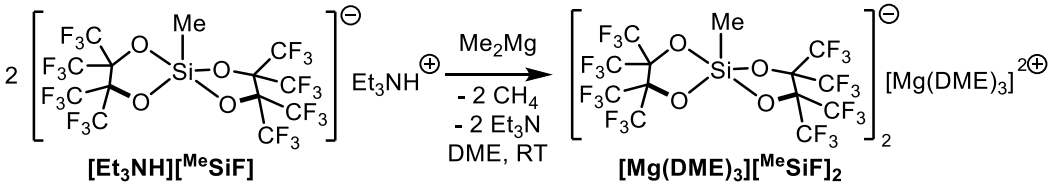

In an N_2-filled glovebox, solid Me_2Mg•0.85(dioxane) (1.16 g, 8.8 mmol) was slowly added to a vigorously stirring solution of **$[Et_3NH][^{Me}SiF]$** (12.1 g, 14.8 mmol) in DME (80 mL), resulting in a slight color change to yellow. *Caution: protonolysis of Me_2Mg is exothermic. Solid Me_2Mg is pyrophoric and must be handled with caution.* An aliquot was drawn and analyzed *via* ^1H NMR spectroscopy to confirm complete consumption of the starting material as evidenced by the presence of excess Me_2Mg. The mixture was concentrated *in vacuo* until a waxy solid was

obtained. The white precipitate was extracted into minimal DME and then layered with Et_2O. The microcrystalline solid was collected, rinsed with additional Et_2O, and dried *in vacuo*. Yield = 9.8 g (78 %).

^{1}H (CD_3CN, 400 MHz): 3.58 (s, 12 H, $CH_3OCH_2CH_2OCH_3$), 3.38 (s, 18 H, $CH_3OCH_2CH_2OCH_3$), 0.19 (s, 6 H, $SiCH_3$).^{19}F (CD_3CN, 376 MHz): -69.84 (app s, 12 F, CF_3), -69.87 (app s, 12 F, CF_3). ^{13}C{^{1}H} (CD_3CN, 101 MHz): 123.65 (q app m, CF_3), 84.47 (br s, $OC(CF_3)_2$), 71.93 (s, $CH_3OCH_2CH_2OCH_3$), 59.46 (s, $CH_3OCH_2CH_2OCH_3$), 0.97 (s, $SiCH_3$). ^{29}Si (CD_3CN, 80 MHz): -73.76 (s). Anal. Calcd. for $C_{38}H_{36}F_{48}MgO_{14}Si_2$ (%): C, 26.71; H, 2.12; Found: C: 26.61; H: 1.93.

$[Mg(DME)_3][^{Ph}SiF]_2$, $[Mg(DME)_3][^{tBu2Ph}SiF]_2$, $[Mg(DME)_3][^{Decyl}SiF]_2$, and **$[Mg(DME)_3][^{C6F5}SiF]_2$** were prepared by an analogous procedure beginning from **$[Et_3NH][^{Ph}SiF]_2$, $[Et_3NH][^{tBu2Ph}SiF]$**, **$[Et_3NH][^{Decyl}SiF]$**, and**$[Et_3NH][^{C6F5}SiF]$**, respectively.

$[Mg(DME)_3][^{Ph}SiF]_2$ *Prepared by Tianyi He*

^{1}H (CD_3CN, 400 MHz): 7.80 (app dd, 4 H, Ar-*H*), 7.30-7.20 (overlapping m, 6 H, Ar-*H*), 3.57 (s, 8 H, $CH_3OCH_2CH_2OCH_3$), 3.38 (s, 12 H, $CH_3OCH_2CH_2OCH_3$). ^{19}F (CD_3CN, 376 MHz): -69.47 (app m, 24 F, CF_3), -69.90 (app m, 24 F, CF_3). ^{13}C{^{1}H} (CD_3CN, 101 MHz): 140.19 (s, Ar-*C*), 137.27 (s, Ar-*C*), 129.38 (s, Ar-*C*), 127.49 (s, Ar-*C*), 123.08 (q app m, CF_3), 84.37 (br s, $OC(CF_3)_2$), 72.14 (s, $CH_3OCH_2CH_2OCH_3$), 59.49 (s, $CH_3OCH_2CH_2OCH_3$). ^{29}Si (CD_3CN, 80 MHz): -89.33 (s). Anal. Calcd. For $C_{48}H_{40}F_{48}MgO_{14}Si_2$ (%): C, 31.45; H, 2.20. Found: C, 31.36; H, 2.06.

$[Mg(DME)_3][^{tBu2Ph}SiF]_2$

^{1}H (CD_3CN, 400 MHz): 7.77 (d, 4 H, Ar-*H*), 7.38 (t, 2 H, Ar-*H*), 3.51 (s, 12 H, $CH_3OCH_2CH_2OCH_3$), , 3.33 (s, 18 H, $CH_3OCH_2CH_2OCH_3$), 1.28 (s, 36 H, $C(CH_3)_3$). ^{19}F (CD_3CN,

376 MHz,): -69.23 (app m, 24 F, C*F*$_3$), -69.81 (app m, 24 F, C*F*$_3$). ^{13}C{^{1}H} (CD_3CN, 101 MHz): 148.84 (s, Ar-*C*), 137.86 (s, Ar-*C*), 132.57 (s, Ar-*C*), 123.14 (s, Ar-*C*), 123.14 (q app m, *C*F_3), 84.33 (br s, O*C*$(CF_3)_2$), 72.23 (s, $CH_3OCH_2CH_2OCH_3$), 59.10 (s, $CH_3OCH_2CH_2OCH_3$), 35.32 (s, *C*$(CH_3)_3$), 31.81 (s, C(*C*$H_3)_3$). ^{29}Si (CD_3CN, 80 MHz): -88.92 (s). Anal. Calcd. for $C_{64}H_{72}F_{48}MgO_{14}Si_2$ (%): C, 37.36; H, 3.53. Found: C, 37.52; H, 3.39.

[Mg(DME)$_3$][^{Decyl}SiF]$_2$

^{1}H (CD_3CN, 400 MHz): 3.51 (s, 12 H, $CH_3OCH_2CH_2OCH_3$), 3.33 (s, 18 H, $CH_3OCH_2CH_2OCH_3$), 1.36 (m, 4 H, alkyl-*H*), 1.25 (br. app. s, 28 H, alkyl-*H*), 0.87 (t, 6 H, alkyl-*H*), 0.76 (t, 4 H, alkyl-*H*). ^{19}F (CD_3CN, 376 MHz,): -69.76 (app m, 24 F, C*F*$_3$), -69.86 (app m, 24 F, C*F*$_3$). ^{13}C{^{1}H} (CD_3CN, 101 MHz): 123.19 (q app m, *C*F_3), 84.51 (br s, O*C*$(CF_3)_2$), 72.25 (s, $CH_3OCH_2CH_2OCH_3$), 59.13 (s, $CH_3OCH_2CH_2OCH_3$), 33.97 (s, alkyl-*C*), 32.65 (s, alkyl-*C*), 30.37 (s, alkyl-*C*), 30.26 (s, alkyl-*C*), 30.10 (s, alkyl-*C*), 30.07 (s, alkyl-*C*) 25.01 (s, alkyl-*C*), 23.40 (s, alkyl-*C*), 18.32 (s, alkyl-*C*), 14.38 (s, alkyl-*C*). ^{29}Si (CD_3CN, 80 MHz): -75.43 (s). Anal. Calcd. For $C_{56}H_{72}F_{48}MgO_{14}Si_2$ (%): C, 34.29; H, 3.70. Found: C, 34.25; H, 3.41.

[Mg(DME)$_3$][^{C6F5}SiF]$_2$

^{1}H (CD_3CN, 400 MHz): 3.52 (s, 12 H, $CH_3OCH_2CH_2OCH_3$), 3.34 (s, 18 H, $CH_3OCH_2CH_2OCH_3$). ^{19}F (CD_3CN, 376 MHz,): -69.96 (br. s, 48 F, -C*F*$_3$), -12.25 (dd, 2F, Ar-*F*), -157.0. (tt, 2 F, Ar-*F*), -165.92 (m, 4 F, Ar-*F*). ^{13}C{^{1}H} (CD_3CN, 101 MHz): 148.57 (d app m, Ar-*C*), 141.81 (d app m, Ar-*C*), 137.70 (d app m, Ar-*C*), 122.75 (q app m, *C*F_3), 114.17 (app t, Ar-*C*), 84.05 (br s, O*C*$(CF_3)_2$), 72.22 (s, $CH_3OCH_2CH_2OCH_3$), 59.16 (s, $CH_3OCH_2CH_2OCH_3$). Anal. Calcd. For $C_{48}H_{30}F_{58}MgO_{14}Si_2$ (%): C, 28.64; H, 1.50. Found: C, 28.56; H, 1.54.

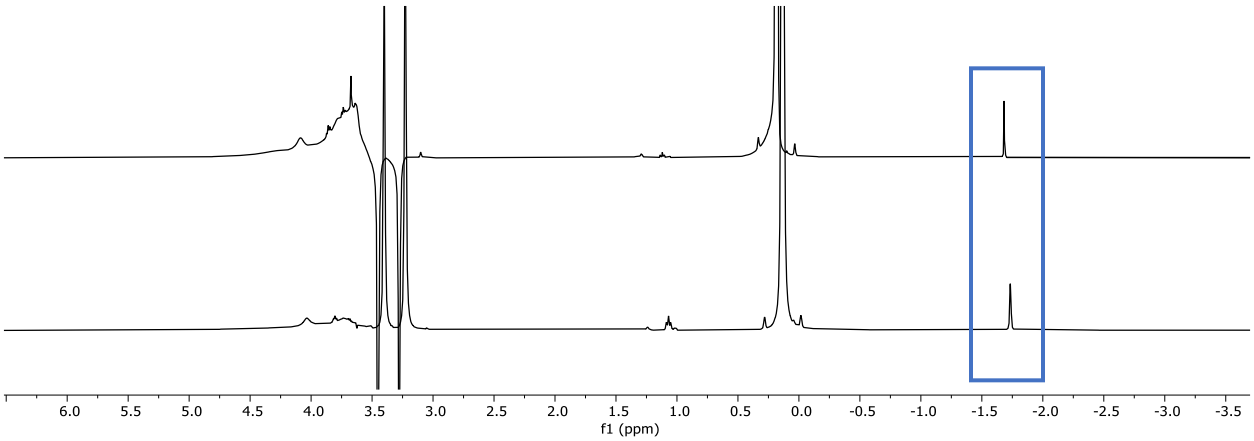

Figure 6.21. Post-CV ^{1}H NMR of 0.26 M $[Mg(DME)_3][^{Me}SiF]_2$ with 0 mM MgMe2 (replicate experiments with different electrolyte batches. The peak at ~0.2 ppm corresponds to -CH_3 of $[^{Me}SiF]^-$

NMR SPECTRA of [Mg(DME)$_3$][^{Me}SiF]$_2$

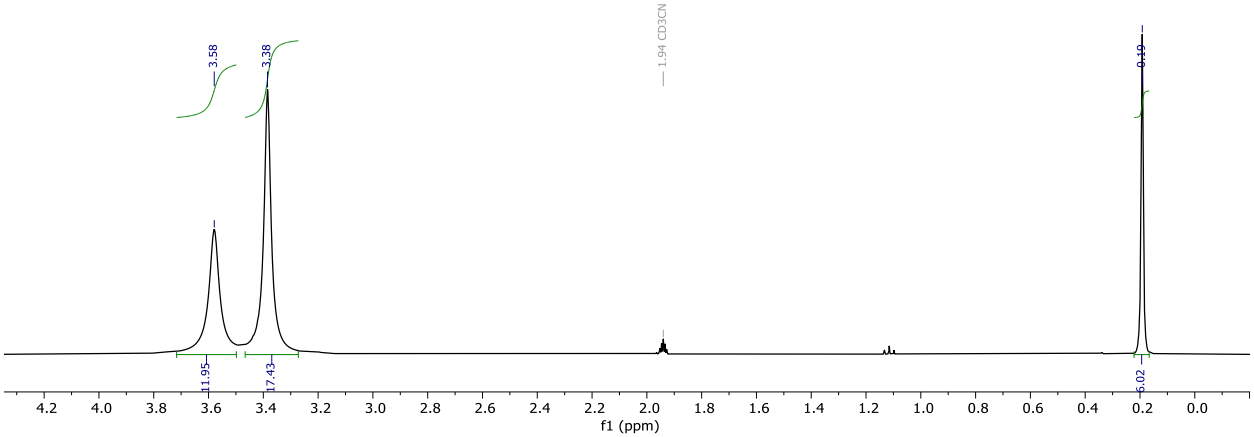

Figure 6.21. ^{1}H NMR of [Mg(DME)$_3$][^{Me}SiF]$_2$ in CD$_3$CN.

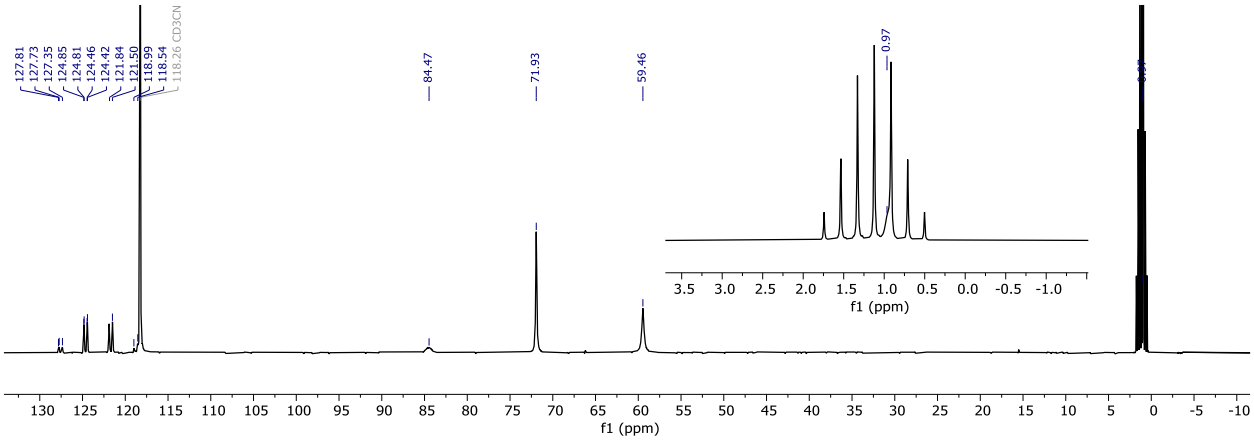

Figure 6.22. ^{13}C NMR of [Mg(DME)$_3$][^{Me}SiF]$_2$ in CD$_3$CN.

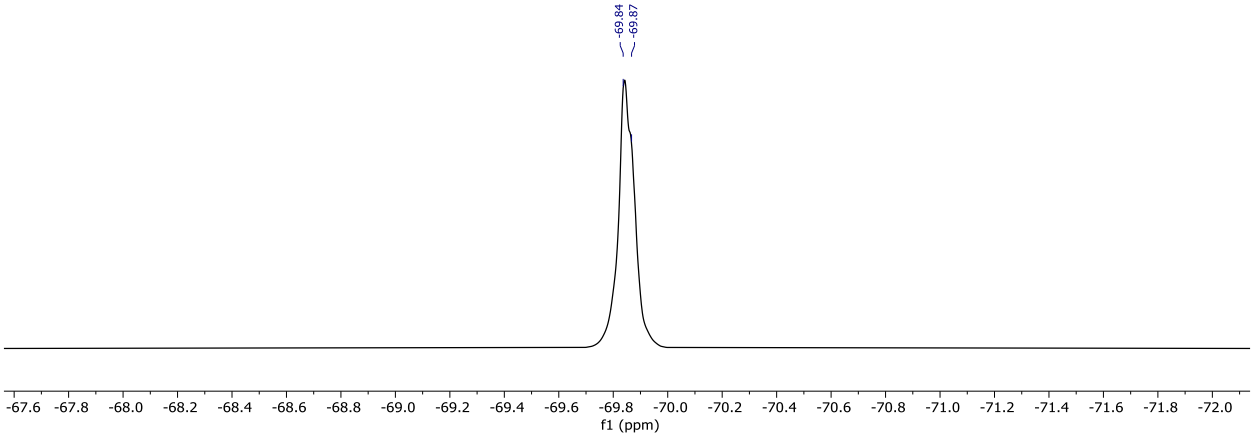

Figure 6.23. ^{19}F NMR of [Mg(DME)$_3$][^{Me}SiF]$_2$ in CD$_3$CN.

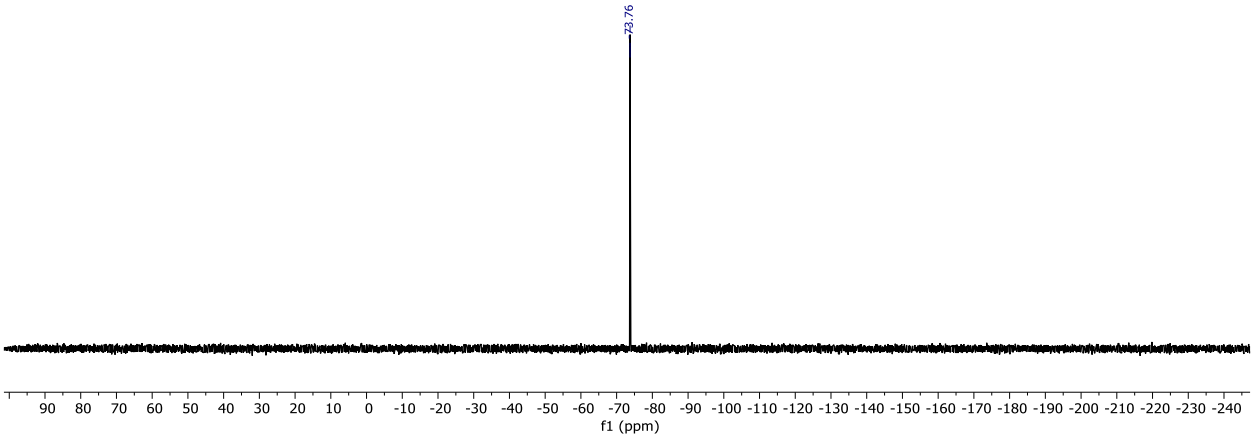

Figure 6.24. ^{29}Si NMR of [Mg(DME)$_3$][^{Me}SiF]$_2$ in CD$_3$CN.

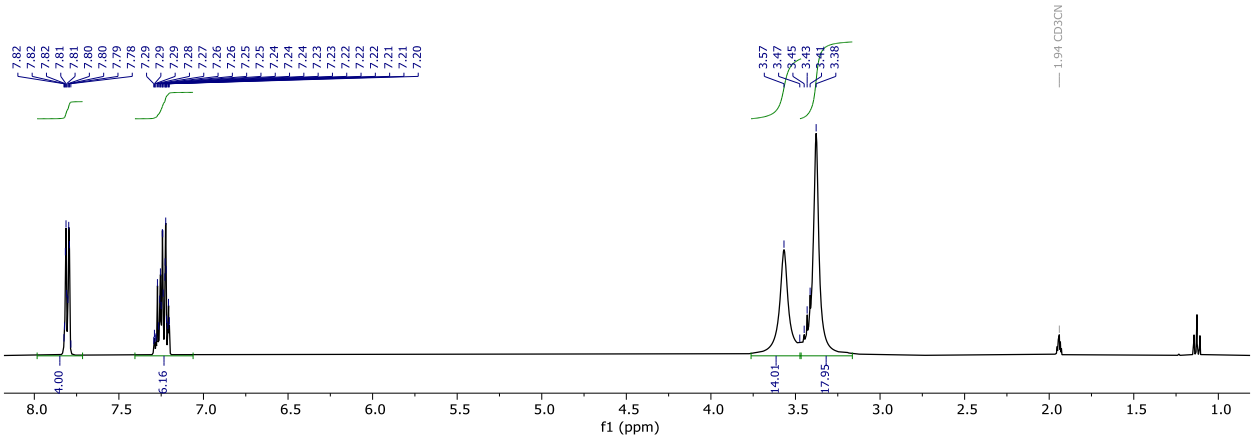

Figure 6.25. ^{1}H NMR of [Mg(DME)$_3$][^{Ph}SiF]$_2$ in CD$_3$CN.

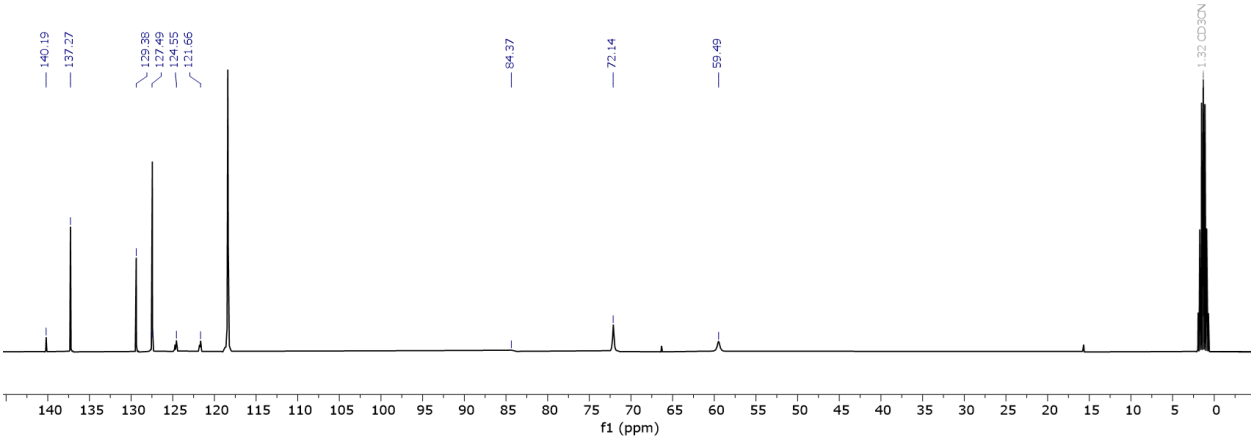

Figure 6.26. ^{13}C NMR of [Mg(DME)$_3$][^{Ph}SiF]$_2$ in CD$_3$CN.

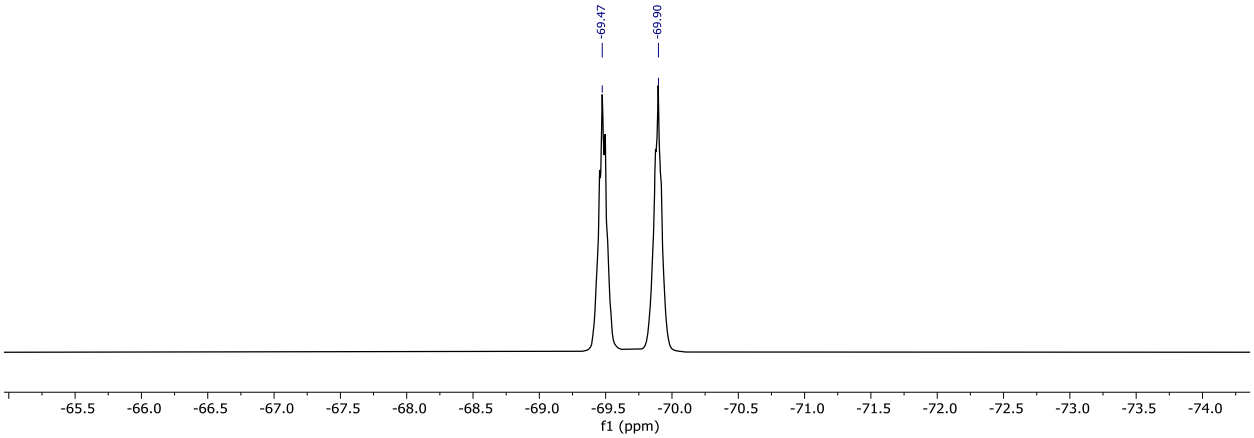

Figure 6.27. ^{19}F NMR of $[Mg(DME)_3][^{Ph}SiF]_2$ in CD_3CN.

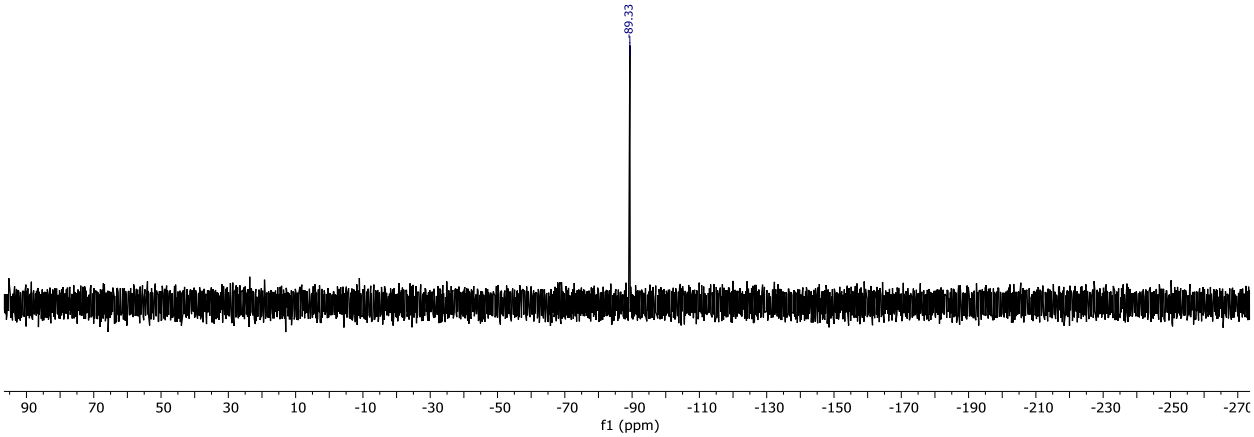

Figure 6.28. ^{29}Si NMR of $[Mg(DME)_3][^{Ph}SiF]_2$ in CD_3CN.

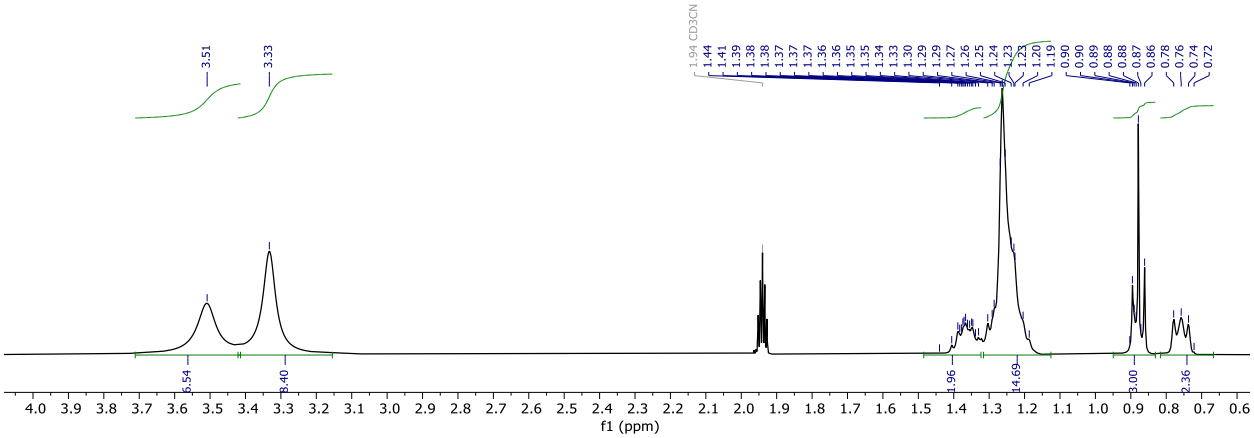

Figure 6.29. ^{1}H NMR of $[Mg(DME)_3][^{Decyl}SiF]_2$ in CD_3CN.

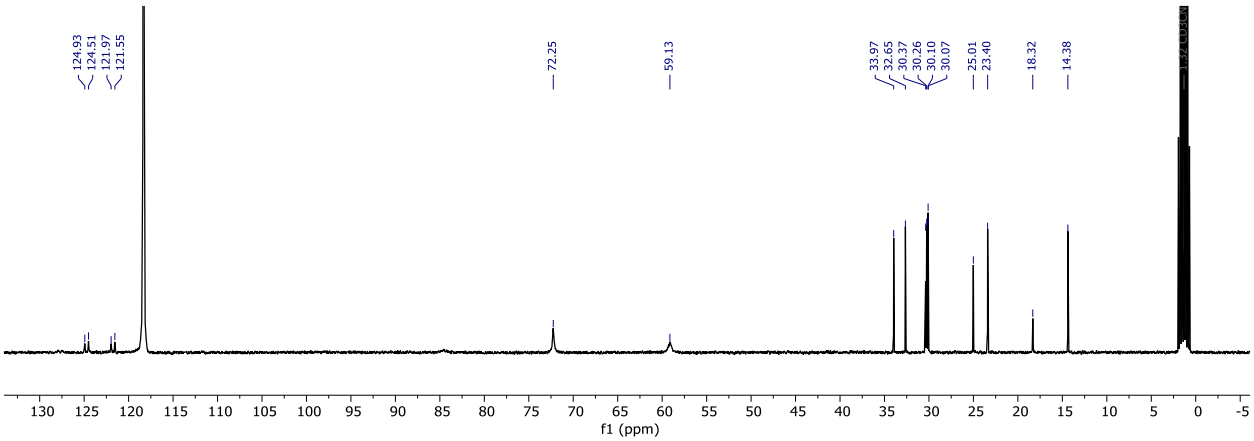

Figure 6.30. ^{13}C NMR of $[Mg(DME)_3][^{Decyl}SiF]_2$ in CD_3CN.

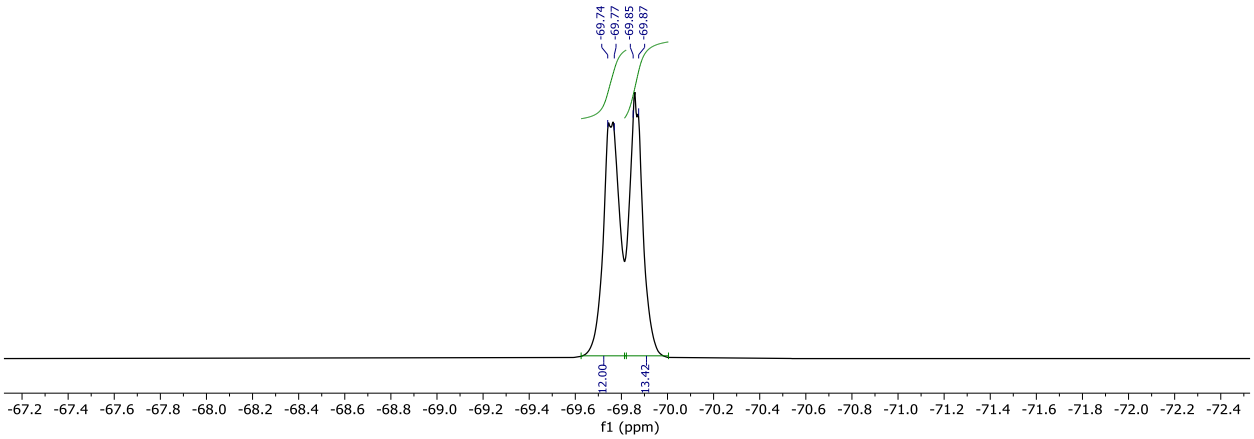

Figure 6.31. ^{19}F NMR of $[Mg(DME)_3][^{Decyl}SiF]_2$ in CD_3CN.

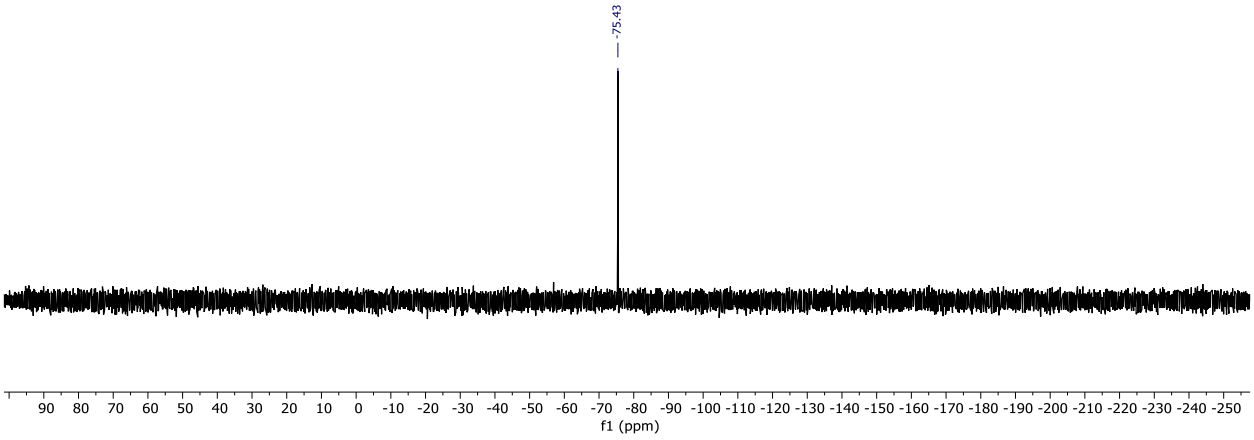

Figure 6.32. ^{29}Si NMR of $[Mg(DME)_3][^{Decyl}SiF]_2$ in CD_3CN.

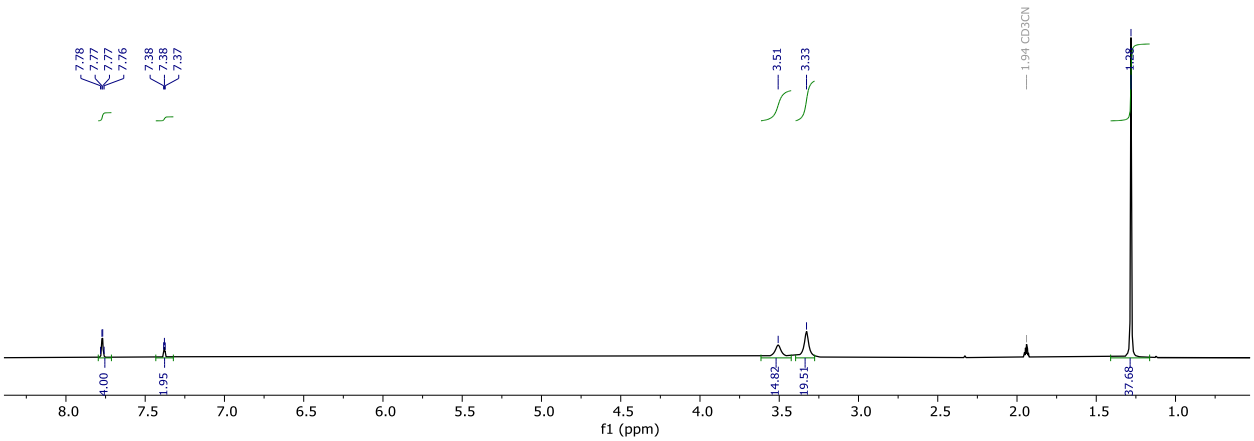

Figure 6.33. ^{1}H NMR of $[Mg(DME)_3][^{tBu2Ph}SiF]_2$ in CD_3CN.

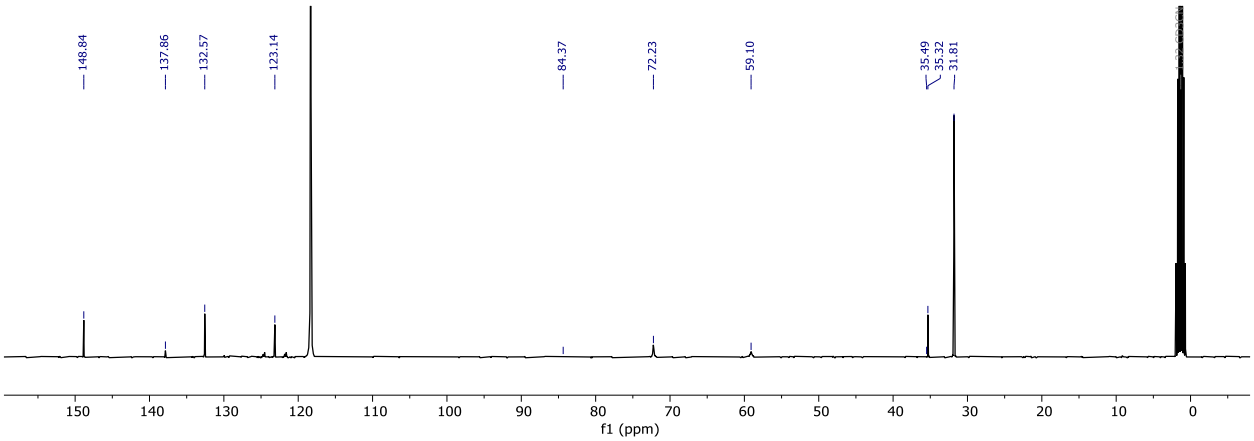

Figure 6.34. ^{13}C NMR of $[Mg(DME)_3][^{tBu2Ph}SiF]_2$ in CD_3CN.

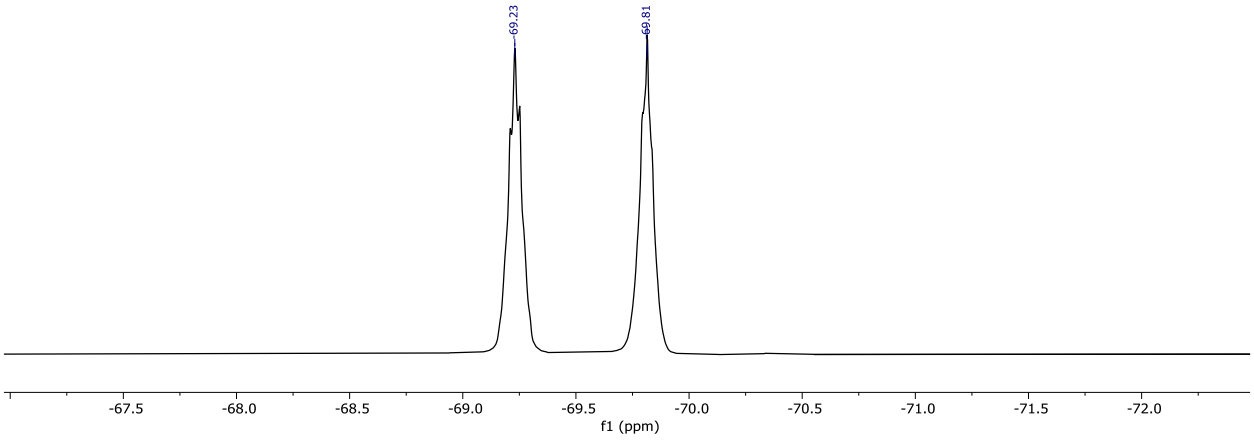

Figure 6.35. ^{19}F NMR of $[Mg(DME)_3][^{tBu2Ph}SiF]_2$ in CD_3CN.

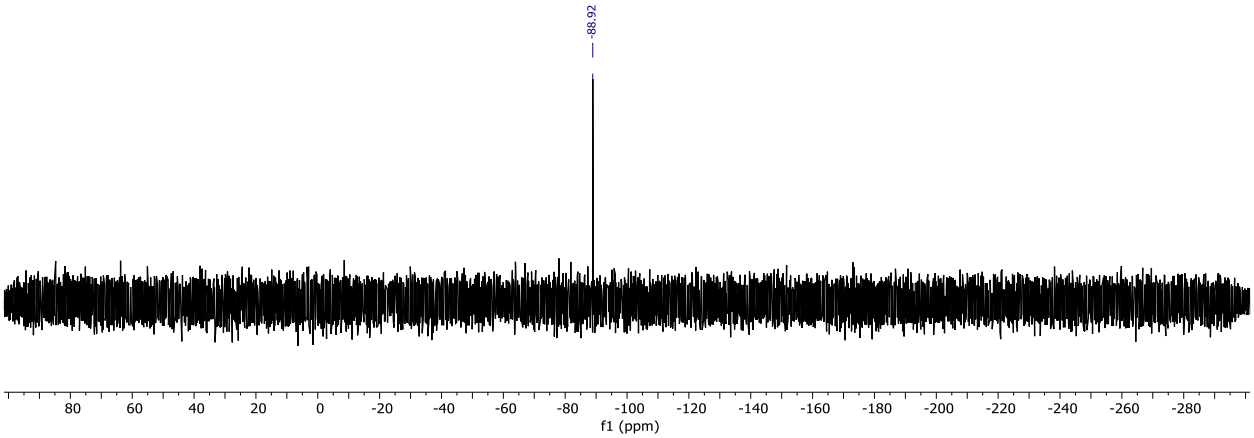

Figure 6.36. ^{29}Si NMR of $[Mg(DME)_3][^{tBu2Ph}SiF]_2$ in CD_3CN.

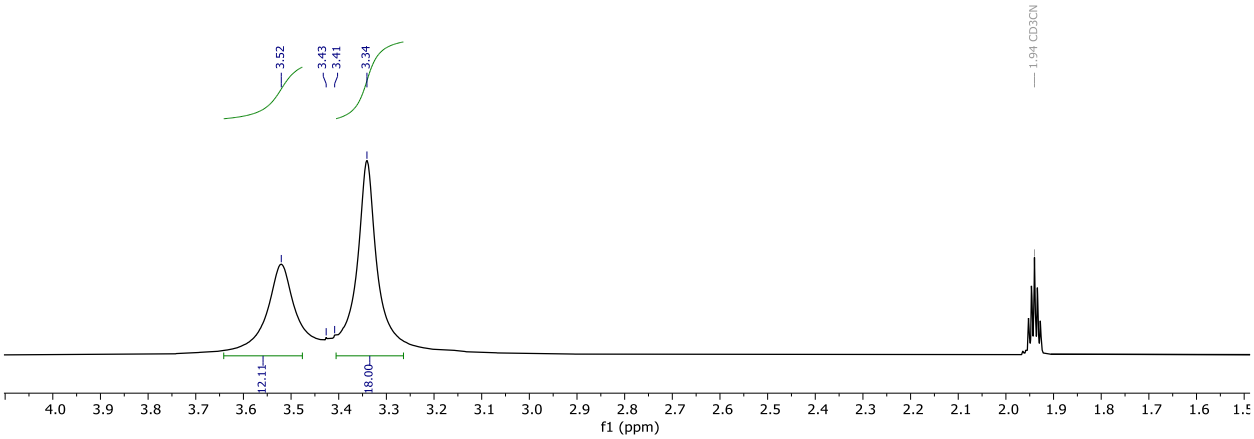

Figure 6.37. ^{1}H NMR of $[Mg(DME)_3][^{C6F5}SiF]_2$ in CD_3CN.

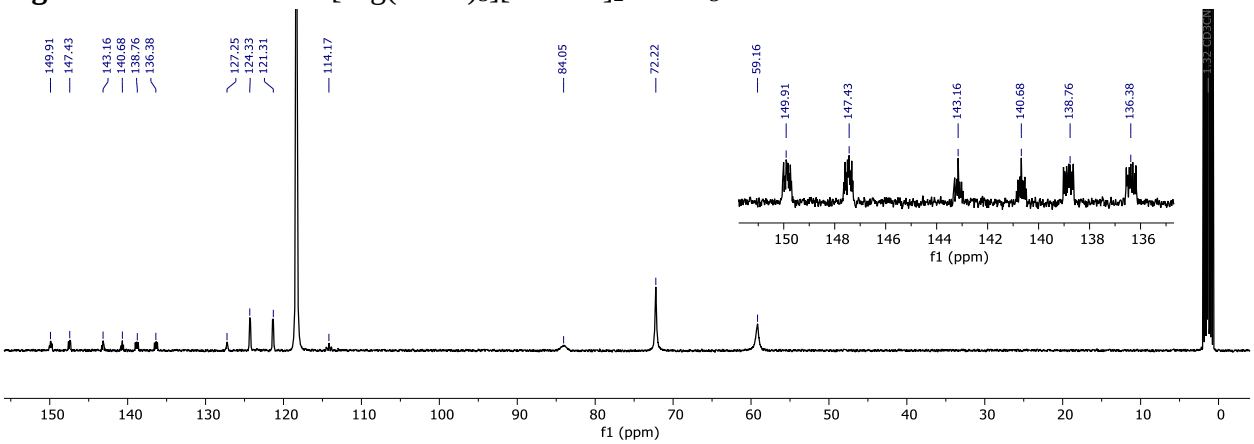

Figure 6.38. ^{13}C NMR of $[Mg(DME)_3][^{C6F5}SiF]_2$ in CD_3CN.

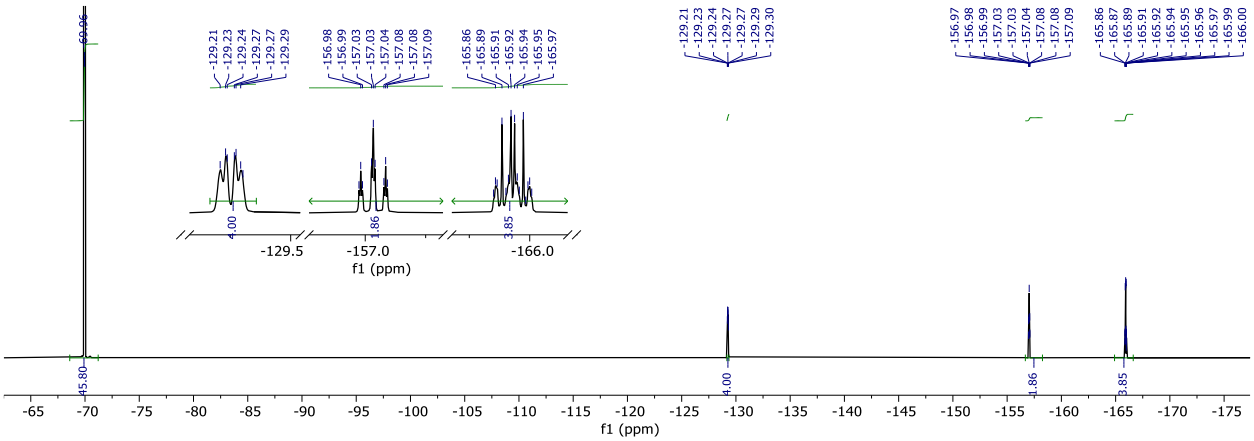

Figure 6.39. ^{19}F NMR of $[Mg(DME)_3][^{C6F5}SiF]_2$ in CD_3CN.

REFERENCES

1. Keyzer, Evan N.; Lee, J.; Liu, Z.; Bond, A. D.; Wright, D. S.; Grey, C. P., A general synthetic methodology to access magnesium aluminate electrolyte systems for Mg batteries. *Journal of Materials Chemistry A* **2019,** *7* (6), 2677-2685. 10.1039/C8TA10295C
2. Dunn, B.; Kamath, H.; Tarascon, J.-M., Electrical Energy Storage for the Grid: A Battery of Choices. *Science* **2011,** *334* (6058), 928-935. 10.1126/science.1212741
3. Yang, Z.; Zhang, J.; Kintner-Meyer, M. C. W.; Lu, X.; Choi, D.; Lemmon, J. P.; Liu, J., Electrochemical Energy Storage for Green Grid. *Chem. Rev.* **2011,** *111* (5), 3577-3613. 10.1021/cr100290v
4. Finance, B. N. E., Electric vehicle outlook 2017. *Bloomberg Finance LP, Tech. Rep* **2017**.
5. Goodenough, J. B.; Park, K.-S., The Li-Ion Rechargeable Battery: A Perspective. *J. Am. Chem. Soc.* **2013,** *135* (4), 1167-1176. 10.1021/ja3091438
6. Nitta, N.; Wu, F.; Lee, J. T.; Yushin, G., Li-ion battery materials: present and future. *Mater. Today* **2015,** *18* (5), 252-264. 10.1016/j.mattod.2014.10.040
7. Tarascon, J.-M., Is lithium the new gold? *Nature Chemistry* **2010,** *2* (6), 510-510. 10.1038/nchem.680
8. Vikström, H.; Davidsson, S.; Höök, M., Lithium availability and future production outlooks. *Applied Energy* **2013,** *110*, 252-266. 10.1016/j.apenergy.2013.04.005
9. Scrosati, B.; Garche, J., Lithium batteries: Status, prospects and future. *J. Power Sources* **2010,** *195* (9), 2419-2430. 10.1016/j.jpowsour.2009.11.048
10. Lau, K.-C.; Seguin, T. J.; Carino, E. V.; Hahn, N. T.; Connell, J. G.; Ingram, B. J.; Persson, K. A.; Zavadil, K. R.; Liao, C., Widening Electrochemical Window of Mg Salt by Weakly Coordinating Perfluoroalkoxyaluminate Anion for Mg Battery Electrolyte. *J. Electrochem. Soc.* **2019,** *166* (8), A1510. 10.1149/2.0751908jes
11. Schmidt, A.; Koger, H.; Barthélemy, A.; Studer, G.; Esser, B.; Krossing, I., Is One of the Least Coordinating Anions Suitable to Serve as Electrolyte Salt for Magnesium-Ion Batteries? *Batteries & Supercaps* **2022,** *5* (12), e202200340. 10.1002/batt.202200340
12. Turcheniuk, K.; Bondarev, D.; Singhal, V.; Yushin, G., Nature Publishing Group: 2018.
13. Olivetti, E. A.; Ceder, G.; Gaustad, G. G.; Fu, X., Lithium-Ion Battery Supply Chain Considerations: Analysis of Potential Bottlenecks in Critical Metals. *Joule* **2017,** *1* (2), 229-243. 10.1016/j.joule.2017.08.019
14. Chen, Y.; Kang, Y.; Zhao, Y.; Wang, L.; Liu, J.; Li, Y.; Liang, Z.; He, X.; Li, X.; Tavajohi, N.; Li, B., A review of lithium-ion battery safety concerns: The issues, strategies, and testing standards. *Journal of Energy Chemistry* **2021,** *59*, 83-99. 10.1016/j.jechem.2020.10.017
15. Feng, X.; Ren, D.; He, X.; Ouyang, M., Mitigating Thermal Runaway of Lithium-Ion Batteries. *Joule* **2020,** *4* (4), 743-770. 10.1016/j.joule.2020.02.010
16. Fang, H., Challenges with the Ultimate Energy Density with Li-ion Batteries. *IOP Conference Series: Earth and Environmental Science* **2021,** *781* (4), 042023. 10.1088/1755-1315/781/4/042023
17. Usiskin, R.; Lu, Y.; Popovic, J.; Law, M.; Balaya, P.; Hu, Y.-S.; Maier, J., Fundamentals, status and promise of sodium-based batteries. *Nature Reviews Materials* **2021,** *6* (11), 1020-1035. 10.1038/s41578-021-00324-w
18. Hosaka, T.; Kubota, K.; Hameed, A. S.; Komaba, S., Research Development on K-Ion Batteries. *Chem. Rev.* **2020,** *120* (14), 6358-6466. 10.1021/acs.chemrev.9b00463

19. Jia, X.; Liu, C.; Neale, Z. G.; Yang, J.; Cao, G., Active Materials for Aqueous Zinc Ion Batteries: Synthesis, Crystal Structure, Morphology, and Electrochemistry. *Chem. Rev.* **2020,** *120* (15), 7795-7866. 10.1021/acs.chemrev.9b00628
20. Hosein, I. D., The Promise of Calcium Batteries: Open Perspectives and Fair Comparisons. *ACS Energy Letters* **2021,** *6* (4), 1560-1565. 10.1021/acsenergylett.1c00593
21. Liu, F.; Wang, T.; Liu, X.; Fan, L.-Z., Challenges and Recent Progress on Key Materials for Rechargeable Magnesium Batteries. *Advanced Energy Materials* **2021,** *11* (2), 2000787. 10.1002/aenm.202000787
22. Ng, K. L.; Amrithraj, B.; Azimi, G., Nonaqueous rechargeable aluminum batteries. *Joule* **2022,** *6* (1), 134-170. 10.1016/j.joule.2021.12.003
23. Faegh, E.; Ng, B.; Hayman, D.; Mustain, W. E., Practical assessment of the performance of aluminium battery technologies. *Nature Energy* **2021,** *6* (1), 21-29. 10.1038/s41560-020-00728-y
24. Das, S. K.; Mahapatra, S.; Lahan, H., Aluminium-ion batteries: developments and challenges. *Journal of Materials Chemistry A* **2017,** *5* (14), 6347-6367. 10.1039/C7TA00228A
25. Yang, H.; Li, H.; Li, J.; Sun, Z.; He, K.; Cheng, H.-M.; Li, F., The Rechargeable Aluminum Battery: Opportunities and Challenges. *Angew. Chem. Int. Ed.* **2019,** *58* (35), 11978-11996. 10.1002/anie.201814031
26. Das, S.; Manna, S. S.; Pathak, B., Recent Trends in Electrode and Electrolyte Design for Aluminum Batteries. *ACS Omega* **2021,** *6* (2), 1043-1053. 10.1021/acsomega.0c04163
27. Lu, Z.; Schechter, A.; Moshkovich, M.; Aurbach, D., On the electrochemical behavior of magnesium electrodes in polar aprotic electrolyte solutions. *J. Electroanal. Chem.* **1999,** *466* (2), 203-217. 10.1016/S0022-0728(99)00146-1
28. Muldoon, J.; Bucur, C. B.; Oliver, A. G.; Zajicek, J.; Allred, G. D.; Boggess, W. C., Corrosion of magnesium electrolytes: chlorides – the culprit. *Energy & Environmental Science* **2013,** *6* (2), 482-487. 10.1039/C2EE23686A
29. Aurbach, D.; Lu, Z.; Schechter, A.; Gofer, Y.; Gizbar, H.; Turgeman, R.; Cohen, Y.; Moshkovich, M.; Levi, E., Prototype systems for rechargeable magnesium batteries. *Nature* **2000,** *407* (6805), 724-727. 10.1038/35037553
30. Li, Y.; Guan, S.; Huo, H.; Ma, Y.; Gao, Y.; Zuo, P.; Yin, G., A Review of Magnesium Aluminum Chloride Complex Electrolytes for Mg Batteries. *Adv. Funct. Mater.* **2021,** *31* (24), 2100650. 10.1002/adfm.202100650
31. Doe, R. E.; Han, R.; Hwang, J.; Gmitter, A. J.; Shterenberg, I.; Yoo, H. D.; Pour, N.; Aurbach, D., Novel, electrolyte solutions comprising fully inorganic salts with high anodic stability for rechargeable magnesium batteries. *Chem. Commun.* **2014,** *50* (2), 243-245. 10.1039/C3CC47896C
32. Mizrahi, O.; Amir, N.; Pollak, E.; Chusid, O.; Marks, V.; Gottlieb, H.; Larush, L.; Zinigrad, E.; Aurbach, D., Electrolyte Solutions with a Wide Electrochemical Window for Rechargeable Magnesium Batteries. *J. Electrochem. Soc.* **2008,** *155* (2), A103. 10.1149/1.2806175
33. Mohtadi, R.; Matsui, M.; Arthur, T. S.; Hwang, S.-J., Magnesium Borohydride: From Hydrogen Storage to Magnesium Battery. *Angew. Chem. Int. Ed.* **2012,** *51* (39), 9780-9783. 10.1002/anie.201204913
34. Palisoc, S.; Joe Santos, D.; Natividad, M., Borohydride-based electrolyte system for Magnesium-Persulfate ($Mg||MgS_2O_8$) rechargeable battery. *Ain Shams Engineering Journal* **2021,** *12* (3), 3021-3030. 10.1016/j.asej.2020.09.032
35. Shao, Y.; Liu, T.; Li, G.; Gu, M.; Nie, Z.; Engelhard, M.; Xiao, J.; Lv, D.; Wang, C.; Zhang, J.-G.; Liu, J., Coordination Chemistry in magnesium battery electrolytes: how ligands affect their performance. *Scientific Reports* **2013,** *3* (1), 3130. 10.1038/srep03130

36. Aurbach, D.; Weissman, I.; Gofer, Y.; Levi, E., Nonaqueous magnesium electrochemistry and its application in secondary batteries. *The Chemical Record* **2003,** *3* (1), 61-73. 10.1002/tcr.10051
37. Ha, S.-Y.; Lee, Y.-W.; Woo, S. W.; Koo, B.; Kim, J.-S.; Cho, J.; Lee, K. T.; Choi, N.-S., Magnesium(II) Bis(trifluoromethane sulfonyl) Imide-Based Electrolytes with Wide Electrochemical Windows for Rechargeable Magnesium Batteries. *ACS Applied Materials & Interfaces* **2014,** *6* (6), 4063-4073. 10.1021/am405619v
38. Ma, Z.; Kar, M.; Xiao, C.; Forsyth, M.; MacFarlane, D. R., Electrochemical cycling of Mg in $Mg[TFSI]_2$/tetraglyme electrolytes. *Electrochem. Commun.* **2017,** *78*, 29-32. 10.1016/j.elecom.2017.03.018
39. Fukutsuka, T.; Asaka, K.; Inoo, A.; Yasui, R.; Miyazaki, K.; Abe, T.; Nishio, K.; Uchimoto, Y., New Magnesium-ion Conductive Electrolyte Solution Based on Triglyme for Reversible Magnesium Metal Deposition and Dissolution at Ambient Temperature. *Chem. Lett.* **2014,** *43* (11), 1788-1790. 10.1246/cl.140704
40. Shterenberg, I.; Salama, M.; Yoo, H. D.; Gofer, Y.; Park, J.-B.; Sun, Y.-K.; Aurbach, D., Evaluation of $(CF_3SO_2)_2N^-$ (TFSI) Based Electrolyte Solutions for Mg Batteries. *J. Electrochem. Soc.* **2015,** *162* (13), A7118. 10.1149/2.0161513jes
41. Jay, R.; Tomich, A. W.; Zhang, J.; Zhao, Y.; De Gorostiza, A.; Lavallo, V.; Guo, J., Comparative Study of $Mg(CB_{11}H_{12})_2$ and $Mg(TFSI)_2$ at the Magnesium/Electrolyte Interface. *ACS Applied Materials & Interfaces* **2019,** *11* (12), 11414-11420. 10.1021/acsami.9b00037
42. Baskin, A.; Prendergast, D., Exploration of the Detailed Conditions for Reductive Stability of $Mg(TFSI)_2$ in Diglyme: Implications for Multivalent Electrolytes. *The Journal of Physical Chemistry C* **2016,** *120* (7), 3583-3594. 10.1021/acs.jpcc.5b08999
43. Rajput, N. N.; Qu, X.; Sa, N.; Burrell, A. K.; Persson, K. A., The Coupling between Stability and Ion Pair Formation in Magnesium Electrolytes from First-Principles Quantum Mechanics and Classical Molecular Dynamics. *J. Am. Chem. Soc.* **2015,** *137* (9), 3411-3420. 10.1021/jacs.5b01004
44. Dlugatch, B.; Mohankumar, M.; Attias, R.; Krishna, B. M.; Elias, Y.; Gofer, Y.; Zitoun, D.; Aurbach, D., Evaluation of Mg[B(HFIP)4]2-Based Electrolyte Solutions for Rechargeable Mg Batteries. *ACS Applied Materials & Interfaces* **2021,** *13* (46), 54894-54905. 10.1021/acsami.1c13419
45. Mandai, T., Critical Issues of Fluorinated Alkoxyborate-Based Electrolytes in Magnesium Battery Applications. *ACS Applied Materials & Interfaces* **2020,** *12* (35), 39135-39144. 10.1021/acsami.0c09948
46. Herb, J. T.; Nist-Lund, C. A.; Arnold, C. B., A Fluorinated Alkoxyaluminate Electrolyte for Magnesium-Ion Batteries. *ACS Energy Letters* **2016,** *1* (6), 1227-1232. 10.1021/acsenergylett.6b00356
47. Luo, J.; Bi, Y.; Zhang, L.; Zhang, X.; Liu, T. L., A Stable, Non-Corrosive Perfluorinated Pinacolatoborate Mg Electrolyte for Rechargeable Mg Batteries. *Angew. Chem. Int. Ed.* **2019,** *58* (21), 6967-6971. 10.1002/anie.201902009
48. Tomich, A. W.; Chen, J.; Carta, V.; Guo, J.; Lavallo, V., Electrolyte Engineering with Carboranes for Next-Generation Mg Batteries. *ACS Central Science* **2024,** *10* (2), 264-271. 10.1021/acscentsci.3c01176
49. Tutusaus, O.; Mohtadi, R.; Arthur, T. S.; Mizuno, F.; Nelson, E. G.; Sevryugina, Y. V., An Efficient Halogen-Free Electrolyte for Use in Rechargeable Magnesium Batteries. *Angew. Chem. Int. Ed.* **2015,** *54* (27), 7900-7904. 10.1002/anie.201412202

50. McArthur, S. G.; Jay, R.; Geng, L.; Guo, J.; Lavallo, V., Below the 12-vertex: 10-vertex carborane anions as non-corrosive, halide free, electrolytes for rechargeable Mg batteries. *Chem. Commun.* **2017,** *53* (32), 4453-4456. 10.1039/C7CC01570D
51. McArthur, S. G.; Geng, L.; Guo, J.; Lavallo, V., Cation reduction and comproportionation as novel strategies to produce high voltage, halide free, carborane based electrolytes for rechargeable Mg batteries. *Inorganic Chemistry Frontiers* **2015,** *2* (12), 1101-1104. 10.1039/C5QI00171D
52. Watanabe, M.; Kanazawa, J.; Hamamura, T.; Shimokawa, T.; Miyamoto, K.; Hibino, M.; Nakura, K.; Inatomi, Y.; Kitazawa, Y.; Uchiyama, M., Boron-vertex modification of carba-closo-dodecaborate for high-performance magnesium-ion battery electrolyte. *Materials Advances* **2021,** *2* (3), 937-941. 10.1039/D0MA00925C
53. Brown, O. R.; McIntyre, R., The magnesium and magnesium amalgam electrodes in aprotic organic solvents a kinetic study. *Electrochim. Acta* **1985,** *30* (5), 627-633. 10.1016/0013-4686(85)80104-3
54. Zhao-Karger, Z.; Gil Bardaji, M. E.; Fuhr, O.; Fichtner, M., A new class of non-corrosive, highly efficient electrolytes for rechargeable magnesium batteries. *Journal of Materials Chemistry A* **2017,** *5* (22), 10815-10820. 10.1039/C7TA02237A
55. Strem Cesium Carborane; 55-5525. (accessed 05/05/24).
56. Metathesis via precipitation of AgCl or AgBr (because of their negligible solubility in organic solvents) is an exception, but silver salt are not common intermediates to Mg-electrolytes.
57. Aldrich, S. Product Specification-Di-n-butylmagnesium solution-1.0 M in heptane. (accessed 05/05/24).
58. Aldrich, S. Product Specification-Lithium aluminum hydride-powder, reagent grade, 95%. (accessed 05/05/24).
59. Aldrich, S. Product Specification-Magnesium bis(hexamethyldisilazide)-97%. (accessed 05/05/24).
60. Mohtadi, R.; Mizuno, F., Magnesium batteries: Current state of the art, issues and future perspectives. *Beilstein Journal of Nanotechnology* **2014,** *5*, 1291-1311. 10.3762/bjnano.5.143
61. Yoo, H. D.; Shterenberg, I.; Gofer, Y.; Gershinsky, G.; Pour, N.; Aurbach, D., Mg rechargeable batteries: an on-going challenge. *Energy & Environmental Science* **2013,** *6* (8), 2265-2279. 10.1039/C3EE40871J
62. Connell, J. G.; Genorio, B.; Lopes, P. P.; Strmcnik, D.; Stamenkovic, V. R.; Markovic, N. M., Tuning the Reversibility of Mg Anodes via Controlled Surface Passivation by H_2O/Cl^- in Organic Electrolytes. *Chem. Mater.* **2016,** *28* (22), 8268-8277. 10.1021/acs.chemmater.6b03227
63. Yang, Z.; Yang, M.; Hahn, N. T.; Connell, J.; Bloom, I.; Liao, C.; Ingram, B. J.; Trahey, L., Toward practical issues: Identification and mitigation of the impurity effect in glyme solvents on the reversibility of Mg plating/stripping in Mg batteries. *Frontiers in Chemistry* **2022,** *10*. 10.3389/fchem.2022.966332
64. Kim, S. S.; See, K. A., Activating Magnesium Electrolytes through Chemical Generation of Free Chloride and Removal of Trace Water. *ACS Applied Materials & Interfaces* **2021,** *13* (1), 671-680. 10.1021/acsami.0c19053
65. Kim, S. S.; Bevilacqua, S. C.; See, K. A., Conditioning-Free Mg Electrolyte by the Minor Addition of Mg(HMDS)2. *ACS Applied Materials & Interfaces* **2020,** *12* (5), 5226-5233. 10.1021/acsami.9b16710
66. Seguin, T. J.; Hahn, N. T.; Zavadil, K. R.; Persson, K. A., Elucidating Non-aqueous Solvent Stability and Associated Decomposition Mechanisms for Mg Energy Storage Applications From First-Principles. *Frontiers in Chemistry* **2019,** *7*. 10.3389/fchem.2019.00175

67. Pavčnik, T.; Lozinšek, M.; Pirnat, K.; Vizintin, A.; Mandai, T.; Aurbach, D.; Dominko, R.; Bitenc, J., On the Practical Applications of the Magnesium Fluorinated Alkoxyaluminate Electrolyte in Mg Battery Cells. *ACS Applied Materials & Interfaces* **2022,** *14* (23), 26766-26774. 10.1021/acsami.2c05141
68. Ely, D. R.; García, R. E., Heterogeneous Nucleation and Growth of Lithium Electrodeposits on Negative Electrodes. *J. Electrochem. Soc.* **2013,** *160* (4), A662. 10.1149/1.057304jes
69. Guan, X.; Wang, A.; Liu, S.; Li, G.; Liang, F.; Yang, Y.-W.; Liu, X.; Luo, J., Controlling Nucleation in Lithium Metal Anodes. *Small* **2018,** *14* (37), 1801423. 10.1002/smll.201801423
70. Zeng, Z.; Barai, P.; Lee, S.-Y.; Yang, J.; Zhang, X.; Zheng, W.; Liu, Y.-S.; Bustillo, K. C.; Ercius, P.; Guo, J.; Cui, Y.; Srinivasan, V.; Zheng, H., Electrode roughness dependent electrodeposition of sodium at the nanoscale. *Nano Energy* **2020,** *72*, 104721. 10.1016/j.nanoen.2020.104721
71. The dioxane precipitation method is not as halide-free as transmetallation between Mg metal and Me_2Hg, it was preferred due to the extreme toxicity of dialkylmercury compounds.
72. Wang, F.; Hua, H.; Wu, D.; Li, J.; Xu, Y.; Nie, X.; Zhuang, Y.; Zeng, J.; Zhao, J., Solvent Molecule Design Enables Excellent Charge Transfer Kinetics for a Magnesium Metal Anode. *ACS Energy Letters* **2023,** *8* (1), 780-789. 10.1021/acsenergylett.2c02525
73. Shriver, D. F.; Drezdzon, M. A., The Manipulation of Air-Sensitive Compounds. Wiley: 1986.
74. Giffin, G. A., The role of concentration in electrolyte solutions for non-aqueous lithium-based batteries. *Nature Communications* **2022,** *13* (1), 5250. 10.1038/s41467-022-32794-z
75. Pangborn, A. B.; Giardello, M. A.; Grubbs, R. H.; Rosen, R. K.; Timmers, F. J., Safe and Convenient Procedure for Solvent Purification. *Organometallics* **1996,** *15* (5), 1518-1520. 10.1021/om9503712
76. Frye, C. L., Pentacoordinate silicon derivatives. IV. Alkylammonium siliconate salts derived from aliphatic 1,2-diols. *J. Am. Chem. Soc.* **1970,** *92* (5), 1205-1210. 10.1021/ja00708a016

APPENDIX A: Copolymerization of Ethylene and Long-Chain Functional α-Olefins by Dinuclear Zirconium Catalysts

This work was published in part as:

Sampson, J.; **Bruening, M.A.**; Akhtar, M.N.; Jaseer, E.A.; Theravalappil, R.; Garcia, N; Agapie, T. Copolymerization of Ethylene and Long-Chain Functional α-Olefins by Dinuclear Zirconium Catalysts. *Orgamometallics*, **2021**, 40,12, 1854-1858. 10.1021/acs.organomet.1c00126

For author contributions, see Page vii.

ABSTRACT

Bimetallic catalysts have shown promise for improving polar comonomer incorporation by late transition metals, but such effects are underexplored using early transition metal catalysts. Herein, the copolymerization of ethylene and α-olefins bearing alcohol groups was performed using mono- and dizirconium bisamine bisphenolate catalysts in the presence of MAO and $Al^{i}Bu_3$. Under these conditions, catalyst activity was retained with comonomer incorporation trends mirroring those observed with unfunctionalized α-olefins, i.e., lower incorporation by bimetallic catalysts. Although incorporation levels are low, these data provide mechanistic insight for polar comonomer incorporation. These results are consistent with our earlier proposal that larger comonomers sterically clash with the distal metal center of the bimetallic catalysts, leading to lower incorporation. Additionally, a bimetallic mechanism for polar comonomer coordination and incorporation is not supported by the current data.

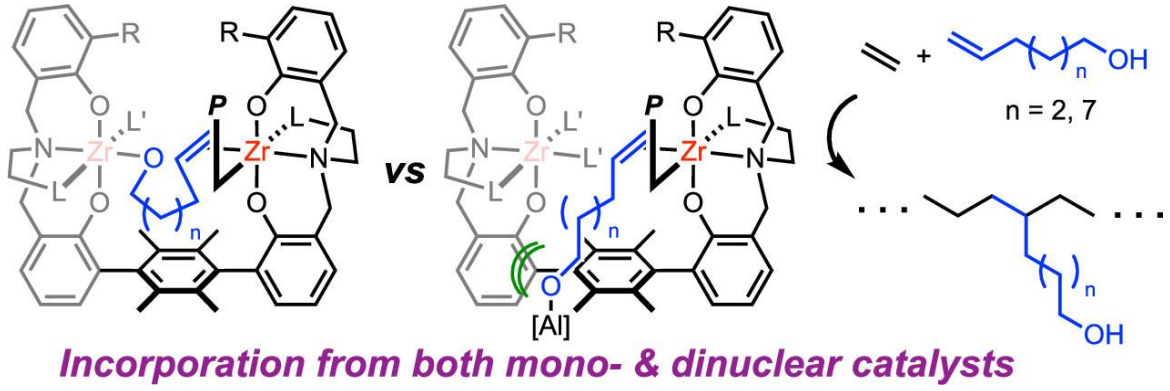

GENERAL INTRODUCTION

Multimetallic catalysts have been pursued as a method for synthesizing functionalized polyethylene *via* a direct copolymerization of ethylene and polar monomers.[1] Examples of bimetallic catalysts with rigid linkers that feature improved performance include enhanced incorporation of functionalized norbornenes using dinickel catalysts (**A**; Figure A.1),[2] higher incorporation of ester-containing comonomers and acrylic anhydride using macrocyclic frameworks to support "double-decker" dinickel or dipalladium catalysts with phenoxy-imine (**B**) or α-diimine (**C**) donors,[3-7] and increased tolerance to amine additives and incorporation of amino olefins by terphenyl-supported bis(phenoxy-imine)dinickel catalysts (**D**).[8-10] Bimetallic catalysts displaying early transition metals have been demonstrated to affect performance by increasing the incorporation of α-olefins (**E** and **F**), [11-19] though not those containing polar groups. A bimetallic mechanism of α-olefin incorporation was proposed where distal C–H bonds interact with the second metal to facilitate enchainment.[15-17, 20-23] An analogous bimetallic mechanism for comonomer incorporation is particularly appealing for polar olefins.

Incorporation of polar comonomers by early transition metal catalysts is desirable due to the high performance of the catalysts and abundance and low cost of those metals. However, catalyst poisoning by Lewis basic functional groups on typical comonomers requires the use of masking agents such as MAO or other alkylaluminum reagents.[24] This strategy has been employed for the copolymerization of long-chain esters by (phenoxy-imine)Ti catalysts, [25] incorporation of allyl alcohol derivatives by metallocenes,[26] modified (phenoxy-imine)Ti catalysts, [27-28] half-metallocene or guanidinate Ti catalysts,[29] and incorporation of halogen- and amine-functionalized comonomers by (pyridylamido)hafnium catalysts.[30-31] Direct polymerization or copolymerization of either silyl ether or amine containing comonomers by metallocenes has been reported.[32-34]

Our previously reported dizirconium olefin polymerization catalysts represent suitable candidates for studies of early transition metals, addressing the differences in performance of bimetallic and monometallic precatalysts in polar comonomer copolymerization.[35-36] We have employed bimetallic versions of the zirconium bisamine bisphenolate catalysts [37] based on a rigid teraryl framework (**G**) and showed that isotactically enriched poly(α-olefins) are generated *via* a site epimerization mechanism.[35] The dizirconium catalysts show enhanced activity relative to monozirconium controls, and a subsequent study demonstrated that such catalysts could also be employed for ethylene-α-olefin copolymerization.[36] These results provide a substantial basis for comparison to probe the effect of the catalyst nuclearity on the copolymerization of ethylene and comonomers bearing functional groups such as alcohols. Herein, we report that the incorporation of polar monomers, including 10-undecen-1-ol (**5**) and 5-hexen-1-ol (**6**), is catalyzed by both monozirconium and dizirconium catalysts, with enhanced incorporation by the monozirconium catalysts. Comparison of the performance of monometallic and bimetallic catalysts with

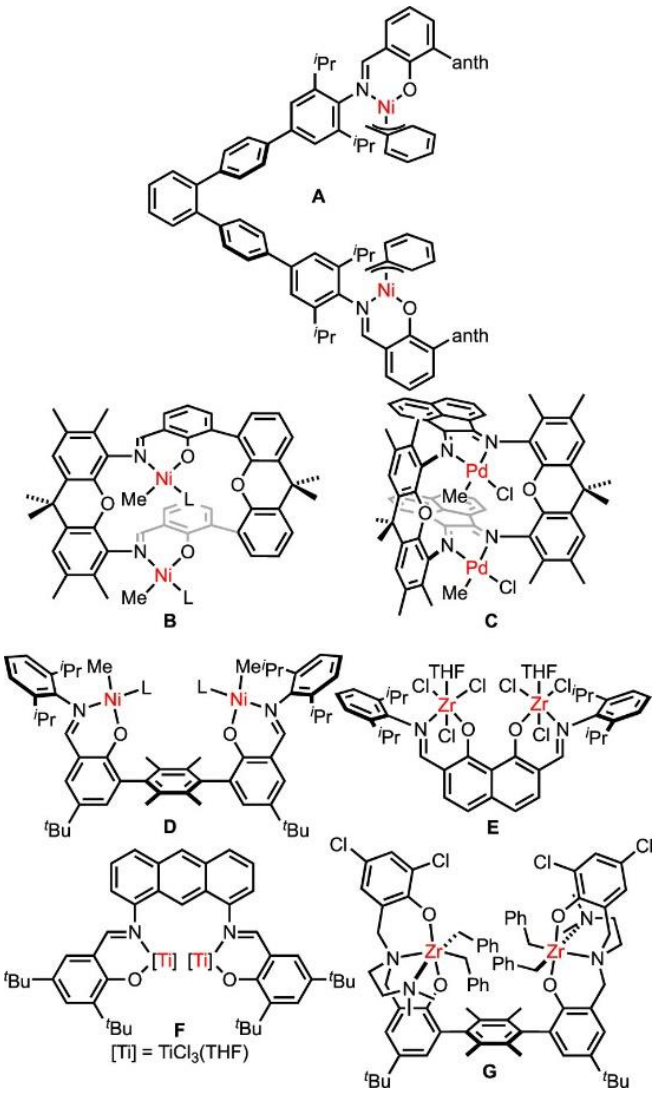

Figure A.1. Bimetallic catalysts for polymer monomer copolymerization

comonomers of different lengths allows for mechanistic insight into dinuclear effects on comonomer incorporation.

RESULTS AND DISCUSSION

Precatalysts **1**–**4** (Figure A.2) were prepared as previously described.[36] These precatalysts were selected for the current study due to the relative ease by which the C_2 isomers of the bimetallic catalysts could be isolated on moderate scales. The reactivities of **1** and **3** with 10-undecen-1-ol (**5**) and ethylene were evaluated over comonomer concentrations ranging from 0.02 to 0.16 M upon treatment of the polar comonomer with Al^{i}Bu$_3$ (TIBA) and precatalyst activation with MAO (Table A.1). Low levels of comonomer incorporation were observed across these concentrations, ranging from 0.13 to 1.4% based on ^{1}H NMR analysis of the resulting polymers. Throughout this concentration range, increased comonomer incorporation was observed from the monometallic **1** compared to the bimetallic **3**. This decreased incorporation by the bimetallic system is similar to what was observed in our previous studies of ethylene and non-polar α-olefin copolymerization by these catalysts; decreasing levels of comonomer incorporation were observed with the increasing comonomer chain length. In agreement with the NMR characterization, the T_M values for the polymers decreased with increased comonomer incorporation.[38] Based on gel permeation chromatography (GPC) characterization, molecular weights produced by **1** and **3** were

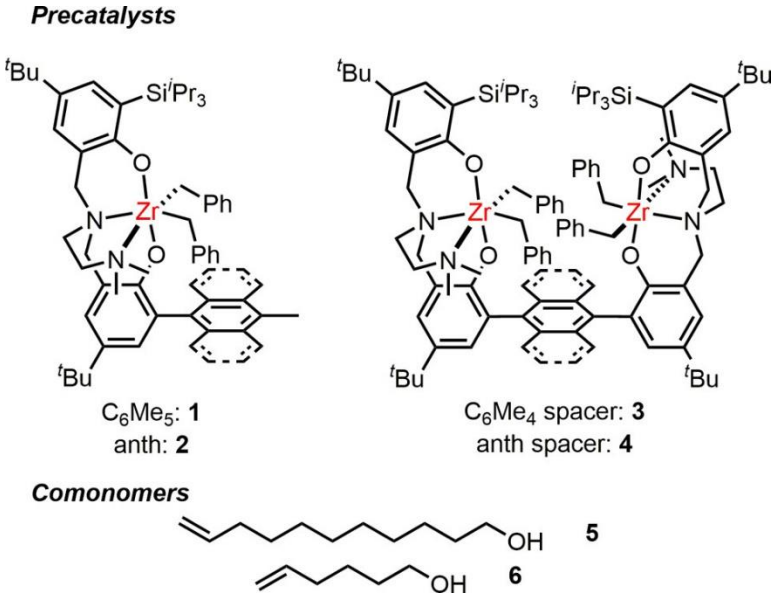

Figure A.2. Compounds evaluated in this study

not substantially impacted by the presence of the comonomer in the reaction mixture. Lower dispersities were observed in the presence of the comonomers, which could result from the interaction of the polar comonomer with MAO.[39]

entry	Cat	C[b]	activity[c]	% I	T_M[d]	M_N[e]	$Đ$[e]
1	**1**	0	0.8		127	1.6	22
2	**1**	0.02	1.23	0.22	126	1.4	9.8
3	**1**	0.04	1.48	0.38	125	1.5	7.3
4	**1**	0.08	1.56	0.47	123	1.2	7.9
5	**1**	0.16	1.58	1.4	121	1.1	5.9
6	**3**	0	1.82		136	10.4	46
7	**3**	0.02	1.78	0.13	132	6.6	26
8	**3**	0.04	1.49	0.21	132	4.3	16
9	**3**	0.08	1.11	0.35	129	8.9	14
10	**3**	0.16	1.08	0.81	126	4.3	13

Table A.1. Copolymerization of **5** with Ethylene[a]

[a]Copolymerizations were run with 10 μmol of Zr, 100 equiv TIBA, and 1000 equiv MAO in 100 mL of toluene for 60 min at a 5 bar ethylene pressure and a temperature of 80 °C. [b]Comonomer concentration in M; the comonomer was pretreated with 1 equiv TIBA prior to copolymerization. [c]Activity in kg $mmol_{Zr}^{-1}h^{-1}$. [d]Based on differential scanning calorimetry (DSC) data (°C). [e]Based on GPC data where M_N is provided in kDa and $Đ = M_W/M_N$

The activity of catalysts **2** and **4** for 10-undecen-1-ol (**5**) copolymerization and the activities of all catalysts for 5-hexen-1-ol (**6**) were evaluated for comparison (Table A.2). Values are provided for those reactions run with an initial comonomer concentration of 0.04 M, except as noted. Diffusion ordered spectroscopy (DOSY) characterization of the products of select copolymerizations of ethylene and 10-undecen-1-ol by **2** confirmed that peaks assigned to the incorporated comonomer were associated with species of a similar diffusion constant as peaks associated with the polymer

backbone (see Figures A.22 and A.23). As observed for precatalysts **1** and **3** in the copolymerization with 10-undecen-1-ol (**5**), precatalysts **2** and **4** incorporate low levels of

entry	cat	comonomer	activity[b]	% I	T_M[c]	M_N[d]	$Đ$[d]
1	**1**	**5**	1.48	0.38	125	1.5	7.3
2	**1**	**6**	1.19	0.26	124	1.2	2.9
3	**3**	**5**	1.49	0.21	132	1.2	16
4	**3**	**6**	1.68	0.08	133	5.9	30
5	**2**	**5**	1.43	0.37	125	1.7	7.4
6[e]	**2**	**5**	1.03	1.7	122	1.4	9.7
7	**2**	**6**	1.39	0.14	127	2.1	2.3
8	**4**	**5**	1.52	0.18	131	7.2	12
9[e]	**4**	**5**	1.79	0.78	126	5.6	17
10	**4**	**6**	1.75	0.04	135	8.2	16.5

Table A.2. Copolymerization of **5** and **6** with Ethylene[a]

[a]Copolymerizations were run with 10μmol of Zr, 100 equiv TIBA, and 1000 equiv MAO in 100 mL of toluene for 60 min at a 5 bar ethylene pressure with a 0.04 M comonomer. Comonomers were pretreated with TIBA prior to copolymerization (1.1 equiv).[b]Activity in kg $mmol_{Zr}^{-1}h^{-1}$. [c]Based on DSC data (°C). [d]Based on GPC data where M_N is provided in kDa and $Đ = M_W/M_N$. [e]Comonomer concentration was 0.16 M in these experiments.

comonomer **5**, with greater incorporation observed from monometallic **2**. This increased incorporation from **2** was observed across a series of experiments where the initial comonomer concentration was increased from 0.02 to 0.16 M (see Table A.4). To compare the behavior of the mono- and bimetallic catalysts as a function of chain length between olefin and alcohol functionality, the activity of all precatalysts was tested for the copolymerization of ethylene and 5-hexen-1-ol (**6**). As with the other comonomers, using the bimetallic catalysts leads to lower incorporation compared with their monometallic conjoiners, though incorporation levels were lower than for **5**.

From these and previous copolymerization studies, a general trend emerges, i.e., lower levels of incorporation are observed starting from bimetallic precatalysts as compared with starting from monometallic precatalysts. These observations suggest that steric repulsion between the distal metal site and the large comonomers, arising from the rigid nature of the teraryl linker, leads to lower incorporation compared with monometallic catalysts that lack this steric constraint (Figure A.3). A similar trend was previously observed in our study of ethylene copolymerization with the non-polar comonomers propylene, 1-hexene, and 1-tetradecene.[36] In that study, the bimetallic precatalysts were observed to incorporate more of the smaller α-olefin (propylene) than the monometallic precatalysts; however, more incorporation of the larger 1-hexene and 1-tetradecene was observed from the monometallic precatalysts. Steric clash between the longer comonomers and the more congested sites of the bimetallic precatalysts is likely exacerbated with comonomers **5** and **6** because of the formation of O–Al bonds with TIBA and MAO. It is worth noting that the large *Đ* values suggest that multiple catalyst structures could be operative under catalytic conditions. From the bimetallic catalysts, two active species may be generated, depending on whether benzyl abstraction occurs at one or two of the Zr sites.

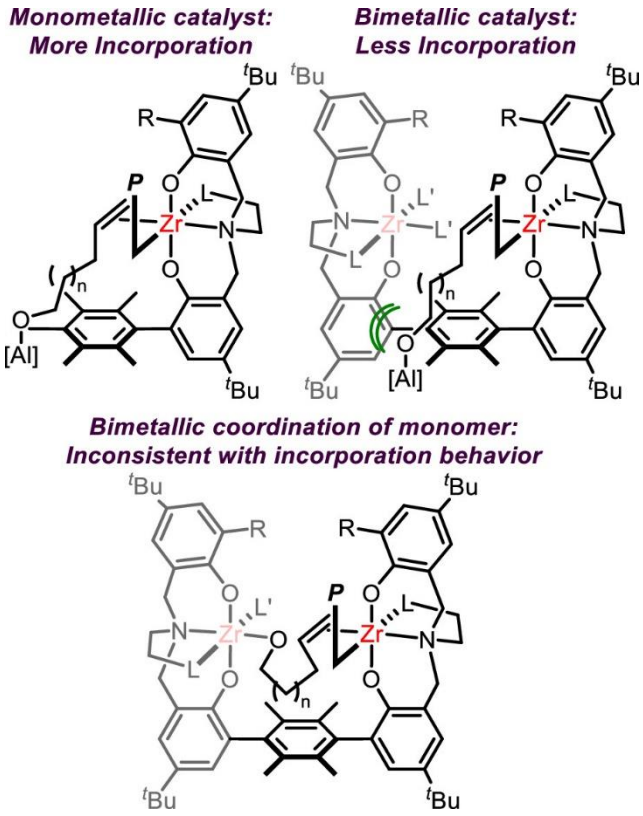

Figure A.3. Models of comonomer incorporation from mono- and bimetallic catalysts highlighting steric inhibition of comonomer coordination as the main reason for decreased incorporation with the bimetallic framework. **P**, growing polymer chain.

The large dispersities may also result from chain transfer, as noted above. Consistent with this hypothesis, the NMR spectra of the polymers show predominant alkyl end groups, with only minor terminal alkene signals (see Figures A.4-A.21).

This pattern of increased comonomer incorporation by monometallic catalysts is furthermore inconsistent with a mechanism for polar monomer incorporation that involves heteroatom and olefin binding across the two metals of the bimetallic catalyst. [15-17, 20-23] Moreover, comparing results with different chain lengths between the olefin and the polar group, **5** and **6**, incorporation is slightly suppressed with the shorter comonomer, one that may be better suited to span the distance between the two metals. The alkylaluminum groups expected to be associated with the alkoxide moieties increase the bulk of the shorter comonomer closer to the olefin, likely exacerbating the steric interaction with the second metal center compared with the monomers where the functionality is further down the chain. These results further support that the second metal center serves as a steric influence on the catalyst behavior, rather than acting as a site for comonomer coordination (Figure A.3).

CONCLUSION

The reactivity of a series of mono- and dizirconium catalysts based on a rigid teraryl framework was tested in the copolymerization of ethylene with alcohol-functionalized comonomers in the presence of MAO and $Al^{i}Bu_3$. Although modest comonomer incorporation was observed, it was sufficient to compare the performance of the different catalysts. The largest incorporation was observed from one of the monometallic catalysts at elevated comonomer concentration. Generally, comonomer incorporation was lower for the bimetallic vs monometallic catalysts. This is consistent with these catalysts' behavior in the copolymerization of ethylene and linear, unfunctionalized α-olefins and supports a mechanism involving steric interactions between the larger comonomers and the distal metal site in the bimetallic catalysts. Our studies do not support a coordinative interaction between the polar group and the second metal center for these catalyst structures. Future bimetallic catalyst designs will require finding the optimal balance of the potential steric repulsion and monomer coordination effects.

EXPERIMENTAL SECTION

General Experimental Considerations

All air- and water-sensitive compounds were manipulated under N_2 or Ar using standard Schlenk or glovebox techniques. Complexes **1**, **2**, **3**, and **4** were prepared as previously reported.[36] Toluene was purified by the method of Grubbs and coworkers[40] and stored over activated molecular sieves. MMAO-12, 10-undecen-1-ol, 5-hexen-1-ol, triisobutylaluminum (TIBA), and toluene (HPLC grade) were purchased from Sigma Aldrich. Polar comonomers treated with 1.1 equiv. Al^iBu_3 (TIBA) prior to polymerization. Ethylene, N_2, and Ar were purified by passage through molecular sieves and a copper-based catalyst (GetterMax 133) to remove moisture and oxygen, respectively.

Polymerization Procedure

The polymerization experiments were carried out in a 0.25 L stainless steel Buchi reactor assembled by Hi-Tech (India). The reactor was heated to 110 °C, purged several times with Ar to remove air and moisture, and then cooled to 80 °C. A stock solution containing TIBA (2.5 mL, 10 wt% in toluene), MAO (7.5 mL, 10 wt% in toluene, 10.0 mmol, 1000 equiv. to Zr), TIBA pacified comonomer (0-16 mmol) was prepared in the glovebox and diluted with toluene to a total volume of 95 mL. This solution was transferred to the reactor, saturated with ethylene at 5 bar, and allowed to equilibrate at the desired polymerization temperature. The reactor vessel was then charged with a solution of the Zr catalyst (10 μmol Zr) in toluene (5 mL). The 5 bar ethylene pressure was maintained for 1 h, after which excess ethylene was allowed to vent and the reaction was quenched by addition of 5% HCl/MeOH (30 mL). The polymer was isolated by filtration, washed with fresh methanol, and dried under high vacuum at 60 °C.

GPC Analysis

Gel permeation chromatographic analyses of ethylene homo- and copolymers were performed at 160 °C using a PL-GPC 220 (Agilent Technologies) equipped with two PLgel Olexis 300 x 7.5 mm columns. BHT (0.0125 wt%) was added to 1,2,4-trichlorobenzene to prevent polymer sample degradation. A sample solution of 5 mg/1.5 mL (w/v) was prepared at 140 °C and 100 µL was injected into the GPC columns. Chromatogram data was analyzed using the Cirrus software, which was calibrated using polystyrene standards. The polystyrene-based calibration curve was converted into the universal one using the MarkHouwink constants of polystyrene ($K = 0.000121$ dL/g and $\alpha = 0.707$) and polyethylene ($K = 0.000406$ dL/g and $\alpha = 0.725$).[41]

Differential Scanning Calorimetry

Differential scanning calorimetric (DSC) analysis was performed using a DSC Q2000 (TA Instruments). The temperature and heat flow of the apparatus were calibrated with an indium standard. Polymer samples were first equilibrated at 25 °C, followed by heating from 25 °C to 200 °C at a rate of 10 °C/min under N_2 flow (5 mL/min). This temperature was maintained for 5 min then samples were cooled to 25 °C at a rate of 10 °C/min. This temperature was maintained for 5 min then samples were reheated to 200 °C at a rate of 10 °C/min. The melting temperature (Tm) was determined from the second heating scan. The percent crystallinity was calculated from ΔH_f (J/g)/ΔH_{std} (J/g), where ΔH_{std} is the heat of fusion for a perfectly crystalline polyethylene; this equals to 290.0 J/g.[42]

NMR Sample Preparation and Analysis Procedure

Polymer NMR spectra were recorded on a Bruker 400 MHz spectrometer at 120 °C in 1,2-dichlorobenzene-D_4. Samples were prepared using ca. 80 mg polymer per mL of solvent. Each sample was pre-heated and agitated by hand, before placing in a pre-heated probe at 120 °C. The sample was equilibrated for 5 minutes in the probe prior to data acquisition and ^{1}H NMR spectra were collected using 128 scans with an acquisition time of 4 s and a d1 of 1 s. Note: an initial spectrum for one of the samples was performed using acquisition times of 8, 16, or 32 s (all with d1 values of 1 s) and no change was observed in the integrals of the signals used to determine % I. While we anticipate there may be some error associated with this pulse sequence, we expect that trends determined from integrals for the same peak will hold, given the similar number of protons attached to the integrated signals and the similar molecular weights of the polymers under consideration.

The %I values were calculated from integration of the ^{1}H NMR spectra according to the formula below. For ease of operation, the value of the integral of the methylene protons adjacent to oxygen (n_i, OC*H*$_2$CH$_2$R, centered at 3.5 ppm) was defined as 2. I_{CH2} = integral of the peaks centered at 1.5 ppm, corresponding to both polymer backbone signals and comonomer methylene signals. n_H = number of protons on the comonomer – n_α.

$$\%\mathrm{I} = \frac{\text{equiv. comonomer}}{(\text{equiv. ethylene})} \times 100\% = \frac{\left(\frac{n_i}{2}\right)}{\left(\frac{I_{CH2} - n_H}{4}\right)} \times 100\% = \frac{4}{(\mathrm{I_{CH2}} - \mathrm{n_H})} \times 100\%$$

Spectra were referenced relative to residual solvent. Signals arising from trace solvents present during sample preparation are observed in some of the ^{1}H NMR spectra; such traces include toluene (s, δ_H = 2.1), diethyl ether (q, δ_H = 3.33), and tetrahydrofuran (m, δ_H = 3.6).

Complete Polymerization Tables

Table A.3. Ethylene homopolymerization

Entry	EXP #	Catalyst	Activity (kg mol$_{Zr}^{-1}$ h^{-1})	Yield (g)	T_M (°C)	M_N (kDa)	Đ
1	PP225	1	800	8.02	127	1.6	22
2	PP237	3	1820	18.18	136	10.4	46
3	PP215	2	740	7.38	128	2.0	20.6
4	PP205	4	1120	11.23	133	6.9	14.1

Conditions: 10 µmol Zr, 100 equiv. Al^{i}Bu$_3$, and 1000 equiv. MAO in 100 mL total volume for 60 min at 5 atm ethylene pressure and 80 °C.

Table A.4. Copolymerization of ethylene and 10-undecen-1-ol

Entry	EXP #	Cat	Comonomer Conc. (M)	Comonomer Conversion (%)	Activity (kg mol$_{Zr}^{-1}$ h^{-1})	Yield (g)	% I	T_M (°C)	M_N (kDa)	Đ
1	PP228	1	0.02	49	1230	12.34	0.22	126	1.4	9.8
2	PP229	1	0.04	49	1480	14.76	0.38	125	1.5	7.3
3	PP230	1	0.08	32	1560	15.55	0.47	123	1.2	7.9
4	PP231	1	0.16	45	1580	15.78	1.4	121	1.1	5.9
5	PP238	3	0.02	41	1780	17.8	0.13	132	6.6	26
6	PP239	3	0.04	27	1490	14.89	0.21	132	4.3	16
7	PP240	3	0.08	17	1110	11.09	0.35	129	8.9	14
8	PP241	3	0.16	19	1080	10.82	0.82	126	4.3	13
9	PP207	2	0.02	64	1220	12.2	0.30	127	2.0	10
10	PP208	2	0.04	46	1430	14.28	0.37	125	1.7	7.4
11	PP209	2	0.08	58	1700	17.03	0.80	125	1.6	7.6
12	PP210	2	0.16	35	1000	10.33	1.7	122	1.4	9.7
13	PP217	4	0.02	26	1430	14.3	0.10	131	6.4	12
14	PP218	4	0.04	25	1520	15.24	0.19	131	7.2	12
15	PP219	4	0.08	17	1380	13.77	0.28	129	5.5	8.4
16	PP220	4	0.16	30	1790	17.86	0.79	126	5.6	17

Conditions: 10 µmol Zr, 100 equiv. Al^{i}Bu$_3$, and 1000 equiv. MAO in 100 mL total volume for 60 min at 5 atm ethylene pressure and 80 °C; 10-undecen-1-ol was treated with 1.1 equiv. Al^{i}Bu$_3$ prior to each polymerization.

Table A.5. Copolymerization of ethylene and 5-hexen-1-ol

Entry	**Exp #**	**Catalyst**	**Comonomer Conversion (%)**	**Activity (kg mol$_{Zr}^{-1}$ h^{-1})**	**Yield (g)**	**% I**	**T_M (°C)**	**M_N (kDa)**	**Đ**
1	PP232	1	28	1190	11.93	0.26	124	1.2	2.9
2	PP242	3	12	1680	16.83	0.08	133	5.9	30.0
3	PP226	2	17	1390	13.91	0.14	127	2.1	2.3
4	PP227	4	6	1750	17.5	0.04	134	8.2	16.5

Conditions: 10 µmol Zr, 100 equiv. Al^{i}Bu$_3$, and 1000 equiv. MAO in 100 mL total volume for 60 min at 5 atm ethylene pressure and 80 °C temperature; 5-hexen-1-ol was treated with 1.1 equiv. Al^{i}Bu$_3$ prior to each polymerization.

Representative Polymer NMRs

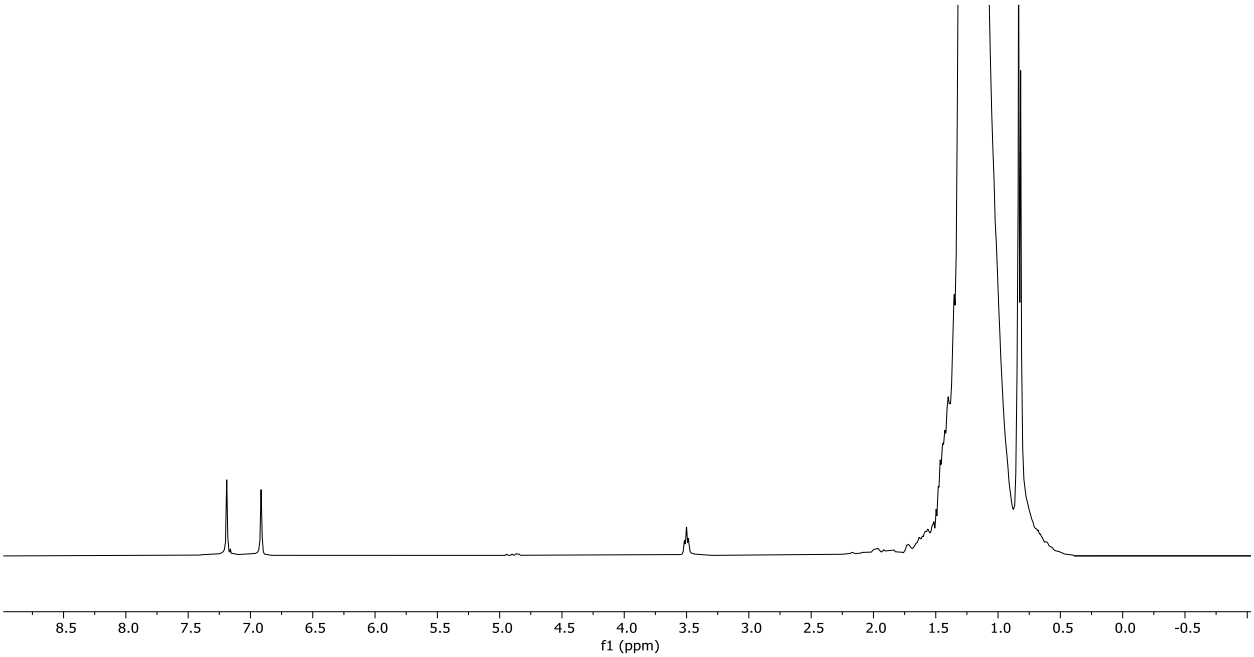

Figure A.4. ^{1}H NMR of ethylene copolymer with 10-undecen-1-ol by **1** at 0.02 M comonomer concentration (Table A.1, Entry 2; Table A.4, Entry 1; PP228)

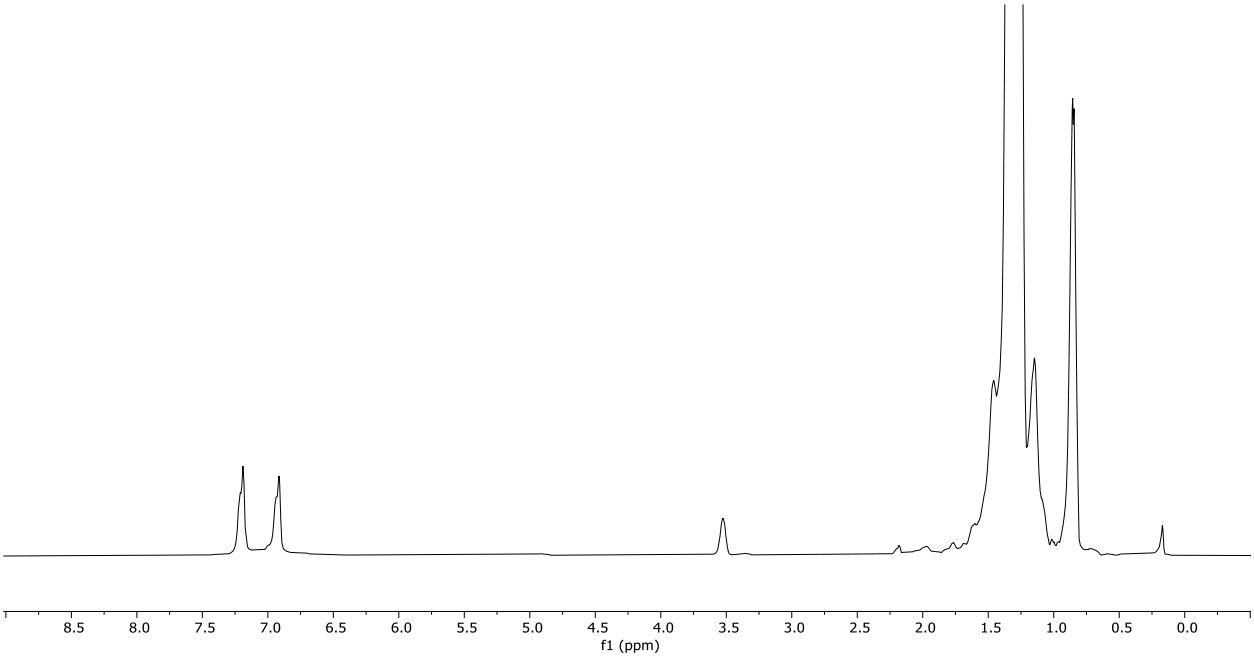

Figure A.5. ^{1}H NMR of ethylene copolymer with 10-undecen-1-ol by **1** at 0.04 M comonomer concentration (Table A.1, Entry 3; Table A.2, Entry 1; Table A.4, Entry 2; PP229)

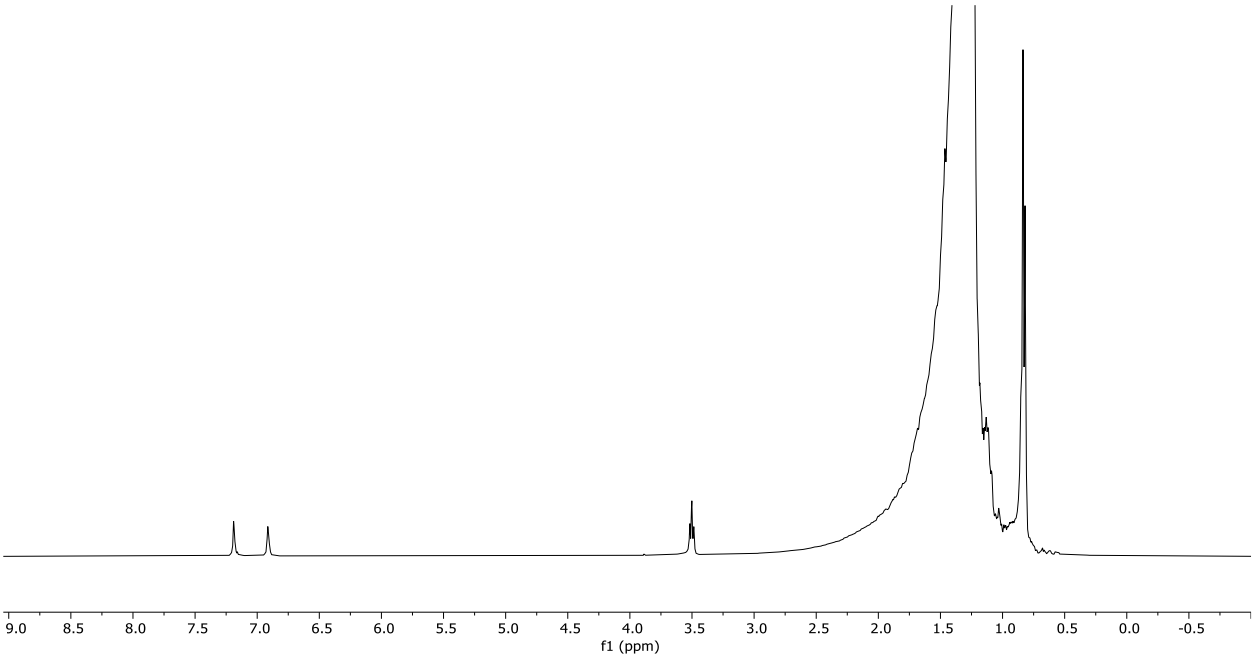

Figure A.6. ^{1}H NMR of ethylene copolymer with 10-undecen-1-ol by **1** at 0.08 M comonomer concentration (Table A.1, Entry 4; Table A.4, Entry 3; PP230)

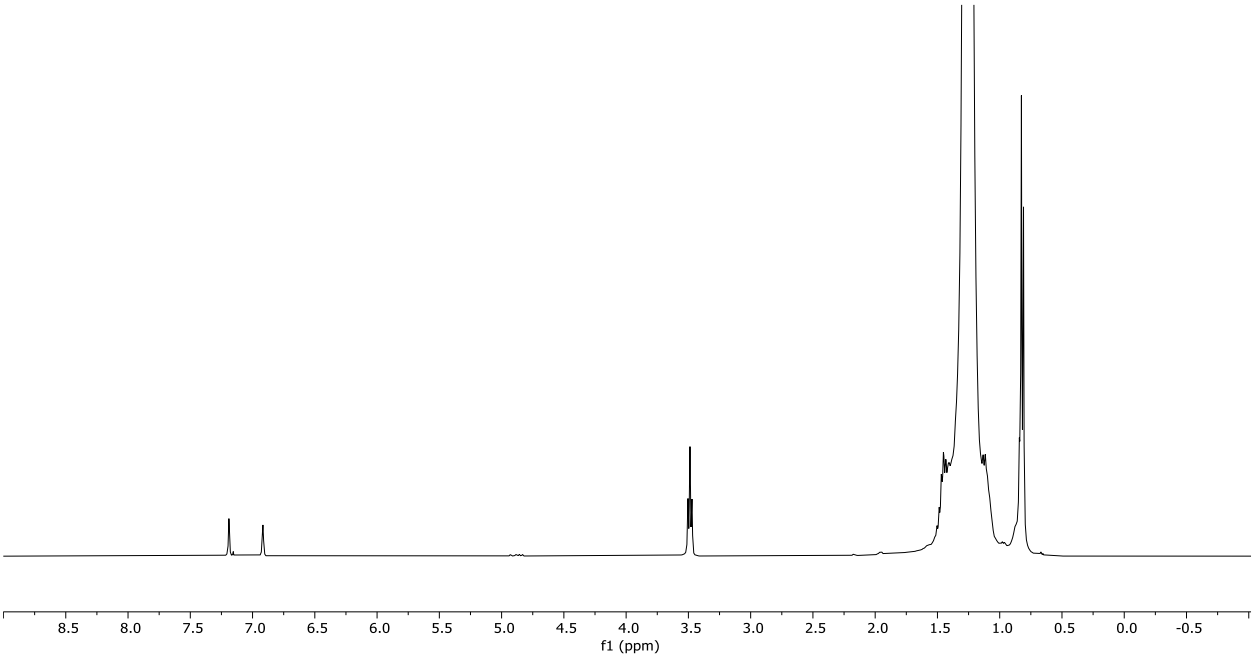

Figure A.7. ^{1}H NMR of ethylene copolymer with 10-undecen-1-ol by **1** at 0.16 M comonomer concentration (Table A.1, Entry 5; Table A.4, Entry 4, PP231)

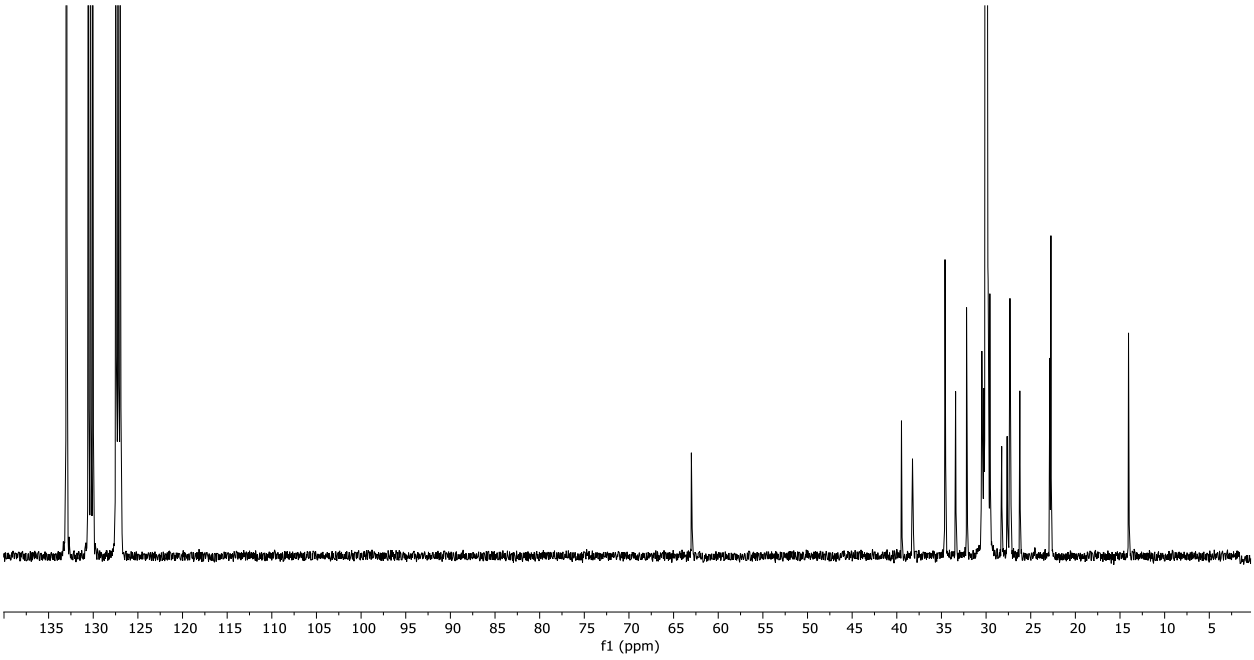

Figure A.8. ^{13}C NMR of ethylene copolymer with 10-undecen-1-ol by **1** at 0.16 M comonomer concentration (Table A.1, Entry 5; Table A.4, Entry 4, PP231)

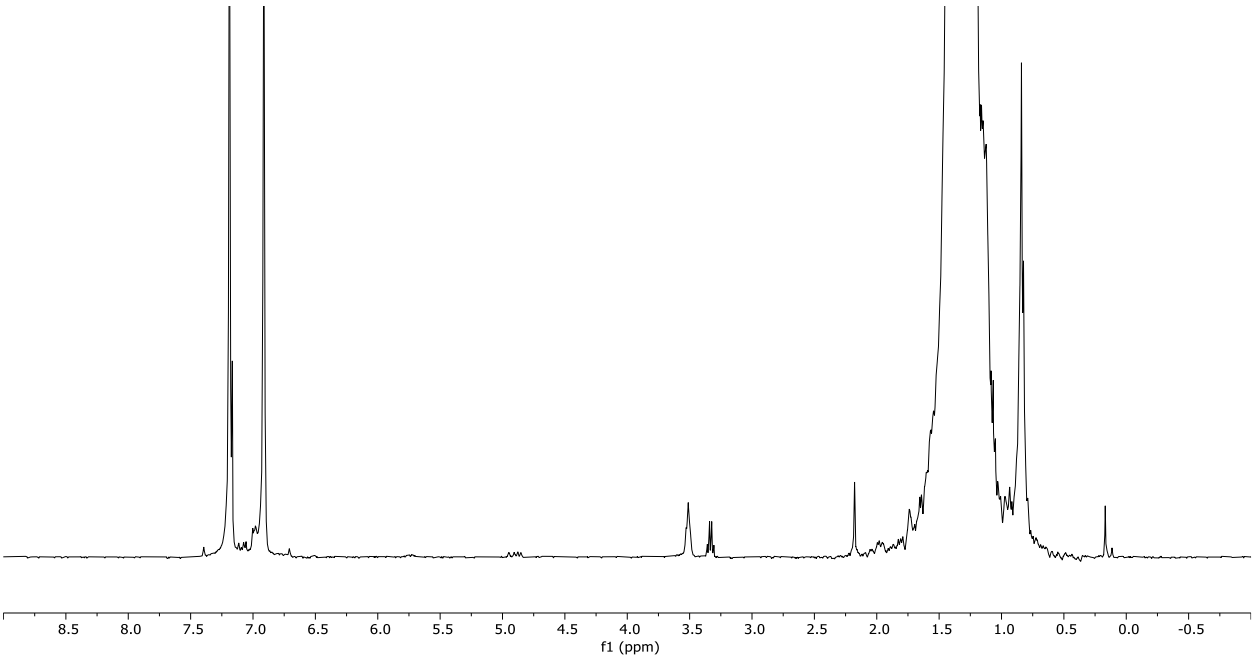

Figure A.9. ^{1}H NMR of ethylene copolymer with 10-undecen-1-ol by **3** at 0.02 M comonomer concentration (Table A.1, Entry 7; Table A.4, Entry 5; PP238)

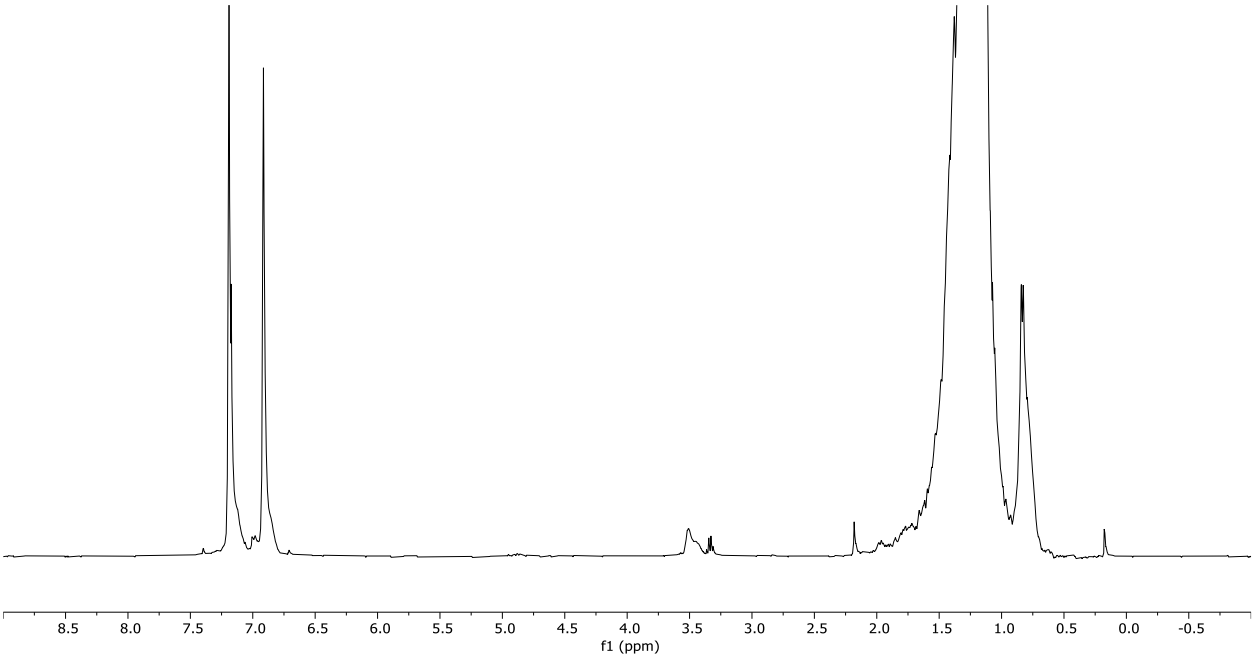

Figure A.10. ^{1}H NMR of ethylene copolymer with 10-undecen-1-ol by **3** at 0.04 M comonomer concentration (Table A.1, Entry 8; Table A.2, Entry 3; Table A.4, Entry 6; PP239)

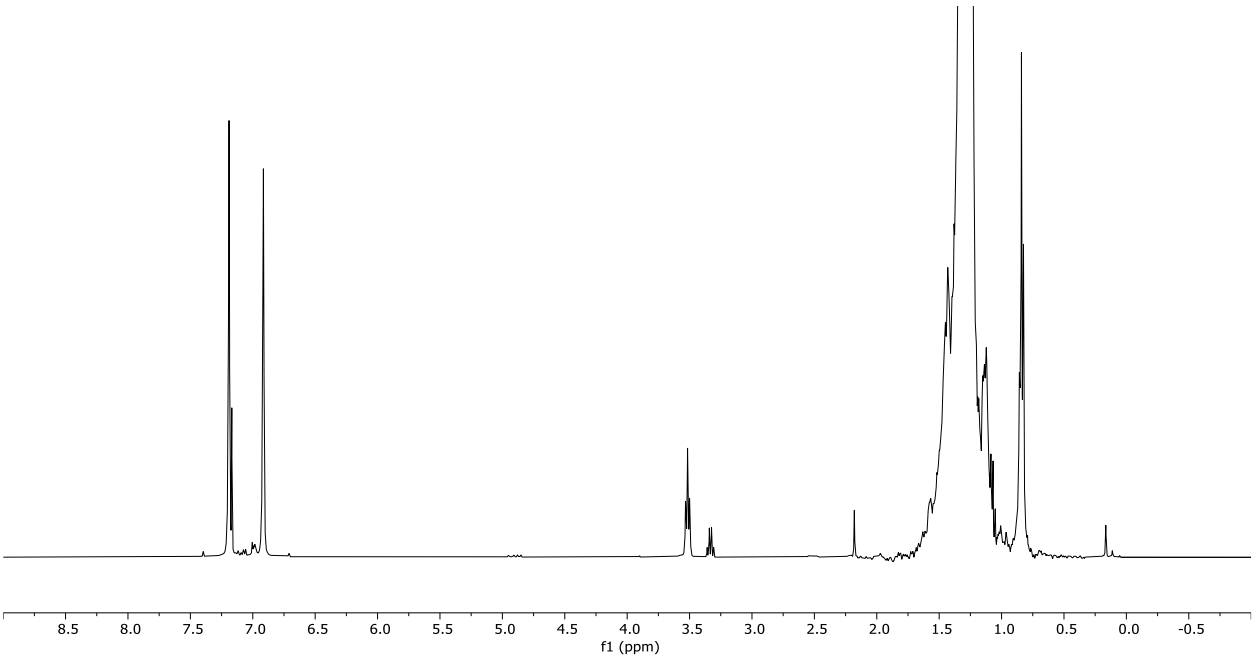

Figure A.11. ^{1}H NMR of ethylene copolymer with 10-undecen-1-ol by **3** at 0.08 M comonomer concentration (Table A.1, Entry 9; Table A.4, Entry 7; PP240)

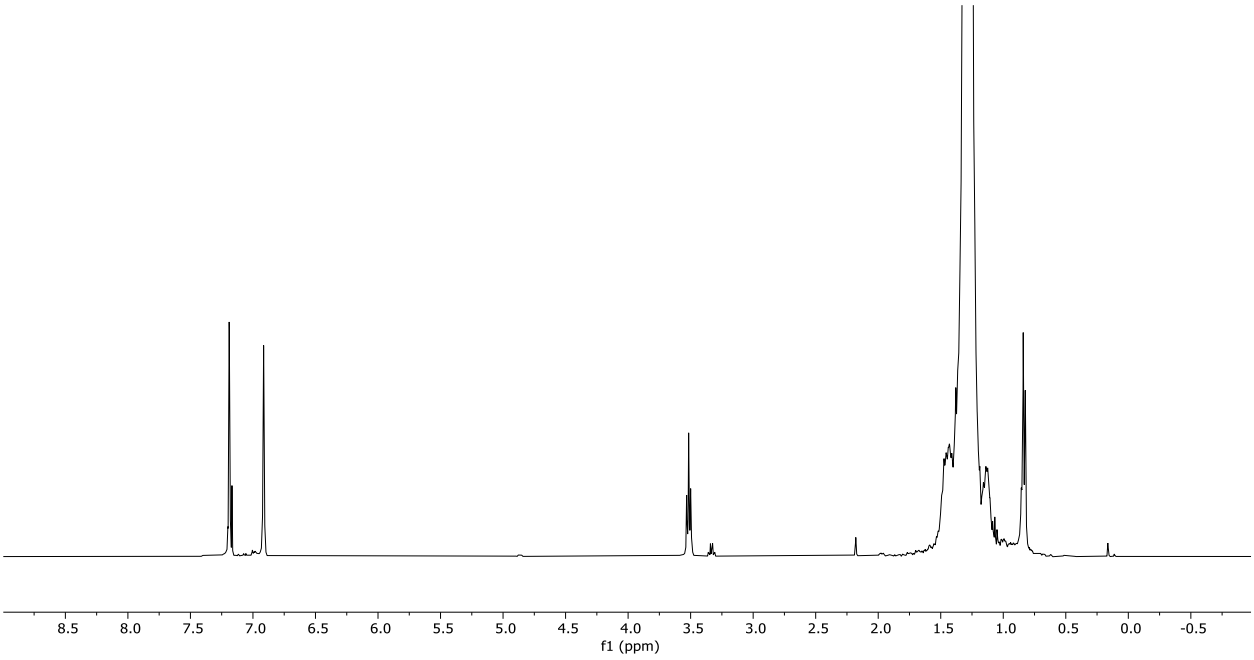

Figure A.12. ^{1}H NMR of ethylene copolymer with 10-undecen-1-ol by **3** at 0.16 M comonomer concentration (Table A.1, Entry 10; Table A.4, Entry 8, PP241)

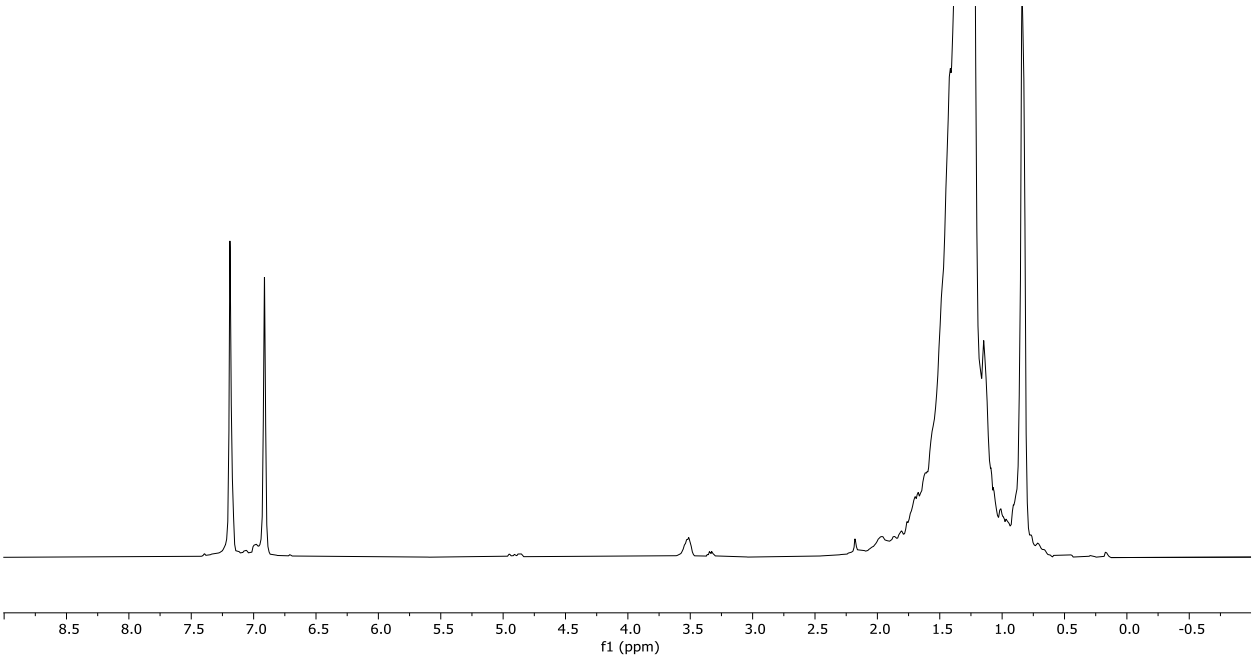

Figure A.13. ^{1}H NMR of ethylene copolymer with 5-hexen-1-ol by **1** at 0.04 M comonomer concentration (Table A.1, Entry 2; Table A.5, Entry 1, PP232)

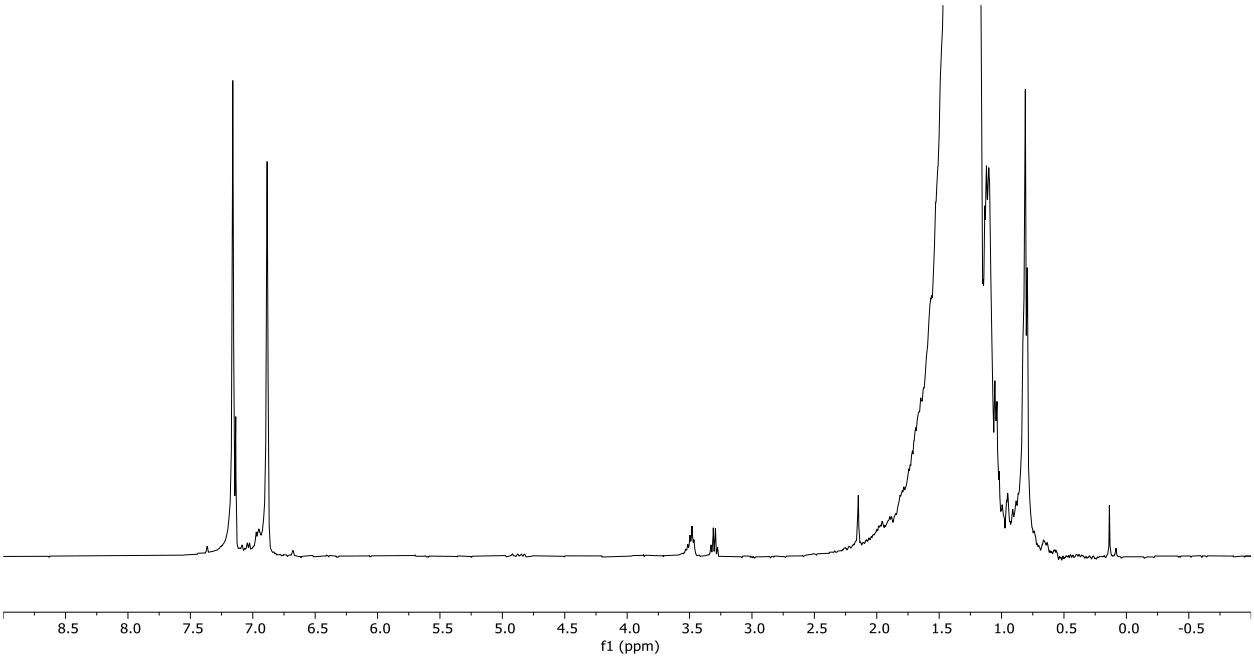

Figure A.14. ^{1}H NMR of ethylene copolymer with 5-hexen-1-ol by **3** at 0.04 M comonomer concentration (Table A.2, Entry 4; Table A.5, Entry 2, PP242)

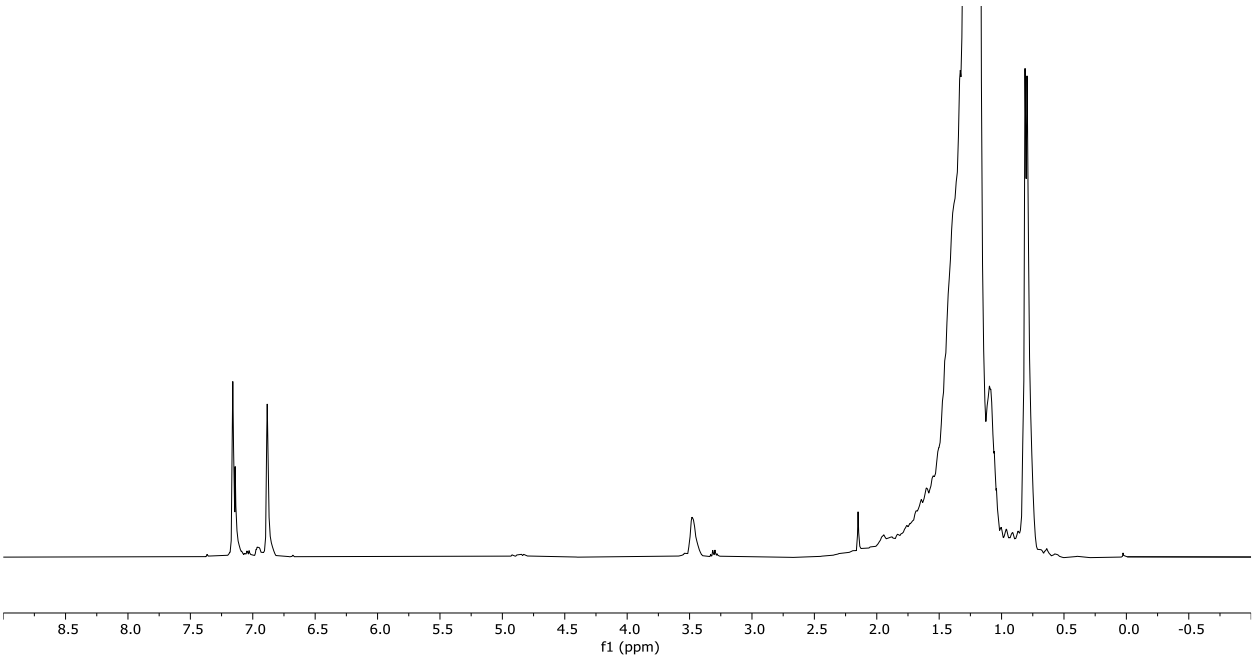

Figure A.15. ^{1}H NMR of ethylene copolymer with 10-undecen-1-ol by **2** at 0.04 M comonomer concentration (Table A.2, Entry 5; Table A.4, Entry 10, PP208)

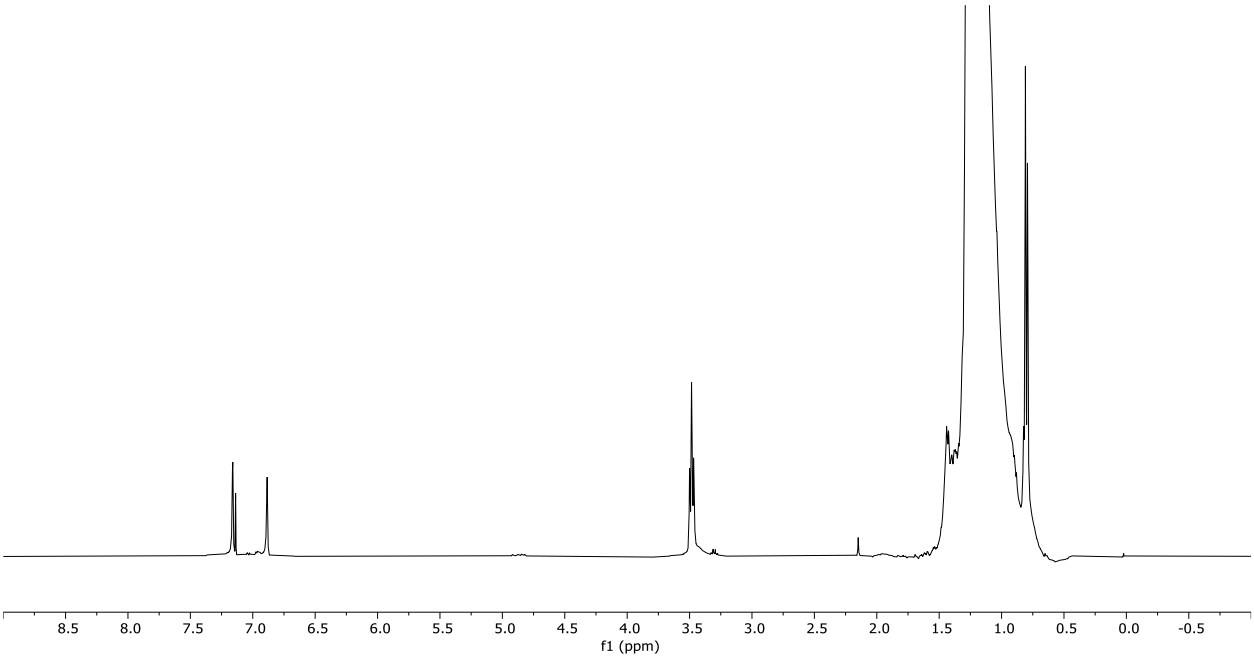

Figure A.16. ^{1}H NMR of ethylene copolymer with 10-undecen-1-ol by **2** at 0.16 M comonomer concentration (Table A.2, Entry 6; Table A.4, Entry 12, PP210)

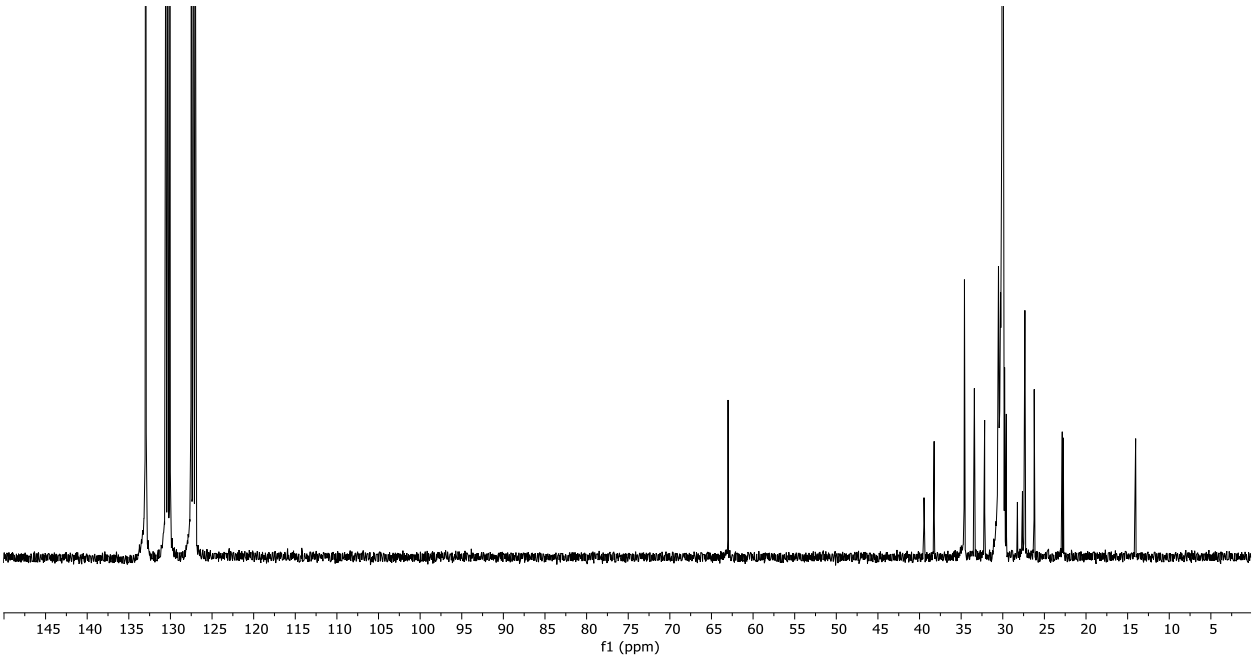

Figure A.17. ^{13}C NMR of ethylene copolymer with 10-undecen-1-ol by **2** at 0.16 M comonomer concentration (Table A.2, Entry 6; Table A.4, Entry 12, PP210)

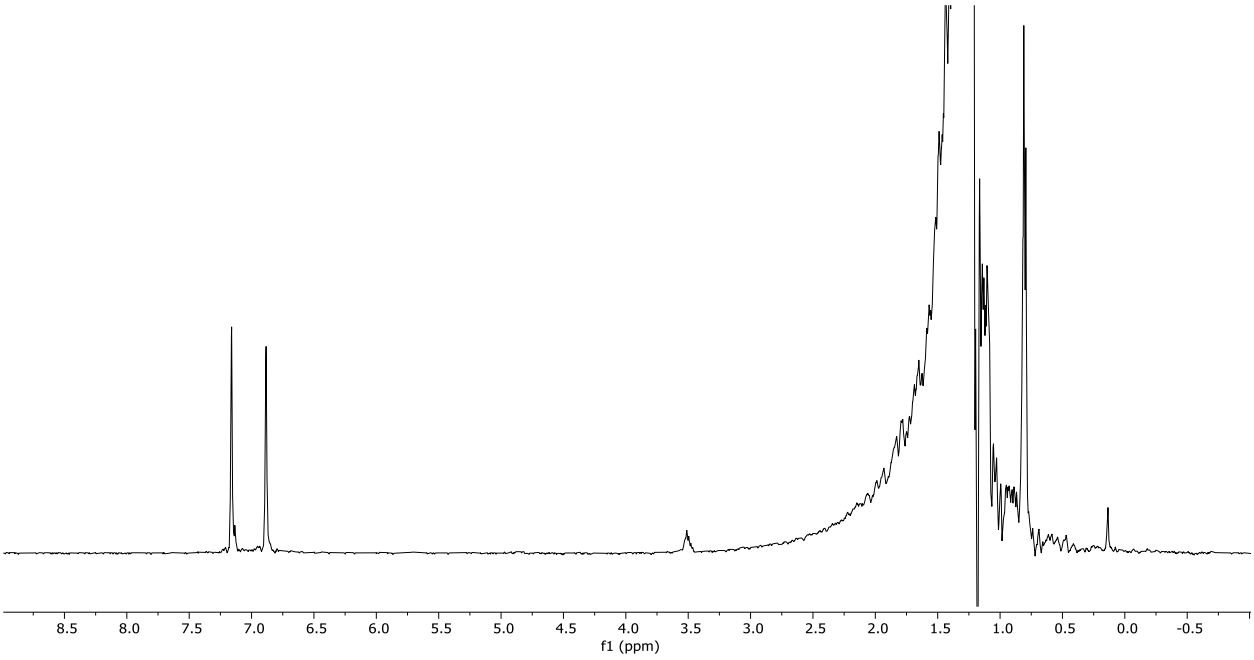

Figure A.18. ^{1}H NMR of ethylene copolymer with 5-hexen-1-ol by **2** at 0.04 M comonomer concentration (Table A.2, Entry 7; Table A.5, Entry 3, PP226)

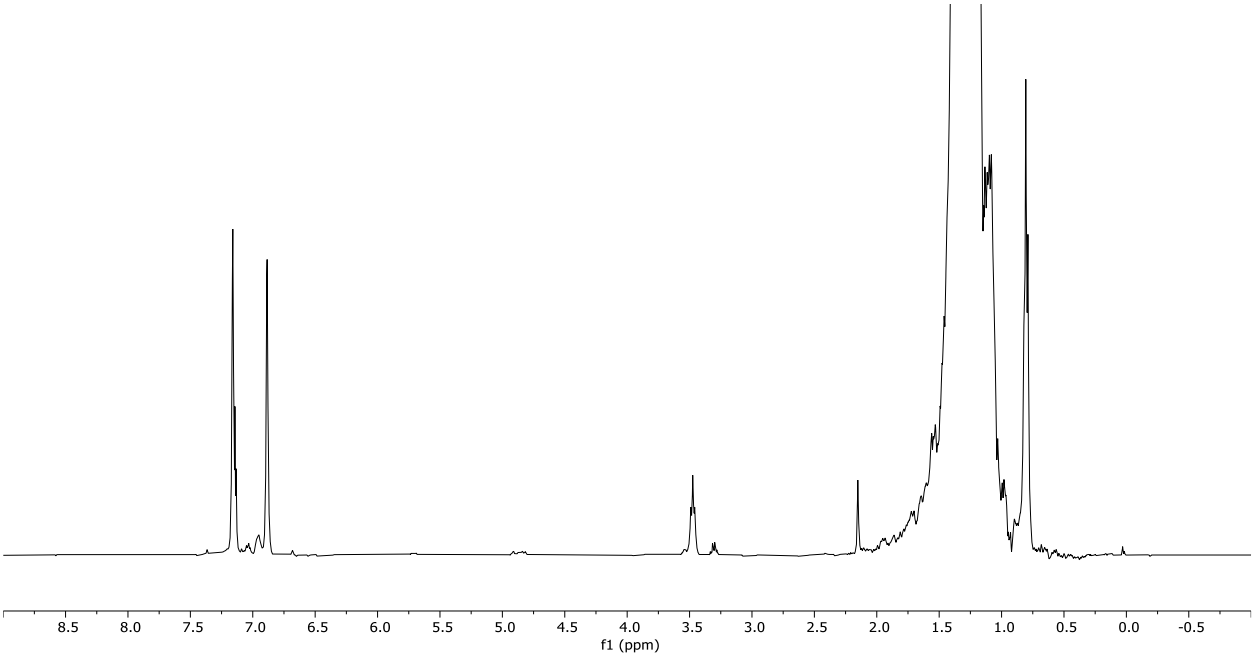

Figure A.19. ^{1}H NMR of ethylene copolymer with 10-undecen-1-ol by **4** at 0.04 M comonomer concentration (Table A.2, Entry 8; Table A.4, Entry 14, PP218)

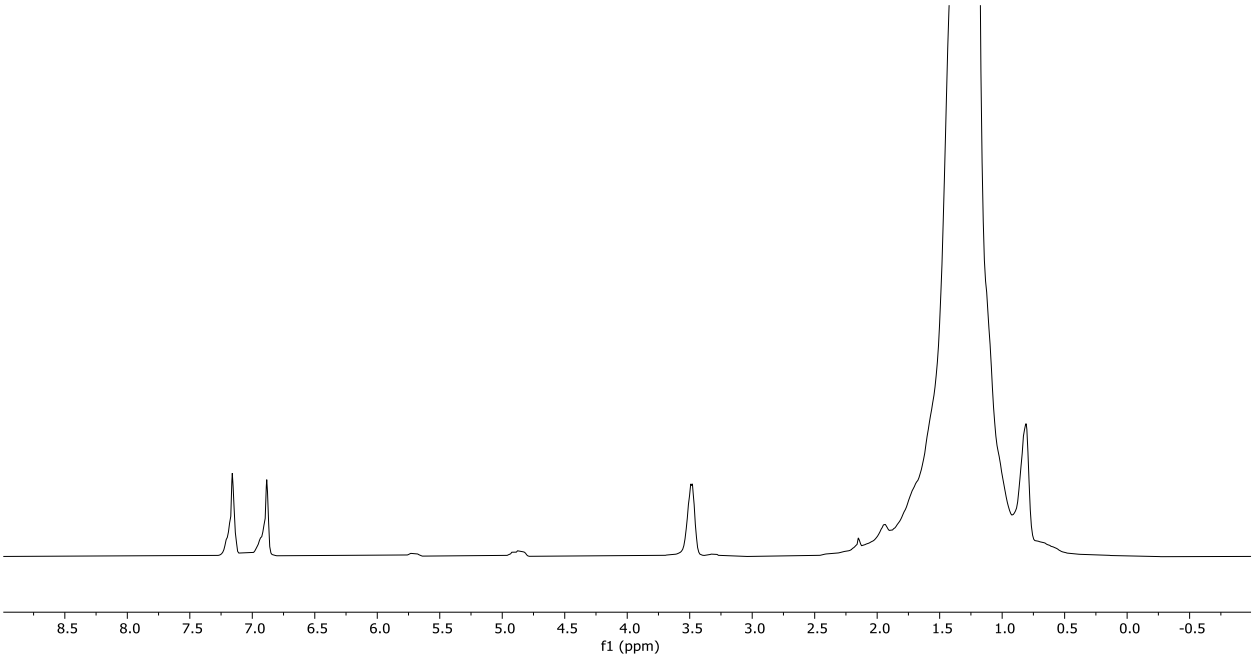

Figure A.20. ^{1}H NMR of ethylene copolymer with 10-undecen-1-ol by **4** at 0.16 M comonomer concentration (Table A.2, Entry 9; Table A.4, Entry 16, PP220)

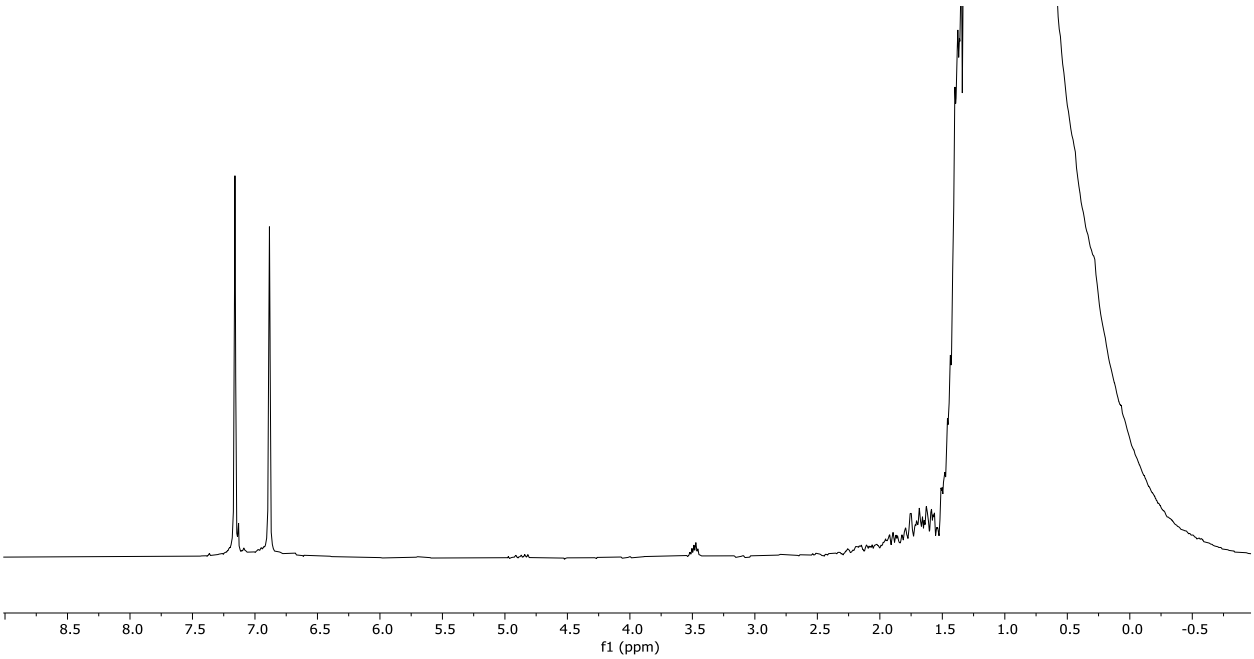

Figure A.21. ^{1}H NMR of ethylene copolymer with 5-hexen-1-ol by **4** at 0.04 M comonomer concentration (Table A.2, Entry 10; Table A.5, Entry 4, PP227)

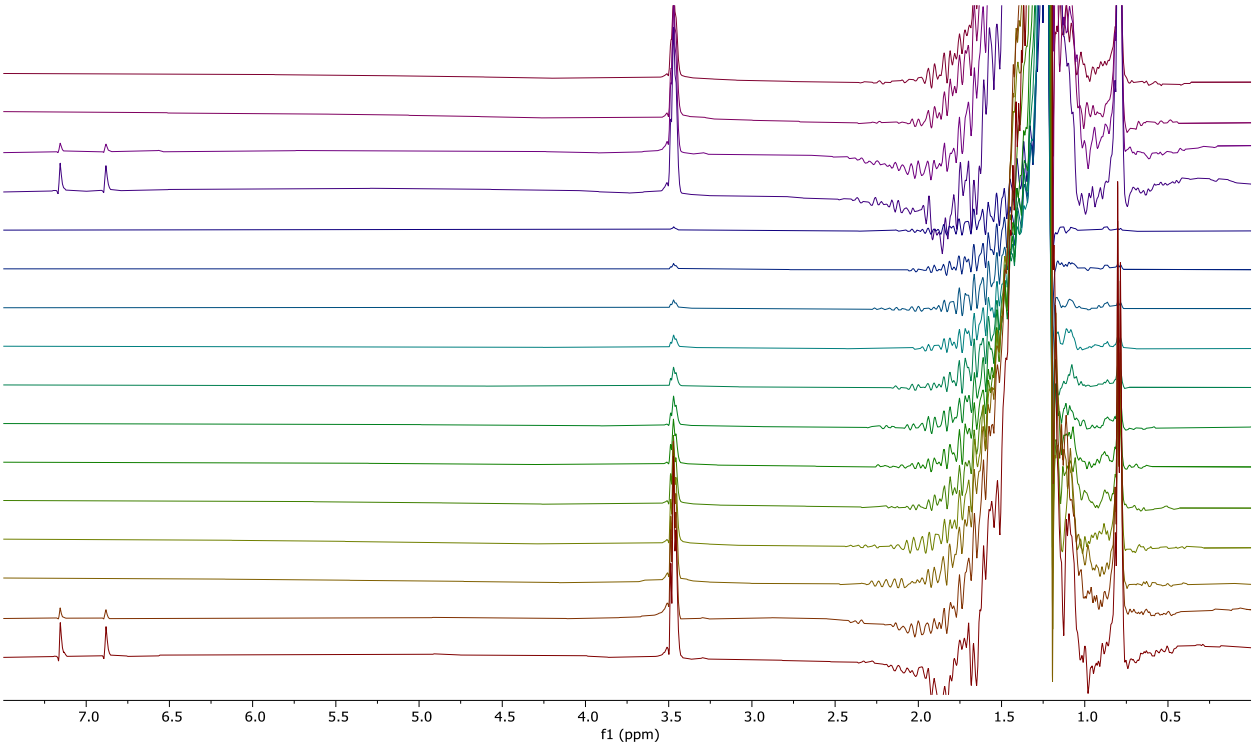

Figure A.22. DOSY spectra of ethylene/10-undecen-1-ol copolymer by **2** (Table A.4, Entry 12; PP210)

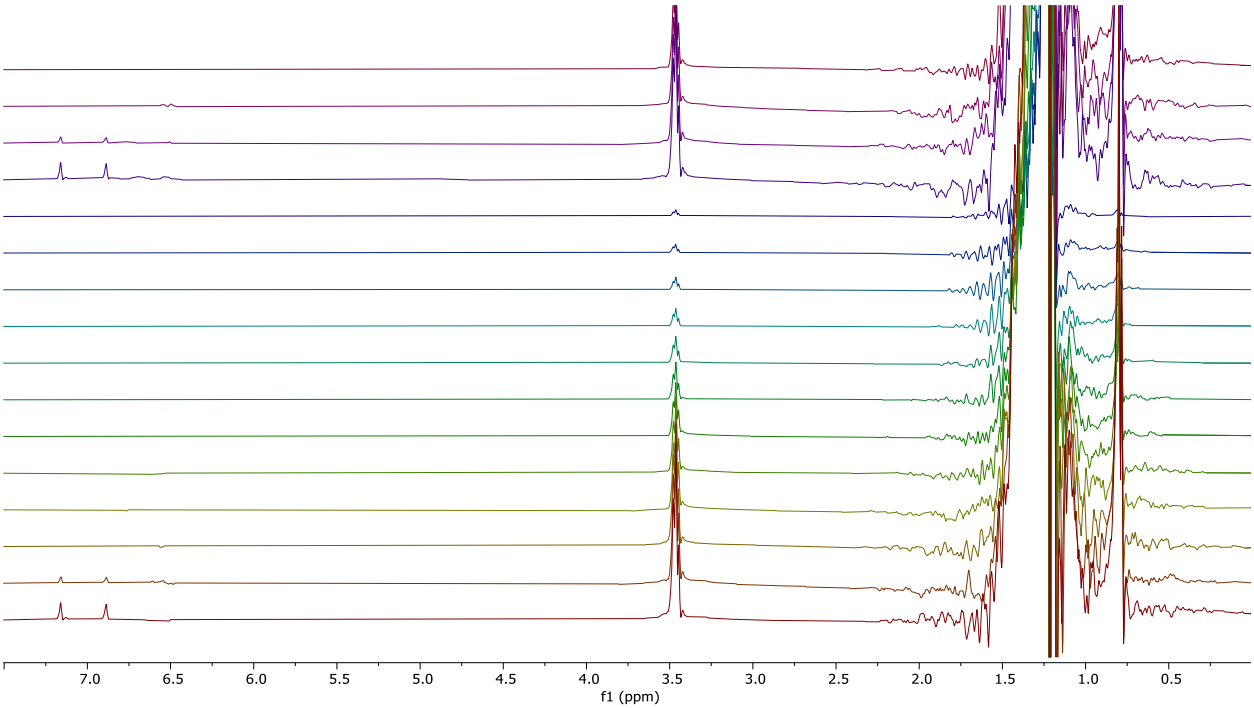

Figure A.23. DOSY spectra of ethylene/10-undecen-1-ol copolymer by **1** (Table A.4, Entry 4; PP231)

REFERENCES

1. Delferro, M.; Marks, T. J., Multinuclear Olefin Polymerization Catalysts. *Chem. Rev.* **2011,** *111* (3), 2450-2485. 10.1021/cr1003634
2. S, S.; Joe, D. J.; Na, S. J.; Park, Y.-W.; Choi, C. H.; Lee, B. Y., Ethylene/Polar Norbornene Copolymerizations by Bimetallic Salicylaldimine−Nickel Catalysts. *Macromolecules* **2005,** *38* (24), 10027-10033. 10.1021/ma051344i
3. Takeuchi, D.; Chiba, Y.; Takano, S.; Osakada, K., Double-Decker-Type Dinuclear Nickel Catalyst for Olefin Polymerization: Efficient Incorporation of Functional Co-monomers. *Angew. Chem. Int. Ed.* **2013,** *52* (48), 12536-12540. 10.1002/anie.201307741
4. Takano, S.; Takeuchi, D.; Osakada, K.; Akamatsu, N.; Shishido, A., Dipalladium Catalyst for Olefin Polymerization: Introduction of Acrylate Units into the Main Chain of Branched Polyethylene. *Angew. Chem. Int. Ed.* **2014,** *53* (35), 9246-9250. 10.1002/anie.201404339
5. Takeuchi, D.; Chiba, Y.; Takano, S.; Kurihara, H.; Kobayashi, M.; Osakada, K., Ethylene polymerization catalyzed by dinickel complexes with a double-decker structure. *Polymer Chemistry* **2017,** *8* (34), 5112-5119. 10.1039/C7PY00333A
6. Takeuchi, D.; Iwasawa, T.; Osakada, K., Double-Decker-Type Dipalladium Catalysts for Copolymerization of Ethylene with Acrylic Anhydride. *Macromolecules* **2018,** *51* (14), 5048-5054. 10.1021/acs.macromol.8b00569
7. Takeuchi, D., Olefin Polymerization and Copolymerization Catalyzed by Dinuclear Catalysts Having Macrocyclic Ligands. *J. Synth. Org. Chem Jpn.* **2019,** *77* (11), 1136-1146. 10.5059/yukigoseikyokaishi.77.1136
8. Radlauer, M. R.; Day, M. W.; Agapie, T., Dinickel Bisphenoxyiminato Complexes for the Polymerization of Ethylene and α-Olefins. *Organometallics* **2012,** *31* (6), 2231-2243. 10.1021/om2011694
9. Radlauer, M. R.; Day, M. W.; Agapie, T., Bimetallic Effects on Ethylene Polymerization in the Presence of Amines: Inhibition of the Deactivation by Lewis Bases. *J. Am. Chem. Soc.* **2012,** *134* (3), 1478-1481. 10.1021/ja210990t
10. Radlauer, M. R.; Buckley, A. K.; Henling, L. M.; Agapie, T., Bimetallic Coordination Insertion Polymerization of Unprotected Polar Monomers: Copolymerization of Amino Olefins and Ethylene by Dinickel Bisphenoxyiminato Catalysts. *J. Am. Chem. Soc.* **2013,** *135* (10), 3784-3787. 10.1021/ja4004816
11. Li, L.; Metz, M. V.; Li, H.; Chen, M.-C.; Marks, T. J.; Liable-Sands, L.; Rheingold, A. L., Catalyst/Cocatalyst Nuclearity Effects in Single-Site Polymerization. Enhanced Polyethylene Branching and α-Olefin Comonomer Enchainment in Polymerizations Mediated by Binuclear Catalysts and Cocatalysts via a New Enchainment Pathway. *J. Am. Chem. Soc.* **2002,** *124* (43), 12725-12741. 10.1021/ja0201698
12. Li, H.; Li, L.; Marks, T. J.; Liable-Sands, L.; Rheingold, A. L., Catalyst/Cocatalyst Nuclearity Effects in Single-Site Olefin Polymerization. Significantly Enhanced 1-Octene and Isobutene Comonomer Enchainment in Ethylene Polymerizations Mediated by Binuclear Catalysts and Cocatalysts. *J. Am. Chem. Soc.* **2003,** *125* (36), 10788-10789. 10.1021/ja036289c
13. Li, H.; Li, L.; Marks, T. J., Polynuclear Olefin Polymerization Catalysis: Proximity and Cocatalyst Effects Lead to Significantly Increased Polyethylene Molecular Weight and Comonomer Enchainment Levels. *Angew. Chem. Int. Ed.* **2004,** *43* (37), 4937-4940. 10.1002/anie.200460288
14. Li, H.; Li, L.; Schwartz, D. J.; Metz, M. V.; Marks, T. J.; Liable-Sands, L.; Rheingold, A. L., Coordination Copolymerization of Severely Encumbered Isoalkenes with Ethylene: Enhanced

Enchainment Mediated by Binuclear Catalysts and Cocatalysts. *J. Am. Chem. Soc.* **2005,** *127* (42), 14756-14768. 10.1021/ja052995x

15. Salata, M. R.; Marks, T. J., Synthesis, Characterization, and Marked Polymerization Selectivity Characteristics of Binuclear Phenoxyiminato Organozirconium Catalysts. *J. Am. Chem. Soc.* **2008,** *130* (1), 12-13. 10.1021/ja076857e
16. Motta, A.; Fragalà, I. L.; Marks, T. J., Proximity and Cooperativity Effects in Binuclear d^0 Olefin Polymerization Catalysis. Theoretical Analysis of Structure and Reaction Mechanism. *J. Am. Chem. Soc.* **2009,** *131* (11), 3974-3984. 10.1021/ja8077208
17. Salata, M. R.; Marks, T. J., Catalyst Nuclearity Effects in Olefin Polymerization. Enhanced Activity and Comonomer Enchainment in Ethylene + Olefin Copolymerizations Mediated by Bimetallic Group 4 Phenoxyiminato Catalysts. *Macromolecules* **2009,** *42* (6), 1920-1933. 10.1021/ma8020745
18. Liu, S.; Xing, Y.; Zheng, Q.; Jia, Y.; Li, Z., Synthesis of Anthracene-Bridged Dinuclear Phenoxyiminato Organotitanium Catalysts with Enhanced Activity, Thermal Stability, and Comonomer Incorporation Ability toward Ethylene (Co)polymerization. *Organometallics* **2020,** *39* (17), 3268-3274. 10.1021/acs.organomet.0c00477
19. Gao, Y.; Mouat, A. R.; Motta, A.; Macchioni, A.; Zuccaccia, C.; Delferro, M.; Marks, T. J., Pyridylamido Bi-Hafnium Olefin Polymerization Catalysis: Conformationally Supported Hf···Hf Enchainment Cooperativity. *ACS Catalysis* **2015,** *5* (9), 5272-5282. 10.1021/acscatal.5b00788
20. Guo, N.; Li, L.; Marks, T. J., Bimetallic Catalysis for Styrene Homopolymerization and Ethylene−Styrene Copolymerization. Exceptional Comonomer Selectivity and Insertion Regiochemistry. *J. Am. Chem. Soc.* **2004,** *126* (21), 6542-6543. 10.1021/ja048761f
21. Amin, S. B.; Marks, T. J., Alkenylsilane Effects on Organotitanium-Catalyzed Ethylene Polymerization. Toward Simultaneous Polyolefin Branch and Functional Group Introduction. *J. Am. Chem. Soc.* **2006,** *128* (14), 4506-4507. 10.1021/ja057947r
22. Amin, S. B.; Marks, T. J., Alkenylsilane Structure Effects on Mononuclear and Binuclear Organotitanium-Mediated Ethylene Polymerization: Scope and Mechanism of Simultaneous Polyolefin Branch and Functional Group Introduction. *J. Am. Chem. Soc.* **2007,** *129* (10), 2938-2953. 10.1021/ja0675292
23. Guo, N.; Stern, C. L.; Marks, T. J., Bimetallic Effects in Homopolymerization of Styrene and Copolymerization of Ethylene and Styrenic Comonomers: Scope, Kinetics, and Mechanism. *J. Am. Chem. Soc.* **2008,** *130* (7), 2246-2261. 10.1021/ja076407m
24. Chen, J.; Gao, Y.; Marks, T. J., Early Transition Metal Catalysis for Olefin–Polar Monomer Copolymerization. *Angew. Chem. Int. Ed.* **2020,** *59* (35), 14726-14735. 10.1002/anie.202000060
25. Terao, H.; Ishii, S.; Mitani, M.; Tanaka, H.; Fujita, T., Ethylene/Polar Monomer Copolymerization Behavior of Bis(phenoxy–imine)Ti Complexes: Formation of Polar Monomer Copolymers. *J. Am. Chem. Soc.* **2008,** *130* (52), 17636-17637. 10.1021/ja8060479
26. Imuta, J.-i.; Kashiwa, N.; Toda, Y., Catalytic Regioselective Introduction of Allyl Alcohol into the Nonpolar Polyolefins: Development of One-Pot Synthesis of Hydroxyl-Capped Polyolefins Mediated by a New Metallocene IF Catalyst. *J. Am. Chem. Soc.* **2002,** *124* (7), 1176-1177. 10.1021/ja0174377
27. Yang, X.-H.; Liu, C.-R.; Wang, C.; Sun, X.-L.; Guo, Y.-H.; Wang, X.-K.; Wang, Z.; Xie, Z.; Tang, Y., [O−NSR]$TiCl_3$-Catalyzed Copolymerization of Ethylene with Functionalized Olefins. *Angew. Chem. Int. Ed.* **2009,** *48* (43), 8099-8102. 10.1002/anie.200903334

28. Chen, Z.; Li, J.-F.; Tao, W.-J.; Sun, X.-L.; Yang, X.-H.; Tang, Y., Copolymerization of Ethylene with Functionalized Olefins by [ONX] Titanium Complexes. *Macromolecules* **2013,** *46* (7), 2870-2875. 10.1021/ma400283p
29. Bouyahyi, M.; Turki, Y.; Tanwar, A.; Jasinska-Walc, L.; Duchateau, R., Randomly Functionalized Polyethylenes: In Quest of Avoiding Catalyst Deactivation. *ACS Catalysis* **2019,** *9* (9), 7779-7790. 10.1021/acscatal.9b01174
30. Wang, X.; Wang, Y.; Shi, X.; Liu, J.; Chen, C.; Li, Y., Syntheses of Well-Defined Functional Isotactic Polypropylenes via Efficient Copolymerization of Propylene with ω-Halo-α-alkenes by Post-metallocene Hafnium Catalyst. *Macromolecules* **2014,** *47* (2), 552-559. 10.1021/ma4022696
31. Shang, R.; Gao, H.; Luo, F.; Li, Y.; Wang, B.; Ma, Z.; Pan, L.; Li, Y., Functional Isotactic Polypropylenes via Efficient Direct Copolymerizations of Propylene with Various Amino-Functionalized α-Olefins. *Macromolecules* **2019,** *52* (23), 9280-9290. 10.1021/acs.macromol.9b00757
32. Kesti, M. R.; Coates, G. W.; Waymouth, R. M., Homogeneous Ziegler-Natta polymerization of functionalized monomers catalyzed by cationic Group IV metallocenes. *J. Am. Chem. Soc.* **1992,** *114* (24), 9679-9680. 10.1021/ja00050a069
33. Chen, J.; Motta, A.; Wang, B.; Gao, Y.; Marks, T. J., Significant Polar Comonomer Enchainment in Zirconium-Catalyzed, Masking Reagent-Free, Ethylene Copolymerizations. *Angew. Chem. Int. Ed.* **2019,** *58* (21), 7030-7034. 10.1002/anie.201902042
34. Huang, M.; Chen, J.; Wang, B.; Huang, W.; Chen, H.; Gao, Y.; Marks, T. J., Polar Isotactic and Syndiotactic Polypropylenes by Organozirconium-Catalyzed Masking-Reagent-Free Propylene and Amino–Olefin Copolymerization. *Angew. Chem. Int. Ed.* **2020,** *59* (46), 20522-20528. 10.1002/anie.202005635
35. Radlauer, M. R.; Agapie, T., Bimetallic Zirconium Amine Bis(phenolate) Polymerization Catalysts: Enhanced Activity and Tacticity Control for Polyolefin Synthesis. *Organometallics* **2014,** *33* (13), 3247-3250. 10.1021/om500608j
36. Sampson, J.; Choi, G.; Akhtar, M. N.; Jaseer, E. A.; Theravalappil, R.; Al-Muallem, H. A.; Agapie, T., Olefin Polymerization by Dinuclear Zirconium Catalysts Based on Rigid Teraryl Frameworks: Effects on Tacticity and Copolymerization Behavior. *Organometallics* **2017,** *36* (10), 1915-1928. 10.1021/acs.organomet.7b00015
37. Tshuva, E. Y.; Goldberg, I.; Kol, M.; Weitman, H.; Goldschmidt, Z., Novel zirconium complexes of amine bis(phenolate) ligands. Remarkable reactivity in polymerization of hex-1-ene due to an extra donor arm. *Chem. Commun.* **2000,** (5), 379-380. 10.1039/B000396O
38. Sworen, J. C.; Smith, J. A.; Wagener, K. B.; Baugh, L. S.; Rucker, S. P., Modeling Random Methyl Branching in Ethylene/ Propylene Copolymers Using Metathesis Chemistry: Synthesis and Thermal Behavior. *J. Am. Chem. Soc.* **2003,** *125* (8), 2228-2240. 10.1021/ja020862v
39. Busico, V.; Cipullo, R.; Cutillo, F.; Friederichs, N.; Ronca, S.; Wang, B., Improving the Performance of Methylalumoxane: A Facile and Efficient Method to Trap "Free" Trimethylaluminum. *J. Am. Chem. Soc.* **2003,** *125* (41), 12402-12403. 10.1021/ja0372412
40. Pangborn, A. B.; Giardello, M. A.; Grubbs, R. H.; Rosen, R. K.; Timmers, F. J., Safe and Convenient Procedure for Solvent Purification. *Organometallics* **1996,** *15* (5), 1518-1520. 10.1021/om9503712
41. Atiqullah, M.; Moman, A. A.; Akhtar, M. N.; Al-Muallem, H. A.; Abu-Raqabah, A. H.; Ahmed, N., Supported SiO_2-$^{n}BuSnCl_3$/MAO/$(^{n}BuCp)_2ZrCl_2$ catalyzing MAO cocatalyst-free

ethylene polymerization: Study of hydrogen responsiveness. *J. Appl. Polym. Sci.* **2007,** *106* (5), 3149-3157. 10.1002/app.26702

42. Dias, P.; Lin, Y. J.; Poon, B.; Chen, H. Y.; Hiltner, A.; Baer, E., Adhesion of statistical and blocky ethylene–octene copolymers to polypropylene. *Polymer* **2008,** *49* (12), 2937-2946. 10.1016/j.polymer.2008.04.022

Appendix B: Ti and Ta Complexes Supported by Bulky Anthracene-Containing Phenoxide Ligands

ABSTRACT

Reported herein is the preparation of series of anthracene-containing bulky *mono*(phenoxide) ligands. Using modified experimental procedures, both *mono*(anthracene) with ethereal donors and *bis*(anthracene) variants were accessed. Metalation studies with titanium and tantalum are reported. Preliminary investigation of ethylene oligomerization activity did not afford selective oligomerization formation. Further study of these complexes was not pursued.

INTRODUCTION

Based on the chemistry that has been developed for the Ti and Zr systems with the bis(phenoxide) ligand platform (discussed in Chapter 2 and previous publications[1]), there is interest in preparation of differentiated mono-ligating anthracene-containing systems to explore the different accessible reactivity, particularly for less-reactive unsaturated olefins (including ethylene) as the complexes may be viable for oligomerization and/or polymerization.

The development of highly active catalysts for selective ethylene oligomerization remains an active area of research, particularly due to the use of 1-hexene and 1-octene as comonomers for the industrial production of linear low-density polyethylene (LLDPE).[2-4] There are literature examples of a variety catalysts including Cr,[2-3, 5-6] Ti,[7-12] and Ta[13] systems that are competent for ethylene oligomerization. For some catalytic systems, the selectivity for oligomer formation over polymer generation is well understood,[14-16] while the selectivity in other systems is less readily explained. In the case of mono(cyclopentadienyl)titaniumtrichloride systems, the polyethylene vs. 1-hexene selectivity can be altered by attachment of a pendent arene group to the cyclopentadienyl ligand, where the hemilability of the arene directs the modification in performance and selectivity.[7] With this in mind, it was hypothesized that Ti and/or Ta systems based on anthracene-containing ligands may be competent for selective ethylene oligomerization.

RESULTS AND DISCUSSION

The design and synthesis of the mono-anthracene monoanionic ligands was targeted (Scheme B.1). The proligands were accessed in three steps from a common intermediate used previously for the *bis*(phenol) proligand. For the 2,6-dimethoybenzene and 2,6-diethoxybenzene variants, use of the di-substituted aryl prevented the formation of different *syn*- and *anti*-isomers. With the quinoline variant, a 1:1 mixture of isomers was formed, and the isomers were separated by column chromatography before deprotection.

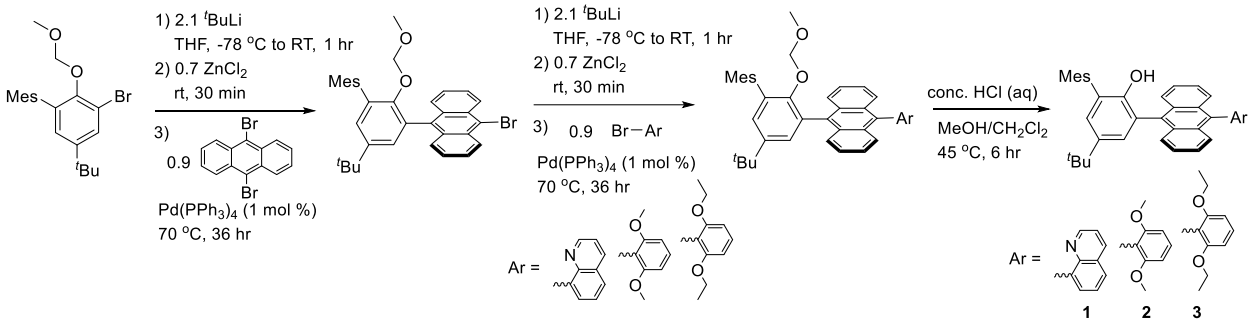

Scheme B.1. Preparation of proligands **S1, A1, 2, 3.**

Using similar synthetic strategies to those discussed above, the synthesis of the bis-anthracene monoanionic ligands was also targeted (Scheme B.2). To avoid formation of complicated mixtures of isomers in later steps of the synthesis, only symmetric aryl groups (2,6-dimethoybenzene and 2,6-diethoxybenzene) were used to modify 1,9-dibromoanthracene.

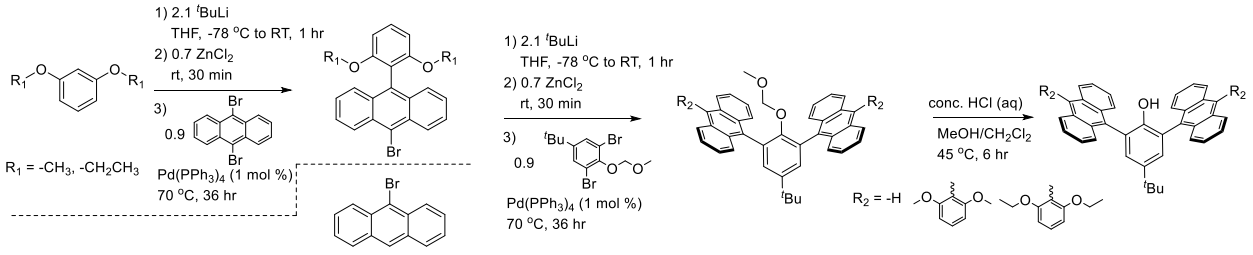

Scheme B.2. Preparation of proligands **4-6**

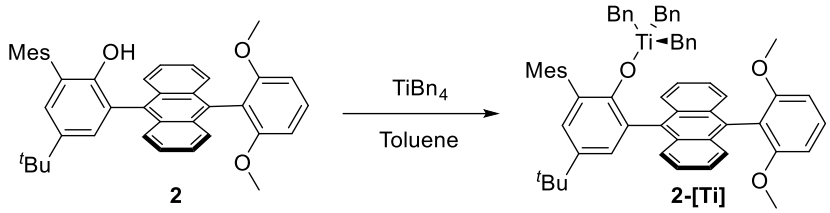

Scheme B.3. Metalation of **2** with $TiBn_4$

Metalation with proligands was carried out by addition of **2** in toluene to a thawing toluene solution of $TiBn_4$ and then warmed to room temperature and stirred overnight. In the ^1H NMR spectrum, a new species (**2-[Ti]**) is observed, consistent with loss of the phenolic proton and the presence of a peak at 1.47 ppm (corresponding to the TiCH_2Ph protons). This peak corresponds to 6 protons, consistent with three benzyl groups in the newly formed species. Solid-state characterization of **2-[Ti]** confirms this initial assignment, where **2-[Ti]** has a phenoxide-bound Ti center with three benzyl groups bound in a tetrahedral geometry. No significant interaction with the ether groups is observed. Analogous titanium complexes were prepared from ligands **S1**, **A1**, and **3** following the same procedure. While solid-state characterization was not collected for **S1-**

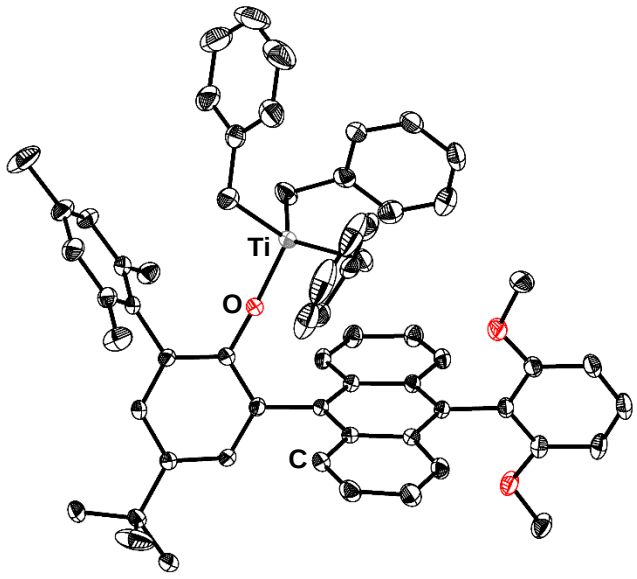

Figure B.1. Solid-state structure of **2-[Ti]**. Thermal ellipsoids shown at 50% probability. Solvent molecules and hydrogen atoms omitted for clarity

[Ti], **A1-[Ti],** and **3-[Ti]**, they are expected to bind in an isostructural fashion, consistent with the similar ^{1}H NMR spectra.

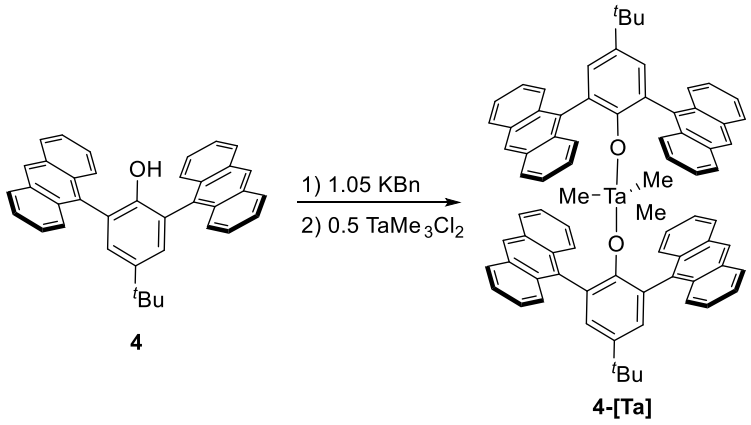

Scheme B.4. Metalation of **4** with **$TaMe_3Cl_2$**

To access the $TaMe_3L_2$ systems, metalation was carried out by deprotonation of LH with KBn, Subsequent addition of $TaMe_3Cl_2$, and the reaction stirred at room temperature overnight. In the ^{1}H NMR spectrum, a new species was observed, with a peak at -2.41 ppm corresponding to the Ta-C*H*$_3$ protons. This peak corresponds to nine protons, consistent with three methyl groups on the Ta center. Preliminary solid-state characterization is consistent with this initial assignment where the Ta center has three methyl ligands and 2 phenoxide ligands. Preliminary solid-state characterization is consistent with a trigonal bipyramidal geometry.

These Ti and Ta complexes have been screened for oligomerization performance at 1 atm C_2H_4, but no selective formation of 1-hexene or 1-octene was observed. Given this observation, additional studies were not pursued.

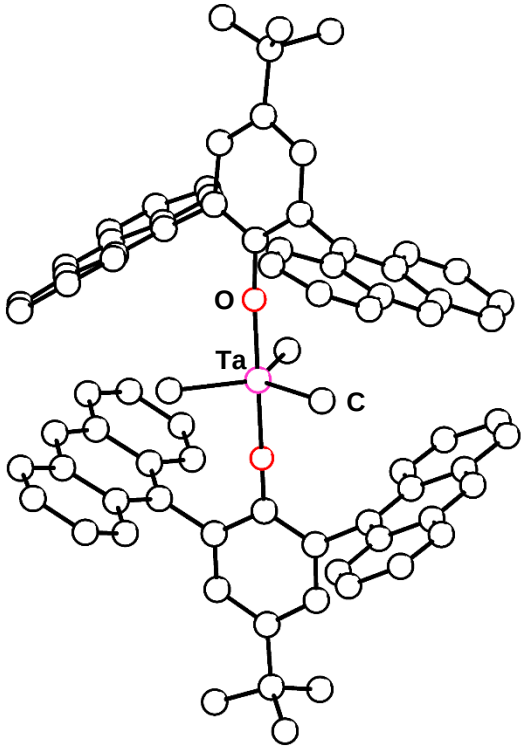

Figure B.2. Preliminary solid-state structure of **4-[Ta]**. Hydrogen atoms and solvent omitted for clarity.

CONCLUSIONS

A series of mono-ligating anthracene-based phenoxide ligands were prepared. By modifying the substituents, a range of proligands was accessed. Metalation of the mono-anthracene proligands (**S1**, **A1**, **2**, **3**) with $TiBn_4$ provides the corresponding *tris*(benzyl) complexes. Solid-state characterization is consistent with formation of the desired species. Metalation of the bis-anthracene proligands (**4**-**6**) by deprotonation and reaction with $TaMe_3Cl_2$ provides the corresponding $TaMe_3L_2$ complexes. Preliminary solid-state characterization is consistent with formation of the desired species.

EXPERIMENTAL SECTION

Unless otherwise specified, all operations involving air- or water-sensitive reagents were carried out in an MBraun drybox under a nitrogen atmosphere or using standard Schlenk and vacuum line techniques. Solvents for air- and moisture-sensitive reactions were dried by the method of Grubbs.1 Deuterated solvents were purchased from Cambridge Isotope Laboratories and C_6D_6 vacuum transferred from sodium benzophenone ketyl before use. All solvents, once dried and degassed, were stored under a nitrogen atmosphere over 4 Å molecular sieves. $TiBn_4$[17] and $TaMe_3Cl_2$[18] were prepared according to literature procedures. All other reagents were used as received. ^{1}H spectra were recorded on Varian Mercury 300 MHz or Varian 400 MHz spectrometers at ambient temperatures, unless otherwise denoted. ^{1}H NMR spectra are reported referenced internally to residual solvent peaks reported relative to tetramethylsilane.

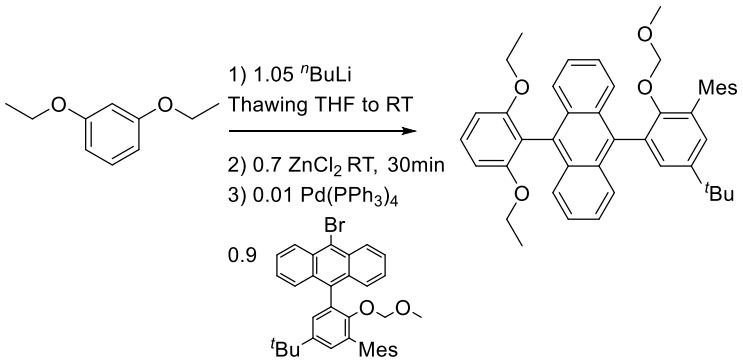

9-(5-(tert-butyl)-2-(methoxymethoxy)-2',4',6'-trimethyl-[1,1'-biphenyl]-3-yl)-10-(2,6-diethoxyphenyl)anthracene. A Schlenk flask fitted with a screw-in Teflon stopper was charged with a solution of 1,3-diethoxybenzene (0.160 g, 0.96 mmol, 1 equiv) in THF (100 mL) and frozen in the cold well. A hexanes solution of ^{n}BuLi (0.4 mL, 2.5 M, 1.05 equiv) was added dropwise to the thawing solution. The reaction was allowed to warm to room temperature and stirred for 1 h forming a dark orange solution. $ZnCl_2$ (0.092 g, 0.67 mmol, 0.7 equiv) was added slowly to the

reaction resulting in the formation of a cloudy pale yellow mixture. The reaction was allowed to stir at room temperature for 30 min after which 9-bromo-10-(5-*tert*-butyl)-2-(methoxymethoxy-2',4',6'-trimethyl-[1,1'-biphenyl]-3-yl)anthracene (0.491 g, 0.86 mmol, 0.9 equiv) and $Pd(PPh_3)_4$ (11 mg, 0.0096 mmol, 0.01 equiv) were added. The flask was sealed and warmed to 70 °C for 48 h. After cooling to room temperature, water (10 mL) was added to quench the reaction, and the mixture was concentrated in vacuo to about 25 mL. The resulting suspension was taken up in CH_2Cl_2 (100 mL) and filtered through a silica gel plug, eluting further with CH_2Cl_2. The filtrate was then washed with water (2 × 50 mL), dried over $MgSO_4$, filtered, and concentrated in vacuo The product was isolated as pale yellow solid. ^{1}H NMR ($CDCl_3$): 8.08 (d, 2 H, Ar-*H*), 7.93 (d, 2 H, Ar-*H*), 7.75 (m, 2 H, Ar-*H*), 7.64 (t, 2 *H*, Ar-*H*), 7.54 (s, 1 H, Ar-*H*), 7.10 (d, 2 H, Ar-*H*), 7.04 (d, 2 H, Ar-*H*), 4.30 (s, 2 H, -OC*H*$_2$OCH$_3$), 4.24 (q, 2 H, -OC*H*$_2$CH$_3$), 4.08 (q, 2 H, -OC*H*$_2$CH$_3$), 2.62 (s, 3 H, Ar-C*H*$_3$), 2.57 (s, 6 H, Ar-C*H*$_3$), 2.16 (s, 3 H, -OC*H*$_2$OCH$_3$), 1.68 (s, 9 H, -C(C*H*$_3$)$_3$), 1.27 (t, 3 H, -OCH$_2$C*H*$_3$), 1.03 (t, 3 H, -OCH$_2$C*H*$_3$).

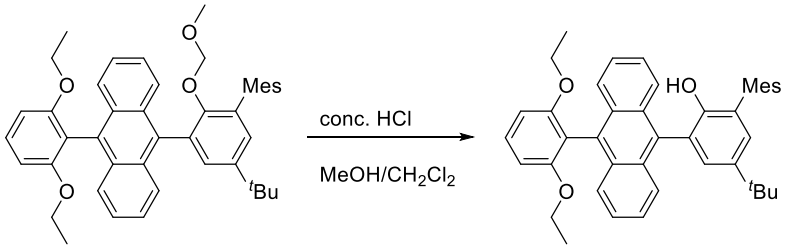

5-(tert-butyl)-3-(10-(2,6-diethoxyphenyl)anthracen-9-yl)-2',4',6'-trimethyl-[1,1'-biphenyl]-2-ol (3). A Schlenk flask fitted with a screw-in Teflon stopper was charged with 9-(5-(tert-butyl)-2-(methoxymethoxy)-2',4',6'-trimethyl-[1,1'-biphenyl]-3-yl)-10-(2,6-diethoxyphenyl)anthracene (100 mg), MeOH (5 mL) and CH_2Cl_2 (10 mL). Concentrated aqueous HCl (1 mL) was added, and the flask sealed and heated to 45 °C. After complete deprotection, about 6 h, the reaction was cooled and concentrated in vacuo. The suspension was taken up in CH_2Cl_2 (25 mL) and washed

with H_2O (2 × 10 mL) and then saturated aqueous $NaHCO_3$ (10 mL). The organic fraction was dried over $MgSO_4$, filtered, and concentrated under reduced pressure to provide the product as a pale yellow solid. ^{1}H NMR ($CDCl_3$): 8.03 (d, 2 H, Ar-*H*), 7.95 (d, 2 H, Ar-*H*), 7.72 (t, 1 H, Ar-*H*), 7.65 (m, 2 *H*, Ar-*H*), 7.63-7.50 (multiple overlapping peaks, 6 H, Ar-*H*), 7.07 (d, 2 H, Ar-*H*), 7.03 (d, 2 H, Ar-*H*), 4.21 (q, 2 H, -OC*H*$_2$CH$_3$), 4.09 (q, 2 H, -OC*H*$_2$CH$_3$), 2.59 (s, 3 H, Ar-C*H*$_3$), 2.48 (s, 6 H, Ar-C*H*$_3$),1.64 (s, 9 H, -C(C*H*$_3$)$_3$), 1.23 (t, 3 H, -OCH$_2$C*H*$_3$), 1.05 (t, 3 H, -OCH$_2$C*H*$_3$).

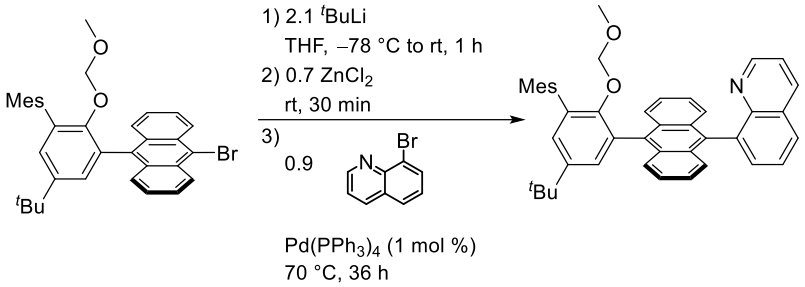

8-(10-(5-(tert-butyl)-2-(methoxymethoxy)-2',4',6'-trimethyl-[1,1'-biphenyl]-3-yl)anthracen-9-yl)quinoline (mixture of isomers). A Schlenk flask fitted with a screw-in Teflon stopper was charged with a solution of 9-bromo-10-(5-*tert*-butyl)-2-(methoxymethoxy-2',4',6'-trimethyl-[1,1'-biphenyl]-3-yl)anthracene (0.5 g, 0.88 mmol, 1 equiv) in THF (100 mL) and frozen in the cold well. A pentane solution of ^{t}BuLi (0.119 g, 1.85 mmol, 2.1 equiv) was added dropwise to the thawing solution. The reaction was allowed to warm to room temperature and stirred for 1 h forming a dark orange solution. $ZnCl_2$ (0.084 g, 0.61 mmol, 0.7 equiv) was added slowly to the reaction resulting in the formation of a cloudy pale yellow mixture. The reaction was allowed to stir at room temperature for 30 min after which 8-bromoquinoline (0.164 g, 0.79 mmol, 0.9 equiv) and $Pd(PPh_3)_4$ (10.2 mg, 0.0088 mmol, 0.01 equiv) was added. The flask was sealed and warmed to 70 °C for 48 h. After cooling to room temperature, water (10 mL) was added to quench the reaction, and the mixture was concentrated in vacuo to about 25 mL. The resulting suspension was

taken up in CH_2Cl_2 (100 mL) and filtered through a silica gel plug, eluting further with CH_2Cl_2. The filtrate was then washed with water (2 × 50 mL), dried over $MgSO_4$, filtered, and concentrated in vacuo The product was isolated as a pale yellow solid. The isomers were separated by column chromatography (95:5, Hexanes:EtOAc)

Isomer 1: ^{1}H NMR ($CDCl_3$): 8.85 (br. s, 1 H, Ar-*H*), 8.38 (d, 1 H, Ar-*H*), 8.07 (d, 1 H, Ar-*H*), 7.81 (d, 2 H, Ar-*H*), 7.76 (d, 1 H, Ar-*H*), 7.71 (d, 1 H, Ar-*H*), 7.54 (s, 1 H, Ar-*H*), 7.46 (m, 1 H, Ar-*H*), 7..37-7.30 (overlapping peaks, 5 H, Ar-*H*), 7.20 (t, 2 H, Ar-*H*), 6.97 (s, 2 H, Ar-*H*), 4.08 (s, 2 H, -OC*H*$_2$OCH$_3$), 2.32 (s, 3 H, Ar-C*H*$_3$), 2.28 (s, 6 H, Ar-C*H*$_3$), 2.07 (s, 3 H, -OCH$_2$OC*H*$_3$), 1.38 (s, 9 H, -C(C*H*$_3$)$_3$).

Isomer 2: ^{1}H NMR ($CDCl_3$): 8.52 (d, 1 H, Ar-*H*), 8.28 (d, 1 H, Ar-*H*), 8.04 (d, 1 H, Ar-*H*), 7.86-7.81 (overlapping peaks, 3 H, Ar-*H*), 7.77 (t, 1 H, Ar-*H*), 7.45 (d, 1 H, Ar-*H*), 7.40- 7.32 (overlapping peaks, 6 H, Ar-*H*), 7.21 (t, 2 H, Ar-*H*), 6.97 (s, 2 H, Ar-*H*), 4.13 (s, 2 H, -OC*H*$_2$OCH$_3$), 2.33 (s, 3 H, Ar-C*H*$_3$), 2.27 (s, 6 H, Ar-C*H*$_3$), 2.05 (s, 3 H, -OCH$_2$OC*H*$_3$), 1.38 (s, 9 H, -C(C*H*$_3$)$_3$).

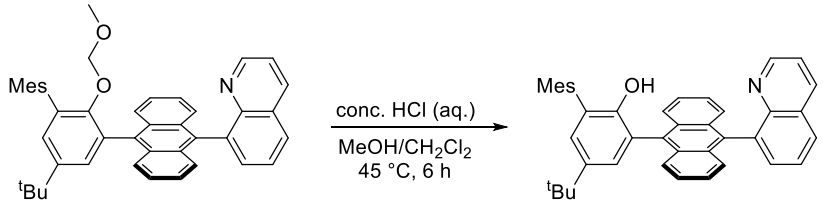

5-(tert-butyl)-2',4',6'-trimethyl-3-(10-(quinolin-8-yl)anthracen-9-yl)-[1,1'-biphenyl]-2-ol (S1 and A1). A Schlenk flask fitted with a screw-in Teflon stopper was charged with 8-(10-(5-(tert-butyl)-2-(methoxymethoxy)-2',4',6'-trimethyl-[1,1'-biphenyl]-3-yl)anthracen-9-yl)quinoline (100 mg), MeOH (5 mL) and CH_2Cl_2 (10 mL). Concentrated aqueous HCl (1 mL) was added, the flask was sealed and heated to 45 °C. After complete deprotection, about 6 h, the reaction was cooled

and concentrated in vacuo. The suspension was taken up in CH_2Cl_2 (25 mL) and washed with H_2O (2 × 10 mL) and then saturated aqueous $NaHCO_3$ (10 mL). The organic fraction was dried over $MgSO_4$, filtered, and concentrated under reduced pressure to provide the product as a pale yellow solid.

Isomer 1: ^{1}H NMR ($CDCl_3$): 8.81 (br. d, 1 H, Ar-*H*), 8.34 (d, 1 H, Ar-*H*), 8.07 (d, 1 H, Ar-*H*), 7.84-7.74 (overlapping peaks, 4 H, Ar-*H*), 7.47 (d, 1 H, Ar-*H*),7.46-7.39 (overlapping peaks, 3 H, Ar-*H*), 7.36 (t, 2 H, Ar-*H*), 7.28 (d, 1 H, Ar-*H*), 7.26-7.21 (overlapping peaks,, 3 H, Ar-*H*), 7.02 (s, 2 H, Ar-*H*), 4.51 (s, 1 H, -O*H*), 2.35 (s, 3 H, Ar-CH_3), 2.24 (s, 6 H, Ar-CH_3), 1.38 (s, 9 H, -C(CH_3)$_3$).

Isomer 2: ^{1}H NMR ($CDCl_3$): 8.66 (d, 1 H, Ar-*H*), 8.34 (d, 1 H, Ar-*H*), 8.08 (d, 1 H, Ar-*H*), 7.87-7.76 (overlapping peaks, 4 H, Ar-*H*), 7.45-7.34 (overlapping peaks, 6 H, Ar-*H*), 7.30 (s, 1 H, Ar-*H*), 7.25 (t, 2 H, Ar-*H*), 7.03 (s, 2 H, Ar-*H*), 5.00 (s, 1 H, -O*H*), 2.36 (s, 3 H, Ar-CH_3), 2.25 (s, 6 H, Ar-CH_3), 1.39 (s, 9 H, -C(CH_3)$_3$).

Representative example of metalation of monophenol anthracene proligands

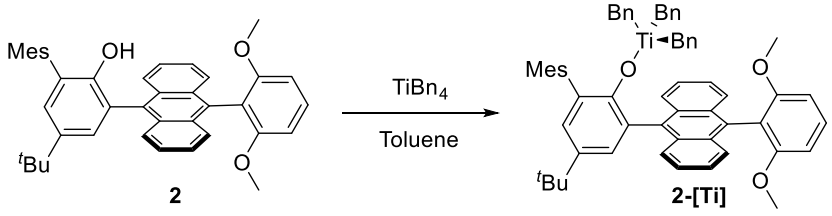

A vial charged with a Teflon-coated stir bar and **2** (0.2 g, 0.34 mmol, 1 equiv) in toluene (5 mL) was frozen in the cold well in a glove box. Allowing it to warm till thawing, it was added to a thawing solution of $TiBn_4$ (0.142 g, 0.2mmol, 1 equiv.) in toluene (3 mL). The reaction was allowed to warm to room temperature, stirring for an additional 2 h. After removal of the volatiles under vacuum, the residue was extracted with benzene and dried in vacuo to yield **2-[Ti]**. Recrystallized from toluene/pentane vapor diffusion in the freezer. ^{1}H NMR (C_6D_6, 400 MHz):

8.31 (d, 2 H, Ar-*H*), 7.89 (d, 2 H, Ar-*H*), 7.43 (app. s, 2 H, Ar-*H*), 7.23 (app t, 3 H, Ar-*H*), 7.08 (app t, 8 H, Ar-*H*), 6.98 (app. t, 3 H, Ar-*H*), 6.78 (app. t, 2 H, Ar-*H*), 6.42 (app. dd, 2 H, Ar-*H*), 5.94 (d, 6 H, Ar-H), 2.99 (s, 3 H, ArOC*H*$_3$), 2.79 (s, 3 H, ArOC*H*$_3$), 2.47 (s, 3 H, ArC*H*$_3$), 2.07 (s, 6 H, ArC*H*$_3$), 1.47 (s, 6 H, TiC*H*$_2$Ph), 1.23 (s, 9 H, ArC(C*H*$_3$)$_3$)

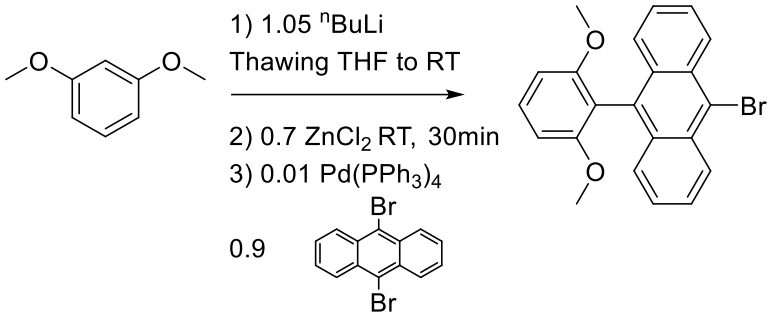

9-bromo-10-(2,6-dimethoxyphenyl)anthracene. A Schlenk flask fitted with a screw-in Teflon stopper was charged with a solution of 1,3-dimethoxybenzene (0.433 g, 3.13 mmol, 1 equiv) in THF (40 mL) and frozen in the cold well. A hexanes solution of *n*BuLi (1.3 mL, 2.5 M, 3.29 mmol, 1.05 equiv) was added dropwise to the thawing solution The reaction was allowed to warm to room temperature and stirred for 1 h forming a dark orange solution. $ZnCl_2$ (0.3 g, 2.19 mmol, 0.7 equiv) was added slowly to the reaction resulting in the formation of a cloudy pale yellow mixture. The reaction was allowed to stir at room temperature for 30 min after which 9,10-dibromoanthracene (1 g, 2.98 mmol, 0.95 equiv) and $Pd(PPh_3)_4$ (36 mg, 0.031 mmol, 0.01 equiv) was added. The flask was sealed and warmed to 70 °C for 48 h. After cooling to room temperature, water (5 mL) was added to quench the reaction, and the mixture concentrated in vacuo to about 10 mL. The resulting suspension was taken up in CH_2Cl_2 (50 mL) and filtered through a silica gel plug, eluting further with CH_2Cl_2. The filtrate was then washed with water (2 × 10 mL), dried over $MgSO_4$, filtered, and concentrated in vacuo The product was isolated as pale yellow solid. ^{1}H NMR (400 MHz,

$CDCl_3$): δ 8.59 (d, 2 H, Ar-*H*), 7.58 (t, 4 H, Ar-*H*), 7.51 (t, 1 H, Ar-*H*), 7.35 (t, 2 H, Ar-*H*), 6.80 (d, 2 H, Ar-*H*), 3.55 (s, 6 H, ArOC*H*$_3$)

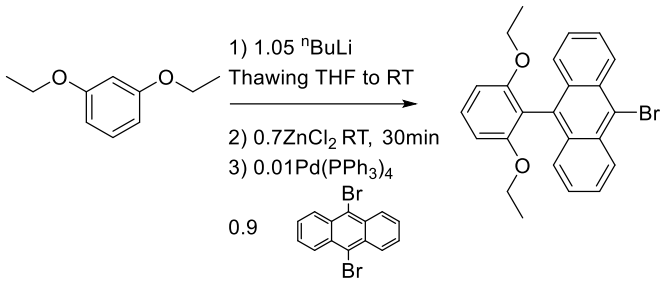

9-bromo-10-(2,6-diethoxyphenyl)anthracene. A Schlenk flask fitted with a screw-in Teflon stopper was charged with a solution of 1,3-diethoxybenzene (0.521 g, 3.13 mmol, 1 equiv) in THF (40 mL) and frozen in the cold well. A hexanes solution of ^{n}BuLi (1.3 mL, 2.5 M, 3.29 mmol, 1.05 equiv) was added dropwise to the thawing solution The reaction was allowed to warm to room temperature and stirred for 1 h forming a dark orange solution. $ZnCl_2$ (0.3 g, 2.19 mmol, 0.7 equiv) was added slowly to the reaction resulting in the formation of a cloudy pale-yellow mixture. The reaction was allowed to stir at room temperature for 30 min after which 9,10-dibromoanthracene (1 g, 2.98 mmol, 0.95 equiv) and $Pd(PPh_3)_4$ (36 mg, 0.031 mmol, 0.01 equiv) was added. The flask was sealed and warmed to 70 °C for 48 h. After cooling to room temperature, water (5 mL) was added to quench the reaction, and the mixture concentrated in vacuo to about 10 mL. The resulting suspension was taken up in CH_2Cl_2 (50 mL) and filtered through a silica gel plug, eluting further with CH_2Cl_2. The filtrate was then washed with water (2 × 10 mL), dried over $MgSO_4$, filtered, and concentrated in vacuo The product was isolated as pale yellow solid. ^{1}H NMR ($CDCl_3$): 8.58 (d, 2 H, Ar-*H*), 7.62 (d, 2 H, Ar-*H*), 7.55 (app. t, 2 H, Ar-*H*), 7.45 (t, 1 H, Ar-*H*), 7.33 (app. t, 2 H, Ar-*H*), 6.76 (d, 2 H, Ar-*H*), 3.85 (q, 4 H, ArOC*H*$_2$CH$_3$), 0.84 (t, 6 H, ArOCH$_2$C*H*$_3$).

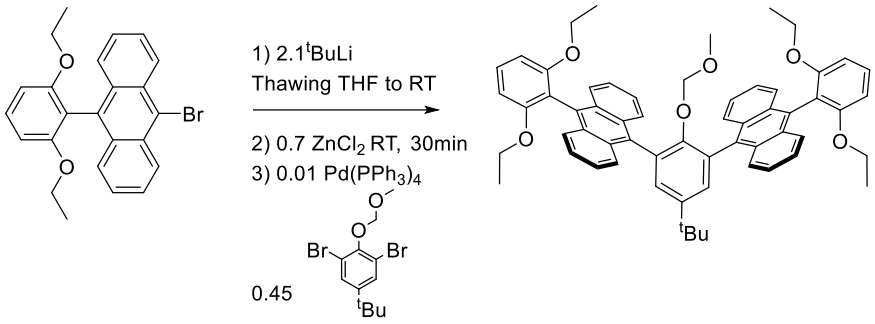

10,10'-(5-(tert-butyl)-2-(methoxymethoxy)-1,3-phenylene)bis(9-(2,6-diethoxyphenyl) anthracene). A Schlenk flask fitted with a screw-in Teflon stopper was charged with a solution of 9-bromo-10-(2,6-diethoxyphenyl)anthracene (0.620 g, 1.48 mmol, 1 equiv) in THF (40 mL) and frozen in the cold well. A pentane solution of *t*BuLi (200 mg, 3.1 mmol, 2.1 equiv) was added dropwise to the thawing solution The reaction was allowed to warm to room temperature and stirred for 1 h forming a dark orange solution. $ZnCl_2$ (0.141 g, 1.03 mmol, 0.7 equiv) was added slowly to the reaction resulting in the formation of a cloudy mixture. The reaction was allowed to stir at room temperature for 30 min after which 1,3-dibromo-5-(*tert*-butyl)-2-(methoxymethoxy)benzene (0.201 g, 0.59 mmol, 0.4 equiv) and $Pd(PPh_3)_4$ (17 mg, 0.0148 mmol, 0.01 equiv) was added. The flask was sealed and warmed to 70 °C for 48 h. After cooling to room temperature, water (5 mL) was added to quench the reaction, and the mixture concentrated in vacuo to about 10 mL. The resulting suspension was taken up in CH_2Cl_2 (50 mL) and filtered through a silica gel plug, eluting further with CH_2Cl_2. The filtrate was then washed with water (2 × 10 mL), dried over $MgSO_4$, filtered, and concentrated in vacuo The product was isolated as pale yellow solid. ^{1}H NMR ($CDCl_3$): 8.04 (d, 4 H, Ar-*H*), 7.70 (s, 2 H, Ar-*H*), 7.64 (d, 4 H, Ar-*H*), 7.50-7.40 (overlapping peaks, 6 H, Ar-*H*), 7.31 (app. t, 4 H, Ar-*H*), 6.82 (d, 2 H, Ar-*H*), 6.72 (d, 2 H, Ar-*H*), 3.97 (q, 4 H, ArOC*H*$_2$CH$_3$), 3.72 (q, 4 H, ArOC*H*$_2$CH$_3$).

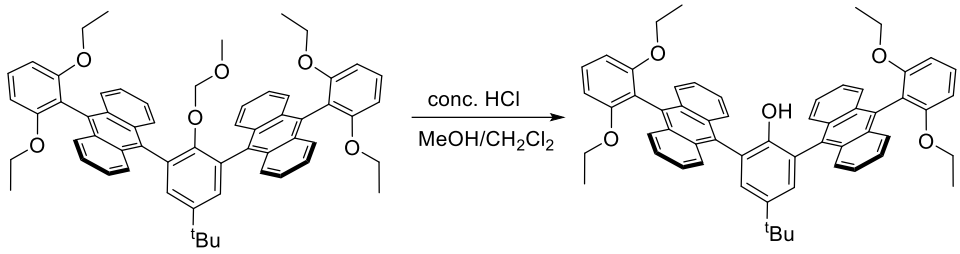

4-(tert-butyl)-2,6-bis(10-(2,6-diethoxyphenyl)anthracen-9-yl)phenol (6). A Schlenk flask fitted with a screw-in Teflon stopper was charged with 10,10'-(5-(tert-butyl)-2-(methoxymethoxy)-1,3-phenylene)bis(9-(2,6-diethoxyphenyl) anthracene) (150 mg), MeOH (5 mL) and CH_2Cl_2 (10 mL). Concentrated aqueous HCl (1 mL) was added, the flask was sealed and heated to 45 °C. After complete deprotection, about 6 h, the reaction was cooled and concentrated in vacuo. The suspension was taken up in CH_2Cl_2 (25 mL) and washed with H_2O (2 × 10 mL) and then saturated aqueous $NaHCO_3$ (10 mL). The organic fraction was dried over $MgSO_4$, filtered and concentrated under reduced pressure to provide the product as a pale yellow solid.^{1}H NMR (400 MHz, $CDCl_3$): δ 7.99 (d, 4 H, Ar-*H*), 7.69-7.61 (overlapping peaks, 6 H, Ar-*H*), 7.45 (m, 6 H, Ar-*H*), 7.32 (m, 4 H, Ar-*H*), 6.81 (d, 2 H, Ar-*H*), 6.74 (d, 2 H, Ar-*H*), 3.96 (q, 4 H, ArOC*H*$_2$CH$_3$), 3.76 (q, 4 H, ArOC*H*$_2$CH$_3$), 0.99 (t, 6 H, ArOCH$_2$C*H*$_3$), 0.73 (t, 6 H, ArOCH$_2$C*H*$_3$).

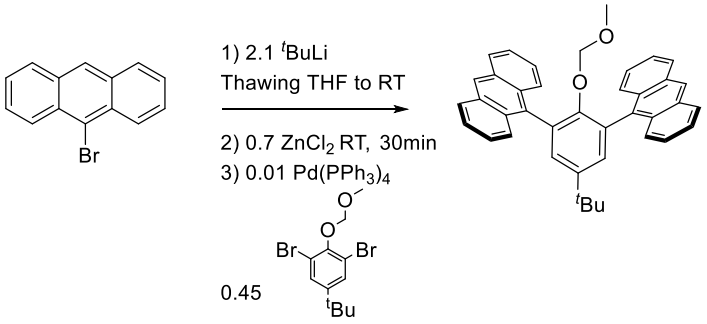

(s)-9,9'-(5-(*tert*-butyl)-2-(methoxymethoxy)-1,3-phenylene)dianthracene. A Schlenk flask fitted with a screw-in Teflon stopper was charged with a solution of 9-bromoanthracene (4.86 g, 18.9 mmol, 1 equiv) in THF (100 mL) and frozen in the cold well. A pentane solution of ^{t}BuLi

(2.57g, 39.7 mmol, 2.1 equiv) was added dropwise to the thawing solution. The reaction was allowed to warm to room temperature and stirred for 1 h forming a dark orange solution. $ZnCl_2$ (1.8 g, 13.2 mmol, 0.7 equiv) was added slowly to the reaction resulting in the formation of a cloudy pale-yellow mixture. The reaction was allowed to stir at room temperature for 30 min after which 1,3-dibromo-5-(*tert*-butyl)-2-(methoxymethoxy)benzene (3 g, 8.5 mmol, 0.45 equiv) and $Pd(PPh_3)_4$ (219 mg, 0.019 mmol, 0.01 equiv) was added. The flask was sealed and warmed to 70 °C for 48 h. After cooling to room temperature, water (10 mL) was added to quench the reaction, and the mixture was concentrated in vacuo to about 25 mL. The resulting suspension was taken up in CH_2Cl_2 (100 mL) and filtered through a silica gel plug, eluting further with CH_2Cl_2. The filtrate was then washed with water (2 × 50 mL), dried over $MgSO_4$, filtered, and concentrated in vacuo The product was isolated as a pale yellow solid. ^{1}H NMR (400 MHz, $CDCl_3$): 8.51 (s, 2 H, Ar-*H*), 8.05 (m, 4 H, Ar-*H*), 7.80 (m, 4 H, Ar-*H*), 7.57-7.46 (overlapping peaks, 10 H, Ar-*H*), 3.76 (s, 2 H, OCH_2OCH_3), 2.06 (s, 2 H, OCH_2OCH_3), 1.40 (s, 9 H, $C(CH_3)_3$).

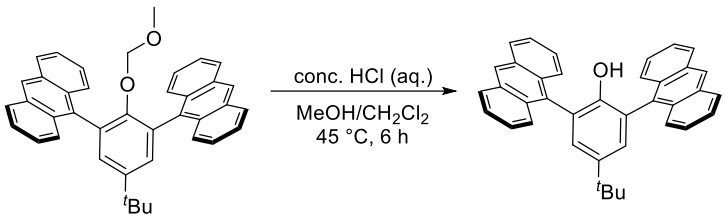

2,6-di(anthracen-9-yl)-4-(*tert*-butyl)phenol (4). A Schlenk flask fitted with a screw-in Teflon stopper was charged with (s)-9,9'-(5-(*tert*-butyl)-2-(methoxymethoxy)-1,3-phenylene)dianthracene (1.5 g), MeOH (25 mL) and CH_2Cl_2 (50 mL). Concentrated aqueous HCl (5 mL) was added, and the flask was sealed and heated to 45 °C. After complete deprotection, about 6 h, the reaction was cooled and concentrated in vacuo. The suspension was taken up in CH_2Cl_2 (50 mL) and washed with H_2O (2 × 25 mL) and then saturated aqueous $NaHCO_3$ (25 mL).

The organic fraction was dried over $MgSO_4$, filtered, and concentrated under reduced pressure to provide the product as a pale yellow solid. ^1H NMR ($CDCl_3$): 8.54 (s, 2 H, Ar-*H*), 8.07 (m, 4 H, Ar-*H*), 7.93 (m, 4 H, Ar-*H*), 7.52-7.46 (overlapping peaks, 10 H, Ar-*H*), 4.35 (s, 1 H, -O*H*), 1.40 (s, 9 H, ArC(CH_3)$_3$).

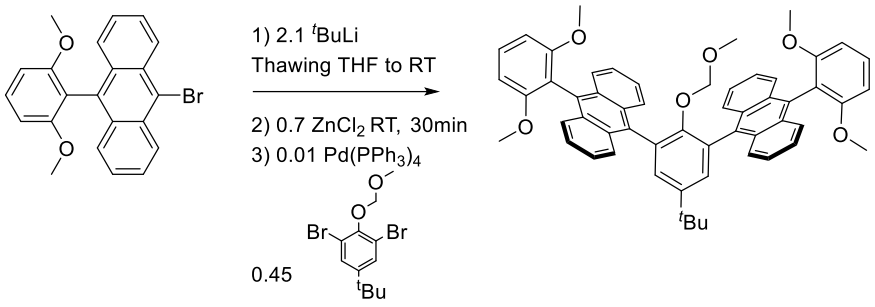

9-((S)-5-(tert-butyl)-3-((r)-10-(2,6-dimethoxyphenyl)anthracen-9-yl)-2-(methoxymethoxy)phenyl)-0-(2,6-dimethoxyphenyl)anthracene.

A Schlenk flask fitted with a screw-in Teflon stopper was charged with a solution of 9-bromo-10-(2,6-dimethoxyphenyl)anthracene (2 g, 5.1 mmol, 1 equiv) in THF (100 mL) and frozen in the cold well. A pentane solution of ^{t}BuLi (0.691 g, 10.7 mmol, 2.1 equiv) was added dropwise to the thawing solution. The reaction was allowed to warm to room temperature and stirred for 1 h forming a dark orange solution. $ZnCl_2$ (0.486 g, 3.57 mmol, 0.7 equiv) was added slowly to the reaction resulting in the formation of a cloudy pale-yellow mixture. The reaction was allowed to stir at room temperature for 30 min after which 1,3-dibromo-5-(*tert*-butyl)-2-(methoxymethoxy)benzene (0.719 g, 2.0 mmol, 0.4 equiv) and $Pd(PPh_3)_4$ (0.059 mg, 0.051 mmol, 0.01 equiv) was added. The flask was sealed and warmed to 70 °C for 48 h. After cooling to room temperature, water (10 mL) was added to quench the reaction, and the mixture was concentrated in vacuo to about 25 mL. The resulting suspension was taken up in CH_2Cl_2 (100 mL) and filtered

through a silica gel plug, eluting further with CH_2Cl_2. The filtrate was then washed with water (2 × 50 mL), dried over $MgSO_4$, filtered, and concentrated in vacuo The product was isolated as a pale yellow solid. Isolated as a mixture of products and used for subsequent deprotection with further purification.

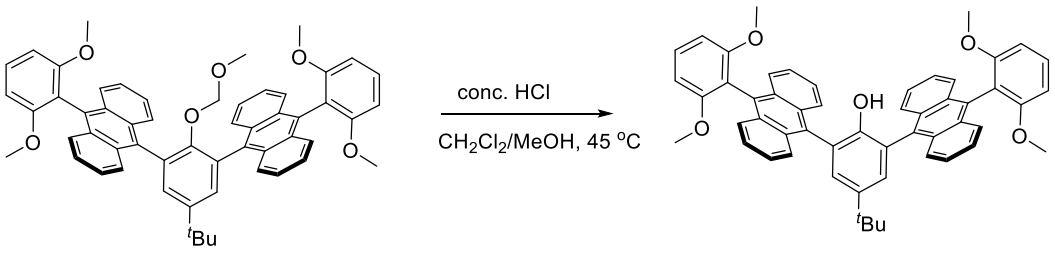

(S)-4-(tert-butyl)-2-((r)-10-(2,6-dimethoxyphenyl)anthracen-9-yl)-6-(10-(2,6-dimethoxyphenyl)anthracen-9-yl)phenol (5). A Schlenk flask fitted with a screw-in Teflon stopper was charged with 9-((S)-5-(tert-butyl)-3-((r)-10-(2,6-dimethoxyphenyl)anthracen-9-yl)-2-(methoxymethoxy)phenyl)-0-(2,6-dimethoxyphenyl)anthracene (1.5 g), MeOH (10 mL) and CH_2Cl_2 (25 mL). Concentrated aqueous HCl (1 mL) was added, and the flask was sealed and heated to 45 °C. After complete deprotection, about 6 h, the reaction was cooled and concentrated in vacuo. The suspension was taken up in CH_2Cl_2 (25 mL) and washed with H_2O (2 × 20 mL) and then saturated aqueous $NaHCO_3$ (10 mL). The organic fraction was dried over $MgSO_4$, filtered, and concentrated under reduced pressure to provide the product as a pale yellow solid.

^{1}H NMR ($CDCl_3$): 8.00 (d, 4 H, Ar-*H*), 7.65 (overlapping peaks, 7 H, Ar-*H*), 7.50 (t, 2 H, Ar-*H*), 7.46 (t, 1 H, Ar-*H*), 7.34 (t, 5 H, Ar-*H*), 6.84 (d, 2 H, Ar-*H*), 6.78 (d, 2 H, Ar-*H*), 4.74 (s, 1 H, -O*H*), 3.65 (s, 6 H, ArOCH_3), 3.47 (s, 6 H, ArOCH_3), 1.45 (s, 9 H, ArC(CH_3)$_3$).

Representative example of metalation of *bis*(anthracene) proligands

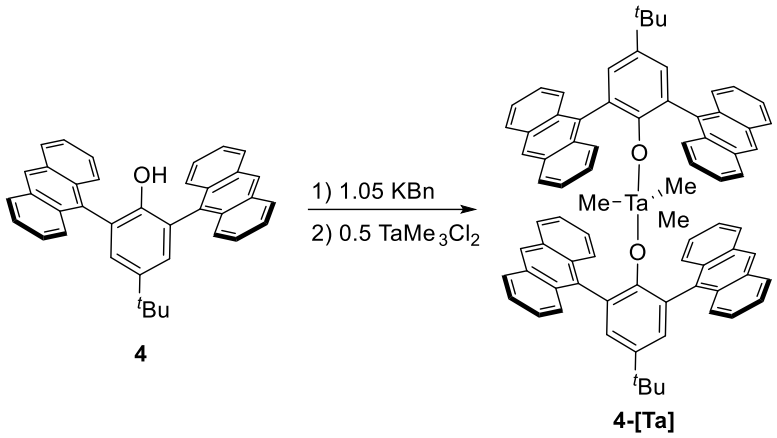

A vial charged with a Teflon-coated stir bar and **4** (0.2 g, 0.39 mmol, 1 equiv) in toluene (5 mL). KBn (0.054 mg, 0.41 mmol, 1.05 equiv) was added as a solid in one portion. After stirring for 10 min at rt, the red-orange mixture was frozen in the old well. $TaCl_2Me_3$ (0.059 g, 0.20 mmol, 0.5 equiv) was added as a solid in one portion. The reaction was warmed to rt and stirring for 16 hr. After removal of the volatiles under vacuum, the residue was extracted with benzene and dried in vacuo to yield **4-[Ta]**. ^{1}H NMR (C_6D_6): 8.12 (s, 4 H, Ar-*H*), 7.84 (app. dd, 16 H, Ar-*H*), 7.36 (s, 4 H, Ar-*H*), 7.21 (app t, 8 H, Ar-*H*), 7.02 (app t, 8 H, Ar-*H*), 1.04 (s, 18 H, -C(C*H*$_3$)$_3$), -2.41 (s, 9 H, Ta-C*H*$_3$).

NMR Spectra

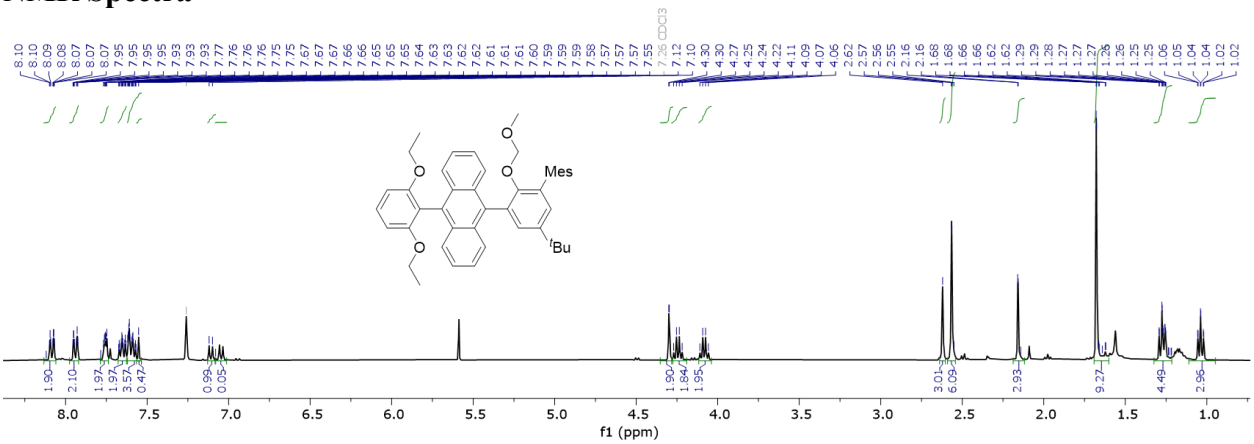

Figure B.3. ^{1}H NMR of **9-(5-(tert-butyl)-2-(methoxymethoxy)-2',4',6'-trimethyl-[1,1'-biphenyl]-3-yl)-10-(2,6-diethoxyphenyl)anthracene** in $CDCl_3$.

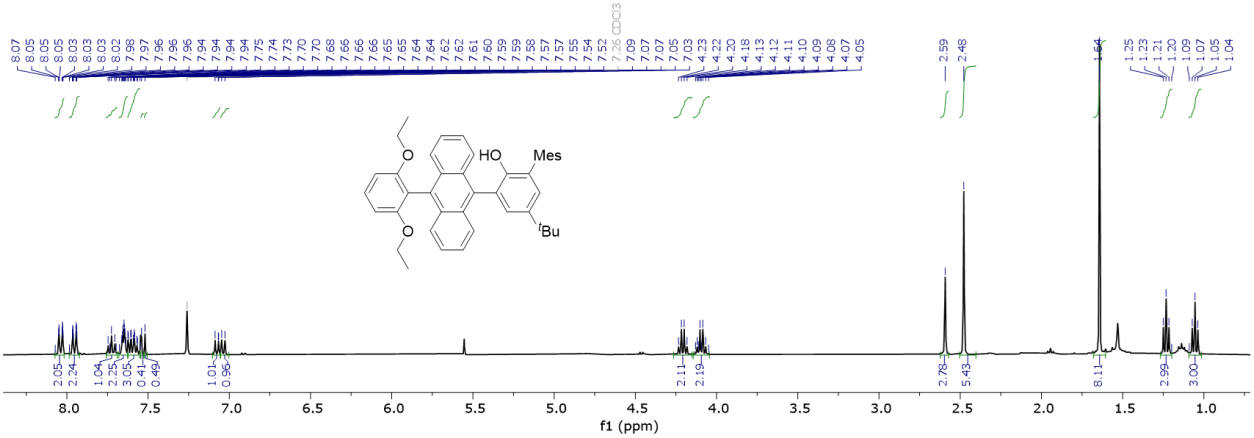

Figure B.4. ^{1}H NMR of **5-(tert-butyl)-3-(10-(2,6-diethoxyphenyl)anthracen-9-yl)-2',4',6'-trimethyl-[1,1'-biphenyl]-2-ol** in $CDCl_3$.

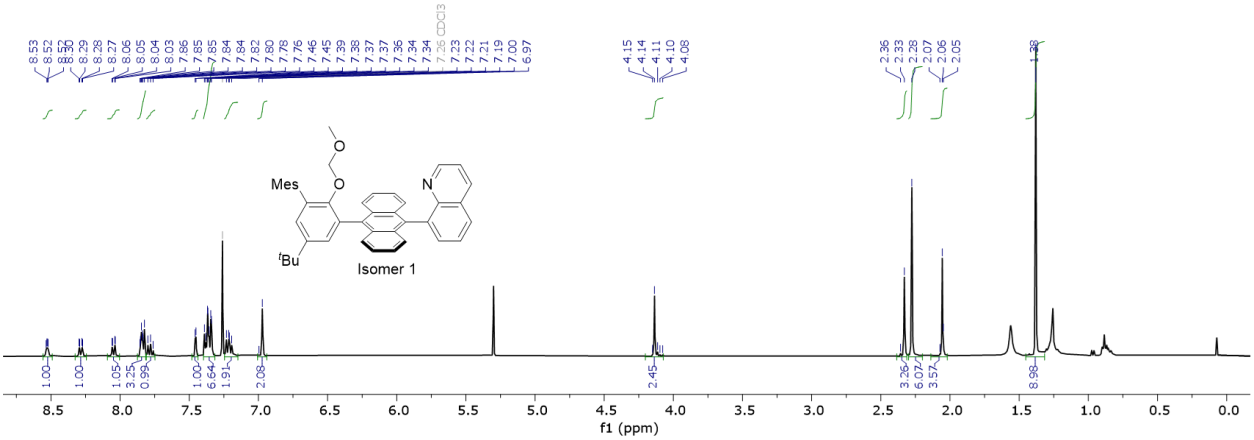

Figure B.5. ^{1}H NMR of **8-(10-(5-(tert-butyl)-2-(methoxymethoxy)-2',4',6'-trimethyl-[1,1'-biphenyl]-3-yl)anthracen-9-yl)quinoline (Isomer 1)** in $CDCl_3$.

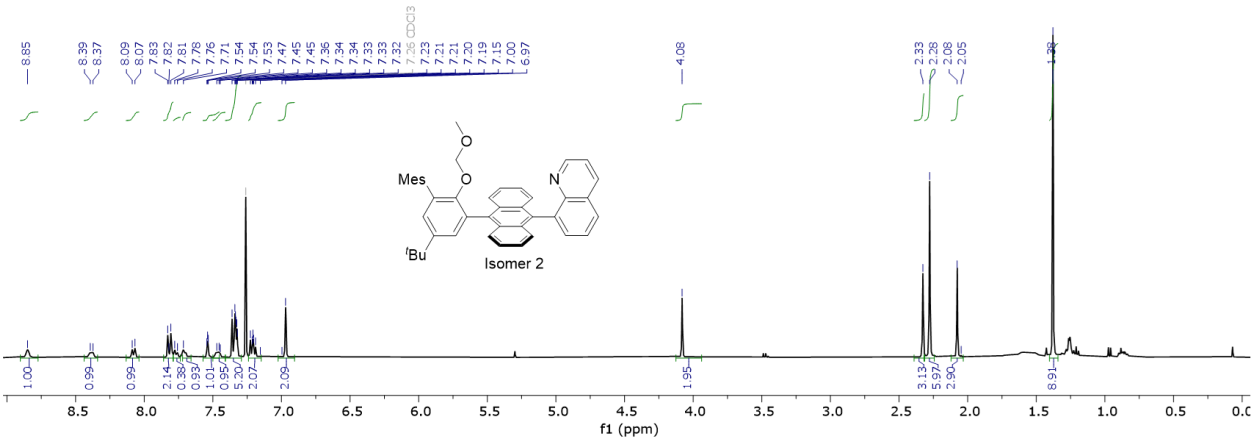

Figure B.6. ^{1}H NMR of **8-(10-(5-(tert-butyl)-2-(methoxymethoxy)-2',4',6'-trimethyl-[1,1'-biphenyl]-3-yl)anthracen-9-yl)quinoline (Isomer 2)** in $CDCl_3$.

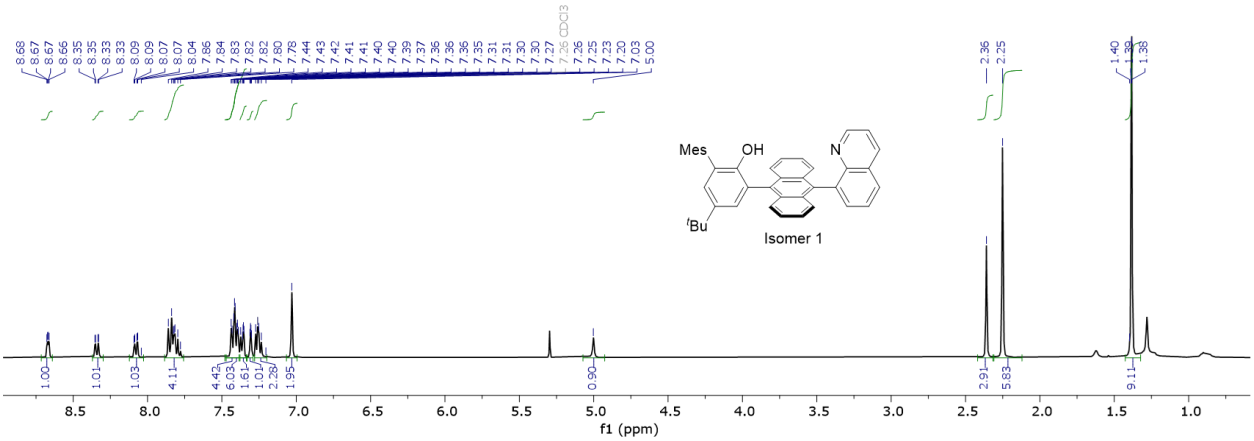

Figure B.7. ^{1}H NMR of **5-(tert-butyl)-2',4',6'-trimethyl-3-(10-(quinolin-8-yl)anthracen-9-yl)-[1,1'-biphenyl]-2-ol (Isomer 1)** in $CDCl_3$.

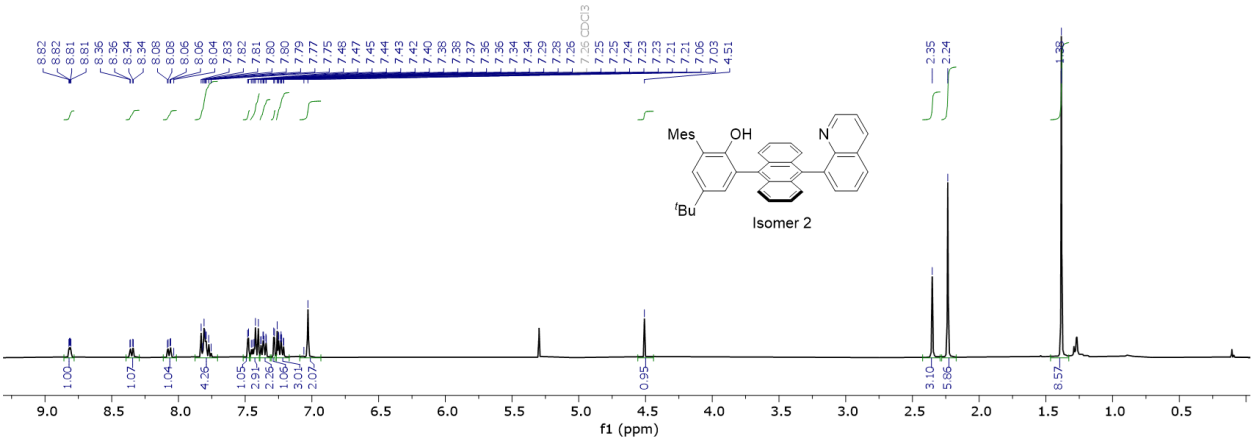

Figure B.8. ^{1}H NMR of **5-(tert-butyl)-2',4',6'-trimethyl-3-(10-(quinolin-8-yl)anthracen-9-yl)-[1,1'-biphenyl]-2-ol (Isomer 2)** in $CDCl_3$.

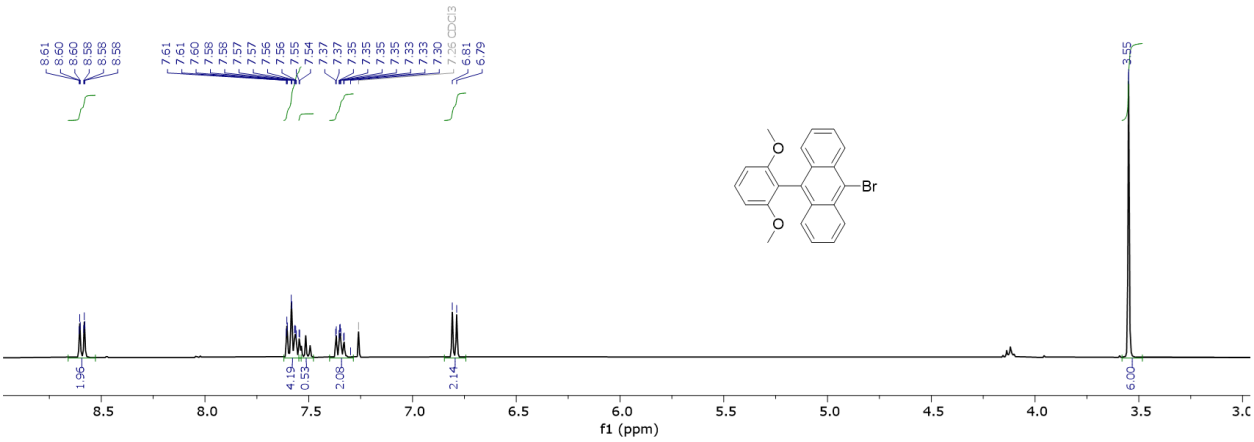

Figure B.9. ^{1}H NMR of **9-bromo-10-(2,6-dimethoxyphenyl)anthracene** in $CDCl_3$.

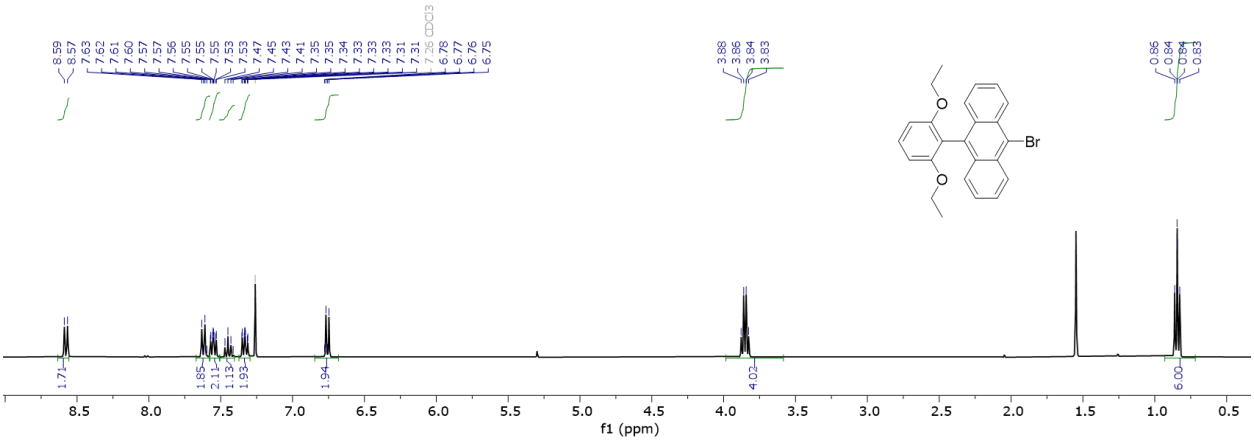

Figure B.10. ^{1}H NMR of **9-bromo-10-(2,6-diethoxyphenyl)anthracene** in $CDCl_3$.

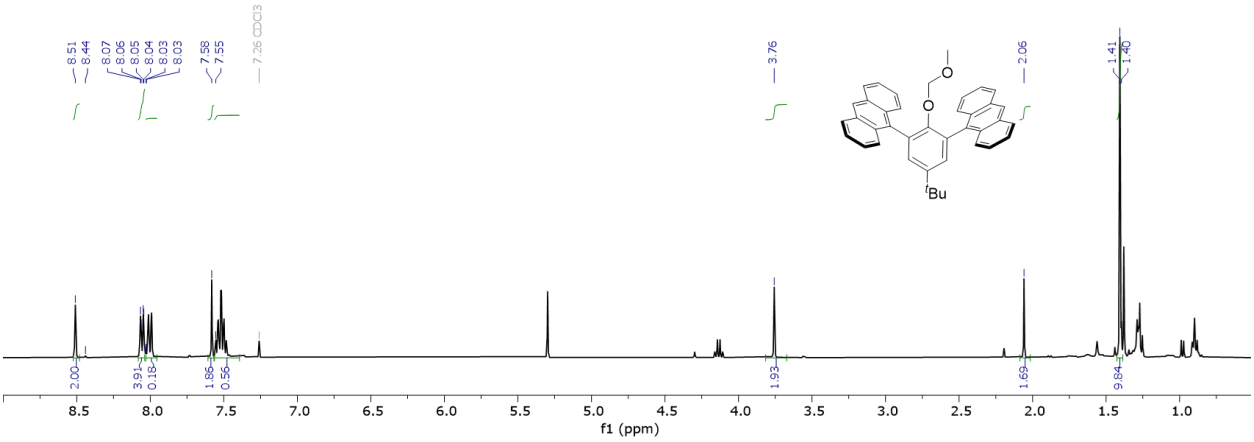

Figure B.11. ^{1}H NMR of **(s)-9,9'-(5-(*tert*-butyl)-2-(methoxymethoxy)-1,3-phenylene) dianthracene** in $CDCl_3$.

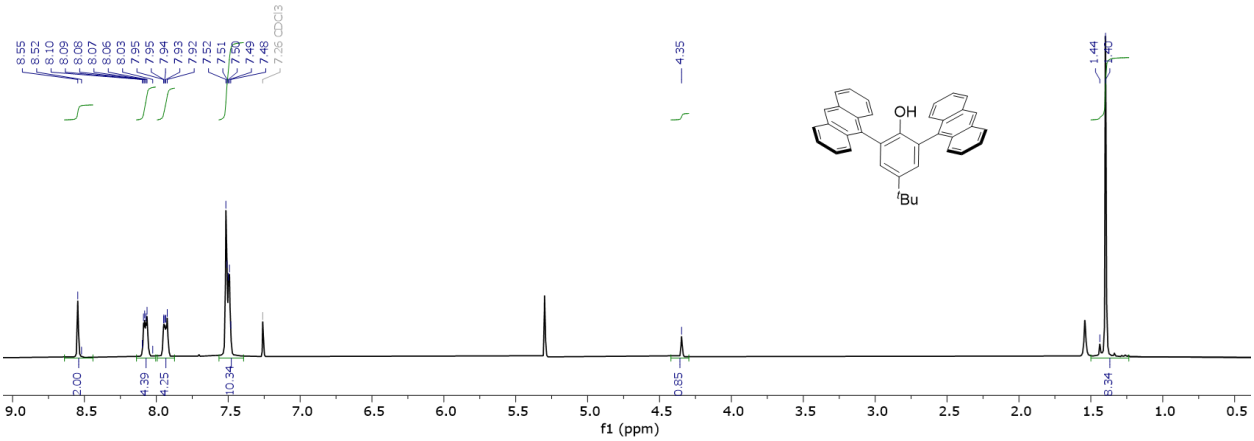

Figure B.12. ^{1}H NMR of **2,6-di(anthracen-9-yl)-4-(*tert*-butyl)phenol (4)** in $CDCl_3$.

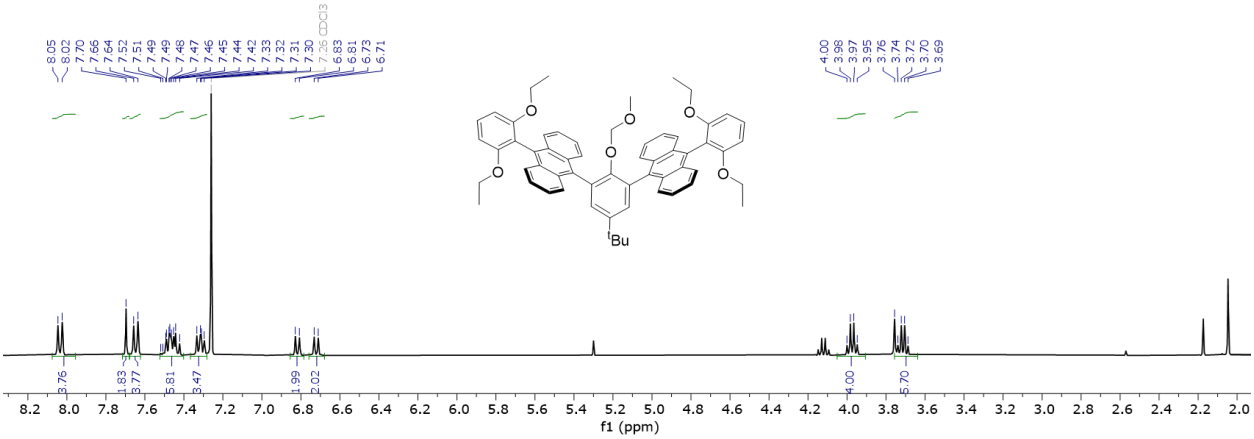

Figure B.13. ^{1}H NMR of **10,10'-(5-(tert-butyl)-2-(methoxymethoxy)-1,3-phenylene)bis(9-(2,6-diethoxyphenyl) anthracene)** in $CDCl_3$.

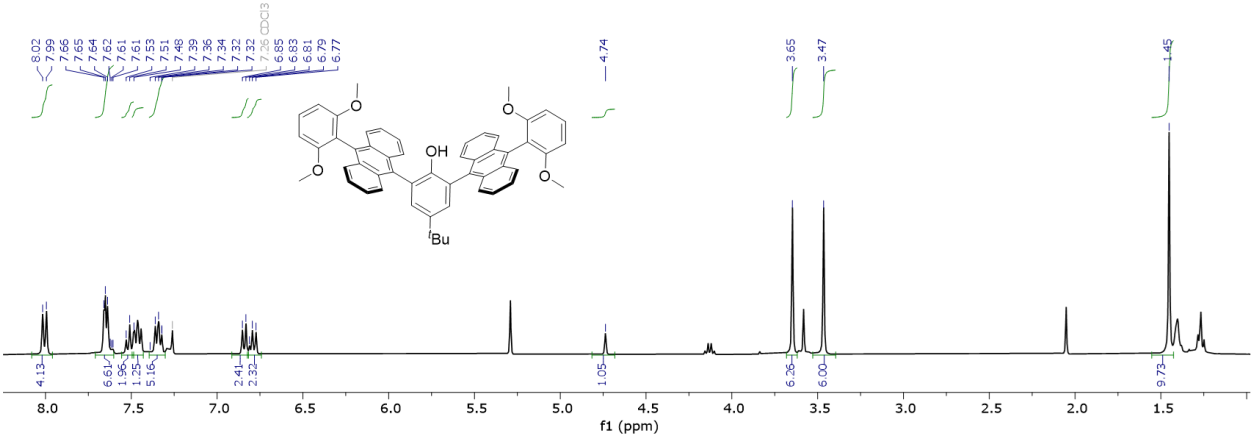

Figure B.14. ^{1}H NMR of **(S)-4-(tert-butyl)-2-((r)-10-(2,6-dimethoxyphenyl)anthracen-9-yl)-6-(10-(2,6-dimethoxyphenyl)anthracen-9-yl)phenol (5)** in $CDCl_3$.

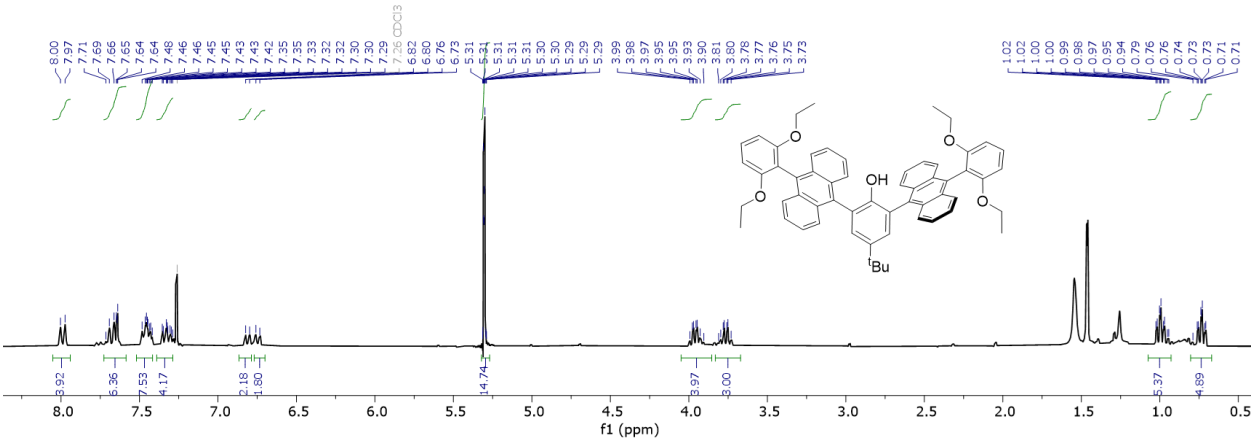

Figure B.15. ^{1}H NMR of **4-(tert-butyl)-2,6-bis(10-(2,6-diethoxyphenyl)anthracen-9-yl)phenol (6)** in $CDCl_3$.

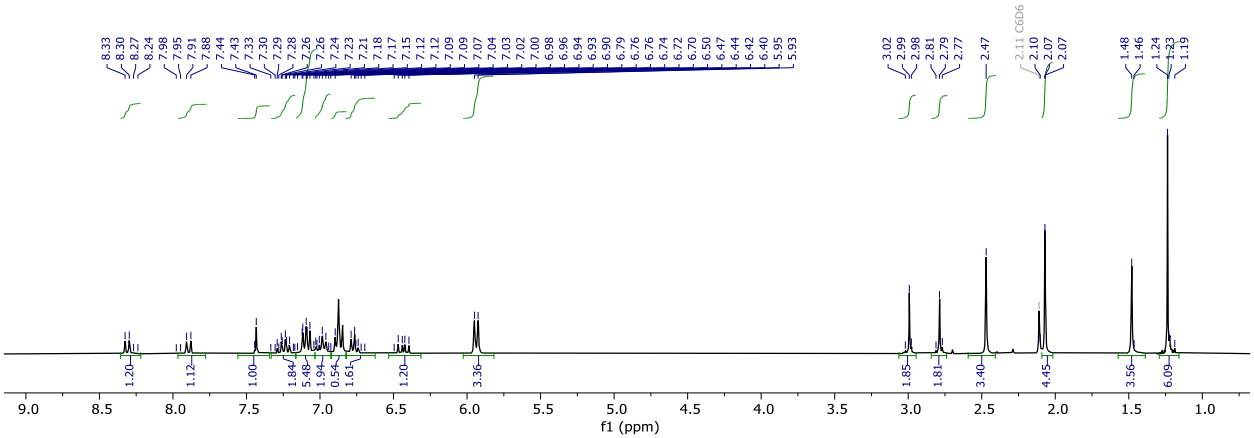

Figure B.16. ^{1}H NMR of **1-[Ti]** in C_6D_6.

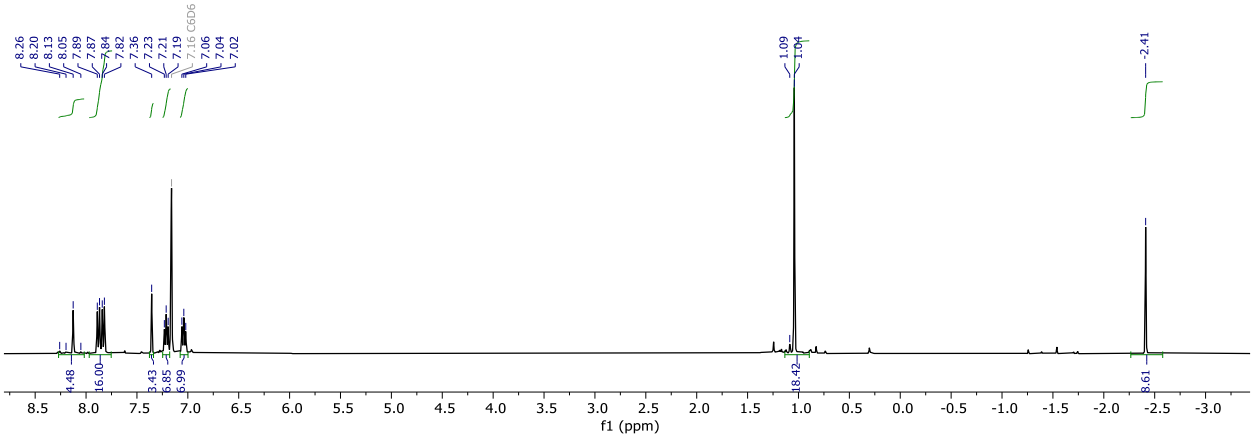

Figure B.17. ^{1}H NMR of **4-[Ta]** in C_6D_6.

REFERENCES

1. Low, C. H.; Rosenberg, J. N.; Lopez, M. A.; Agapie, T., Oxidative Coupling with Zr(IV) Supported by a Noninnocent Anthracene-Based Ligand: Application to the Catalytic Cotrimerization of Alkynes and Nitriles to Pyrimidines. *J. Am. Chem. Soc.* **2018,** *140* (38), 11906-11910. 10.1021/jacs.8b07418
2. McGuinness, D. S., Olefin Oligomerization via Metallacycles: Dimerization, Trimerization, Tetramerization, and Beyond. *Chem. Rev.* **2011,** *111* (3), 2321-2341. 10.1021/cr100217q
3. Agapie, T., Selective ethylene oligomerization: Recent advances in chromium catalysis and mechanistic investigations. *Coord. Chem. Rev.* **2011,** *255* (7), 861-880. 10.1016/j.ccr.2010.11.035
4. Sydora, O. L., Selective Ethylene Oligomerization. *Organometallics* **2019,** *38* (5), 997-1010. 10.1021/acs.organomet.8b00799
5. Hirscher, N. A.; Perez Sierra, D.; Agapie, T., Robust Chromium Precursors for Catalysis: Isolation and Structure of a Single-Component Ethylene Tetramerization Precatalyst. *J. Am. Chem. Soc.* **2019,** *141* (14), 6022-6029. 10.1021/jacs.9b01387
6. Boelter, S. D.; Davies, D. R.; Margl, P.; Milbrandt, K. A.; Mort, D.; Vanchura, B. A., II; Wilson, D. R.; Wiltzius, M.; Rosen, M. S.; Klosin, J., Phospholane-Based Ligands for Chromium-Catalyzed Ethylene Tri- and Tetramerization. *Organometallics* **2020,** *39* (7), 976-987. 10.1021/acs.organomet.9b00722
7. Deckers, P. J. W.; Hessen, B.; Teuben, J. H., Switching a Catalyst System from Ethene Polymerization to Ethene Trimerization with a Hemilabile Ancillary Ligand. *Angewandte Chemie International Edition* **2001,** *40* (13), 2516-2519. 10.1002/1521-3773(20010702)40:13<2516::Aid-anie2516>3.0.Co;2-v
8. Deckers, P. J. W.; Hessen, B.; Teuben, J. H., Catalytic Trimerization of Ethene with Highly Active Cyclopentadienyl−Arene Titanium Catalysts. *Organometallics* **2002,** *21* (23), 5122-5135. 10.1021/om020765a
9. Otten, E.; Batinas, A. A.; Meetsma, A.; Hessen, B., Versatile Coordination of Cyclopentadienyl-Arene Ligands and Its Role in Titanium-Catalyzed Ethylene Trimerization. *J. Am. Chem. Soc.* **2009,** *131* (14), 5298-5312. 10.1021/ja810089f
10. Huang, J.; Wu, T.; Qian, Y., Ethylene trimerization with a half-sandwich titanium complex bearing a pendant thienyl group. *Chem. Commun.* **2003,** (22), 2816-2817. 10.1039/B309749H
11. Wu, T.; Qian, Y.; Huang, J., Catalytic trimerization of ethylene by half-sandwich titanium complexes bearing a pendant ethereal group. *J. Mol. Catal. A: Chem.* **2004,** *214* (2), 227-229. 10.1016/j.molcata.2003.12.018
12. Suzuki, Y.; Kinoshita, S.; Shibahara, A.; Ishii, S.; Kawamura, K.; Inoue, Y.; Fujita, T., Trimerization of Ethylene to 1-Hexene with Titanium Complexes Bearing Phenoxy−Imine Ligands with Pendant Donors Combined with MAO. *Organometallics* **2010,** *29* (11), 2394-2396. 10.1021/om1003368
13. Chen, Y.; Credendino, R.; Callens, E.; Atiqullah, M.; Al-Harthi, M. A.; Cavallo, L.; Basset, J.-M., Understanding Tantalum-Catalyzed Ethylene Trimerization: When Things Go Wrong. *ACS Catalysis* **2013,** *3* (6), 1360-1364. 10.1021/cs400349p
14. Johnson, L. K.; Killian, C. M.; Brookhart, M., New Pd(II)- and Ni(II)-Based Catalysts for Polymerization of Ethylene and .alpha.-Olefins. *J. Am. Chem. Soc.* **1995,** *117* (23), 6414-6415. 10.1021/ja00128a054

15. Zhang, J.; Qiu, P.; Liu, Z.; Liu, B.; Batrice, R. J.; Botoshansky, M.; Eisen, M. S., Mechanistic Studies on the Switching from Ethylene Polymerization to Nonselective Oligomerization over the Triphenylsiloxy Chromium(II)/Methylaluminoxane Catalyst. *ACS Catalysis* **2015,** *5* (6), 3562-3574. 10.1021/acscatal.5b00240
16. Despagnet-Ayoub, E.; Takase, M. K.; Henling, L. M.; Labinger, J. A.; Bercaw, J. E., Mechanistic Insights on the Controlled Switch from Oligomerization to Polymerization of 1-Hexene Catalyzed by an NHC-Zirconium Complex. *Organometallics* **2015,** *34* (19), 4707-4716. 10.1021/acs.organomet.5b00472
17. Hamaed, A.; Hoang, T. K. A.; Trudeau, M.; Antonelli, D. M., Optimization of hydrogen storage capacity in silica-supported low valent Ti systems exploiting Kubas binding of hydrogen. *J. Organomet. Chem.* **2009,** *694* (17), 2793-2800. 10.1016/j.jorganchem.2009.02.034
18. Sattler, A.; Ruccolo, S.; Parkin, G., Structural characterization of $TaMe_3Cl_2$ and $Ta(PMe_3)_2Me_3Cl_2$, a pair of five and seven-coordinate d^0 tantalum methyl compounds. *Dalton Transactions* **2011,** *40* (30), 7777-7782. 10.1039/C1DT10806A

Appendix C: Magnesium Aryl Borohydrides as Electrolytes for Next-Generation Batteries

ABSTRACT:

Discussed herein is the targeted preparation of new electrolytes for next-generation Mg batteries. While $Mg(BH_4)_2$ and $Ca(BH_4)_2$ systems have demonstrated reversible deposition and stripping of Mg or Ca, respectively, these systems suffer from poor solubility, poor oxidative stability, and limited conductivity (in the absence of added salts). The report synthetic efforts towards the preparation of mixed aryl/hydride borates including $Mg(DME)_2[H_3BAr]_2$ and $Mg(DME)_3[HBAr_3]_2$.

GENERAL INTRODUCTION:

In Chapter 6, $Mg(DME)_3[^RSiF]_2$ anions were developed as electrolytes for next-generation Mg batteries. This appendix discusses other classes of electrolytes targeted.

For both Mg (and Ca-based) systems, $M^{2+}(BH_4)_2$ has been demonstrated to reversibly plate magnesium[1-4] or calcium,[2, 5-10] respectively, in solution-phase electrolytes. However, these systems are limited by (1) the limited solubility of the $[BH_4]^-$ anion, (2) poor solution conductivity, (3) limited oxidative stability (~1.7 V vs. Mg/Mg^{2+}), and (4) these systems have challenges with reproducibility arising from different levels of purity in commercially available $Mg(BH_4)_2$ and $Ca(BH_4)_2$.[10] Based on the previously reported electrochemistry, we hypothesized that by using mixed aryl/hydride borates, a more soluble, tunable electrolyte could be developed.

RESULTS AND DISCUSSION:

The preparation of several Mg compounds was investigated with mixed hydride/aryl borates. The attempted scheme for preparation of $Mg[H_3BAr]_2$ is shown in Figure C.1. It is well-established that reaction of a Grignard or ArLi with $BH_3{\cdot}SMe_2$ generally affords a mixture of $[BH_4]$, $[BH_3Ar]$, and $[BH_2Ar_2]$ due to the facile hydride and aryl exchange.[11-12] Similar to the previous reports, in the presence of most aryl groups, a mixture of Ar_xBH_{4-x} anions was obtained. Attempts were made to remove and purify the mixture (with limited success). Solid state characterization revealed formation of the desired $Mg(DME)_2[H_3BAr]_2$ compound (Figure C.1).

However, large-scale preparation and purification was not successful. Alternative preparation pathways were attempted, beginning with from $Li[H_3BAr]$, where formation of a single product

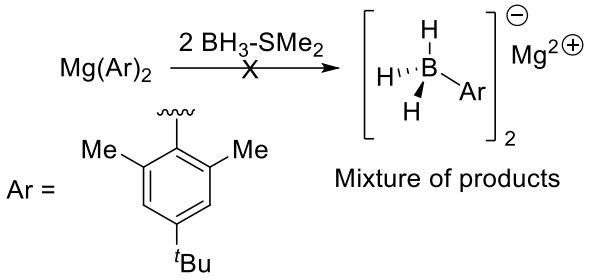

Scheme C.1. Attempted preparation of $Mg[H_3BAr]_2$ salts

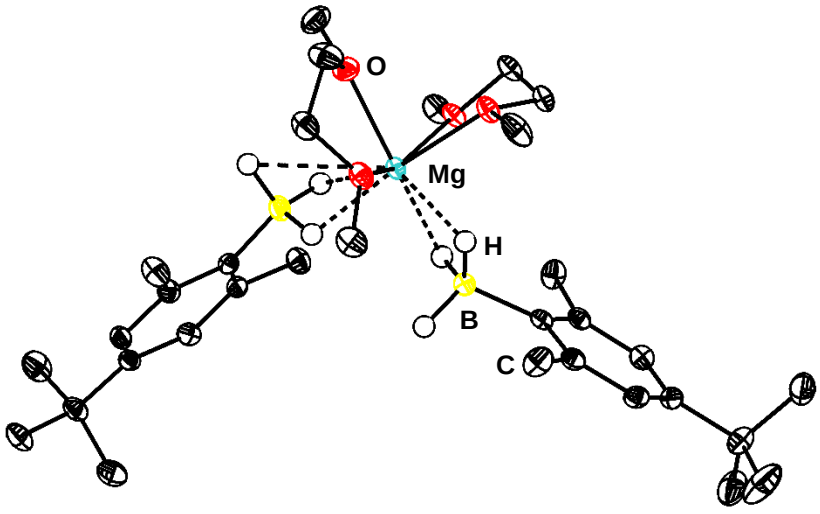

Figure C.1. Solid-state structure of $Mg(DME)_2[H_3BAr]_2$. Hydrogen atoms (except B-H) omitted for clarity.

avoids the distribution of hydride-containing species. However, subsequent transmetallation to Mg was continually plagued by incomplete removal of Li salts. Intermediate formation of K[H_3BAr] was hypothesized to ensure complete removal of any Li impurities. While enriched materials were accessed, complete removal of Li (and K) salts was not possible, even with repeated treatment. Similar to above, sufficiently clean material (required for meaningful electrochemical studies) was not able to be obtained.

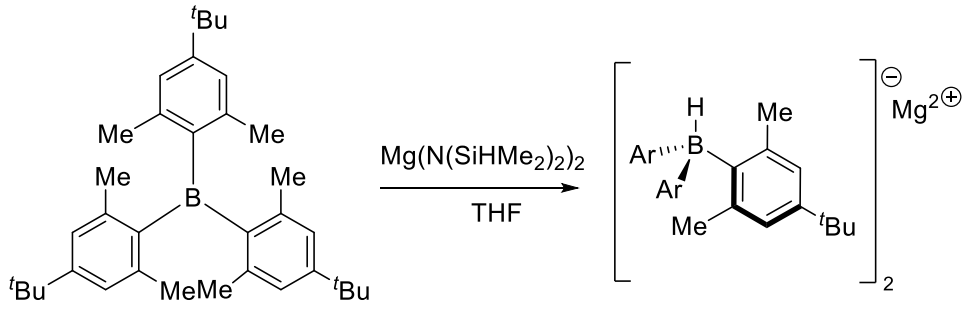

Scheme C.2. Preparation of Mg[$HBAr_3$]$_2$ salts

Alternative mixed aryl/hydride borates were targeted. Inspired by the previously reported preparation of Mg(THF)$_6$[$HBPh_3$]$_2$,[13] where the desired product is accessed by treatment of the BPh_3 with Mg(N(SiHMe_2)$_2$)$_2$ by BPh_3-mediated β-SiH abstraction. Gratifyingly, treatment of BAr_3 with an excess of Mg(TMDS)$_2$ in THF (Scheme C.2) resulted in formation of the desired Mg(THF)$_x$[$HBAr_3$]$_2$ complexes and recrystallization with dimethoxyethane (DME) generated the corresponding DME-solvated species (Mg(DME)$_3$[$HBAr_3$]$_2$). While not amenable to solid-state characterization, the ^{1}H and ^{11}B NMR spectra are consistent with formation of the desired species, with a diagnostic 1:1:1:1 quartet (at 3.69 ppm) corresponding to the B-*H* proton and a sharp singlet at 14.54 ppm corresponding to the Ar_3*B*H, respectively. Preliminary electrochemistry experiments conducted by others demonstrate reversible performance, but the data is not discussed further in this thesis.

CONCLUSIONS:

Towards the investigation of new next-generation Mg electrolytes, mixed hydride/aryl borates were targeted. While $Mg(DME)_2[H_3BAr]_2$ was characterized by crystallography, purification was severely hindered due to the similarity in solubility between the generated $[BH_4]$, $[BH_3Ar]$, and $[BH_2Ar_2]$ species. Alternative salt metathesis routes were also unsuccessful. $Mg(DME)_3[HBAr_3]_2$ was targeted by treatment of the corresponding neutral borane with $Mg(N(SiHMe_2)_2)_2$. While not amenable to solid-state characterization, ^1H and ^{11}B NMR are consistent with formation of the desired species $Mg(DME)_3[HBAr_3]_2$. Preliminary electrochemical experiments were conducted by others and are not discussed.

EXPERIMENTAL SECTION:

General Considerations - Unless otherwise specified, all operations were carried out in an MBraun drybox under a nitrogen atmosphere or using standard Schlenk line or high vacuum techniques. Solvents for air- and moisture-sensitive reactions were dried by the method of Grubbs[14] (THF, Et_2O, toluene, pentane, benzene). Solvents, once dried and degassed, were vacuum transferred directly and stored under inert atmosphere over 3 Å molecular sieves. C_6D_6, C_7D_8, CD_3CN, CD_2Cl_2 were purchased from Cambridge Isotope Laboratories and vacuum transferred from CaH_2 (CD_3CN) after three freeze-pump-thaw cycles. $Mg(TMDS)_2$,[15] 2-bromo-5-(tert-butyl)-1,3-dimethylbenzene[16] were prepared by previously reported procedures.

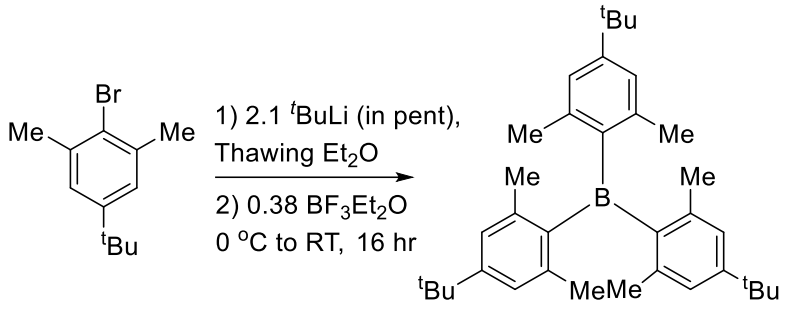

Preparation of BAr_3 (Ar = 2,6-dimethyl,4-*tert*(butyl)benzene): 1-Bromo-2,6-dimethyl-4-*tert*(butyl)benzene (5 g, 20.82 mmol, 1.0 equiv) was dissolved in Et_2O (50 mL) and frozen. ^{t}BuLi (2.8 g, 43.74 mmol, 2.1 equiv) was dissolved in pentane (10 mL) and added dropwise to the thawing solution. The reaction was allowed to warm to RT and stir for 30 min. The reaction was re-cooled to 0 ºC followed by addition of $BF_3{\cdot}Et_2O$ (0.99 mL, 7.98 mmol, 0.383 equiv). The reaction was warmed to RT and stirred for 16 hr. The reaction was quenched by exposure to air. The volatiles were concentrated *in vauco* and the product was purified by column chromatography. The product BAr_3 (Ar = 2,6-dimethyl,4-*tert*(butyl)benzene) was isolated as a white solid. 2.3 g (60%) ^{1}H ($CDCl_3$, 400 MHz): 6.88 (s, 6 H, Ar-H), 2.01 (s, 18 H, Ar-C*H*$_3$), 1.28 (s, 27 H, -C(C*H*$_3$)$_3$). ^{11}B ($CDCl_3$, 128 MHz): 77.72 (vr. br. s)

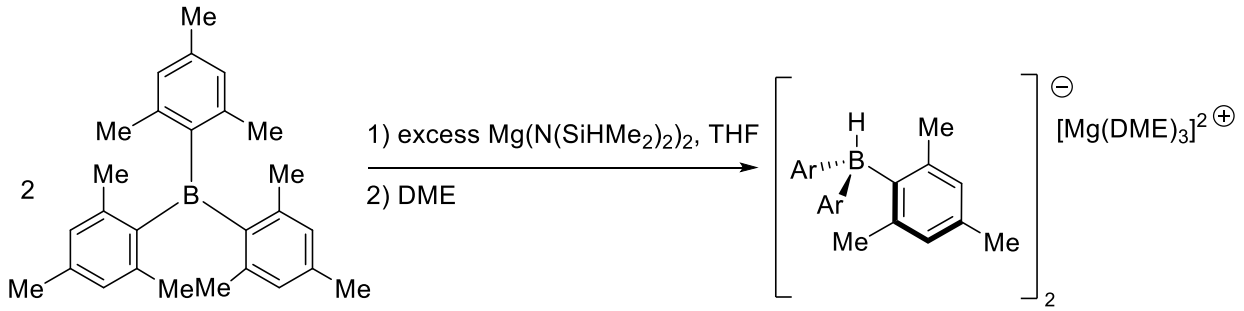

Preparation of $Mg(DME)_3[HB(Mes)_3]_2$: A vial charged with a Teflon-coated stir bar and $BMes_3$ (500 mg, 1.36 mmol, 1 equiv) in THF (10 mL) in a glove box. A solution of $Mg(N(SiHMe_2)_2)_2$ (1.17 g, 4.07 mmol, 3 equiv) in THF was added dropwise, and the reaction was stirred at RT for 16 hr, with precipitation of a white solid. The reaction was filtered, and the white solid was washed extensively with THF. The product was extracted into DME, and the volitates were concentrated *in vacuo*. The product was recrystallized by DME/HMDSO vapor diffusion. The product was isolated as a white solid. ^1H (CD_3CN, 400 MHz): 6.44 (br. app. d, 12 H, Ar-*H*), 3.69 (1:1:1:1, 2 H, B-*H*), 3.47 (s, 12 H, $CH_3OC\mathit{H}_2C\mathit{H}_2OCH_3$), 3.30 (s, 18 H, $C\mathit{H}_3OCH_2CH_2OC\mathit{H}_3$), 2.13 (s, 18 H, Mes-*H*) 1.96 (br. app. s, 18 H, Mes-*H*), 1.69 (br. app. s, 18 H, Mes-*H*). ^{11}B (CD_3CN, 128 MHz): 14.54 (s)

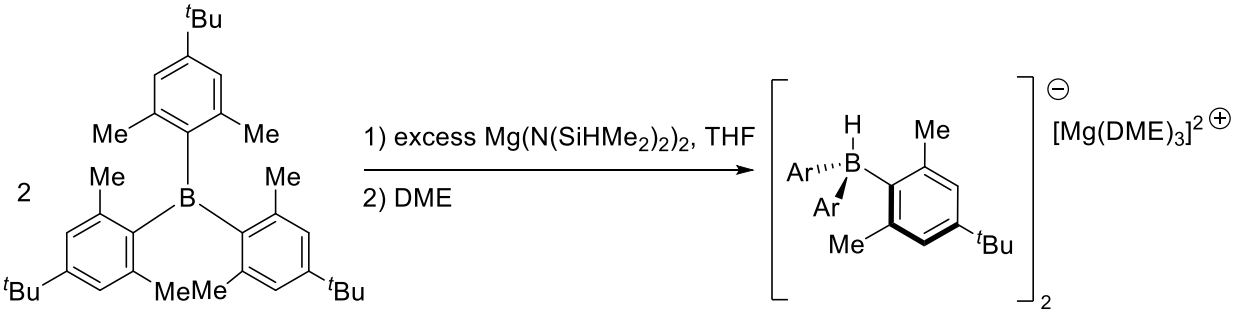

Preparation of $Mg(DME)_3[HB(Ar)_3]_2$ (Ar = 2,6-dimethyl,4-*tert*(butyl)benzene): A vial charged with a Teflon-coated stir bar and BAr_3 (1.37 mg, 2.8 mmol, 1 equiv) in THF (10 mL) in a glove box. A solution of $MgN(SiHMe_2)_2)_2$ (2.40 g, 8.3 mmol, 3 equiv) in THF was added dropwise, and the reaction was stirred at RT for 16 hr, with precipitation of a white solid. The reaction was

filtered, and the white solid was washed extensively with THF. The product was extracted into DME, and the volatiles were concentrated *in vacuo*. The product was isolated as a white solid. ^{1}H (CD_3CN, 400 MHz): 6.65 (br. app. s, 12 H, Ar-*H*), 3.65 (1:1:1:1, 2 H, B-*H*), 3.50 (s, 12 H, $CH_3OCH_2CH_2OCH_3$), 3.32 (s, 18 H, $CH_3OCH_2CH_2OCH_3$), 1.93 (br. app. s, 18 H, Mes-*H*), 1.81 (br. app. s, 18 H, Mes-*H*), 1.24 (s, 54 H, $C(CH_3)_3$. ^{11}B (CD_3CN, 128 MHz): 14.62 (s).

REFERENCES:

1. Mohtadi, R.; Matsui, M.; Arthur, T. S.; Hwang, S.-J., Magnesium Borohydride: From Hydrogen Storage to Magnesium Battery. *Angew. Chem. Int. Ed.* **2012,** *51* (39), 9780-9783. 10.1002/anie.201204913
2. Hahn, N. T.; Self, J.; Seguin, T. J.; Driscoll, D. M.; Rodriguez, M. A.; Balasubramanian, M.; Persson, K. A.; Zavadil, K. R., The critical role of configurational flexibility in facilitating reversible reactive metal deposition from borohydride solutions. *Journal of Materials Chemistry A* **2020,** *8* (15), 7235-7244. 10.1039/D0TA02502J
3. Palisoc, S.; Joe Santos, D.; Natividad, M., Borohydride-based electrolyte system for Magnesium-Persulfate ($Mg||MgS_2O_8$) rechargeable battery. *Ain Shams Engineering Journal* **2021,** *12* (3), 3021-3030. 10.1016/j.asej.2020.09.032
4. Shao, Y.; Liu, T.; Li, G.; Gu, M.; Nie, Z.; Engelhard, M.; Xiao, J.; Lv, D.; Wang, C.; Zhang, J.-G.; Liu, J., Coordination Chemistry in magnesium battery electrolytes: how ligands affect their performance. *Scientific Reports* **2013,** *3* (1), 3130. 10.1038/srep03130
5. Melemed, A. M.; Skiba, D. A.; Steinberg, K. J.; Kim, K.-H.; Gallant, B. M., Impact of Differential Ca^{2+} Coordination in Borohydride-Based Electrolyte Blends on Calcium Electrochemistry and SEI Formation. *The Journal of Physical Chemistry C* **2023,** *127* (40), 19886-19899. 10.1021/acs.jpcc.3c03800
6. Melemed, A. M.; Skiba, D. A.; Gallant, B. M., Toggling Calcium Plating Activity and Reversibility through Modulation of Ca^{2+} Speciation in Borohydride-Based Electrolytes. *The Journal of Physical Chemistry C* **2022,** *126* (2), 892-902. 10.1021/acs.jpcc.1c09400
7. Wang, D.; Gao, X.; Chen, Y.; Jin, L.; Kuss, C.; Bruce, P. G., Plating and stripping calcium in an organic electrolyte. *Nature Materials* **2018,** *17* (1), 16-20. 10.1038/nmat5036
8. Jie, Y.; Tan, Y.; Li, L.; Han, Y.; Xu, S.; Zhao, Z.; Cao, R.; Ren, X.; Huang, F.; Lei, Z.; Tao, G.; Zhang, G.; Jiao, S., Electrolyte Solvation Manipulation Enables Unprecedented Room-Temperature Calcium-Metal Batteries. *Angew. Chem. Int. Ed.* **2020,** *59* (31), 12689-12693. 10.1002/anie.202002274
9. Ta, K.; Zhang, R.; Shin, M.; Rooney, R. T.; Neumann, E. K.; Gewirth, A. A., Understanding Ca Electrodeposition and Speciation Processes in Nonaqueous Electrolytes for Next-Generation Ca-Ion Batteries. *ACS Applied Materials & Interfaces* **2019,** *11* (24), 21536-21542. 10.1021/acsami.9b04926
10. McClary, S. A.; Long, D. M.; Sanz-Matias, A.; Kotula, P. G.; Prendergast, D.; Jungjohann, K. L.; Zavadil, K. R., A Heterogeneous Oxide Enables Reversible Calcium Electrodeposition for a Calcium Battery. *ACS Energy Letters* **2022,** *7* (8), 2792-2800. 10.1021/acsenergylett.2c01443
11. Samigullin, K.; Bolte, M.; Lerner, H.-W.; Wagner, M., Facile Synthesis of $(3,5\text{-}(CF_3)_2C_6H_3)2BX$ (X = H, OMe, F, Cl, Br): Reagents for the Introduction of a Strong Boryl Acceptor Unit. *Organometallics* **2014,** *33* (13), 3564-3569. 10.1021/om500476d
12. Wang, L.; Samigullin, K.; Wagner, M.; McQuilken, A. C.; Warren, T. H.; Daniliuc, C. G.; Kehr, G.; Erker, G., An Ethylene-Bridged Phosphane/Borane Frustrated Lewis Pair Featuring the -$B(Fxyl)_2$ Lewis Acid Component. *Chemistry – A European Journal* **2016,** *22* (31), 11015-11021. 10.1002/chem.201601583
13. Mukherjee, D.; Shirase, S.; Spaniol, T. P.; Mashima, K.; Okuda, J., Magnesium hydridotriphenylborate $[Mg(thf)_6][HBPh_3]_2$: a versatile hydroboration catalyst. *Chem. Commun.* **2016,** *52* (89), 13155-13158. 10.1039/C6CC06805G

14. Pangborn, A. B.; Giardello, M. A.; Grubbs, R. H.; Rosen, R. K.; Timmers, F. J., Safe and Convenient Procedure for Solvent Purification. *Organometallics* **1996,** *15* (5), 1518-1520. 10.1021/om9503712
15. Song, S.; Ma, H.; Yang, Y., Magnesium complexes supported by salan-like ligands: Synthesis, characterization and their application in the ring-opening polymerization of rac-lactide. *Dalton Transactions* **2013,** *42* (39), 14200-14211. 10.1039/C3DT51344K
16. Yan, C.; Shang, R.; Nakamoto, M.; Yamamoto, Y.; Adachi, Y., The Substituent Effect of Bridged Triarylamine Helicenes on Light-emitting and Charge Transfer Properties. *Chem. Lett.* **2020,** *49* (5), 457-460. 10.1246/cl.200089

Appendix IV: Additional Crystal Structures

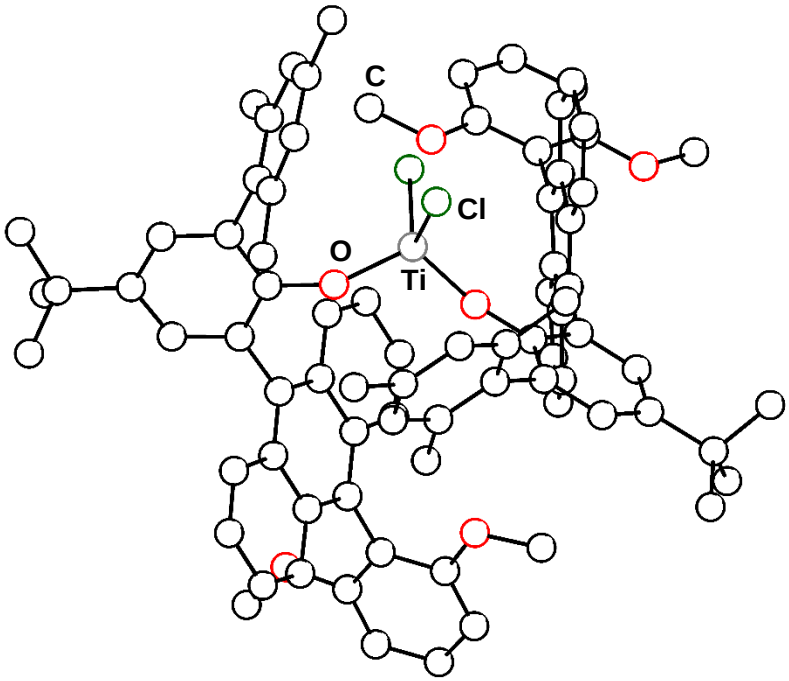

Figure D.1. Crystal from reaction $TiCl_2(OOMeAnth)_2$

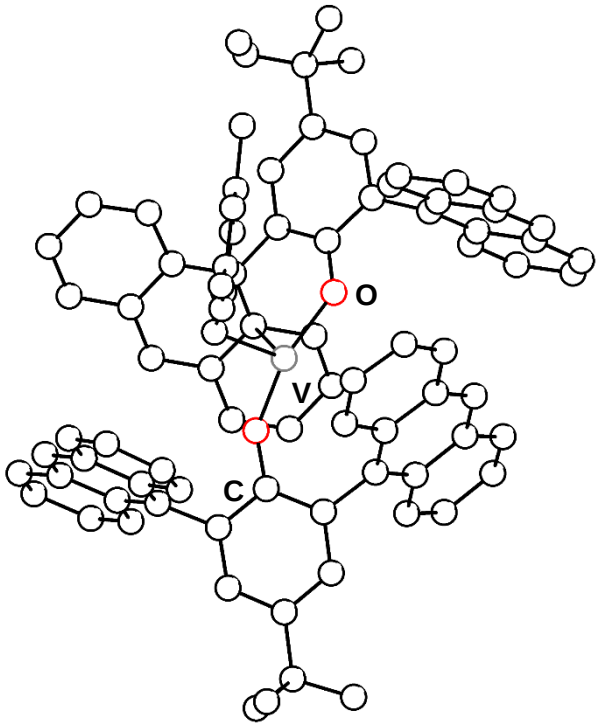

Figure D.2. Crystal from reaction $V(Mes)(OAnth_2)_2$

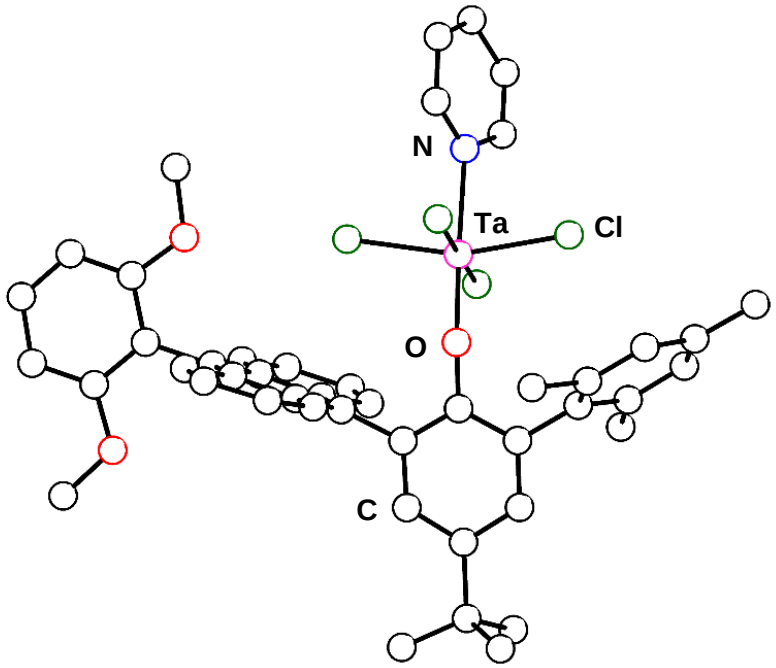

Figure D.3. Crystal from reaction $TaCl_4Py(OOMeAnth)$

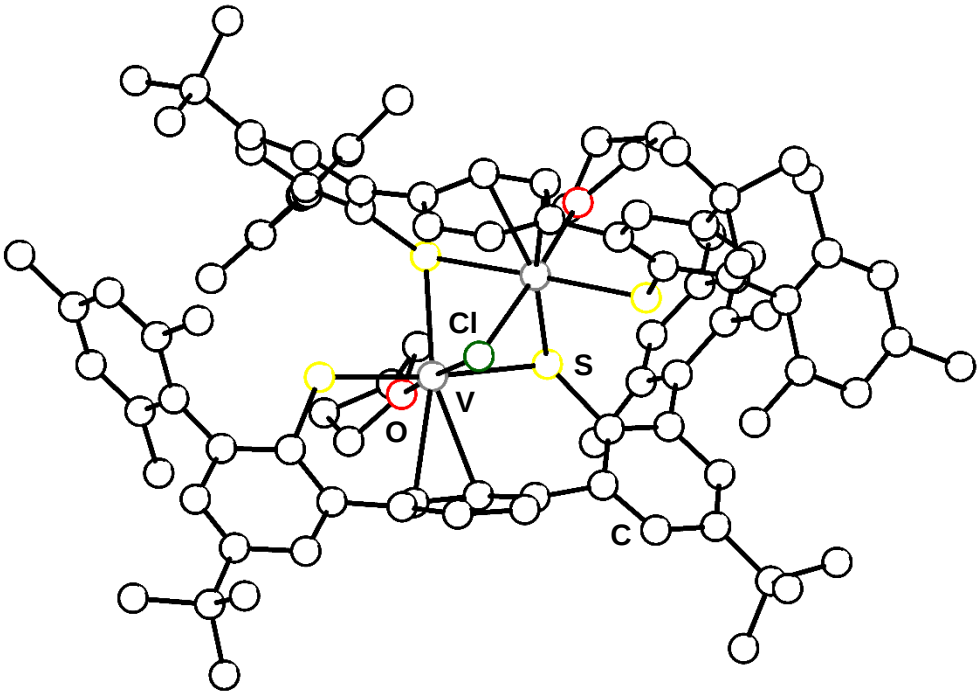

Figure D.4. Crystal from reaction $[V(S_2Benz)THF]_2Cl$

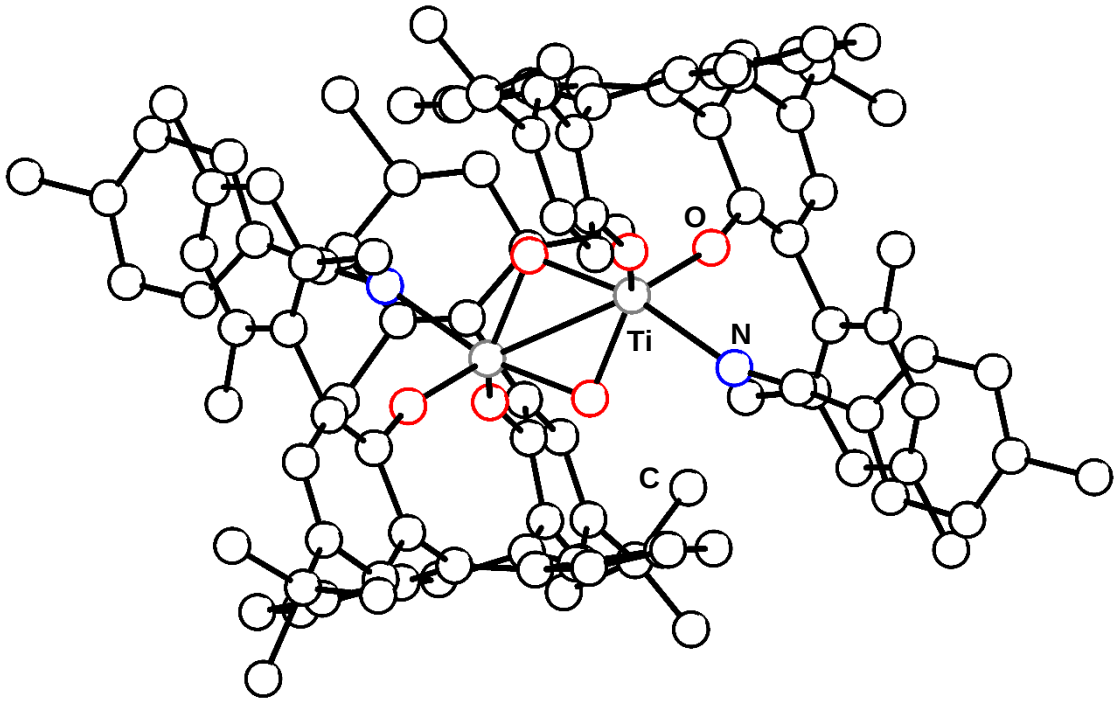

Figure D.5. Crystal from reaction $[Ti(O_2Anth)(TolCN)O]_2$

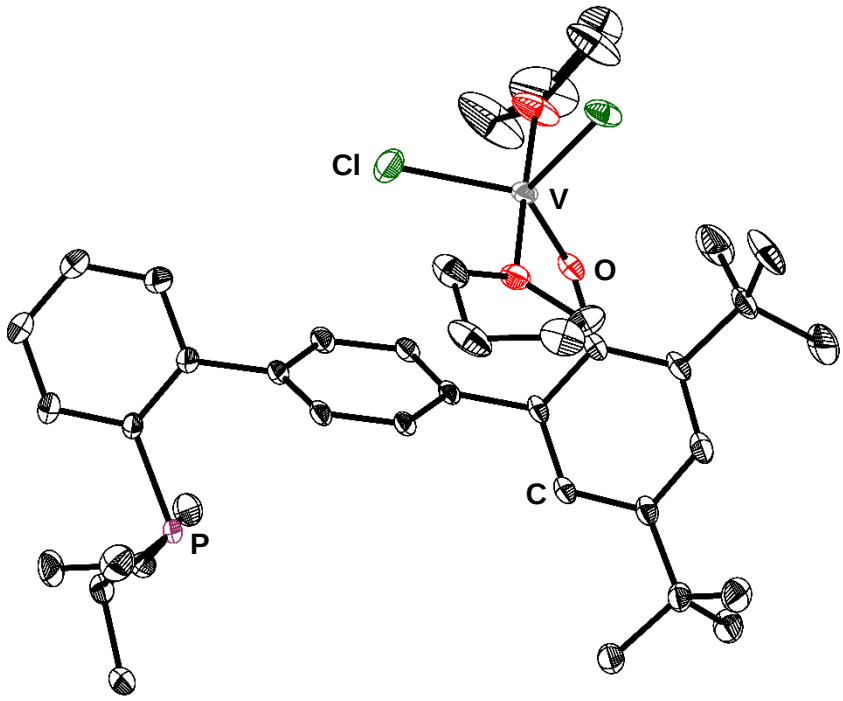

Figure D.6. Crystal from reaction $VCl_2(O^iPr_2PBenz)(THF)_2$

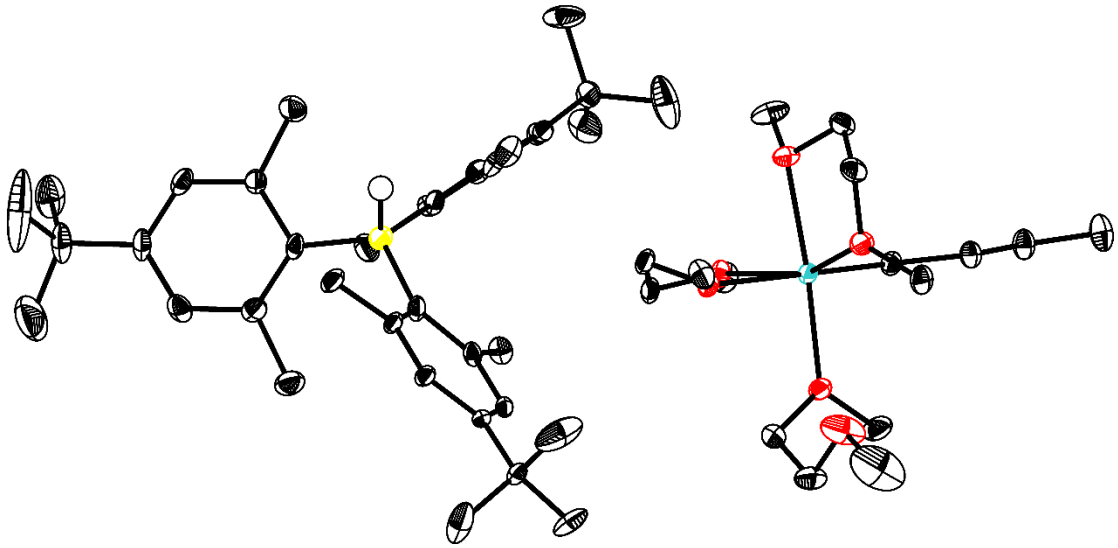

Figure D.7. Crystal from reaction $(Mg(DME)_3{}^nBu)[HBAr_3]$

ABOUT THE AUTHOR

Meaghan Bruening was born in Marshfield, WI on November 29th, 1994. She and her older brother (Robert) grew up in Mosinee, WI and she graduated from high school in 2013. She completed her undergraduate studies at Saint Catherine University in St. Paul, MN. As an undergraduate, she worked in the labs of Prof. Daron Janzen (St. Kate's), Prof. Mark Distefano (University of Minnesota), and Prof. Richard Van Duyne (Northwestern), before graduating from St. Kate's in 2017 with a B.S. in Chemistry. She completed her PhD at the California Institute of Technology in the lab of Prof. Theodor Agapie. When not in lab, she is often found cross-stitching, eating ice cream, and teaching her cats to talk with buttons.

That old familiar body ache

The snaps from the same little breaks in my soul

I know…

When it's time to go

-Taylor Swift

Evermore

"it's time to go"